Peter Pivonka *Editor*

# Multiscale Mechanobiology of Bone Remodeling and Adaptation

Springer

# CISM International Centre for Mechanical Sciences

Courses and Lectures

Volume 578

The series presents lecture notes, monographs, edited works and proceedings in the field of Mechanics, Engineering, Computer Science and Applied Mathematics. Purpose of the series is to make known in the international scientific and technical community results obtained in some of the activities organized by CISM, the International Centre for Mechanical Sciences.

Peter Pivonka

Editor

# Multiscale Mechanobiology of Bone Remodeling and Adaptation

Springer

*Editor*
Peter Pivonka
School of Chemistry, Physics and
    Mechanical Engineering
Queensland University of Technology
Brisbane, QLD
Australia

*To my Mother and Father who have provided
a lifetime of encouragement and support and
to my wife Carolina in appreciation of her
love, spirit and compassion, and who
continuously inspires my work and life.*

# Preface

Osteoporosis (OP) is a major health problem in society. OP is characterised by low bone mass and deterioration of bone strength, resulting in fragile bones which are more prone to fracture. Osteoporosis is often called the "silent disease" because bone loss occurs without symptoms. New drugs are continually being developed and trialled in animals, and the most promising ones tested on humans. However, many bone diseases including OP do not have a proven means of prevention or effective treatment.

On the one hand, precision medicine is an emerging field for disease treatment and prevention that takes into account the variability in genes, environment, and lifestyle factors for each individual. Any comprehensive approach for understanding bone disease progression and effective drug interventions requires integration of experimental findings and computational modelling. Particularly, over the last few decades, a large number of regulatory factors in bone homeostasis and pathology have been identified together with interactions of bone tissue with other tissues such as muscles, blood vessels, and the nervous system which all have been shown to regulate bone responses. Furthermore, links between bone quality and environmental factors such as nutrition and mechanical loading have been established.

On the other hand, material engineering has made significant progress in characterising and modelling of biomaterials such as bone with high accuracy at various scales of observation. In particular, micromechanical approaches have proven to be very powerful in integrating different experimental information from different scales. A long-standing missing link between the mechanical aspects of bone and the biochemical and mechanobiological regulations has recently been established by developing cell-based models of bone remodeling and adaptation. These models allow to integrate subject-specific data and can be used to predict changes in bone mass and the respective mechanical properties. The ultimate goal of any of these models is to predict the fracture risk of a patient in order to start an intervention of either drug or physiological exercise in a timely manner.

The present book is a summary of the course notes of the 20th CISM-IUTAM International Summer School on *Multiscale Mechanobiology of Bone Remodeling*

*and Adaptation*. This course gathered experts from the fields of applied mechanics and biomedical engineering, complex systems modelling, bone biology, mechanobiology, and materials science, in order to give, in an unprecedented interdisciplinary fashion, the cutting-edge view on bone mechanobiology with emphasis on disease progression analysis in osteoporosis and assessment of changes in material properties. These include disease systems analysis of osteoporosis (P. Pivonka) in order to predict disease progression and drug interventions; musculoskeletal modelling (J. Fernandez) in order to accurately estimate muscle forces acting on bone; bone biology (D. Findlay) including interactions of bone tissue with other tissues such as muscle, cartilage, vascularisation, and central nervous system (CNS); bone mechanobiology (T. Skerry) including Frost's mechanostat theory, animal models of bone mechanical loading, and osteocytes and their role as mechanosensing cells; multiscale bone adaptation algorithms (T. Adachi); and bone quality assessment at different scales using experimental and computational approaches (Ch. Hellmich), including fundamentals of continuum micromechanics with application to bone and merging quantitative computed tomography (qCT) with micromechanics as a new clinical tool.

The individual chapters of this book were prepared by the respective lecturers and their collaborators with the exception of Prof. Tim Skerry who was not able to contribute due to many other commitments at that time. Fortunately, Prof. Mark Forwood with the assistance of myself was able to summarise the content of the *Bone Mechanobiology* chapter.

It is a pleasure to thank the six lecturers and the 25 attendees who came from 12 different countries and actively participated in the numerous discussions throughout the course. I would like to also extend my thanks and appreciation to the administrative staff of CISM for their help. Last but not least, support by the International Union for Theoretical and Applied Mechanics (IUTAM) is also gratefully acknowledged.

Brisbane, Australia                                                                           Peter Pivonka
March 2017

# Contents

# Contributors

**Taiji Adachi** Department of Biosystems Science, Institute for Frontier Life and Medical Sciences, Kyoto University, Kyoto, Japan

**Thor Besier** Auckland Bioengineering Institute, University of Auckland, Auckland, New Zealand; Department of Engineering Science, University of Auckland, Auckland, New Zealand

**Justin Fernandez** Auckland Bioengineering Institute, University of Auckland, Auckland, New Zealand; Department of Engineering Science, University of Auckland, Auckland, New Zealand

**David M. Findlay** Discipline of Orthopaedics and Trauma, University of Adelaide, Adelaide, SA, Australia

**Mark R. Forwood** School of Medical Science and Menzies Health Institute Queensland, Griffith University, Gold Coast, QLD, Australia

**Christian Hellmich** Institute for Mechanics of Materials and Structures, TU Wien – Vienna University of Technology, Vienna, Austria

**Peter Hunter** Auckland Bioengineering Institute, University of Auckland, Auckland, New Zealand

**Yoshitaka Kameo** Department of Biosystems Science, Institute for Frontier Life and Medical Sciences, Kyoto University, Kyoto, Japan

**David G. Lloyd** Menzies Health Institute Queensland, Griffith University, Gold Coast, QLD, Australia

**Claire Morin** Ecole Nationale Supérieure des Mines de Saint Etienne, CIS-EMSE-INSERM U1059, SAINBIOSE, Saint-Etienne, France

**Jacob T. Munro** School of Medicine, University of Auckland, Auckland, New Zealand; Auckland City Hospital, University of Auckland, Auckland, New Zealand

**David P. Nickerson**  Auckland Bioengineering Institute, University of Auckland, Auckland, New Zealand

**Aaron Park**  School of Medical Science and Menzies Health Institute Queensland, Griffith University, Gold Coast, QLD, Australia

**Peter Pivonka**  St Vincent's Department of Surgery, The University of Melbourne, Melbourne, VIC, Australia; Australian Institute of Musculoskeletal Science, Melbourne, VIC, Australia; School of Chemistry, Physics and Mechanical Engineering, Queensland University of Technology, Brisbane, QLD, Australia

**Massimo Sartori**  Department of Neurorehabilitation Engineering, Göttingen University, Gottingen, Germany

**Stefan Scheiner**  Institute for Mechanics of Materials and Structures, TU Wien – Vienna University of Technology, Vienna, Austria

**Vickie Shim**  Auckland Bioengineering Institute, University of Auckland, Auckland, New Zealand

**Silvia Trichilo**  St Vincent's Department of Surgery, The University of Melbourne, Melbourne, VIC, Australia; Australian Institute of Musculoskeletal Science, Melbourne, VIC, Australia

**Viktoria Vass**  Institute for Mechanics of Materials and Structures, TU Wien – Vienna University of Technology, Vienna, Austria

**Ju Zhang**  Auckland Bioengineering Institute, University of Auckland, Auckland, New Zealand

# Functional Adaptation of Bone: The Mechanostat and Beyond

**Peter Pivonka, Aaron Park and Mark R. Forwood**

**Abstract** The conceptual model of the mechanostat proposed by Harold Frost in 1983 is among the most significant contributions to musculoskeletal research today. This model states that bone and other musculoskeletal tissues including cartilage, tendon and muscle respond to habitual exercise/loading and that changes in the loading environment lead to adequate structural adaptation of (bone) tissue architecture. The analogy with a thermostat clearly indicates presence of a physiological feedback system which is able to adjust bone mass and structure according to the engendered loads. In the bioengineering community, the mechanostat has been mathematically formulated as a feedback algorithm using a set point criterion based on a particular mechanical quantity such as strain, strain energy density among others. As pointed out by Lanyon and Skerry, while it is widely thought that in a single individual, there exists a single mechanostat set point, this view is flawed by the fact that different bones throughout the skeleton require a specific strain magnitude to maintain bone mass. Consequently, different bones respond differently to increases or decreases in loading depending on the sensitivity of the mechanostat. Osteocytes, i.e., cells embedded in the bone matrix are believed to be the major bone cells involved in sensing and transduction of mechanical loads. The purpose of this chapter is to review the concept of the mechanostat and its role in bone pathophysiology. To do this we provide examples of why and how the skeleton responds to complex loading stimuli made up of numerous different parameters including strain magnitude,

P. Pivonka
St Vincent's Department of Surgery, University of Melbourne, Melbourne, VIC, Australia
e-mail: peter.pivonka@qut.edu.au

P. Pivonka
School of Chemistry, Physics and Mechanical Engineering,
Queensland University of Technology, Brisbane, QLD, Australia

A. Park · M.R. Forwood (✉)
School of Medical Science and Menzies Health Institute Queensland,
Griffith University, Gold Coast, QLD, Australia
e-mail: m.forwood@griffith.edu.au

A. Park
e-mail: aaron.park2@griffithuni.edu.au

frequency and rest intervals among others. We describe latest in vivo and ex vivo loading models, which allow exploration of various mechanobiological relations in the mechanostat model utilising controlled mechanical environments. A review of the bone cells and signalling transduction cascades involved in mechanosensation and bone adaptation will also be provided. Furthermore, we will discuss the mechanostat in a clinical context, e.g., how factors such as sex, age, genetic constitution, concomitant disease, nutrient availability, and exposure to drugs all affect bone's response to mechanical loading. Understanding the mechanostat and mechanobiological regulatory factors involved in mechanosensation and desensitisation is essential for our ability to control bone mass based on physiological loading, either directly through different exercise regimens, or by manipulating bone cells in a targeted manner using tailored site and individual specific stimuli including pharmaceuticals.

**Keywords** Bone adaptation · Wolff's law · Mechanostat · Physiological exercise · Dynamic loading · Disuse-related resorption · Mechanotransduction · Mechanobiology · Osteocytes

## 1 Introduction

Let's start with the famous quote by Huiskes [115]: "If bone is the answer then what is the question?". Finding answers to the structural – functional relationship in bone has occupied scientists from many different disciplines over the last centuries. Indeed, as stated by Carter and Beaupre [35]: "The close relationship between form and function inherent in the design of animals is perhaps nowhere more evident than in the musculoskeletal system. In the bones, cartilage, tendons, ligaments and muscles of all vertebrates there is a graceful and efficient physical order."

This chapter is about how function determines form. In particular, it addresses the role of mechanical factors in the adaptation, maintenance, and aging of bone tissue. This process is now commonly referred to as mechanobiology of bone. We first provide a historical overview of the events that led to the development of Wolff's law and Frost's mechanostat concept. Based on a comprehensive review of the literature we summarise major findings related to physical loading patterns leading to anabolic bone responses. Furthermore, we review important steps in the signal mechanotransduction cascade leading to anabolic and catabolic responses together with describing the signalling molecules involved in mechanosensation. Finally, we review recent developments of in silico models of bone adaptation which aim to formulate algorithms which capture essential features of experimental findings.

To achieve and maintain adequate bone mass functional loading of the skeleton is essential. Both bone modelling and remodelling are locally regulated by physiological levels of loading, i.e., via site-specific activation of osteoblastic and osteoclastic cells [188]. This highly regulated, mechanically mediated, targeted bone turnover allows for adaptive changes and repair of damage in bone structure. Reductions in functional loading as a result of a less active lifestyle might manifest through metabolic (for example, obesity and/or diabetes), disease-induced (chronic bedrest),

injury (paraplegia, cast immobilization), occupation related (spaceflight) or natural (aging) means, culminating in a weakened bone structure that is more susceptible to bone fracture.

*Background bone adaptation to exercise*: The "use it or lose it" tenet of bone physiology also referred to as Wolff's law [79] is based on the fact that bone structure is reduced by disuse and enhanced by exercise. As reviewed in detail in by Rubin and co-workers [188], retrospective studies illustrate the response of bone to physical extremes, for example astronauts enduring microgravity lose up to 2% of hip bone density each month [142], whereas professional tennis players possess up to 35% more bone in the dominant (i.e., playing) arm compared to the non-dominant arm [123]. Indeed, a range of site-specific benefits can be correlated to the special tasks of elite sportsmen and women trained over extended periods [105].

Several studies indicate that new loading challenges can also induce focal accretions of bone mass. Intense exercise in young army recruits stimulated increases in bone mineral density (BMD) [150], while a 10-month, high-impact strength-building regimen in children significantly increased femoral neck BMD [175]. Despite the apparent anabolic nature of the mechanical signal, moderate exercise regimens generally result in only modest, if any, increases in bone mass. For example, a 1-year high-resistance strength-training study in young women significantly increased muscle strength but failed to influence bone mass [106]. Non-mechanical co-determinants of any mechanical signal to drive bone adaptation are: genetic factors, sex, ethnicity, age and diet all able to enhance or suppress bone anabolism. The inherent complexity of exercise-generated mechanical stimuli to the skeleton indicates that some components of the mechanostat might be more potent regulators than others. Hence, before we can utilise mechanical stimuli as effective clinical interventions for the treatment of osteoporosis and other bone pathologies, identifying the cellular and molecular nature of these mechanobiological regulatory mechanism is essential.

Recently, progress has been made in characterising the ability of bone cells, i.e., osteoblasts, osteocytes and osteoclasts, to respond to physical signals and so add to our knowledge of the biological basis of the mechanostat. As pointed out by Rosen and Bouxsein, the mechanical sensitivity of the bone-marrow-derived stem-cell population and, in particular, mesenchymal stem cells (MSCs), has significant influence on the bone, and fat, phenotype [215]. Importantly, the mechanical influence on stem-cell activity is critical not only to tissue health, but to the regenerative capacity of organ systems. For example, if the mechanical signals that arise from weight bearing disappear during long-term spaceflight, and result in osteoporosis for an astronaut, the consequences of microgravity might be compounded if an injury were to occur (for example, hip fracture from a fall), as the progenitor cell population critical to bone repair might have collapsed in the absence of mechanical signals [281]. Therefore, interventions that are being designed to retain and/or reestablish a healthy, functional skeleton by targeting existing bone cells might also define the fate of the stem-cell niche, ensuring the capacity of these cells to proliferate and differentiate to higher-order connective tissues.

This chapter is organised as follows: In Sect. 2 we review the origins and evolution of the mechanostat. We then survey some of the latest in vivo animal models of

bone adaptation that are designed to dissect the complex regulatory mechanisms of the mechanostat (Sect. 3). The fundamental cellular and molecular regulatory mechanisms governing the mechanostat bone cell responses, in particular signal transduction and transcription are reviewed in Sect. 4. Loading physiology including type of loading and exercise together with timing in young and old are discussed in Sect. 5. In Sect. 6 on in silico models of bone adaptation an attempt is made to integrate the experimental findings from Sects. 2–5 into comprehensive computational models. These models can be used as hypothesis generation tools and allow prediction of the effects of various loading pattern on bone adaptation responses.

## 2   Functional Adaptation: Origins and Evolution of the Mechanostat and Its Physiological Properties

### 2.1   Why Should Bones Respond to Exercise?

Bones of the skeleton have many functions, with one of them being support for locomotion. This latter function determines bone size, shape, structure and material properties. The mechanical function of the skeleton provides support and protection for the vital soft tissues essential for maintenance of life (i.e., the central nervous and cardiovascular systems), and a rigid structure that allows the contractile properties of muscle to act and result in locomotion. Bone mass and structural organisation varies in different individuals based on the mechanical requirements of locomotion and weight bearing which has previously been investigated looking at different activities [46, 99]. As pointed out by Skerry, it is fascinating that the skeleton at the time of intrauterine development or even growth and adult life of any individual is not conditioned towards physiological activities that will take place in the future [240]. Hence, the existence of a dynamic regulatory system that tunes bone's stiffness and strength by altering the amount of bone and orientation of bone present at each location in the skeleton is not surprising.

### 2.2   What Happens When Bones Respond to Exercise or a Lack of It?

This regulatory system provides the mechanism for functional adaptation in the skeleton, so that the mass of load-bearing tissue we carry around is not so excessive as to waste energy in growth, maintenance and use. However, it must be sufficiently strong to provide a safety margin that protects against fracture in response to unlikely events such as those experienced in falls and impacts [50]. As stated by Skerry, it is likely that the adaptive mechanism that arose as a result of evolutionary pressures, when there were animals with genetically massive skeletons, resistant to all but the

most extreme traumatic insults, but unable to evade more nimble predators or to capture prey [240]. The development of animals with optimal (i.e., not excessively massive) skeletons would permit better survival for the species even if the individuals resistance to trauma were reduced. It seems likely that this evolutionary process was advanced at early stages of vertebrate evolution. In sections of fossil dinosaur bones from over 100 million years ago, it is possible to recognise the same organised trabecular structures that led to the foundation of understanding of functional adaptation − Wolff's law. Remarkably, high magnification pictures of dinosaur bones reveal morphological structures such as secondary osteons formed by targeted Haversian remodelling that can also be found in vertebrates. These morphological features are consistent with the highly orchestrated control of bone mass and architecture that underlies the adaptive mechanism as we understand it today.

## 2.3 Wolff's Law and the Mechanostat

Central to the notion of functional bone adaptation is Wolff's law, which is a precursor of Frost's mechanostat theory exclusively focusing on mechanical aspects. An elegant description of the historical events and discoveries that led to the formulation Wolff's law is presented by Carter and Beaupre (Chap. 1, [35]).

First relations between bone dimensions and body size where established in the early 15th century by Galileo who noted, that "bones must consequently also disproportionately increase in girth, adapting to load-bearing rather than mere size" (translation of Galileo [172]). It is not known whether Galileo believed that this adaptation was merely a scaling phenomenon, or whether it occurred during each individuals life. A major advance in the field of bone adaptation to mechanical loads occurred in the 18th century when von Meyer, an anatomist, and Culmann, an engineer who was a pioneer in graphical methods for analysis of truss structures, compared pictures of the trabecular arrangements in the human femur with calculated stress patterns in crane structures. Their work came to the attention of Roux and Wolff who both associated a link between bone structure and mechanical function (i.e., loading), while with slightly different interpretations. Roux was the first using a term implying functional adaptation, while Wolff proposed a trajectorial theory on the structure of compact and cancellous bone. The history of Wolff's law, as the law of bone transformation is often called, took a peculiarly ambivalent course where both Roux and Wolff insisted on validity of their own hypothesis. Between 1870 and 1890 the trajectorial hypothesis of Wolff and the theory of functional adaptation by Roux amalgamated to *Wolff's law* [214].

This "law" translates as: "Every change in the form and function of a bone or their function alone is followed by certain definite secondary alterations in their internal architecture, and equally definite secondary alterations in their external conformation in accordance with mathematical laws," and this could imply that bone form was related to function during development, but not as a dynamic self regulating system. Wolff's law and the process of functional adaptation suggests responsiveness to

increased loads with stronger, more mechanically competent bones, but its natural corollary is that reductions in loading or usage lead to bone loss. Without such a negative aspect to the feedback system, gains in bone that were no longer appropriate would not be reduced to a new optimal level for a lower level of habitual activity. Ruff et al. provide a detailed review of various interpretations and misinterpretations of Wolff's law [225].

This dynamic balance between form and function raises some fundamental questions: What are the variables to which the skeleton's bone forming and bone resorbing cells respond? How are mechanical stimuli translated in signal transduction and transcription events? The former question is still a source of debate as various opinions exist on the type of stimulus, i.e., role of interstitial fluid flow, streaming potentials, or direct cellular strain in controlling adaptive responses [118].

## 2.4   What Initiates and Controls Bone's Adaptive Response?

In the following sections, we will review the second question, i.e., signalling pathways and regulatory molecules that are activated during mechanical loading in more detail (Sect. 4). However, in order to answer the first question one can take a reductionist view and argue that whatever the mechanical stimuli, they are ultimately consequences of tissue deformation or strain, which is evident when bone is physically loaded. Mechanical strain ($\varepsilon$) is a dimensionless quantity defined as the ratio of deformation (i.e., new length − original length) divided by original length. Strain magnitudes in mammalian bones under physiological loading are around $10^{-3}$ and a commonly used convention is to use so-called microstrain ($\mu\varepsilon$) measures, i.e., $1 \ \mu\varepsilon = 10^{-6} \ \varepsilon$. Consequently, physiological strains are in the range of 1,000s $\mu\varepsilon$. Tissue strain as controlling factor of bone adaptation was first recognised by Lance Lanyon beginning of the 1970s, after the first pioneering in vivo bone strain gauge experiments conducted by Evans [62]. Lanyon and co-workers made the first accurate assessments of strain in bone in an in vivo setting [143, 145, 146]. Quantification of the "habitual" bone strain environment has been a central part of the continuing investigation of the mechanism by which bone adapts to loading. Using strain gauges, peak bone strain and strain rates have been measured during various activities in numerous species, including humans. These studies have been comprehensively reviewed by Fritton and Rubin [75]. For most animals, peak functional strains range from 200–1,000 $\mu\varepsilon$ during walking [76, 145] and from 2,000–3,200 $\mu\varepsilon$ for more vigorous activities, and can almost reach 5,000 $\mu\varepsilon$ in galloping racehorses [76]. For humans, strains vary significantly between low impact exercises such as walking and running and high impact exercises such as zig–zag hopping and basketball rebounding ranging between 500 and 2,000 $\mu\varepsilon$ [32, 275].

Utilising peak strain as major variable driving bone adaptation is a useful first approximation. However, this has also led to the notion that bone remodels exclusively to minimise strains [77]. It is now well accepted that bone curvature is induced and maintained not only to minimise strain magnitude, but to also allow a preferential strain distribution, i.e., to provide a more strategic directional reinforcement of

individual elements of the skeleton during adaptation than would be possible with a simple column design of bone loaded purely in axial compression due to habitual loads [23, 24, 144].

The narrow range of habitual strains observed in various species has led to the misconception that peak long bone strains are universal quantities, i.e., strain magnitudes are the same in all bones. Following this assumption, rules for adaptation have been considered based on the same strain threshold values for changes due to overload ($>1,500\ \mu\varepsilon$) or disuse ($<1,000\ \mu\varepsilon$) independent of the type of bone and spatial location. It is now well established that there are many factors apart from strain magnitude that are important for bone adaptation and that this response is site and bone-type specific. From an experimental point of view, strain magnitude is certainly an important quantity which directly governs the effectiveness of an exercise regimen both in animals and humans [219, 242]. The strain rate, strain gradient (i.e., spatial distribution of strains), number of loading cycles and repetitions (i.e., duration of loading and frequency), the dwell times (hold or rest times during an individual cycle) all appear to have effects on bone's adaptive response [186, 211, 244].

High strain rates are profoundly more potent stimuli than low strain rates. Strain rates of less than 4,000 $\mu\varepsilon$ per second are ineffective at inducing bone formation, while high strain rates experienced during footfall at high speeds, or when landing from jumps (in the range around of 1–200,000 $\mu\varepsilon$ per second) are highly osteogenic [180, 239, 258]. In vivo animal models indicate that the direction of strain may be less important. Applying compressive strains at strain waveforms with high rate ($>100,000\ \mu\varepsilon$ per second) but slow release (4,000 $\mu\varepsilon$ per second) were associated with bone formation that was indistinguishable from animals loaded with the opposite waveform of slow rate load and high rate unloading [241]. Currently no good experimental models exist which properly control for alteration of strain rates with high frequency loading [258]. Experimental data of Rubin and co-workers indicate that an inverse relationship between strain frequency and magnitude exists [222]. The effect of parameters other than peak strain magnitude may explain the observations that in humans, loading that induces unusual distributions of strain, even of a customarily experienced magnitude, alter bone mass.

## 2.5 Cellular and Molecular Machinery of the Mechanostat

### The Mechanostat's Stimulus

The findings described above led to the hypothesis that strain magnitude was the target variable to which bones respond in an adaptive way. Frost among others adopted this hypothesis and proposed that the stimulus for bone functional adaptation is strain magnitude. However, as evidenced from the literature review above, there are a number of other strain-related characteristics that have been shown to play a role in the functional adaptation of bone including strain rate, the frequency of loading cycles, the amount of rest between loading cycles and bouts of loading, and the distribution of strain within the bone structure [240]. Skerry coined a new
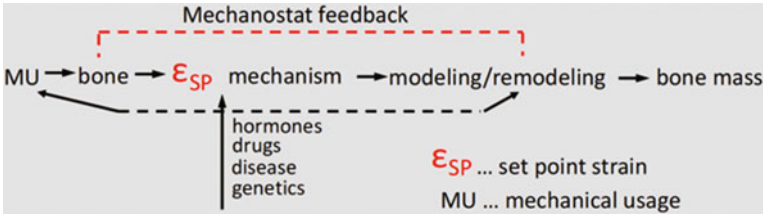
**Fig. 1** Conceptual model of the mechanostat as proposed by H. Frost: $MU$ = mechanical usage; $\varepsilon_{SP}$ = set point strain; Increasing the mechanical load compared to the habitual load (i.e., the set point) leads to gain in bone mass, while decreased mechanical loading leads to bone loss until a new equilibrium is established. Biological regulatory factors such as hormones, drugs and pathologies may affect the set point strain [79]

term for the stimulus of bone functional adaptation that incorporates these various strain characteristics into a unified concept the customary strain stimulus (CSS). It is important to note that Skerry, as well as Frost, acknowledged the fact that CSS (or the set point strain) is both sex and site specific and that it is genetically, biochemically, and pharmacologically regulated [240]. Frost's mechanostat model in its original form is shown in Fig. 1 which also indicates the feedback loop.

The above findings have been summarized by Turner into essentially three physical rules [251]: ($i$) bone adaptation is driven by dynamic, rather than static, loading; ($ii$) only a short duration of mechanical loading is necessary to initiate an adaptive response. Extending the loading duration has a diminishing effect on further bone adaptation and ($iii$) bone cells accommodate to a customary mechanical loading environment (i.e., habitual loading), making them less responsive to routine loading signals. These rules have been subsequently expanded by Skerry as follows [240]: ($i$) the number of cycles of loading applied to bones appears to be relatively unimportant once some threshold level has been reached. The first study to demonstrate this showed that in experimental animals, 36 cycles of loading per day (occupying ~2 min in each 24-h period) induced bone formation that could not be increased by greater numbers of cycles of the same magnitude and waveform [221]; ($ii$) additional osteogenic benefits can be gained by inserting rest periods between individual load cycles [244]. Rest periods of less than 9 s are not effective in rodents, and periods of over 15 s induce no greater benefit than 15 s [96]. While this phenomenon is currently not fully explained, it has been hypothesised that it is related to fluid flow in the different porosities of bone, i.e., the bone micro porosity (i.e., lacunar canalicular porosity) and the bone tissue porosity (i.e., vascular porosity). As discussed in Scheiner et al., typical physiological loads exhibit a variety of characteristic loading times which are intricately linked to the ability of fluid to drain out of the respective porosity of bone [236]; and ($iii$) it has been shown that the division of a saturating number of load cycles (360) into several shorter bouts separated by rest periods ($2 \times 180$, $3 \times 120$, $4 \times 90$) increases the bone formation response in vivo [211]. These findings have one unifying principle, each suggesting that at some level, bone retains the effect of loading events, and the information stored is used to modify subsequent events.
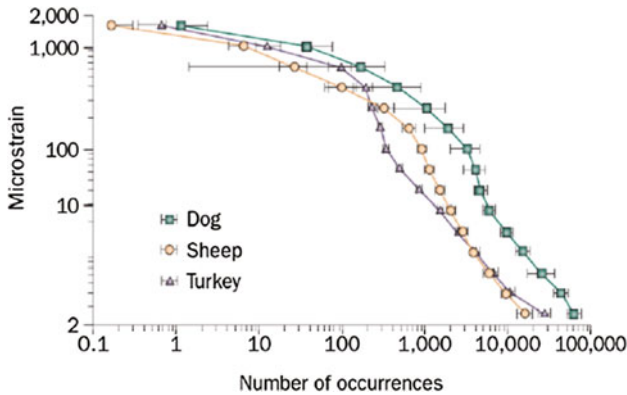
**Fig. 2** Bone is subjected to a wide range of mechanical loading conditions ranging from high magnitude, low frequency loading to low magnitude, high frequency loading: strain recordings from the tibia of a diverse range of animals over a 12-h period are remarkably similar. (Image adapted from [76])

Rapid repetition of single load cycles appears to cause desensitisation to immediate subsequent events (in the next 9 s), while once a saturating number of cycles has been applied, the "memory" system is not stimulated further within the same bout of loading. However, a rest period of 1–4 h appears to allow for the re-sensitising of the mechanobiological sensory system to cause potentiated effects.

As has been reviewed by Rubin and co-workers, over the daily course of functional challenges, bone will be subjected to very few high-strain (2,000–3,000 $\mu\varepsilon$), low-frequency (1–3 Hz, or cycles per second) events, but to a persistent bombardment of low-strain ($<5$ $\mu\varepsilon$), high frequency events (10–50 Hz), stemming from muscle contractions engaged to retain posture (Fig. 2) [76]. The occurrence of omnipresent, high-frequency, low- magnitude mechanical events in the axial and appendicular skeleton decreases in parallel with the sarcopenia of aging or disuse [112], perhaps contributing to the etiology of the bone loss that correlates with the deterioration of muscle.

Note that functional loading parameters that correlate with signal intensity imply that a "goal" of mechanical adaptation is to minimise tissue strain for a given load, while simultaneously minimising tissue mass [188]. Alternatively, bone cells might actually be responding to biological parameters of the functional milieu that are not necessarily linked to the magnitude of the signal. Examples of biological systems that are tuned to perceive and respond to "other than peak" exogenous signals are vision, hearing and touch. It is well accepted that too much loading will damage the bone, leading to failure − just as too much light, noise or pressure will overwhelm sight, hearing and touch. The nature of the mechanical stimulus of the mechanostat has most precisely been characterised for the turkey ulnar loading model (Fig. 3). In this in vivo loading model, bone's adaptation to mechanical signals is nonlinear with a well-defined curve representing bone homeostasis, a region of bone anabolism and a region of bone catabolism (Fig. 3). The mechanical stimulus can be generated either
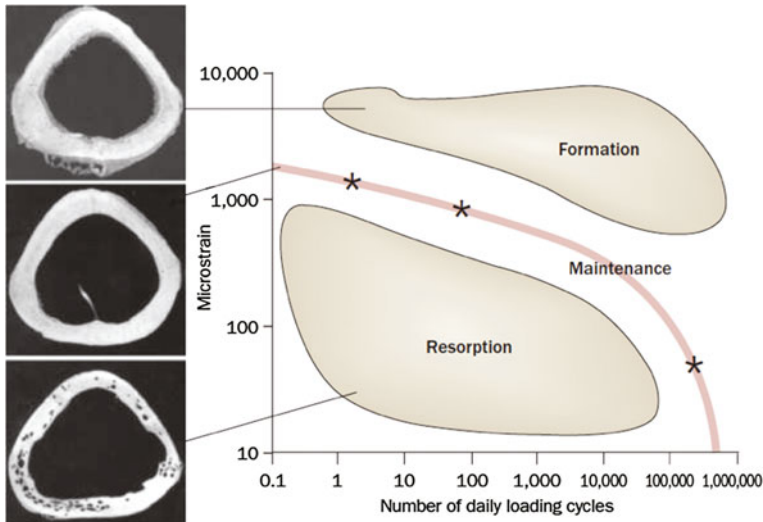
**Fig. 3** Effects of loading magnitude and frequency on bone adaptation using the turkey ulna model. A nonlinear relationship between cycle number and strain magnitude is observed which uniquely maintains bone mass (*solid line*) via different loading patterns: bone is preserved with either four cycles per day of 2,000 $\mu\varepsilon$, 100 cycles per day of 1,000 $\mu\varepsilon$, or hundreds of thousands of cycles of signals of well below 10 $\mu\varepsilon$ (each represented as a *star*). These data indicate that bone loss is induced above this "preferred strain history", while bone formation occurs above the maintenance envelope. (Image adapted from [200])

by very few high-magnitude strain events, or by many thousands of low-magnitude strain events [200] (Fig. 3).

**The Mechanostat's Effector Mechanism**

After having discussed the various stimuli leading to bone's adaptive responses due to mechanical loading, we briefly discuss the biological machinery necessary to respond to these stimuli (for more details see the next section). It is now well established that the cells responsible for bone formation and bone resorption are osteoblasts and osteoclasts, respectively. Based on technological developments in bone histomorphometry in the late 1950s, it was Frost who first observed the two distinct and dynamic effector processes carried out by these cell types, i.e., bone modelling and bone remodelling. The process of bone modelling involves the spatially and temporarily separated action of osteoclasts and osteoblasts on bone surfaces. Based on the mode of action, Frost distinguished between "formation modelling" and "resorption modelling" which refer to bone being added along some surface or removed from others. Consequently, modelling affects the size and shape of bones and is therefore a critical process for reshaping long bones during growth [190].

The second major effector process is bone remodelling which refers to a localised process that involves the spatio-temporal coupled action of osteoclasts and osteoblasts in so-called basic multicellular units (BMUs). Remodelling starts with osteoclasts

resorbing a small trench of bone, and osteoblasts are subsequently recruited to the site to form and mineralise new bone. Frost was the first to identify this coupled action of osteoblasts and osteoclasts [103]. Except in disuse, the amount of bone formed is generally equivalent to the amount of bone resorbed in each BMU [83]. Nonetheless, this processes of bone resorption followed by formation can take several weeks to months to complete, and consequently, there is a temporary increase in porosity caused by remodelling [104] that can transiently alter whole bone strength.

While the two distinct processes of modelling and remodelling are responsible for altering bone's material properties, structure, and strength in response to changes in the mechanical environment, there still remains confusion as to the different roles of these effector mechanisms in various mechanical states such as in disuse or overload. Understanding the biology of a third cell type of bone, osteocytes, in bone functional adaptation helped to clarify both the stimuli for, and effects of, these two distinct processes of bone adaptation.

### The Mechanostat's Sensory Mechanism

As mentioned, the mechanostat's effector cells have been well characterised. However, the sensory cells of bone have only recently received more attention. This role is fulfilled by members of the mesenchymal stromal cell lineage: osteoblasts, osteocytes, and bone lining cells. Of these cells, osteocytes are highly connected by dendritic processes (through canaliculi), are linked to the dendrites of neighboring osteocytes by gap junctions, and are abundantly distributed throughout the bone matrix allowing them to provide local indications of changes in the mechanical environment [26]. As discussed below, recent evidence reveals a crucial role for osteocytes in resorbing, forming, and maintaining bone mass in response to alterations in the mechanical environment.

Although bone mechanotransduction pathways are just beginning to be identified, it does appear that osteocytes provide a pivotal function in bone adaptation to mechanical demands (Fig. 4). If an adequate strain stimulus is generated from customary (i.e., habitual) loading, osteocytes will remain viable and bone will neither be lost nor gained. This state is generally denoted as homoeostasis or equilibrium. Note that identifying the customary loading stimulus in an individual is difficult. Conversely, if strain stimuli are lower than the CSS, osteocyte apoptosis and subsequent bone loss will occur (Fig. 4b). For the case that the strain stimulus is greater than the CSS, osteocytes will regulate anabolic factors resulting in bone formation. It is still a matter of debate whether the CSS is a single point or whether it is defined by a region, the so-called lazy zone, characterised by upper and lower threshold values (see Fig. 4a).

The remodelling response of bone appears to be regulated via a disruption in the osteocyte syncytium due to microdamage and microcrack formation, or loss of chemo-transport. This type of remodelling is often referred to as "targeted remodelling", and it prevents microdamage from accumulating in bone matrix. For loading stimuli larger than the CSS, microdamage accumulates and is remodelled at a higher rate (Fig. 4a). On the other hand, if the loading stimulus is lower than the CSS
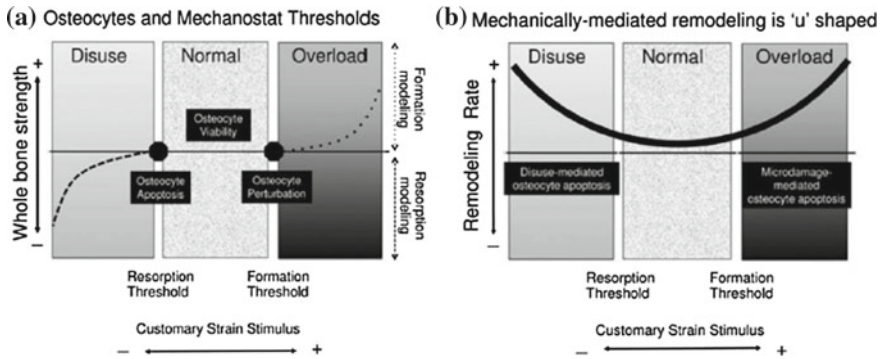
**Fig. 4** Schematic illustration of mechanostat feedback regulation by osteocytes via **a** bone modelling − whole bone strength is altered by formation modelling (*dotted line*) and resorption modelling (*dashed line*) and **b** bone remodelling processes mechanically mediated remodelling also occurs in response to mechanical loading but in a *U*-shaped manner such that the rate of remodelling increases with both increased loading as well as unloading. Upper and lower bounds of the customary strain stimulus (CSS) regulate osteocyte faith, i.e., apoptosis and consequently bone modelling and/or remodelling events. (Image adapted from [113])

**Table 1** Summary of the role of osteocytes in the different processes of mechanically-mediated bone modelling and remodelling in response to changing customary strain stimulus (CSS)

| Customary strain stimulus | | | |
|---|---|---|---|
| | Low | Normal | High |
| **Modelling** | | | |
| Osteocytes | Apoptosis | Maintenance of viability | Perturbation |
| Bone mass | Decreased | Maintained | Increased |
| Primary surfaces of action | Endocortical, trabecular | N/A | Periosteal, trabecular |
| Whole bone strength | Decreased | Maintained | Increased |
| **Remodelling** | | | |
| Remodelling rate | Increased | Baseline | Increased |
| Osteocytes | Apoptosis | Maintenance of viability | Apoptosis |
| Stimulus for osteocyte action | ↓ nutrients/waste removal | Pulsatile fluid flow | Microdamage |
| Result | Transient loss of bone negative bone balance | No change | Maintenance of material quality |

(i.e., mechanical disuse scenario), osteocytes undergo apoptosis leading to increased remodelling (Fig. 4b).

The functional responses of osteocytes due to mechanical loading regulating bone modelling and remodelling events have been summarized in Table 1.

# 3 Animal Models for Structural Adaptations to Mechanical Loading

There is a long history of applying different models to understand functional adaptation of the skeleton, from natural observations to engineering analogies and genetic modification of mice. In the 1600s, Galileo discussed allometric scaling of bones for animal size in relation to the change in volume required for a given increase in a bone's cross sectional area [90]. He also showed how structural adaptations, such as a hollow diaphysis, adapt bones for strength and lightness in the same way that "…men have discovered, therefore, that in order to make lances strong as well as light they must make them hollow" [90]. Darwin observed that domestic ducks on the Falkland islands walked more and flew less than their wild counterparts, and hence had lighter wing bones and heavier leg bones [53]. Classically, Julius Wolff applied the engineering principles he observed from Culmanns crane to the arrangement of trabeculae in sections of the proximal femur [271], which incorrectly led to Wolff's law being cited as the basis for functional adaptation (see previous section for more detailed discussion). It was in fact Roux, influenced by Darwin and Wallace, who introduced a dynamic concept of functional adaptation [216]. While Wolff had the biology wrong [57], Roux argued that it was the functional stimulus that shaped the bone, providing an example of a fibula that had thickened in the absence of a tibia [216].

To understand the biology, in the context of complex mechanical loads, investigators had to develop in vivo and in vitro models to control the applied loads and differentiate them from habitual activity. In vitro preclinical models have been reviewed extensively, elsewhere [16, 55], and enable specific mechanotransduction pathways to be investigated. Unfortunately, most of those studies focus on osteoblastic/osteocytic responses, leaving the effects of loading on osteoclasts largely unexplored [224], particularly in terms of resorptive activity. Regardless of the model, they are nonetheless employed to examine two principal questions: (1) what is the nature of the stimulus that drives functional adaptation; and (2) what is the cell biology that transduces mechanical stimuli into tissue adaptation?

Since the nineteenth century, several highly developed and biologically relevant theories have attempted to describe the dynamic relationship between mechanical loading stimuli and the biological response in bone [20, 33, 79, 251]. The essential features of these theories have been reviewed elsewhere, and most predict that adaptation responds to factors in the strain environment, is driven by errors outside of physiological thresholds, and is surface-specific [31]. In Sect. 6 we will discuss some of the proposed in silico models of bone adaptation. Frost's mechanostat theory [79] (see also previous section), later referred to as the Utah Paradigm [82] is unique among these in its distinction between modelling and remodelling processes, thresholds for activating lamellar or woven bone formation and its application to the aetiology of osteopenia and osteoporosis. The Utah Paradigm maintains that bone adapts by different biological processes within four mechanical usage windows (Fig. 5), with thresholds defined by minimum effective strains (MES) for activating adaptive

**Fig. 5** Mechanical usage windows defined in Frost's Utah Paradigm [79, 82]: MES = minimum effective strain. (Image adapted from [79])
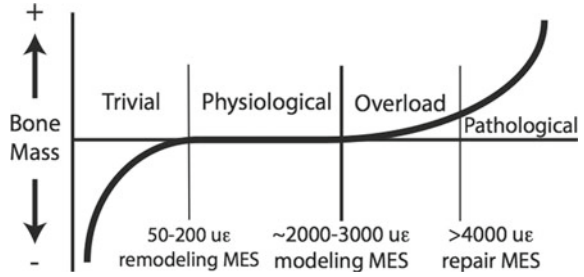


processes [78]. The change in bone mass described in Fig. 5 is similar to Carter's model [33], except that Frost defines the set-points for activation and the biological processes underlying the changes in bone mass.

Remodelling by basic multicellular units (BMUs) tends to remove or conserve bone and is activated by reduced mechanical usage in the trivial loading zone, or microdamage (extreme loading) in the pathological loading zone, but suppressed by physiological loads (Fig. 5).

Conversely, modelling can add cortical and trabecular bone, reshape surfaces by resorption or lamellar formation drifts, is activated by increased mechanical usage in the overload zone and remains within, or below, the physiological loading zone. It also predicts rapid addition of woven bone to surfaces in response to excessive loading in the pathological loading zone. Moreover, the threshold loads for activation, "set points", may be influenced by humoral or local factors (such as hormones, steroids or drugs) or metabolic bone diseases such that the adaptation effected by them mimics the response expected for the perceived change in mechanical loads [30, 79, 81].

In this subsection we will focus on the numerous animal models that have been developed to test these relationships and the cell biology driving them, all of which involve application of forces and moments to deform bones. Those forces can be applied intrinsically, such as muscle force during exercise, or surgical manipulation of a skeletal region (e.g., use of an osteotomy to overload the adjacent bone). Alternatively, forces and moments can be applied extrinsically through surgical application of actuators; or via direct external pressure to the limb from a loading system that deforms the underlying bone(s). The loads generated by ground reaction force during exercise, may also be considered extrinsic, but for convenience will be discussed in terms of intrinsic loading. To understand cell responses, ex vivo systems have also been developed that apply stress to cells in a variety of culture systems.

## 3.1 Physiological Models

Similar to humans, a range of activity models have been used to investigate loading/unloading responses to mechanical factors. These naturally include running [69] and swimming, but also jumping [261], spaceflight [272], hind-limb suspension

[91, 218] and unilateral hind-limb immobilisation (overloading the un-bandaged limb) [119, 120]. This section will focus on loading models. In relation to physical activity, animal studies demonstrate that growing bone responds to low or moderate exercise through significant additions of new bone. This occurs in both cortical and trabecular bone, and results in adaptation through both periosteal expansion and endocortical contraction [68]. Intracortical activation frequency declines in growing bone in response to exercise, reducing porosity and the remodelling space [173]. In the adult skeleton, the effect of loading tends to be one of conservation, not acquisition [68]. The range of animal species, exercise protocols and training volumes varies widely in these studies making it difficult to draw unequivocal conclusions about the loading stimulus and mechanotransduction. Such problems led investigators to use controlled, extrinsic loading studies in which the load magnitude, frequency and rate can be accurately applied.

## 3.2 Externally Applied Loading Models

Extrinsic models that have been systematically applied to test hypotheses about mechanically adaptive modelling have included the isolated turkey ulna and rat ulnar loading model from Lanyon's laboratory [219–221, 250], Turner's tibial four-point loading model [254, 257] and Chamber's vertebral loading model [45] in rats. These approaches have subsequently been adapted to enable study in mice [149], and the approach adapted to axial loading of tibiae in rodents [54] and the rabbit [17]. In concert with other models, these have advanced our knowledge of mechanically-induced bone formation considerably during the past 30 years. These recent models for small animals are quite accessible to many researchers, often adaptable to commercial testing devices, and enable testing in genetically modified animals, broadening the range of hypotheses that can be tested.

## 3.3 Surgical Approaches

One of the first extrinsic models to deliver controlled loads to bones in vivo was developed by Hert and his colleagues in the 1960s and 70s [108, 109]. They applied continuous and intermittent loading using an external electromagnetically operated device to the tibia of rabbits through surgically implanted pins, demonstrating that static, or isometric, loading provides very little stimulus to adaptation. Although this observation was subsequently supported in other animal models, Hert's experiments lacked verification of the strain environment generated through the loading apparatus, making it more descriptive than mechanistic.

This was rectified by the pioneering experiments undertaken in Lanyon's laboratory in the 1980s. They used implanted strain gauges to measure the loading stimuli applied through controlled loading experiments, leading to a paradigm shift in the

**Fig. 6** Rubin and Lanyon surgically isolated the ulna of turkeys to control the strain rate and magnitude, pioneering studies of functional adaptation to mechanical loading [219–221]. (Image adapted from Rubin et al. [217])
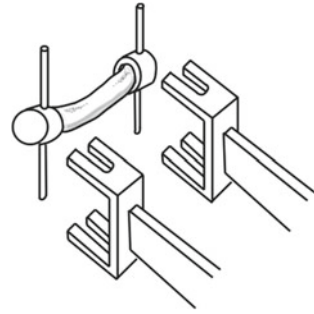
investigation of functional adaptation. Lanyon's experiments started in a sheep model [186], but with Rubin, they developed the isolated avian ulna (Fig. 6) in which applied loads of known strain rate and magnitude could be distinguished from the turkey's habitual activity [219]. These experiments unveiled the key characteristic of loading that very few loading cycles are actually required to elicit new bone formation [219–221]; and, that the effect saturates very quickly. So much so that increasing the duration of loading beyond 40 cycles per day had little additional effect on new bone formation [219].

The avian model certainly created a paradigm shift in studies of functional adaptation, but there are limitations. The surgical approach limits its utility for many investigators, and the periosteal modelling response tends to be of woven bone, which has different regulatory characteristics to lamellar bone [257]. In addition, the ulnar is exposed to relative disuse between loading bouts, potentially activating a remodelling response, which loading has to moderate; and avian biology is less amenable to molecular probes for mammalian targets. Chambers recognised that these models were specific to cortical bone adaptation and applied this method of external actuators to deform rat tail vertebrae [37, 45]. By placing pins in the 7th and 9th caudal vertebra, they were able to deform the interposed 8th caudal vertebra, initiating (re)modelling responses in the trabecular bone, without the confounding effects of surgery in the vertebra being studied. This model was subsequently extended and perfected by Mueller and co-workers to perform in vivo imaging of bone adaptation in combination with micro finite element modelling [141].

## 3.4 Non-invasive Approaches

Charles Turner developed a new approach for producing mechanical strains in vivo that did not require surgical intervention and allowed normal activity between loading sessions [254]. A four-point bending device applied force to the leg of a rat, thus generating strain in the tibia (Fig. 7). The loading points were padded so damage to the muscle tissue was minimised during loading. Many methods used to study bone adaptation cause callus-like, woven bone formation as a primary response to loading
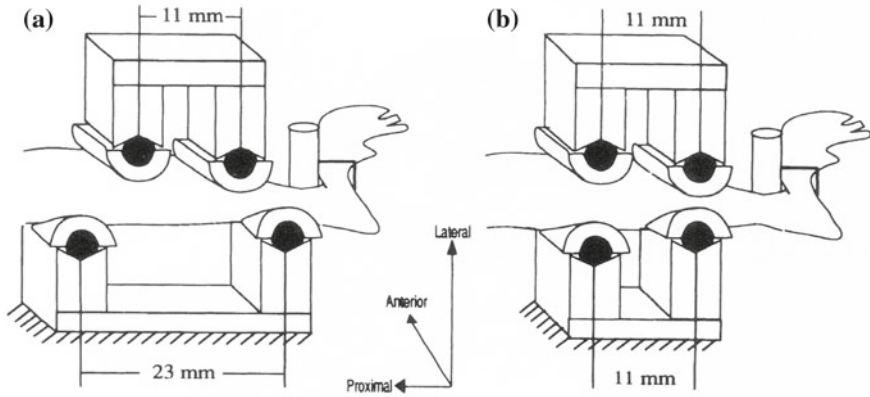
**Fig. 7** Arrangement of the four-point loading apparatus to apply bending (**a**) or sham (**b**) loads to the right tibia of rats [254]. The limb between the inner loaders in bending provides a region of uniform strain, which could not be achieved with 3-point bending. (Image adapted from [71])

[219]. Although woven bone is important for bone healing and rapid growth, it is not a response seen in healthy adults, except in extraordinary conditions [31]. In the case of extreme mechanical loading, woven bone provides a rapid, and almost immediate, increase in sectional geometry, following which it remodels and consolidates into a lamellar structure over time [223, 255]. Depending on the mechanical loading conditions, the 4-point bending model produces a lamellar bone response at the endocortical and periosteal surfaces [201, 257].

Furthermore, lamellar bone formation on the endocortical surface of rat tibiae increased linearly with increasing load after a threshold of 40 N (approximately 1050 $\mu\varepsilon$) was reached; and that new woven bone formed on the periosteal surface was independent of the magnitude of applied strain [257]. Sham loading (Fig. 7b), in which no bending moment was introduced, did not significantly increase lamellar bone formation at the endocortical surface. The original device was driven by an open-loop spring-linkage driven by a stepper motor [254]. To increase the range of available frequencies, Forwood modified this device by driving the system with an electromagnetic vibrator offering a range of applied loads to 70 N and frequencies up to 20 Hz [71].

The clear advantages of this approach were that the loads from habitual activity could be subtracted from the applied loads, there was no surgical intervention, the model offered a sham loading to control for the effects of periosteal pressure, and rat tissue was more amenable to cell and molecular probes for analysis. At low loading magnitudes, the periosteal response was quite variable, producing lamellar bone at low magnitudes, but rapidly switching to woven bone once a strain of more than about 1000 microstrain was reached. This was a disadvantage that tended to leave the endocortical surface as the valid region for analysis, which in humans tends to be associated with remodelling, rather than modelling.
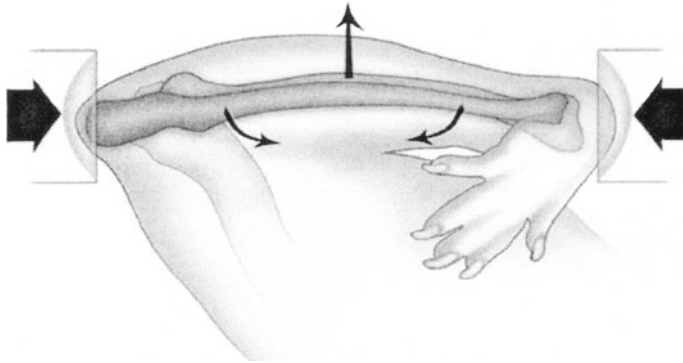
**Fig. 8** Axial loading of the rat forelimb creates a bending moment in the ulna, approximating physiological loading conditions. (Image adapted from [228])

To overcome some of those limitations, different approaches have been developed. A cantilever model was first developed in which the knee and the ankle of the mouse were placed in cups to move the ankle laterally in relation to the knee [95]. This generated a bending moment in the tibio-fibula. While this avoided periosteal woven bone, allowing analysis of periosteal and endosteal surface, it still did not model physiological loading. Torrance then developed an innovative loading system that avoided direct application of loads to the surface of a bone, by applying axial loads through the epiphyses [250]. This model applies compressive end-loads to the forearm of rats, inducing a bending moment in the ulna [181], a mode of loading analogous to that occurring physiologically. Short daily periods of dynamic loading, to a peak of 4000 microstrain over 10 days, increase modelling activity furthest from the axis of bending [181]. New bone formation increases along the lateral surface, while at the medial surface, the normal resorptive activity is arrested and new bone formation is activated. At the cranial and caudal cortices (along the neutral axis) little adaptive activity is observed (Fig. 8). It is also important to note that differential modelling also occurs along the ulnar diaphysis. When compared with the unloaded contralateral ulna, increased periosteal apposition is observed in the loaded limb toward the distal end, but the mineral apposition rate is reduced toward the proximal end. That is, the whole bone adapts to the mechanical perturbation as a structure, highlighting the site specificity of adaptive changes.

The ulnar loading model has now been used by a large number of groups to examine characteristics of loading that initiate functional adaptation, and optimise skeletal responses. In addition to adaptive modelling, repetitive loading of the rat ulnar creates an excellent model of microcracking and stress fracture [22, 130, 264]. It is non-invasive, avoids external trauma to the periosteum and its clinical characteristics are very similar to stress fracture in humans and animals. In this mode, repetitive cyclical loading is applied for a large number of cycles until an increase in displacement, of between 10 and 40% [22, 130, 262], is observed, at which time microcracking and a small non-displaced fracture occurs in the ulnar

diaphysis. Stress fractures created by ulnar loading heal by a combination of woven bone formation, that stabilises the region, and remodelling that progresses directly along the fracture line [130]. This stress fracture repair shows no evidence of an inflammatory response and does not rely on endochondral ossification for fracture healing [130]. It is also, therefore, a useful model for investigating remodelling activation at a known time-point and anatomical location in rat cortical bone.

The concept of applying axial loads to a limb, to generate bending moments in the diaphysis of the bones, has now also been modified for the mouse tibia [54]. Non-invasive controlled axial loading of the mouse tibia not only generates an adaptive response in the diaphysis, but loading through the tibial plateau also allows trabecular responses to be studied in the tibial metaphysis. This is an advantage because this is a common region for studying remodelling changes in rodents. Like ulnar loading, it also enables studies of functional adaptation in mice genetically modified to test specific molecular hypotheses. Ulnar and tibial cyclic compression in rats and mice have therefore become favoured models for investigating mechanobiology. However, even though remodelling can be activated by fatigue loading in rodents, they do not have intracortical Haversian bone as the natural microstructure. This can be problematic for translating the effects of pharmaceutical interventions to humans.

Building on knowledge gained through the rodent models of axial loading, Baumann et al. developed an ulnar loading system for the rabbit [17] fulfilling this unmet need. Although strain thresholds for activating lamellar bone formation were higher than those observed in rodents, the model provided a dose-dependent anabolic stimulus for periosteal bone formation. At strains above 5000 microstrain, significant woven bone was also produced on periosteal surfaces. In addition, rabbits exhibited remodelling within the intracortical envelope, but it was not clear that this was a response to loading, or baseline intracortical remodelling. This may be a useful pre-clinical model to combine with loading because rabbits exhibit osteopenia, including cortical bone loss, after ovariectomy [193], and respond to current therapies [4, 110].

## 4   Bone Cell Responses to Loading: Involved Regulatory Factors, Receptors and Environmental Factors

When subjected to mechanical stimuli, bone responds via the process of mechan-otransduction. This involves cascades of signalling pathways that lead to adaptive changes to bone geometry at the stress site. When the receptor cells, arguably the osteocytes, detect a mechanical stimulus, a signalling cascade is initiated promoting tissue adaptation. A large volume of work has elucidated key cellular events that occur over seconds to hours, and, lead to increased bone formation and modulation of bone remodelling. Different approaches have identified the cellular transducer(s), focussing on G protein-coupled mechanoreceptors or focal adhesion signalling molecules [39, 40]. Fluid flow has been identified as a key signal driving mechanotrans-duction [256]. This generates fluid shear stress in the osteocyte membrane, activating

mechanically sensitive ion channels in osteocytes [12], which are exquisitely more sensitive to this signal than osteoblasts [133]. Attention has focused on the key molecules in the cascade that leads to adaptation.

## 4.1 Early Responses: ATP, Calcium, PGE2, Nitric Oxide

**ATP and Calcium**

ATP is the earliest regulatory factor of bone cell mechanotransduction that acts as an acute mediator of signalling cascade. ATP can be released via vesicles and hemi-channels such as connexin-43 (Cx43) and pannexin 1 [139, 249]. Vesicular ATP release is mediated by fluid shear stress arising from mechanical loading which puts strain on the plasma membrane of bone cells, subsequently activating mechanosensitive calcium channels (MSCC) (Fig. 9) [249]. This causes local depolarisation that activates voltage sensitive calcium channel (VSCC) to initiate influx of calcium ions that facilitates exocytosis of vesicular ATP [139, 249]. For example, verapamil, a VSCC blocker, significantly reduces loading effects in rat bone when introduced in vivo [153]. The involvement of Cx43 and pannexin 1 in loading-related ATP release in osteocytes is yet to be elucidated, and it is speculated that another unknown hemi-channel might be involved in this process [139].

Following its release, ATP acts in autocrine or paracrine fashion to increase intracellular calcium concentration by binding to purinergic receptors: P2X and P2Y. P2X, notably $P2X_2$ and $P2X_7$ in bone cells, is an ionotropic receptor that causes influx
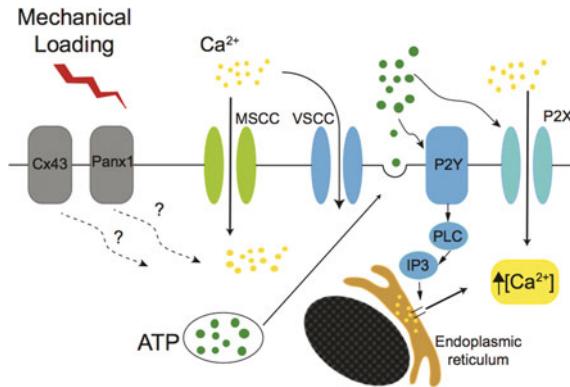


**Fig. 9** Mechanical loading activates mechanosensitive calcium channels (MSCC) and voltage sensitive calcium channels (VSCC). Influx of calcium facilitates exocytosis of vesicular ATP. ATP binds to P2X to allow influx of calcium. Binding of ATP to P2Y activates PLC-IP3 response that causes calcium release from endoplasmic reticulum. The responses from P2X and P2Y results in increased intracellular calcium concentration ($\left[Ca^{2+}\right]_i$). Involvement of hemi-channel Cx43 and pannexin 1 (Panx1) remains questionable

of extracellular calcium ions [139, 154]. P2Y is a G protein coupled receptor that, upon its activation, produces phospholipase C (PLC)-induced inositol triphosphate (IP3) which binds to a receptor linked to a channel on the endoplasmic reticulum to release calcium from intracellular stores [39, 40, 212, 277]. Pharmacological inhibition of IP3 and PLC, which generates IP3, obliterated the calcium response [39, 276]. This early calcium response is essential for expression of regulatory factors such as COX-2, nitric oxide, and osteopontin expression that mediate load-induced bone formation [39, 40, 153, 276].

## Prostaglandin

Prostaglandin (PG) is another early response activated by mechanical stimulation that is essential for bone formation. Its production involves phospholipase A2 releasing arachidonic acid, which is converted into $PGH_2$ by prostaglandin G/H synthases (PGHS), also known as cyclooxygenases (COX). $PGH_2$ then becomes $PGD_2$, $PGF_{2\alpha}$, $PGE_2$, prostacyclin ($PGI_2$), or thromboxane $A_2$ by their respective terminal synthases.

COX has two isoforms: COX-1 and COX-2. COX-2 plays an important role in producing PG for mechanotransduction [134], as pharmacological treatments such as indomethacin (a non-specific COX blocker) and NS-398 (a specific COX-2 blocker) are able to suppress bone formation [44, 66] (Fig. 10). On the other hand, COX-1 is not involved in this process as SC-560 (specific COX-1 blocker) does not alter PG level in response to loading [13]. Of interest, COX-1 is upregulated in COX-2 knockout mice and replaces function of COX-2 as a compensatory pathway [2].

Of all the $PGH_2$ terminal products, PGE2 in particular has been put under a spotlight and extensively studied. Several studies observed sustained release of PGE2 through auto-amplification to potentiate long term effects of PGE2 upon the application of pulsating fluid flow (PFF), or steady shear flow [41, 132–134, 205, 243]. Sakuma et al. demonstrated that compared to the other prostanoids, PGE2 was the most effective inducer of COX-2 (i.e., autoamplification) and cAMP, which plays a significant role in PGE2-induced bone formation [227].



Fig. 10 Effect of a single dose of non-specific COX (indomethacin) and specific COX-2 (NS-398) inhibition on relative bone formation rate (%) following 4-point loading of the rat tibia. rBFR is the BFR of left (control) limb subtracted from the right (loaded). (Image adapted from [66])
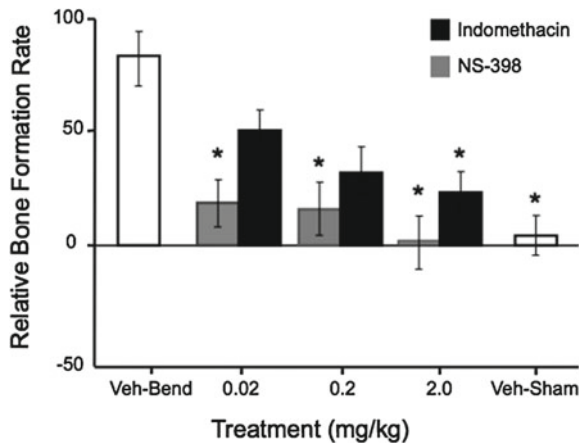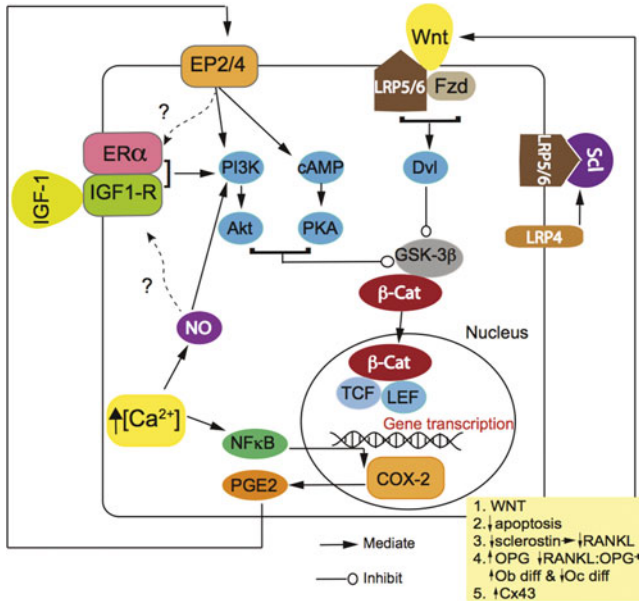
**Fig. 11** Increased intracellular calcium concentration ($[Ca^{2+}]_i$) induces NFkB nuclear transloca-tion [40] which results in COX-2 expression and subsequent PGE2 formation. PGE2 binds to EP2 and EP4 receptors to activate cAMP/PKA and PI3K/Akt pathways which inhibit GSK-3 to release $\beta$-catenin ($\beta$-cat). $\beta$-catenin then translocates into nucleus and controls a number of gene tran-scriptions by forming a complex with TCF and LEF. Nitric oxide (NO) increases PI3K-dependent Akt activation that enhances $\beta$-catenin nuclear translocation. In addition, ER physically associates with IGF-1 receptor to also activate PI3K/Akt pathway. PGE2 and NO are required to mediate IGF-1-mediated activation of PI3K/Akt, but their exact cellular contribution is unknown. Wnt binds to Lrp5/6 and Frizzled (Fzd) to activate Dishevelled (Dvl) that inhibits GSK-3 to promote $\beta$-catenin nuclear translocation. $\beta$-catenin/TCF/LEF complex expresses more Wnt to enhance Wnt/$\beta$-catenin signalling. Sclerostin (Scl) physically binds to Lrp5/6 to disrupt Wnt/$\beta$-catenin signalling. Lrp4 facilitates sclerostin inhibition of Wnt signal. (Ob diff = osteoblast differentiation; Oc diff = osteoclast differentiation)

PGE2 engenders bone anabolic responses both in vivo [43, 128, 129, 158, 167, 203] and in vitro [3, 129, 177]. Although the exact molecular signalling pathway is yet to be established, two PGE2 receptor isoforms, EP2 and EP4, have been identified to be involved in loading related bone formation. While both receptors elicit bone formation, Minamizaki et al. illustrated that each receptor activates separate MAPK pathways to mediate anabolic action of PGE2 [177]. No study has yet reported on EP1 and EP3 receptor involvement in bone formation.

The anabolic response of PGE2 may be mediated by the combined effects arising from nuclear translocation of a transcription factor $\beta$-catenin, a crucial signalling pathway for normal bone homeostasis (Fig. 11). In osteocyte-specific $\beta$-catenin-deficient mice, dramatically impaired bone formation was observed along with enhanced osteoclast number and activity [138]. Similar results were observed in

mice with $\beta$-catenin-deficient osteoblasts [94, 111]. Moreover, bone loading and PGE2 induce $\beta$-catenin nuclear translocation [93, 124, 131, 147, 273]. By acting on EP2 and EP4 receptors, PGE2 produced by mechanical loading activates cAMP/PKA and PI3K/Akt pathways which inhibit GSK-3 to relieve $\beta$-catenin from its proteasomal degradation [138, 273]. $\beta$-catenin then translocates into the nucleus to form a complex with members of TCF/LEF family which controls gene transcription [138]. Lara-Castillo et al. highlighted the observation that early $\beta$-catenin activation is mediated by PGE2, independent of the Lrp5/Wnt pathway, a potent signal for $\beta$-catenin activation [147].

How then do PGE2 and $\beta$-catenin bring about the bone anabolism? In this section, four mechanisms will be described:

(i) Prevention of bone cell apoptosis: Bone cell apoptosis is associated with diminished bone formation as seen in excess glucocorticoid administration [267]. Thus, several studies speculated that mechanical loading supports bone formation by preventing osteoblast apoptosis [192, 247]. It was later found that both PGE2 and $\beta$-catenin exhibit protective effects on osteocyte apoptosis and that inhibition of $\beta$-catenin abrogated PGE2s protective effects [131], confirming their association. The same mechanism is utilised by PTH, an anabolic agent for osteoporosis treatment [122].

(ii) Downregulation of sclerostin: Sclerostin is a Sost gene product which is a potent inhibitor of bone formation by blocking the Wnt/$\beta$-catenin pathway (Wnt and sclerostin detailed in Sect. 4.3) [155]. Through $\beta$-catenin translocation, PGE2 reduces sclerostin expression [87, 93, 147], and this downregulation relieves antagonism of Wnt/$\beta$-catenin signalling which promotes proliferation of osteoblasts and contributes to the functional adaptation of bone mass and architecture [87]. In other cell systems, however, there is contradictory evidence of PGE2 enhancing sclerostin expression in human dermal fibroblast culture by acting on EP1 receptor [85]. Its relationship to bone formation has not been tested.

(iii) Increase in OB differentiation and suppression of OC differentiation: PGE2 is associated with enhanced expression of osteoblastic differentiation markers (alkaline phosphatase and osteocalcin) and subsequent augmentation of bone mineralisation [3, 43]. In both osteocytes and osteoblasts, $\beta$-catenin deficiency increases the ratio of receptor activator of nuclear factor kappa-B ligand (RANKL) to osteoprotegerin (OPG) (RANKL:OPG ratio), a gauge for the magnitude of osteoclastogenesis, and consequently heightened osteoclasts bone resorptive activity [94, 111, 138]. Conversely, $\beta$-catenin upregulates osteoprotegerin (OPG), an antagonist of osteoclast differentiation, and enhances bone formation by inhibiting osteoclastic differentiation [94, 111]. Lutter et al. observed direct evidence of PGE2 inhibiting precursor osteoclast differentiation which is hypothesised to control the area of bone resorption by restricting the number of active osteoclasts [162]. These findings suggest that $\beta$-catenin promotes differentiation of osteoblasts and inhibits osteoclast differentiation in order to reinforce the responses to loading.

(iv) Upregulation of Cx43 gap junction expression: Cx43 takes a significant role in mediating the initial response to bone loading by acting as gap junctions for neighbouring osteocytes, allowing communication with other bone cells to harmonise their interactions. For example, Cx43 deficiency engenders local reduction in mineralisation [25]. On the other hand, PGE2-induced $\beta$-catenin binds to the Cx43 promoter to upregulate Cx43 expression, which is associated with increased bone mineralisation [273].

**Nitric Oxide**

Along with PGE2, nitric oxide (NO) is released within minutes upon bone loading [12, 74] in a stress magnitude-dependent manner [8]. Interestingly, an increase in NO precedes the PGE2 response [132], and NO is required for the progressive increase in loading-induced PGE2 [125]. Moreover, NO appears to play pivotal role in transduction of mechanical stimulus as inhibition of nitric oxide synthase (NOS) significantly reduces mechanically-induced bone formation [74, 259].

Mechanically-induced NO release was believed to be mediated through endothelial NOS (eNOS) [135]. However, emerging evidences made this belief doubtful. eNOS knockout mice (eNOS$^{-/-}$) did not exhibit any differences in bone quality compared to wild-type (WT) and both osteoblastic cultures of WT and eNOS$^{-/-}$ mice produced significant amounts of NO upon PFF [14]. Furthermore, the role of NOS in NO production became questionable as triple knockout of all three isoforms of NOS increased bone density [226].

The cellular response mediated by NO is still poorly understood. NO may modulate osteoblastic mechanotransduction by activating cGMP/protein kinase G II-dependent Src that increases PI3K-dependent Akt activation and subsequent $\beta$-catenin nuclear translocation (Fig. 11) [204]. Moreover, NO is a required element to engender loading-induced stabilisation and activation of $\beta$-catenin in MLO-Y4 osteocyte cultures [230]. It is possible that the bone anabolic effect of NO may occur through reduction in bone resorption [168] and decreased sclerostin expression [56]. In summary, there are still many unknown mechanisms by which NO is produced and mediates its cellular response.

## *4.2 Oestrogen Receptor Involvement in Load Sensing*

Millions of women are predisposed to osteoporosis when their levels of oestrogen decline at the menopause. It is therefore hypothesised that oestrogen is involved in adaptive bone responses to load bearing through the two isoforms of oestrogen receptors (ER$\alpha$ and ER$\beta$). An unequivocal role for oestrogen in mechanotransduction has been difficult to ascertain because oestrogen levels, in vivo, have not been directly linked to mechanical sensitivity of bone cells. Lanyons group argues that this is in fact consistent with observations in vitro and in vivo that oestrogen receptors (ER$\alpha/\beta$), rather than oestrogen itself, mediate the adaptive response [52].

## Oestrogen Receptor $\alpha$

In vitro studies on ER$\alpha$ illustrated that ER$\alpha$ mediates proliferation of osteoblastic cells in response to mechanical strain by using pharmacological ER$\alpha$ antagonist [52, 88, 279] and ER$\alpha$-deficient osteoblastic cells [121, 148, 149]. These in vitro data were mirrored in several in vivo studies which demonstrated lower adaptive response to mechanical loading in cortical bones of ER$\alpha$ knockout female mice, suggesting ER$\alpha$ may contribute to mechanosensitivity in cortical bone formation [148, 149, 233, 269] (Fig. 11). Interestingly, ER$\alpha$ exhibited sex-dependent effects on the adaptive response whereby ER$\alpha$ promoted cortical adaptation in females without affecting cancellous bone, whereas it suppressed mechanosensitivity for both cortical and cancellous bone in males [233].

Conversely, bone cell-specific knockout of ER$\alpha$ in female mice produced greater cortical and cancellous adaptive responses than their littermate controls, whereas male counterparts had similar responses [176]. This suggests that ER$\alpha$ in female osteoblasts and osteocytes can repress mechanotransduction, but is not the case for ER$\alpha$ in males. Similar findings were seen in female mice treated with tamoxifen (ER$\alpha$ antagonist and ER$\beta$ agonist) in vivo [245]. Melville et al. stated the difference could have arisen from using global ER$\alpha$ knockout mice in other in vivo studies in contrast to using bone cell-specific ER$\alpha$-deficient mice [176]. Global ER$\alpha$ knockout mice exhibit altered hormone levels which could indirectly affect bone remodelling and bone mass [161, 238], possibly confounding the results. More studies utilising bone cell-specific ER$\alpha$-deficient mice are required to elucidate the role of ER$\alpha$ in mechanotransduction.

Although the role of ER$\alpha$ in mechanotransduction remains unclear, several studies have suggested potential signalling pathways ER$\alpha$ may mediate to promote bone formation in response to mechanical loading. ER$\alpha$ contributes to PGE2 signalling by sensitising mechanically induced COX-2 expression [159]. Moreover, ER$\alpha$ is associated with phosphorylation of ERK1/2 and activation of Wnt/$\beta$-catenin pathway [1, 6], which are also observed in application of mechanical loading and PGE2 [27, 273]. Therefore, ER$\alpha$ may act as one of the necessary components to engender adaptive bone response to loading. Moreover, insulin-like growth factor-1 (IGF-1) appears to be involved in ER$\alpha$-mediated osteoblastic proliferation [121]. Activation function 1 (AF-1), one of the transactivation domains of ER$\alpha$, may physically associate with the IGF-1 receptor to activate PI3K/Akt/$\beta$-catenin pathway to stimulate the bone adaptive response (Fig. 11) [246, 269]. It was revealed that PGE2 and nitric oxide are also required for IGF-1-mediated activation of Akt [246]. Lastly, ER$\alpha$ upregulates mechanically related Cx43 expression in MLO-Y4 cells in ligand-dependent manner, suggesting that ER$\alpha$ sensitises osteocyte to strain-induced bone formation [207]. Thus, pathways mediated by ER$\alpha$ orchestrate the transduction of mechanical forces into an adaptive response.

## Oestrogen Receptor $\beta$

Similar to ER$\alpha$, there is inconsistency present in ER$\beta$ studies. In-vitro studies agree that ER$\beta$ suppresses ER$\alpha$−mediated osteoblast proliferation to mechanical strain

[88, 121, 149]. However, female ER$\beta$ knockout mice exhibit lower loading-related osteogenic responses, suggesting that ER$\beta$ contributes to mechanosensitivity [149]. Unfortunately, the in vitro data from the same study was not reflected by this in vivo result. ER$\beta$ may engender bone formation by downregulating sclerostin [88], which supports the in vivo data by Lee et al. [149].

Conversely, female ER$\beta$ knockout mice show increased cortical adaptation to mechanical loading, meaning ER$\beta$ suppresses mechanical loading response in cortical bone [232, 233]. The increased cortical mechanosensitivity in ER$\beta$ knockout mice may be explained by upregulation of ER$\alpha$ [36]. ER$\alpha$ is associated with activation of loading-related $\beta$-catenin signalling [6] and hence, the upregulation of ER$\alpha$ in ER$\beta$ knockout mice may enhance the mechanical adaptation [36]. Of interest, Saxon et al. suggests that ER$\alpha$ and ER$\beta$ compete against each other such that signalling through ER$\alpha$ enhances adaptation at trabecular and endocortical surfaces, while signalling through ER$\beta$ suppresses the response at the periosteal surface [232]. In comparison to ER$\alpha$ studies, there are less studies of ER$\beta$ available, and more studies need to be performed to fully delineate how ER$\beta$ participates in mechanotransduction.

## 4.3 Intermediate Responses: RANKL and Wnt

**RANKL**

RANKL is a membrane bound factor which is essential for osteoclastogenesis since RANKL deficiency causes severe osteopetrosis due to a complete lack of osteoclasts [184]. Two in vivo studies [184, 274] illustrated that osteocytes are the primary sources of RANKL that contribute to the bone remodelling process and that osteocytes can act as mechanosensors to regulate bone mass by adjusting RANKL expression level. Consistent with this effect, osteocytes under high strain can inhibit osteoclastic bone resorption [140]. Moreover, in vitro loading of osteocytic cells enhances the expression of OPG and reduces the RANKL/OPG ratio, attenuating osteocytes potential to promote osteoclastogenesis [140, 191, 248, 278]. Kulkarni et al. reported that matrix extracellular phosphoglycoprotein (MEPE) was implicated in this response [140]. The diminished osteoclast formation was also observed in primary osteocyte cultures in serum from rheumatoid arthritis patients after the application of pulsatile fluid flow [191].

The repression of RANKL in response to mechanical loading is, in fact, orchestrated by other mechanically responsive elements. Nitric oxide takes part in this process because NOS inhibition prevents the strain-related suppression of RANKL and osteoclastogenesis in vitro [202, 248]. PGE2 and $\beta$-catenin may indirectly attenuate RANKL expression by downregulating the expression of sclerostin which dose-dependently reduces OPG and potentiates the osteocyte's ability to form osteoclasts in RANKL-dependent manner [268]. Osteocytic RANKL expression was not significantly altered in osteocyte-specific $\beta$-catenin-deficient mice [138], suggesting that Wnt/$\beta$-catenin signalling does not directly influence RANKL level.

### Wingless-Related Integration Site (Wnt) Signalling

Wnt is a group of secreted glycoproteins that are one of the most critical elements of bone mass regulation. Here, two different Wnt signalling pathways (canonical and non-canonical) will be discussed briefly in relation to mechanical loading.

Canonical Wnt signalling pathway (or Wnt/$\beta$-catenin signalling) involves secreted Wnt forming a complex with low-density lipoprotein receptor-related protein 5 or 6 (Lrp5/6) and the 7 transmembrane domain receptor Frizzled (Fzd) (12) [138]. The complex triggers Dishevelled (Dvl) activation [28] which leads to inhibition of GSK-3, promoting $\beta$-catenin nuclear translocation. Mechanical loading enhances Wnt3a gene expression and the canonical signalling pathway [229, 231], and this response could be produced by early PGE2 mediated $\beta$-catenin activation independent of Lrp5/Wnt. The activated $\beta$-catenin upregulates the expression of Wnt which further enhances $\beta$-catenin activation via the canonical pathway [28]. Numerous functions of canonical Wnt signalling in response to mechanical stress are heavily shared with those of PGE2 and are addressed in the previous Sect. 4.1. The significance of the canonical Wnt pathway is accentuated by sclerostin's ability to severely abrogate bone cell responses to mechanical stimuli (sclerostin detailed in the next Sect. 4.4).

Non-canonical Wnt signalling is different to canonical Wnt signalling in that it interacts with Fzd and Dvl in $\beta$-catenin- and Lrp5/6-independent fashion to trigger alternative intracellular events [178]. Unfortunately, there are a limited number of available studies on the role of non-canonical signalling on bone cell mechanotransduction. Instead, several studies on this signalling pathway have been performed on mesenchymal stem cells. In planar cell polarity (PCP) pathway, one of the non-canonical Wnt pathways, the binding of Wnt to Fzd activates Dvl which forms a complex with Daam1 [15]. This complex activates RhoA/ROCK pathway that mediates cytoskeletal reorganisation (Fig. 12) [178]. Thompson et al. summarised the importance of the cytoskeleton reorganisation [249]. In response to fluid shear



**Fig. 12** Planar cell polarity (PCP) pathway: Wnt binds to Fzd to form a complex of Dvl/Daam1 which activates RhoA/ROCK pathway to mediate cytoskeletal reorganisation
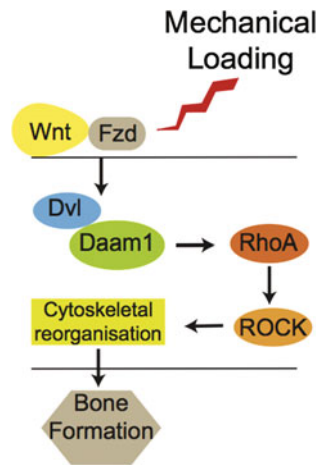
stress, actin fibres rearrange themselves to form the contractile stress fibres which sense loading at the cell membrane level and mediate osteogenic differentiation. Comparably, in murine mesenchymal stem cells, non-canonical Wnt5a signalling involving Ror2 and RhoA was required for mechanically induced osteogenic differentiation [7], and in human adipose tissue-derived mesenchymal stromal cells, Wnt5a was associated with ROCK upregulation and the subsequent stress fibre formation that stimulated osteogenic response [231]. Although these findings have not been tested in bone cells directly, based on the current knowledge, it can be hypothesised that the non-canonical Wnt pathway may participate in mechanically induced stress fibre formation in bone cells since the reorganisation of actin cytoskeleton is one of the important steps of mechanotransduction [39].

Despite a limited number of studies, it is becoming evident that non-canonical Wnt signalling is implicated in mechanotransduction. A recent study on osteoblastic cells illustrated that RhoA was activated by flow treatment and was required for loading-induced cellular responses such as PI3K/Akt and ERK1/2 signalling [101]. Furthermore, osteoblasts utilised both canonical Wnt and Wnt/PCP pathways to fine-tune bone architecture in terms of rate and orientation of osteoblast division [89]. More studies need to be performed to fully elucidate how non-canonical Wnt signalling contributes to mechanotransduction.

## *4.4   Sclerostin as a Master Regulator of Mechanical Loading*

Sclerostin is a protein encoded by the Sost gene, which is centrally expressed by osteocytes [270]. It was discovered by deciphering the pathogenesis of the high bone mass disorders, sclerosteosis and Van Buchem disease. In these conditions, sclerostin is absent or present in significantly small amounts [263]. The impaired sclerostin level seen in these disorders led to speculation that sclerostin may be involved in regulation of bone homeostasis and extensive studies have since proven its role.

Sclerostin is a potent suppressor of bone formation. Absence of sclerostin in Sost knockout mice elicited similar skeletal characteristics to sclerosteosis patients, whereby the mice had greater bone mass density, bone volume, bone formation rate, and bone strength [156]. Corresponding results were observed in aged osteoporotic ovariectomised mice [157] and gonad-intact female cynomolgus monkeys [187] when they were treated with sclerostin-neutralising monoclonal antibody (Scl-Ab). Interestingly, Scl-Ab treatment in osteoporotic mice not only reversed osteoporosis caused by one year of oestrogen deficiency, but also produced greater bone mass and bone strength than controls [157]. On the other hand, transgenic mice overexpressing Sost had significantly reduced osteoblastic activity, leading to decreased bone mass, bone strength, and bone formation [270]. These results clearly indicate the role of sclerostin as a negative regulator of bone mass.

Several studies have shed light on how sclerostin mediates its effect. Sclerostin antagonises canonical Wnt signalling by physically interacting with Wnt coreceptor LRP5/6 and disrupting Wnt-induced Frizzled-Lrp complex formation (Fig. 11) [58, 155, 160, 237]. This suggests that lack of Sost function hyperactivates Wnt

signalling, leading to pathological bone overgrowth seen in sclerosteosis patients [237]. Recently, the $\beta$-propeller domain of LRP4 was shown to facilitate sclerostin inhibition of Wnt signaling [152], and this mutation was reported in a sclerostic patient who did not have a mutation in Sost [65].

Osteocytes adjust their sclerostin levels depending on the types of mechanical signals to which they are exposed (loading and unloading). Robling et al. demonstrated that ulnar loading of mice dramatically reduced Sost transcripts and sclerostin-positive osteocytes, and these effects were greater in portions of the ulnar cortex receiving greater strain [213]. Moustafa et al. added that the amount of loading-related osteogenesis was reflected in the magnitude of loading-related decreases in the percentage of sclerostin-positive osteocytes [182]. In contrast, Sost expression was significantly increased in mice exposed to unloading (tail suspension or sciatic neurectomy) [160, 182, 213] and in immobilised postmenopausal patients [92]. The disuse-induced increase in sclerostin-positive osteocytes was reversed by mechanical loading [182], and Sost knockout mice were immune to bone loss from unloading [160], suggesting that sclerostin is involved in the disuse response. Given its expression pattern, sclerostin provides a mechanism for osteocytes to locally regulate mechanotransduction by adjusting sclerostin output to modulate Wnt signalling and the subsequent bone response [213].

Since sclerostin acts as a strong regulator of mechanical loading, use of an antibody against sclerostin has opened up a new possibility to a more potent osteoporosis treatment. Romosozumab (AMG 785), a sclerostin monoclonal antibody, has been tested in phase 1 [189] and phase 2 [174] clinical trials with promising results. Currently, there are four phase 3 clinical trials in progress and they are reviewed by Chapurlat [38]. A schematic illustration of the mechanical loading induced molecular cascade is shown in Fig. 13. Loading induces fluid shear on osteocyte processes which regulates NO, PGE2 and Scl concentration in the local bone environment [253].

## 5 Loading Physiology: Translating Findings from Animal Models to Clinical Applications in Humans

### 5.1 Changes of Bone Mass with Age

Sections 3 and 4 of this chapter described mechanical characteristics derived from controlled loading studies in animals that might optimise the biological response to loading the skeleton. A key question is whether these characteristics can optimise bone mass during growth to reduce the risk of fracture in adulthood and old age. Osteoporotic fractures occur because reduced bone mass decreases the safety factor for skeletal loading. This can result from age-related bone loss or failure to maximise peak bone mass [114]. During childhood and adolescence the skeleton undergoes rapid change due to growth, modelling and remodelling, the processes that effect bone accrual. Bone mass increases substantially during adolescence, reaching a plateau,
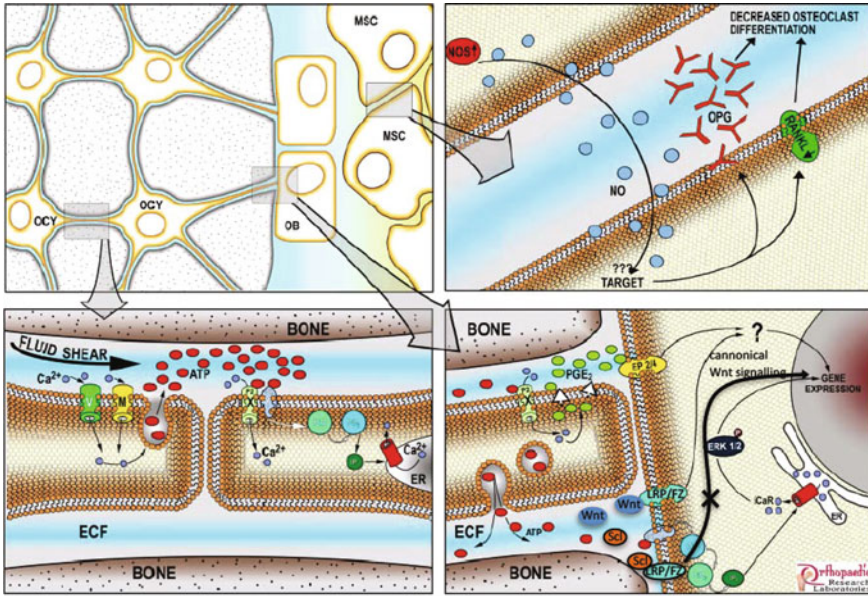
**Fig. 13** Fluid shear on osteocytes (OCYs) induces a cascaded of molecular events including influx of extracellular $Ca^{2+}$ via voltage-sensitive (V) and perhaps mechanosensitive (M) channels. Shear stress also causes vesicular ATP release, which binds to the purinergic receptors P2X (ionotropic) and P2Y (metabotropic). P2Y is required for $Ca^{2+}$ release from intracellular stores. NO, PGE2 and sclerostin are also regulated in response to fluid shear stress. Catabolic response due to mechanical disuse is mediated via a decreased NO production which subsequently upregulates NF-kB ligand (RANKL) and downregulates OPG, ultimately leading to increased RANKL/OPG ratio driving osteoclast formation. Disuse upregulates sclerostin leading to inhibition of canonical Wnt signalling and consequently reduced proliferation of OB. Anabolic response due to overloading is mediated via decrease in sclerostin production and increased $\beta$-catenin signalling leading to increased OB formation. At the same time the RANKL/OPG ratio decreases due to overloading. (OB = osteoblast; Wnt = wingless, Scl = sclerostin; LRP/FZ = LRP5/6 and Frizzled receptor complex) (Image adapted from Turner and Robling [253])

being peak bone mass (PBM), in the late teen or early adult years [19]. Longitudinal data measured from childhood (age 8) to young adulthood (up to age 30), demonstrates that PBM occurs by the end of the teenage years, or early twenties [19]. Importantly, 33−46% of adult bone mineral is accrued over a 4-year period of the adolescent growth spurt. In females, this accrual represents double the amount of bone mineral that will subsequently be lost during the post-menopausal years from age 50 to 80 years [5].

Some fields of clinical practice are sceptical that physical activities can provide sufficient mechanical stimulus for adaptation that reduces fracture risk in the elderly. Certainly, there is evidence that the growing skeleton has greater potential for functional adaptation than adaptation in adults [68, 126, 170, 171]. The fact that the difference in bone density and strength between dominant and non-dominant arms

of tennis players is greater in players who started before puberty, is a classical example of this observation [126, 137]. These activities certainly provide a controlled test for the efficacy of physical activity during growth and maturation, but do not provide a guide to optimise bone strength in the public health context.

Studies of general physical activity overwhelmingly demonstrate that the skeleton is more sensitive to mechanical loading during the pre-pubertal and early pubertal periods, than post-puberty or adulthood [11, 29, 73, 165, 170, 171, 179, 196]. Physical activity that loads the skeleton will therefore optimise peak bone mass during these periods, and be more effective for skeletal adaptation than in adults, where the outcome of loading is conservation, rather than acquisition. There is also evidence that the increase in oestrogen levels in males and females during adolescence augments the expression of functional oestrogen receptors (ER$\alpha$) available to effect adaptive responses in bone [52, 280], explaining the enhanced sensitivity to physical activity during early puberty.

Unilateral activities provide a well-controlled model, and physical activity demonstrates positive effects, but experiments to optimise the osteogenic effects of exercise are difficult to accomplish in humans. The heterogeneity of exercise designs for animals also varies widely, making it difficult to draw conclusions about optimising skeletal adaptation during growth. Another important issue is that areal bone mineral density (aBMD), as assessed by dual energy x-ray absorptiometry (DEXA), is an inappropriate and misleading variable to use as an endpoint for physical activity, or especially as a surrogate for bone strength. This is partly because DEXA fails to distinguish variations in geometry and density [67, 199], but also because its resolution is too low to detect small changes in bone dimensions that elicit substantial increases in bone strength. Consequently, the loading models described in Sect. 3 enabled controlled loading in which the load magnitude, frequency and partitioning could be controlled and quantified. That set of models has advanced our knowledge of dynamic skeletal adaptation considerably during the past 20 years and defined the characteristics of an optimal loading environment.

## 5.2   Effective Loading Characteristics

Controlled loading studies provide biological and mechanical guidelines to understand the key parameters to maximise effects of physical activities. As described above, static loading provides little adaptive stimulus to bone adaptation [108, 109, 219, 258] and, new bone formation is stimulated when a threshold magnitude of loading is exceeded [257]. This depends on the interaction between strain rate and loading amplitude that modulates this threshold [180, 186, 257, 258]. In one clever experiment, Turner et al. varied the proportion of static and dynamic loading applied to rat tibiae [258], creating equivalent peak strains in the tissue but with varying strain rates. After 36 cycles per day for 10 days, bone formation was significantly increased in the two experimental groups with the highest strain rate, compared to the groups with lower strain rate, and was not increased at all in the group subjected
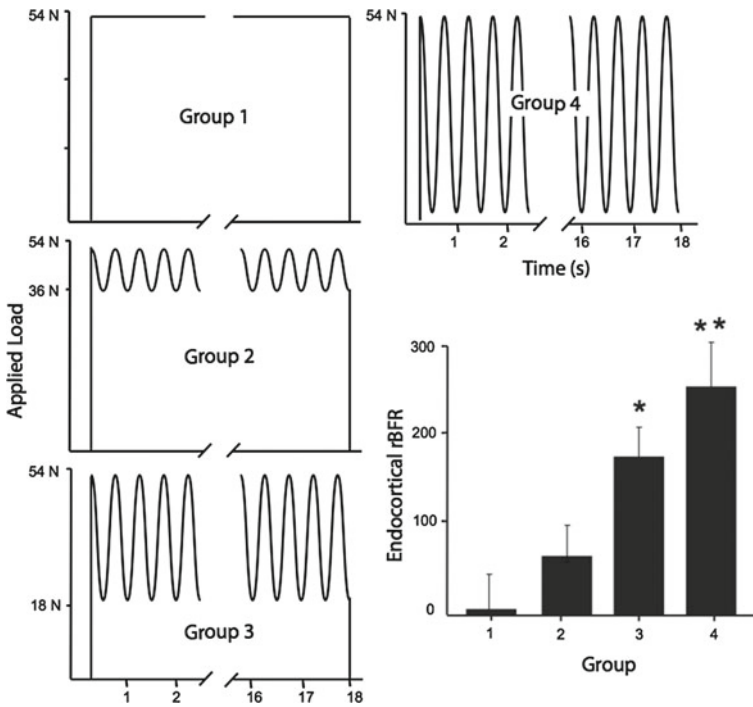
**Fig. 14** Turner et al. [258] varied the proportion of static and dynamic loading as shown in Groups 1–4. Relative bone formation rate (rBFR:*right* minus *left*) was proportional to strain rate and not peak strain, and unaffected by static loading (Group 1). The peak strain for all groups was about 1300 microstrain (max applied load of 54 N), while strain rates for Groups 1–4 were approximately 0, 0.013, 0.026, and $0.039\,s^{-1}$. * = significant to Group 1 and ** = significant to Group 1, 2 ($P < 0.05$). ( Image adapted from [258])

to a static 54 N load (Fig. 14). The effect of strain rate occurs because bone tissue is viscoelastic and fluid flow mechanics underlie mechanotransduction [117, 256]. For externally applied loads, during exercise for example, these responses are optimal in a range of loading frequencies up to about 2.0 Hz [257, 258]. In the context of exercise, activities like jumping, that create relatively high strain rates, will be more adaptive than simply walking or doing isometric exercises.

A key observation from controlled loading is that only a small number of loading cycles are required to activate bone formation [70, 219, 221]. This effect saturates relatively quickly so that increasing the duration of loading beyond about 40 cycles per session has little additional effect [219]. In terms of bone strength, long exercise sessions are therefore unnecessary to achieve a training effect. Importantly, a given physical activity will have greater skeletal effect if it is divided into short bouts with rest periods [209–211]. This is because bone cells accommodate quickly to loading stimuli, but sensitivity returns after a period of rest. For example, adaptive bone formation was 80% greater when loading was partitioned into 4 bouts of 90 cycles

per day for 2 weeks, compared to one bout of 360 cycles [209]. Over a 16-week period, groups that received 4 × 90 cycles per day also had significantly greater bone strength compared to those receiving a single session of 360 cycles [211]. The increased strength was attributed to efficient geometric adaptations that resist axial bending.

Based on these relationships, Turner and Robling developed an osteogenic index (OI) that accounts for loading intensity (essentially peak load × loading frequency), bone cell desensitisation and the time between sessions [252]. Using a relatively simple calculation, the index estimates how changes to design of an exercise program can optimise its osteogenic characteristics. For example, a program of 300 jumps per day, done twice a week, generates an OI of 33, whereas a program of 120 jumps/d, 5 times/week produces an OI of 70. The OI of 600 jumps/week is therefore doubled if performed 5 times, rather than just 2 times. While this doesn't predict the exact nature of an adaptation, it can effectively inform our design of programs to maximise the skeletal outcomes, while reducing unnecessary exercise duration or training sessions.

## 5.3 Translating Controlled Loading to Physical Activity

Although stronger bones are evident in children who undertake greater levels of normal physical activity [73], or compete in gymnastics [59, 60, 63], the principles learned above are being adopted increasingly for exercise programs [84, 165, 170, 171, 175, 196]. Although many controlled trials applied some of the loading principles to childhood physical activity, the Healthy Bones II [169, 171] and "Action Schools! BC" programs [165, 175] specifically aimed to optimise the osteogenic index in a practical and sustainable activity program. In Action Schools! BC, bone loading was simply an extra 15 min of activities each school day, and "bounce at the bell" [175] in which three minutes of jumping activities were undertaken at each school bell (three times a day). This program resulted in greater bone mass (BMC) at the lumbar spine and femoral neck of about two percent in boys and girls.

It's difficult to assess the structural adaptation, and changes in bone strength, using DEXA-based outcomes. But the program in Action Schools! BC, used quantitative computed tomography (pQCT) to demonstrate the adaptation, showing increases in indices of bone strength at the distal tibia [164]. In addition to this structural adaptation, increases were observed in spine and total body BMC of pre-pubertal boys, and BMC and section modulus of the femoral neck (an index of bending strength) in peri-pubertal girls [165]. By optimising the osteogenic index, this program was able to achieve modest, but significant increases in parameters of bone strength that were equivalent to outcomes in other studies that used more intensive bone-loading programs.

**Fig. 15** After 16 weeks of axial loading of the rat ulna, small increases in bone mineral density (aBMD) imparted large increases in ultimate force (64−87%) because the new bone formation was strategically placed at the most biomechanically relevant sites (Image adapted from [211])
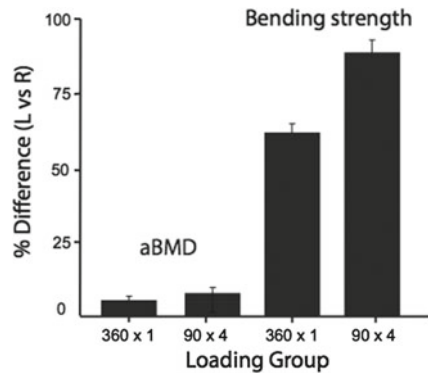


## 5.4 Maximising Bone Strength

As noted above, the goal of any program is not simply to alter bone mass, but to increase bone strength through appropriate changes in geometry. This can occur independently of material properties, which can also be adapted through altered remodelling. This principle is exemplified where a small increase (5%) in aBMD of rat ulnae is contrasted with an incredible 64% increase in ultimate breaking strength after 16 weeks of axial loading [211] (Fig. 15). The improvement in strength occurs because appositional bone formation at the periosteal surface provides a disproportionate mechanical advantage at the locations of greatest strain. Following the principle of an I-beam, the small addition of lamellar bone is strategically placed distant to the axis of bending, where it provides the maximum resistance to bending moments.

Unfortunately, most studies of exercise rely upon DEXA to assess skeletal outcomes in terms of aBMD, missing any subtle geometric improvements. To partially overcome this limitation, a novel analysis program for the hip was developed for DEXA to provide mechanical indices to assess changes in bone strength [21] and has been applied to numerous studies [63, 72, 73]. However, direct assessment of density and geometry has been achieved through the increased use of pQCT [51, 107, 163, 164, 166]. This specifically enables distinction between geometry and density, proving that increased bone strength, not mass, is the goal of adaptation. The most difficult challenge to overcome has been to provide evidence that adaptations achieved during childhood and adolescence are carried forward into adulthood and old age.

## 5.5 Persistence of Childhood Bone Adaptation

It is practically and experimentally impossible to prove that adaptations developed in childhood and adolescence, reduce the risk of osteoporotic fracture in old age.

This would require well-designed longitudinal trials over such a long life-span that they are simply not possible. There are, however, some longitudinal cohorts that have followed children from a young age in to adulthood, and these are starting to provide evidence for continuity of mechanical adaptations [10]. Other cohorts have used retrospective analysis to examine this question, but confounding variables, such as self-selection for physique in particular activities, reduce the certainty that a given sporting involvement created long-lasting fracture resistance [260]. Studies of sporting populations into adulthood led to evidence that higher bone mass achieved by athletes during childhood was lost as adults [98, 127, 185]. Some of these studies were cross-sectional, or started relatively late in adolescence, when it is harder to control for confounding variables such as maturity. Effective longitudinal studies through adolescence have now reported sustained effects on BMC accrual up to 8 years after training, or cessation of a physical activity intervention [18, 97, 234]. In addition, physically active children achieve greater bone mass during adolescence than inactive children [11, 73], and their higher bone mass is maintained into adulthood [18].

As noted above, modest increases in bone mass can be associated with substantial improvements in bone strength, as a result of improved geometry. It is very likely that studies using DEXA alone have misinterpreted the distinction between preservation of bone mass or architecture in ageing adults. Because rodents achieve old age over a two-year period, they provide a good experimental model to test this principle. To test the conservation of bone structure into old age, the forearm of rapidly growing rodents was subjected to a short 7-week exercise program, following which they were limited to cage activity for up to 92 weeks (equivalent to senescence for rodents) [265]. Increases in "bone mass" induced by exercise (aBMD and BMC) were not retained into adulthood. However, bone structural changes were retained throughout life, manifested in greater strength and fatigue properties in the trained animals [265]. Similar retention of exercise-induced structural adaptation from childhood is evident following cessation of racquet sports in tennis players who had started training at 10 years of age [100, 136], and in baseball players in whom the benefits of throwing-related physical activity during youth were maintained lifelong [266]. These data from excellent animal studies, and long-term evaluation of athletes, support the hypothesis skeletal adaptations achieved during childhood effect structural improvements in the skeleton that persist well in to adulthood. The greater strength afforded by these structural changes potentially reduce the risk of fracture in adults, more than that predicted by bone mass alone.

# 6   In Silico Models of Bone Adaptation

The experimental observations on bone adaptation and the premise of Wolff's law were early recognised by the engineering community which identified similarities between bone adaptation and the problem of structural and material optimisation commonly found in the design of engineering structures. Indeed, it was again Galileo

Galilei who first investigated optimal shapes of structural elements [90]. In his book, *Discorsi*, Galileo performed systematic analysis into the fracture behaviour of brittle materials. In this context, he described the influence of the shape of a body (hollow bodies, bones, blades of grass) on its strength, thus posing and answering questions addressing the "Theory of bodies with equal strength". The other pioneer in this area was Robert Hook (1653–1703) who established classical theory of linear elasticity.

Continuous improvements in materials and structural developments has led to the emergence of a new area with scope on computer aided engineering, which focuses on the optimisation of structures. This field is commonly referred to as *Structural Optimisation* or *Topology Optimisation*. A comprehensive review on different approaches in topology optimisation is given by Eshenauer and Olhoff [61]. Most commonly bone's adaptive responses are, considered to be, governed by an "optimisation process" making bone a "least weight" structure with respect to its actual mechanical loading [9, 151]. Topology design in the field of bone mechanics has been addressed by, e.g., Reiter [206], Fernandes et al. [64], and Bagge [9] and the use of special material models for topology design combined with bone remodelling schemes is, e.g., discussed in Mullender et al. [183] and Pettermann et al. [197].

In the following, we will focus on the mathematical modelling of bone adaptation with a focus on cortical bone modelling and remodelling. One key feature in all the developed computational models is the use of an a priori assumed "error signal" to drive the (re)modelling process. The error signal is commonly assumed to be the difference between the mechanical state in its equilibrium configuration (i.e., the CSS defined in Sect. 2) and the current mechanical state (following some perturbation to the bone such as a change in mechanical loading). The error signal is then used to drive the net adaptation process. The differences in the various bone (re)modelling theories lie mainly in the mechanical variables that are used to drive (re)modelling, while some use tensorial quantities, such as the strain tensor, others use scalar quantities such as effective stress or strain energy density.

It should be noted that most adaptation models developed today are based on purely mechanical considerations, with no direct links being established between mechanical loading and cellular activities in the (re)modelling process. One of the few mechanobiological models which explicitly takes into account bone-cell interactions in the remodelling process together with including a mechanical feedback based on biochemical regulatory factors was developed by Pivonka and co-workers [198, 235]. We will briefly discuss the major features of this model.

Another aspect most commonly not addressed in these models is to take into account the dynamical loading pattern. Instead most models only use peak strain or peak strain energy density as the error signal. In order to take into account the temporal/dynamical aspect of the loading pattern one needs to define characteristic loading times and include superposition of different loading scenarios such as walking and running. We will discuss how to include the dynamical patterns in bone adaptation models.

## 6.1 Cowin's Theory of Adaptive Elasticity

One of the earliest models of bone adaptation was proposed by Cowin and Hegedus who developed the theory of adaptive elasticity [47]. In their framework bone remodelling was described in thermomechanical continuum theory sense as chemical reaction and mass transfer between constituents. The theory developed by Cowin and co-workers is general in the sense that it can be applied to both, cortical [48] and trabecular bone remodelling [49].

Using the notation of Cowin and van Buskirk the rate of surface remodelling can be defined for a point with coordinates $\mathbf{Q}$ and surface normal $\mathbf{n}$ as:

$$U = C_{ij}(\mathbf{n}, \mathbf{Q}) \left\{ E_{ij}(\mathbf{Q}) - E_{ij}^0(\mathbf{Q}) \right\} \tag{1}$$

with $C_{ij}$, $E_{ij}$ and $E_{ij}^0$ corresponding respectively to the tensors of remodelling rate, strain and reference strain.

For net internal remodelling, Cowin and Hegedus proposed [47]:

$$\dot{e} = a(e) + tr\left\{ A(e)\mathbf{E} \right\} \tag{2}$$

where $\dot{e}$ is the rate of change in solid fraction of bone, $A$ is a remodelling rate parameter, and $\mathbf{E}$ is the strain tensor.

Hart and colleagues employed this formulation to predict cortical adaptation for different mechanobiological models in an idealised cylindrical shaft and to an ulnar osteotomy model [102]. Cowin and co-workers simulated trabecular bone remodelling at the apparent level by introducing a continuum fabric tensor that changes its degree of anisotropy, and accounting for changes in volume fraction over time. Note that in this formulation no coupling in bone formation and resorption events is enforced and consequently the adaptation response could be also interpreted as bone modelling response.

## 6.2 Stanford Model of Daily Stress Stimulus

Fyhrie and Carter developed a model of trabecular bone adaptation at the continuum level. In this model the apparent density of bone $\rho$ is proportional to a scalar quantity, i.e., the local energy effective stress [86]:

$$\rho \propto \bar{\sigma} = \sqrt{2E_{avg}U} \tag{3}$$

where $E_{avg}$ is the average Young's modulus and $U$ denotes the apparent strain energy density (SED). This formulation provided the foundations for many models developed subsequently based on the so-called daily stress stimulus [20, 35]. The goal of this model was to develop some function that is able to map the stress or strain
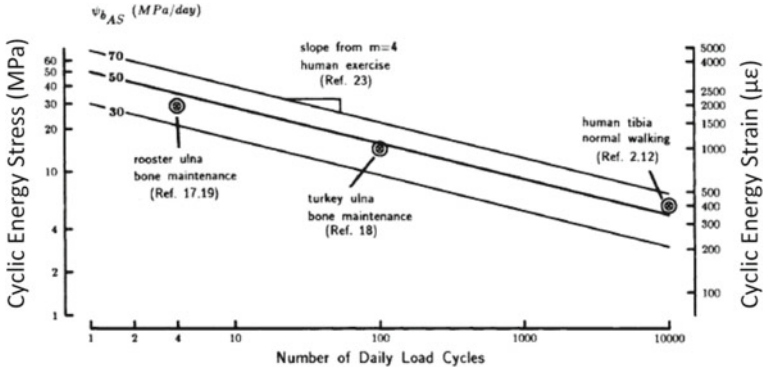
**Fig. 16** Graph of cyclic energy stress and cyclic energy strain versus the number of loading cycles per day required to maintain cortical bone mass. Experimental data points taken from studies by Rubin and Lanyon [221] and Lanyon and Hampson [146]. Curve fitting (log–log) of these data delivers estimates of the stress attractor ($\psi_{AS}$) of between 30 and 70 MPa/day and an $m$ value of about 4. (Image adapted from Carter [34])

stimuli experienced by a particular bone over an entire day into a single scalar quantity. As a first approximation, the daily stress (or strain) history is characterised by the magnitude of the energy effective stress (or strain) and the number of cycles of stress that is imposed at a specific location. Functions that have been proposed for defining the daily stress stimulus ($\psi$) are [35]:

$$\psi = \left( \sum_{day} n_i \bar{\sigma}_i^m \right)^{1/m} \tag{4}$$

were $n_i$ is the number of cycles of load type $i$, $\bar{\sigma}_i$ is the magnitude of the cyclic energy effective stress and $m$ is an empirical constant that is used to weight the relative contribution of stress magnitude and the number of loading cycles. The energy stress term does not distinguish between tension, compression and shear components of the stress tensor with respect to the local bone organization. It does, however, provide a simple measure of the local magnitude of the total cyclic strain energy stored at a point in the tissue. Note that the form of Eq. (4) is identical to that used to estimate the amount of fatigue damage created in the bone matrix.

Based on this definition one can mathematically express Fig. 16 in terms of the influence of the daily stress history on the net linear deposition of bone at periosteal and endosteal surfaces. When the daily tissue stress stimulus is equal to some "attractor stimulus" ($\psi_{AS}$), no bone apposition or resorption will occur. Carter and colleagues used the term attractor stimulus in analogy to stable non-linear dynamic systems which when perturbed aim to attain the original stable configuration. Furthermore, a so-called lazy zone has been introduced in this model formulation to indicate a region of homeostatic state rather than a point only. If the stress stimulus

exceeds this region bone formation will occur, while if the loading is reduced such that the stress stimulus is lower than the homeostatic region, bone resorption will occur. The local modelling error ($\psi - \psi_{AS}$) drives the bone modelling simulation.

## 6.3 Huiskes' Strain Energy Density Model

Huiskes and co-workers developed a continuous phenomenological model, conceptually similar to Cowin's adaptive elasticity and Carter's remodelling law, which accounts for adaptation in shape and material properties [116]. Strain energy density $U$ was used as the mechanical driver and replaced the remodelling equilibrium state from one single point by a range of mechanical stimulus values where the bone is assumed not to adapt, i.e., Carter's lazy zone. Huiskes and colleagues combined two three-linear remodelling curve models for (external) geometry modelling and (internal) stiffness remodelling. The relation between surface adaptation rate and SED, using the notation from their work, was linear as follows [116]:

$$\frac{dX}{dt} = \begin{cases} C(U - (1+s)U_n), & U > (1+s)U_n \\ 0, & (1-s)U_n \leq U \leq (1+s)U_n \\ C(U - (1-s)U_n), & U < (1-s)U_n \end{cases} \tag{5}$$

with $dX/dt$ as the rate of periosteal adaptation, $s$ the relative width of the lazy zone, $C$ a proportionality constant and $U_n$ the homeostatic SED. A similar equation was used for the variation of the elastic modulus $E$. This formulation was used to simulate the bone-density distribution (assuming that it is proportional to $E$) in a $2D$ model of the proximal femur, and in a $2D$ stress-shielding model of an intramedullary fixation. They showed the different bone configurations for variations of stem diameters, adaptation model thresholds and bonding characteristics of the implant. In later simulations Huiskes and co-workers also assessed trabecular orientation due to mechanical loading [115], indicating that the number and orientation of trabecular struts may be associated with the directions of applied loads.

## 6.4 Turner's Model of Dynamic Loading Stimulus

To incorporate Turner's three rules of bone adaptation into a mathematical formula, one must consider that peak strain rate is proportional to the frequency of the loading waveform and strain magnitude. Assuming a simple experimental system, where a long bone is subjected to either static or periodic cyclic loads $F(t)$, the applied load is given as follows [251]:

$$F(t) = A + B \sin(\omega t) \tag{6}$$

where $A$ is the magnitude of the stationary load, $2B$ is the peak-to-peak magnitude of the cyclic load, $\omega$ is the angular frequency (2 times frequency) of the cyclic load, and $t$ is time. If the bone is assumed to be a perfect cylinder (length $= L$ and radius $= R$) loaded in bending (i.e., $F$ acting in $L/2$), the peak surface strain (at $r = R$) is given by:

$$\varepsilon = \frac{M}{EI} R = \frac{FL/4}{E(\pi/4)R^4} R = \frac{4L(A + B\sin(\omega t))}{E\pi R^3} \tag{7}$$

where $M$, $I$ and $E$ are the cross sectional moment, moment of inertia (for a circular cross section) and the Young's modulus of bone respectively.

The strain rate on the bone surface is found by taking the derivative of Eq. (7):

$$\dot{\varepsilon} = \frac{4LB\omega\cos(\omega t)}{E\pi R^3} \tag{8}$$

The peak strain rate is proportional to $\omega B$, the stationary load $A$ does not affect the strain rate. Because the peak-to-peak dynamic strain ($\varepsilon$) is proportional to $2B$ and the loading frequency ($f$) is proportional to $\omega$, the strain rate is proportional to $f$. If we assume that the strain rate determines the tissue-level strain stimulus, an assumption supported by experimental studies then:

$$E = k_1 \varepsilon f \tag{9}$$

where $E$ is the strain stimulus, $k_1$ is a proportionality constant, is the peak-to-peak strain magnitude and $f$ is the frequency. Equation (9) gives the strain stimulus for a sinusoidal loading waveform. However, the result can be generalized using the Fourier method that allows any periodic loading condition (e.g., walking, running, or experimentally applied loading) to be expanded into a series of $n$ sine waves at different amplitudes and frequencies. For example, the trapezoidal loading waveform used by Rubin and Lanyon for studying bone adaptation in the avian ulna [219] shown in Fig. 17 (left) is expanded into a Fourier series (Fig. 17 (right)). It seems a reasonable assumption that, if a single sine wave creates a strain stimulus proportional to $\varepsilon f$, the strain stimulus from a series of sine waves is given by:

$$E = k_1 \sum_{i=1}^{n} \varepsilon_i f_i \tag{10}$$

where $n = \infty$. However, the majority of information in a typical Fourier series is contained in the first 10–20 terms, so $n = 20$ may serve as a reasonable approximation. See Turner et al. for further discussions [212, 251].

Equation (10) predicts all of the results that were discussed for *Rule 1* in Sect. 2 regarding the dynamic nature of the loading stimulus. As reviewed by Turner: Eq. (10) demonstrates that static loads characterised by $f = 0$ are not affecting bone adaptation [219], because $E = 0$; it predicts that bone adaptation is proportional to the applied dynamic strain magnitude [220] and that higher frequency loading is more
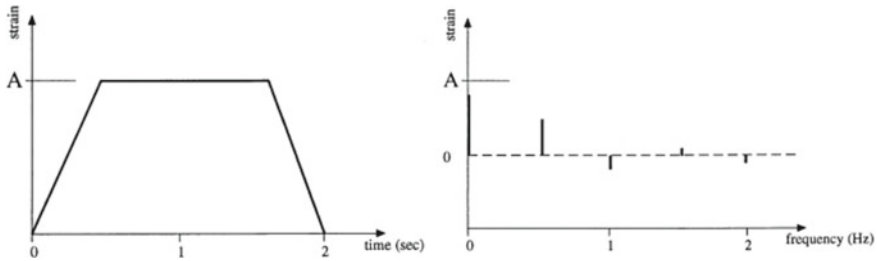
**Fig. 17** Dynamic nature of loading stimulus: (*left*) the trapezoidal loading waveform used by Rubin and Lanyon [219] can be expanded into a Fourier series (*right*), which shows a static loading component of about 0.75 $A$, a major dynamic component at 0.5 Hz, and several higher frequency components with progressively lower amplitudes. The strain stimulus from this waveform is the sum of strain magnitude × frequency for each of these components (Eq. (10))

effective at stimulating bone adaptation. It was demonstrated, using the isolated avian ulna model, that 2000 $\mu\varepsilon$ applied at 1 Hz could reverse the effects of disuse and stimulate new bone formation. According to Eq. (10), we should expect a similar response if 100 $\mu\varepsilon$ were applied at 20 Hz. This is precisely what was observed by Rubin and McLeod [222] when they showed that 150 $\mu\varepsilon$ at 20 Hz reversed the effects of disuse and stimulated bone ingrowth around transcortical, porous-coated titanium implants.

*Rule 2* states that extending the duration of skeletal loading does not yield proportional increases in bone mass. As loading duration is increased, the bone formation response tends to fade as if the cells become desensitized. Based on experimental data a logarithmic relation is proposed for the bone formation response [212]:

$$\text{bone formation} = k_2 \log (1 + N) \tag{11}$$

where $k_2$ is a proportionality constant and $N$ is the number of loading cycles applied to a bone during a training session. Equation (11) demonstrates that bone tissue sensitivity to mechanical loading is proportional to $1/(N + 1)$. Thus, bone loses more than 95% of its mechanosensitivity after only 20 loading cycles. Presumably, bone cells will resensitise to loading if they are given a period of rest between loading bouts.

The interaction between the strain stimulus ($\varepsilon f$) and duration of loading (number of loading cycles per day, $N$) can be described mathematically combining Eqs. (10) and (11) which give the following logarithmic relationship [251]:

$$S = \sum_{j=1}^{k} \log (1 + N_j) E_j \tag{12}$$

with $E_j$ defined in Eq. (10). $k$ represents the number of daily loading conditions, and $N_j$ represents the number of frequency components for each loading condition. Ch. Turner also pointed out the relation between the more heuristically derived for-

mula of Carter and Beaupre (Eq. (4)) in taking into account dynamic loading stimuli on bone adaptation. The formula proposed by Carter and co-workers is limited because the effect of loading frequency is not taken into account. However, the idea of the weighting factor $m$ was an important step forward. The experimental data clearly dictate that $m$ should be $>1$; Carter and colleagues estimated $m = 4$.

## 6.5  Recent Theories of Bone Adaptation

Roberts and Hart used strain energy density, along with other stimuli [208], including von Mises stress, axial strain and dilatational stress, to simulate long bone alignment of idealised shapes, described by Frost [80]. The last two were able to produce a straightened configuration, starting with a curved solid cylinder. Simulations using SED and von Mises stress, on the other hand, did not obtain the desired result. The fact that both of these quantities are always positive did not allow resorptive signals to be specified to the tensile side, while adding bone in regions in compression. B-spline curves were used to delimit the boundaries of cortical bone, allowing re-meshing the geometry at each iteration, guaranteeing high quality of elements throughout the simulation. For more details see Sect. 3 in the Ph.D. thesis of Pereira [194].

Jasiuk and co-workers utilised a similar approach to Huiskes et al. based on SED to account for external bone adaptation in the axial loading model of the rat ulna [42]. The proposed bone adaptation algorithm simulates surface modelling events by iteratively calculating the nodal displacements on the periosteal surface based on the modelling formation rate equation. This allows updating of the cross sectional geometry and the respective moment of inertia. Utilising this procedure reduces the surface SED at periosteal nodes until a homeostatic value is reached. The simulation results were compared to changes in second moment of area about the minor axis ($\Delta I_{min}/I_{min}$) measured experimentally by Robling et al. [211] (Fig. 18). This experimental study highlighted the advantages of separating loading periods into



**Fig. 18** Comparison of the percent change in the minimum principal moments of inertia $I_{min}$ between the original and adapted rat ulna from in-silico simulations and experiments [211]. ($I_{min}$ = current configuration; $I_{min}^0$ = original configuration; (Image adapted from [42])
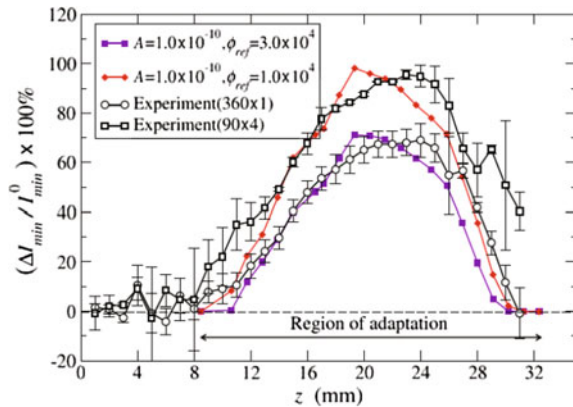
smaller bouts and this was introduced in the in silico model by changing the stimulus threshold. They also conducted a parametric study to the reference stimulus and remodelling rate coefficient, concluding that the former regulated the area extent of surface adaptation and the latter controlled the amount of formed bone.

Pereira et al. used the finite-element method to analyse bone adaptation responses in the mouse tibia loading model [195]. This allowed them to take into account the complex geometry of the mouse tibia and to calculate the mechanical fields that result from the external application of the loads. The algorithm starts with the local mechanical signal, i.e., the strain energy $\Psi$ that results from an external applied load $F$. The cellular response to the stimulus is denoted as $\Lambda$ (i.e., effective mechanical stimulus), a value ranging between $-1$ (resorptive response) and $+1$ (formation response), with different responses being triggered if $\Psi$ is above or below a certain threshold. The obtained local remodelling rate $\dot{u}$ was considered to be linearly proportional to the integral in time of the perceived stimulus.

The mechanosensing signal calculated at node $n$ (periosteal or endosteal) and time instant $t$, $\Psi(n, t)$, can elicit three different discrete responses of bone activity, $\Lambda(n, t)$, dictated by the relative value of the signal compared with the apposition and resorption limits of the homeostatic interval, $\Psi_A$ and $\Psi_R$. The value of $\Lambda$ is a dimensionless quantity and can be expressed as the following set of equations [195]:

$$\Lambda(n, t) = \begin{cases} 1, & \Psi \geq \Psi_A \\ 0, & \Psi_R \leq \Psi \leq \Psi_A \\ -1, & \Psi < \Psi_R \end{cases} \tag{13}$$

where $\Lambda$ takes positive values at time periods were the mechanical signal is above the apposition set point $\Psi_A$. The corresponding local remodelling rate $\dot{u}$ (units of length per iteration) is linearly proportional to the integral of $\Lambda$ over time:

$$\dot{u}(n) = C \int_t \Lambda(n, t) dt \tag{14}$$

where $C$ is a proportionality constant (units of length per iteration). Equation (14) indicates that the remodelling rate is higher the longer the signal stays above the threshold (Fig. 19).

In order to account for non-local mechanotransductive signals the average at a node $n$, $\bar{\dot{u}}(n)$ was calculated as the mean between the value $\dot{u}(n)$ and it weighted average at the other nodes inside the zone of influence:

$$\bar{\dot{u}}(n) = \frac{1}{2} \left( \dot{u}(n) + \frac{\int_\Omega w(r) \dot{u}(r) d\Omega}{\int_\Omega w(r)} \right) \tag{15}$$

with weighting function $w(r) = (R - r)/R$ and $\Omega$ as a spherical region of integration with centre at $n$ (excluding its centre). The value of $R$ was set to $150\,\mu m$, the average radius of an osteon representing the network of osteocytes over which the mechanical signal is sensed.
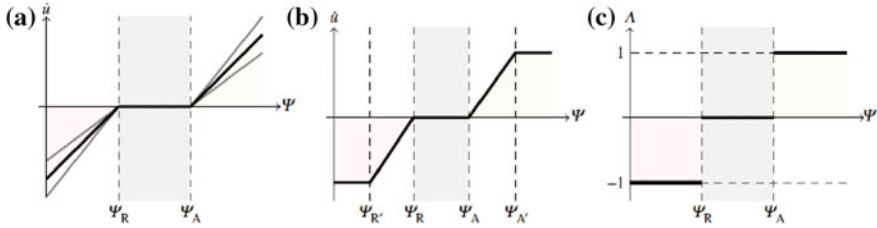
**Fig. 19** Schematic presentation of the relationship between mechanical stimulus versus bone adaptation response $\dot{u}$: **a** generic *tri-linear curves* (different slopes indicate different modeling rates), **b** *tri-linear curve* including an upper threshold (i.e., maximum remodelling rates of apposition and resorption), and **c** on off relationship. ($\psi_R$ and $\psi_A$ are the apposition and resorption limits of the homeostasis interval, i.e., the lazy zone; image adapted from Pereira et al. [195])
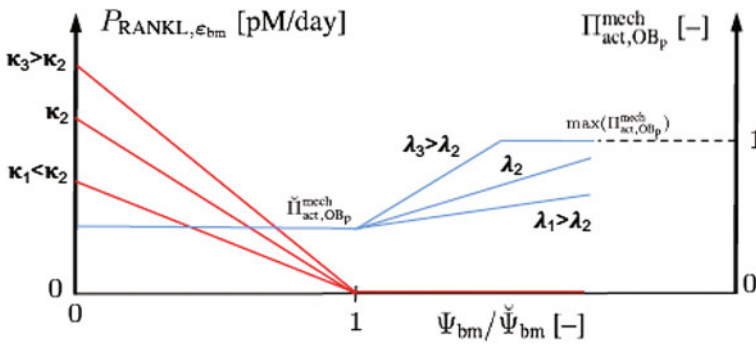


**Fig. 20** Mechanobiological model of Pivonka and co-workers [198, 235] including mechanical feedback based on biological regulatory functions. The mechanical stimulus is assumed to be proportional to the strain energy density in the bone matrix ($\psi_{bm}$) and the adaptive signal is the ratio of the current loading stimulus and the habitual loading stimulus. Bone anabolic response is taken into account via a proliferation Hill-type function $\pi_{load}$ which controls proliferation of osteoblast precursor cells. Bone catabolic response is taken into account via a production term of RANKL, i.e., a regulatory factor which promotes osteoclast formation. (*dashed* and *dotted lines* represent different magnitudes of the regulatory functions)

## Mechanobiological Models by Pivonka and co-workers

The last type of model considered in this section is based on a mechanobiological feedback rather than a mechanical only feedback. Pivonka and co-workers coupled a "bone remodelling" model of bone cell interactions with a mechanical model of bone stiffness to formulate a mechanical feedback system [198, 235]. Notably, the bone cell population model takes into account anabolic and catabolic regulatory pathways such as the RANKL/RANKL/OPG pathway, TGF-$\beta$ and osteoblast precursor proliferation via Wnt signalling (see Sect. 4 for more details on molecular pathways). The novelty of this approach is to use clearly defined biological regulatory mechanisms to define the mechanostat feedback. Figure 20 shows the anabolic and catabolic regulatory functions due to mechanical loading that control bone cell numbers in the remodelling process.

# 7 Conclusion

Bone adaptation due to mechanical loading is among the most comprehensively studied biological system. The close relationship between form and function is clearly evident in the design of the skeletal system of vertebrates. Many prominent researchers including Wolff, Frost, Cowin, Turner, Lanyon, Carter, and Huiskes, among others, have contributed to our current mechanistic understanding of mechanobiological regulation of bone adaptation. Particularly, the conceptual model of the mechanostat, originally proposed by H. Frost and subsequently adapted by T. Skerry, has proven very useful in formulating research hypotheses for loading induced bone adaptation studies.

A variety of controlled loading models, such as those applying known strains to turkey, rat, or mouse bones, have contributed to our knowledge of functional adaptation. Insights from these models reveal that static loads do not play a role in mechanotransduction and that bone formation is threshold driven and dependent on strain rate, amplitude, and partitioning of the load. That is, only a few cycles of loading are required at any time to elicit an adaptive response, and distributed bouts of loading, incorporating rest periods, are more osteogenic than single sessions of long duration. Recent development of a model in rabbits also provides potential to examine intracortical Haversian remodelling. These parameters of loading are being translated into feasible public health interventions that exploit the insights gained from animal experiments. Investigators, have a range of models available to them that are accessible, non-invasive and produce physiologically relevant responses. It requires selection of the model to most effectively provide a valid test of hypotheses.

The attempts to decrypt the cellular processes involved in the mechanotransduction have revealed diverse signalling elements. These are delicately arranged in a hierarchical order to orchestrate the functional adaptation of bone mass and architecture in response to mechanical loading. ATP, calcium, PGE2, and NO are released in an acute setting to initiate the downstream chain reactions that employ oestrogen receptors and modulate expression of RANKL, Wnt, and sclerostin. The advancement in our knowledge has enabled the clinical trials of a new medical treatment such as Romosozumab and there will be more to come in the future.

Children and adolescents have greater potential to adapt their skeleton in response to physical loading. The peri-pubertal stage of maturation is the optimal period in which the skeleton is most accessible to structural adaptation. Experimental loading studies show that static or isometric exercises elicit minimal skeletal response, but repetitive cyclical loads, including a range of strain magnitudes and directions (such as running and jumping) provide the most effective stimulus. Because relatively few cycles of loading elicit an adaptive response, disseminated bouts of loading with interspersed rest periods will activate a greater response than fewer sessions of long duration. These principles have been transformed into practical public health programs that have improved the mass and strength of the skeleton in children and adolescents. Both human and animal studies provide strong evidence that the structural adaptations also persist in to adulthood, where they will reduce the fracture risk.

Many in silico models of bone adaptation have been developed over the past 30 years with the aim to predict bone modelling and remodelling responses due to mechanical loading. These models are based on a "Wolff's law"−type algorithm that computes bone density or porosity as a function of the applied mechanical loads. This adaptation algorithm ultimately optimises bone density similar to topological optimisation problems in materials engineering.

It can be anticipated that our understanding of the mechanostat and the mechanobiological regulatory factors involved in mechanosensation and desensitisation will continue to evolve in the next years. Ultimately sports scientists, physiotherapists, clinicians and surgeons will be able to control bone mass based on a precisely prescribed physiological exercise regimen that is based on in silico patient specific models. These models may also provide insights into combined therapies of physical exercise and pharmaceuticals in order to manipulate bone cells in a targeted, i.e., site and individual specific manner.

# References

1. J.I. Aguirre, L.I. Plotkin, A.R. Gortazar, M.M. Millan, C.A. O'Brien, S.C. Manolagas, T. Bellido, A novel ligand-independent function of the estrogen receptor is essential for osteocyte and osteoblast mechanotransduction. J. Biol. Chem. **282**(35), 25501–25508 (2007)
2. I. Alam, S.J. Warden, A.G. Robling, C.H. Turner, Mechanotransduction in bone does not require a functional cyclooxygenase-2 (cox-2) gene. J. Bone Miner. Res. **20**(3), 438–446 (2005). ISSN 0884-0431
3. C.B. Alander, L.G. Raisz, Effects of selective prostaglandins e2 receptor agonists on cultured calvarial murine osteoblastic cells. Prostaglandins Other Lipid Mediat. **81**(3), 178–183 (2006). ISSN 1098-8823
4. M.R. Allen, J.J. Turek, R.J. Phipps, D.B. Burr, Greater magnitude of turnover suppression occurs earlier after treatment initiation with risedronate than alendronate. Bone **49**(1), 128–132 (2011). ISSN 1873-2763
5. M.E. Arlot, E. Sornay-Rendu, P. Garnero, B. Vey-Marty, P.D. Delmas, Apparent pre- and postmenopausal bone loss evaluated by dxa at different skeletal sites in women: the ofely cohort. J. Bone Miner. Res. **12**(4), 683–690 (1997)
6. V.J. Armstrong, M. Muzylak, A. Sunters, G. Zaman, L.K. Saxon, J.S. Price, L.E. Lanyon, Wnt/$\beta$-catenin signaling is a component of osteoblastic bone cell early responses to load-bearing and requires estrogen receptor $\alpha$. J. Biol. Chem. **282**(28), 20715–20727 (2007)
7. E.J. Arnsdorf, P. Tummala, C.R. Jacobs, Non-canonical wnt signaling and n-cadherin related $\beta$-catenin signaling play a role in mechanically induced osteogenic cell fate. PLoS ONE **4**(4), e5388 (2009)
8. R.G. Bacabac, T.H. Smit, M.G. Mullender, S.J. Dijcks, J.J.W.A. Van Loon, J. Klein-Nulend, Nitric oxide production by bone cells is fluid shear stress rate dependent. Biochem. Biophys. Res. Commun. **315**(4), 823–829 (2004)
9. M. Bagge, A model of bone adaptation as an optimization process. J. Biomech. **33**(11), 1349–1357 (2000)
10. D.A. Bailey, The saskatchewan pediatric bone mineral accrual study: bone mineral acquisition during the growing years. Int. J. Sports Med. **18**(Suppl 3), S191–S194 (1997)
11. D.A. Bailey, H.A. McKay, R.L. Mirwald, P.R. Crocker, R.A. Faulkner, A six-year longitudinal study of the relationship of physical activity to bone mineral accrual in growing children: the university of saskatchewan bone mineral accrual study. J. Bone Miner. Res. **14**(10), 1672–1679 (1999)

12. A.D. Bakker, K. SoeJima, J. Klein-Nulend, E.H. Burger, The production of nitric oxide and prostaglandin e2 by primary bone cells is shear stress dependent. J. Biomech. **34**(5), 671–677 (2001). ISSN 0021-9290

13. A.D. Bakker, J. Klein-Nulend, E.H. Burger, Mechanotransduction in bone cells proceeds via activation of cox-2, but not cox-1. Biochem. Biophys. Res. Commun. **305**(3), 677–683 (2003). ISSN 0006-291X

14. A.D. Bakker, C. Huesa, A. Hughes, R.M. Aspden, R.J. vant Hof, J. Klein-Nulend, M.H. Helfrich, Endothelial nitric oxide synthase is not essential for nitric oxide production by osteoblasts subjected to fluid shear stress in vitro. Calcif. Tissue Int. **92**(3), 228–239 (2013)

15. R. Baron, M. Kneissel, Wnt signaling in bone homeostasis and disease: from human mutations to treatments. Nat. Med. **19**(2), 179–192 (2013)

16. N. Basso, J.N.M. Heersche, Characteristics of in vitro osteoblastic cell loading models. Bone **30**(2), 347–351 (2002). ISSN 8756-3282

17. A.P. Baumann, M.W. Aref, T.L. Turnbull, A.G. Robling, G.L. Niebur, M.R. Allen, R.K. Roeder, Development of an in vivo rabbit ulnar loading model. Bone **75**, 55–61 (2015)

18. A.D. Baxter-Jones, S.A. Kontulainen, R.A. Faulkner, D.A. Bailey, A longitudinal study of the relationship of physical activity to bone mineral accrual from adolescence to young adulthood. Bone **43**(6), 1101–1107 (2008)

19. A.D. Baxter-Jones, R.A. Faulkner, M.R. Forwood, R.L. Mirwald, D.A. Bailey, Bone mineral accrual from 8 to 30 years of age: an estimation of peak bone mass. J. Bone Miner. Res. **26**(8), 1729–1739 (2011)

20. G.S. Beaupre, T.E. Orr, D.R. Carter, An approach for time-dependent modeling and remodeling - theoretical development. J. Orthop. Res. **8**, 651–661 (1990)

21. T.J. Beck, C.B. Ruff, K.E. Warden Jr., W.W. Scott Jr., G.U. Rao, Predicting femoral neck strength from bone mineral data. a structural approach. Invest. Radiol. **25**(1), 6–18 (1990)

22. V. Bentolila, T.M. Boyce, D.P. Fyhrie, R. Drumb, T.M. Skerry, M.B. Schaffler, Intracortical remodeling in adult rat long bones after fatigue loading. Bone **23**(3), 275–81 (1998)

23. J.E.A. Bertram, A.A. Biewener, Bone curvature: sacrificing strength for load predictability? J. Theor. Biol. **131**(1), 75–92 (1988). ISSN 0022-5193

24. J.E.A. Bertram, A.A. Biewener, Allometry and curvature in the long bones of quadrupedal mammals. J. Zool. **226**(3), 455–467 (1992). ISSN 1469-7998

25. N. Bivi, M.T. Nelson, M.E. Faillace, J. Li, L.M. Miller, L.I. Plotkin, Deletion of cx43 from osteocytes results in defective bone material properties but does not decrease extrinsic strength in cortical bone. Calcif. Tissue Intern. **91**(3), 215–224 (2012). ISSN 0171-967X

26. L.F. Bonewald, Mechanosensation and transduction in osteocytes. BoneKEy Osteovision **3**(10), 7–15 (2006). ISSN 1533-4368

27. L.F. Bonewald, The amazing osteocyte. J. Bone Miner. Res. **26**(2), 229–238 (2011)

28. L.F. Bonewald, M.L. Johnson, Osteocytes, mechanosensing and wnt signaling. Bone **42**(4), 606–615 (2008)

29. M. Bradney, G. Pearce, G. Naughton, C. Sullivan, S. Bass, T. Beck, J. Carlson, E. Seeman, Moderate exercise during growth in prepubertal boys: changes in bone mass, size, volumetric density, and bone strength: a controlled prospective study. J. Bone Miner. Res. **13**(12), 1814–1821 (1998)

30. D.B. Burr, R.B. Martin, Errors in bone remodeling: toward a unified theory of metabolic bone disease. Am. J. Anat. **186**(2), 186–216 (1989)

31. D.B. Burr, M.B. Schaffler, K.H. Yang, M. Lukoschek, N. Sivaneri, J.D. Blaha, E.L. Radin, Skeletal change in response to altered strain environments: is woven bone a response to elevated strain? Bone **10**(3), 223–233 (1989)

32. D.B. Burr, C. Milgrom, D. Fyhrie, M. Forwood, M. Nyska, A. Finestone, S. Hoshaw, E. Saiag, A. Simkin, In vivo measurement of human tibial strains during vigorous activity. Bone **18**(5), 405–410 (1996). ISSN 8756-3282

33. D.R. Carter, The relationship between in vivo strains and cortical bone remodelling. CRC Crit. Rev. Biomed. Eng. **8**, 1–28 (1982)

34. D.R. Carter, Mechanical loading histories and cortical bone remodeling. Calcif. Tissue Int. **36**(1), S19–S24 (1984)
35. D.R. Carter, G.S. Beaupre, *Skeletal Funtion and Form - Mechanobiology of Skeletal Development, Aging, and Regeneration* (Cambridge University Press, New York, 2001). ISBN 978-0-521-79000-0
36. A.B. Castillo, J.W. Triplett, F.M. Pavalko, C.H. Turner, Estrogen receptor-$\beta$ regulates mechanical signaling in primary osteoblasts. Am. J. Physiol.-Endocrinol. Metab. **306**(8), E937–E944 (2014)
37. T.J. Chambers, M. Evans, T.N. Gardner, A. Turner-Smith, J.W. Chow, Induction of bone formation in rat tail vertebrae by mechanical loading. Bone Miner. **20**(2), 167–178 (1993)
38. R. Chapurlat, Cathepsin k inhibitors and antisclerostin antibodies. the next treatments for osteoporosis? Joint Bone Spine **83**(3), 254–256 (2016)
39. N.X. Chen, K.D. Ryder, F.M. Pavalko, C.H. Turner, D.B. Burr, J. Qiu, R.L. Duncan, Ca2+ regulates fluid shear-induced cytoskeletal reorganization and gene expression in osteoblasts. Am. J. Physiol. Cell Physio. **278**(5), C989–C997 (2000)
40. N.X. Chen, D.J. Geist, D.C. Genetos, F.M. Pavalko, R.L. Duncan, Fluid shear-induced nfb translocation in osteoblasts is mediated by intracellular calcium release. Bone **33**(3), 399–410 (2003). ISSN 8756-3282
41. B. Cheng, Y. Kato, S. Zhao, J. Luo, E. Sprague, L.F. Bonewald, J.X. Jiang, Pge2 is essential for gap junction-mediated intercellular communication between osteocyte-like mlo-y4 cells in response to mechanical strain. Endocrinology **142**(8), 3464–3473 (2001). ISSN 0013-7227
42. N. Chennimalai Kumar, J.A. Dantzig, I.M. Jasiuk, A.G. Robling, C.H. Turner, Numerical modeling of long bone adaptation due to mechanical loading: correlation with experiments. Ann. Biomed. Eng. **38**(3), 594–604 (2010)
43. S. Choudhary, C. Alander, P. Zhan, Q. Gao, C. Pilbeam, L.G. Raisz, Effect of deletion of the prostaglandin ep2 receptor on the anabolic response to prostaglandin e2 and a selective ep2 receptor agonist. Prostaglandins Other Lipid Mediat. **86**(1), 35–40 (2008). ISSN 1098-8823
44. J.W. Chow, T.J. Chambers, Indomethacin has distinct early and late actions on bone formation induced by mechanical stimulation. Am. J. Physiol.-Endocrinol. Metab. **267**(2), E287–E292 (1994). ISSN 0193-1849
45. J.W. Chow, C.J. Jagger, T.J. Chambers, Characterization of osteogenic response to mechanical stimulation in cancellous bone of rat caudal vertebrae. Am. J. Physiol. **265**(2 Pt 1), E340–E347 (1993). ISSN 0002-9513 (Print)
46. L.A. Colletti, J. Edwards, L. Gordon, J. Shary, N.H. Bell, The effects of muscle-building exercise on bone mineral density of the radius, spine, and hip in young men. Calcif. Tissue Int. **45**(1), 12–14 (1989). ISSN 1432-0827
47. S.C. Cowin, D.H. Hegedus, Bone remodeling i: theory of adaptive elasticity. J. Elast. **6**(3), 313–326 (1976)
48. S.C. Cowin, W.C. Van Buskirk, Surface bone remodeling induced by a medullary pin. J. Biomech. **12**(4), 269–276 (1979)
49. S.C. Cowin, A.M. Sadegh, G.M. Luo, An evolutionary wolff's law for trabecular architecture. J. Biomech. Eng. **114**(1), 129–136 (1992)
50. J.D. Currey, What should bones be designed to do? Calcif. Tissue Int. **36**(1), S7–S10 (1984). ISSN 1432-0827
51. R.M. Daly, L. Saxon, C.H. Turner, A.G. Robling, S.L. Bass, The relationship between muscle size and bone geometry during growth and in response to exercise. Bone **34**(2), 281–287 (2004)
52. E. Damien, J.S. Price, L.E. Lanyon, Mechanical strain stimulates osteoblast proliferation through the estrogen receptor in males as well as females. J. Bone Miner. Res. **15**(11), 2169–2177 (2000)
53. C. Darwin, *The Origin of Species by Means of Natural Selection or the Preservation of Favoured Races in the Struggle for Life* (John Murray, London, 1872)
54. R.L. De Souza, M. Matsuura, F. Eckstein, S.C. Rawlinson, L.E. Lanyon, A.A. Pitsillides, Non-invasive axial loading of mouse tibiae increases cortical bone formation and modifies

trabecular organization: a new model to study cortical and cancellous compartments in a single loaded element. Bone **37**(6), 810–818 (2005)

55. R.M. Delaine-Smith, B. Javaheri, J.H. Edwards, M. Vazquez, R.M.H. Rumney, Preclinical models for in vitro mechanical loading of bone-derived cells. Bonekey Rep. **4**, 728 (2015)

56. J. Delgado-Calle, J.A. Riancho, J. Klein-Nulend, Nitric oxide is involved in the down-regulation of sost expression induced by mechanical loading. Calcif. Tissue Int. **94**(4), 414–422 (2014)

57. J.M.H. Dibbets, One century of wolff's law, *Bone Biodynamics in Orthodontic and Orthopedic Treatment*, vol. 1, 1st edn. (Centre for Human growth and Development, University of Michigan, Ann Arbor, 1991), pp. 1–13

58. D.L. Ellies, B. Viviano, J. McCarthy, J.P. Rey, N. Itasaki, S. Saunders, R. Krumlauf, Bone density ligand, sclerostin, directly interacts with lrp5 but not lrp5g171v to modulate wnt activity. J. Bone Miner. Res. **21**(11), 1738–1749 (2006)

59. M.C. Erlandson, S.A. Kontulainen, A.D. Baxter-Jones, Precompetitive and recreational gymnasts have greater bone density, mass, and estimated strength at the distal radius in young childhood. Osteoporos. Int. **22**(1), 75–84 (2011)

60. M.C. Erlandson, S.A. Kontulainen, P.D. Chilibeck, C.M. Arnold, A.D. Baxter-Jones, Bone mineral accrual in 4- to 10-year-old precompetitive, recreational gymnasts: a 4-year longitudinal study. J. Bone Miner. Res. **26**(6), 1313–1320 (2011)

61. H.A. Eschenauer, N. Olhoff, Topology optimization of continuum structures: a review. Appl. Mech. Rev. **54**(4), 331–390 (2001)

62. F.G. Evans, Methods of studying the biomechanical significance of bone form. Am. J. Phys. Anthropol. **11**(3), 413–436 (1953). ISSN 1096-8644

63. R.A. Faulkner, M.R. Forwood, T.J. Beck, J.C. Mafukidze, K. Russell, W. Wallace, Strength indices of the proximal femur and shaft in prepubertal female gymnasts. Med. Sci. Sports Exerc. **35**(3), 513–518 (2003)

64. P. Fernandes, H. Rodrigues, C. Jacobs, A model of bone adaptation using a global optimization criterion based on the trajectorial theory of wolff. Comp. Meth. Biomech. Biomed. Eng. **2**(2), 125–138 (1999)

65. I. Fijalkowski, E. Geets, E. Steenackers, V. Van Hoof, F.J. Ramos, G. Mortier, A.M. Fortuna, W. Van Hul, E. Boudin, A novel domain specific mutation in a sclerosteosis patient suggests a role of lrp4 as an anchor for sclerostin in human bone. J. Bone Miner. Res. **31**(4), 874–881 (2016)

66. M.R. Forwood, Inducible cyclo-oxygenase (cox-2) mediates the induction of bone formation by mechanical loading in vivo. J. Bone Miner. Res. **11**(11), 1688–1693 (1996)

67. M.R. Forwood, Mechanical effects on the skeleton: are there clinical implications? Osteoporos. Int. **12**(1), 77–83 (2001)

68. M.R. Forwood, D.B. Burr, Physical activity and bone mass: exercises in futility? Bone Miner. **21**, 89–112 (1993)

69. M.R. Forwood, A.W. Parker, Repetitive loading, in vivo, of the tibiae and femora of rats: effects of repeated bouts of treadmill-running. Bone Miner. **13**(1), 35–46 (1991)

70. M.R. Forwood, C.H. Turner, The response of rat tibiae to incremental bouts of mechanical loading: a quantum concept for bone formation. Bone **15**(6), 603–609 (1994)

71. M.R. Forwood, M.B. Bennett, A.R. Blowers, R.L. Nadorfi, Modification of the in vivo four-point loading model for studying mechanically induced bone adaptation. Bone **23**(3), 307–310 (1998)

72. M.R. Forwood, D.A. Bailey, T.J. Beck, R.L. Mirwald, A.D. Baxter-Jones, K. Uusi-Rasi, Sexual dimorphism of the femoral neck during the adolescent growth spurt: a structural analysis. Bone **35**(4), 973–81 (2004)

73. M.R. Forwood, A.D. Baxter-Jones, T.J. Beck, R.L. Mirwald, A. Howard, D.A. Bailey, Physical activity and strength of the femoral neck during the adolescent growth spurt: a longitudinal analysis. Bone **38**(4), 576–583 (2006)

74. S.W. Fox, T.J. Chambers, J.W. Chow, Nitric oxide is an early mediator of the increase in bone formation by mechanical stimulation. Am. J. Physiol. - Endocrinol. Metab. **270**(6), E955–E960 (1996)

75. S.P. Fritton, C.T. Rubin, In vivo measurement of bone deformations using strain gauges, in *Bone Mechanics Handbook*, vol. 1, 1st edn., ed. by S.C. Cowin (CRC Press, Boca Raton, 2001), pp. 8–34

76. S.P. Fritton, K.J. McLeod, C.T. Rubin, Quantifying the strain history of bone: spatial uniformity and self-similarity of low-magnitude strains. J. Biomech. **33**(3), 317–325 (2000). ISSN 0021-9290

77. H.M. Frost, Review article mechanical determinants of bone modeling. Metab. Bone Dis. Relat. Res. **4**(4), 217–229 (1982). ISSN 0221-8747

78. H.M. Frost, A determinant of bone architecture. the minimum effective strain. Clin. Orthop. Relat. Res. **1**(175), 286–292 (1983)

79. H.M. Frost, Bone mass and the mechanostat: a proposal. Anat. Rec. **219**(1), 1–9 (1987). ISSN 1097-0185

80. H.M. Frost, Skeletal structural adaptations to mechanical usage (satmu): 1. Redefining wolff's law: the bone modeling problem. Anat. Rec. **226**(4), 403–413 (1990)

81. H.M. Frost, The utah paradigm of skeletal physiology: an overview of its insights for bone, cartilage and collagenous tissue organs. J. Bone Miner. Metab. **18**(6), 305–16 (2000)

82. H.M. Frost, From wolff's law to the utah paradigm: insights about bone physiology and its clinical applications. Anat. Rec. **262**(4), 398–419 (2001)

83. H.M. Frost, Bone's mechanostat: a 2003 update. Anat. Rec. **275A**(2), 1081–1101 (2003)

84. R.K. Fuchs, J.J. Bauer, C.M. Snow, Jumping improves hip and lumbar spine bone mass in prepubescent children: a randomized controlled trial. J. Bone Miner. Res. **16**(1), 148–156 (2001)

85. M. Fujiwara, T. Kubota, W. Wang, Y. Ohata, K. Miura, T. Kitaoka, D. Okuzaki, N. Namba, T. Michigami, Y. Kitabatake, Successful induction of sclerostin in human-derived fibroblasts by 4 transcription factors and its regulation by parathyroid hormone, hypoxia, and prostaglandin e2. Bone **85**, 91–98 (2016). ISSN 8756-3282

86. D.P. Fyhrie, D.R. Carter, A unifying principle relating stress to trabecular bone morphology. J. Orthop. Res. **4**(3), 304–317 (1986)

87. G.L. Galea, Sost down-regulation by mechanical strain in human osteoblastic cells involves pge2 signaling via ep4. FEBS Lett. **585**(15), 2450–2454 (2011). ISSN 0014-5793

88. G.L. Galea, L.B. Meakin, T. Sugiyama, N. Zebda, A. Sunters, H. Taipaleenmaki, G.S. Stein, A.J. van Wijnen, L.E. Lanyon, J.S. Price, Estrogen receptor $\alpha$ mediates proliferation of osteoblastic cells stimulated by estrogen and mechanical strain, but their acute down-regulation of the wnt antagonist sost is mediated by estrogen receptor $\beta$. J. Biol. Chem. **288**(13), 9035–9048 (2013)

89. G.L. Galea, L.B. Meakin, D. Savery, H. Taipaleenmaki, P. Delisser, G.S. Stein, A.J. Copp, A.J. van Wijnen, L.E. Lanyon, J.S. Price, Planar cell polarity aligns osteoblast division in response to substrate strain. J. Bone Miner. Res. **30**(3), 423–435 (2015)

90. G. Galileo, *Discorsi e demonstrazioni matematiche, intorno a due nuove scienze attentanti all meccanica ed a muovementi locali*. Reprinted by University of Wisconsin Press, Madison (1638)

91. M.A. Garber, D.L. McDowell, W.C. Hutton, Bone loss during simulated weightlessness: a biomechanical and mineralization study in the rat model. Aviat. Space Environ. Med. **71**(6), 586–952 (2000)

92. A. Gaudio, P. Pennisi, C. Bratengeier, V. Torrisi, B. Lindner, R.A. Mangiafico, I. Pulvirenti, G. Hawa, G. Tringali, C.E. Fiore, Increased sclerostin serum levels associated with bone formation and resorption markers in patients with immobilization-induced bone loss. J. Clin. Endocrinol. Metab. **95**(5), 2248–2253 (2010)

93. D.C. Genetos, C.E. Yellowley, G.G. Loots, Prostaglandin e2 signals through ptger2 to regulate sclerostin expression. PloS One **6**(3), e17772 (2011). ISSN 1932-6203

94. D.A. Glass, P. Bialek, J.D. Ahn, M. Starbuck, M.S. Patel, H. Clevers, M.M. Taketo, F. Long, A.P. McMahon, R.A. Lang, Canonical wnt signaling in differentiated osteoblasts controls osteoclast differentiation. Dev. Cell **8**(5), 751–764 (2005). ISSN 1534-5807

95. T.S. Gross, S. Srinivasan, C.C. Liu, T.L. Clemens, S.D. Bain, Noninvasive loading of the murine tibia: an in vivo model for the study of mechanotransduction. J. Bone Miner. Res. **17**(3), 493–501 (2002). ISSN 0884-0431

96. T.S. Gross, S.L. Poliachik, B.J. Ausk, D.A. Sanford, B.A. Becker, S. Srinivasan, Why rest stimulates bone formation: a hypothesis based on complex adaptive phenomenon. Exerc. Sport Sci. Rev. **32**(1), 9–13 (2004)

97. K. Gunter, A.D. Baxter-Jones, R.L. Mirwald, H. Almstedt, R.K. Fuchs, S. Durski, C. Snow, Impact exercise increases bmc during growth: an 8-year longitudinal study. J. Bone Miner. Res. **23**(7), 986–993 (2008)

98. A. Gustavsson, T. Olsson, P. Nordstrom, Rapid loss of bone mineral density of the femoral neck after cessation of ice hockey training: a 6-year longitudinal study in males. J. Bone Miner. Res. **18**(11), 1964–1969 (2003)

99. H. Haapasalo, P. Kannus, H. Sievnen, M. Pasanen, K. Uusi-Rasi, A. Heinonen, P. Oja, I. Vuori, Effect of long-term unilateral activity on bone mineral density of female junior tennis players. J. Bone Miner. Res. **13**(2), 310–319 (1998). ISSN 1523-4681

100. H. Haapasalo, S. Kontulainen, H. Sievnen, P. Kannus, M. Jrvinen, I. Vuori, Exercise-induced bone gain is due to enlargement in bone size without a change in volumetric bone density: a peripheral quantitative computed tomography study of the upper arms of male tennis players. Bone **27**(3), 351–357 (2000)

101. K. Hamamura, G. Swarnkar, N. Tanjung, E. Cho, J. Li, S. Na, H. Yokota, Rhoa-mediated signaling in mechanotransduction of osteoblasts. Connect. Tissue Res. **53**(5), 398–406 (2012)

102. R.T. Hart, Bone modeling and remodeling: theories and computation, in *Bone Mechanics Handbook*, vol. 1, 2nd edn., ed. by S.C. Cowin (CRC Press, London, 2001), pp. 31.1–31.42

103. R. Hattner, B.N. Epker, H.M. Frost, Suggested sequential mode of control of changes in cell behaviour in adult bone remodelling. Nature **206**(4983), 489–490 (1965)

104. R.P. Heaney, Is the paradigm shifting? Bone **33**(4), 457–465 (2003). ISSN 8756-3282

105. A. Heinonen, P. Oja, P. Kannus, H. Sievanen, H. Haapasalo, A. Mnttri, I. Vuori, Bone mineral density in female athletes representing sports with different loading characteristics of the skeleton. Bone **17**(3), 197–203 (1995). ISSN 8756-3282

106. A. Heinonen, H. Sievnen, P. Kannus, P. Oja, I. Vuori, Effects of unilateral strength training and detraining on bone mineral mass and estimated mechanical characteristics of the upper limb bones in young women. J. Bone Miner. Res. **11**(4), 490–501 (1996). ISSN 1523–4681

107. A. Heinonen, H. Sievanen, P. Kannus, P. Oja, M. Pasanen, I. Vuori, High-impact exercise and bones of growing girls: a 9-month controlled trial. Osteoporos. Int. **11**(12), 1010–1017 (2000)

108. J. Hert, M. Liskova, B. Landrgot, Influence of the long-term, continuous bending on the bone. An experimental study on the tibia of the rabbit. Folia Morphol. (Praha) **17**(4), 389–399 (1969)

109. J. Hert, M. Liskova, J. Landa, Reaction of bone to mechanical stimuli. 1. Continuous and intermittent loading of tibia in rabbit. Folia Morphol. (Praha) **19**(3), 290–300 (1971)

110. T. Hirano, D.B. Burr, C.H. Turner, M. Sato, R.L. Cain, J.M. Hock, Anabolic effects of human biosynthetic parathyroid hormone fragment (1–34), ly333334, on remodeling and mechanical properties of cortical bone in rabbits. J. Bone Miner. Res. **14**(4), 536–545 (1999). ISSN 0884-0431

111. S.L. Holmen, C.R. Zylstra, A. Mukherjee, R.E. Sigler, M.-C. Faugere, M.L. Bouxsein, L. Deng, T.L. Clemens, B.O. Williams, Essential role of $\beta$-catenin in postnatal bone acquisition. J. Biol. Chem. **280**(22), 21162–21168 (2005). ISSN 0021-9258

112. R.P. Huang, C.T. Rubin, K.J. McLeod, Changes in postural muscle dynamics as a function of age. J. Gerontol. Ser. A: Biol. Sci. Med. Sci. **54**(8), B352–B357 (1999)

113. J.M. Hughes, M.A. Petit, Biological underpinnings of frosts mechanostat thresholds: the important role of osteocytes. J. Musculoskelet. Neuronal Interact. **10**(2), 128–135 (2010)

114. S.L. Hui, C.W. Slemenda, C.C. Johnston Jr., The contribution of bone loss to postmenopausal osteoporosis. Osteoporos. Int. **1**(1), 30–34 (1990)

115. R. Huiskes, If bone is the answer, then what is the question? J. Anat. **197**(2), 145–156 (2000). ISSN 1469-7580

116. R. Huiskes, H. Weinans, H.J. Grootenboer, M. Dalstra, B. Fudala, T.J. Slooff, Adaptive bone-remodeling theory applied to prosthetic-design analysis. J. Biomech. **20**(11), 1135–1150 (1987)

117. C.R. Jacobs, C.E. Yellowley, B.R. Davis, Z. Zhou, J.M. Cimbala, H.J. Donahue, Differential effect of steady versus oscillating flow on bone cells. J. Biomech. **31**(11), 969–976 (1998)

118. C.R. Jacobs, S. Temiyasathit, A.B. Castillo, Osteocyte mechanobiology and pericellular mechanics. Annu. Rev. Biomed. Eng. **12**(1), 369–400 (2010). ISSN 1523-9829

119. W.S. Jee, X.J. Li, M.B. Schaffler, Adaptation of diaphyseal structure with aging and increased mechanical usage in the adult rat: a histomorphometrical and biomechanical study. Anat. Rec. **230**(3), 332–338 (1991)

120. W.S.S. Jee, X.J. Li, Skeletal adaptations to mechanical usage in the rat. Cells Mater. Suppl. **1**(Supplement 1), 131–142 (1991)

121. H.L. Jessop, R.F.L. Suswillo, S.C.F. Rawlinson, G. Zaman, K. Lee, V. Das-Gupta, A.A. Pitsillides, L.E. Lanyon, Osteoblast like cells from estrogen receptor $\alpha$ knockout mice have deficient responses to mechanical strain. J. Bone Miner. Res. **19**(6), 938–946 (2004)

122. R.L. Jilka, R.S. Weinstein, T. Bellido, P. Roberson, A.M. Parfitt, S.C. Manolagas, Increased bone formation by prevention of osteoblast apoptosis with parathyroid hormone. J. Clin. Investig. **104**(4), 439–446 (1999). ISSN 0021-9738

123. H.H. Jones, J.D. Priest, W.C. Hayes, C.C. Tichenor, D.A. Nagel, Humeral hypertrophy in response to exercise. J. Bone Joint Surg. **59**(2), 204–208 (1977)

124. M.A. Kamel, J.L. Picconi, N. Lara-Castillo, M.L. Johnson, Activation of $\beta$-catenin signaling in mlo-y4 osteocytic cells versus 2t3 osteoblastic cells by fluid flow shear stress and pge2: implications for the study of mechanosensation in bone. Bone **47**(5), 872–881 (2010). ISSN 8756-3282

125. M. Kanematsu, K. Ikeda, Y. Yamada, Interaction between nitric oxide synthase and cyclooxy-genase pathways in osteoblastic mc3t3 e1 cells. J. Bone Miner. Res. **12**(11), 1789–1796 (1997)

126. P. Kannus, H. Haapasalo, M. Sankelo, H. Sievanen, A. Pasanen, A. Heinonen, P. Oja, I. Vuori, Effect of starting age of physical activity on bone mass in the dominant arm of tennis and squash players. Ann. Intern. Med. **123**(1), 27–31 (1995)

127. M.K. Karlsson, C. Linden, C. Karlsson, O. Johnell, K. Obrant, E. Seeman, Exercise during growth and bone mineral density and fractures in old age. Lancet **355**(9202), 469–70 (2000)

128. H.Z. Ke, V.W. Shen, H. Qi, D.T. Crawford, D.D. Wu, X.G. Liang, K.L. Chidsey-Frink, C.M. Pirie, H.A. Simmons, D.D. Thompson, Prostaglandin e2 increases bone strength in intact rats and in ovariectomized rats with established osteopenia. Bone **23**(3), 249–255 (1998). ISSN 8756-3282

129. S. Keila, A. Kelner, M. Weinreb, Systemic prostaglandin e2 increases cancellous bone formation and mass in aging rats and stimulates their bone marrow osteogenic capacity in vivo and in vitro. J. Endocrinol. **168**(1), 131–139 (2001). ISSN 0022-0795

130. L.J. Kidd, A.S. Stephens, J.S. Kuliwaba, N.L. Fazzalari, A.C. Wu, M.R. Forwood, Temporal pattern of gene expression and histology of stress fracture healing. Bone **46**(2), 369–378 (2010). ISSN 1873-2763

131. Y. Kitase, L. Barragan, H. Qing, S. Kondoh, J.X. Jiang, M.L. Johnson, L.F. Bonewald, Mechanical induction of pge2 in osteocytes blocks glucocorticoid induced apoptosis through both the $\beta$ catenin and pka pathways. J. Bone Miner. Res. **25**(12), 2657–2668 (2010). ISSN 1523-4681

132. J. Klein-Nulend, C.M. Semeins, N.E. Ajubi, P.J. Nijweide, E.H. Burger, Pulsating fluid flow increases nitric oxide (no) synthesis by osteocytes but not periosteal fibroblasts-correlation with prostaglandin upregulation. Biochem. Biophys. Res. Commun. **217**(2), 640–648 (1995). ISSN 0006-291X

133. J. Klein-Nulend, A. Van der Plas, C.M. Semeins, N.E. Ajubi, J.A. Frangos, P.J. Nijweide, E.H. Burger, Sensitivity of osteocytes to biomechanical stress in vitro. FASEB J. **9**(5), 441–445 (1995). ISSN 0892-6638

134. J. Klein-Nulend, E.H. Burger, C.M. Semeins, L.G. Raisz, C.C. Pilbeam, Pulsating fluid flow stimulates prostaglandin release and inducible prostaglandin g/h synthase mrna expression in primary mouse bone cells. J. Bone Miner. Res. **12**(1), 45–51 (1997). ISSN 1523-4681

135. J. Klein-Nulend, M.H. Helfrich, J.G.H. Sterck, H. MacPherson, M. Joldersma, S.H. Ralston, C.M. Semeins, E.H. Burger, Nitric oxide response to shear stress by human bone cell cultures is endothelial nitric oxide synthase dependent. Biochem. Biophys. Res. Commun. **250**(1), 108–114 (1998)

136. S. Kontulainen, P. Kannus, H. Haapasalo, H. Sievnen, M. Pasanen, A. Heinonen, P. Oja, I. Vuori, Good maintenance of exercise-induced bone gain with decreased training of female tennis and squash players: a prospective 5-year follow-up study of young and old starters and controls. J. Bone Miner. Res. **16**(2), 195–201 (2001)

137. S. Kontulainen, H. Sievanen, P. Kannus, M. Pasanen, I. Vuori, Effect of long-term impact-loading on mass, size, and estimated strength of humerus and radius of female racquet-sports players: a peripheral quantitative computed tomography study between young and old starters and controls. J. Bone Miner. Res. **17**(12), 2281–2289 (2002)

138. I. Kramer, C. Halleux, H. Keller, M. Pegurri, J.H. Gooi, P.B. Weber, J.Q. Feng, L.F. Bonewald, M. Kneissel, Osteocyte wnt/$\beta$-catenin signaling is required for normal bone homeostasis. Mol. Cell. Biol. **30**(12), 3071–3085 (2010). ISSN 0270-7306

139. T.M. Kringelbach, D. Aslan, I. Novak, M. Ellegaard, S. Syberg, C.K.B. Andersen, K.A. Kristiansen, O. Vang, P. Schwarz, N.R. Jorgensen, Fine-tuned atp signals are acute mediators in osteocyte mechanotransduction. Cell. Signal. **27**(12), 2401–2409 (2015). ISSN 0898-6568

140. R.N. Kulkarni, A.D. Bakker, V. Everts, J. Klein-Nulend, Inhibition of osteoclastogenesis by mechanically loaded osteocytes: involvement of mepe. Calcif. Tissue Int. **87**(5), 461–468 (2010)

141. F.M. Lambers, G. Kuhn, C. Weigt, K.M. Koch, F.A. Schulte, R. Mller, Bone adaptation to cyclic loading in murine caudal vertebrae is maintained with age and directly correlated to the local micromechanical environment. J. Biomech. **48**(6), 1179–1187 (2015). ISSN 0021-9290

142. T. Lang, A. LeBlanc, H. Evans, Y. Lu, H. Genant, A. Yu, Cortical and trabecular bone mineral loss from the spine and hip in long-duration spaceflight. J. Bone Miner. Res. **19**(6), 1006–1012 (2004). ISSN 1523-4681

143. L.E. Lanyon, Analysis of surface bone strain in the calcaneus of sheep during normal loco-motion. J. Biomech. **6**(1), 41–49 (1973). ISSN 0021-9290

144. L.E. Lanyon, The influence of function on the development of bone curvature. An experimental study on the rat tibia. J. Zool. **192**(4), 457–466 (1980). ISSN 1469-7998

145. L.E. Lanyon, R.N. Smith, Bone strain in the tibia during normal quadrupedal locomotion. Acta Orthop. Scand. **41**(3), 238–248 (1970). ISSN 0001-6470

146. L.E. Lanyon, W.G.J. Hampson, A.E. Goodship, J.S. Shah, Bone deformation recorded in vivo from strain gauges attached to the human tibial shaft. Acta Orthop. Scand. **46**(2), 256–268 (1975). ISSN 0001-6470

147. N. Lara-Castillo, N.A. Kim-Weroha, M.A. Kamel, B. Javaheri, D.L. Ellies, R.E. Krumlauf, G. Thiagarajan, M.L. Johnson, In vivo mechanical loading rapidly activates $\beta$-catenin signaling in osteocytes through a prostaglandin mediated mechanism. Bone **76**, 58–66 (2015). ISSN 8756-3282

148. K. Lee, H. Jessop, R. Suswillo, G. Zaman, L.E. Lanyon, Endocrinology: bone adaptation requires oestrogen receptor-$\alpha$. Nature **424**(6947), 389 (2003)

149. K.C. Lee, H. Jessop, R. Suswillo, G. Zaman, L.E. Lanyon, The adaptive response of bone to mechanical loading in female transgenic mice is deficient in the absence of oestrogen receptor-$\alpha$ and -$\beta$. J. Endocrinol. **182**(2), 193–201 (2004). ISSN 0022-0795

150. I. Leichter, A. Simkin, J.Y. Margulies, A. Bivas, R. Steinberg, M. Giladi, Ch. Milgrom, Gain in mass density of bone following strenuous physical activity. J. Orthop. Res. **7**(1), 86–90 (1989). ISSN 1554-527X

151. T. Lekszycki, Functional adaptation of bone as an optimal control problem. J. Theor. Appl. Mech. **43**(3), 555–574 (2005)

152. O. Leupin, E. Piters, C. Halleux, S. Hu, I. Kramer, F. Morvan, T. Bouwmeester, M. Schirle, M. Bueno-Lozano, F.J.R. Fuentes, Bone overgrowth-associated mutations in the lrp4 gene impair sclerostin facilitator function. J. Biol. Chem. **286**(22), 19489–19500 (2011)

153. J. Li, R.L. Duncan, D.B. Burr, V.H. Gattone, C.H. Turner, Parathyroid hormone enhances mechanically induced bone formation, possibly involving l-type voltage-sensitive calcium channels. Endocrinology **144**(4), 1226–1233 (2003)

154. J. Li, D. Liu, H.Z. Ke, R.L. Duncan, C.H. Turner, The p2x7 nucleotide receptor mediates skeletal mechanotransduction. J. Biol. Chem. **280**(52), 42952–42959 (2005)

155. X. Li, Y. Zhang, H. Kang, W. Liu, P. Liu, J. Zhang, S.E. Harris, D. Wu, Sclerostin binds to lrp5/6 and antagonizes canonical wnt signaling. J. Biol. Chem. **280**(20), 19883–19887 (2005). ISSN 0021-9258

156. X. Li, M.S. Ominsky, Q.T. Niu, N. Sun, B. Daugherty, D. D'Agostin, C. Kurahara, Y. Gao, J. Cao, J. Gong, F. Asuncion, M. Barrero, K. Warmington, D. Dwyer, M. Stolina, S. Morony, I. Sarosi, P.J. Kostenuik, D.L. Lacey, W.S. Simonet, H.Z. Ke, C. Paszty, Targeted deletion of the sclerostin gene in mice results in increased bone formation and bone strength. J. Bone Miner. Res. **23**(6), 860–869 (2008)

157. X. Li, M.S. Ominsky, K.S. Warmington, S. Morony, J. Gong, J. Cao, Y. Gao, V. Shalhoub, B. Tipton, R. Haldankar, Q. Chen, A. Winters, T. Boone, Z. Geng, Q.T. Niu, H.Z. Ke, P.J. Kostenuik, W.S. Simonet, D.L. Lacey, C. Paszty, Sclerostin antibody treatment increases bone formation, bone mass, and bone strength in a rat model of postmenopausal osteoporosis. J. Bone Miner. Res. **24**(4), 578–588 (2009)

158. X.J. Li, W.S.S. Jee, Y.L. Li, P. Patterson-Buckendahl, Transient effects of subcutaneously administered prostaglandin e2 on cancellous and cortical bone in young adult dogs. Bone **11**(5), 353–364 (1990). ISSN 8756-3282

159. A. Liedert, L. Wagner, L. Seefried, R. Ebert, F. Jakob, A. Ignatius, Estrogen receptor and wnt signaling interact to regulate early gene expression in response to mechanical strain in osteoblastic cells. Biochem. Biophys. Res. Commun. **394**(3), 755–759 (2010)

160. C. Lin, X. Jiang, Z. Dai, X. Guo, T. Weng, J. Wang, Y. Li, G. Feng, X. Gao, L. He, Sclerostin mediates bone response to mechanical unloading through antagonizing wnt/$\beta$ catenin signaling. J. Bone Miner. Res. **24**(10), 1651–1661 (2009)

161. M.K. Lindberg, S.L. Alatalo, J.M. Halleen, S. Mohan, J.-A. Gustafsson, C. Ohlsson, Estrogen receptor specificity in the regulation of the skeleton in female mice. J. Endocrinol. **171**(2), 229–236 (2001)

162. A.-H. Lutter, U. Hempel, U. Anderer, P. Dieter, Biphasic influence of pge 2 on the resorption activity of osteoclast-like cells derived from human peripheral blood monocytes and mouse raw264.7 cells. Prostaglandins, Leukot. Essent. Fat. Acids (PLEFA) **111**, 1–7 (2016). ISSN 0952-3278

163. H. Macdonald, S. Kontulainen, M. Petit, P. Janssen, H. McKay, Bone strength and its determinants in pre- and early pubertal boys and girls. Bone **39**(3), 598–608 (2006)

164. H.M. Macdonald, S.A. Kontulainen, K.M. Khan, H.A. McKay, Is a school-based physical activity intervention effective for increasing tibial bone strength in boys and girls? J. Bone Miner. Res. **22**(3), 434–446 (2007)

165. H.M. Macdonald, S.A. Kontulainen, M.A. Petit, T.J. Beck, K.M. Khan, H.A. McKay, Does a novel school-based physical activity model benefit femoral neck bone strength in pre- and early pubertal children? Osteoporos. Int. **19**(10), 1445–1456 (2008)

166. H.M. Macdonald, D.M. Cooper, H.A. McKay, Anterior-posterior bending strength at the tibial shaft increases with physical activity in boys: evidence for non-uniform geometric adaptation. Osteoporos. Int. **20**(1), 61–70 (2009)

167. M. Machwate, S. Harada, C.T. Leu, G. Seedor, M. Labelle, M. Gallant, S. Hutchins, N. Lachance, N. Sawyer, D. Slipetz, Prostaglandin receptor ep4 mediates the bone anabolic effects of pge2. Mol. Pharmacol. **60**(1), 36–41 (2001). ISSN 1521-0111

168. I. MacIntyre, M. Zaidi, A.S. Alam, H.K. Datta, B.S. Moonga, P.S. Lidbury, M. Hecker, J.R. Vane, Osteoclastic inhibition: an action of nitric oxide not mediated by cyclic gmp. Proc. Natl. Acad. Sci. **88**(7), 2936–2940 (1991)

169. K.J. MackElvie, H.A. McKay, K.M. Khan, P.R. Crocker, A school-based exercise intervention augments bone mineral accrual in early pubertal girls. J. Pediatr. **139**(4), 501–508 (2001)

170. K.J. MacKelvie, H.A. McKay, M.A. Petit, O. Moran, K.M. Khan, Bone mineral response to a 7-month randomized controlled, school-based jumping intervention in 121 prepubertal boys: associations with ethnicity and body mass index. J. Bone Miner. Res. **17**(5), 834–844 (2002)

171. K.J. MacKelvie, M.A. Petit, K.M. Khan, T.J. Beck, H.A. McKay, Bone mass and structure are enhanced following a 2-year randomized controlled trial of exercise in prepubertal boys. Bone **34**(4), 755–764 (2004)

172. B.R. Martin, A genealogy of biomechanics: Presidential lecture, in *23rd Annual Conference of the American Society of Biomechanics*, 23 Oct: pp. 1–8 (1999)

173. R.N. McCarthy, L.B. Jeffcott, Effects of treadmill exercise on cortical bone in the third metacarpus of young horses. Res. Vet. Sci. **52**, 28–37 (1992)

174. M.R. McClung, A. Grauer, S. Boonen, M.A. Bolognese, J.P. Brown, A. Diez-Perez, B.L. Langdahl, J.-Y. Reginster, J.R. Zanchetta, S.M. Wasserman, Romosozumab in postmenopausal women with low bone mineral density. N. Engl. J. Med. **370**(5), 412–420 (2014)

175. H. McKay, L. MacLean, M. Petit, K. MacKelvie-O'Brien, P. Janssen, T. Beck, K. Khan, "bounce at the bell": a novel program of short bouts of exercise improves proximal femur bone mass in early pubertal children. Br. J. Sports Medi. **39**(8), 521–526 (2005)

176. K.M. Melville, N.H. Kelly, G. Surita, D.B. Buchalter, J.C. Schimenti, R.P. Main, F.P. Ross, M.C.H. van der Meulen, Effects of deletion of er$\alpha$ in osteoblast lineage cells on bone mass and adaptation to mechanical loading differ in female and male mice. J. Bone Miner. Res. **30**(8), 1468–1480 (2015)

177. T. Minamizaki, Y. Yoshiko, K. Kozai, J.E. Aubin, N. Maeda, Ep2 and ep4 receptors differentially mediate mapk pathways underlying anabolic actions of prostaglandin e2 on bone formation in rat calvaria cell cultures. Bone **44**(6), 1177–1185 (2009). ISSN 8756-3282

178. D.G. Monroe, M.E. McGee-Lawrence, M.J. Oursler, J.J. Westendorf, Update on wnt signaling in bone cell biology and bone disease. Gene **492**(1), 1–18 (2012)

179. F.L. Morris, G.A. Naughton, J.L. Gibbs, J.S. Carlson, J.D. Wark, Prospective ten-month exercise intervention in premenarcheal girls: positive effects on bone and lean mass. J. Bone Miner. Res. **12**(9), 1453–1462 (1997)

180. J.R. Mosley, L.E. Lanyon, Strain rate as a controlling influence on adaptive modeling in response to dynamic loading of the ulna in growing male rats. Bone **23**(4), 313–318 (1998). ISSN 8756-3282

181. J.R. Mosley, B.M. March, J. Lynch, L.E. Lanyon, Strain magnitude related changes in whole bone architecture in growing rats. Bone **20**(3), 191–198 (1997)

182. A. Moustafa, T. Sugiyama, J. Prasad, G. Zaman, T.S. Gross, L.E. Lanyon, J.S. Price, Mechanical loading-related changes in osteocyte sclerostin expression in mice are more closely associated with the subsequent osteogenic response than the peak strains engendered. Osteoporos. Int. **23**(4), 1225–1234 (2012)

183. M.G. Mullender, R. Huiskes, H. Weinans, A physiological approach to the simulation of bone remodeling as a self-organizational control process. J. Biomech. **27**(11), 1389–1394 (1994)

184. T. Nakashima, M. Hayashi, T. Fukunaga, K. Kurata, M. Oh-hora, J.Q. Feng, L.F. Bonewald, T. Kodama, A. Wutz, E.F. Wagner, Evidence for osteocyte regulation of bone homeostasis through rankl expression. Nat. Med. **17**(10), 1231–1234 (2011)

185. A. Nordstrom, T. Olsson, P. Nordstrom, Bone gained from physical activity and lost through detraining: a longitudinal study in young males. Osteoporos. Int. **16**(7), 835–841 (2005)

186. J.A. O'Connor, L.E. Lanyon, H. MacFie, The influence of strain rate on adaptive bone remodelling. J. Biomech. **15**(10), 767–781 (1982). ISSN 0021-9290

187. M.S. Ominsky, F. Vlasseros, J. Jolette, S.Y. Smith, B. Stouch, G. Doellgast, J. Gong, Y. Gao, J. Cao, K. Graham, Two doses of sclerostin antibody in cynomolgus monkeys increases bone formation, bone mineral density, and bone strength. J. Bone Miner. Res. **25**(5), 948–959 (2010)

188. E. Ozcivici, Y.K. Luu, B. Adler, Y.-X. Qin, J. Rubin, St Judex, C.T. Rubin, Mechanical signals as anabolic agents in bone. Nat. Rev. Rheumatol. **6**(1), 50–59 (2010). ISSN 1759-4790

189. D. Padhi, G. Jang, B. Stouch, L. Fang, E. Posvar, Single dose, placebo controlled, randomized study of amg 785, a sclerostin monoclonal antibody. J. Bone Miner. Res. **26**(1), 19–26 (2011)

190. A.M. Parfitt, The two faces of growth: Benefits and risks to bone integrity. Osteoporos. Int. **4**(6), 382–398 (1994). ISSN 1433-2965

191. J.L. Pathak, N. Bravenboer, F.P. Luyten, P. Verschueren, W.F. Lems, J. Klein-Nulend, A.D. Bakker, Mechanical loading reduces inflammation-induced human osteocyte-to-osteoclast communication. Calcif. Tissue Int. **97**(2), 169–178 (2015)

192. F.M. Pavalko, R.L. Gerard, S.M. Ponik, P.J. Gallagher, Y. Jin, S.M. Norvell, Fluid shear stress inhibits tnf induced apoptosis in osteoblasts: A role for fluid shear stress induced activation of pi3kinase and inhibition of caspase3. J. Cell. Physiol. **194**(2), 194–205 (2003). ISSN 1097-4652

193. B.L. Pennypacker, L.T. Duong, T.E. Cusick, P.J. Masarachia, M.A. Gentile, J.Y. Gauthier, W.C. Black, B.B. Scott, R. Samadfam, S.Y. Smith, D.B. Kimmel, Cathepsin k inhibitors prevent bone loss in estrogen-deficient rabbits. J. Bone Miner. Res. **26**(2), 252–262 (2011). ISSN 1523-4681

194. A.F. Pereira, *Cortical Bone Adaptation - A finite-element study of the mouse tibia*. Ph.d. thesis, Imperial College, London, UK (2014)

195. A.F. Pereira, B. Javaheri, A.A. Pitsillides, S.J. Shefelbine, Predicting cortical bone adaptation to axial loading in the mouse tibia. J. R. Soc. Interface **12**(110), 1–14 (2015)

196. M.A. Petit, H.A. McKay, K.J. MacKelvie, A. Heinonen, K.M. Khan, T.J. Beck, A randomized school-based jumping intervention confers site and maturity-specific benefits on bone structural properties in girls: a hip structural analysis study. J. Bone Miner. Res. **17**(3), 363–372 (2002)

197. H.E. Pettermann, T.J. Reiter, F.G. Rammerstorfer, Computational simulation of internal bone remodeling. Arch. Comput. Methods Eng. **4**(4), 295–323 (1997)

198. P. Pivonka, P.R. Buenzli, S. Scheiner, C. Hellmich, C.R. Dunstan, The influence of bone surface availability in bone remodelling a mathematical model including coupled geometrical and biomechanical regulations of bone cells. Eng. Struct. **47**, 134–147 (2013)

199. A. Prentice, T.J. Parsons, T.J. Cole, Uncritical use of bone mineral density in absorptiometry may lead to size-related artifacts in the identification of bone mineral determinants. Am. J. Clin. Nutr. **60**(6), 837–842 (1994)

200. Y.-X. Qin, C.T. Rubin, K.J. McLeod, Nonlinear dependence of loading intensity and cycle number in the maintenance of bone mass and morphology. J. Orthop. Res. **16**(4), 482–489 (1998). ISSN 1554-527X

201. D.M. Raab-Cullen, M.P. Akhter, D.B. Kimmel, R.R. Recker, Bone response to alternate-day mechanical loading of the rat tibia. J. Bone Miner. Res. **9**(2), 203–211 (1994)

202. J. Rahnert, X. Fan, N. Case, T.C. Murphy, F. Grassi, B. Sen, J. Rubin, The role of nitric oxide in the mechanical repression of rankl in bone stromal cells. Bone **43**(1), 48–54 (2008)

203. L.G. Raisz, F.N. Woodiel, Effects of selective prostaglandin ep 2 and ep 4 receptor agonists on bone resorption and formation in fetal rat organ cultures. Prostaglandins Other Lipid Mediat. **71**(3), 287–292 (2003). ISSN 1098-8823

204. H. Rangaswami, R. Schwappacher, T. Tran, G.C. Chan, S. Zhuang, G.R. Boss, R.B. Pilz, Protein kinase g and focal adhesion kinase converge on src/akt/$\beta$-catenin signaling module in osteoblast mechanotransduction. J. Biol. Chem. **287**(25), 21509–21519 (2012)

205. K.M. Reich, J.A. Frangos, Effect of flow on prostaglandin e2 and inositol trisphosphate levels in osteoblasts. Am. J. Physiol.Cell Physiol. **261**(3), C428–C432 (1991). ISSN 0363-6143

206. T.J. Reiter, *Functional adaptation of bone and application in optimal structural design*. Ph.d. thesis, Vienna University of Technology, Vienna, Austria (1995)

207. J. Ren, X.-H. Wang, G.-C. Wang, J.-H. Wu, 17$\beta$ estradiol regulation of connexin 43-based gap junction and mechanosensitivity through classical estrogen receptor pathway in osteocyte-like mlo-y4 cells. Bone **53**(2), 587–596 (2013)

208. M.D. Roberts, R.T. Hart, Shape adaptation of long bone structures using a contour based approach. Comput. Methods Biomech. Biomed. Eng. **8**(3), 145–156 (2005)

209. A.G. Robling, D.B. Burr, C.H. Turner, Partitioning a daily mechanical stimulus into discrete loading bouts improves the osteogenic response to loading. J. Bone Miner. Res. **15**(8), 1596–1602 (2000)

210. A.G. Robling, D.B. Burr, C.H. Turner, Recovery periods restore mechanosensitivity to dynamically loaded bone. J. Exp. Biol. **204**(Pt 19), 3389–3399 (2001)
211. A.G. Robling, F.M. Hinant, D.B. Burr, Ch.H Turner, Improved bone structure and strength after long-term mechanical loading is greatest if loading is separated into short bouts. J. Bone Miner. Res. **17**(8), 1545–1554 (2002). ISSN 1523-4681
212. A.G. Robling, A.B. Castillo, C.H. Turner, Biomechanical and molecular regulation of bone remodeling. Annu. Rev. Biomed. Eng. **8**, 455–498 (2006). ISSN 1523-9829
213. A.G. Robling, P.J. Niziolek, L.A. Baldridge, K.W. Condon, M.R. Allen, I. Alam, S.M. Mantila, J. Gluhak-Heinrich, T.M. Bellido, S.E. Harris, Mechanical stimulation of bone in vivo reduces osteocyte expression of sost/sclerostin. J. Biol. Chem. **283**(9), 5866–5875 (2008)
214. H. Roesler, The history of some fundamental concepts in bone biomechanics. J. Biomech. **20**(11), 1025–1034 (1987). ISSN 0021-9290
215. C.J. Rosen, M.L. Bouxsein, Mechanisms of disease: is osteoporosis the obesity of bone? Nat. Clin. Pract. Rheum. **2**(1), 35–43 (2006). ISSN 1745-8382
216. W. Roux, Beitrage zur morphologie der funktionellen anspassung. Arch. Anat. Physiol. Abt. **9**, 120–158 (1885)
217. C. Rubin, T. Gross, Y.X. Qin, S. Fritton, F. Guilak, K. McLeod, Differentiation of the bone-tissue remodeling response to axial and torsional loading in the turkey ulna. J. Bone Joint Surg. Am. **78**(10), 1523–1533 (1996)
218. C. Rubin, G. Xu, S. Judex, The anabolic activity of bone tissue, suppressed by disuse, is normalized by brief exposure to extremely low-magnitude mechanical stimuli. FASEB J. **15**(12), 2225–2229 (2001)
219. C.T. Rubin, L.E. Lanyon, Regulation of bone formation by applied dynamic loads. J. Bone Joint Surg. **66**(3), 397–402 (1984)
220. C.T. Rubin, L.E. Lanyon, Regulation of bone mass by mechanical strain magnitude. Calcif. Tissue Int. **37**(4), 411–417 (1985)
221. C.T. Rubin, L.E. Lanyon, Osteoregulatory nature of mechanical stimuli: function as a determinant for adaptive remodeling in bone. J. Orthop. Res. **5**(2), 300–310 (1987). ISSN 1554-527X
222. C.T. Rubin, K.J. McLeod, Promotion of bony ingrowth by frequency-specific, low-amplitude mechanical strain. Clin. Orthop. **298**, 165–174 (1994)
223. C.T. Rubin, T.S. Gross, K.J. McLeod, S.D. Bain, Morphologic stages in lamellar bone formation stimulated by a potent mechanical stimulus. J. Bone Miner. Res. **10**(3), 488–495 (1995)
224. J. Rubin, X. Fan, D.M. Biskobing, W.R. Taylor, C.T. Rubin, Osteoclastogenesis is repressed by mechanical strain in an in vitro model. J. Orthop. Res. **17**(5), 639–645 (1999)
225. Ch. Ruff, B. Holt, E. Trinkaus, Who's afraid of the big bad wolff?: wolff's law and bone functional adaptation. Am. J. Phys. Anthropol. **129**(4), 484–498 (2006). ISSN 1096-8644
226. K. Sabanai, M. Tsutsui, A. Sakai, H. Hirasawa, S. Tanaka, E. Nakamura, A. Tanimoto, Y. Sasaguri, M. Ito, H. Shimokawa, Genetic disruption of all no synthase isoforms enhances bmd and bone turnover in mice in vivo: involvement of the renin angiotensin system. J. Bone Miner. Res. **23**(5), 633–643 (2008)
227. Y. Sakuma, Z. Li, C.C. Pilbeam, C.B. Alander, D. Chikazu, H. Kawaguchi, L.G. Raisz, Stimulation of camp production and cyclooxygenase-2 by prostaglandin e2 and selective prostaglandin receptor agonists in murine osteoblastic cells. Bone **34**(5), 827–834 (2004). ISSN 8756-3282
228. S.J. Sample, R.J. Collins, A.P. Wilson, M.A. Racette, M. Behan, M.D. Markel, V.L. Kalscheur, Z. Hao, P. Muir, Systemic effects of ulna loading in male rats during functional adaptation. J. Bone Miner. Res. **25**(9), 2016–2028 (2010). ISSN 1523-4681
229. A. Santos, A.D. Bakker, B. ZandiehDoulabi, C.M. Semeins, J. Klein Nulend, Pulsating fluid flow modulates gene expression of proteins involved in wnt signaling pathways in osteocytes. J. Orthop. Res. **27**(10), 1280–1287 (2009)
230. A. Santos, A.D. Bakker, J.M.A. de Blieck-Hogervorst, J. Klein-Nulend, Wnt5a induces osteogenic differentiation of human adipose stem cells via rho-associated kinase rock. Cytotherapy **12**(7), 924–932 (2010)

231. A. Santos, A.D. Bakker, B. Zandieh-Doulabi, J.M.A. de Blieck-Hogervorst, J. Klein-Nulend, Early activation of the $\beta$-catenin pathway in osteocytes is mediated by nitric oxide, phosphatidylinositol-3 kinase/akt, and focal adhesion kinase. Biochem. Biophys. Res. Commun. **391**(1), 364–369 (2010)

232. L.K. Saxon, A.G. Robling, A.B. Castillo, S. Mohan, C.H. Turner, The skeletal responsiveness to mechanical loading is enhanced in mice with a null mutation in estrogen receptor-$\beta$. Am. J. Physiol.-Endocrinol. Metab. **293**(2), E484–E491 (2007)

233. L.K. Saxon, G. Galea, L. Meakin, J. Price, L.E. Lanyon, Estrogen receptors $\alpha$ and $\beta$ have different gender-dependent effects on the adaptive responses to load bearing in cancellous and cortical bone. Endocrinology **153**(5), 2254–2266 (2012)

234. T.A. Scerpella, J.N. Dowthwaite, P.F. Rosenbaum, Sustained skeletal benefit from childhood mechanical loading. Osteoporos. Int. **22**(7), 2205–2210 (2011)

235. S. Scheiner, P. Pivonka, C. Hellmich, Coupling systems biology with multiscale mechanics, for computer simulations of bone remodeling. Comput. Methods Appl. Mech. Eng. **254**, 181–196 (2013)

236. S. Scheiner, P. Pivonka, C. Hellmich, Poromicromechanics reveals that physiological bone strains induce osteocyte-stimulating lacunar pressure. Biomech. Model. Mechanobiol. **15**(1), 9–28 (2016). ISSN 1617-7940

237. M. Semnov, K. Tamai, X. He, Sost is a ligand for lrp5/lrp6 and a wnt signaling inhibitor. J. Biol. Chem. **280**(29), 26770–26775 (2005). ISSN 0021-9258

238. N.A. Sims, S. Dupont, A. Krust, P. Clement-Lacroix, D. Minet, M. Resche-Rigon, M. Gaillard-Kelly, R. Baron, Deletion of estrogen receptors reveals a regulatory role for estrogen receptors in bone remodeling in females but not in males. Bone **30**(1), 18–25 (2002)

239. T.M. Skerry, Mechanical loading and bone: what sort of exercise is beneficial to the skeleton? Bone **20**(3), 179–181 (1997). ISSN 8756-3282

240. T.M. Skerry, One mechanostat or many? modifications of the site-specific response of bone to mechanical loading by nature and nurture. J. Musculoskelet. Neuronal Interact. **6**(2), 122–127 (2006)

241. T.M. Skerry, The response of bone to mechanical loading and disuse: fundamental principles and influences on osteoblast/osteocyte homeostasis. Arch. Biochem. Biophys. **473**(2), 117–123 (2008). ISSN 0003-9861

242. E.L. Smith, C. Gilligan, Dose-response relationship between physical loading and mechanical competence of bone. Bone **18**(1), S45–S50 (1996). ISSN 8756-3282

243. D. Somjen, I. Binderman, E. Berger, A. Harell, Bone remodelling induced by physical stress is prostaglandin e2 mediated. Biochimica et Biophysica Acta (BBA)-Gen. Subj. **627**(1), 91–100 (1980). ISSN 0304-4165

244. S. Srinivasan, D.A. Weimer, S.C. Agans, S.D. Bain, T.S. Gross, Low-magnitude mechanical loading becomes osteogenic when rest is inserted between each load cycle. J. Bone Miner. Res. **17**(9), 1613–1620 (2002). ISSN 1523-4681

245. T. Sugiyama, G.L. Galea, L.E. Lanyon, J.S. Price, Mechanical loading-related bone gain is enhanced by tamoxifen but unaffected by fulvestrant in female mice. Endocrinology **151**(12), 5582–5590 (2010)

246. A. Sunters, V.J. Armstrong, G. Zaman, R.M. Kypta, Y. Kawano, L.E. Lanyon, J.S. Price, Mechano-transduction in osteoblastic cells involves strain-regulated estrogen receptor $\alpha$-mediated control of insulin-like growth factor (igf) i receptor sensitivity to ambient igf, leading to phosphatidylinositol 3-kinase/akt-dependent wnt/lrp5 receptor-independent activation of $\beta$-catenin signaling. J. Biol. Chem. **285**(12), 8743–8758 (2010)

247. S.D. Tan, A.M. Kuijpers-Jagtman, C.M. Semeins, A.L.J.J. Bronckers, J.C. Maltha, J.W. Von den Hoff, V. Everts, J. Klein-Nulend, Fluid shear stress inhibits tnf-induced osteocyte apoptosis. J. Dent. Res. **85**(10), 905–909 (2006). ISSN 0022-0345

248. S.D. Tan, T.J. de Vries, A.M. Kuijpers-Jagtman, C.M. Semeins, V. Everts, J. Klein-Nulend, Osteocytes subjected to fluid flow inhibit osteoclast formation and bone resorption. Bone **41**(5), 745–751 (2007)

249. W.R. Thompson, C.T. Rubin, J. Rubin, Mechanical regulation of signaling pathways in bone. Gene **503**(2), 179–193 (2012). ISSN 0378-1119

250. A.G. Torrance, J.R. Mosley, R.F. Suswillo, L.E. Lanyon, Noninvasive loading of the rat ulna in vivo induces a strain-related modeling response uncomplicated by trauma or periostal pressure. Calcif. Tissue Int. **54**(3), 241–247 (1994)

251. C.H. Turner, Three rules for bone adaptation to mechanical stimuli. Bone **23**(5), 399–407 (1998). ISSN 8756-3282

252. C.H. Turner, A.G. Robling, Designing exercise regimens to increase bone strength. Exerc. Sport Sci. Rev. **31**(1), 45–50 (2003)

253. C.H. Turner, A.G. Robling, Mechanical loading and bone formation. BoneKEy **1**(9), 15–23 (2004)

254. C.H. Turner, M.P. Akhter, D.M. Raab, D.B. Kimmel, R.R. Recker, A noninvasive, in vivo model for studying strain adaptive bone modeling. Bone **12**(2), 73–79 (1991)

255. C.H. Turner, T.A. Woltman, D.A. Belongia, Structural changes in rat bone subjected to long-term, in vivo mechanical loading. Bone **13**, 417–422 (1992)

256. C.H. Turner, M.R. Forwood, M.W. Otter, Mechanotransduction in bone: do bone cells act as sensors of fluid flow? FASEB J. **8**(11), 875–878 (1994)

257. C.H. Turner, M.R. Forwood, J.Y. Rho, T. Yoshikawa, Mechanical loading thresholds for lamellar and woven bone formation. J. Bone Miner. Res. **9**(1), 87–97 (1994). ISSN 0884-0431 (Print)

258. C.H. Turner, I. Owan, Y. Takano, Mechanotransduction in bone: role of strain rate. Am. J. Physiol. Endocrinol. Metab. **269**(3), E438–E442 (1995)

259. C.H. Turner, Y. Takano, I. Owan, G.A. Murrell, Nitric oxide inhibitor l-name suppresses mechanically induced bone formation in rats. Am. J. Physiol. Endocrinol. Metab. **270**(4), E634–E639 (1996)

260. M. Tveit, B.E. Rosengren, J.A. Nilsson, M.K. Karlsson, Exercise in youth: High bone mass, large bone size, and low fracture risk in old age. Scand. J. Med. Sci. Sports **25**(4), 453–461 (2015)

261. Y. Umemura, T. Ishiko, T. Yamauchi, M. Kurono, S. Mashiko, Five jumps per day increase bone mass and breaking force in rats. J. Bone Miner. Res. **12**(9), 1480–1485 (1997)

262. B.A. Uthgenannt, M.J. Silva, Use of the rat forelimb compression model to create discrete levels of bone damage in vivo. J. Biomech. **40**(2), 317–324 (2007). ISSN 0021-9290

263. A.H. van Lierop, N.A.T. Hamdy, M.E. van Egmond, E. Bakker, F.G. Dikkers, S.E. Papapoulos, Van buchem disease: clinical, biochemical, and densitometric features of patients and disease carriers. J. Bone Miner. Res. **28**(4), 848–854 (2013)

264. O. Verborgt, G.J. Gibson, M.B. Schaffler, Loss of osteocyte integrity in association with microdamage and bone remodeling after fatigue in vivo. J. Bone Miner. Res. **15**(1), 60–7 (2000)

265. S.J. Warden, R.K. Fuchs, A.B. Castillo, I.R. Nelson, C.H. Turner, Exercise when young provides lifelong benefits to bone structure and strength. J. Bone Miner. Res. **22**(2), 251–259 (2007)

266. S.J. Warden, S.M. Mantila Roosa, M.E. Kersh, A.L. Hurd, G.S. Fleisig, M.G. Pandy, R.K. Fuchs, Physical activity when young provides lifelong benefits to cortical bone size and strength in men. Proc. Natl. Acad. Sci. **111**(14), 5337–5342 (2014)

267. R.S. Weinstein, R.L. Jilka, A.M. Parfitt, S.C. Manolagas, Inhibition of osteoblastogenesis and promotion of apoptosis of osteoblasts and osteocytes by glucocorticoids. potential mechanisms of their deleterious effects on bone. J. Clin. Investig. **102**(2), 274–282 (1998)

268. A.R. Wijenayaka, M. Kogawa, H.P. Lim, L.F. Bonewald, D.M. Findlay, G.J. Atkins, Sclerostin stimulates osteocyte support of osteoclast activity by a rankl-dependent pathway. PLoS ONE **6**(10), e25900 (2011)

269. S.H. Windahl, L. Saxon, A.E. Brjesson, M.K. Lagerquist, B. Frenkel, P. Henning, U.H. Lerner, G.L. Galea, L.B. Meakin, C. Engdahl, Estrogen receptor $\alpha$ is required for the osteogenic response to mechanical loading in a ligand independent manner involving its activation function 1 but not 2. J. Bone Miner. Res. **28**(2), 291–301 (2013)

270. D.G. Winkler, M.K. Sutherland, J.C. Geoghegan, C. Yu, T. Hayes, J.E. Skonier, D. Shpektor, M. Jonas, B.R. Kovacevich, K. Staehling, Hampton. Osteocyte control of bone formation via sclerostin, a novel bmp antagonist. EMBO J. **22**(23), 6267–6276 (2003)

271. J. Wolff, *Das Gesetz der Transformation der Knochen* (Hirschwald, Berlin, 1892)

272. T.J. Wronski, E. Morey-Holton, W.S. Jee, Skeletal alterations in rats during space flight. Adv. Space Res. **1**(14), 135–140 (1981)

273. X. Xia, N. Batra, Q. Shi, L.F. Bonewald, E. Sprague, J.X. Jiang, Prostaglandin promotion of osteocyte gap junction function through transcriptional regulation of connexin 43 by glycogen synthase kinase 3/$\beta$-catenin signaling. Mol. Cell. Biol. **30**(1), 206–219 (2010). ISSN 0270-7306

274. J. Xiong, M. Onal, R.L. Jilka, R.S. Weinstein, S.C. Manolagas, C.A. O'Brien, Matrix-embedded cells control osteoclast formation. Nat. Med. **17**(10), 1235–1241 (2011)

275. P.F. Yang, G.P. Brggemann, J. Rittweger, What do we currently know from in vivo bone strain measurements in humans? J. Musculoskelet. Neuronal Interact. **11**(1), 8–20 (2011)

276. J. You, G.C. Reilly, X. Zhen, C.E. Yellowley, Q. Chen, H.J. Donahue, C.R. Jacobs, Osteopontin gene regulation by oscillatory fluid flow via intracellular calcium mobilization and activation of mitogen-activated protein kinase in mc3t3e1 osteoblasts. J. Biol. Chem. **276**(16), 13365–13371 (2001)

277. J. You, C.R. Jacobs, T.H. Steinberg, H.J. Donahue, P2y purinoceptors are responsible for oscillatory fluid flow-induced intracellular calcium mobilization in osteoblastic cells. J. Biol. Chem. **277**(50), 48724–48729 (2002)

278. L. You, S. Temiyasathit, P. Lee, C.H. Kim, P. Tummala, W. Yao, W. Kingery, A.M. Malone, R.Y. Kwon, C.R. Jacobs, Osteocytes as mechanosensors in the inhibition of bone resorption due to mechanical loading. Bone **42**(1), 172–179 (2008)

279. G. Zaman, M.Z. Cheng, H.L. Jessop, R. White, L.E. Lanyon, Mechanical strain activates estrogen response elements in bone cells. Bone **27**(2), 233–239 (2000)

280. G. Zaman, H.L. Jessop, M. Muzylak, R.L. De Souza, A.A. Pitsillides, J.S. Price, L.E. Lanyon, Osteocytes use estrogen receptor alpha to respond to strain but their eralpha content is regulated by estrogen. J. Bone Miner. Res. **21**(8), 1297–1306 (2006)

281. M. Zayzafoon, W.E. Gathings, J.M. McDonald, Modeled microgravity inhibits osteogenic differentiation of human mesenchymal stem cells and increases adipogenesis. Endocrinology **145**(5), 2421–2432 (2004). ISSN 0013-7227

# Application of Disease System Analysis to Osteoporosis: From Temporal to Spatio-Temporal Assessment of Disease Progression and Intervention

**Silvia Trichilo and Peter Pivonka**

**Abstract**  Osteoporosis (OP) is a progressive bone disorder regarded as an important worldwide health issue. OP is characterised by a slow reduction of the bone matrix and changes in the bone matrix properties. Novel drug treatments are continuously developed to reduce the risk of bone fractures. Assessing the effects of novel and existing treatments on OP can be challenging. This is due to the difficulties of establishing the effects of the drug on the disease progression as reflected in the slowly changing bone mineral density (BMD). In recent years, our understanding of the pathophysiology of OP has considerably improved. Biomarkers reflecting bone physiology have been identified at the cellular, tissue and organ levels. Cellular biomarkers reflect the dynamics of bone remodelling (i.e., bone formation and resorption) on a short time scale. On the other hand, tissue and organ scale biomarkers show changes of BMD and bone structural arrangements on a larger time scale. Biomarkers can be used to characterise bone remodelling and to quantify the effect of the drug on OP. Recently, the concept of disease system analysis (DSA) has been proposed as a novel approach to quantitatively characterise drug effects on disease progression. This approach integrates physiology, disease progression and drug treatment in a comprehensive mechanism-based modelling framework using a large amount of complementary biomarker data. This chapter will provide an overview of the use of DSA to characterise drug effects on OP. We will review classical (i.e., non-mechanistic) pharmacokinetic-pharmacodynamic (PK/PD) models used to study *drug dose-effect* responses. Latest mechanistic bone remodelling models will be presented together with the study of the effect of the drug denosumab on

S. Trichilo · P. Pivonka (✉)
St Vincent's Department of Surgery, The University of Melbourne,
Melbourne, VIC, Australia
e-mail: peter.pivonka@qut.edu.au

S. Trichilo · P. Pivonka
Australian Institute of Musculoskeletal Science, Melbourne, VIC, Australia
e-mail: strichilo@student.unimelb.edu.au

P. Pivonka
School of Chemistry, Physics and Mechanical Engineering, Queensland University
of Technology, Brisbane, QLD, Australia

disease progression in postmenopausal osteoporosis (PMO). Finally, we will provide an outlook on how to extend the temporal mechanistic model towards a spatio-temporal description. We conclude that the development of fully mechanistic disease system models of OP has great potential to adequately predict the long-term effects of drug treatments on clinical outcomes. This may provide a means for patient-specific estimation of bone fracture risk.

# 1 Introduction

The objective of this chapter is to introduce the theoretical framework of disease system analysis (DSA) to analyse disease progression and therapeutic intervention in osteoporosis (OP). Firstly, we will introduce the classical pharmacokinetic (PK), pharmacodynamic (PD) and pharmacokinetic-pharmacodynamic (PK/PD) modelling approaches in the context of OP and drug interventions. The PK/PD framework will then be expanded towards DSA allowing for the classification of disease status and progression, together with assessment of various drug interventions. Two types of models will be discussed: (i) the one treating the symptoms of a disease and their response to the treatment directly, i.e., without consideration of the underlying biological system; (ii) the one treating the disease progression as a turnover model allowing the distinction between the disease progress and the effects of the drug on the disease status. Based on the limitations of current DSA models of OP, we introduce a comprehensive mechanism-based disease progression model. Key variables in this model are: bone cells concentrations (active osteoblasts, active osteoclasts and their precursor cells); cell-cell signalling pathway (RANK-RANKL-OPG pathway); hormonal (PTH) and local (TGF-$\beta$) regulatory factors; mechanical strains both at the macroscopic level of cortical and trabecular bone and at the microscopic level of the extra-vascular bone matrix. The latter variable provides the ability to account for the biomechanical feedback coming from osteocytes. Subsequently, this model is used to investigate postmenopausal osteoporosis (PMO) and its treatment with the anti-catabolic drug denosumab. Finally, we will provide an outlook on how to extend temporal models of bone remodelling to spatio-temporal models, a necessary prerequisite to accurately estimate the risk of bone fracture.

OP is a progressive disease characterised by fractures of spine, hip and wrist as primary clinical manifestations. It is a major health problem in the society placed alongside diseases such as breast cancer, cardiovascular diseases and diabetes mellitus when considering prevalence, lifetime risk and socio-economical impact [76, 143]. Most often, OP is diagnosed only after a fracture occurs, it is therefore referred to as *silent disease*. Because of its importance, many researchers are currently studying to understand the origin of the disease and to find effective treatments [13]. New drugs are continually being developed and trialled on animals, only the most promising ones are then tested on humans. Drug efficacy and safety are usually assessed using biomarkers. In general, biomarkers can be divided into two categories: *site-specific* and *non-site specific*. The former category allows to assess bone mineral density

(BMD) and bone quality at a particular bone site using X-ray imaging technologies. The latter category, also referred to as bone turnover markers (BTMs), allows to assess the activity of bone cells in the entire body by measuring bone molecular product concentrations in blood and/or urine [23].

Several scientific communities have approached the problem of OP aiming to better understand the deterioration of bone mechanical properties, to predict bone fracture risk and to quantify the effects of drugs on disease progression. The approach taken by materials, structural mechanics and biomedical engineering researchers is based on the development of deterministic methods including experimental testing techniques (e.g., mechanical characterisation and imaging-based methods) and computational models assessing bone mechanical behaviour at different scales [177].

On the other hand, the approach taken by clinical researchers investigating drug efficacy and safety is mainly based on the use of statistical methods, including randomised controlled trials (RCTs) [91]. The development of new drug treatments, however, is challenging. The trials require a large cohort of patients, due to the necessity of establishing a statistically significant anti-fracture benefit, and are long in duration, due to the slow progression of the disease.

Finally, basic bone scientists are concerned with the development of animal models (including genetically engineered animals) in order to investigate intra- and inter-cellular aspects of bone diseases and interventions [71]. This approach has significantly improved the knowledge of the bone physiology and the underlying mechanisms of OP. In particular, a number of biomarkers reflecting different aspects and levels of bone physiology and disease are now available.

DSA is a promising methodology which combines all the insights gained from these different but complementary approaches, via computational modelling. DSA aims to include the major signalling mechanisms and the experimentally observable results (e.g., temporal or spatio-temporal data on biomarkers) in order to create a mechanistic view of the underlying bone physiology and disease progression. Purely experimental approaches establish statistical correlations between individual risk factors and disease progression biomarkers. Mechanism-based models instead, allow for the integration of different factors into a comprehensive model of bone remodelling, providing a more holistic view of the disease progression and the effect of interventions. Moreover, once that the computational model has been developed, it can either be used to predict outcomes or as hypothesis generating tool to design new experiments [120].

Traditionally, PK/PD modelling was used to characterise the time course of a drug effect with the primary objective of optimising the dosing regimen and the delivery profile. Recently, PK/PD models have also been applied in the drug development process [41, 124]. The approach of conventional PK/PD models is descriptive, empirical and driven by a large amount of data. Due to their nature, these models are not able to predict clinical responses beyond the data which they are based on. For this reason, mechanism-based PK/PD models have been developed [41, 126, 147]. These are more sophisticated models which take into account the underlying mechanisms of a pathology and the action of the drug, with the aim of characterising the intermediate processes between the drug administration and the drug effect. This

characterisation relies on biomarker data and on two categories of parameters: the ones describing the properties of the drug (e.g., affinity and target activation) and the ones describing the properties of the biological system [40, 41, 124]. The separation between drug and system is crucial for the prediction and the extrapolation of treatment effects, in particular when the model takes into account disease-modifying agents that specifically target the underlying time course of the disease.

Nevertheless, both PK/PD and DSA models have had, so far, limited success in predicting fracture risk in osteoporotic subjects. Potential limitations of these approaches can be the non-detailed modelling of the underlying mechanical properties of bone, and the use of temporal assessment alone to study the effects of anti-catabolic and anabolic drugs on bone biomarkers. With the continuous improvement of bone imaging technologies, however, different spatial regions can be distinguished in bone and local BMD or bone volume (BV/TV) can be monitored. Given that bone structural properties strongly depend on the spatial distribution of BV/TV, understanding the effects of drugs on spatial changes is critical.

Here we will present our group effort over the past years to incorporate bone mechanical behaviour in mechanism based PK/PD models and extend the DSA approach to spatio-temporal models. In Sect. 2 we introduce the basic principles of bone physiology including: (i) a summary of the hierarchical structure of bone material; (ii) the mechanical and physiological function of bone modelling and remodelling; (iii) the major cell-cell signalling pathways; (iv) the mechanical and hormonal regulatory factors controlling bone homeostasis. In Sect. 3 we introduce the notion of bone biomarkers which provide the *signature* of a particular bone in terms of bone mass and turnover. The latter parameter indicates the amount of bone replaced in a certain period of time and can be used in the characterisation of bone homeostasis and bone diseases such as OP. Biomarkers will be discussed with respect to their catabolic or anabolic characteristics. BMD is discussed with respect to different measurement technologies. In Sect. 4 we discuss bone pathologies, in particular age-related bone loss and OP. Diagnosis and currently available treatment options are also described in this section. DSA in the context of conventional PK/PD models is reviewed in Sect. 5, introducing the notion of linear and asymptotic disease progression models together with symptomatic and protective disease interventions. In Sect. 6 we extend the concept of PK/PD modelling in bone with respect to mechanism-based PK/PD models and we introduce the bone remodelling model by Pivonka et al. [121] and extensions thereof. This mechanistic PK/PD model contains specific expressions of signalling pathways, hormones and growth factors that allow to quantitatively characterise processes and interactions from the drug administration to its effect. As an example, we show the effect that the anti-catabolic drug denosumab has on PMO. Finally, in Sect. 7 we provide a summary of the chapter with future directions in the application of DSA in OP research with emphasis on spatio-temporal modelling.

## 2 Relationship Between Structure and Function of Bone: An Overview

### 2.1 Bone Structure and Function

**Material Characterisation: Organic/Inorganic**

The skeletal system is a major constituent of the human body. It is an extensive connective tissue composed of bones, tendons, ligaments and cartilage. Bone is a dynamic living tissue which refers to a family of materials with different structural motifs, but all having in common the mineralised collagen fibril as the basic building block [170]. These materials have evolved to fulfil a variety of mechanical functions for which the structures are fine-tuned and adapted. Bone structure is highly complex and it can be described by up to seven hierarchical levels of organization (Fig. 1) [129]. The basic building block of bone, i.e., the mineralised collagen fibril, is composed of three major components. The first component is the *organic* part, mainly composed of Type I collagen present in the structural form that can also be found in skin, tendon and other soft tissues. Collagen constitutes the main component of the osteoid matrix (with proteoglycans and non-collagenous proteins forming additional constituents) into which, and in some cases onto which, the mineral forms. The second component is the bone mineral, which represents the *inorganic* part of bone tissue composed of dahllite, also known as carbonated apatite ($Ca_5 (PO_4, CO_3)_3 (OH)$). Water represents the third component. During the biological process of bone remodelling (see also Sect. 2.2), osteoblasts and osteocytes assemble these three components into an ordered structure known as mineralised collagen fibril.

**Cortical and Trabecular Bone**

Based on morphological structure, mechanical properties and metabolic functions, two types of bone can be distinguished: *cortical* and *trabecular* (Fig. 1). Cortical or dense bone forms the outer shell of bones. It consists of layers of bone (i.e., lamellae) organized around a central canal in which blood vessels, nerves, connective tissue and lymphatic vessels are found. This functional unit is referred to as Haversian system or osteon. Approximately 80% of the skeletal mass is cortical bone. On the other hand, trabecular or cancellous bone consists of an interconnected network of struts and plates. Pore spaces within this network are filled with blood vessels, nerves and bone marrow. Trabecular bone is found at the distal end of long bones, in short bones, in the inner surfaces of flat bones and in irregular bones such as vertebrae. Approximately 20% of the skeletal mass is trabecular bone.

**Bone Mechanical Properties, Bone Quality and Fracture Risk**

Cortical bone is a dense calcified tissue having high resistance to bending and torsion. It provides mechanical strength and protection to vital internal organs and bone marrow. Cortical bone also forms the basis for muscles attachment, supporting locomotion. On the other hand, trabecular bone is less dense and composed of thin
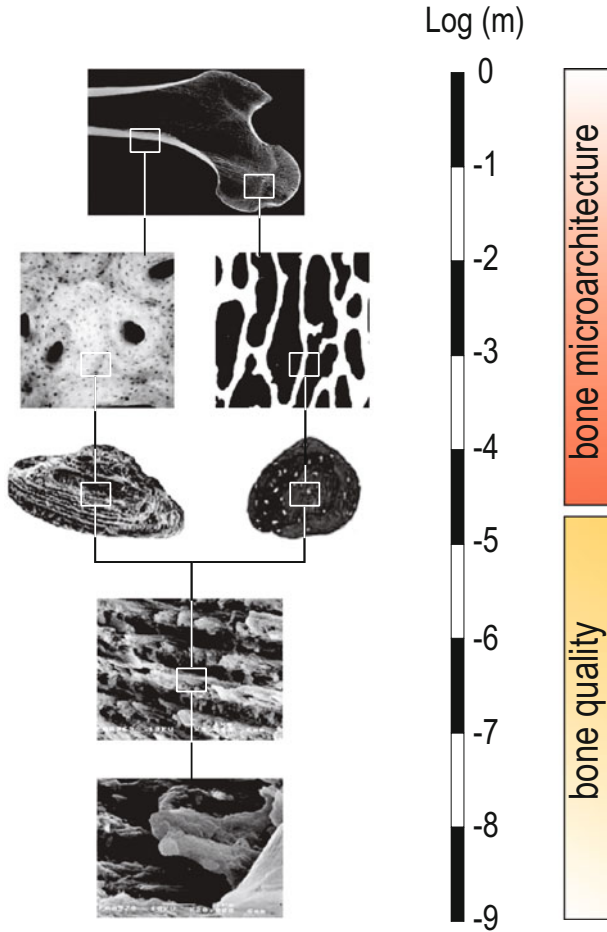
**Fig. 1** Hierarchical structure of bone: from whole organ scale (cortical and cancellous bone) to cylindrical arrangements in osteons and features of bone quality (composition and arrangement of mineralised collagen fibrils, size of bone mineral crystals, collagen molecules and non-collagenous proteins)

trabeculae which form a robust 3D structural framework with elastic properties. It contributes to provide mechanical support, particularly in bones such as vertebrae, femoral head and neck. Due to its high turnover rate, trabecular bone has a major function in metabolic processes serving as a reservoir of calcium and phosphate for the maintenance of mineral homeostasis (see also Sect. 2.2). Cortical bone instead, is involved in metabolic processes only in situations of severe or prolonged mineral deficit [58, 87, 150].

In order to determine the biomechanical function of bone, mechanical testing is commonly applied. Traditional mechanical testing provides detailed information on

the whole-bone mechanical properties and on the properties of the matrix material, however, it does not reveal local failure characteristics. High correlation has been established between the elastic properties of bone and its density [27]. Utilising multiscale modelling techniques based on micromechanics, it is now possible to link individual bone constituents in a hierarchical way so that anisotropic elastic properties of bone can be predicted [60]. A correlation has also been shown between bone strength and bone density [27]. However, computational prediction of bone strength is challenging because of the non-linear and inelastic material behaviour of bone tissue. Bone failure is a complex process that depends on: (i) the applied loading regimen (uniaxial vs. multiaxial); (ii) the loading rate (static vs. dynamic); (iii) the structural and material properties. When exposed to a slow and monotonous loading condition, bone initially deforms elastically. After reaching the yield limit, the deformation becomes inelastic. Close to the ultimate load (i.e., maximum structural load) high local deformations occur, together with local growth and propagation of microcracks that eventually lead to a macroscopic failure [103]. Another important quantity characterising bone resistance to failure is the bone toughness, i.e., the integral of the stress-strain curve in the post elastic regimen [134]. During ageing, bone becomes more brittle due to the loss of ultrastructural water in the bone matrix that significantly reduces bone toughness [113]. Furthermore, anti-resorptive drug treatments have been associated with increased brittleness of bones [153]. Although some work has been done to clarify the characteristics of bone failure, fundamental knowledge on how failure originates within trabecular and cortical bone is still lacking. However, to be able to estimate the fracture risk of a specific patient, a detailed understanding of bone failure behaviour is essential.

The emergence of accurate and precise bone densitometry over the last two decades resulted in bone density becoming a primary target in the diagnosis and monitoring of OP. Bone strength and fracture risk are generally assessed by measuring BMD. Although large population studies demonstrated a strong correlation between bone density and bone mechanical properties of trabecular bone [149, 164], bone mechanical properties also depend on the architecture and the intrinsic material properties of the tissue [25]. In fact, the risk of fracture in a 75 year old woman is 4–7 times higher than the risk of fracture in a 45 year old woman having the same bone mass [68]. This demonstrates that bone fragility is not determined by bone mass only. In agreement with this idea, it has recently been observed that all the anti-resorptive treatments for OP have about the same fracture efficacy, although there is a seven-fold difference in their effect on BMD. Consequently, it is difficult to achieve an accurate assessment of bone fracture risk in a clinical environment solely on the basis of bone densitometry. Other factors such as bone microarchitecture, bone turnover (i.e., proportion of bone replaced in a certain unit time, usually expressed as %/year), microcrack and microdamage distributions and bone matrix material properties also have important roles. All these factors, together with BMD, are often referred to as *bone quality* [25]. In the following, two factors of bone quality, i.e., bone turnover and degree of mineralisation of bone tissue, will be discussed in the context of bone physiology and pathology.

## *2.2   Bone Physiology*

Bone has multiple functions within the body. Among these, the most important one is to enable locomotion by providing support to muscles, ligaments, tendons and joints. To carry out this function, bone needs to maintain structure and strength with minimal weight. Bone also provides a readily accessible store of calcium to support calcium homeostasis. Other roles of bone include: providing a protected environment for bone marrow, providing support for a haematopoietic stem cell niche [26], acting as an endocrine organ regulating energy metabolism potentially via osteocalcin [31].

### Bone Modelling and Remodelling

To accomplish all its functions, bone needs several cellular mechanisms. To meet the biomechanical demand, for example, bone requires a control system able to detect bone strain and/or other mechanical quantities (e.g., hydrostatic pressure and fluid flow) and microdamage. Signalling systems inducing a reparative response, i.e., inducing bone resorption to remove damaged bone and bone formation to replace it with new one, are also needed [80]. The main processes by which bone is able to continuously adapt and renew in response to biomechanical and metabolic demands are *bone modelling* and *bone remodelling*.[1]

Bone modelling refers to the process in which bone formation and bone resorption occur at spatially distinct sites [7, 72]. It shapes skeletal elements and ensures the acquisition of the appropriate bone morphology and mass during growth. Bone modelling occurs at a low rate throughout life. It is required for both bone repair and bone adaptation to mechanical loading, being the latter in control of the size, structure and shape of bones.

On the other hand, bone remodelling refers to the process of bone renewal in which bone resorption and bone formation occur spatially at the same site and turn bone tissue over at regular intervals. In remodelling, bone resorption and formation are coupled, occurring in packages of cells along specific sites on the same bone surface. This warrants that old bone sites that have been resorbed will be filled with new bone. While bone modelling predominantly occurs in the growing skeleton, bone remodelling occurs throughout life. Moreover, bone remodelling has been suggested to regulate calcium and phosphorus homeostasis and to repair microcracks.

### Bone Cells in (Re)modelling

To translate local mechanical and autocrine/paracrine biochemical signals into tailored bone remodelling responses, certain requirements need to be fulfilled. Less structurally important bone, for example, should be targeted for calcium mobilization during times of high calcium demand [93]. To achieve all the diverse requirements, three bone cell types are present in bone microenvironment:

---

[1]Following the notation of L. Lanyon we will use (re)modelling to denote both modelling and remodelling.

*Osteocytes* reside within the bone matrix. They interact with the surrounding bone matrix and communicate to adjacent osteocytes via a dense and interconnecting canaliculi network which contains osteocyte cell processes. Osteocytes orchestrate the detection and the response to microdamage, fracture, and changing bone strain. They represent about 90% of all bone cells [84].

*Osteoblasts* are cells of mesenchymal origin which line the surface of bone. They form bone by progressive bone matrix deposition and subsequent mineralisation. Cells of this lineage have receptors for parathyroid hormone (PTH), 1,25-dihydroxyvitamin D, and a number of local regulatory factors [136]. After completing the bone formation process, these cells can either undergo apoptosis (i.e., cell death), remain on the newly formed bone surface and become lining cells, or be trapped in the bone matrix and further differentiate into osteocytes.

*Osteoclasts* are large multinucleated cells of haematopoietic origin able to resorb bone. Adhering to bone surface, they secrete acid to demineralise bone and proteolytic enzymes to break down the collagenous bone matrix [22, 165]. Osteoclasts are typically unable to respond directly to pro-resorptive hormones and require the presence of osteoblasts to locally regulate their differentiation and activity.

Communication between osteocytes, osteoblasts and osteoclasts enables a spatio-temporal coordinated response to both physiological and pathological demands via the integration of multiple catabolic and anabolic signals. Bone cells are organised into clusters named *basic multicellular units* (BMUs) by Frost who was the first to describe them as the basic functional unit of bone remodelling [44, 50, 51]. In a normal adult skeleton, there are about $1.7 \cdot 10^6$ BMUs [50, 52, 169]. At the front of a BMU, osteoclasts dissolve the bone matrix creating a resorption cavity (also known as cutting cone). Towards the rear of a BMU, osteoblasts secrete osteoid, an organic matrix of collagen fibres gradually refilling the resorbed cavity. This organic matrix becomes gradually mineralised and forms new bone (Fig. 2). The osteoid mineralisation process is believed to be partly regulated by osteoblasts and osteocytes. In cortical bone, BMUs proceed through the bulk of the tissue leaving new secondary osteons in their wake. Osteons are cylindrical tissue structures having a diameter of about 100–200 µm, have a length of up to 10 mm and are aligned with the main loading direction [85, 159, 160]. In trabecular bone, BMUs proceed along the surface of plates and struts, forming hemi-osteons or trenches of new bone tissue about 60–70 µm deep [159].

Since trabecular bone remodelling operates on bone surface, it can be associated with either negative bone balance (net bone loss) or positive bone balance (net bone gain). In cortical bone the situation depends on the mode of remodelling: if a new Haversian canal (type I osteon) is created, the remodelling process always implies net bone loss; if a pre-existing Haversian canal (type II osteon) is used, net bone gain occurs if the diameter of the Haversian canal is reduced by the passage of the BMU [116, 135]. The exact proportion of type I over type II osteons in cortical bone remodelling is controversial, in fact, vascular channels increase with age [116], but age-related bone loss is due to increased pore area rather than increased pore density [167].
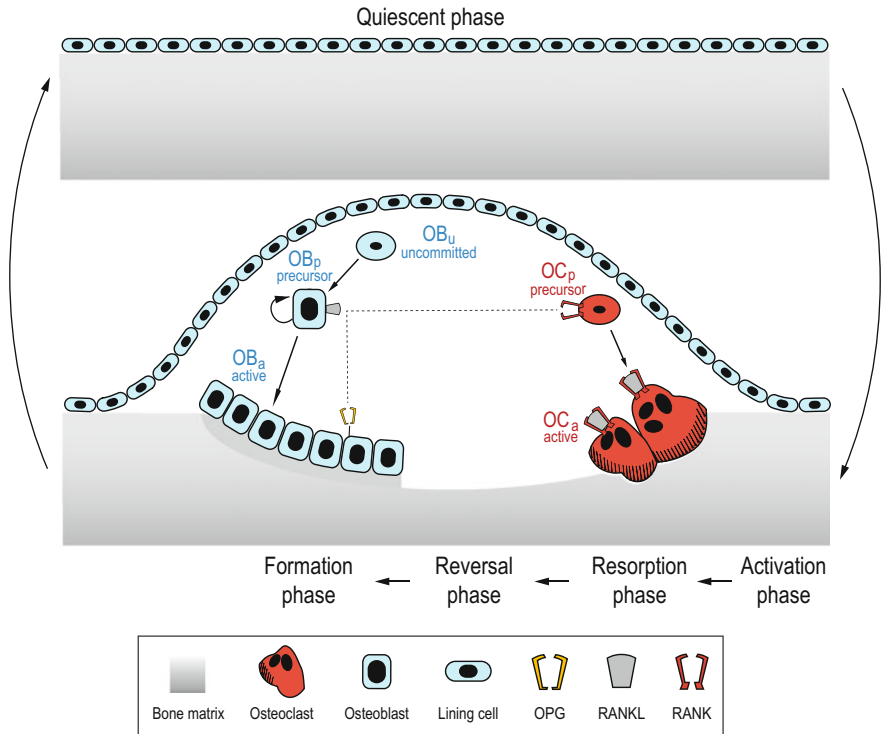
**Fig. 2** Bone remodelling and BMU on a trabecular bone surface: bone lining cells retract from bone surfaces and form a closed canopy over the remodelling site (activation phase), osteoclasts remove bone (resorption phase), bone surface is prepared for bone formation (reversal phase), osteoblasts form bone matrix (formation phase) and eventually either undergo apoptosis, become enclosed in bone to develop into osteocytes or differentiate into lining cells (return into a quiescent phase)

Dynamic histomorphometry techniques, such as tetracycline labelling and radionuclide imaging, have considerably helped in the elucidation of kinetic properties of matrix apposition and cell development within BMUs [69, 70, 118]. Whilst trabecular bone exhibits the same sequence of surface activation, resorption and formation, its three-dimensional organisation is difficult to visualise from two-dimensional histological sections. Latest imaging techniques apply synchrotron radiation (SR micro-CT) to visualize the morphology of 3D osteonal structures ex vivo [33]. Phase-contrast agents have been used in combination with SR micro-CT to visualize osteonal structures in vivo [59].

## Cell Signalling Pathways and Regulatory Factors (Mechanical, Hormonal, Local)

### Catabolic pathway: RANK-RANKL-OPG

Bone resorption is regulated via the integration of multiple pro- and anti-resorptive stimuli with convergence of output into a dominant mediating pathway. Cells of

the osteoblast lineage integrate hormonal, mechanical and pathological signals that change their expression of the cytokine receptor activator of nuclear factor kappa-B ligand (RANKL) [82, 176] and its inhibitor osteoprotegerin (OPG) [157, 168]. RANKL is either expressed as a membrane bound cytokine or released in a soluble form by cells of the osteoblast lineage. Osteocytes, osteoblasts and osteoblast precursors can express RANKL and currently there is some controversy regarding which predominate. Apparently, selective knock-down of RANKL in osteocytes produces a moderately severe osteopetrosis in mice, indicating that osteocytes have a significant role as source for RANKL [108]. RANKL binds to its receptor RANK (receptor activator of nuclear factor kappa-B) expressed on the surface of osteoclast precursor cells. The RANKL-RANK binding induces intracellular signalling pathways driving the differentiation into an osteoclast phenotype, activating osteoclastic bone resorption and increasing osteoclast survival (Fig. 3a) [107]. OPG is a decoy receptor for RANKL naturally secreted by cells of the osteoblast lineage and involved in the regulation of the resorption process. OPG, in fact, binds to RANKL to prevent its association with RANK. Consequently, osteoclast differentiation and activity are inhibited and osteoclast apoptosis is promoted (Fig. 3b). Therefore, if RANKL expression exceeds OPG expression, bone resorption is promoted, vice versa, if OPG expression exceeds RANKL expression, bone resorption is inhibited (http://www.rankligand.com/).

Pro-resorptive hormones, such as PTH and calcitriol, increase RANKL expression within bone and decrease the OPG one, leading to increased bone resorption. These hormones and other local regulatory factors bind to their own specific receptors expressed on osteoblasts and activate signalling pathways leading to an increased RANKL expression. On the other hand, bone protective agents such as estradiol and testosterone tend to increase the expression of OPG relative to RANKL, reducing bone resorption [67, 101]. Local regulatory factors such as PTHrP, IL-1 and TNF-$\alpha$ increase the expression of RANKL on cells of the osteoblast lineage in case of pathological bone loss related to cancer (PTHrP) or inflammation (IL-1 and TNF-$\alpha$). Local regulatory factors such as mechanical signals, on the other hand, alter RANKL and OPG expressions in a spatially restricted manner. Reduced bone strain and the presence of either microfractures or fatigue damage increase the RANKL/OPG ratio, while increased bone strain tends to decrease the RANKL/OPG ratio via osteocytes [81].

While RANKL-RANK signalling is necessary and dominant in the regulation of bone resorption, other modulating molecules can directly signal osteoclasts to magnify or diminish their response to RANKL. Inflammatory cytokines, for example, can enhance the osteoclast response [83]. In contrast, the systemic hormone calcitonin inhibits (reversibly) the osteoclast response via the activation of the calcitonin receptor on mature osteoclasts [28]. In addition, there are other sources of RANKL in bone that tend to contribute to the regulation of bone resorption during disease. Activated T-cells, in particular, secrete RANKL and can induce bone resorption during infection or chronic inflammation [166].

**Fig. 3** Role of the
RANK-RANKL-OPG
pathway in
osteoclastogenesis:
osteoblasts express RANKL
on either cell surface or in
soluble form (shown here).
**a** Osteoclastogenesis is
promoted by osteoblasts via
the RANKL-RANK binding
which induce osteoclast
precursor cells to
differentiate into active
osteoclasts.
**b** Osteoclastogenesis is
inhibited by osteoblasts via
the production of OPG which
blocks RANKL-RANK
interactions [22]



(a)



(b)
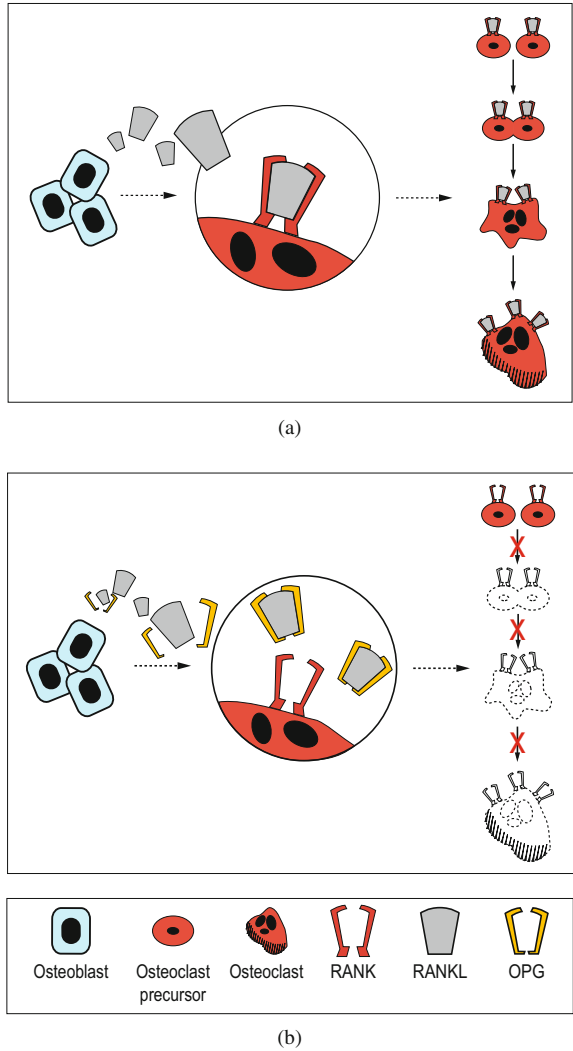
*Anabolic Pathway: Wnt Signalling*

The Wnt family of growth factors, together with their receptors, co-factors and
inhibitors, represent one source of regulation of both the mesenchymal stem cell
lineage commitment and the osteoblast precursors population. There is evidence that
mature osteoblasts can secrete Wnt that in turn acts on early mesenchymal precursors
to induce differentiation in the osteoblast lineage [7]. However, the understanding of
the Wnt action is complicated due to the presence of 19 Wnt ligands, 10 Wnt recep-
tors and multiple Wnt receptor co-factors and inhibitors [77]. Another contribution to
lineage commitment for osteoblast precursors may come from bone morphogenetic
proteins (BMPs), a group of growth factors produced by osteoblast lineage cells and

sequestered in bone matrix [1]. However, it is difficult to separate this action from their differentiation activity. During the inflammation typical of fracture repair, the transient exposure to TNF-$\alpha$ may also influence the commitment of mesenchymal stem cells to the osteoblast lineage [95].

**Association Between Bone Remodelling and Bone Mineralisation**

The measurement of the degree of mineralisation of bone (DMB), also known as tissue mineral density (TMD), is relatively recent compared with the assessment of bone vascular porosity. The most accurate way to assess TMD is microscopically (i.e., at the bone matrix level) using high-resolution imaging techniques. This approach translates the linear X-ray attenuation coefficient for a given beam energy in grey level values in the 3D reconstructed micro-CT or SR micro-CT images [112, 139]. The X-ray attenuation depends on the material composition and in a bone sample it is related to the mineral component of the bone. The amount of mineral per unit volume of bone matrix $\left(\text{in g/cm}^3\right)$ in a bone sample can be estimated using a calibration technique based on *phantoms* of known compositions. These calibration phantoms can either be solid and made of different concentrations of calcium hydroxyapatite ($CaHA$) or liquid and made of homogeneous solutions of water and different concentrations of dipotassium hydrogen phosphate ($K_2HPO_4$) [109]. The distribution of the grey levels within different regions of interest (ROIs) can be obtained from the histogram of the bone images normalized by the total volume (TV).

TMD has been directly associated with bone mechanical properties either at the bone structural unit level [150, 161] or at the whole bone tissue level [38, 39, 47]. Moreover, TMD has also been associated with the bone remodelling activity (Fig. 4a) [4]. According to the model recently developed by Bala and co-workers, an increase in bone remodelling leads to an increase of BMUs birthrate and to a decrease in TMD related to the lower probability to complete the secondary mineralisation, being the latter a slow phase of mineralisation which can take up to several years with a large fraction completed within one year [3, 18, 140, 141]. In case of hyperparathyroidism, for example, the proportion of bone structural units (BSUs) undergoing primary mineralisation decreases, the mean TMD decreases and its distribution broadens (Fig. 4b). The opposite occurs when the remodelling activity is low or reduced due to drugs and/or pathologies (Fig. 4b). In this case, the different BSUs have more time to complete mineralisation before being resorbed in a further remodelling event [16]. As a consequence, the proportion of bone highly mineralised maximally increases and its distribution becomes more homogeneous, the mean TMD increases and its distribution narrows [19, 137]. This conceptual model has been widely validated by the observation of pathologies and drugs altering remodelling activity.

In normal bone, the evolution of TMD with age has been widely studied and the overall result is the absence of correlation with age. More generally, it has been found that the TMD mean was age, sex, race, bone site and bone envelope independent and that the inter-individual variation was low [8, 11, 17, 48, 138]. However, some studies revealed a positive correlation between TMD and age [49, 138, 163]. This discrepancy may have several causes. Among these, one example is the fact that most of the samples were collected at the autopsy or drawn from anthropologic
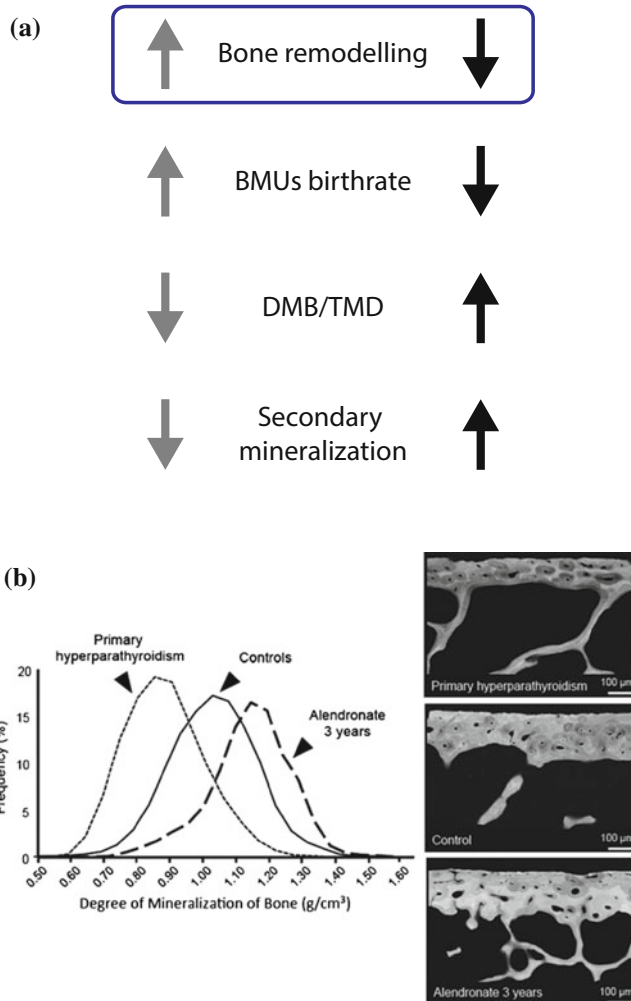
**Fig. 4** Bone mineralisation and bone turnover: **a** the degree of TMD is regulated by the rate of bone turnover, higher turnover rates lead to lower TMD and vice versa. **b** Bone diseases characterised by high bone turnover rates (e.g., primary hyperparthyrodism) lead to a decreased TMD, anti-catabolic drugs (e.g., Alendronate) inhibit bone turnover and result in increased TMD, modified from [4] with permission

collections with few medical history details. Moreover, anthropologic collections comprised specimens from populations in the ninetieth century (before the industrial revolution) which are not representative of our modern population [11]. Another cause of the discrepancy can be that age classes are often not well balanced, with fewer individuals in both youngest and oldest categories. Furthermore, most of the results are reported on iliac crest samples because they are easier to collect. However, even if data suggest that changes in the iliac crest are correlated to the changes in

other bone sites with a mixture of cortical and trabecular bone, e.g., femoral neck and vertebral bodies [42, 127], extrapolations to the femoral shaft are limited. In fact, the differences between femur and iliac crest are striking: the femur is a weight bearing bone, entirely cortical and a site of osteoporotic fracture, all characteristics that are absent in the iliac crest. Another cause of discrepancy can be the fact that most of the studies investigated the cortical bone as a homogeneous bulk, masking the radial and circumferential regional inhomogeneities. A recent study highlighted that the DMB assessed in the femoral midshaft using SR micro-CT decreased from the periosteal to the endosteal surface [144]. Further investigations regarding spatial inhomogeneities of TMD are required.

## 3 Biomarkers Characterising Mass, Quality and Turnover of Bone

Currently, there is no standard practice to monitor patients receiving treatment for OP. Repeated dual-energy X-ray absorptiometry (DXA) is a diagnostic test commonly used to assess the change in BMD following a therapeutic intervention. However, this technology has several limitations such as long time interval between two consecutive BMD measurements (6–9 months are needed to be able to detect changes in BMD), limited access to the DXA machine, elevated cost of the technology and low correlation between BMD monitoring and fracture risk estimate. A recent review pointed out that BTMs measuring bone resorption and formation may offer an alternative monitoring strategy [61]. Some advantages that BTMs have over DXA in monitoring the response to OP therapies are, for example, their non-invasive nature, their relatively cheap cost and the capability to detect changes in bone turnover rates after 3–6 months of therapy and in some cases already after 2 weeks.

More generally, these clinical quantities used to characterise OP and therapeutic interventions can be divided in two groups: *specific biomarkers* and *non-specific biomarkers*. Specific biomarkers such as BMD are specific to a particular bone site (e.g., femoral neck, lumbar vertebra, wrist) and reflect the effects of disease and treatment as changes in BMD over time. On the other hand, BTMs are non-specific biomarkers as they reflect bone remodelling activities in the whole skeleton and, as such, they are not specific to a particular bone site. In the following, we will review the use of these biomarkers in the context of OP and various therapeutic interventions having in mind to use these quantities for DSA.

### 3.1 Bone Structure and Bone Mineral Density

Imaging is essential to the evaluation of bone and joint diseases. In this context, many studies were conducted in order to find non-invasive analytical techniques to quantify

the changes occurring in bones and joints over time, both in health and disease [103]. Several methods are used to measure BMD at different skeletal sites, such as ultrasound, radiographic absorptiometry, dual photon absorptiometry, quantitative computed tomography (QCT), quantitative ultrasound and DXA [37, 76, 174]. The application of a particular technique depends on the accessibility of a particular bone site. In particular, latest high resolution QCT (HR-pQCT) techniques can mainly be applied at sites of the peripheral skeleton such as wrist and proximal tibia.

The gold standard in clinical practice for the assessment of BMD is DXA, which measures the mineral content of bone per unit area $\left(\text{in g/cm}^2\right)$ involving a low radiation exposure. The most relevant sites for the clinical assessment of the fracture risk using DXA are the spine (predominantly trabecular), the hip (mixed trabecular-cortical) and the wrist (predominantly cortical), and are routinely assessed using this technology to monitor the changes in BMD [173, 174]. One major drawback of DXA is that cortical and trabecular bone cannot be distinguished. DXA calculates BMD using a projected areal density (i.e., 2D image) and it does not measure a true density [158]. Hence, the quantification of bone structure, material composition or cortical porosity is not possible with this technology.

HR-pQCT is an imaging technique that allows to better understand bone and joint diseases at the microarchitectural level. It provides high resolution 3D images (82 µm isotropic voxel size) using a relatively low radiation dose (3–5 µSv) compared to total body CT scans [56]. With this technology, properties and microarchitecture of cortical and trabecular bone can be analysed separately. It also allows the in vivo assessment of the spatial distribution and dimension of cortical bone erosions. Furthermore, micro-finite element analysis (micro-FEA) can be performed on HR-pQCT data to calculate bone mechanical properties at the distal sites of the skeleton (i.e., distal radius and distal tibia). HR-pQCT can also be used to evaluate patient specific drug effects on bone.

BMD and structural parameters of bone such as trabecular thickness (Tb.Th) and trabecular numbers (Tb.N) are specific biomarkers that can be used to assess the changes in bone microarchitecture due to OP. One example of specific bone biomarkers is shown in Fig. 5a where micro-CT reconstructions of biopsy specimens of the iliac crest at baseline (left) and after three years (right) clearly show that both cortical and trabecular bone become thinner and connectivity is lost with the disease progression in an untreated patient [150].

## 3.2 Bone Turnover Markers

BTMs characterise the dynamic activity of bone cells via measurements of their biochemical concentrations in blood, serum or urine. BTMs are defined as non-specific biomarkers of bone because they provide information related to the whole body as opposed to site-specific information on a particular bone site. For this reason, the effectiveness of a particular treatment needs to be evaluated carefully. BTMs can be distinguished in three different types according to their relation to bone (re)modelling
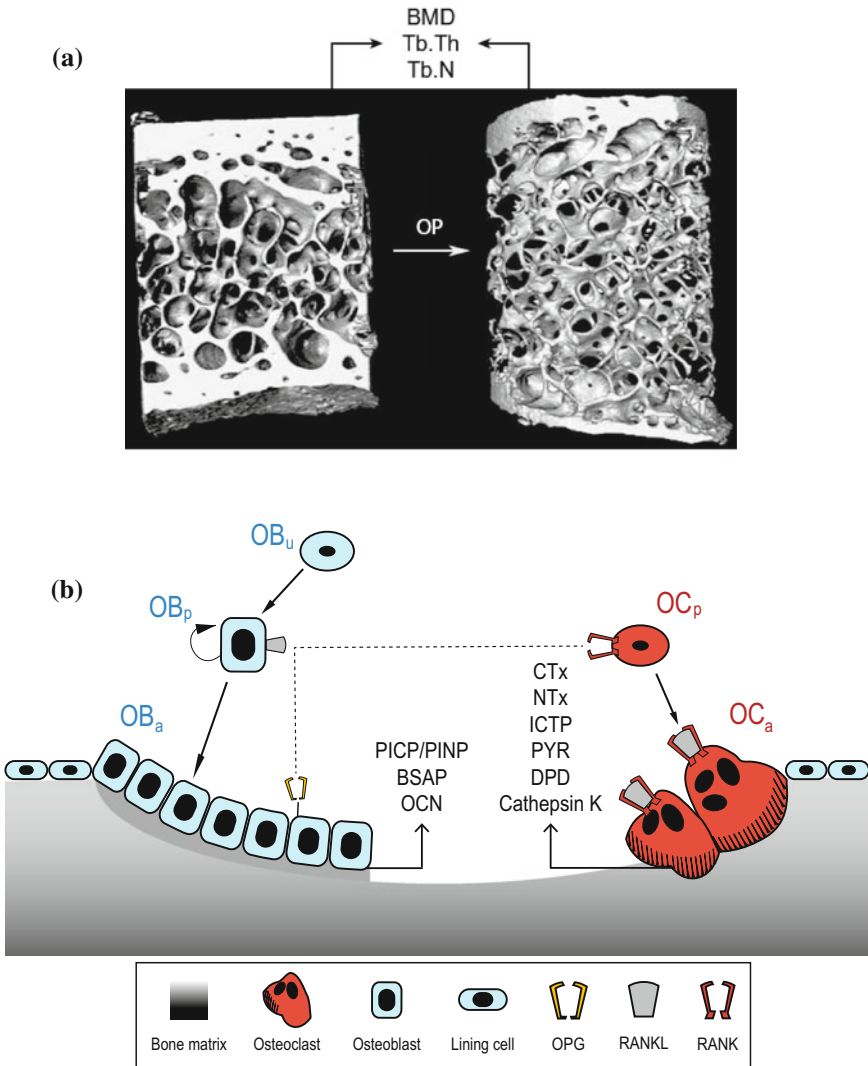
**Fig. 5** Biomarkers reflecting bone physiology: **a** specific biomarkers such as BMD, Tb.Th and Tb.N, from micro-CT images of biopsy specimens of the iliac crest at baseline (*left*) and after 3 years (*right*), modified from [150]. **b** Non-specific biomarkers of bone turnover in relation to their origination during bone remodelling process

activity: (i) collagenous bone resorption markers, (ii) bone formation markers, (iii) markers of osteoclast regulatory proteins [36, 87, 151]. An overview of various markers of bone turnover in relation to their origin and function is provided in Fig. 5b and Table 1 [125]. Collagenous resorption markers are degradation products of bone collagen and their concentrations reflect the rate of bone resorption [36, 151]. Bone formation can be measured based on the enzyme activity of osteoblasts, on the bone protein composing the bone matrix and on the pro-collagen markers. Osteoclast regulatory proteins are divided into markers reflecting the rate of osteoclastogenesis and the osteoclast numbers. Measurements of calcium and phosphate concentrations provides additional information on bone turnover and reflect the net balance between bone resorption and bone formation in the whole body [104]. It is worth to mention that calcium balance studies are costly, time consuming and difficult to perform [117].

BTMs have advantages over BMD measurements as they are non-invasive, relatively cheap and can detect changes in bone turnover rates earlier. However, the disadvantage of a particularly high within- and between-patient variability needs to be taken into account when using BTMs. Moreover, their ability to identify treatment non-responders and predict future fracture risk has yet to be established.

## 3.3  Characteristic Time Scale and Variability of Bone Biomarkers

In order to use bone biomarkers in the diagnosis and treatment of OP and other bone disorders, it is important to understand the dynamics and the variability of BMD and BTMs due to both technical and biological causes. From the technical point of view, variability in BMD measurements depends on the type of device used (e.g., lunar or hologic DXA scanners). The precision of a measurement can vary due to device errors, technician variability, intra- and inter-observer variability and between-centre variations [15, 43]. Nevertheless, the overall reproducibility of DXA measurements has been proven satisfactory with phantom measurements [155]. To overcome the issues of comparing numerical measures of BMD obtained from different scanners, each device manufacturer provides the user with a reference distribution that allows to internally normalize the individual measure with respect to the peak bone density of young adults. This normalised parameter is known as T-score and represents the number of standard deviation (SD) of the BMD measurement above or below the BMD of a young healthy adult of the same sex. The use of the T-score allows a better comparison between measurements taken with different scanners. To evaluate the precision error, repeated scans are performed on a set of patients and the reproducibility is characterised. Generally, this characterisation take place over a short period of time (about 2 weeks) so that no real change in the BMD is expected and the short-term precision error is quantified [43]. The BMD precision error can be expressed as coefficient of variation (CV [%]), which is the ratio of the SD to the

**Table 1** Non-specific biomarkers of bone turnover [125]

| Marker | Sample | Remarks |
|---|---|---|
| **Bone resorption** | | |
| *Collagenous bone resorption markers* | | |
| CTx | Urine and serum | Bone degradation products reflecting resorption and composition rates. |
| NTx | Urine and serum | Bone degradation products reflecting resorption and composition rates. |
| ICTP | Serum | Bone degradation products reflecting resorption and composition rates. |
| PYR/DPD | Urine and serum | Bone degradation products reflecting resorption and composition rates, derived from mature type I collagen. |
| **Bone formation** | | |
| *Enzyme activity marker* | | |
| BSAP | Serum | Osteoblast products, related to osteoblast and osteoblast precursor activity, involved in bone mineralisation. |
| *Bone protein marker* | | |
| OCN | Serum or plasma | Non-collagenous protein of bone matrix, osteoblast products, bone degradation product, correlated to histomorphometric measurements. |
| *Pro-collagen marker* | | |
| PICP/PINP | Serum or plasma | Osteoblast and fibroblast proliferation, released from newly synthesized pro-collagen, PINP correlates to histomorphometric measurements. |
| **Osteoclast regulatory proteins** | | |
| *Markers of osteoclastogenesis* | | |
| RANKL | Serum | Active osteoblasts and activated T-cells products. |
| OPG | Serum | Osteoblasts products. |
| *Markers of osteoclast numbers* | | |
| Cathepsin K | Serum or plasma | Type I collagen degradation enzyme. |

CTx = C-terminal cross-linked telopeptide of type I collagen; NTx = N-terminal cross-linked telopeptide of type I collagen; ICTP = C-telopeptide pyridinoline cross-links of type I collagen; PYR = pyridinoline; DPD = deoxypyridinoline; BSAP = bone-specific alkaline phosphatase; OCN = osteocalcin; PICP = C-terminal pro-peptide of type I collagen; PINP = procollagen type I N-propeptide; RANKL = receptor activator of NF-kB ligand; OPG = osteoprotegerin.

mean of the measurement, or as SD $[g/cm^2]$. Studies have shown that the short-term precision error in SD for lumbar spine and total hip is constant and ranges from 0.01 to 0.15 $g/cm^2$, corresponding to a CV between 1 and 1.5% with 1 $g/cm^2$ used as reference [175]. This implies that CV increases with decreasing BMD. Therefore, when assessing for significant changes in BMD, it is common practice to use SD rather than CV. The reproducibility of a measurement can also be quantified measuring the smallest detectable difference (SDD) that represents the minimum meaningful BMD change that can be detected with a certain device. The SDD is measured using the Bland and Altman's 95% limit of agreement method [14, 43] and is generally preferred to CV because is expressed in absolute units $[g/cm^2]$ and is independent of the BMD level. It has been shown that in older subjects, the measurement error increases for the spine and total hip. The long-term precision error in a clinical study increased by 6.5–9.2% with each additional year of monitoring [142].

Biological variability reflected in BMD measurements instead, arise from the effect that factors such as age, sex, demographics, seasonal variation, recent fractures, drug treatment, disease, mobility and lifestyle (including diet and vitamin D intake) have on the underlying bone physiology [87, 151].

BTMs exhibit high intra- and inter-individual variability. The technical causes for this are determined by the type of marker measured, e.g., resorption markers are often a mixture of molecular entities, and the type and precision of the assay used to detect a specific marker. The CV for the inter- and intra-assay variability are typically within 10% [87]. Other technical sources of variability are the inter-laboratory variation, the mode of sampling (e.g., 24-h or second morning void for urinary markers), the timing of sampling (e.g., diurnal variation), the type of sample taken (e.g. urine or serum) and the status of the subject before the sample collection (e.g. fasting, exercised). To control all these factors it is necessary to have an appropriate study design, a specimen collection protocol and to use standardised assays and working protocols [151, 152].

On the other hand, the biological causes of variability in the measures of BTMs are more difficult to control. These are the same factors mentioned previously for BMD measurements, such as age, sex, recent fractures, drugs, disease, lifestyle and also temporal variability (e.g., diurnal variation, menstrual rhythm) [36, 151]. However, in contrast to BMD, the influence of several of these factors on BTMs concentration can be observed on a daily to monthly basis. In general, the variability in BTMs increases with age and after menopause.

In Sect. 6 we will discuss how a mechanistic model can aid in comparing disease and treatment effects based on these heterogeneous sets of biomarkers. This type of model captures the underlying dynamics present in the data independently of the measured markers, assays used and reported assay units. It can also detect differences in the methodology used to analyse the markers in different studies. In addition, the previously mentioned difference in BMD values due to different devices can be incorporated in a mechanistic model.

# 4    Bone Pathology: Osteoporosis and Treatments

OP and its related skeletal complications are amongst the most important diseases impacting on both quality of life of the ageing population and costs of the health care system. Bone diseases in the elderly, are associated with high morbidity and increased mortality. OP in particular, is characterised by low bone mass due to increased (macroscopic) porosity, which leads to the deterioration of bone microstructure. Cortical bone deterioration is characterised by an increased intra-cortical porosity and trabecularisation of endocortical bone regions. On the other hand, trabecular bone loses connectivity between trabecular struts and plates. Furthermore, OP changes the mechanical properties of the bone matrix. The increased mineralisation, in fact, induces a more brittle material behaviour. These changes in bone structure and quality enhance bone fragility and consequently the fracture risk [173].

Different types of OP can be distinguished: PMO, senile or age-related OP, idiopathic and juvenile OP, OP resulting from other diseases (e.g., hypogonadism, endocrine states, diabetes) or conditions in the mechanical environment (e.g., immobilization) and OP due to deficiencies (e.g., vitamin D, calcium) and medications (e.g., corticosteroids) [130, 132]. Among all these types, age-related OP and PMO are the most frequent ones. It is now well established that normal ageing leads to trabecular and cortical bone loss, in both women and men. This bone loss starts from the fourth or fifth decade of life onwards, with a more pronounced effect in women after menopause (Fig. 6). Due to this accelerated bone loss, prevalence of OP and probability of fractures beyond age 50 is about 3 times higher in women than in men [76]. In women, age-related bone loss starts approximately 10–15 years preceding menopause affecting primarily trabecular bone. A study measuring BMD using DXA suggested that cortical bone is not damaged until menopause [2], however, this might be related to limitations in the imaging resolution. Intra-cortical bone loss and how this is affected by oestrogen can be better investigated using latest technologies such as HR-pQCT [24, 56].

## 4.1    RANK-RANKL-OPG Pathway

As pointed out in Sect. 2.2, the RANK-RANKL-OPG pathway is responsible for catabolic regulations and if altered towards an increase in the RANKL/OPG ratio it leads to enhanced osteoclastic activity. This process has been associated with various metabolic bone diseases, including OP [64, 155, 172]. Age-related bone loss is thought to be a combination of several factors, which includes: reduced bone formation, cumulative effects of calcium and vitamin D deficiency, decreased physical activity, lack of mechanoresponsiveness of osteocytes and age-related decrease in gonadal function [143]. Deficiency in calcium and vitamin D has been associated with increased osteoclastic activity via the action of PTH [117]. To react to low levels of calcium in blood the parathyroid gland secretes PTH in excess (secondary
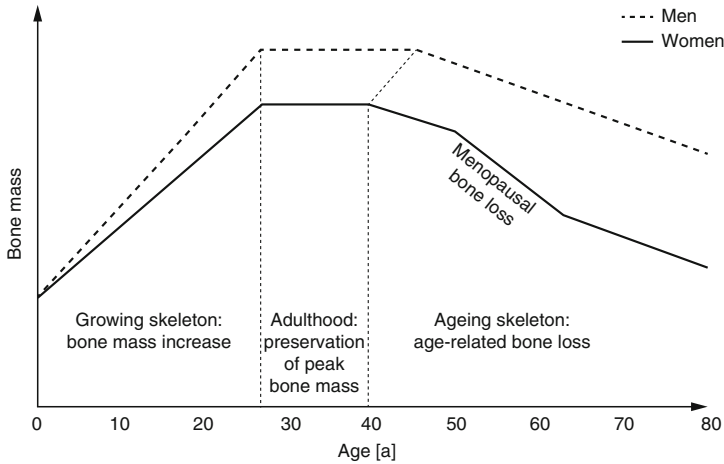
**Fig. 6** Bone mass variation with age in men and women: during growth bone mass increases reaching a peak at around 30 years of age (greater in men than in women). At around 40–45 years of age, age-related bone loss is observed in both men and women, but it is more pronounced in women (for about 10 years) due to menopause

hyperparathyroidism) to induce a calcium release from bone via osteoclastic bone resorption. This process is reflected in the variation of BTMs such as OPG and RANKL. On the other hand, it has been shown that serum OPG concentrations increase with age, both in men and women [78]. Although unexpected, this OPG increase does not exclude the possibility of bone site-specific increases in RANKL concentrations which drive bone resorption.

Oestrogen concentration is positively correlated with OPG concentration and BMD, but inversely correlated with markers of bone turnover [78]. The increase of bone fracture risk in women has been associated with the elevated bone loss observed in the period following menopause (10–15 years) characterised by a rapid decline in oestrogen concentration, an increase in BTM concentrations and a decrease in BMD [128]. Onset of this postmenopausal phase occurs between 50 and 65 years of age (Fig. 6). The higher rate of bone loss (compared to the age-related bone loss) is mainly observed in trabecular bone due to its higher turnover rate and the larger surface area. A recent research however, indicates that cortical bone might also be strongly affected during this phase and characterised by cortical bone trabecularisation [5]. RANKL has been positively correlated with markers of bone turnover, while OPG is negatively correlated with bone turnover [64, 78]. The accelerated phase is then followed by a phase of slow bone loss (Fig. 6).

## 4.2 Risk Factors for Osteoporosis and Osteoporotic Fractures

As highlighted in many reviews, peak bone mass is a major determinant of the risk of osteoporotic fractures [125]. Peak bone mass is usually reached in the third decade of life (Fig. 6) and is strongly governed by environmental factors during growth, with physical activity and nutrition playing major roles. Once the peak is reached, bone mass stays constant until the forth to fifth decade of life and after that bone loss commences. Due to the fact that women have a lower peak bone mass and an accelerated phase of bone loss due to menopause, bone fracture risk is higher in women compared to men [76]. Peak bone mass and the rate of bone loss during life are influenced by both genetic and environmental factors [173]. These factors include risk factors that can be either non-modifiable or modifiable, such as age, race, sex, life expectancy, menarche, early menopause, family history of OP or fractures, history of fragility fractures, diseases, medications, physical activity, nutritional status, low bodyweight, lifestyle, smoking, excessive consumption of alcohol [74–76, 125, 173]. Bone mass, quality and consequently strength are determined by the combination of these risk factors. In turn, bone strength and the mechanical loading determine the fracture risk. The mechanical load acting on bone can be estimated from either quasi-static loading conditions such as for lumbar spine, or from dynamic loading conditions such as frequency and direction of falls for femoral fractures.

To estimate the individual contribution of genetic and environmental factors on the overall fracture risk is difficult [74, 76]. Considering the complex interactions of these factors in OP, one should distinguish between patient-specific diagnosis of OP and population-specific fracture risk assessment, the latter being a not very accurate measure of fracture risk for an individual [173]. The WHO endorsed a tool named FRAX® which takes into account all these risk factors for the prediction of the 10-year risk of osteoporotic fracture in men and women. A link to this tool and other programs that calculate cost effectiveness and quality of life can be found on the website of the *International Osteoporosis Foundation* (https://www.iofbonehealth. org). It is worth to mention that FRAX® is far from accurate and the development of more sophisticated tools based on bone DSA is required.

## 4.3 Current Diagnosis of Osteoporosis and Whole Bone Strength

BMD is the best single predictor of bone strength, accounting for the 60–85%. Consequently, OP diagnosis is commonly based on BMD measurements [125, 171, 173, 174]. The WHO defined four diagnostic categories for women, based on the T-score evaluation (see Sect. 3.3): (i) *normal* (T-score $> -1$); (ii) *osteopenia* ($-1 <$T-score$< -2.5$); (iii) *osteoporosis* (T-score$< -2.5$); (iv) *severe osteoporosis* (T-score$< -2.5$ in the presence of at least 1 osteoporotic fragility fracture) [173].

Nevertheless, these categories are considered arbitrary thresholds strongly dependent on the reference population characteristics, e.g., race and demographics [94].

Despite the strong connection between BMD and bone strength, it is important to recognise that low BMD alone accounts for maximum 44% of the fracture risk [162]. The reason for this is that clinical scientists have exclusively focused on the material side of bone, neglecting entirely the loading conditions. In an attempt to improve the prediction of individual risk of OP and osteoporotic fractures, the BMD value was augmented with other bone material properties contributing to the whole bone strength such as shape, geometry, microarchitecture, bone tissue composition, mineralisation, microdamage and rate of bone turnover. These properties are summarized in the term bone quality [21, 25]. There have been many discussions regarding the suitability of the term bone quality in the context of bone fracture risk assessment. As pointed out by Sievänen and co-workers, bone quality is an imprecise term that should be avoided due to the difficulty of quantitatively include all the factors in a bone strength model and translate their effect into anti-fracture efficacy [156]. It is worth to notice that BMD measurements also contain the mineralisation of bone, consequently it is not possible to separate BMD from bone quality.

More quantitative approaches to estimate bone strength and fracture risk have continuously been developed by the biomechanical community. They result from the combination of 3D micro-CT or HR-pQCT imaging data and multiscale modelling using micromechanical models and finite element (FE) simulations [178]. Based on biomechanical arguments, the concept of bone quality was further discussed. In a review, Hernandez and Keaveny state that, since a bone fracture can be considered a mechanical event, all the clinically relevant modifications of bone quality are likely to affect bone mechanical performance (i.e., strength) relative to bone mass (i.e., BMD) [63]. Based on this consideration, Hernandez proposed a comprehensive hierarchical framework to quantify the biomechanical effect of changes in bone quality parameters at different scales. In particular, this framework was used to investigate how bone turnover could independently influence fracture risk [62].

## 4.4   Current and Emerging Treatments

The aim of OP treatments is to reduce the frequency of bone fractures, especially vertebral and hip fractures which are mainly responsible for morbidity associated with this disease. Different drug treatments can be distinguished according to the following characteristics: mechanisms of action; specific sites and modes of action; route of administration (oral, intravenous, nasal); dosage regimens; degrees of efficacy and effectiveness [13, 32]. Current bone therapeutic guidelines use BMD and BTMs as classification criteria for anabolic and anti-catabolic (previously also referred to as antiresorptive) drugs [131]. According to the terminology of Riggs and Parfitt, anti-catabolic drugs, e.g., bisphosphonates (BPs) and denosumab, act to reduce bone turnover (i.e., reduce bone remodelling) causing an increase in bone strength. These drugs are also associated with a moderately increase of bone mass resulting from

the increased mineralisation of the existing bone matrix. On the other hand, anabolic drugs, e.g., intermittent PTH and sclerostin antibody, strongly increase bone mass by increasing bone remodelling (i.e., high bone turnover) and consequently bone strength. Interestingly, most agents decrease bone resorption (i.e., anti-catabolic treatment), some increase bone formation (i.e., anabolic treatment) and others have been reported to do both [30].

In bone remodelling, osteoblastic and osteoclastic actions are coupled (see Sect. 2.2): osteoblasts are necessary to activate osteoclasts, and osteoclasts secrete factors which stimulate osteoblasts activity. Due to this coupling, anti-catabolic drugs inhibiting bone resorption will also inhibit to a certain extent bone formation. This results in reduced concentrations of bone resorption markers, followed by decreased concentrations of bone formation markers (BP in Fig. 7a). In contrast, anabolic drugs stimulating bone formation will also stimulate bone resorption, resulting in increased concentrations of bone formation markers, followed by increased concentrations of bone resorption markers (PTH in Fig. 7a). The different kinetics driving the changes in bone formation and resorption markers following the anabolic treatment generates a period of time known as the *anabolic window* where bone mass increases. According to this conceptual model, the effect of the anabolic treatment appears to wear off after a certain period of time [12].

The effects on bone microarchitecture of the anti-catabolic treatment with risedronate and of the anabolic treatment with teriparatide are illustrated in Fig. 7b. Based on micro-CT imaging data of iliac crest biopsy specimens, treatment with the anti-catabolic agent maintains bone structure, whereas treatment with the anabolic agent promotes bone deposition and both cortical and trabecular thickening. In the following, a brief summary is given on currently available therapies to treat OP together with new emerging strategies, including combined and sequential therapies [45, 55].

**Anti-catabolic Therapies**

In clinical practice the most prescribed anti-catabolic drugs are BPs and denosumab. Nitrogen-containing BPs bind to bone surfaces and inhibit the mevalonate pathway in osteoclasts resulting in osteoclast apoptosis. The effects of long-acting BPs such as zoledronate and alendronate can persist for a long time after the end of the treatment [57]. On the other end, denosumab is a fully human monoclonal antibody that binds to RANKL with high affinity and inhibits osteoclast differentiation and activation. The inhibition of osteoclasts ceases within 1 year after discontinuation of the treatment, depending on the dose administered [102]. Other anti-catabolic drugs commonly used in the treatment of OP are oestrogen, selective oestrogen receptor modulators (SERMs), calcitonin and cathepsin-K inhibitors [45]. Alendronate, risedronate, zoledronate and denosumab have a broad spectrum of fracture prevention in patients with OP: the risk of vertebral fractures can decrease by more than 50%, the risk of non-vertebral fractures decreases by 20–25% and the risk of hip fractures decreases by 40–50% [105]. Long-term studies with alendronate and zoledronate indicated a favourable effect on vertebral fractures [9, 148].

During treatments with anti-catabolic drugs the birth of new BMUs is suppressed, resorption cavities become fewer and shallower and bone structure is maintained.

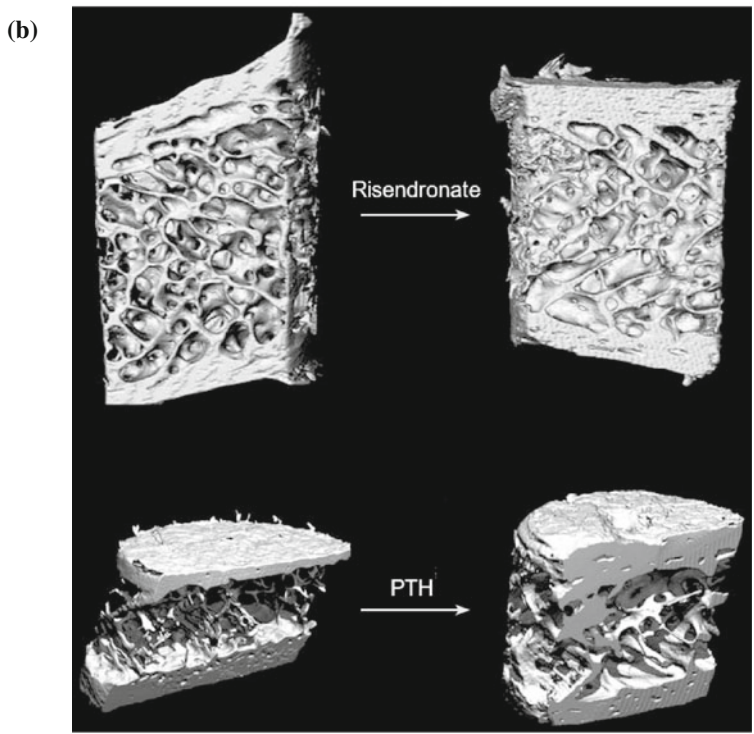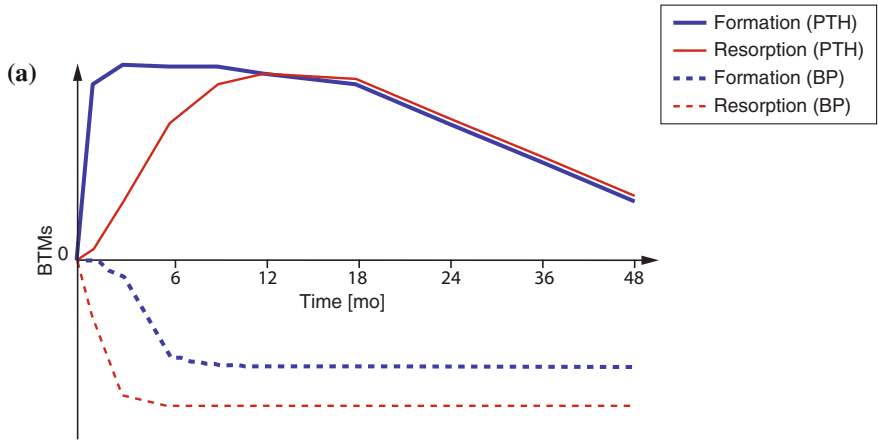**Fig. 7** Effect of anti-catabolic and anabolic drugs on bone biomarkers: **a** BTMs for PTH (*continuous lines*) and BP (*dashed lines*) treatments. *Thicker curves* indicate bone formation BTMs. *Thinner curves* indicate bone resorption BTMs. **b** Bone microstructural changes of iliac crest biopsy specimens at baseline (*left*) and after 18 months of treatment with risedronate or PTH (*right*), modified from [150]

Moreover, since the remodelling process is slowed down, a more complete mineralisation of the tissue can be obtained: the newly formed bone has time to reach the secondary mineralisation and the older bone keeps mineralising instead of being removed (if remodelling was higher) [98]. As a consequence, bone regions become more homogeneous. Based on the fact that changes in BMD plateau after a rather long period of time (approximately 2–3 years), it seems that secondary mineralisation may be a good candidate to explain the increase in BMD.

## Anabolic Therapies

Physiological exercise and related mechanical stimuli can act as anabolic agents on bone [114]. Large intense challenges to the skeleton, as well as brief exposure to mechanical signals of high frequency and low intensity, have been shown to provide a significant anabolic stimulus to bone. Physical activity has been proven to have a positive effect on building peak bone mass and density [111]. It directly affects osteoblast and osteocyte activities, but can also bias mesenchymal stem cell differentiation towards osteoblastogenesis instead of adipogenesis [114]. This fact in particular indicates that, at least during growth, physical activity targets bone marrow stem cells, hence, it might be considered as a novel drug-free anabolic therapy.

Currently, the only anabolic drug available is teriparatide, a recombinant 1–34 N-terminal fragment of endogenous human PTH [rhPTH(1-34)]. In patients with severe OP, daily subcutaneous injections of teriparatide during 18 months decreased the risk of vertebral fractures by 65% and the risk of non-vertebral fractures by 53% [92, 110]. The mechanisms behind the increased bone formation driven by the intermittent administration of PTH (i.e., daily injection of the drug) are still not fully understood. The overall action of the treatment is to increase osteoblast differentiation and proliferation, while reducing osteoblast apoptosis. In trabecular bone, teriparatide increases BMD and trabecular thickness [73]. In cortical bone, teriparatide increases endosteal bone remodelling and periosteal bone formation [20]. These results indicate that teriparatide has an effect on both bone modelling and remodelling [6]. The duration of a treatment with teriparatide is generally between 18 and 24 months and the action of the drug is believed to be maximally anabolic during the anabolic window (as mentioned above). After 18–24 months of treatment, bone resorption appears to catch up with bone formation and the newly formed and lowly mineralised bone is quickly lost [6, 12]. To preserve the new bone and allow further mineralisation, the established treatment protocol requires the administration of an anti-catabolic drug at the cessation of the treatment with teriparatide.

In animal studies, the use of anti-sclerostin monoclonal antibodies appears to directly stimulate bone formation via bone modelling, i.e., at least partially independent of the activation frequency and bone remodelling [6]. In addition, these antibodies stimulated the production of OPG resulting in decreased bone resorption and leading to the uncoupling of bone formation and bone resorption processes. Potentially, the use of sclerostin antibodies could result in an even greater anabolic window compared to teriparatide. Subcutaneous injections of the anti-sclerostin antibody romosozumab have been studied in phase I and II trials [99, 115]. In postmenopausal women with low bone mass, a 12-month treatment with a monthly dose of 210 mg of

romosozumab was associated with a significant increase in BMD (11.3% at the spine, 4.1% total hip and 3.7% at the femoral neck) greater than the ones obtained with weekly alendronate or daily teriparatide treatments. There was a transient increase in bone formation markers during the first 3 months together with an initial 2-month decrease in bone resorption markers, which was to a lesser degree sustained during the 12 months.

**Combined Therapies**

Despite the development of new therapeutic treatments for OP in the past decades, the currently approved drugs are not able to restore normal bone integrity in the majority of osteoporotic patients. To increase the therapeutic efficacy, latest OP treatments combine anabolic and anti-catabolic drugs. Clinical trials showed that the effect of the combined therapy on BMD depends on the timing of the anabolic drug administration (i.e., before, during or after the administration of the anti-catabolic drug), on the specific drugs used and on the particular bone site analysed [34, 46]. The most consistent effect of the combined therapy is a greater BMD increase at the hip compared to the treatment with the anabolic agent alone, in particular when teriparatide is associated with BPs or denosumab [34]. On the contrary, no benefit of the combined therapy has been shown on the BMD at the spine. In patients treated with BPs only and who still develop bone fractures or loose BMD, switching to a treatment with teriparatide is advocated. In addition, the continuation of the anti-catabolic treatment when starting the teriparatide one resulted in a better response of the BMD at the hip [35]. On the other hand, an anti-catabolic treatment is indicated after stopping the administration of teriparatide in order to preserve the increased bone architecture and enhance its mineralisation.

In conclusion, the site and the mode of action of a particular treatment depend on the PK properties of the specific drug (or combination of drugs) and the underlying bone pathology of the single individual. Consequently, the duration of the effects on BTMs and BMD after the withdrawal of a treatment can be different, perhaps indicative of disease modification or at least suggesting an appropriate treatment duration [125]. In order to compare treatments on a common basis, conceptual and mathematical models describing these combined dynamics can play a crucial role. Progresses in development of such models are given in the next sections.

# 5 Basics of Disease System Analysis

## 5.1 *PK/PD Modelling*

The development of PK/PD models in the last 20 years has had as primary objective the characterisation of the drug effect over time, then used to optimise dosing regimen and delivery profile of both new and existing drugs. Recently, PK/PD models have also been applied during the drug development process [41, 124]. To clarify the
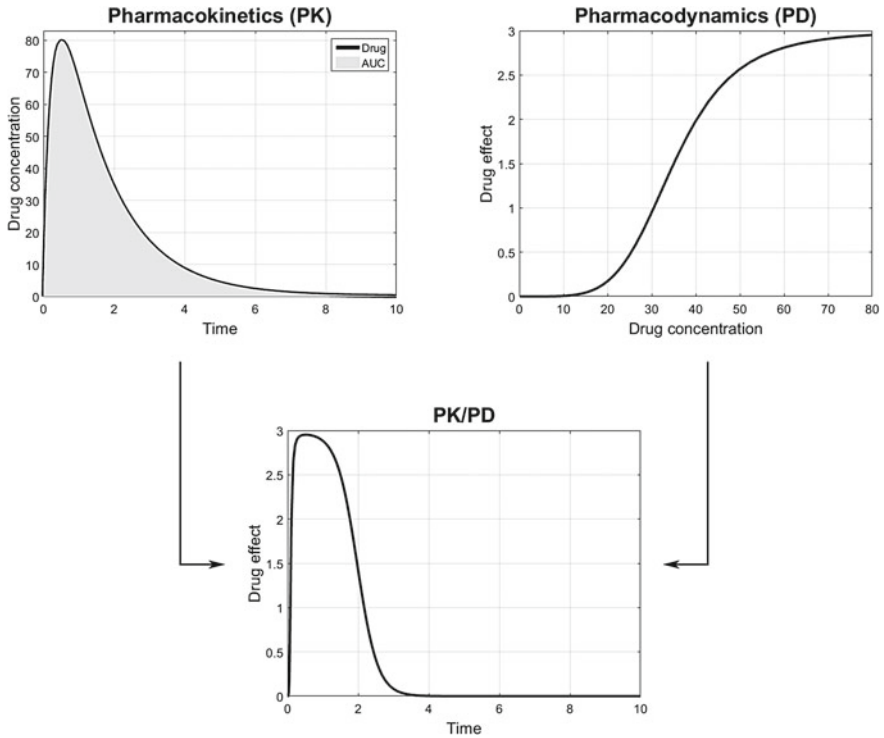
**Fig. 8** Combination of a PK model and a PD model in the PK/PD modelling process (AUC indicates the area under the curve)

difference between pharmacokinetics and pharmacodynamics, Holford and Sheiner came up with these simple and practical definitions: pharmacokinetics is *what the body does to the drug*, whereas pharmacodynamics defines *what the drug does to the body* [66]. A PK model is a mathematical description of the change over time of the drug concentration in the body fluid (i.e., blood, plasma or serum)[2] after the administration of a certain drug dose. PK models are used to simulate the rate of drug absorption, distribution and elimination in order to describe and predict the drug concentration in the body over time. A PD model, on the other end, describes the intensity of the drug effect relative to its concentration in the body fluid. The combination of a PK model and a PD model is known as PK/PD model of the drug (Fig. 8) and allows the description of the drug effect over time [100].

A common tool used to describe the pharmacokinetics of a drug is the *compartment-based* PK model [154]. According to this model, the drug is assumed to enter, distribute and leave an hypothetical compartment containing a volume of

---

[2]It is important to distinguish between blood, plasma, and serum. Blood includes fluid, white and red cells and platelets; plasma is the fluid portion of blood including only soluble proteins; serum is the plasma without the soluble protein.

fluid that equilibrates with the drug. This compartment is not an anatomical structure, but it represents a group of tissues with similar blood flow and drug affinity, balancing with the drug in an uniform way. In the one-compartment open model, the drug is added to and eliminated from a single compartment, also denoted as *central compartment*, which represents the plasma and the highly perfused tissues. In the two-compartment open model, the central compartment communicates with a second compartment (*tissue compartment*) and the drug disposition is related to the exchange between the two. The one-compartment open model for an intravenous injection (IV bolus) is the simplest mathematical way to describe the process of drug distribution and elimination. In this model the drug is assumed to be injected all at once, the distribution is assumed instantaneous and homogeneous throughout the central compartment and the drug elimination starts immediately after the injection.

To describe the change over time of the drug concentration in the compartment following the injection of a certain dose, two primary PK parameters need to be considered: the *volume of distribution* of the compartment and the *clearance* of the drug [154]. The volume of distribution is a proportionality factor that correlates the amount of drug in the body to the drug concentration measured in the biological fluid. Although it has the dimension of a volume, it is not a physiological measurable quantity, hence, it is often referred to as *apparent* volume of distribution. The volume of distribution is linked to the dose of drug administered and to the plasma drug concentration immediately after the dose injection by means of the following equation:

$$D = V_D \cdot C_p, \tag{1}$$

where $D$ is the drug dose expressed in mg, $V_D$ is the volume of distribution in $mm^3$ and $C_p$ is the plasma drug concentration in $mg/mm^3$. A drug dose is generally proportional to the volume of distribution, i.e., the larger the volume of distribution, the larger the dose has to be to achieve the target concentration. In an adult, approximately 60% of the total body weight is water, made up of intracellular fluid (35%) and extracellular fluid (25%). The extracellular fluid includes plasma (4%) and the interstitial fluid surrounding the cells outside the vascular system (21%). According to this partition, low $V_D$ indicates that the drug is distributed only in the extracellular fluid. If $V_D$ is close to the total body water ($\approx 40$ l), the drug distribution involves the total body water. When $V_D$ is larger than the total body water, the drug is probably concentrated in the tissues outside the plasma and in the interstitial fluid, consequently resulting in a low plasma concentration.

The concentration of the drug is also regulated by the amount of drug eliminated per unit of time (*elimination rate*). For most drugs, the elimination process is assumed to be a *first order reaction* [154], meaning that the elimination rate is directly proportional to the amount of drug present in the system (Eqs. (2) and (4)). For other drugs instead, the amount of drug is assumed to decrease at a constant rate and the elimination process is defined as *zero-order reaction*. When considering a first order reaction we can describe the elimination process as follows:

$$\frac{dD}{dt} = -k \cdot D, \tag{2}$$

where $\frac{dD}{dt}$ is the elimination rate expressed in mg/h and $k$ is the *first order elimination rate constant*. Integrating Eq. (2) we obtain the expression of the change over time of the amount of drug in the body:

$$D = D_0 \cdot e^{-k \cdot t}, \tag{3}$$

where $D_0$ is the initial drug dose. The same considerations can be done expressing Eqs. (2) and (3) in terms of drug concentration:

$$\frac{dC_p}{dt} = -k \cdot C_p, \tag{4}$$

$$C_p = C_{p_0} \cdot e^{-k \cdot t}, \tag{5}$$

where $C_p$ is the concentration of the drug in µg/ml. The time required for a certain drug concentration to decrease by one half is a characteristic parameter of the drug pharmacokinetics defined as drug *half-life*. It is generally expressed in h and in case of first order elimination is constant and equal to:

$$t_{1/2} = \frac{0.693}{k}, \tag{6}$$

where $t_{1/2}$ indicates the half life.

Drug clearance is another fundamental parameter used to describe the drug elimination process in pharmacokinetics. It is defined as the volume of either plasma or blood cleared from the drug per unit of time. Clearance is measured in ml/h and consists of a constant parameter related to the volume of distribution and to the elimination rate constant as follows:

$$CL = k \cdot V_D, \tag{7}$$

where $CL$ is the clearance.

When the drug is not administered intravenously (e.g., oral administration or subcutaneous injection), the PK model needs also to account for the *absorption process* of the drug from the site of administration into the plasma, and for the *bioavailability* of the drug in the systemic circulation. For such cases, additional pharmacokinetics parameters are necessary (see also example of OP treatment with denosumab in Sect. 6.1). Most PK models for extra-vascular drug administration consider the absorption process as a first order reaction. As for the elimination process, the absorption of the drug is described via a rate constant. Drug absorption is usually faster than its elimination. It is important to mention that the elimination process begins as soon as the drug enters the plasma and starts to be distributed in all tissues, even if the absorption process is not complete. During the absorption phase, the rate of drug

absorption is greater than the rate of drug elimination. When the plasma drug concentration reaches its peak, the rate of drug elimination equals the rate of drug absorption (i.e., the amount of drug in the body does not change). In the post-absorption phase, the elimination rate is higher than the absorption rate. As soon as the amount of drug at the absorption site is null, the absorption rate equals zero and the system is described by the elimination phase only.

The actual exposure of the body to the drug, following the administration of a certain dose, can be quantified measuring the *area under the curve* (AUC) of the *plasma concentration versus time* curve (Fig. 8). During clinical trials, the plasma, blood or serum drug concentration in a patient can be measured at several time points and used to create a patient specific profile of the drug concentration change over time. From this profile AUC can be estimated. Mathematically, AUC is defined as the integral of the drug concentration versus time curve and is generally expressed in μgh/ml. It depends on the drug elimination and absorption rates and the administered dose. For drugs following linear kinetics, AUC is directly proportional to the dose and inversely proportional to the clearance. In particular, the higher the clearance, the shorter the time that the drug spends in the systemic circulation and the faster the reduction of the drug concentration. Consequently, the exposure of the body to the drug is shorter and AUC is smaller. Therefore, AUC is related to the amount of drug absorbed in the systemic circulation.

Following an intravenous injection, the dose administered is assumed to entirely enter the systemic circulation in an active form. In case of extra-vascular administration instead, only a part of the entire dose reaches the systemic circulation in an active form. Following this considerations, AUC can be used to define another important PK parameter: the drug bioavailability. This parameter represents the fraction of the administered dose that enters the system circulation in an active form. By definition, a drug administered intravenously has bioavailability equal to 100 %, therefore it is used as reference for the computation of the bioavailability of a drug following an extra-vascular administration. Numerically, the bioavailability of a certain dose of a specific drug is computed as the ratio between AUC corresponding to an extra-vascular administration and AUC corresponding to an intravenous administration. Often, volume of distribution and clearance are given as function of the bioavailability.

Taking into account absorption, elimination and bioavailability of the drug, the rate of drug variation in the body and the drug concentration can be expressed as follows:

$$\frac{dD}{dt} = rate_{in} - rate_{out} = F \cdot k_a \cdot D_0 \cdot e^{-k_a \cdot t} - k \cdot D, \tag{8}$$

$$C_p = \frac{F}{V_D} \cdot \frac{k_a \cdot D_0}{(k_a - k)} \cdot (e^{-k \cdot t} - e^{-k_a \cdot t}), \tag{9}$$

where $F$ is the bioavailability, $k_a$ is the absorption rate constant expressed in 1/h and $\frac{F}{V_D}$ is the inverse of the volume of distribution given as a function of the bioavailability. As previously mentioned, at the peak plasma concentration the rate of drug absorption

equals the rate of drug elimination. This assumption allows the computation of the *peak time*, i.e., the time required to reach the peak drug concentration:

$$t_{max} = \frac{ln(k_a/k)}{k_a - k},$$

(10)

where $t_{max}$ indicates the peak time, generally expressed in h. Note that the peak time is a parameter of the drug independent of the administered dose.

Once the mathematical description of the drug concentration time course in the body fluid is completed, a PD analysis is used to quantify the relationship between the drug concentration and its effect. Ideally, the drug concentration should be measured at the effect site (i.e., site where the drug interacts with its receptor), in case of OP for example it should be at the interested bone site. Since this is generally not possible, it is common practise to use either the plasma or the blood drug concentration and to assume that, under PK steady-state conditions, the concentration in plasma or blood is in equilibrium with the pharmacologically active, unbound, drug concentration at the effect site [100]. The effect of the drug can be evaluated measuring the variation of physiological parameters. In OP for example, changes in the bone resorption and formation activities are monitored. Several PD models have been developed so far, such as fixed effect, linear, log-linear, $E_{max}$ and *sigmoid $E_{max}$* models. Among these, the $E_{max}$ and the *sigmoid $E_{max}$* are the most commonly used (Fig. 8). In the $E_{max}$ model, the effect of the drug is expressed as function of the *intrinsic activity* of the drug (i.e., maximum effect possible) and the *potency* of the drug (i.e., concentration that causes 50% of the intrinsic activity) [100, 154]:

$$E = E_0 \pm \frac{E_{max} \cdot C}{E_{50} + C},$$

(11)

where $C$ is the drug concentration, $E_{max}$ is the intrinsic activity, $E_{50}$ is the potency and $E_0$ is the baseline effect existing in the absence of the drug. The latter can be either stimulated $(+)$ or inhibited $(-)$ by the drug effect. $E_0$ is assumed equal to zero (i.e., in the absence of the drug the effect is null) when the receptor theory is applied to the equilibrium interaction of the drug with the site of action. The $E_{max}$ model describes two key features of the pharmacologic response: (i) the hyperbolic pharmacologic response versus drug concentration curve, and (ii) the max response induced by a certain drug concentration beyond which no more increase in the response is obtained. The sigmoid $E_{max}$ model is an extension of the $E_{max}$ model describing the pharmacologic response versus drug concentration curve for s-shaped rather than hyperbolic drugs. The effect is calculated as:

$$E = E_0 \pm \frac{E_{max} \cdot C^n}{E_{50}^n + C^n},$$

(12)

with $n$ being a parameter denoting the steepness of the curve. Theoretically, $n$ should be related to the number of drug molecules that combine with each receptor, however,

it is mainly used as a phenomenological factor that allows a good fit of the experimental data. The larger $n$, the steeper the linear phase of the plasma concentration (log) versus effect curve [100, 154].

The conventional PK/PD models described so far are characterised by a descriptive approach which is empirical and driven by a large amount of data. As a consequence, they cannot predict a clinical response beyond the data which they are based on. To overcome this limitation, more sophisticated models have been developed which take into account both the underlying mechanisms of the disease and the drug action [41, 126, 147]. They are referred to as *mechanism-based* or *mechanistic* PK/PD models and aim to characterise the intermediate processes between the drug administration and its effect, relying on biomarker data such as receptor binding and activation and feedback pathways. There are two types of parameters used to describe these models: the ones describing the properties of the drug (e.g., affinity and target activation) and the ones describing the properties of the biological system [41, 124]. In the context of mechanism-based PK/PD modelling, the sequence of events following the activation induced by the drug and governing the in vivo pharmacological response is referred to as *transduction*. This process is generally non-linear and can either be fast (rate constants between milliseconds and seconds) or slow (rate constants in the order of hours to days). In the first case, since the rate constants controlling the disposition of the drug are typically between minutes and hours, the transduction does not cause a delay in the pharmacological effect. In the second case instead, it becomes a fundamental parameter in the definition of the drug action over time [41, 124].

## *5.2 Disease Progression Analysis*

Another limitation of the conventional PK/PD analysis worth to mention is the representation of the system baseline using constant parameters (e.g., $E_0$ in Eqs. (11) and (12)). In case of degenerative diseases such as OP, Alzheimer's disease, Parkinson's disease, sarcopenia and osteoarthritis, this approach is not realistic because the biological functions deteriorate over time due to slow changes in the disease status. To take into account the changes in the system due to the progression of the disease, mechanism-based PK/PD models also include a *disease progression analysis* [29, 65, 124]. Furthermore, the use of disease progression models is fundamental when drug treatments specifically aim to modify the progression of the disease [41]. In particular, clinical pharmacology can be described in terms of *disease progression*, i.e. changes in the disease status over time, and *drug action*, i.e. the effect of the drug on the disease progression [29]. Disease progression can be analysed at different levels of the pathophysiology (Fig. 9) [124]. Bone healthy remodelling state, for example, can initially be perturbed at the molecular level (level 1) where the interactions between genetic and transcription events and receptor-ligand binding reactions take place. The result of these molecular changes may affect the behaviour of bone cells regulating bone resorption and bone formation events (level 2). These changes

**Fig. 9** DSA in OP: individual levels represent stages of bone disease. Bone biological function within the homeostatic state of remodelling may be disturbed at level 1 or 2, resulting in an imbalance of bone resorption and bone formation. This imbalance can be observed at the bone tissue level (level 3) as an increase in porosity and/or variation in bone quality. At the clinical endpoint, these changes may result in bone fractures. The 3 stages of the disease specifically represent the combined outcome of disease progression and pharmacodynamic effect
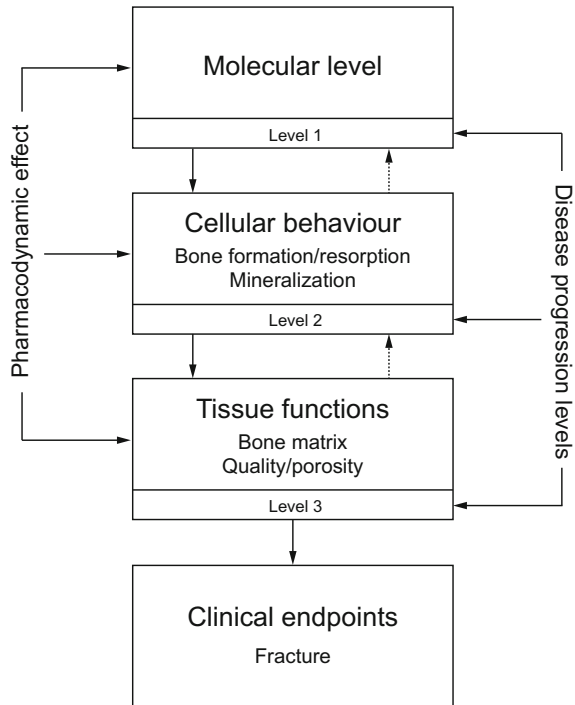
in turn regulate bone tissue properties such as porosity and bone quality (level 3). At the clinical endpoint these changes may eventually result in bone fractures. At each of the mentioned levels, disease progression and pharmacodynamic effect are combined to produce a certain outcome on the disease over time behaviour. The level at which the disease behaviour is described in the disease progression analysis, depends on the information available.

In ageing, the natural progression of the disease involves phenomena such as cell death and loss of organ functions. An interesting aspect worth to investigate is whether the development of degenerative diseases is exclusively driven by ageing or if other factors are also involved. From a statistical prospective, the occurrence of degenerative diseases appears to be mainly age-related. However, ageing alone cannot explain the different disease progression pattern and the faster rate of cell loss found in patients with either Alzheimer's or Parkinson's disease [29].

**Aims of Drug Treatments**

Drug treatments aim to either reduce, stop or reverse the natural process of a disease. According to the way in which the drug affects the disease status, its effect can be defined either *symptomatic* or *protective*. A symptomatic treatment effect improves the severity of the symptoms without modifying the disease progression. A protective treatment effect, on the other hand, involves a modification of the underling disease progression leading to an improved disease status. A combination of both

symptomatic and protective effects is also possible. In general, symptomatic effect action is faster compared to the protective effect one. A review of several disease progression models based on clinical endpoints is provided by Chan and Holford for diseases such as Parkinson's, Alzheimer's, and OP [29].

Similarly to the use of drug concentration in a PK model and drug effect in a PD model, the disease status is used in a disease progression model to identify the disease pathway [65]. A simple disease progression model can be described with the following equation:

$$S(t) = S_0 + \frac{E_{max} \cdot C_e(t)}{E_{50} + C_e(t)}, \tag{13}$$

where, similarly to Eq. (11), $S(t)$ is the time course of the disease status determined by both the underlying disease and the drug action, $S_0$ refers to the baseline disease status and $C_e$ is the drug concentration at the effect site [65]. The downside of this model is that it does not account for a time course of the disease status independent of the drug effect. Even though it could be reasonable to use this model when the observation time is short, however, modelling the changes of the disease status over time independently of the drug effect is necessary. From this prospective, Chan and colleagues [29] and Holford and co-authors [65] proposed two models of natural disease progression (i.e., without the drug effect on the disease progression), one linear and one asymptotic. The linear model is expressed as follows:

$$S(t) = S_0 + \alpha \cdot t, \tag{14}$$

where the rate of disease progression is linear with a constant slope defined by the parameter $\alpha$. In the asymptotic model on the other hand, the worsening of the disease status is considered exponential and approaching to a steady state as follows:

$$S(t) = S_0 \cdot e^{-\frac{ln(2) \cdot t}{TP}} + S_{ss} \cdot \left[ 1 - e^{-\frac{ln(2) \cdot t}{TP}} \right], \tag{15}$$

where $TP$ indicates the half-life of the drug and $S_{ss}$ is the maximum burnt-out disease status. The natural disease progression curves for the linear and the asymptotic models are shown as black solid lines in Fig. 10a, b respectively.

According to the type of treatment simulated (i.e., symptomatic or protective), model parameters reflecting the action of the drug are conveniently modified. In particular, in the case of a symptomatic drug effect, the parameters describing the underlying disease progression (i.e., $\alpha$ in the linear model, $TP$ and $S_{ss}$ in the asymptotic model) do not change. Consequently, the symptomatic effect is generally included in the disease progression model as an additive term. In a linear model for example we can have:

$$S(t) = S_0 + \alpha \cdot t + E(t), \tag{16}$$

where $E(t)$ represents the symptomatic effect. Assuming that this effect is constant for a given time interval, one can observe a constant offset from the natural disease
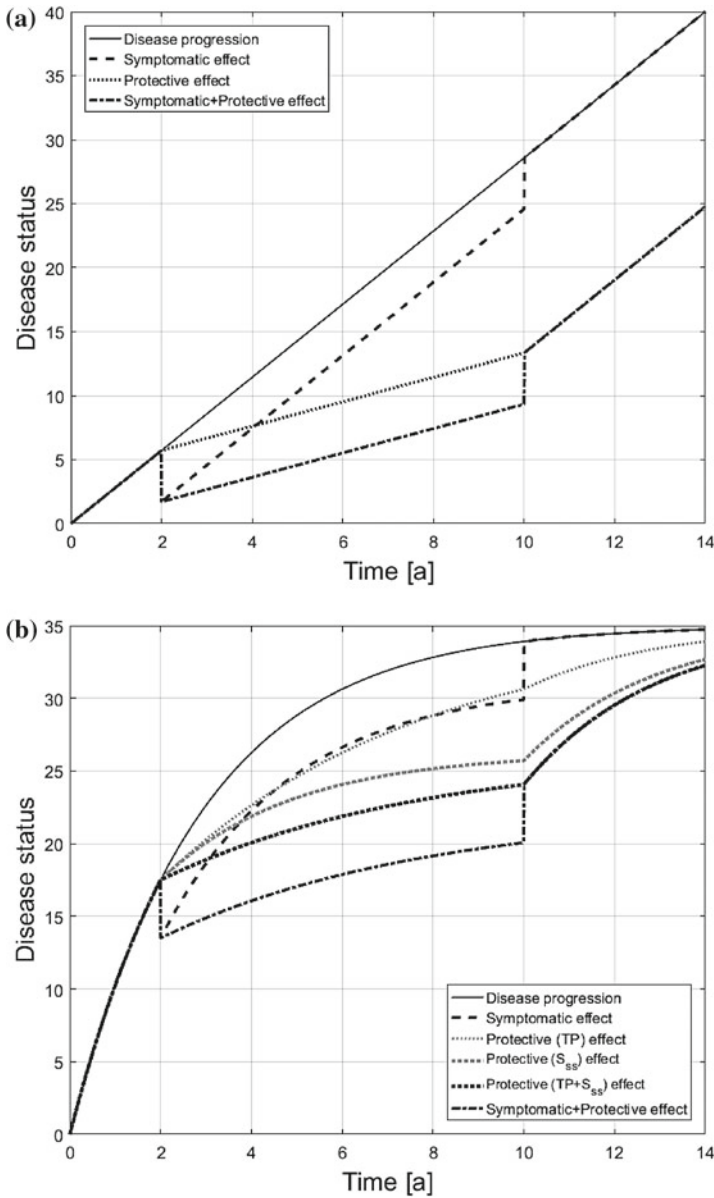
**Fig. 10** Disease progression and drug intervention models: disease status versus time for a linear model (**a**) and an asymptotic model (**b**). *Black solid curves* represent the disease progression without drug intervention, *black dashed curves* represent the symptomatic treatment effect, *black dot curves* represent the protective treatment effect, *black dash-dot curves* represent the combined symptomatic and protective treatment effect. *Gray dot curves* in (**b**) represent the $TP$ protective treatment effect (light) and the $S_{ss}$ protective treatment effect (thick) separately

progression (dashed black curves in Fig. 10a, b) indicating a delay in the time needed by the disease to reach the same status as at the start of the treatment. When the treatment is stopped, the natural disease progression pattern is followed.

In the case of protective effect, the action of the drug influences the rate of disease progression and it is described as a change in the slope of the disease progression curve. In a linear model it follows that:

$$S(t) = S_0 + [\alpha + E(t)] \cdot t, \tag{17}$$

where $E(t)$ represents the protective effect. Assuming that this effect is constant for a given time interval, the effect of the drug action on the disease status is shown in the dotted curves in Fig. 10a, b. When an asymptotic model is used, the protective effect can act either on $TP$, resulting in a change of the curvature of the natural disease progress model (see grey light dotted curve in Fig. 10b), on $S_{ss}$ (see grey thick dotted curve in Fig. 10b) or on both (see black dotted curve in Fig. 10b). The protective effect is shown in Fig. 10a, b as the difference between the untreated disease status curve (black solid line) and the treated one (dotted line) at the end of the treatment, when the rate of disease progression returns to the natural value, indicating that the treatment benefit continues also after drug effects have ceased.

Sometimes the ability to distinguish between symptomatic and protective effects can be challenging and both the effects may occur together. In this case, the total effect is defined as *symptomatic + protective* and, in a linear model for example, can be described with an additive term and a change of the slope of the disease progression model:

$$S(t) = S_0 + E_0(t) + [\alpha + E_s(t)] \cdot t, \tag{18}$$

where $E_0(t)$ is the additive term and $E_s(t)$ is the change in the slope. Assuming that these two variables are constant for a given time interval, the combined symptomatic + protective effect of the drug results in the dash-dot curves in Fig. 10a, b.

**Disease Progression Model of Postmenopausal Osteoporosis**

The disease progression models described above are here applied to PMO, together with symptomatic and protective effects acting on the disease progression to either reduce or slow down the bone loss. As already mentioned in Sect. 3, BMD and BV/TV are the clinical parameters most commonly monitored in OP patients. In general, BMD in OP decreases over time (Fig. 6). In particular, PMO in women induces a BMD decline at a rate of up to 2%/yr. As previously pointed out, the loss of BMD is largely linked to the increase in bone porosity, for this reason, either BMD, BV/TV or porosity itself can be used as parameters describing the disease status. Assuming a linear disease progression model, the BMD variation over time in PMO is reported in Fig. 11. The dashed curves represent the natural PMO progression, whereas symptomatic, protective and combined treatment effects are shown as solid lines in the top, middle and bottom panels respectively. It is worth to notice that comparing the natural disease progression curve reported in Fig. 11 with the
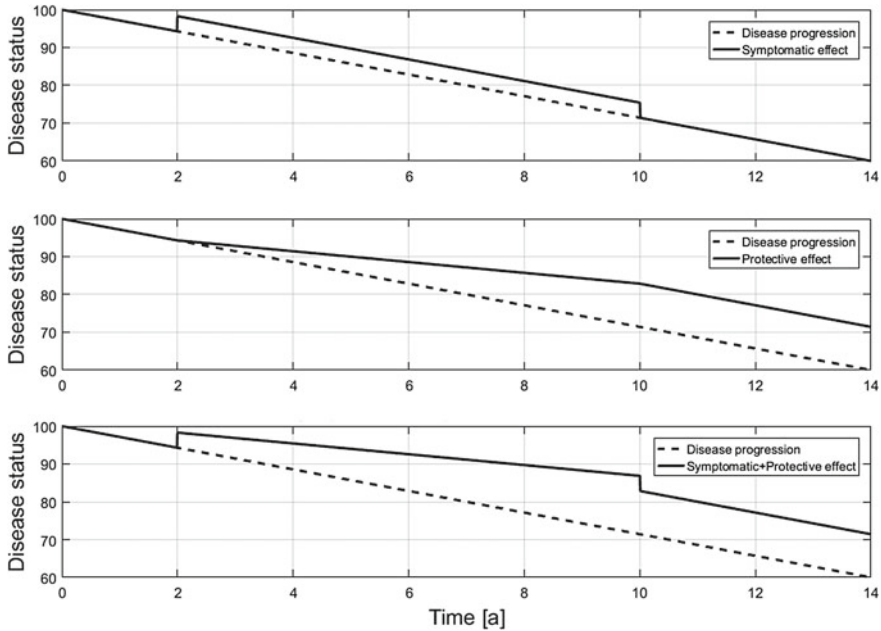
**Fig. 11** Disease progression and drug intervention in PMO: PMO status (e.g., BMD change) versus time in a linear model. *Dashed curves* represent the disease progression without drug intervention. *Solid curves* represent respectively symptomatic (*top panel*), protective (*middle panel*) and combined symptomatic + protective (*bottom panel*) treatment effects

schematic curve representing PMO in Fig. 6, it is evident that the change in bone loss rate is not well represented with a linear model. A piecewise linear model in fact, would represent more realistically the non-linear disease progression. On the other hand, assuming an asymptotic disease progression model, the BMD variation over time is represented in Fig. 12. The dashed curves represent the natural PMO progression, whereas the treatment effects are shown as solid lines. The asymptotic model is able to well represent the non-linear natural disease progression of PMO, which is characterised by a rapid BMD reduction in the first 5 years of the disease followed by a relatively linear progression thereafter. A symptomatic effect is shown in the top panel of Fig. 12a, whereas different protective effects are shown in the middle and bottom panels of Fig. 12a and in the top panel of Fig. 12b. The bottom panel of Fig. 12b shows a combined treatment effect. Due to the slow changes in BMD over time, however, it is not clear how to estimate when the full treatment effect is reached and how to distinguish between protective and symptomatic effects.

All the cases discussed so far assumed a drug effect acting instantaneously on the disease progression. A more consistent way to represent the action of a drug on the disease status is to take into account the time required for a drug to exert its effect (*wash-in*) and the time required for the drug to lose its effect (*wash-out*) [65]. In more detail, the drug wash-in represents the time delay between the starting point of the treatment and the achievement of a constant drug action. This delay might be
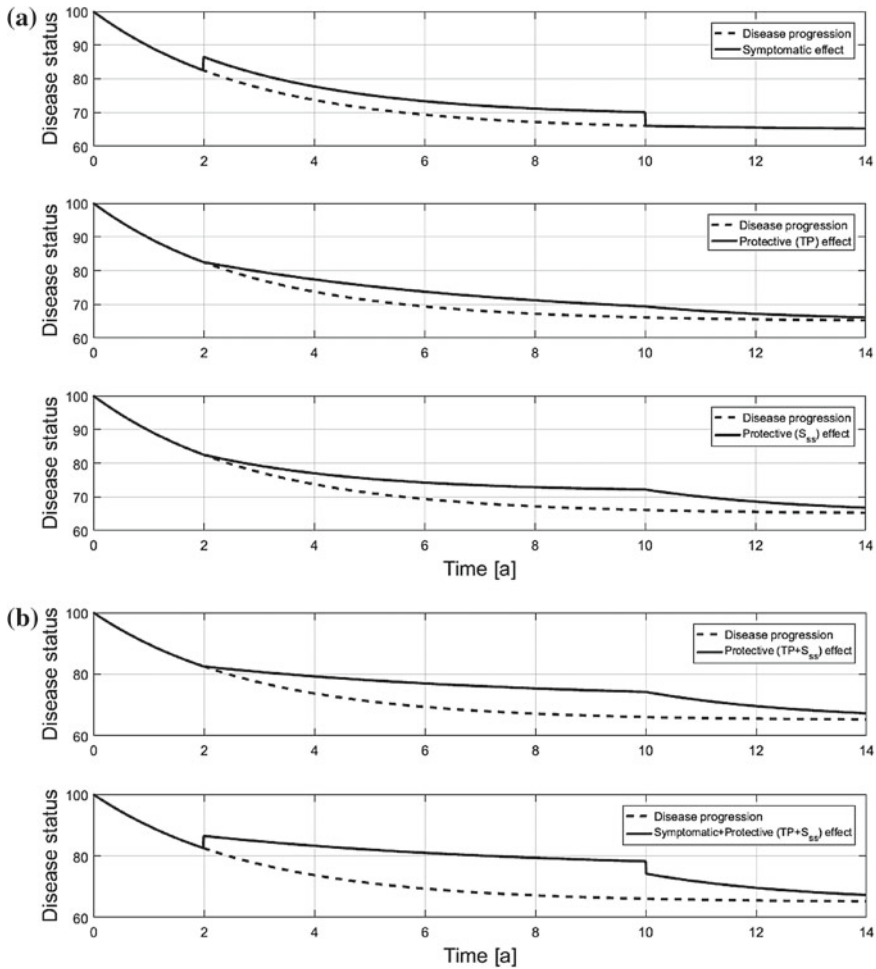
**Fig. 12** Disease progression and drug intervention in PMO: PMO status (e.g., BMD change) versus time in an asymptotic model. *Dashed curves* represent the disease progression without drug intervention. *Solid curves* represent respectively symptomatic treatment effect ((**a**), *top panel*), protective treatment effect acting on $TP$ ((**a**), *middle panel*), protective treatment effect acting on $S_{ss}$ ((**a**), *bottom panel*), combined protective treatment effect $TP + S_{ss}$ ((**b**), *top panel*), combined symptomatic + protective $TP + S_{ss}$ treatment effect ((**b**), *bottom panel*)

due to the drug absorption process, to its distribution to the effect site and to binding reactions with its receptors. On the other hand, the drug wash-out is the time needed to completely remove the drug effect after the withdrawal of the treatment. The BMD change over time in a linear disease progression model taking into account also the wash-in and the wash-out of the drug are reported in Fig. 13. The dashed curves represent the natural PMO progression model, whereas symptomatic, protective and combined treatment effects are shown as solid lines in the top, middle and bottom panels respectively.
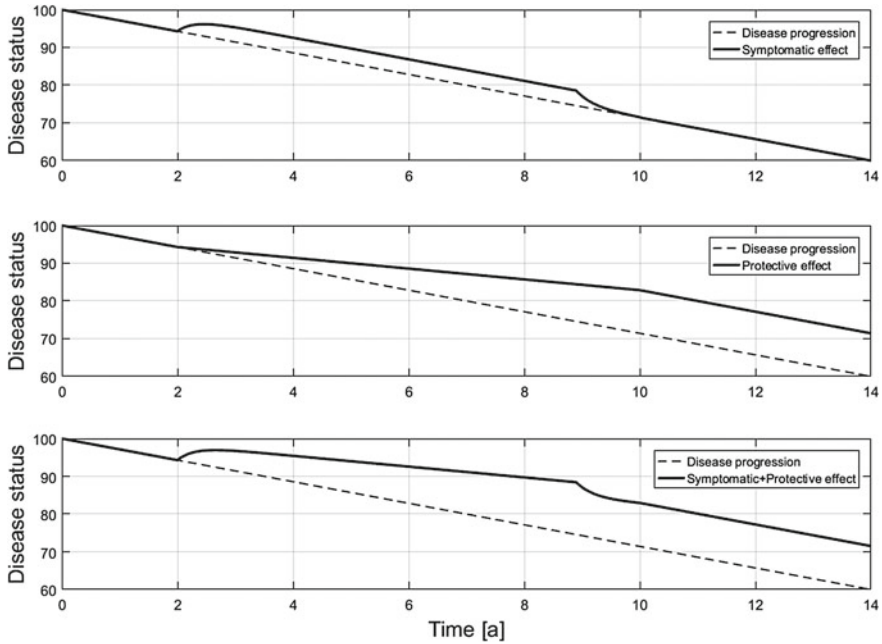
**Fig. 13** Disease progression and drug intervention in PMO: PMO status (e.g., BMD change) versus time in a linear model taking into account the time required for the drug to exert its effect (wash-in) and for losing its effect (wash-out). *Dashed lines* represent the disease progression without drug intervention, *solid curves* represent respectively symptomatic (*top panel*), protective (*middle panel*) and combined symptomatic + protective (*bottom panel*) treatment effects

## 6 Disease System Analysis of Osteoporosis

As introduced in Sect. 5.1, mechanistic PK/PD models use specific expressions to characterise pharmacokinetics and mechanism of action of a drug, as well as physiological processes. A feature specific to this type of models is the differentiation between drug-specific and system-specific parameters. In Sect. 5.2, PMO and the associated bone remodelling process were described via linear and asymptotic disease progression models in which all the details of the underlying molecular actions were lumped into phenomenological parameters describing, for example, the rate of bone loss. In this section, we will formulate a mechanistic model of the bone remodelling process that takes into account the major molecular regulatory pathways. Successively, we will apply this mechanism-based disease progression model to the analysis of PMO progression and its treatment with the anti-catabolic drug denosumab. In this regard, we will closely follow the approach taken by Scheiner and co-workers [146].

A PK model of denosumab has been developed based on the experimental data from Bekker et al. [10] and used to predict blood serum concentrations of the drug

after subcutaneous administration of different doses (see Sect. 6.1). Subsequently, this PK model has been linked to the mechanobiological model of bone remodelling developed by Pivonka and co-workers [121, 122, 145] which takes into account key features of the known physiology of bone remodelling, including the most significant biochemical and biomechanical regulatory mechanisms (see Sect. 6.2). This mechanobiological model allowed the simulation of disease progression in PMO based on molecular and cellular mechanisms. The time-dependent increase of RANKL expression together with the decreased mechanosensitivity of osteocytes have been included in the model to accurately reflect the disease progression in PMO (see Sect. 6.3). Furthermore, this model allowed the introduction of the PD effect of the drug in different points of action, such as cell differentiation, proliferation and apoptosis. In particular, the action of denosumab has been incorporated in the RANK-RANKL-OPG pathway according to the receptor-ligand binding reaction theory (see Sect. 6.4). Eventually, this mechanistic model has been used to simulate PMO with and without the administration of denosumab. The results obtained were investigated and compared with experimental biomarker data (BMD and BTMs) from the literature (see Sect. 6.5).

## 6.1 Denosumab PK Model

As previously mentioned, denosumab is a fully human monoclonal antibody that binds to RANKL with high affinity and inhibits osteoclast differentiation and activation. Denosumab is administrated via subcutaneous injections in either the thigh, the abdomen or the back of the arm. From the site of injection, the drug is absorbed in the blood serum over time and reaches the surfaces of metabolising bone through the blood circulation. The serum drug concentration over time for denosumab has been modelled using the one-compartment PK model illustrated in Fig. 14 (see also Sect. 5.1) which takes into account the extra-vascular administration of the drug and the consequent absorption process from the injection site to the blood serum [97]. The blood serum represent the central compartment of the PK model, characterised by concentration, volume of distribution and bioavailability of the drug (i.e., $m_{den,ser}$ and $V_d/F$). The process of drug absorption is described as a first order rate process characterised by the absorption rate $k_{abs}$. The drug was assumed to be cleared from the central compartment by both organs and enzymes. The elimination by organs was accounted for via the degradation rate $k_{org}$, whereas the elimination by enzymes was included via the degradation rate $k_{enz}$ [146].

The degradation of the drug is assumed to be proportional to its concentration in the central compartment, however experimental data [90] suggested that the elimination process becomes limited above a certain threshold concentration $(m_{den,ser}^{crit})$. According to enzyme kinetics [106], this limitation of the degradation has to be attributed to a limited capacity of the enzymes involved in the elimination process. The governing equations for the serum concentration of denosumab used in the PK model are the following:

**Fig. 14** Denosumab PK model: one-compartment PK model with central compartment characterized by concentration $(m_{den,ser})$, volume of distribution and bioavailability of the drug $(V_d/F)$. Absorption process described via the absorption rate constant $k_{abs}$. Elimination process described via the two elimination constants $k_{org}$ and $k_{enz}$
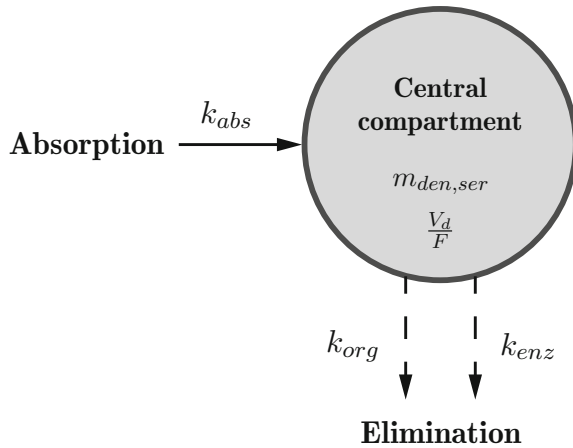


$$\frac{dm_{den,ser}}{dt} = \begin{cases} k_{abs} \cdot m_{den,sub} - (k_{org} + k_{enz}) \cdot m_{den,ser} & \text{if } m_{den,ser} \leq m_{den,ser}^{crit}, \\ k_{abs} \cdot m_{den,sub} - k_{org} \cdot m_{den,ser} - k_{enz} \cdot m_{den,ser}^{crit} & \text{if } m_{den,ser} \geq m_{den,ser}^{crit}, \end{cases} \quad (19)$$

where $m_{den,sub}$ is the amount of drug injected. From the start of the absorption process until when $m_{den,ser}^{crit}$ is reached, the system is described via the first equation in Eq. (19). After this time the system follows the second equation. When the peak concentration is reached, $m_{den,ser}$ starts to decrease reaching again $m_{den,ser}^{crit}$. From this point onwards the system follows the first equation.

To determine the parameters $k_{abs}$, $k_{org}$ and $k_{enz}$, clinical data measuring the temporal evolutions of denosumab serum concentration have been used [10]. Among the six different administration doses investigated in the clinical study, three have been used for the calibration of the model. Since denosumab is generally administered with a small number of high-doses injections, only the higher doses (ranging between 0.3 and 3 mg/kg) have been taken into account, assumed to be practically more relevant. Moreover, since the experimental data showed a limitation on denosumab degradation above a serum concentration of 750 ng/ml, this value has been assumed as threshold concentration $m_{den,ser}^{crit}$ in the PK model. Since denosumab doses are administered according to the patient body mass, to compute the drug concentration in the model knowing the administered dose, an average subject of 70 kg body weight and a 3 litres volume of distribution central compartment (i.e., $F = 1$ and $V_d/F = 3$ l) have been taken into account. The comparison between clinical data and the results obtained using the PK model for three different doses are illustrated in Fig. 15, where the markers indicate the experimental data and the curves the computed values. In particular, triangles, dots and circles represent measurements of denosumab concentration in patients for an administered dose of 0.3, 1 and 3 mg/kg respectively, and dotted, solid and dashed curves are the corresponding concentrations computed with the drug PK model. The continuous horizontal line indicates the threshold concentration.
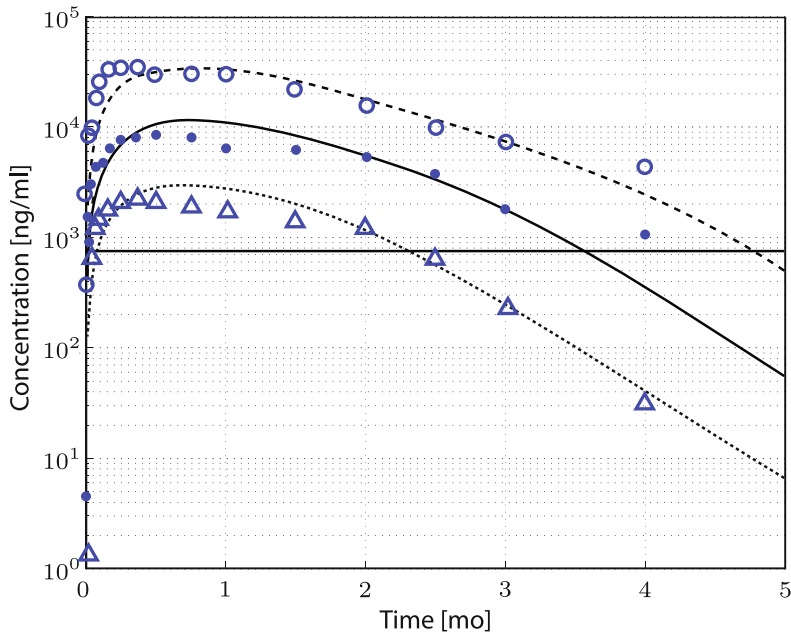
**Fig. 15** Calibration of the denosumab PK model: comparison between experimental (markers) and model-computed (curves) serum concentrations of denosumab over time. *Triangles* and *dotted curve* correspond to a drug dose of 0.3 mg/kg, *dots* and *solid curve* correspond to a dose of 1 mg/kg, *circles* and *dashed curve* correspond to a dose of 3 mg/kg. Solid horizontal line indicates $m_{den,ser}^{crit}$

## 6.2   Mechanistic PK/PD Model of Osteoporosis

The biochemical interactions between bone cells and regulatory factors acting in the remodelling process were summarised in Sect. 2.2. Bone cell responses such as differentiation, proliferation and apoptosis are initiated via ligand-receptor binding reactions occurring on a particular cell. These reactions are based on the physical chemistry principles of mass balance and mass action kinetics applied to the receptor and its corresponding ligand [79]. Detailed development of the equations describing the law of mass action in the remodelling process can be found in the book chapter on bone cell interactions by Pivonka and co-workers [123].

The first mechanism-based model of bone remodelling was proposed by Lemaire and co-authors [88] and successively refined by Pivonka and co-workers [121, 122]. Since both those models took into account the major bone cell types involved in the remodelling process, together with the most significant regulatory factors, they are also referred to as *bone cell population models*. It is worth to mention that the model by Pivonka et al. also accounted for the changes in bone volume, providing in this way the pathway for a biomechanical extensions of the model. Previous models of bone remodelling and adaptation were mainly driven by mechanical loading. In this

context, a major advantage of the mechanism-based models is to provide a translation towards bone biology and clinical bone research. However, both the model from Lemaire et al. and the model from Pivonka et al. had the limitation of not including the concept of Frost's *mechanostat* [53], i.e., they lacked the inclusion of a biomechanical feedback. According to the mechanostat mechanism of action, bone overloading leads to increased bone formation responses, whereas bone underloading leads to increased bone resorption responses. This feedback warrants that, after sufficient time, bone reaches an equilibrium. Given the importance of a biomechanical feedback in the remodelling process, as a further development of the mechanism-based model, Pivonka and co-workers combined the bone cell population model with a micromechanical model of bone stiffness including the mechanostat concept [145]. The biomechanical feedback was included via the strain energy density (SED) induced in the bone matrix by the mechanical loading applied on bone at the macroscopic level. In particular, the loading at the macroscopic level has been linked to the loading at the microscopic level inducing microscopic deformations represented in the model by the SED, the latter parameter in turn affected the bone formation and resorption events by entering the bone cell population model. This mechanism-based model of bone remodelling has been used in combination with the denosumab PK model described in Sect. 6.1 to simulate PMO progression with and without drug intervention.

Due to the complexity of the bone remodelling process, it is not feasible to include into a mathematical model all the cell types and the regulatory factors involved. Therefore, the aim of a comprehensive model is to include sufficient details to address the scientific problem at hand. The mechanobiologically driven evolution of osteoblasts and osteoclasts were mathematically modelled by means of the bone cell population model, which explicitly considered several developmental stages of these cells. In particular, with reference to Fig. 16, the bone cell populations included in the model were: uncommitted osteoblast progenitors (OBu), osteoblast precursors (OBp), active osteoblasts (OBa), osteoclast precursors (OCp) and active osteoclasts (OCa). The progression of osteoblasts and osteoclasts along various developmental stages (i.e., OBu $\rightarrow$ OBp $\rightarrow$ OBa and OCp $\rightarrow$ OCa) was implemented considering several regulatory mechanism (dashed arrows) which either activate ($+$) or repress ($-$) a certain cell function. Among these regulatory factors, there were the RANK-RANKL-OPG pathway regulating the differentiation of osteoclasts via the osteoblast lineage, and the effect of TGF-$\beta$ on OBu, OBp and OCa. Moreover, osteocytes were assumed to sense the SED ($\Psi_{bm}$) induced in the bone matrix by the mechanical loading ($\sigma$) and accordingly send a signal to OBp to promote either their proliferation (i.e., anabolic response) or the RANKL production (i.e., catabolic response). In addition, the action of denosumab and the progression of PMO were also included in the model as regulatory mechanisms. The former was accounted for via competitive binding reactions in the RANK-RANKL-OPG pathway, while the latter was included via disease-related RANKL increased production and mechanoresponsiveness reduction. Note that in Fig. 16 the fine dashed lines indicate binding reactions (i.e., RANK-RANKL-OPG plus denosumab and PTH binding to its recep-
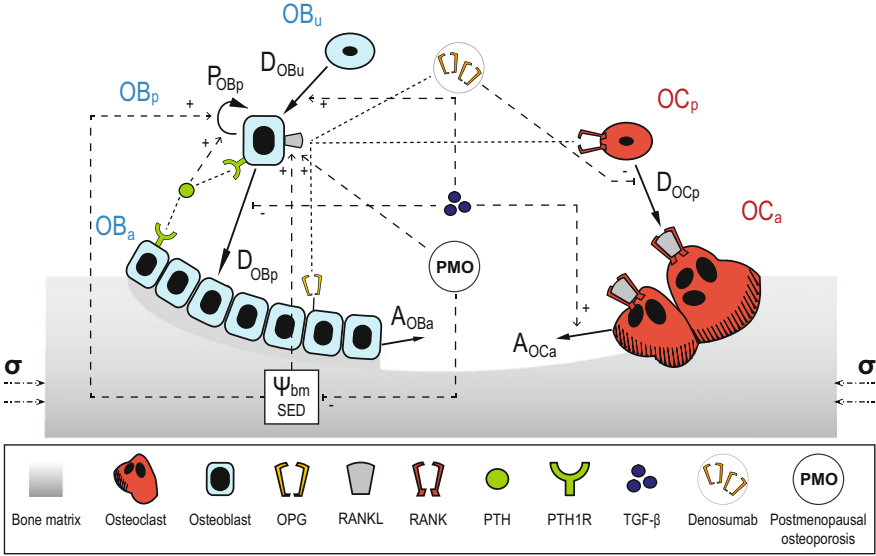
**Fig. 16** Mechanism-based model of bone remodelling showing: (i) osteoblast lineage comprising marrow stromal cells (uncommitted osteoblasts, OBu), osteoblast precursors (OBp), active osteoblasts (OBa); (ii) osteoclast lineage comprising osteoclast precursors (OCp) and active osteoclasts (OCa); (iii) RANK-RANKL-OPG pathway; (iv) TGF-$\beta$ action; (v) PTH action; (vi) denosumab competitive binding in the RANK-RANKL-OPG pathway; (vii) PMO effect; (viii) tissue scale loading ($\sigma$) inducing the SED ($\psi_{bm}$) in the bone matrix [121, 122, 145]

tor), the dashed arrows represent regulatory mechanisms and the solid arrows indicate either cells differentiation, proliferation or apoptosis.

The governing equations of the bone cell population model have been formulated as cell balance equations describing in and out flows of cells from the respective cell pools. Three ordinary differential equations (ODEs) were used to describe the changes in osteoblast precursor, active osteoblast and active osteoclast pool concentrations respectively. In addition, an ODE was used to describe the change in the bone matrix volume fraction ($f_{bm}$) computed as the difference between the amount of bone resorbed and formed. The 4 ODEs constituting the system of equation governing the bone remodelling process are as follows:

$$
\begin{aligned}
\frac{dOBp}{dt} &= D_{OBu} \cdot OBu \cdot \pi_{act,OBu}^{TGF\beta} + P_{OBp} \cdot OBp \cdot \Pi_{act,OBp}^{mech} - D_{OBp} \cdot OBp \cdot \pi_{rep,OBp}^{TGF\beta}, \\
\frac{dOBa}{dt} &= D_{OBp} \cdot OBp \cdot \pi_{rep,OBp}^{TGF\beta} - A_{OBa} \cdot OBa, \\
\frac{dOCa}{dt} &= D_{OCp} \cdot OCp \cdot \pi_{act,OCp}^{RANKL} - A_{OCa} \cdot OCa \cdot \pi_{act,OCa}^{TGF\beta}, \\
\frac{df_{bm}}{dt} &= -K_{res} \cdot OCa + K_{form} \cdot OBa,
\end{aligned}
\tag{20}
$$

where $D_{OBu}$, $D_{OBp}$ and $D_{OCp}$ are differentiation rates of uncommitted osteoblast progenitors, osteoblast precursors and osteoclast precursors respectively. $P_{OBp}$ denotes the proliferation rate of osteoblast precursors. $A_{OBa}$ and $A_{OCa}$ are respectively the apoptosis rates of active osteoblasts and osteoclasts. $K_{res}$ and $K_{form}$ are respectively the bone resorption and bone formation rates. All the $\pi$ together with $\Pi$ represent regulatory functions.

At the core of any mechanism-based model of bone pathophysiology is how various regulatory factors govern the cell behaviour. When dealing with extracellular ligands that bind to their specific receptors on a cell surface (e.g., systemic hormones, autocrine and paracrine factors, growth factors) the behaviour of the cell is modulated by the activation of specific intracellular signalling pathways initiated by the receptor-ligand binding. These intracellular pathways induce an overall cell response that can be either cell differentiation, proliferation and apoptosis or the expression of signalling molecules and receptors. The formulation of binding reactions based on the law of mass action kinetics allows the derivation of phenomenological Hill-type functions that can either activate or repress a particular cell behaviour [86]. In the bone cell population model described so far, these regulatory functions were introduced both as *activator* ($\pi_{act}$) and *repressor* ($\pi_{rep}$) functions, i.e. functions that can either promote or inhibit differentiation, proliferation and apoptosis of the cells. In particular, TGF-$\beta$ binding to its receptors has been accounted for via $\pi_{act,OBu}^{TGF\beta}$, $\pi_{rep,OBp}^{TGF\beta}$ and $\pi_{act,OCa}^{TGF\beta}$; the competitive binding between RANK, RANKL, OPG and denosumab has been included via $\pi_{act,OCp}^{RANKL}$; $\Psi_{bm}$ regulating the proliferation of OBp has been introduced via $\Pi_{act,OBp}^{mech}$. For a complete description and derivation of the governing equations refer to [146].

## 6.3 Modelling Disease Progression in PMO

Experimental studies investigating the pathophysiology of PMO indicated that the disease progression could depend on several regulatory mechanisms perturbed at the same time. Among the potential pathogenic mechanisms driving PMO, oestrogen deficiency has been widely accepted as the principal cause of PMO [96, 133] resulting in increased osteoclast and osteoblast concentrations and consequently increased bone turnover compared to the normal remodelling homeostasis [54]. Furthermore, it appears that another effect of oestrogen deficiency is a decrease in bone mechanoresponsiveness due to increased osteocyte apoptosis. In the initial phase of the oestrogen deficiency, the increase in osteoclast concentration is higher than the increase in osteoblast concentration, inducing a significant bone loss right after the onset of PMO (we also refer to this as first phase of PMO). Simultaneously, the first phase of PMO is also characterised by an increased RANKL/OPG ratio. After a period of time that can vary between some months and few years, the rate of bone loss decreases and bone is subjected to a long-lasting moderate bone loss thereafter (second phase of PMO).

In the mechanism-based model of bone remodelling described in Sect. 6.2 PMO has been modelled introducing a disease-related increase in the RANKL production, which led to an increased osteoclast differentiation. In order to account for the moderate bone loss characterising the second phase of PMO, the excessive production of RANKL has been assumed to reduce over time. The reduction in bone mechanoresponsiveness has also been introduced in the model by varying the parameters governing the sensitivity of bone remodelling to a changing mechanical load [146].

## 6.4   Modelling the Action of Denosumab

Denosumab acts similarly to OPG and competes with RANK and OPG in the binding with RANKL. Specifically, the higher the denosumab concentration, the lower the concentration of RANKL-RANK complexes. In the mechanism-based model of bone remodelling described in Sect. 6.2 denosumab has been introduced as co-regulator factor of osteoclast differentiation by means of the activator function $\pi_{act,OCp}^{RANKL}$. Precisely, the simulation of denosumab treatment induced a reduction of the RANKL-RANK complexes concentration, which consequently downregulated the activator function and eventually resulted in a lower fraction of osteoclast precursor cells differentiated into active osteoclasts. This reduction in the active osteoclast number induced a decreased bone resorption. Adapting the approach used by Pivonka and co-authors [121], the concentration of RANKL was expressed via Eq. (21) taking into account the action of denosumab in the competitive binding:

$$
\begin{aligned}
RANKL = RANKL^{max} \cdot \frac{\beta_{RANKL} + P_{RANKL}}{\beta_{RANKL} + \tilde{D}_{RANKL} \cdot RANKL^{max}} \cdot (1+ \\
+ K_{a,RANKL-OPG} \cdot OPG + K_{a,RANKL-RANK} \cdot RANK+ \\
+ \zeta \cdot K_{a,RANKL-d} \cdot den)^{-1},
\end{aligned}
\tag{21}
$$

where $K_{a,RANKL-OPG}$, $K_{a,RANKL-RANK}$ and $K_{a,RANKL-d}$ are the equilibrium association binding constants respectively for the binding of RANKL to OPG, RANKL to RANK and RANKL to denosumab. $OPG$, $RANK$ and $den$ represent the molar concentrations of OPG, RANK, and denosumab respectively. $\beta_{RANKL}$ is the intrinsic RANKL production rate, $P_{RANKL}$ is the external RANKL dosage term, $\tilde{D}_{RANKL}$ is the constant degradation rate. $RANKL^{max}$ is the maximum concentration of RANKL [146]. It is worth to notice that the concentrations of regulatory factors in the model (i.e., RANKL, OPG, RANK and TGF-$\beta$) have been formulated for a specific representative volume element (RVE) of bone tissue, while the concentration of denosumab was expressed in blood serum using the PK model described in Sect. 6.1. To be able to express the concentration of denosumab in the bone RVE, an additional compartment has been taken into account in the model, i.e., the bone RVE compartment. Assuming an instantaneous distribution from the serum compartment

into the bone RVE compartment, the concentration in the bone RVE compartment was considered to be equal to the serum concentration. To include the possibility of limited accessibility of the drug in the bone RVE compartment, the accessibility factor $\zeta$ has been introduced in Eq. (21). In particular, $\zeta = 1$ was assumed to indicate unrestricted access to denosumab and $\zeta < 1$ reflected access restrictions. Knowing the RANKL concentration from Eq. (21), the concentration of the RANKL-RANK complexes was expressed as follows:

$$[RANKL - RANK] = K_{a,RANKL-RANK} \cdot RANKL \cdot RANK. \qquad (22)$$

Consequently, the activator function was defined as:

$$\pi_{act,OCp}^{RANKL} = \frac{[RANK - RANKL]}{K_{d,RANKL-d} + [RANK - RANKL]}, \qquad (23)$$

where $K_{d,RANKL-d}$ indicates the corresponding equilibrium dissociation binding constant.

## 6.5 Numerical Simulations

The results of the numerical simulations of PMO progression and denosumab treatments are illustrated in Fig. 17 showing the change of $f_{bm}$ over time. The solid curves represent the disease progression of PMO over 5 (Fig. 17a) and 10 years (Fig. 17b) respectively. It is clearly visible that the bone loss obtained in the simulations is rapid in the first 5 years, while it slows down thereafter. In addition, it is worth to notice that the shape of the PMO progression curve obtained with the mechanism-based model of bone remodelling appears similar to the shape of the asymptotic disease progression reported in Fig. 12. However, while in Fig. 12 the shape of the curve was decided a priori by choosing an asymptotic disease progression model, in Fig. 17 the shape of the curve resulted from the structure of the mechanism-based bone remodelling model and the way in which the biochemical and biomechanical feedback and PMO were modelled.

The results of the simulations of PMO treatments with single and multiple injections of denosumab are reproduced in Fig. 17a, b respectively. The three non-solid curves represent simulations with three different drug doses, specifically: the dashed curves correspond to 0.3 mg/kg, the dot curves correspond to 1.0 mg/kg and the dash-dot curves correspond to 3.0 mg/kg. The results for the single injection indicate that the bone loss was rapidly reduced after the injection of the drug. In addition, even though the increase in the $f_{bm}$ appeared to be independent of the dose level, the higher the dose of denosumab the longer the effect on $f_{bm}$ (i.e., time in which $f_{bm}$ stays constant at a certain level). Overall, the observed bone gain was small and once denosumab was cleared, the bone loss continued along the trajectory of PMO. Therefore, the action of a treatment with a single injection of denosumab can be assumed as

**Fig. 17** Changes of cortical $f_{bm}$ over time for PMO and different denosumab administration regimes: **a** single injection, **b** multiple injections. *Solid curves* indicate PMO progression without drug treatment, *dashed curves* indicate treatment with a denosumab dose of 0.3 mg/kg, *dotted curves* indicates treatment with a denosumab dose of 1.0 mg/kg, *dash-dot curves* indicate treatment with a denosumab dose of 3.0 mg/kg
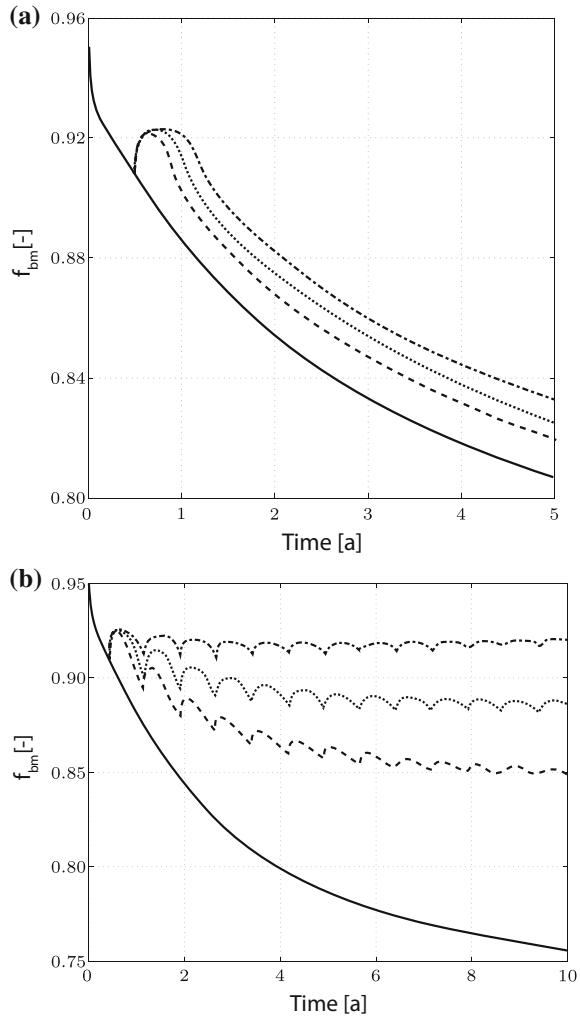
symptomatic because it does not affect the disease progression. In the investigation of multiple injections of denosumab, the drug administration has been modelled as one injection every 9 months. The reduced bone loss appeared to be dependent on the dose level with a lower anti-catabolic effect corresponding to lower doses. The highest dose significantly reduced the bone loss maintaining the $f_{bm}$ at a higher and almost constant level.

# 7 Summary and Conclusions

This chapter reviewed the complexity of the pathophysiology of the skeletal system and the numerous regulatory factors involved at multiple scales in bone homeostasis and OP. Current approaches taken to understand this system include clinical research, basic bone biology and biomechanical assessment. It is evident that none of these approaches alone will be able to provide a comprehensive picture of the skeletal system and that a combination of all the information gained separately is required. In this context, DSA is a promising framework which allows to link together various disciplines and to utilise information on bone pathophysiology based on the major bone biomarkers in a quantitative way. It also provides the ability to define clearer clinical endpoints and better assess drug efficacy. If based on subject-specific data, the DSA approach gives the possibility to formulate subject-specific models allowing the optimisation of individual treatments rather than drawing conclusions on a population basis.

The use of comprehensive mechanism-based models of bone remodelling in DSA allows quantitative assessment of treatment efficacy at various levels of bone pathophysiology. To continuously improve these models good experimental data and up-to-date computational modelling tools are crucial. As with any mathematical approach, the identification from available experimental data of the essential time and rate limiting steps in the bone remodelling process is necessary. Moreover, in order for those models to be relevant for clinical and basic bone biology research, the most important aspects of bone physiology need to be incorporated.

In conclusion, the ultimate goal of DSA is to develop a quantitative simulation tool which allows the prediction of short-term and long-term effects of various drug treatments (including combinations of drugs) on disease progression in OP and other bone diseases. As such, the computational model needs to undergo continuous development according to the latest discoveries in the bone remodelling process and associated biomarkers, in order to increase its ability to compare, predict and extrapolate drug treatment effects. Currently, the development of fully mechanistic disease system models for OP is an ongoing process, it is anticipated that in the near future these models will be able to adequately predict the long-term effects of drug treatment on the clinical outcome, i.e., bone fractures.

**Outlook to Future Model Extensions**

One possible model extension is towards a whole organ scale description of calcium and phosphate homeostasis. Key regulatory factors in the endocrine control of calcium concentration are PTH and vitamin D. Bone plays an important part in the calcium and phosphate homeostasis, other organs involved include gut (responsible of mineral absorption) and kidneys (responsible for calcitriol formation). Many endocrine diseases such as hyperparathyroidism and hypoparathyroidism have a high impact on the bone remodelling balance and consequently on bone health. The loss of kidney functions has a significant impact on bone health as well. In this context, Peterson and Riggs have developed a physiologically based mathematical model of

integrated calcium homeostasis and bone remodelling containing 46 ODEs which describe the concentration of calcium and phosphate in the different body compartments such as blood, gut [119].

Another important model extension is towards *spatio-temporal* disease progression models. As previously discussed, bone fractures result from the combination of the applied mechanical load and the material properties of bone (including porosity and TMD). Bone fractures are localised phenomena which initiate at a particular spatial location within bone. In order to predict bone fracture and the evolving failure pattern more accurately, spatio-temporal mechanical models of bone are required. Researchers in the field of materials engineering developed a large variety of constitutive models of bone which are able to simulate bone fracture under known mechanical loading conditions. However, these models did not integrate the bone remodelling process in their framework, but were purely mechanical. A first attempt to develop spatio-temporal models of bone disease progression were made by Pivonka and co-workers who studied the age-related expansion of the marrow cavity and the trabecularisation of cortical bone using a mechanobiological model [89].

# References

1. E. Abe, M. Yamamoto, Y. Taguchi, B. Lecka-Czernik, C.A. O'Brien, A.N. Economides, N. Stahl, R.L. Jilka, S.C. Manolagas, Essential requirement of BMPs-2/4 for both osteoblast and osteoclast formation in murine bone marrow cultures from adult mice: Antagonism by noggin. J. Bone Mineral Res. **15**(4), 663–673 (2000)
2. M.E. Arlot, E. Sornay-Rendu, P. Garnero, B. Vey-Marty, P.D. Delmas, Apparent pre- and postmenopausal bone loss evaluated by DXA at different skeletal sites in women: the OFELY cohort. J. Bone Mineral Res. **12**(4), 683–690 (1997)
3. Y. Bala, D. Farlay, P.D. Delmas, P.J. Meunier, G. Boivin, Time sequence of secondary mineralization and microhardness in cortical and cancellous bone from ewes. Bone **46**(4), 1204–1212 (2010). ISSN 8756-3282
4. Y. Bala, D. Farlay, G. Boivin, Bone mineralization: from tissue to crystal in normal and pathological contexts. Osteoporosis Int. **24**(8), 2153–2166 (2013). ISSN 1433-2965
5. Y. Bala, R. Zebaze, E. Seeman, Role of cortical bone in bone fragility. Current Opinion Rheumatol. **27**(4), 406–413 (2015)
6. R. Baron, E. Hesse, Update on bone anabolics in osteoporosis treatment: rationale, current status, and perspectives. J. Clin. Endocrinol. Metaboli. **97**(2), 311–325 (2012). ISSN 0021972X
7. R. Baron, M. Kneissel, WNT signaling in bone homeostasis and disease: from human mutations to treatments. Nat. Med. **19**(2), 179–92 (2013). ISSN 1546-170X
8. C.A. Baud, M. Gossi, Degree of mineralization of bone tissue as determined by quantitative microradiograhy: effect of age, sex and pathological conditions, in *Proceedings Fourth International Conference on Bone Measurement* (1980)
9. D.C. Bauer, A. Schwartz, L. Palermo, J. Cauley, M. Hochberg, A. Santora, S.R. Cummings, D.M. Black, Fracture prediction after discontinuation of 4 to 5 years of alendronate therapy. JAMA Int. Med. **174**(7), 1126–34 (2014). ISSN 2168-6106

10. P.J. Bekker, D.L. Holloway, A.S. Rasmussen, R. Murphy, S.W. Martin, P.T. Leese, G.B. Holmes, C.R. Dunstan, A.M. DePaoli, A single-dose placebo-controlled study of AMG 162, a fully human monoclonal antibody to RANKL, in postmenopausal women. J. Bone Mineral Res. **19**(7), 1059–1066 (2004). ISSN 0884-0431

11. C. Bergot, Y. Wu, E. Jolivet, L.Q. Zhou, J.D. Laredo, V. Bousson, The degree and distribution of cortical bone mineralization in the human femoral shaft change with age and sex in a microradiographic study. Bone **45**(3), 435–442 (2009)

12. J.P. Bilezikian, Combination anabolic and antiresorptive therapy for osteoporosis: opening the anabolic window. Current Osteoporosis Rep. **6**(1), 24–30 (2008). ISSN 1544-2241

13. D.M. Black, C.J. Rosen, Postmenopausal osteoporosis. N. Engl. J. Med. **374**(3), 254–262 (2016)

14. J.M. Bland, D.G. Altman, Statistical methods for assessing agreement between two methods of clinical measurement. Lancet **1**(8476), 307–310 (1986). ISSN 01406736

15. R.D. Blank, D.G. Malone, R.C. Christian, N.L. Vallarta-Ast, D.C. Krueger, M.K. Drezner, N.C. Binkley, K.E. Hansen, Patient variables impact lumbar spine dual energy X-ray absorptiometry precision. Osteoporosis Int. **17**(5), 768–774 (2006). ISSN 1433-2965

16. G. Boivin, P. Meunier, Effects of bisphosphonates on matrix mineralization. J. Musculoskelet. Neuronal Interact. **2**(6), 538–543 (2002)

17. G. Boivin, P.J. Meunier, The degree of mineralization of bone tissue measured by computerized quantitative contact microradiography. Calcif. Tissue Int. **70**(6), 503–511 (2002)

18. G. Boivin, D. Farlay, Y. Bala, A. Doublier, P.J. Meunier, P.D. Delmas, Influence of remodeling on the mineralization of bone tissue. Osteoporosis Int. **20**(6), 1023–1026 (2009). ISSN 1433-2965

19. G.Y. Boivin, P.M. Chavassieux, A.C. Santora, J. Yates, P.J. Meunier, Alendronate increases bone strength by increasing the mean degree of mineralization of bone tissue in osteoporotic women. Bone **27**(5), 687–694 (2000)

20. J. Borggrefe, C. Graeff, T.N. Nickelsen, F. Marin, C.C. Gler, Quantitative computed tomographic assessment of the effects of 24 months of teriparatide treatment on 3D femoral neck bone distribution, geometry, and bone strength: results from the EUROFORS study. J. Bone Mineral Res. **25**(3), 472–481 (2010). ISSN 1523-4681

21. M.L. Bouxsein, Mechanisms of osteoporosis therapy: a bone strength perspective. Clin. Cornerstone **5**, S13–S21 (2003). ISSN 1098-3597

22. W.J. Boyle, W.S. Simonet, D.L. Lacey, Osteoclast differentiation and activation. Clin. Calcium **17**(4), 484–492 (2003). ISSN 0028-0836

23. J. Burch, St. Rice, H. Yang, A. Neilson, L. Stirk, R. Francis, P. Holloway, S. Peter, D. Craig, Systematic review of the use of bone turnover markers for monitoring the response to osteoporosis treatment: the secondary prevention of fractures, and primary prevention of fractures in high-risk groups. Report ISSN1366-5278, National Institute for Health Research (2014)

24. A.J. Burghardt, G.J. Kazakia, S. Ramachandran, T.M. Link, S. Majumdar, Age and gender related differences in the geometric properties and biomechanical significance of intra-cortical porosity in the distal radius and tibia. J. Bone Mineral Res. **25**(5), 983–993 (2010). ISSN 0884-0431

25. D.B. Burr, Bone quality: understanding what matters. J. Musculoskelet. Neuronal Interact. **4**(2), 184–186 (2004). ISSN 11087161

26. L.M. Calvi, G.B. Adams, K.W. Weibrecht, J.M. Weber, D.P. Olson, M.C. Knight, R.P. Martin, E. Schipani, P. Divieti, F.R. Bringhurst, L.A. Milner, H.M. Kronenberg, D.T. Scadden, Osteoblastic cells regulate the haematopoietic stem cell niche. Nature **425**(6960), 841–846 (2003)

27. D.R. Carter, W.C. Hayes, Bone compressive strength: the influence of density and strain rate. Science **194**(4270), 1174–1176 (1976)

28. T.J. Chambers, Osteoblasts relase osteoclasts from calcitonin-induced quiescence. J. Cell Sci. **57**, 247–260 (1982)

29. P.L.S. Chan, N.H.G. Holford, Drug treatment effects on disease progression. Annu. Rev. Pharmacol. Toxicol. **41**(1), 625–659 (2001)

30. L. Cianferotti, F. DAsta, M.L. Brandi, A review on strontium ranelate long-term antifracture efficacy in the treatment of postmenopausal osteoporosis. Therapeutic Adv. Musculoskelet. Disease **5**(3), 127–139 (2013). ISSN 1759-720X

31. T.L. Clemens, G. Karsenty, The osteoblast: an insulin target cell controlling glucose homeostasis. J. Bone Mineral Res. **26**(4), 677–680 (2011)

32. P. Close, A. Neuprez, J.-Y. Reginster, Developments in the pharmacotherapeutic management of osteoporosis. Expert Opinion Pharmacother. **7**(12), 1603–1615 (2006). ISSN 1465-6566

33. D.M.L. Cooper, B. Erickson, A.G. Peele, K. Hannah, C.D.L. Thomas, J.G. Clement, Visualization of 3D osteon morphology by synchrotron radiation micro-CT. J. Anatomy **219**(4), 481–489 (2011). ISSN 0021-8782

34. F. Cosman, Anabolic and antiresorptive therapy for osteoporosis: combination and sequential approaches. Current Osteoporosis Rep. **12**(4), 385–395 (2014). ISSN 1544-2241

35. F. Cosman, R.A. Wermers, C. Recknor, K.F. Mauck, L. Xie, E.V. Glass, J.H. Krege, Effects of teriparatide in postmenopausal women with osteoporosis on prior alendronate or raloxifene: differences between stopping and continuing the antiresorptive agent. J. Clin. Endocrinol. Metab. **94**(10), 3772–3780 (2009). ISSN 0021-972X

36. S. Cremers, P. Garnero, Biochemical markers of bone turnover in the clinical development metastatic bone disease potential uses and pitfalls. Drugs **66**(16), 2031–2058 (2006)

37. S.R. Cummings, D. Bates, D.M. Black, Clinical use of bone densitometry: scientific review. JAMA **288**(15), 1889–1897 (2002)

38. J.D. Currey, The mechanical properties of bone. Clin. Orthop. Relat. Res. **73**, 210–231 (2006)

39. J.D. Currey, K. Brear, P. Zioupos, The effects of ageing and changes in mineral content in degrading the toughness of human femora. J. Biomech. **29**(2), 257–260 (1996)

40. M. Danhof, G. Alvan, S.G. Dahl, J. Kuhlmann, G. Paintaud, Mechanism-based pharmacokinetic-pharmacodynamic modeling − a new classification of biomarkers. Pharm. Res. **22**(9), 1432–1437 (2005). ISSN 0724-8741

41. M. Danhof, J. de Jongh, E.C.M. De Lange, O. Della Pasqua, B.A. Ploeger, R.A. Voskuyl, Mechanism-based pharmacokinetic-pharmacodynamic modeling: biophase distribution, receptor theory, and dynamical systems analysis. Annu. Rev. Pharmacol. Toxicol. **47**, 357–400 (2007). ISSN 0362-1642

42. D.W. Dempster, M.W. Ferguson-Pell, R.W. Mellish, G.V. Cochran, F. Xie, C. Fey, W. Horbert, M. Parisien, R. Lindsay, Relationships between bone structure in the iliac crest and bone structure and strength in the lumbar spine. Osteoporos. Int. **3**(2), 90–96 (1993)

43. A. El Maghraoui, L. Achemlal, A. Bezza, Monitoring of dual-energy X-ray absorptiometry measurement in clinical practice. J. Clin. Densitom. **9**(3), 281–286 (2006). ISSN 1094-6950

44. E.F. Eriksen, Cellular mechanisms of bone remodeling. Rev. Endocr. Metab. Disord. **11**(4), 219–227 (2010). ISSN 13899155

45. S. Ferrari, Future directions for new medical entities in osteoporosis. Best Pract. Res. Clin. Endocrinol. Metab. **28**(6), 859–870 (2014). ISSN 15321908

46. J.S. Finkelstein, J.J. Wyland, H. Lee, R.M. Neer, Effects of teriparatide, alendronate, or both in women with postmenopausal osteoporosis. J. Clin. Endocrinol. Metab. **95**(4), 1838–1845 (2010). ISSN 0021-972X

47. H. Follet, G. Boivin, C. Rumelhart, P.J. Meunier, The degree of mineralization is a determinant of bone strength: a study on human calcanei. Bone **34**(5), 783–789 (2004)

48. H. Follet, S. Viguet-Carrin, B. Burt-Pichat, B. Depalle, Y. Bala, E. Gineyts, F. Munoz, M.E. Arlot, G. Boivin, R. Chapurlat, P.D. Delmas, M.L. Bouxsein, Effects of pre-existing microdamage, collagen cross-links, degree of mineralization, age and architecture on compressive mechanical properties of elderly human vertebral trabecular bone. J. Orthop. Res. **29**(4), 481–488 (2011)

49. N. Fratzl-Zelman, P. Roschger, B.M. Misof, S. Pfeffer, F.H. Glorieux, K. Klaushofer, F. Rauch, Normative data on mineralization density distribution in iliac bone biopsies of children, adolescents and young adults. Bone **44**(6), 1043–1048 (2009)

50. H.M. Frost, in *Bone Remodelling Dynamics*, ed. by C.R. Lam (Charles C. Thomas, Springfield, 1963)

51. H.M. Frost, Dynamics of bone remodeling, in *Bone Biodymanics*, ed. by H.M. Frost (Little, Brown & Co, 1964), pp. 315–333
52. H.M. Frost, The skeletal intermediary organization. Metab. Bone Disease Relat. Res. **4**(5), 281–290 (1983). ISSN 02218747
53. H.M. Frost, Bone mass and the mechanostat: a proposal. Anat Record **219**(1), 1–9 (1987)
54. P. Garnero, E. Sornay-Rendu, M.C. Chapuy, P.D. Delmas, Increased bone turnover in late postmenopausal women is a major determinant of osteoporosis. J. Bone Mineral Res. **11**(3), 337–349 (1996). ISSN 0884-0431
55. P. Geusens, New insights into treatment of osteoporosis in postmenopausal women. RMD Open **1**(Suppl 1), e000051 (2015). ISSN 2056-5933
56. P. Geusens, R. Chapurlat, G. Schett, A. Ghasem-Zadeh, E. Seeman, J. de Jong, J. van den Bergh, High-resolution in vivo imaging of bone and joints: a window to microarchitecture. Nat. Rev. Rheumatol. **10**(5), 304–313 (2014). ISSN 1759-4790
57. A. Grey, M. Bolland, B. Mihov, S. Wong, A. Horne, G. Gamble, I.R. Reid, Duration of antiresorptive effects of low-dose zoledronate in osteopenic postmenopausal women: a randomized, placebo-controlled trial. J. Bone Mineral Res. **29**(1), 166–172 (2014). ISSN 1523-4681
58. D.J. Hadjidakis, I.I. Androulakis, Bone remodeling. Ann. N. Y. Acad. Sci. **1092**, 385–396 (2006). ISSN 00778923
59. K.D. Harrison, D.M.L. Cooper, Modalities for visualization of cortical bone remodeling: the past, present, and future. Front. Endocrinol. **6**, 122 (2015). ISSN 1664-2392
60. Ch. Hellmich, F.-J. Ulm, L. Dormieux, Can the diverse elastic properties of trabecular and cortical bone be attributed to only a few tissue-independent phase properties and their interactions? Biomech. Model. Mechanobiol. **2**(4), 219–238 (2004). ISSN 1617-7940
61. K. Henriksen, D.J. Leeming, C. Christiansen, M.A. Karsdal, Use of bone turnover markers in clinical osteoporosis assessment in women: current issues and future options. Women's Health **7**(6), 689–698 (2011). ISSN 1745-5057
62. C.J. Hernandez, How can bone turnover modify bone strength independent of bone mass? Bone **42**(6), 1014–1020 (2008). ISSN 87563282
63. C.J. Hernandez, T.M. Keaveny, A biomechanical perspective on bone quality. Bone **39**(6), 1173–1181 (2006). ISSN 8756-3282
64. L.C. Hofbauer, M. Schoppet, Clinical implications of the osteoprotegerin/RANKL/RANK system for bone. J. Am. Med. Assoc. **292**(4), 490–495 (2004)
65. N.H.G. Holford, Clinical pharmacology = disease progression + drug action. Br. J. Clin. Pharmacol. **79**(1), 18–27 (2013). ISSN 1365-2125
66. N.H.G. Holford, L.B. Sheiner, Kinetics of pharmacologic response. Pharmacol. Ther. **16**(2), 143–166 (1982). ISSN 01637258
67. N.J. Horwood, J. Elliott, T.J. Martin, M.T. Gillespie, Osteotropic agents regulate the expression of osteoclast differentiation factor and osteoprotegerin in osteoblastic stromal cells. Endocrinology **139**(11), 4743 (1998)
68. S.L. Hui, C.W. Slemenda, C.C. Johnston, Age and bone mass as predictors of fracture in a prospective study. J. Clin. Investig. **81**(6), 1804–1809 (1988). ISSN 0021-9738
69. Z.F.G. Jaworski, C. Hooper, Study of cell kinetics within evolving secondary haversian systems. J. Anat. **131**(1), 91–102 (1980)
70. Z.F.G. Jaworski, B. Duck, G. Sekaly, Kinetics of osteoclasts and their nuclei in evolving secondary haversian systems. J. Anat. **133**, 397405 (1981)
71. W.S.S. Jee, W. Yao, Overview: animal models of osteopenia and osteoporosis. J. Musculoskelet. Neuron Interact. **1**(3), 193–207 (2001)
72. W.S.S. Jee, X.Y. Tian, R.B. Setterberg, Cancellous bone minimodeling-based formation: a Frost Takahashi legacy. J. Musculoskelet. Neuronal Interact. **7**(3), 232–239 (2007)
73. B. Jobke, B. Muche, A.J. Burghardt, J. Semler, T.M. Link, S. Majumdar, Teriparatide in bisphosphonate-resistant osteoporosis: Microarchitectural changes and clinical results after 6 and 18 months. Calcif. Tissue Int. **89**(2), 130–139 (2011). ISSN 1432-0827
74. J.A. Kanis, Diagnosis of osteoporosis and assessment of fracture risk. Lancet **359**(9321), 1929–1936 (2002). ISSN 0140-6736

75. J.A. Kanis, N. Burlet, C. Cooper, P.D. Delmas, J.Y. Reginster, F. Borgstrom, R. Rizzoli, European guidance for the diagnosis and management of osteoporosis in postmenopausal women. Osteoporos. Int. **19**(4), 399–428 (2008). ISSN 0937941X

76. J.A. Kanis, E.V. McCloskey, H. Johansson, C. Cooper, R. Rizzoli, J.Y. Reginster, European guidance for the diagnosis and management of osteoporosis in postmenopausal women. Osteoporos. Int. **24**(1), 23–57 (2013). ISSN 1433-2965

77. Y. Kawano, R. Kypta, Secreted antagonists of the Wnt signalling pathway. J. Cell Sci. **116**(13), 2627–2634 (2003)

78. A.E. Kearns, S. Khosla, P.J. Kostenuik, Receptor activator of nuclear factor $\kappa$b ligand and osteoprotegerin regulation of bone remodeling in health and disease. Endocr. Rev. **29**(2), 155–192 (2008). ISSN 0163-769X

79. J. Keener, J. Sneyd, *Mathematical Physiology*, 2nd edn. (Springer, Berlin, 2009). ISBN 9780387758466

80. L.J. Kidd, A.S. Stephens, J.S. Kuliwaba, N.L. Fazzalari, A.C.K. Wu, M.R. Forwood, Temporal pattern of gene expression and histology of stress fracture healing. Bone **46**(2), 369–378 (2010)

81. R. Kulkarni, A. Bakker, V. Everts, J. Klein-Nulend, Inhibition of osteoclastogenesis by mechanically loaded osteocytes: Involvement of MEPE. Calcif. Tissue Int. **87**(5), 461–468 (2010)

82. D.L. Lacey, E. Timms, H.L. Tan, M.J. Kelley, C.R. Dunstan, T. Burgess, R. Elliott, A. Colombero, G. Elliott, S. Scully, H. Hsu, J. Sullivan, N. Hawkins, E. Davy, C. Capparelli, A. Eli, Y.X. Qian, S.. Kaufman, I. Sarosi, V. Shalhoub, G. Senaldi, J. Guo, J. Delaney, W.J. Boyle, Osteoprotegerin ligand is a cytokine that regulates osteoclast differentiation and activation. Cell **93**, 165–176 (1998). ISSN 00928674

83. J. Lam, S. Takeshita, J.E. Barker, O. Kanagawa, F.P. Ross, S.L. Teitelbaum, TNF-$\alpha$ induces osteoclastogenesis by direct stimulation of macrophages exposed to permissive levels of RANK ligand. J. Clin. Invest. **106**(12), 1481–1488 (2000)

84. L.E. Lanyon, Osteocytes, strain detection, bone modeling and remodeling. Calcif. Tissue Int. **53**, S102–S107 (1993)

85. L.E. Lanyon, S. Bourn, The influence of mechanical function on the development and remodeling of the tibia. an experimental study in sheep. J. Bone Joint Surg. Am. **61**(2), 263–273 (1979)

86. D.A. Lauffenburger, J. Linderman, *Receptors: Models for Binding, Trafficking, and Signaling* (Oxford University Press, New York, 1993)

87. D.J. Leeming, P. Alexandersen, M.A. Karsdal, P. Qvist, S. Schaller, L.B. Tankó, An update on biomarkers of bone turnover and their utility in biomedical research and clinical practice. Eur. J. Clin. Pharmacol. **62**(10), 781–792 (2006). ISSN 00316970

88. V. Lemaire, F.L. Tobin, L.D. Greller, C.R. Cho, L.J. Suva, Modeling the interactions between osteoblast and osteoclast activities in bone remodeling. J. Theor. Biol. **229**(3), 293–309 (2004)

89. C. Lerebours, P.R. Buenzli, S. Scheiner, P. Pivonka, A multiscale mechanobiological model of bone remodelling predicts site-specific bone loss in the femur during osteoporosis and mechanical disuse. Biomech. Model. Mechanobiol. **15**(1), 43–67 (2015)

90. E.M. Lewiecki, Treatment of osteoporosis with denosumab. Maturitas **66**, 182–186 (2010). ISSN 03785122

91. T. Lin, C. Wang, X.Z. Cai, X. Zhao, M.M. Shi, Z.M. Ying, F.Z. Yuan, C. Guo, S.G. Yan, Comparison of clinical efficacy and safety between denosumab and alendronate in postmenopausal women with osteoporosis: a meta-analysis. Int. J. Clin. Pract. **66**(4), 399–408 (2012). ISSN 1742-1241

92. R. Lindsay, W.H. Scheele, R. Neer, et al, Sustained vertebral fracture risk reduction after withdrawal of teriparatide in postmenopausal women with osteoporosis. Arch. Intern. Med. **164**(18), 2024–2030 (2004). ISSN 0003-9926

93. X.S. Liu, L. Ardeshirpour, J.N. VanHouten, E. Shane, J.J. Wysolmerski, Site-specific changes in bone microarchitecture, mineralization, and stiffness during lactation and after weaning in mice. J. Bone Mineral Res. **27**(4), 865–875 (2012). ISSN 15234681

94. Y. Lu, H.K. Genant, J. Shepherd, S. Zhao, A. Mathur, T.P. Fuerst, S.R. Cummings, Classification of osteoporosis based on bone mineral densities. J. Bone Mineral Res. **16**(5), 901–910 (2001). ISSN 1523-4681

95. Z.F. Lu, G. Wang, C.R. Dunstan, H. Zreiqat, Short-term exposure to tumor necrosis factor-α enables human osteoblasts to direct adipose tissue-derived mesenchymal stem cells into osteogenic differentiation. Stem Cells Dev. **21**(13), 2420–2429 (2012)

96. S.C. Manolagas, Birth and death of bone cells: basic regulatory mechanisms and implications for the pathogenesis and treatment of osteoporosis. Endocr. Rev. **21**(2), 115–137 (2000)

97. A. Marathe, M.C. Peterson, D.E. Mager, Integrated cellular bone homeostasis model for denosumab pharmacodynamics in multiple myeloma patients. J. Pharmacol. Exp. Ther. **326**(2), 555–562 (2008). ISSN 1521-0103

98. T.J. Martin, E. Seeman, New mechanisms and targets in the treatment of bone fragility. Clin. Sci. **112**(2), 77–91 (2007). ISSN 1470-8736

99. M.R. McClung, A. Grauer, S. Boonen, M.A. Bolognese, J.P. Brown, A. Diez-Perez, B.L. Langdahl, J.-Y. Reginster, J.R. Zanchetta, S.M. Wasserman, L. Katz, J. Maddox, Y.-C. Yang, C. Libanati, H.G. Bone, Romosozumab in postmenopausal women with low bone mineral density. N. Engl. J. Med. **370**(5), 412–420 (2014). ISSN 0028-4793

100. B. Meibohm, H. Derendorf, Basic concepts of pharmacokinetic/pharmacodynamic (PK/PD) modelling. Int. J. Clin. Pharmacol. Ther. **35**(10), 401–13 (1997)

101. H. Michael, P.L. Hrknen, H.K. Vnnen, T.A. Hentunen, Estrogen and testosterone use different cellular pathways to inhibit osteoclastogenesis and bone resorption. J. Bone Mineral Res. **20**(12), 2224–2232 (2005)

102. P.D. Miller, M.A. Bolognese, E.M. Lewiecki, M.R. McClung, B. Ding, M. Austin, Y. Liu, J. San Martin, Effect of denosumab on bone density and turnover in postmenopausal women with low bone mass after long-term continued, discontinued, and restarting of therapy: a randomized blinded phase 2 clinical trial. Bone **43**(2), 222–229 (2008). ISSN 8756-3282

103. R. Müller, Hierarchical microimaging of bone structure and function. Nat. Rev. Rheumatol. **5**(7), 373–381 (2009). ISSN 1759-4790

104. G.R. Mundy, Cellular and molecular regulation of bone turnover. Bone **24**(5 Suppl), 35S–38S (1999). ISSN 8756-3282

105. M.H. Murad, M.T. Drake, R.J. Mullan, K.F. Mauck, L.M. Stuart, M.A. Lane, N.O. Abu Elnour, P.J. Erwin, A. Hazem, M.A. Puhan, T. Li, V.M. Montori, Comparative effectiveness of drug treatments to prevent fragility fractures: a systematic review and network meta-analysis. J. Clin. Endocrinol. Metab. **97**(6), 1871–1880 (2012). ISSN 19457197

106. J.D. Murray, *Mathematical Biology: I. An Introduction*, vol. 1, 3rd edn. (Springer, New York, 2002)

107. N. Nakagawa, M. Kinosaki, K. Yamaguchi, N. Shima, H. Yasuda, K. Yano, T. Morinaga, K. Higashio, RANK is the essential signaling receptor for osteoclast differentiation factor in osteoclastogenesis. Biochem. Biophys. Res. Commun. **253**(2), 395–400 (1998)

108. T. Nakashima, M. Hayashi, T. Fukunaga, K. Kurata, M. Oh-hora, J.Q. Feng, L.F. Bonewald, T. Kodama, A. Wutz, E.F. Wagner, J.M. Penninger, H. Takayanagi, Evidence for osteocyte regulation of bone homeostasis through RANKL expression. Nat. Med. **17**(10), 1231–1234 (2011). ISSN 1078-8956

109. A. Nazarian, B.D. Snyder, D. Zurakowski, R. Müller, Quantitative micro-computed tomography: A non-invasive method to assess equivalent bone mineral density. Bone **43**(2), 302–311 (2008). ISSN 87563282

110. R.M. Neer, C.D. Arnaud, J.R. Zanchetta, R. Prince, G.A. Gaich, J.Y. Reginster, A.B. Hodsman, E.F. Eriksen, S. Ish-Shalom, H.K. Genant, O. Wang, B.H. Mitlak, Effect of parathyroid hormone (1–34) on fractures and bone mineral density in postmenopausal women with osteoporosis. N. Engl. J. Med. **344**(19), 1434–1441 (2001). ISSN 0028-4793

111. M. Nilsson, C. Ohlsson, A. Odn, D. Mellström, M. Lorentzon, Increased physical activity is associated with enhanced development of peak bone mass in men: a five-year longitudinal study. J. Bone Mineral Res. **27**(5), 1206–1214 (2012). ISSN 1523-4681

112. S. Nuzzo, M.H. Lafage-Proust, R. Martin-Badosa, G. Boivin, T. Thomas, C. Alexandre, F. Peyrin, Synchrotron radiation microtomography allows the analysis of three-dimensional microarchitecture and degree of mineralization of human iliac crest biopsy specimens: effects of etidronate treatment. J. Bone Mineral Res. **17**(8), 1372–1382 (2002)

113. J.S. Nyman, A. Roy, X. Shen, R.L. Acuna, J.H. Tyler, X. Wang, The influence of water removal on the strength and toughness of cortical bone. J. Biomech. **39**(5), 931–938 (2006). ISSN 0021-9290

114. E. Ozcivici, Y.K. Luu, B. Adler, Y.-X. Qin, J. Rubin, S. Judex, C.T. Rubin, Mechanical signals as anabolic agents in bone. Nat. Rev. Rheumatol. **6**(1), 50–59 (2010). ISSN 1759-4790

115. D. Padhi, M. Allison, A.J. Kivitz, M.J. Gutierrez, B. Stouch, C. Wang, G. Jang, Multiple doses of sclerostin antibody romosozumab in healthy men and postmenopausal women with low bone mass: a randomized, double-blind, placebo-controlled study. J. Clin. Pharmacol. **54**(2), 168–178 (2014). ISSN 1552-4604

116. A.M. Parfitt, The physiological and clinical significance of bone histomorphometric data, *Bone Histomorphometry: Techniques and Interpretation* (CRC Press, Boca Raton, 1983)

117. A.M. Parfitt, *Calcium Homeostasis*, vol. 107 (Springer, Heidelberg, 1993), pp. 1–65

118. A.M. Parfitt, Osteonal and hemi-osteonal remodeling: the spatial and temporal framework for signal traffic in adult human bone. J. Cell. Biochem. **55**(3), 273–86 (1994). ISSN 0730-2312

119. M.C. Peterson, M.M. Riggs, A physiologically based mathematical model of integrated calcium homeostasis and bone remodeling. Bone **46**(1), 49–63 (2010). ISSN 1873-2763

120. P. Pivonka, S.V. Komarova, Mathematical modeling in bone biology: from intracellular signaling to tissue mechanics. Bone **47**(2), 181–189 (2010). ISSN 1873-2763

121. P. Pivonka, J. Zimak, D.W. Smith, B.S. Gardiner, C.R. Dunstan, N.A. Sims, T.J. Martin, G.R. Mundy, Model structure and control of bone remodeling: a theoretical study. Bone **43**(2), 249–263 (2008)

122. P. Pivonka, J. Zimak, D.W. Smith, B.S. Gardiner, C.R. Dunstan, N.A. Sims, T.J. Martin, G.R. Mundy, Theoretical investigation of the role of the RANK-RANKL-OPG system in bone remodeling. J. Theor. Biol. **262**(2), 306–316 (2010)

123. P. Pivonka, P.R. Buenzli, C.R. Dunstan, A systems approach to understanding bone cell interactions in health and disease, in *Cell Interact*, ed. by S. Gowder (chapter 7) (InTech, 2012), pp. 169–204

124. T.M. Post, J.I. Freijer, J. DeJongh, M. Danhof, Disease system analysis: basic disease progression models in degenerative disease. Pharm. Res. **22**(7), 1038–1049 (2005). ISSN 07248741

125. T.M. Post, S.C.L.M. Cremers, T. Kerbusch, M. Danhof, Bone physiology, disease and treatment. Clin. Pharmacokinet. **49**(2), 89–118 (2010). ISSN 0312-5963

126. T.M. Post, S. Schmidt, L.A. Peletier, R. de Greef, T. Kerbusch, M. Danhof, Application of a mechanism-based disease systems model for osteoporosis to clinical data. J. Pharmacokinet. Pharmacodyn. **40**(2), 143–56 (2013). ISSN 1573-8744

127. S. Qiu, D.S. Rao, S. Palnitkar, A.M. Parfitt, Reduced iliac cancellous osteocyte density in patients with osteoporotic vertebral fracture. J. Bone Mineral Res. **18**(9), 1657–1663 (2003)

128. R.R. Recker, J. Lappe, K.M. Davies, R. Heaney, Remodeling increases substantially in the years after menopause and remains increased in older osteoporosis patients. J. Bone Mineral Res. **19**(10), 1628–1633 (2004)

129. J.-Y. Rho, L. Kuhn-Spearing, P. Zioupos, Mechanical properties and the hierarchical structure of bone. Med. Eng. Phys. **20**(2), 92–102 (1998). ISSN 1350-4533

130. B.L. Riggs, Overview of osteoporosis. West. J. Med. **154**(1), 63–77 (1991)

131. B.L. Riggs, A.M. Parfitt, Drugs used to treat osteoporosis: the critical need for a uniform nomenclature based on their action on bone remodeling. J. Bone Mineral Res. **20**(2), 177–184 (2005). ISSN 0884-0431

132. B.L. Riggs, H.W. Wahner, L.J. Melton, L.S. Richelson, H.L. Judd, K.P. Offord, J. Clin. Invest. **77**(5), 1487–1491 (1986). ISSN 00219738

133. B.L. Riggs, S. Khosla, L.J. Melton, A unitary model for involutional osteoporosis: estrogen deficiency causes both type I and type II osteoporosis in postmenopausal women and contributes to bone loss in aging men. J. Bone Mineral Res. **13**(5), 763–773 (1998). ISSN 0884-0431

134. R.O. Ritchie, The conflicts between strength and toughness. Nat. Mater. **10**(11), 817–22 (2011). ISSN 14761122

135. A.G. Robling, S.D. Stout, Morphology of the drifting osteon. Cells Tissues Organs **164**, 192–204 (1998)

136. G. Rodan, T.J. Martin, Role of osteoblasts in hormonal control of bone resorption a hypothesis. Calcif. Tissue Int. **33**(1), 349–351 (1981)

137. P. Roschger, S. Rinnerthaler, J. Yates, G.A. Rodan, P. Fratzl, K. Klaushofer, Alendronate increases degree and uniformity of mineralization in cancellous bone and decreases the porosity in cortical bone of osteoporotic women. Bone **29**(2), 185–191 (2001)

138. P. Roschger, H.S. Gupta, A. Berzlanovich, G. Ittner, D.W. Dempster, P. Fratzl, F. Cosman, M. Parisien, R. Lindsay, J.W. Nieves, K. Klaushofer, Constant mineralization density distribution in cancellous human bone. Bone **32**(3), 316–323 (2003)

139. P. Roschger, E.P. Paschalis, P. Fratzl, K. Klaushofer, Bone mineralization density distribution in health and disease. Bone **42**(3), 456–466 (2008)

140. D. Ruffoni, P. Fratzl, P. Roschger, K. Klaushofer, R. Weinkamer, The bone mineralization density distribution as a fingerprint of the mineralization process. Bone **40**(5), 1308–1319 (2007)

141. D. Ruffoni, P. Fratzl, P. Roschger, R. Phipps, K. Klaushofer, R. Weinkamer, Effect of temporal changes in bone turnover on the bone mineralization density distribution: a computer simulation study. J. Bone Mineral Res. **23**(12), 1905–1914 (2008)

142. M. Sadatsafavi, A. Moayyeri, L. Wang, and W. D. Leslie. Heteroscedastic regression analysis of factors affecting bmd monitoring. *Journal of Bone and Mineral Research*, 23 (11): 1842–1849, 2008. ISSN 1523-4681

143. P. Sambrook, C. Cooper, Osteoporosis. Lancet **367**, 2010–2018 (2006)

144. V. Sansalone, V. Bousson, S. Naili, C. Bergot, F. Peyrin, J.D. Laredo, G. Haiat, Anatomical distribution of the degree of mineralization of bone tissue in human femoral neck: impact on biomechanical properties. Bone **50**(4), 876–884 (2012)

145. S. Scheiner, P. Pivonka, C. Hellmich, Coupling systems biology with multiscale mechanics, for computer simulations of bone remodeling. *Comput. Methods Appl. Mech. Eng.***254**(1), 181–196 (2013). ISSN 00457825

146. S. Scheiner, P. Pivonka, D.W. Smith, C.R. Dunstan, C. Hellmich, Mathematical modeling of postmenopausal osteoporosis and its treatment by the anti-catabolic drug denosumab. Int. J. Numer. Method Biomed. Eng. **30**(1), 1–27 (2014). ISSN 2040-7947

147. S. Schmidt, T.M. Post, L.A. Peletier, M.A. Boroujerdi, M. Danhof, Coping with time scales in disease systems analysis: application to bone remodeling. J. Pharmacokinet. Pharmacodyn. **38**(6), 873–900 (2011). ISSN 1567567X

148. A.V. Schwartz, D.C. Bauer, S.R. Cummings, J.A. Cauley, K.E. Ensrud, L. Palermo, R.B. Wallace, M.C. Hochberg, A.C. Feldstein, A. Lombardi, D.M. Black, Efficacy of continued alendronate for fractures in women with and without prevalent vertebral fracture: the FLEX trial. J. Bone Mineral Res. **25**(5), 976–982 (2010). ISSN 08840431

149. E. Seeman, Is a change in bone mineral density a sensitive and specific surrogate of anti-fracture efficacy? Bone **41**(3), 308–317 (2007). ISSN 8756-3282

150. E. Seeman, P.D. Delmas, Bone quality − the material and structural basis of bone strength and fragility. N. Engl. J. Med. **354**(21), 2250–2261 (2006). ISSN 1533-4406

151. M.J. Seibel, Biochemical markers of bone turnover − Part I: biochemistry and variability. Clin. Biochem. Rev. **26**(4), 97–122 (2005). ISSN 0159-8090

152. M.J. Seibel, Biochemical markers of bone turnover Part II: clinical applications in the management of osteoporosis. Clin. Biochem. Rev. **27**(3), 123–138 (2006). ISSN 0159-8090

153. E. Shane, D. Burr, P.R. Ebeling, B. Abrahamsen, R.A. Adler, T.D. Brown, A.M. Cheung, F. Cosman, J.R. Curtis, R. Dell, D. Dempster, T.A. Einhorn, H.K. Genant, P. Geusens, K. Klaushofer, K. Koval, J.M. Lane, F. McKiernan, R. McKinney, A. Ng, J. Nieves, R. O'Keefe, S. Papapoulos, H.T. Sen, M.C.H. van der Meulen, R.S. Weinstein, M. Whyte. Atypical subtrochanteric and diaphyseal femoral fractures: Report of a task force of the american society for bone and mineral research. J. Bone Mineral Res. **25**(11), 2267–2294 (2010). ISSN 1523-4681

154. L. Shargel, S. Wu-Pong, A.B.C. Yu, *Applied Biopharmaceutics & Pharmacokinetics*, 5th edn. (McGraw-Hill, New York, 2004) (Medical)
155. J.A. Shepherd, Y. Lu, K. Wilson, T. Fuerst, H. Genant, T.N. Hangartner, C. Wilson, D. Hans, E.S. Leib. Cross-calibration and minimum precision standards for Dual-Energy X-ray absorptiometry: the 2005 ISCD official positions. J. Clin. Densitom. **9**(1), 31–36 (2006). ISSN 1094-6950
156. H. Sievänen, P. Kannus, T.L.N. Järvinen, Bone quality: an empty term. PLoS Med. **4**(3), e27 (2007)
157. W.S. Simonet, D.L. Lacey, C.R. Dunstan, M. Kelley, M.S. Chang, R. Lüthy, H.Q. Nguyen, S. Wooden, L. Bennett, T. Boone, G. Shimamoto, M. DeRose, R. Elliott, A. Colombero, H.L. Tan, G. Trail, J. Sullivan, E. Davy, N. Bucay, L. Renshaw-Gegg, T.M. Hughes, D. Hill, W. Pattison, P. Campbell, S. Sander, G. Van, J. Tarpley, P. Derby, R. Lee, W.J. Boyle, Osteoprotegerin: a novel secreted protein involved in the regulation of bone density. Cell **89**(2), 309–319 (1997)
158. R.E. Small, Uses and limitations of bone mineral density measurements in the management of osteoporosis. Medscape General Med. **7**(2), 3–29 (2005). ISSN 1531-0132
159. T.H. Smit, E.H. Burger, Is BMU-coupling a strain-regulated phenomenon? A finite element analysis. J. Bone Mineral Res. **15**(2), 301–307 (2000)
160. T.H. Smit, E.H. Burger, J.M. Huyghe, A case for strain-induced fluid flow as a regulator of bmu-coupling and osteonal alignment. J. Bone Mineral Res. **17**(11), 2021–2029 (2002)
161. L.J. Smith, J.P. Schirer, N.L. Fazzalari, Bone mineralization density distribution in health and disease. J. Biomech. **43**(16), 3144–3149 (2010)
162. K.L. Stone, D.G. Seeley, L.-Y. Lui, J.A. Cauley, K. Ensrud, W.S. Browner, M.C. Nevitt, S.R. Cummings, BMD at multiple sites and risk of fracture of multiple types: long-term results from the study of osteoporotic fractures. J. Bone Mineral Res. **18**(11), 1947–1954 (2003). ISSN 1523-4681
163. P. Sutton-Smith, H. Beard, N. Fazzalari, Quantitative backscattered electron imaging of bone in proximal femur fragility fracture and medical illness. J. Microsc. **229**(Pt 1), 60–66 (2007)
164. P. Szulc, E. Seeman, Thinking inside and outside the envelopes of bone. Osteoporos. Int. **20**(8), 1281–1288 (2009). ISSN 1433-2965
165. S.L. Teitelbaum, F.P. Ross, Genetic regulation of osteoclast development and function. Nat. Rev. Genet. **4**(8), 638–649 (2003). ISSN 1471-0056
166. A.Y.-T. Teng, H. Nguyen, X. Gao, Y.-Y. Kong, R.M. Gorczynski, B. Singh, R.P. Ellen, J.M. Penninger, Functional human T-cell immunity and osteoprotegerin ligand control alveolar bone destruction in periodontal infection. J. Clin. Invest. **106**(6), R59–R67 (2000)
167. C.D.L. Thomas, S.A. Feik, J.G. Clement, Increase in pore area, and not pore density, is the main determinant in the development of porosity in human cortical bone. J. Anat. **209**, 219–230 (2006)
168. E. Tsuda, M. Goto, S. Mochizuki, K. Yano, F. Kobayashi, T. Morinaga, K. Higashio, Isolation of a novel cytokine from human fibroblasts that specifically inhibits osteoclastogenesis. Biochem. Biophys. Res. Commun. **234**(1), 137–142 (1997)
169. S.S.J. Webster, Integrated bone tissue physiology: anatomy and physiology, *Bone Mechanics Handbook*, 2nd edn. (CRC Press, Boca Raton, 2001)
170. S. Weiner, H.D. Wagner, The material bone: structure-mechanical function relations. Annu. Rev. Mater. Sci. **28**(8), 271–298 (1998)
171. R.S. Weinstein, True strength. J. Bone Mineral Res. **15**(4), 621–625 (2000). ISSN 1523-4681
172. M.N. Weitzmann, R. Pacifici, Estrogen deficiency and bone loss: an inflammatory tale. J. Clin. Investig. **116**(5), 1186–1194 (2006)
173. WHO: Assessment of fracture risk and its application to screening for postmenopausal osteoporosis. World Health Organ. Techn. Rep. Ser. **843** (1994)
174. WHO: Prevention and management of osteoporosis. World Health Organ. Techn. Rep. Ser. **921**, 1–164 (2003). ISSN 0512-3054
175. J.C. Wong, M.R. Griffiths, Precision of bone densitometry measurements: when is change true change and does it vary across bone density values? Australas. Radiol. **47**(3), 236–239 (2003)

176. H. Yasuda, N. Shima, N. Nakagawa, K. Yamaguchi, M. Kinosaki, S. Mochizuki, A. Tomoyasu, K. Yano, M. Goto, A. Murakami, E. Tsuda, T. Morinaga, K. Higashio, N. Udagawa, N. Takahashi, T. Suda, Osteoclast differentiation factor is a ligand for osteoprotegerin/osteoclastogenesis-inhibitory factor and is identical to TRANCE/RANKL. Proc. Natl. Acad. Sci. USA **95**(7), 3597–602 (1998). ISSN 0027-8424
177. E.A. Zimmermann, B. Busse, R.O. Ritchie, The fracture mechanics of human bone: influence of disease and treatment. BoneKEy Rep. **4**(September), 743 (2015). ISSN 2047-6396
178. P.K. Zysset, E. Dall'Ara, P. Varga, D.H. Pahr, Finite element analysis for prediction of bone strength. BoneKEy Rep. **2**(386), e1–e9 (2013). ISSN 2047-6396

# Musculoskeletal Modelling and the Physiome Project

**Justin Fernandez, Ju Zhang, Vickie Shim, Jacob T. Munro,
Massimo Sartori, Thor Besier, David G. Lloyd, David P. Nickerson
and Peter Hunter**

**Abstract**  This chapter presents developments as part of the International Union of Physiological Sciences (IUPS) Physiome Project. Models are multiscale, multispatial and multiphysics, hence, suitable numerical tools and platforms have been developed to address these challenges for the musculoskeletal system. Firstly, we present modelling ontologies including several markup languages used to facilitate storage, sharing and exchange of numerical models. Secondly, custom software tools, CMISS and CMGUI, are then presented in the development of anatomically based geometrical models. Customisation methods are also presented to morph generic models into subject-specific representations. Thirdly, population based modelling and statistical shape analysis methods are presented as efficient techniques that harness the power of big data and imaging databases. These allow prediction of human anatomy from minimal geometric information. Fourthly, a specific example of our framework is presented in the context of a validated orthopaedic clinical tool used for assessing osteolytic defects around implants. Finally, EMG-informed muscle modelling is presented combined with medical imaging to better understand musculoskeletal injury. The problem of NaF PET CT is used to highlight the problem of patellofemoral pain.

J. Fernandez (✉) · J. Zhang · V. Shim · T. Besier · D.P. Nickerson · P. Hunter
Auckland Bioengineering Institute, University of Auckland, Auckland, New Zealand
e-mail: j.fernandez@auckland.ac.nz

J. Fernandez · T. Besier
Department of Engineering Science, University of Auckland, Auckland, New Zealand

J.T. Munro
School of Medicine, University of Auckland, Auckland, New Zealand

J.T. Munro
Auckland City Hospital, University of Auckland, Auckland, New Zealand

M. Sartori
Department of Neurorehabilitation Engineering, Göttingen University, Gottingen, Germany

D.G. Lloyd
Menzies Health Institute Queensland, Griffith University, Gold Coast, QLD, Australia

# 1 The Physiome Project

Models of physiological processes across multiple spatial and temporal scales are used to interpret diagnostic measurements, or to guide clinical intervention or device design, or just to improve our quantitative understanding of the relative influence of genetics and environmental factors on a particular disease. Whatever the reason, the complexity of these processes can be daunting and often calls for modular approaches based on model encoding standards. Developing such standards, with standards-based and freely-accessible databases for data and models, and open source software for authoring, curating, annotating, visualising and running these models, is the goal of the Physiome Project. Here we briefly review the history, current state and future ambitions of the international Physiome Project.

## 1.1 Introduction

The overarching goal of the Physiome Project is to establish a framework for computational modelling of the anatomy and physiology of humans and other species in order to explain function (phenotype) at the tissue, organ and whole organism level in terms of the biophysical processes that operate at all spatial and temporal scales. This requires dealing with multiple interacting physical processes based on principles of continuum mechanics at the tissue/organ level as well as with their underpinning molecular processes. It requires a modular approach based on experimentally validated and reproducible models encoded in community-accepted modelling standards and annotated with community-accepted ontological terms. Much of the initial effort in establishing the Physiome Project was directed towards (i) the development of modelling standards CellML and FieldML and to some extent data standards (BioSignalML), (ii) to developing the Physiome Model Repository (PMR) database for models (with accompanying data) that are encoded with these standards, and (iii) to developing software (OpenCOR and OpenCMISS) for simulating physiological processes described by combinations of CellML and FieldML models. Other important complementary parallel efforts by the systems biology community have been the development of minimum information standards, a standard for models of biochemical reactions (SBML) and, together with the bioengineering physiome community, a standard for describing the simulation itself (SED-ML). All of these developments are described further below but first we give some historical background to the Physiome Project.

## 1.2 History of the Physiome Project

The Physiome Project was initiated by the International Union of Physiological Sciences (IUPS) to meet the challenge of understanding physiological processes that span spatial scales from molecular interactions to the interaction of a whole organism

with its environment. The IUPS Physiome committee (co-chaired by the last author) was established at the 33rd international IUPS congress in St Petersburg in 1997 to lead the project [1]. Significant more recent events have been the recognition by NIH of the importance of developing a computational modeling infrastructure for human biology NIH (and the funding under the Framework 7 ICT call by the European Commission (VPH) for a Network of Excellence to co-ordinate the EuroPhysiome contribution to a Virtual Physiological Human (http://www.vph-institute.org/).

## 1.3 Objectives of the Physiome Project

Interpreting the wealth of quantitative data now available on cellular and subcellular processes requires a new level of international collaboration between biological, physical (including engineering), mathematical, computer and computational scientists. Biological processes operate primarily at the molecular scale (ligand/ protein/DNA/RNA interactions) but are influenced by, or in turn create an in-fluence on, the physiological systems of cells, tissues, organs and whole body organ systems. This influence therefore encompasses a 109 range of spatial scales (nm to m) and a 1015 range of temporal scales (from s for molecular interactions to the 109 s of a human life span). Our ability to investigate human disease with the tools of genetics and proteomics as well as physiological tests and diagnostic imaging on an individual patient (MRI, CT, etc.) is a tribute to astonishing developments in instrumentation at the two ends of this spectrum of spatial scales. But our current ability to link our knowledge of structure and function across these spatial and temporal scales is, with few exceptions, dismal. Mathematics is the language of quantitative science and the only way to address this challenge is through mathematical modeling. In particular, multiscale modeling based on bio-physical principles (mechanistic modeling) is needed, along with numerical techniques that can adequately represent the highly complex three dimensional structures of biological systems from proteins to organs.

Building mathematical models of biological systems plays an important role in understanding those systems. Early work on building models for computational simulation conflated the model with the techniques to simulate it, and used procedural programming languages. The mathematical equations in the model were published, rather than the computational code, and so reproducing the simulation results involved a significant amount of work.

More recently, declarative formats for marking up mathematical models have been developed. CellML [26] and SBML [63], for example, both use an XML based format to represent models. The focus of CellML is on representing mathematical models, while SBML contains constructs specific to modelling biochemical reaction networks, but allows certain additional forms of algebraic and rate equations. The benefit of these declarative representations is that the numerical algorithm to be used is completely separated from the mathematical specification of the model. This means that the same model description can be used to solve the model with many different tools and numerical algorithms. It also means that all or parts of the model can be more easily taken and put into a different model.

The benefit of having models in a few widely used standard formats is that the tools needed to run simulations are gradually becoming ubiquitous within the bio-logical systems modelling community, or at least readily available. There are well-developed APIs to simplify the development of tools for working with CellML [82] and SBML [7] models. In addition, model users can choose from a wide range of programs for running analyses on CellML [40] and SBML [4, 57, 106] models. Thus, modellers can share their models with members of the community, who can not only easily reproduce the results described in a paper, but also build on the work of other modellers.

This benefit becomes even more significant when common parts of models can be shared between multiple models. CellML 1.1 provides for model composition by allowing hierarchies of components to be imported from one model into another, where they can be connected to other components. For example, CellML model composition has been used to build a library of models for standard synthetic biology parts [22]. In order for model sharing to occur, it is important that members of the community can easily obtain models. A number of repositories have been developed for sharing models, including the PMR2 software [145] (which is used to run the CellML Model Repository [75]) and the BioModels Database [92]. No repository described in the literature had until then the ability to store detailed information on the revision history of the representation of the model.

Under a DVCS based repository, such as PMR, curators and model authors can directly push and pull changes to and from each other. They can also share a model which is not yet ready for publication through a workspace in the repository, and create an exposure for the model when they are ready. Alternatively, they can share a model by pushing to or pulling from their respective local repositories directory, and all revisions made will be added to the repository when the changes are pushed to the repository. In many existing repositories, access to create revisions of a model is restricted to authorised curators. This is done so that curators can ensure that models that are to be made public meet the standards of the repository. However, this also has the side effect that model authors cannot create revisions except by submitting their changes to the curators, and usually means that a record of the revision is only created when a model is accepted by the curator (which may require a number of changes). DVCSs work by recording changes locally, and only later pushing them to another repository. This means that model authors can make revisions and store them on their own computer without the need to be granted access by the repository curators. It is the act of pushing these changes into the central repository that requires access to be granted. In PMR2, model authors are given access to their own workspace, and it is only the final step of creating a public exposure of a particular revision on the repository web-site which is restricted to authorised curators. This approach allows the quality of exposed models to be maintained, while not preventing model authors from creating as many revisions as required to accurately describe the revision history of their model.

## 1.4 Recent Developments and Future Directions for the Physiome Project

CellML, SBML and similar standards have successfully begun to address the problem of sharing and reusing mathematical models. To address the issues of dissemination and reproducibility of computational simulations, two main community-based efforts have emerged involving not just the Physiome community but also the computational systems biology and computational biology communities. The first was the establishment of the minimal information guidelines Minimum Information About a Simulation Experiment (MIASE) [136]. These guidelines define the minimal set of information that must be provided in order to make the description of a simulation experiment available to others, and thus enable dissemination and replication by the community at large. As an implementation of the MIASE guidelines, the second effort was the creation of the Simulation Experiment Description Markup Language (SED-ML) [136].

SED-ML enables users to unambiguously describe the computational simulations they perform in order to produce a given output. This includes the models used, any pre-processing of the models, the numerical algorithms to apply and the parameterization of those algorithms, any post-processing to perform on the data which results from performing the actual simulation, and the data to extract from the resultant data. The first version of SED-ML focused on the most commonly used simulation task, the uniform time course. The second version of SED-ML introduced the ability to describe complicated simulation tasks through the combination of an ordered set of sub-tasks. Some features being considered for future versions of SED-ML are the inclusion of data (e.g., for parameterization or optimization), more comprehensive description of the extraction of data for simulation outputs, and greater flexibility in the addressing of model entities within the simulation description to enable, for example, generic experiment descriptions to be applied to many different mathematical models.

In concert with the development of SED-ML, the Kinetic Simulation Algorithm Ontology (KiSAO) [25] is being developed to describe simulation algorithms and their inter-relationships through their characteristics and parameters. SED-ML makes use of KiSAO to identify simulation algorithms and their parameters. This allows software tools to make use of similar algorithms if the specific algorithm used in the SED-ML is not to that tool. Thus enabling SED-ML documents to describe the use of proprietary algorithms or implementations to be exchanged and potentially executed by open-source tools.

FieldML [20] is a model representation format being developed as part of the Physiome Project to encode the spatially distributed aspects of physiological models. Adopting the fundamental design philosophy from CellML of a modular and reusable model-encoding format, FieldML is attempting to become a standard for the archiving, dissemination, and interchange of spatially distributed multi-scale computational field models. Given the often large size of the computational models and high performance nature of the computational tools which use them, for example,

in visualisation or numerical simulation tasks, FieldML is addressing a much more complex set of requirements than those of CellML. The scope of FieldML efforts have recently focused on the representation of the finite element models routinely used in Physiome-style models e.g. [89, 121].

While FieldML will be able to represent both temporally and spatially varying computational fields, it is often useful to consider the time variation of a quantity of interest at a single point in space. Such physiological signals can arise from computational simulations and analyses or direct measurement. BioSignalML [10, 11] is an abstract model for such physiological time-series data and arose from a need to standardise the description and interpretation of such data stored in a variety of formats, from hardware vendor specific to various standard formats originating in different geographical regions. The provision of a standard description of such data and the development of software tools for extracting such information from the commonly used formats facilitates the integration of biosignal data into physiological modelling applications.

In addition to standardisation efforts and the development of controlled vocabularies, it is essential to develop Minimum Information Standards to ensure that sufficient information is being provided for the data to be understandable in a certain context. The broad computational modelling in biology community has seen the development of several such standards regarding experimental [102], modelling [91], and simulation [136] data. Recent initiatives in this area are in the parameter identifiability (tentatively called the Minimal Information for Model Inference and Parametrisation MIMIP) and mathematical classification (the Mathematical Modelling Ontology MAMO).

The modelling and simulation goals of the Physiome Project often require the development of high performance software to provide the capabilities needed to create, edit, manage, simulate, visualise, disseminate, and interact with the computational models and work-flows. In addition to ensuring such software development is freely available as open-source projects, appropriate use of the standardisation efforts directly under the Physiome Project as well as related efforts is always encouraged. Furthermore, the adoption of similar practices in the software tools as the standards (i.e., modularity and reuse) ensures that reusable software modules are created which can be assembled to meet the specific needs of given application. The established standards provide the obvious method for data interchange between such modules and the ontologies and minimal information guidelines can be utilised to automate a large portion of common tasks, e.g., model composition [87], interaction and visualisation of simulation results [90], ranked retrieval from repositories [50]. The MAP Client (http://map-client.readthedocs.org/) and OpenCOR (http://opencor.ws) are examples of frameworks enabling the flexible assembly of such modules. A recent example [47] describes the application of Physiome software and standards to modelling the chemo-electromechanical behaviour of skeletal muscle.

## 2   Geometrical Musculoskeletal Modelling

The International Union of Physiological Sciences (IUPS) Physiome Project was established as a framework for creation, sharing and dissemination of multiscale mathematical models of human physiology. One key aspect of this work was the development of anatomically-based geometries of the Virtual Human to serve as a common source for computational investigation and sharing in the scientific community. In this section we present the techniques used to develop subject-specific musculoskeletal models that were developed for the Physiome repository and are available for sharing. This process starts with using high-order cubic Hermite elements suitable for describing the topology of complex musculoskeletal structures accurately and with minimal element numbers. These geometries are able to be customised using free-form deformation (FFD) techniques with data from Computed Tomography (CT), Magnetic Resonance Imaging (MRI) or anthropometric information derived from motion capture. Building upon these same anatomical geometries we describe complex fibre orientations throughout the soft tissue structures. These are used later in understanding the deformations of soft tissues, which are referred to a microstructural curvilinear coordinate system based on these fibre orientations. The constitutive laws that describe the stress-strain behaviour of soft tissue are also referred to this anatomically based material coordinate system and the muscle contractions are also based on these fibre pennation angles. The FFD method is then further extended to a hybrid technique coupling mechanics for added constraints and anatomical realism during motion. This coupled mechanics-FFD approach is used to measure musculotendon lengths and inform moment arms for rigid body mechanics.

### 2.1   Challenges in Subject-Specific Modelling

The challenges faced in subject-specific modelling are similar in all organ systems. In this chapter we focus on musculoskeletal modelling, which has strong links with orthopaedics and physiotherapy where patient-based treatment is increasingly being sought in clinical practice. Some of these modelling challenges include: (i) how to model the anatomy and tissue structure in a parametrically efficient way; (ii) how to morph generic templates efficiently to patient data using known geometrical landmarks and features of underlying mechanics; and (iii) how to make efficient use of population data to construct patient-specific models. Objectives i and ii are developed in this chapter and the use of population data (objective iii) via principal component analysis methods is presented in Sect. 3.

## *2.2  Geometry Development*

One goal of the IUPS Physiome project [67] was to develop a database of anatomically-based geometries as the first step in computational mechanics. Figure 1 shows how this database was developed from a number of sources including an anatomical skeleton model (SOMSO, www.somso.de), scanned using a Polhemus laser scanner and the soft tissues digitised from the Visible Man (VM) [1]. The Somso skeleton allowed for accurate depiction of the complex joint articular surfaces at the end of the bones and attachment points, while the VM high resolution images provided information about the detailed three-dimensional relationships between muscles, tendons, ligaments and other organs. These were collected in a supine reference pose as this was the position the data were imaged. Over the last 10 years additional images have been collected from the Visible Female [122] which is sliced at every 0.33 mm (as opposed to 1 mm for the VM) providing greater detail around the knee joint region where structures like the menisci and cartilage are typically a few millimetres thick. Additional imaging modalities have also been used including Magnetic Resonance Imaging (MRI) and Computed Tomography (CT) to add to the growing collection of data. The additional modalities offer further benefits by allowing customisation of generic models and validation of model mechanics by comparison with Tagged MRI, dynamic X-ray (fluoroscopy) and dynamic ultrasound. The geometries are being collected into hierarchical modelling ontologies (Hunter and Borg 2003) to facilitate data exchange among scientists contributing to the Physiome Project. The collected datasets utilise AnatML (www.physiome.org. nz/anatml_viewer), a markup language describing the linkages between the different structures using definitions from Greys anatomy [42] and Anatomica [31].

Once the raw segmented data is acquired, a set of 3D parameterised FE meshes suitable for mechanics are developed. The three-dimensional FE meshes have basis (or shape) functions determined from the tensor product of 1D interpolation functions. These four 1D cubic Hermite basis functions are given by

$$\psi_1^0(\xi) = 1 - 3\xi^2 + 2\xi^3 \tag{1}$$
$$\psi_2^0(\xi) = \xi^2(3 - 2\xi)$$
$$\psi_1^1(\xi) = \xi(\xi - 1)^2$$
$$\psi_2^1(\xi) = \xi^2(\xi - 1),$$

where $\xi$ is the normalised local or element coordinate which is defined from 0 to 1. These cubic Hermite elements differ from the usual Lagrange family finite elements in that they preserve both the continuity of the nodal values (C0 continuity), and their first derivatives (C1 continuity). This provides many advantages in constructing a finite element geometry, particularly of biological structures such as muscles and other organs that typically have smooth surfaces [144]. Moreover, the realistic geometries are useful in such applications as virtual surgery and medical education. Another attractive feature of cubic Hermite elements is that fewer numbers

of elements are required for complex geometries. C1-continuos interpolation also provides a smooth change in the surface normal across element boundaries and this provides numerical benefits when solving contact mechanics problem. Interpolation of the spatial coordinates of line elements in space with cubic Hermite basis functions is given by

$$\mathbf{u}(\xi) = \psi_1^0(\xi)\mathbf{u}_1 + \psi_2^0(\xi)\mathbf{u}_2 + \psi_1^1(\xi)\frac{d\mathbf{u}}{ds}\bigg|_1 L + \psi_2^1(\xi)\frac{d\mathbf{u}}{ds}\bigg|_2 L. \tag{2}$$

where u is x, y or z if the field is geometry and du/ds is the derivative of the spatial coordinate with respect to a measure of distance, chosen to be arc-length here. Subscripts 1 and 2 refer to node numbers and superscripts 0 and 1 are the zeroth and first derivatives, respectively. L is the physical arc length along the curve. To ensure we have continuity with respect to arc-length we enforce the condition that the magnitude of du/ds should be 1. The interpolation can be any field in general such as stress, temperature or fibre information and more details can be found in Fernandez et al. [35]. Now that we have established the element primitive we fit the elements to segmented data using a least-squares fitting procedure. We employ a face fitting routine for surfaces of the volume mesh and define a face objective function, F(un), consisting of two components, namely the data error and a smoothing constraint given by

$$F(\mathbf{u}_n) = \sum_{d=1}^{N} w_d \| \mathbf{u}(\xi_{1d}, \xi_{2d}) - \mathbf{z}_d \|^2 + F_s(\mathbf{u}_n), \tag{3}$$

where the data error is the summation of the square of the distances between each data point, zd, and its orthogonal projection u($\xi_{1d}$ and $\xi_{2d}$) on the relevant face. Each point can be weighted based on importance using wd. The smoothing constraint, Fs($ui_n$), is appended to the objective function as a penalty function defined by

$$F_s(\mathbf{u}_n) = \int_0^1\!\!\int_0^1 \left\{ \alpha_1 \left\| \frac{\partial \mathbf{u}}{\partial \xi_1} \right\|^2 + \alpha_2 \left\| \frac{\partial \mathbf{u}}{\partial \xi_2} \right\|^2 + \alpha_3 \left\| \frac{\partial^2 \mathbf{u}}{\partial \xi_1^2} \right\|^2 \right. \tag{4}$$
$$\left. + \alpha_4 \left\| \frac{\partial^2 \mathbf{u}}{\partial \xi_2^2} \right\|^2 + \alpha_5 \left\| \frac{\partial^2 \mathbf{u}}{\partial \xi_1 \partial \xi_2} \right\|^2 \right\} d\xi_1 d\xi_2,$$

which is the second order Sobolev norm [8] used as the smoothing constraint to account for sparse and scattered data. Constants $a_i(i = 1 \ldots 5)$ are the Sobolev weights (penalty parameters) and each term has a distinct effect on the final shape of the fitted object. The first two terms ($a_1$, $a_2$) control the arc-length, while the third and fourth terms ($a_3$, $a_4$) control the arc-curvature in the $\xi_1$ and $\xi_2$ directions, respectively. The last term ($a_5$) represents the face area. For instance, if the weight associated with the cross-derivative term is set to a relatively higher value, one might end up with a smaller face area. All Sobolev weights must be at least an order lower

than the weight associated with the data error component, $w_d$, which is usually taken as 1.0.

We highlight two examples of model fitting depicted in Fig. 2. If the data set is sparse, such as shown with the rectus femoris muscle (one of the quadriceps) and if the Sobolev weights are all set to have minimal effect then the fitting will produce an oscillatory shape in the muscle. This is an artefact arising from the data being dense in the radial direction but sparse in the longitudinal direction. If, however, we place more weight on the curvature in the longitudinal direction and increase smoothing on the face area we arrive at a more anatomically correct shape. This shows that the Sobolev weights can account for incomplete or non-uniform data sets. In the second example we have a bone to fit (the femur) with a uniform and dense cloud of data from a scanned source. There is usually less need to increase Sobolev smoothing parameters in such a case as the data is sufficient and homogenously distributed for an accurate fit. However, if we want to place more emphasis on a particular region such as the greater and lesser trochanters then we can increase the data point weights for those features. The fitting algorithm will then ensure a better fit in those regions.

## 2.3 Subject-Specific Customisation

A database of geometries is extremely useful for sharing and disseminating models amongst the scientific community, especially using the popular Visible Human dataset. They can be used to study population-based mechanics primarily in healthy individuals. However, when studying diseased joints, pathology leading to deformed geometry (such as cerebral palsy) or for focussed studies aimed at predicting the outcomes of intervention a subject-specific geometry is required. The original database of geometries serves as a good basis to morph and fit to patient data obtained from MRI, CT or motion capture. We utilise a technique, based on free-form, to rapidly morph complex geometries using only a few control points [36].

Free form deformation (FFD) is a computer graphics technique used to efficiently morph an underlying geometry with many degrees of freedom using a coarse mesh with only a few degrees of freedom. The coarse mesh is morphed so as to minimise the distance between strategically chosen control points and this deformation is passed to the embedded geometry within. This idea was extended to musculoskeletal structures and biomechanics by Fernandez et al. [36] using generic template muscle meshes developed from the popular Visible Human data set [22]. Figure 2 shows a subset of these geometries from the lower limb with one representative muscle, the rectus femoris, customised to subject-specific data using MR identified control points. The FFD method provides shape control over muscle curvature and length by using shape-based constraints called Sobolev smoothing [144]. To evaluate the FFD method the actual target rectus femoris muscle was manually segmented and shown to match the host-meshed muscle with an error of less than 2 mm RMS. This technique was further evaluated for the complete lower limb by Oberhofer et al. [93] by matching MR segmented geometries at 15° and 45° flexion with host-mesh predicted muscle

shapes producing errors less than 3.7 mm RMS. The FFD morphing method provides complex muscle scaling to patient data beyond the simple scaling currently offered in OpenSIM.

The host-mesh fitting method described below is a free-form deformation technique used to perform geometric transformations consisting of both Euclidean (translation and rotation) and Affine (Euclidean plus scaling and shearing) operations on arbitrary parameterised meshes. The structure of the host mesh is a parallelepiped in these examples, but can in general be any shape. The size of the host mesh is determined from experience, however, as a general rule it should be close to the size of the object being deformed and the number of degrees freedom of the host mesh depends on the control the user wishes to have over the deformation and object anatomy. The object being morphed is embedded within the host and when the host is morphed the object within it also undergoes the same transformation. For most cases one to three-element host meshes will suffice to provide enough degrees of freedom to control its deformation. We demonstrate this method in a couple of scenarios shown in Fig. 2 including changing the articular features of femoral bone, changing the attachments of ligaments and morphing the rectus femoris muscle.

The host-mesh technique permits morphing of anatomical geometries given a limited number of data points. This is most useful where only a limited data set is available, such as a partial MRI or CT, or only discrete measures can be obtained (such as motion capture). The quality of fit can be controlled through weighting the data points (placing more weight on important regions) or through constraining the host that the body lies within. A useful illustration is the femur, which is known to vary between patients and is influenced by gender (with females having a wider quadriceps angle) and pathology (such as children with cerebral palsy with highly curved femurs). When performing finite element analyses the resulting stress distribution is influenced by the geometric profile and so obtaining a quick fit is desirable when performing large population studies. In this case 24 landmark points were identified from a CT-scanned femur but could also be obtained from other modalities. Each data point represents a distinct extremity such as a peak or groove in the bone. The host was divided into 3 segments (elements) for separate control of the shaft, proximal and distal ends. Greater freedom was allowed for the femur ends while the shaft, which had limited data available, was allowed only to radially expand, twist and lengthen. The blue markers indicate the landmark points and the red markers show their desired final positions. The undeformed host (blue) was distorted to the red host in order to minimise the distance between the blue and red markers in a weighted least squares sense. The fitting procedure used to distort the mesh in order to minimise the data error is identical to that described in Eqs. 3 and 4 for fitting.

The host mesh can also be used to adjust small features while maintaining the remaining geometric shape. Ligament attachments vary between patients, as observed in MRI, and can be modified due to surgery to correct pathology. Illustrated in Fig. 2 is a new ligament attachment specified by green markers on the femur. The medial collateral ligament was morphed so as to match the insertion into the femur while maintaining the original ligament origin at the tibia. In this example only a sparse set of data existed (the insertion points), so we increased the Sobolev smooth-

ing to assist the fit by placing weights on the host-mesh curvature. This ensured that the new ligament was not distorted.

Soft tissues can come in a variety of deformed poses and shape depending on the orientation the subject is imaged. While muscles typically have textbook profiles defined based on cadaveric studies it may be useful to rapidly customise a generic muscle to another subject. Here we have chosen an extreme example whereby the generic rectus femoris muscle (one of the quadriceps) derived from the Visible Male is customised to a subset of points taken from the Visible Female dataset. Muscle size is useful because it affects the force generation capacity in computation. We identified a set of landmarks at the ends of the muscle and radially along the length of the axis (a total of 20 points). The same sites were located on the female muscle set using Visible Female images and we performed the fit to minimise the distance between the marker sets. The resulting mesh closely resembled the female muscle and to check we performed a least squares fit against the fully segmented female muscle giving an RMS of less than 3 mm.

FFD can be performed at the individual muscle and bone level or be applied to the outer skin and whole muscle groups. Figure 3 shows FFD being used where the host is now the skin (rather than the originally proposed box mesh) with embedded muscles being deformed based on skin motion. Control points can be located on the skin surface or within the limb and be used to control internal muscle deformation. For example, CT images only identify muscle groups as grey thresholds with no individual muscle boundaries, which can be used to inform the shape of the collective quadriceps or hamstring muscle groups.

In gait analysis, continuum muscles are often used to inform rigid body mechanics simulations with anatomically correct musculotendon arc-length paths and muscle moment arms. FFD requires high numbers of control markers, which is difficult to achieve in practice. This limitation has been partially addressed by introducing additional non-kinematic information including material behaviour (constitutive laws), tissue interaction (contact mechanics) and volume conservation constraints [5]. Muscle arc-length centroids can be used to perform a virtual tendon excursion and evaluate moment arms. Figure 4 shows a hybrid finite element-FFD approach with wrapping surfaces, muscle sliding and bone interactions for the semimembranosus and semitendinosus muscles through 45° hip flexion. This extension to traditional FFD couples FE analysis allowing different material laws to be included accounting for stiffer tendon, spatially varying fibre fields, soft tissue sliding and volume conservation of muscle generating a more anatomically realistic shape with only a few control points needed.

Muscle fibre information is a key component of muscle function, as it controls the direction of muscle contractile behaviour and shape in 3D, and the pennation components of force in 1D Hill-type models. In 3D finite element muscle models, extracted fibre information from both cadaver dissections and Magnetic Resonance Imaging has been used to inform spatially varying fibre architecture [6–9]. Figure 5 shows a representative dissected cadaveric human rectus femoris muscle with visible fibre pennation angle. Discrete fibre angle measurements were made at different slices and mapped to a continuum fibre field, which becomes part of the generic

muscle template. One possible solution proposed is to solve the complete muscle contraction problem at the continuum level. Using statistical methods, such as partial least squares regression, muscle shape, stress/strain fields and musculotendon force can be computed directly from muscle tendon length and activation levels. These muscle parameters can be directly linked to skeletal models in OpenSim by applying the muscle forces directly to bones.

## 2.4   Conclusions

The modelling framework presented in this section demonstrates a collection of techniques that can be used to aid patient-specific analysis using computational methods. This chapter primarily demonstrates efforts towards efficient methods of building subject-specific geometries. However, accurate boundary conditions and material properties are necessary before results can be used with confidence. Patient derived geometries are paramount for both bone and soft tissue when informing clinical decisions. Accurate descriptions of bone provide correct anatomical surface topology and articular features. This is especially important for diseased states like cerebral palsy, which differ significantly from the healthy condition, or when informing implant design for patient surgery. Furthermore, predicting joint contact areas requires accurate models of joint articulations. The anatomical axis is also influenced by the curvature of bone shaft, which in turn allows for accurate moment arm predictions and more meaningful muscle force estimates. Improved soft tissue profiles are important for volume prediction of muscle, which is used to estimate cross-sectional area and hence predict the power generation capacity.

## 3   Musculoskeletal Statistical Shape Analysis

Statistical shape modelling has been extensively used to model the 3-D shape variations of many biological structures. Using statistical methods such as principal component analysis to reduce the dimensionality of 3-D data, complex geometric variations can be modelled using a just a few parameters. These models have been used to greatly improve the robustness and efficiency of patient-specific model generation from images and sparse or incomplete data. This section will outline the basic theory of statistical shape modelling, and describe how it has been applied to the human femur as an example of its application.

## 3.1 Introduction

Understanding and making predictions using femur shape has a long history in anthropology, forensics, and clinical medicine. Traditional measurements of lengths, widths and angles have been used to predict fracture risk [86, 95] and estimate anthropometric information [138], amongst other applications. However, traditional measurements are time consuming to perform, and do not capture the full three-dimensional shape of the femur. Shape can be strictly defined as geometric information invariant to translation, rotation and scaling [33]. Statistical shape analysis is the use of statistical methods to model variations in shape. It provides the means to, in three dimensions, quantify shape differences, generate representative shapes, or correlate shape to other measurements.

Statistical shape analysis has been used for three main applications: image segmentation, model generation, and classification and prediction. It has led to more accurate and automated femur modelling for finite-element analysis or computer-guided surgery, and new predictors for fracture and disease risk. A comprehensive review of shape modelling in image segmentation can be found in [48]. With respect to the femur, shape model driven automatic segmentation methods have been applied to the knee [38, 104] and hip [70, 113]. When images do not capture the whole femur or pelvis, for example due to limited field of view, a shape model can approximate the missing portions based on what is present. Often, only sparse geometrical data, e.g. anatomical landmarks, are available. Numerous work have shown that shape models can be used to approximate femur shape from landmarks and partial data [3, 103, 124]. The ability of shape models to generate representative femur models was use by Bryan et al. [12, 13] to study the variations in mechanical response due to variations in shape (and bone density). Finally, shape models allow pathological shape differences to be quantified, for example femurs with high fracture risk [43] and osteoarthritis [135].

The key steps in statistical shape analysis are (i) describing each object in a training set using a shape descriptor; (ii) aligning the descriptions to remove translational, rotational, and size variations; (iii) statistical analysis and modelling of the variations in the aligned shape descriptions.

The shape descriptor is a mathematical way to encode shape information, and is dependent on what aspects of an objects shape are of interest. Shape descriptions range in complexity from simple hand-placed landmark points, to parametric meshes [149], to deformation fields [107]. Whatever the description, the variables of the description must be correspondent between shape instances so that statistics on variables can be computed.

Removal of translational, rotational, and scale variation between objects is required to obtain pure shape information. In some cases, scale variation is preserved to study allometric variations. Given a training set of shapes, the variations above can be removed by aligning the shapes to a common coordinate system. The coordinate system can be anatomical or functional, or general for any shape but dependent on a reference shape in the case of the commonly used General Procrustes Analysis [33].

Statistical analysis commonly involves decomposing variations in shape information into significant modes or components the shape model. The shape model can then be used for shape generation and classification. Principal component analysis (PCA) [69], the most common method for shape analysis [48], decomposes a training set of observations (e.g. shape instances) into a mean, and orthogonal principal components, ranked in descending significance. Assuming linear Gaussian variations, the first few components will capture most of the variation, meaning that shapes can be approximately reconstructed by linear combinations of just the first few components. Other statistical method can also be used, e.g. ICA [126], kernel PCA [27], to model non-linear or non-Gaussian variations.

To demonstrate the power of statistical shape analysis in musculoskeletal modelling, the remainder of this article will summarise a body of work focused on shape modelling of the human femur. In the next section, we present an anatomical region-based shape model of the femur, using piecewise parametric meshes as the shape description. In Sect. 3, this femur shape model is used to drive automatic femur segmentation from X-ray computed tomography (CT) images, and in Sect. 4, it is used to generate femur models from sparse anatomical landmarks from motion capture.

## 3.2 Training the Femur Shape Model

Anatomic features can be better represented in a shape model if the shape description incorporates regions that correspond to the features. Explicitly defined regions constrain the shape description in regions that have are known to be correspondent, thereby improving overall correspondence. In addition, a region-based shape model of the femur allows these regions to be analysed independently, or compared against other regions, which may reveal local shape variations not found in a whole-femur shape model.

Our method for training an anatomical region-based femur shape model is detailed in [149]. Briefly, the method is composed of a region partitioning clustering stage and a shape model training stage. To identify the best conserved anatomical regions on the femur, 31 femoral surfaces segmented from CT images were partitioned based on local Gaussian curvature. The regions from all 31 femurs were then clustered based on their geometric properties. The most tightly clustered regions were the femoral head, the greater trochanter, the medial condyle, and lateral condyle. Template piecewise parametric meshes were created for each of these four regions, plus two regions for the femoral shaft (Fig. 6).

In the shape model training stage (Fig. 7), for each of the six regions, the template mesh was fitted to the corresponding regions from the 31 femur surfaces. Fitting minimised the sum of squared distances between data points (vertices on the segmented surface) and their orthogonal projections on the mesh:
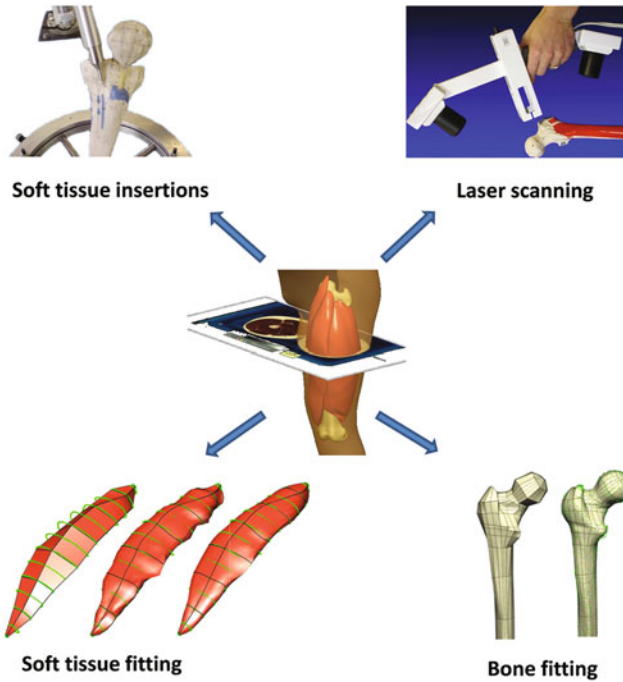
**Fig. 1** A subset of the lower limb model derived from the Visible Man dataset with bone geometry and soft tissue insertions from a physical Somso model. The process of fitting the rectus femoris (quadriceps) muscle and femur (thigh) bone to data is illustrated

$$\xi = \sum_{i=1}^{n} \| \mathbf{d}_i - \mathbf{p}_i \|^2 \qquad (5)$$

Equation 1 was minimised in a coarse to fine scale manner, first using rigid-body registration, then free form deformation, and finally optimising the position of each mesh node independently.

The fitted meshes were aligned to remove translational and rotation variations then used to train a shape model of the region using PCA. For each mesh, node coordinates were concatenated into a column vector, and the matrix formed by the column vectors from all the meshes was the PCA input matrix. Node coordinates of the mean mesh was calculated by taking the mean across each row, $\bar{\mathbf{x}}$. Singular value decomposition was performed on the mean-subtracted $\mathbf{X}$

$$\mathbf{X} - \bar{\mathbf{x}} = \overline{\mathbf{X}} + \mathbf{U} \sum \mathbf{V}^T \qquad (6)$$

to obtain the principal components (columns of $V^T$) and their variance ($diag(\sum)^2$). To improve the correspondence of fitted mesh nodes across the training set, the fitting

**Fig. 2** Host-mesh customisation of the femur (*top*), medial collateral ligament insertion (*middle*) and rectus femoris muscle (*bottom*)
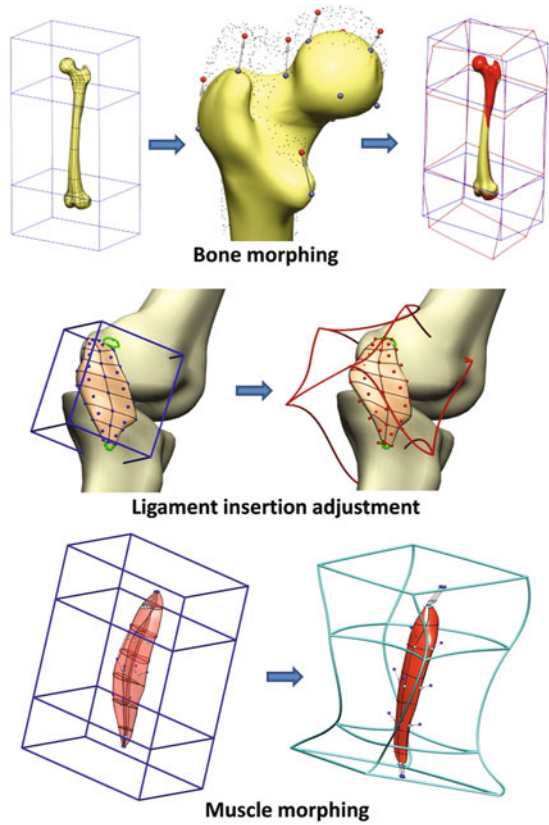
process was repeated using the mean mesh from the shape model as the template mesh, and using the principal components of variation to deform the mesh instead of freeform deformation. Mesh node coordinates were generated as a linear combination of the first principal components and the mean,

$$x' = \overline{\mathbf{X}} + \sum_{i=1}^{k} a_i b_i{}^2 \tag{7}$$

which were then subject to a rigid-body translation and rotation to minimised Eq. 1. This form of fitting was efficient since it optimised very few parameters ($k$ is typically four or five), and was robust since mesh deformations are constrained by the shape model to be realistic. For each femur, its fitted region meshes were assembled into a full femur mesh, which was then aligned and used to training a whole femur shape model using PCA.

Across the training set, root-mean squared (RMS) fitting accuracy was 0.52 mm with 0.09 mm standard deviation, which was 9 mm lower than fitting using region

**Fig. 3 a** Complete lower limb skin host-mesh with embedded muscles deformed using motion capture surface markers. **b** Initial embedded muscle pose and **c** resulting deformed muscle pose after 30° flexion
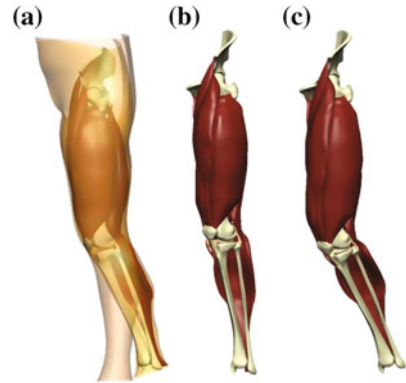
meshes. In leave-one-out experiments, the region-based shape model could fit to unseen femurs with greater accuracy than the non-regional-based shape mode. The region-based shape model also produced a more compact shape model, describing more variation in the first 5 principal components than the non-region-based model.

The first four principal components of the femur shape model accounted for over 95% of total variation, and reflected anatomically significant changes in shape and size (Fig. 8). The first component was dominated by size variation, plus a small increase in the femoral neck angle with size. The second component accounted for variation in anteversion. The third component accounted for femoral neck angle, inversely related to widths throughout the femur, while the fourth component reflected an increase in the neck angle, correlated with an increase in the sizes of the proximal and distal femur.

The shape model captured the great majority of femur shape variation with just a few parameters, and as described above, enabled an efficient and robust fitting method. This fitting method was applied in work of the next two sections to rapidly generate femur shapes that match imaging and motion-capture data.

## 3.3 Automatic Femoral Cortex Segmentation

The femoral cortex is a vital consideration in nearly all femur-related analysis. Cortical morphology, in terms of shape and thickness, is correlated to anthropological factors [78, 96], hip fracture risk [56, 81], and the accuracy of finite-element models of femur mechanics [147]. The cortical thickness mapping method [132] allows cortical thickness and cortical boundaries to be estimated over the femur surface from CT images to sub-voxel accuracy. However, the method requires an initial segmentation of the surface. Manual segmentation is prohibitively time consuming, so we combined active shape modelling [23], a well-established shape model-based automatic segmentation method, with cortical thickness mapping to produce an auto-
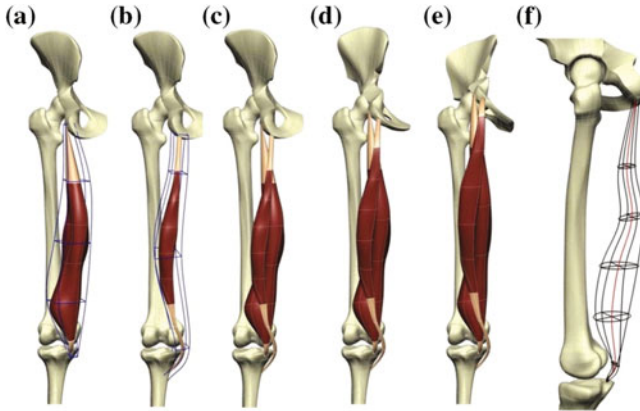
**Fig. 4 a** Semimembranosus and **b** semitendinosus muscles embedded inside hybrid mechanics host volume meshes. **c–e** Finite elastic mechanics simulations of muscle deformation, sliding and wrapping through 45° of hip flexion; and **f** muscle arc-length changes through muscle centroid (*red*) (color figure online)

matic femur cortex segmentation method [148]. The mean femur mesh produced in the previous section was customized to represent the inner and outer cortical surfaces in a CT image in three main steps (Fig. 9): active shape model segmentation of the outer surface, cortical thickness mapping to estimate cortical thickness and inner and outer cortical surface positions, mesh duplication and fitting to produce meshes of the inner and outer cortical surfaces.

First, following the active shape modelling method, the mesh was deformed according to the principal components of the femur shape model to textures in the image matching the femoral surface. The principal components constrained the deformation of the mesh to realistic shapes found in the training set, making the segmentation robust to noise in the image. Statistical models of image texture normal to the mesh surface were first trained at a dense distribution of points (material points) over the femur mesh. During each segmentation iteration, image texture normal to the mesh at each material point was compared to the material point's texture model. The coordinates of the best matching texture sample for each material point generated a dense cloud of points to which the mesh was fitted through optimisation of principal component weights and rigid-body transformations. The mean femur mesh was thus iteratively deformed to the image femur surface.

Cortical thickness mapping was performed on the active shape model-deformed mesh. As detailed in [132], cortical thickness mapping is based on a model of one-dimensional cortical bone appearance normal to the cortical surface, taking into account image blurring. This model was fitted to 1-D image profiles sampled normal to the mesh at the dense distribution of material points. The result was that each material point was associated with a cortical thickness value, a position of the outer cortical surface, and a position of the inner cortical surface. The thickness values were represented over the femur mesh as a scalar thickness field. The mesh was
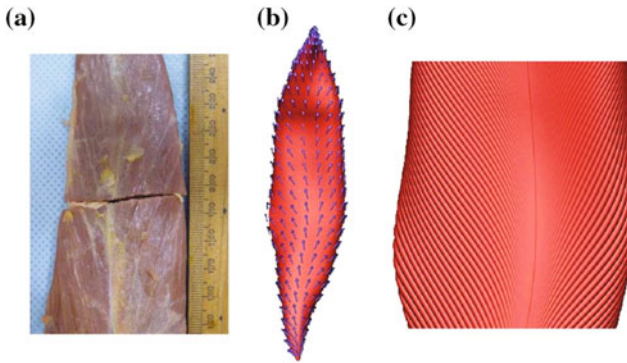
**Fig. 5** **a** Cadaveric human rectus femoris muscle showing fibre pennation angle; **b** identified muscle points used to measure pennation angle; and **c** fitted fibre field inside continuum muscle

fitted to the outer surface points to create the outer cortical surface mesh. It was then duplicated and its nodes projected inwards by their thickness field values to create the inner cortical surface. Figure 10 shows three examples of automatically segmented cortical surface meshes.

Seventeen unseen femur CT images were used to validate segmentation accuracy. Automatic segmentation results were compared to manual segmentation and cortical thickness mapping performed on the Stradwin software. The outer cortical surface mesh was, on average, 0.75 mm RMS from the corresponding Stradwin surface, and 0.89 mm for the inner surface. Cortical thickness had an average RMS error of 0.61 mm. All errors were less than voxel dimensions.

The automatic segmentation method allowed a large number of femurs to be segmented and statistical models to be produced of not only shape, but cortical thickness. The large population allowed femur models to be generated with more confidence about their representativeness. In the next section, we describe how the femur shape model has been implemented in software for robust femur model generation from motion capture landmarks and partial segmentations.

## 3.4 Model Generation and the Musculoskeletal Atlas Project

We have shown that statistical shape modelling provides powerful tools for model customisation and the ability to automatically collect large amounts of geometric data. Being able to share these methods and data allows the greater musculoskeletal modelling community to validate, improve, and develop new methodologies. The Musculoskeletal Atlas Project (MAP) being developed at the Auckland Bioengineering Institute, University of Auckland, New Zealand, aims to establish a unified database of musculoskeletal models as well as computational methods for research and clinical application in the field of orthopaedic biomechanics. A component of
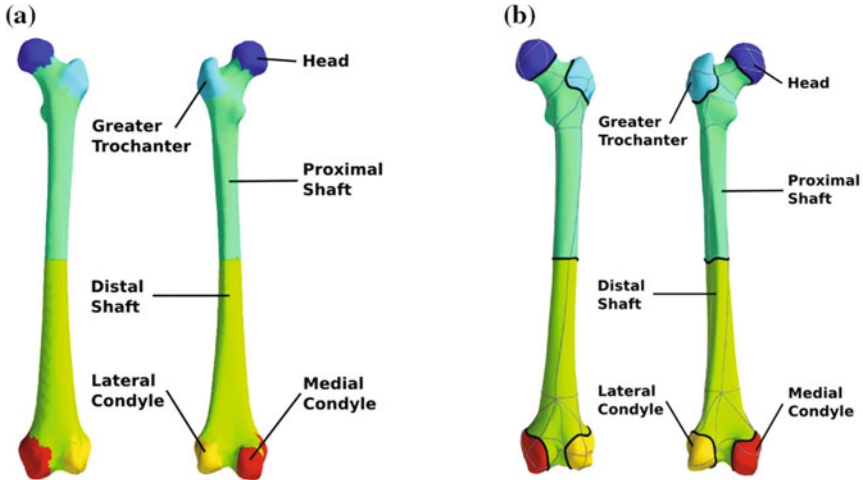
**Fig. 6** **a** Anterior and posterior views of the automatically partitioned regions on a typical femur. **b** Anterior and posterior views of the assembled femur mesh composed of six region meshes. Region boundaries are shown in *black*, and parametric patch boundaries in *grey*

the MAP is the MAP Client (Fig. 11), a plug-ins based workflow software for model generation [149]. A number of MAP Client plugins, or steps, have been implemented that makes use of femur and pelvis shape models for rapid model generation, as a part of a patient-specific model generation workflow.

Creating patient-specific femur models to predict in vivo knee joint loading is a common task in musculoskeletal modeling [37]. Femur position and general size and shape can be reconstructed from sparse anatomical landmarks in motion-capture data. Detailed distal femur geometry can be segmented from high resolution knee magnetic resonance (MR) images. The MAP Client workflow for this task begins by loading motion-capture landmarks (in the TRC format) using the TRC Source step. Landmarks are then passed to the Pelvis Reconstruction by Landmarks step and the Femur Reconstruction by Landmarks step (Fig. 12, left). In each of these two steps, the mean bone mesh is fitted to the input landmarks by optimising rigid body translation, rotation, and principal component weights to minimise the sum of squared distances between given landmarks and their corresponding predefined positions on the mesh. Predefined landmark positions on the mesh are defined in terms of the mesh parametric coordinate system so that as the mesh deforms, their 3-D coordinates are re-evaluated, by stay correspondent to their anatomical position on the bone. The Femur Reconstruction by Landmarks step was validated on 12 femur meshes unseen to the shape model. Mean RMS distance between the actual and registered models was $4.3 \pm 2.2$ mm, which was roughly half of the error produced by rigid-body and isotropic scaling registration ($8.5 \pm 3.6$ mm).

On a parallel workflow path, the Image Source step loads an MR image stack and sends it to the Manual Segmentation step for segmentation. The Point Cloud
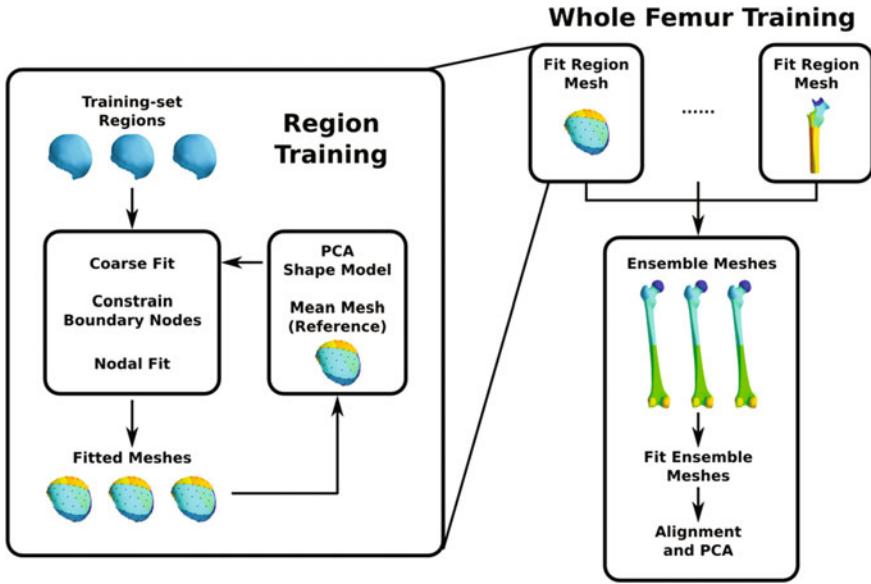
**Fig. 7** Overview of the ensemble and region shape model training process. A shape model is trained for each femoral region in an iterative fitting-PCA process. Fitted region meshes are then assembled into whole-femur meshes to train the femur shape model

**Fig. 8** Shape variations along the first four principal components of the femur shape model. For each principal components, the *left* and *right* shapes are at −2 and +2 standard deviations from the mean shape



(a) component 1

(b) component 2

(c) component 3

(d) component 4
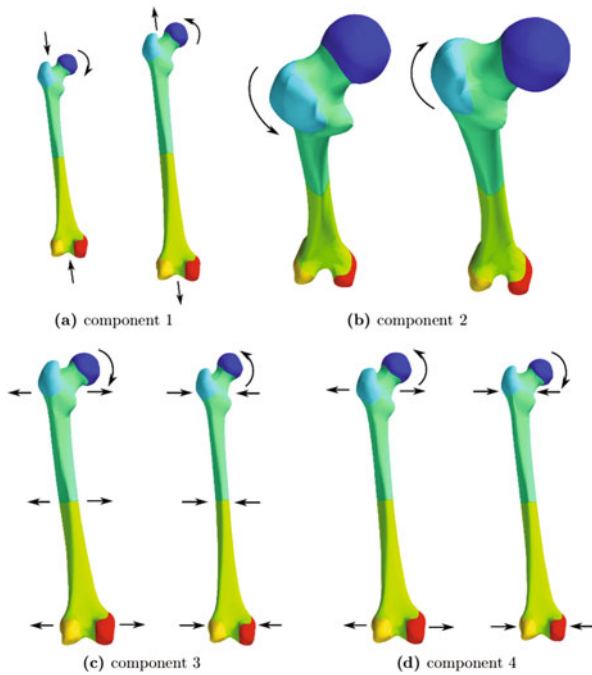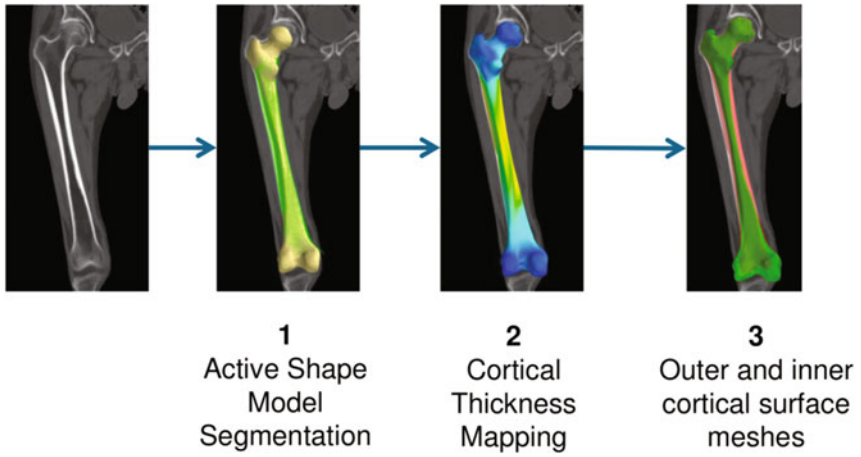
Fig. 9 The key steps of automatic femur cortical surface segmentation
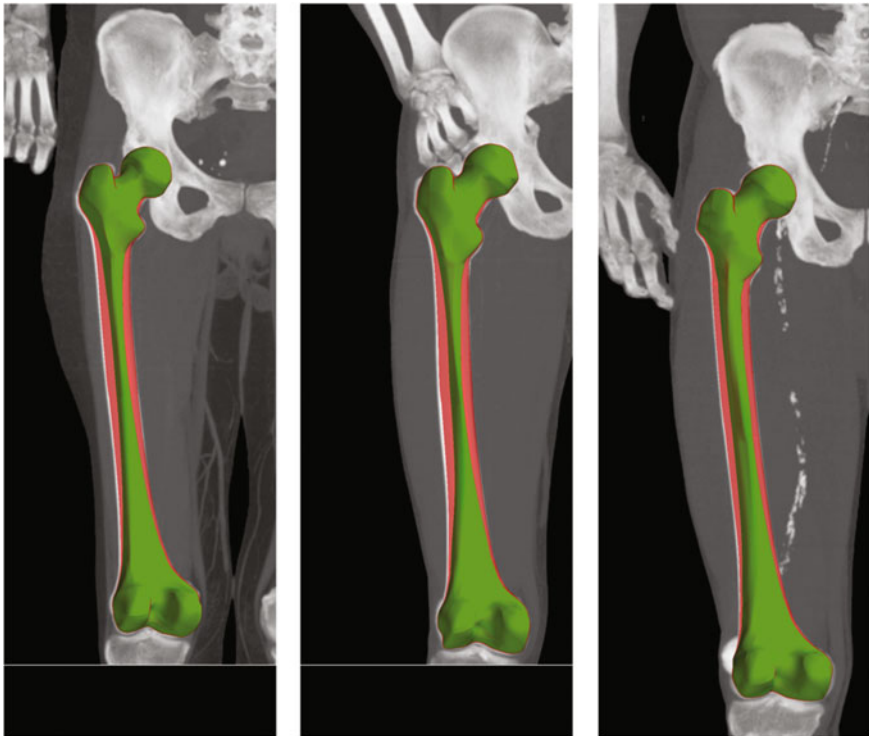


Fig. 10 Examples of automatically segmented inner and outer cortical surface meshes
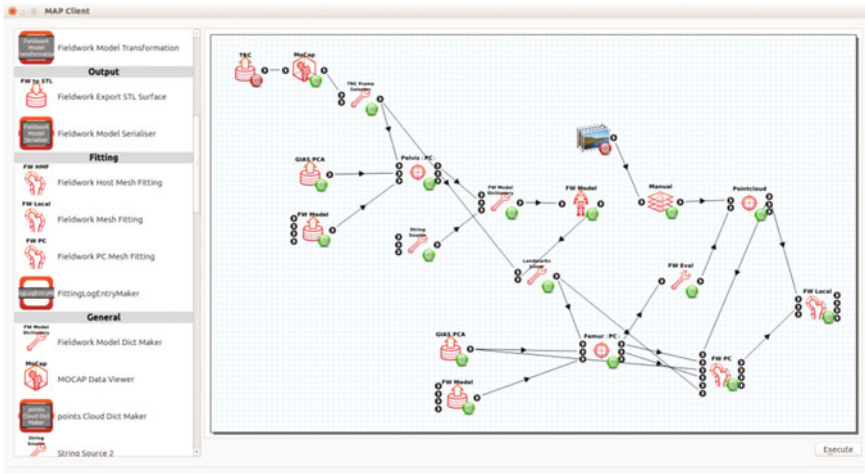
**Fig. 11** The MAP Client software. Installed plug-ins/steps are listed in the *left* area. The workspace area to the *right* shows the patient-specific femur generation workflow



Femur Reconstruction by Landmarks                    Principal Components Fitting
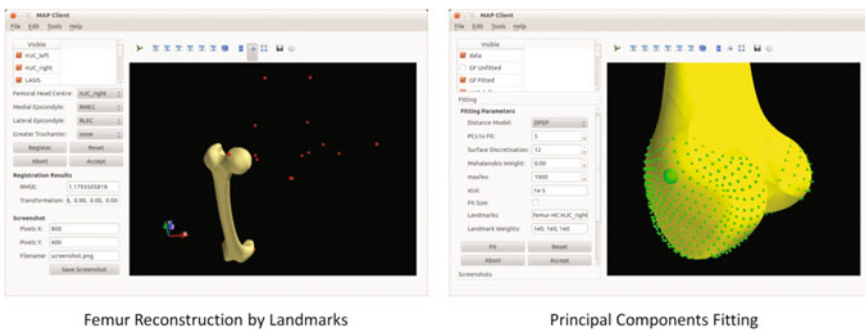
**Fig. 12** MAP Client plugins/steps using the femur shape model. The graphical user interface for the Femur Reconstruction by Landmarks step is shown on the *left* and the Principal Components Fitting step on the *right*

Registration step aligns the segmented point cloud to the femur mesh before they are passed to the Principal Components Fitting step (Fig. 12, right) which fits the femur mesh to the point cloud according to the femur shape model. In this workflow, principal components-based fitting is used to fit the femur mesh to incomplete femur geometry (segmented femoral condyles). The shape model reconstructs the rest of femur geometry based on the condyle geometry and motion-capture landmarks. In leave-one-out experiments using 31 femurs, the average RMS fitting error was $1.2 \pm 0.3$ mm using ten principal components, which was superior to the commonly-used host-mesh fitting method (2.5 to 4.0 mm RMS) [35]. A subsequent unconstrained Mesh Fitting step can reduce the fitting error to around 0.5 mm RMS.

The resulting femur mesh exhibits high accuracy in the condylar region where detailed geometry is available, and elsewhere is formed by the optimal shape model approximation, based on a real population of femur geometry. The steps of the workflow are modular and can be easily rearranged for other model generation tasks.

### 3.5 Conclusions

In this article, we have demonstrated statistical shape modelling on the femur, and given two examples of how a shape model can be used in musculoskeletal model generation. In training a shape model of the femur, we chose a piecewise parametric mesh description of femur shape, and used an iterative fitting-PCA process to obtain correspondent fits of the mesh to a training set of femur segmentations, paying special attention to anatomical regions. While this is by no means the only to create a shape model, the region-based approach improved the correspondence of the mesh to anatomically significant features. The main goal was to create a compact model of femur shape variation, and this was achieved by PCA on the fitted femur meshes.

The shape model then drove an automatic segmentation method. Combined with cortical thickness mapping, the inner and outer cortical surfaces, and cortical thickness could be automatically extracted from CT images. This allowed the training set size of the shape model to be greatly increased, improving the robustness of the model.

Finally, we showed that the shape model can be used to rapidly create patient-specific femur models from sparse and incomplete motion-capture and imaging data. The software tools for doing this have been made available as a part of the open-source Musculoskeletal Atlas Project, so that the community can benefit from, and improve upon statistical shape modelling methodology in musculoskeletal modelling.

## 4 Modelling Towards a Clinical Tool

Finite element analysis has been used widely in orthopaedic biomechanics mainly as a research tool. We present our work that show how finite element models can be efficiently generated from clinical CT scans and used in post-surgical monitoring of a patient who received a total hip replacement implant and developed osteolytic defects around the implant.

### 4.1 Introduction

Since its introduction in 1972 [9] the finite element(FE) method has been widely used in orthopaedic biomechanics. It has many applications from stress strain calculation

to microstructural modelling of bones [65, 66]. However, it has not yet reached widespread clinical use mainly due to the intensive labour that is needed in generating accurate FE meshes. There have been numerous attempts to develop an automated method for generating FE models to be used in orthopaedic areas. Keyak and coworkers have developed an efficient and robust automatic mesh generation (AMG) method [71] that has proved to be useful in many research areas [21, 72, 73]. Viceconti and coworkers have also pioneered in developing a mesh generation method [133] for generating patient-specific FE models of various different types of bones other than the femur [134].

All the aforementioned methods use computed tomography (CT) to obtain patient specific geometry and material properties. The data requirements are quite intensive, most of them requiring very dense FE meshes with thousands of elements. This will inevitably lead to increased radiation exposure to subjects/patients.

There have been a number of concerns about the possible adverse effects of CT radiation exposure [98, 105, 112]. Moreover, it is common for clinical CT datasets to be limited to the part of a bone that is a region of clinical interest such as the acetabulum of the pelvis. Data describing a structure such as the iliac region of the pelvis may be very limited or missing. However, to have a full FE model of a bone for mechanical simulations, it is vital to have structural information for the whole bone.

In this section we first introduce a hybrid method for generating pelvic FE models, which supplements sparse patient pelvic data with geometric data from the visible human dataset [1]. The models use high order cubic Hermite elements which have the advantage of capturing complex geometry using few elements [8]. Then the validation of the model generated with the hybrid method is presented.

## 4.2 Generation of FE Models from Clinical CT Datasets and Model Validation

A new method of supplementing patient CT images with images from the Visible Human CT was developed [117]. This method uses the previously described cubic Hermite elements and least squares fitting procedures. Figure 13 outlines the method starting with dividing the patient CT and Visible Human CT into the same number of anatomically defined regions. Second, within each region we transformed slices from the Visible Human CT slice to the patient CT slice using landmarks at the beginning and end of each region. Third, we selected a minimal number of slices within each region of the Visible Human CT to transform and fill the gaps in the patient CT set. It was found that with only 12 CT slices we were able to generate smooth and accurate meshes of the proximal femur with a geometric root mean square (RMS) error of less than 1 mm and peak errors less than 8 mm. We tested this method on three patient data sets, generating FE meshes of the pelvis using only 10 CT slices with an overall RMS error less than 3 mm. Considering that linear meshes usually
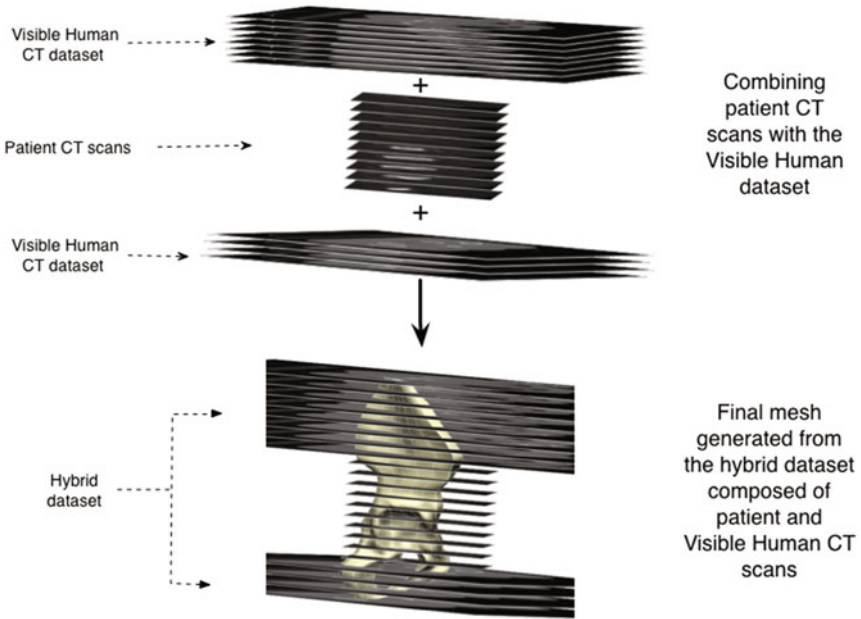
**Fig. 13** Generation of a subject-specific model of the pelvis from a sparse CT data set by complementing it with the Visible Human CT data set

require about 70100 pelvic CT slices (in axial mode) to generate FE models, our method has brought a significant data reduction to the automatic mesh generation step.

Models generated with this technique were validated with mechanical experiments [118]. Three cadaveric embalmed pelvises were strain gauged and FE models were generated from the CT scans using the hybrid technique. Material properties for cancellous bone were obtained from the CT scans and assigned to the FE mesh using a spatially varying field embedded inside the mesh while the mechanical characteristics of other materials used in the model were obtained from the literature. For each pelvis, five different FE meshes with a varying number of patient CT slices (812) were generated to determine how many patient CT slices were needed for good accuracy. All five mesh types showed good agreement between the model and experimental strains with an R2 of 0.9. Meshes generated with incomplete data sets showed very similar stress distributions to those obtained from the FE mesh generated with complete data sets. The model developed using the hybrid method was validated with mechanical experiments. Three cadaveric embalmed pelvises were strain gauged and FE models were generated from the CT scans using the hybrid method. Material properties for cancellous bone were obtained from the CT scans and assigned to the FE mesh using a spatially varying field embedded inside the mesh while other materials used in the model were obtained from the literature. For each pelvis, five different FE meshes with a varying number of patient CT slices

(812) were generated to determine how many patient CT slices were needed for good accuracy. All five mesh types showed good agreement between the model and experimental strains with an R2 of 0.9. Meshes generated with incomplete data sets showed very similar stress distributions to those obtained from the FE mesh generated with complete data sets. The validated model was then used in analyzing clinical situations in total hip arthroplasty as described in the following sections.

## 4.3 Development and Validation of Retroacetabular Osteolytic Defect Model

The validated model was used to investigate a common clinical symptom of total hip arthroplasty, that is the formation of retroacetabular osteolytic defects [85]. Cementless, metal acetabular components are known to alter the transfer of stress in pelvic bone whereby loads applied to the cup are transferred to the cortical bone while the cancellous bone remains shielded. The remodeling that follows results in cancellous bone mineral density (BMD) loss [99]. Further to this mechanical effect, wear particles from the articulating surfaces have a well-established biologic role in cellular mediated osteolysis [68, 101]. This can lead to profound bone loss with resulting cystic defects, which is often termed a silent disease as substantial osteolysis can occur before symptoms become apparent. How retroacetabular bone loss affects stress transfer is less clear. We do not know how much bone can be lost before risk of fracture increases significantly. Further, during reconstructive surgery, it may not be necessary to complicate the procedure by using bone graft to fill defects if cup stability can be established by other means. Therefore the motivation for this study was to develop and validate a 3D FE model of retroacetabular bone loss behind a cementless hip replacement and investigate its biomechanical role.

An experimental system with a 4th generation composite pelvis (Sawbones, Pacific Research Laboratories, Vashon, Washington, USA) where the pelvis was positioned in a mounting pane to mimic a single leg standing position (Fig. 14). The left acetabulum was prepared with hemispherical reamers and press-fitted with a 58 mm, acetabular prosthesis (Harris-Galante I, Zimmer, Warsaw, Indiana). Eight, three-element, rectangular ($0° − 45° − 90°$) rosette strain gauges (KFW-5-120-D17-11L1M2S, Kyowa Electronic Instruments, Minatoku, Tokyo, Japan) were attached to locations on the medial and lateral walls. The strain gauges were positioned in regions of interest, notably the cortex of the superior dome, the posterior column and the medial wall (Fig. 14 right). The experimental model was then positioned in a mechanical testing system (Instron, Norwood, Massachusetts, USA). A vertically oriented load in the direction of single leg weight bearing was applied in 4 increments (150N, 300N, 450N, 600N).

Following initial testing and data collection, the acetabular cup position was marked and the cup was removed. A retro-acetabular defect measuring approximately 30 by 60 by 30 mm was created in the cancellous region of the model, using a

Experimental set-up          Strain gauge location
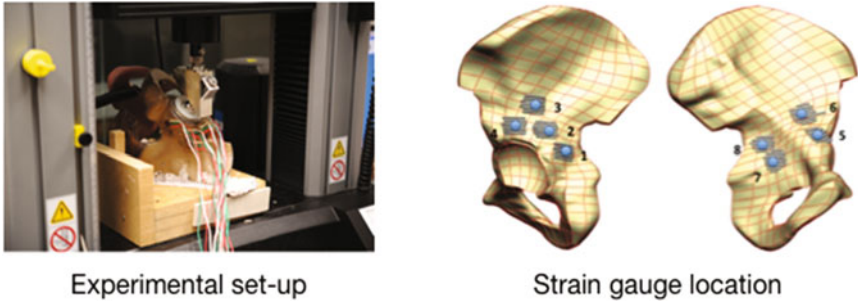
**Fig. 14** An experimental set up using a composite pelvis that mimics the single leg stance (*left*) and locations of strain gauges used (*right*)



Osteolytic defect indicated          Retroacetabular defect created
in a X-ray scan (arrorw)            in the composite pelvis
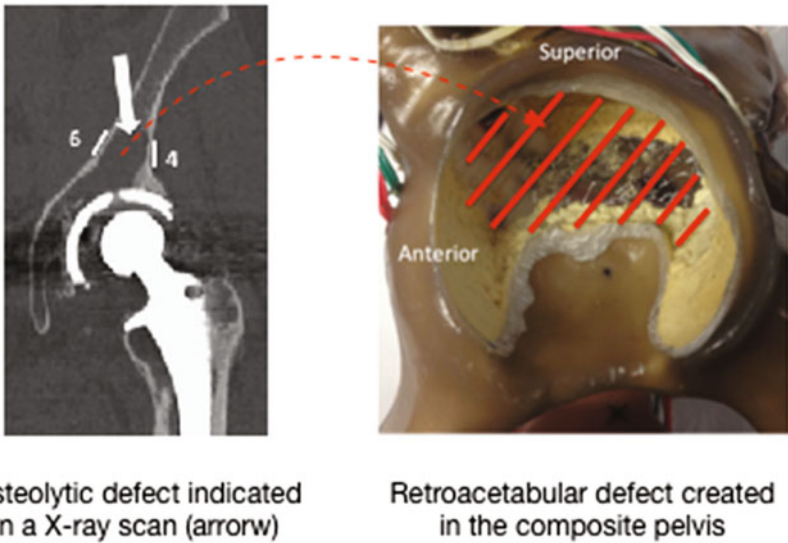
**Fig. 15** CT scan showing osteolytic defect of a patient with THA (*left*) and creation of defect in the composite pelvis used in the experiment (*right*)

high-speed burr (Fig. 15). Care was taken to avoid perforation of the cortical regions of the model. The cup was then re press-fit in its original position and orientation. Mechanical testing was conducted with the same protocol described above. Strain measurements from each gauge were used to calculate the principal and von Mises stresses at each gauge location.

The composite pelvis mode used in the experiment was CT scanned in a Lightspeed VCT Helical scanner (GE Medical Systems, NY, USA) obtaining axial cuts according to the anatomic plane. The CT scans were processed with Image J (National Institutes of Health, Bethesda, Maryland, USA) and a model generated with the

Correlation between experimental
and predicted principal strains

Max principal strain in the lateral
and medial cortices of the pelvis
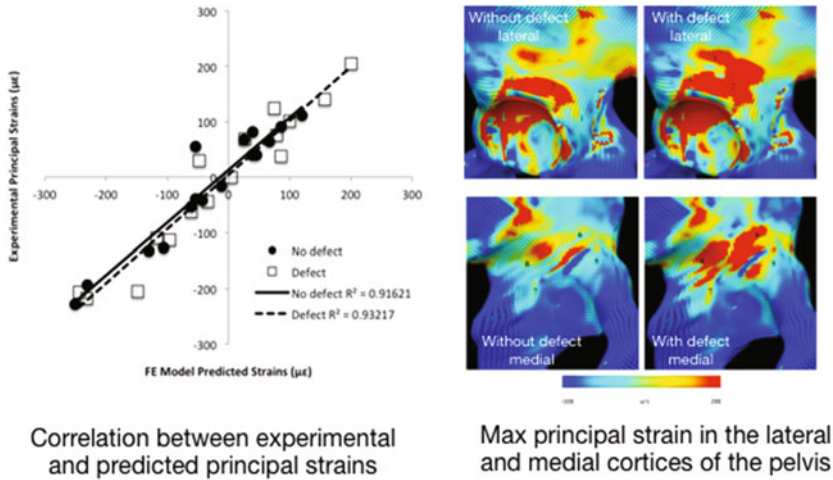
**Fig. 16** Correlation between experimental and predicted strains (*left*) and the changes in the maximum principal strain distribution due to the presence of defects, which increased the peak strain regions

method described in Sect. 1. The final FE mesh consisted of 621 nodes and 309 large volume, 8 node elements with high order cubic Hermite basis functions. The root mean square error (RMSE) comparing the final mesh to the surface data points was 0.843 (average 0.482 ± 0.690). Mesh density was established by convergence analysis of peak regional von Mises stresses. The acetabulum of the mesh was than reamed by fitting the element surfaces to a model of the hemispherical titanium cup used in the experiment. Nodes were fixed at the sacrum and iliac crest according to the experimental conditions. Contact between the cup and acetabular bone was simulated as frictional contact. Material properties were assigned to Gauss points within the elements [119]. Simulations were conducted to establish the correlation of the experimental saw-bone and FE models with regard to surface strain and calculated von Mises stresses for both defect and non-defect cases to analyze changes in the stress pattern due to the presence of the defect.

Surface strains were highly correlated for both models with and without defects (Fig. 16 left). The presence of a retroacetabular defect increased strain in the adjacent cortical bone both medially and laterally, with the medial wall region receiving the highest increase (Fig. 16 right), which corresponds to Gauge number 6 in Fig. 14.

## 4.4 Investigation of Osteolytic Defects with Clinical CT Data

This method was then used to investigate the influence of osteolytic defects on stress transfer patterns in actual clinical situations. High-resolution spiral multislice CT

**Fig. 17** The volume of defects measured from CT scan. The volume of defects increased over 3 years period both in cancellous and cortical bones (*left*) and the interfaces incorporated in the FE model (*right*)

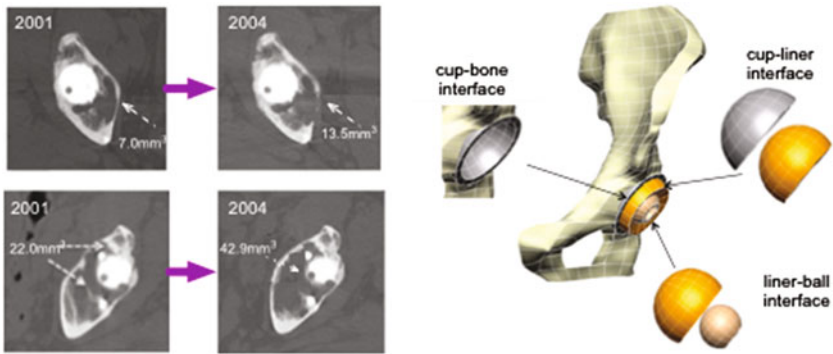imaging was obtained from a 65 kg male patient in his 8th decade who underwent bilateral primary THA in 1989 with Harris-Galante I (Zimmer, War-saw, IN, USA) cementless acetabular components. Scans were conducted in 2001 and 2004. A validated technique employing metal artifact reduction software (Voxel Q FALCON, Picker International Inc, Cleveland, OH) was used to provide accurate identification of osteolytic defect position and volume [59, 123] (Fig. 17 left) Individual CT slices were analysed using ImageJ (Opensource, National Institutes of Health, Bethesda, Maryland, USA) to identify cortical bone boundary and the regions where defects are present.

The validated mesh described above then fitted to the surface data points from each of the patient-specific CT scans. The root mean square error (RMSE) comparing the fitted mesh to surface data points ranged from 0.598 mm (average error 0.301 ± 545) to 0.671 mm (average error 0.395 ± 0.622) across the models.

Hounsfield unit values from the CT slice internal data were converted to relative density correlated to values from the concomitantly scanned phantom and assigned to model using the method described in Shim et al. [119]. Contact between the cup and acetabular bone was simulated as bonded contact. Likewise the PE liner cup interface was modeled as fully bonded. The ball liner interface was modeled as free sliding with coefficient of friction at 0.065 (Fig. 17 right). Load was applied through the femoral head. Contributing forces from 23 muscle units crossing the hip joint calculated from electromyography assisted methods were included [34, 108]. These were applied to the FE model using muscle belly centroid paths matched to the origin and insertion of the muscles in question. Vectors for each force were plotted based on the gait cycle with forces distributed over the origin insertion areas of the pelvis mesh. Details of this procedure can be found in Fernandez and colleagues [34]. Forces for slow walking that were originally calculated from young male subjects were used [108]. Nodes at the pubic symphysis and sacroiliac joint were fixed. Two loading situations were simulated: a vertical load of 1300N (2BW) representing the stance

**(a)** Numbered ROI for statistical analysis

**(b)** Pelvis meshes from 2004 showing defects on the right (a) and left (b) around the implant
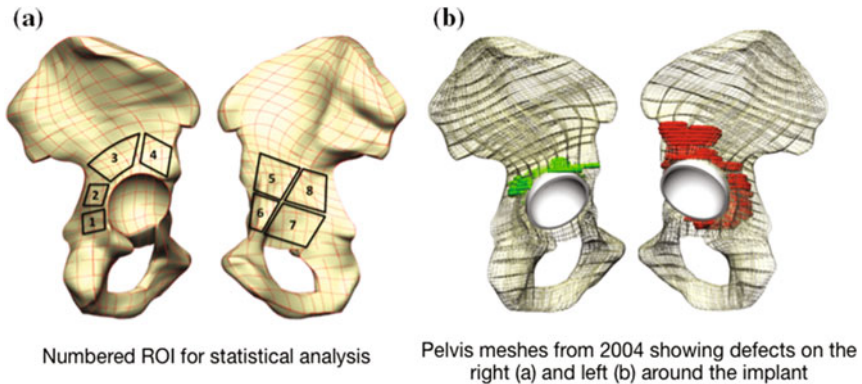
**Fig. 18** Regions of interest used in stress analysis (*left*) and the pelvis mesh showing the location and volume of defects (*right*)



Right hemipelvis

Left hemipelvis

No defect     2001     2004

No defect     2001     2004

0          MPa          15
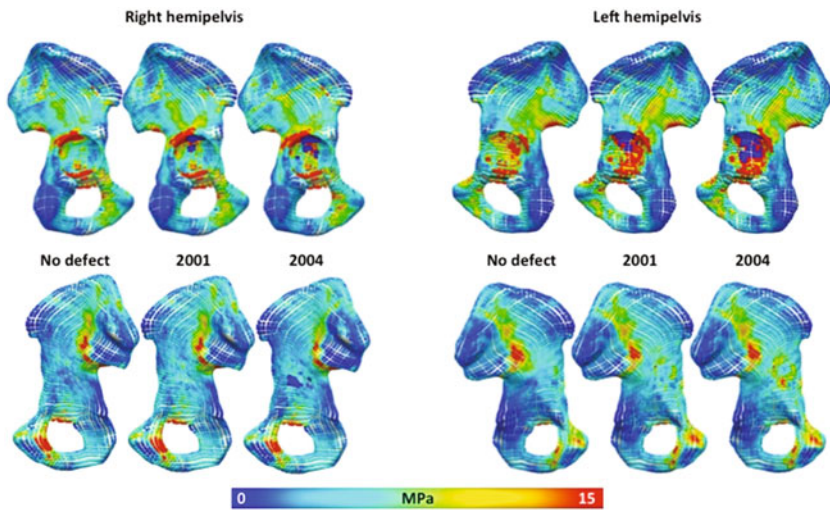
**Fig. 19** The von Mises stresses during single leg stance for *left* and *right* hemipelvis comparing models without a defect to defects present in 2001 and 2004. Note the *dark blue* regions in the acetabulum and medial wall of the *right* pelvis in 2004 indicating cortical bone loss (color figure online)

phase of gait and a lateral load of 5000N (7.5BW) representing a fall directly onto the side. CMISS was used to solve the FE analysis.

Simulations were conducted to establish differences in load transfer when defects were present compared to those where defects were filled by assigning a modulus of 155 MPa to the defect region. The von Mises stresses were compared for all data points within defined regions of interest (ROI) on the cortical bone (Fig. 18).
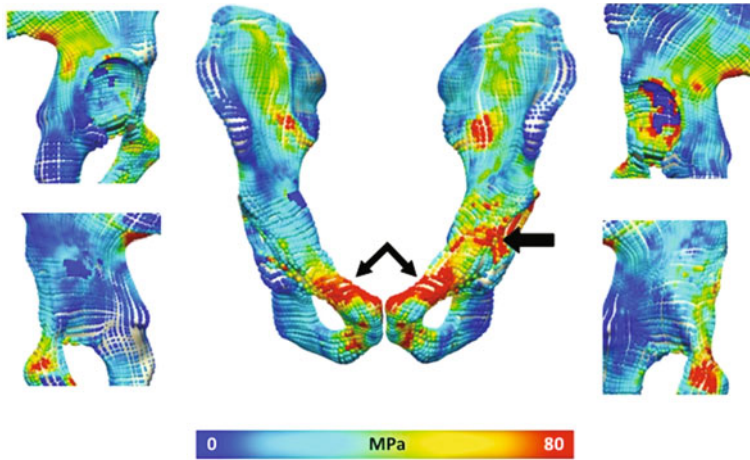
**Fig. 20** The von Mises stresses following a fall directly onto the side for models based on 2004 data. Force is directed medially for the respective sides. Note high stress concentrations at the pubic symphysis (*double arrow*) and at the anterior wall on the *left side* with the larger cancellous defect (44.9 cm$^3$) compared to the *rights side* with a smaller defect (13.5 cm$^3$)

The presence of a retroacetabular defect significantly increased cortical von Mises stress in the medial and lateral walls of both the left and the right hemipelvis during normal gait. On the left, higher stress regions were observed in the lateral cortex extending form the postero-superior acetabulum towards the sciatic notch and in the anterior column extending towards the medial wall (Fig. 19). Stress increased as defect volume increased. This was most prominent in the medial wall (ROI 6,7 and 8).

While a similar load pattern occurred on the right (Fig. 19), mean increases and peak von Mises stresses were slightly lower. The defect in the cortical wall did not produce large increases in von Mises stress in the local region (ROI 6). Again stress was seen to increase as defect volume increased although this was greatest in the lateral cortical bone (ROI 1, 2 and 4).

During a fall directly onto the side, von Mises stresses were also increased in the presence of a defect for both the left and the right side. On the left side, the greatest increase in stress occurred in the medial wall and the anterior and posterior columns as well as the pubic rami (Fig. 20). All regions except ROI 2 showed significant increases in stress from 2001 to 2004 as defect volume increased.

While the proportionate changes in cortical von Mises stress in the presence of defects were high, the absolute increases were not. During single leg stance, the largest observed mean increase of 89.5% in ROI 6 of the left hemipelvis represents an increase from 4 to 7.5 MPa. Likewise the highest peak stresses predicted in ROI 3 in both models were still less than 20 MPa. The true yield and failure values for pelvic bone are unknown and the reported values in the literature ranges from 50 to 130 MPa. Even taking into account the variability, the von Mises stresses predicted

in our model for single leg stance are likely to be well below yield for cortical structures. During a fall, peak stresses do approach levels that can be considered a risk for fracture but periprosthetic fracture around acetabular implants are fairly uncommon. These results support observation of smaller volume osteolytic defects where the cup is well fixed and suggest that strategies to stop lysis progression may be justified in reducing need for revision surgery.

## 5 Understanding the Mechanical Aetiology of Musculoskeletal Injury and Disease using EMG-Informed Muscle Modelling and Medical Imaging

### 5.1 Introduction

It is well established that the growth, development, regeneration and ageing of musculoskeletal tissue is regulated by mechanical processes [17, 18]. The local mechanical environment at a cellular or tissue level also plays a critical role in the onset, development and severity of musculoskeletal injury and disease [19, 84, 143]. Osteoarthritis at the hip and knee for example, has been shown to correlate to walking gait mechanics [52, 97, 111]. Indeed, several attempts have been made (authors included) to alter the mechanics of gait in the hope that changing the local mechanical environment of the joint will slow the progression of cartilage degeneration [120]. However, if we are to develop appropriate intervention strategies to treat these disorders we must first characterise the local mechanical environment of skeletal tissues and understand the role of mechanical environment in maintaining tissue health. Herein lies one of the greatest challenges in biomechanics how do we characterise the local mechanical environment and load history of a tissue?

A common goal of our research is to understand the mechanical aetiology of musculoskeletal injury and disease by combining traditional experimental methods with computational models that account for the underlying physics and physiology of the musculoskeletal system. Ultimately, we want to develop musculo-skeletal models that can predict clinical outcome and personalise treatment strategies. To do this we must estimate in vivo muscle forces during various activities of daily living as these loads are main determinants of the mechanical environment experienced by musculoskeletal tissues.

The following chapter provides an overview of our neuromusculoskeletal modelling framework to estimate muscle and joint forces using electromyography (EMG) as input. We present some applications of our modelling work and introduce some novel imaging methods to investigate tissue function.

## 5.2  Estimating Muscle Forces Using EMG

Muscle forces are critical for producing motion at our joints and they are also the primary determinant of joint contact forces [52] and are consequently important for distributing stress through the cartilage and underlying subchondral bone. It is currently not feasible to measure muscle forces experimentally so we must rely on computational methods to resolve the age-old problem of muscle indeterminacy. That is, there are more muscles that cross a joint than degrees of freedom of that joint. One approach to solve this problem has been to arrive at a neural solution that distributes muscle forces subject to some pre-determined optimisation criteria [114], such as minimising metabolic cost or total muscle activation [97]. Of course, we do not know a priori what the central nervous system is actually trying to optimise (if anything at all!), and we cannot begin to assume that this criteria is consistent across or even within individuals or maintained with impairment or injury. Indeed, for the same exactly the joint moments and angles, where optimisation will lead to the same neural solution, it has been well shown that the activation of motor units within muscles [128–131] and synergies between muscles [14, 28, 55] vary due to the control task, learning and disease [46, 58, 61, 62]. This variation in the activations patterns can occur within the same person [14, 28, 128–130] and between people [77]. Therefore, another method is required to determine muscle activity.

An alternate approach to solve the muscle indeterminacy problem is to distribute muscle forces based upon measured muscle activity such that the combined muscle forces produce a net joint moment that is consistent with inverse dynamics [76]. In the past we have referred to this as EMG-driven modelling, but now we now generalise it as EMG-informed modelling. Although EMG-informed modelling is not a new concept [54], the ability of these models to predict joint moments across a range of dynamic tasks is reliant on modelling the complex non-linear behaviour inherent in the activation and contraction dynamics of skeletal muscle [45], which has been a major challenge. However, being able to calibrate and tune the behaviour of EMG-informed models to match, or well predict, experimentally measured inverse dynamics loads [15, 76], and now EMG linear envelopes [110], are relatively new achievements.

Our EMG-informed musculoskeletal model consists of four components [15, 16, 76]: (1) an anatomical model of the musculoskeletal system to estimate muscle tendon lengths and moment arms; (2) an EMG-to-activation model that uses raw EMG as input to estimate the neural activation and activation dynamics of a muscle; (3) a Hill-type muscle model to represent the muscle contraction dynamics; and (4) a calibration procedure to adjust model parameters to match a specific subject.

## 5.3  Anatomical Model of the Musculoskeletal System

Developing an accurate representation of the muscles, their origins and insertions, and the underlying skeletal system is critical to understanding in vivo muscle and joint function (see Sect. 2). Our current modelling pipeline relies on an open source

musculoskeletal modelling package called OpenSim [29]. OpenSim represents the three-dimensional bone surface geometry as a polygonal surface with muscle-tendon units represented as line-segment actuators with defined origin and insertion points. Wrapping surfaces or via points can be used to approximate the wrapping of muscles around bone and other soft tissues. Joints describe the three dimensional position and orientation of one segment relative to another and an inverse kinematics analysis can be performed to track the motion of a subject using experimental motion capture data (typically from an optical-based motion capture system).

OpenSim is built around a multibody dynamics engine called SimBody [116], providing capability to perform inverse and forward dynamic simulation of complex biomechanical systems. The EMG-informed model relies on OpenSim to provide muscle tendon lengths and three dimensional moment arms for a motion of interest. We also use OpenSim to calculate joint moments that are dynamically consistent with the reconstructed motion and experimentally measured ground reaction forces using inverse dynamics with a reduced residual analysis [29, 30, 110]. Joint moments predicted by the EMG-informed model are then compared to joint moments computed from inverse dynamics during a calibration process, which adjusts model parameters to best-fit the experimental data.

Scaling an OpenSim model to match the anthropometry of a subject remains a major challenge and is the first and potentially, most important step in developing a realistic simulation of human movement and muscle function. The most common approach to generate a subject-specific OpenSim model is to scale a generic model to match anatomical markers from a static motion capture trial. This length scaling is susceptible to error due to difficulty in identifying bony landmarks and poor placement of static markers. Functional scaling of joints and segment lengths using dynamic motion trials can be performed to alleviate some of these errors [76]. To overcome these problems, we are investigating new methods of scaling a generic model using a statistical shape model that represents a population of bone geometries to constrain the geometric fit (see Sect. 3). Another approach, although time consuming, is to build a geometric model directly from medical imaging (see Sect. 2). To facilitate rapid generation of accurate musculoskeletal models we have developed an open source project called the Musculoskeletal Atlas Project (MAP; https://map-client.readthedocs.org). This project will build a repository of musculoskeletal models and apply statistical modelling methods to characterise the morphology of various structures across a population.

One limitation of using the simplified line segment OpenSim models is that they do not adequately represent the complex muscle geometry and architecture, which are extremely important with regard to estimating muscle function (see Sect. 2). Another limitation imposed by the use of simple line segments to represent muscles wrapping around bones and soft tissue is that wrapping surfaces and via points can create discontinuities in the predicted muscle tendon kinematics [39]. Discontinuities can be overcome by fitting multi-dimensional B-splines to fit muscle moment arms and muscle tendon lengths across a range of generalised coordinates without a loss of accuracy [108]. This method has the added advantage of being numerically efficient for real-time computation. Our future plans involve the use of imaging methods

coupled with finite element models of muscles with embedded fibre architecture (see Sect. 2) to characterise realistic muscle tendon lengths and moment arms.

## 5.4 EMG-to-Activation Model

Surface EMG recordings are inherently noisy and a bi-product of the underlying activation of a muscle. The transformation from EMG to muscle activation is not trivial and should account for the underlying activation dynamics.

The first step in this process involves filtering the raw EMG signals using a zero-lag 4th order Butterworth high-pass filter using a cut-off frequency of 30 Hz. This filter will remove any DC offsets from the raw signal and eliminate artifacts due to electrode movement. Next, the signal is full wave rectified and normalised to a maximum voluntary activations across a range of tasks. Normalisation of EMG signals can be problematic as it is difficult to voluntarily recruit all motor units to achieve a true maximum value. Interpolated twitch response methods can also be used to assist in normalising the EMG signal, particularly in patients who might have neural inhibition of their motor units due to pain or dysfunction.

The rectified, normalised EMG signal is then smoothed using a zero-lag 4th or-der Butterworth low-pass filter using a cut-off frequency of 6 Hz. This process is used to approximate the summed motor units within the muscle. We call this excitation, $e(t)$, and this case this is termed EMG-derived excitation to distinguish these from excitations derived from optimisation. When a muscle is activated by a single action potential, the muscle generates a twitch response. This response can be represented by a critically damped second-order differential system [83], which is modelled using a discrete recursive filter:

$$u_j(t) = \alpha_j \bullet e_j(t - d) - \beta_{1j} \bullet u_j(t - 1) - \beta_{2j} \bullet u_j(t - 2)$$

where $u_j(t)$ is the neural activation of muscle j at time t and $\alpha_j, \beta_{1j}, \beta_{2j}$ are the coefficients that define the second-order dynamics. Electromechanical delay, $d$, is also represented in this filter, which accounts for the delay between the neural signal and the start of the resulting twitch force. We keep this value between 10 msec and 100 msec [24].

To realise a positive stable solution of Eq. 1, a set of constraints are used:

$$\beta_1 = C_1 + C_2$$
$$\beta_2 = C_1 \cdot C_2$$

where $|C1| < 1$ and $|C2| < 1$. In addition to these constraints, the unit gain of this filter is maintained by ensuring $\alpha - \beta_1 - \beta_2 = 1.0$.

As a recursive filter, the neural activation is dependent on its current level of excitation as well as its recent neural activation history. Previous work on cats [44,

51] reveals why many researchers have experienced difficulties predicting muscle force from rectified and low-pass filtered EMG. This was due to an inability to (a) attain the best time delay between EMG onset and force onset, and (b) account for the observation that the EMG signal was shorter in duration than the resulting force. Both of these issues are resolved by the discrete second-order system presented above.

The final step in the EMG-to-activation model is to account for the linear or non-linear relationship between muscle activation and force, which has been shown experimentally [142] and known to vary between individuals and across different muscles. We model this using an exponential function (similar to [100]):

$$a_j(t) = \frac{e^{A_j u_j(t)} - 1}{e^{A_j} - 1}$$

where $a_j(t)$ is the activation of muscle $j$ at time $t$, $u_j(t)$ is excitation (from the step above) and $A_j$ is a non-linear shape factor for muscle $j$. This simple equation scales the muscle excitation and accounts for the potential non-linear EMG-to-force relationship using a single parameter for each muscle, $A_j$. We also use an alternative formulation [80] that represents the EMG-joint moment relationship of Woods and Bigland-Ritchie [109], which is also controlled by a single parameter $A_j$.

## 5.5 Hill-Type Muscle Model

Following the estimation of muscle activations, the next step in the process is to estimate muscle force accounting for muscle contraction dynamics. For this we rely on a phenomenological Hill-type muscle model, which describes the force-length and force-velocity relationship of muscle [53]. Although Hill-type models do not represent the underlying physiology of muscle contraction, they adequately represent whole muscle behaviour and are computationally efficient compared to more complex cross-bridge models, as the contraction dynamics can be governed by one differential equation per muscle.

Our muscle model is based on a normalised Hill-type model with a non-linear tendon function as defined by Zajac [146]. It accounts for changes in pennation angle and uses generic force-length and force-velocity curves for each muscle to estimate muscle fibre force. These curves are normalised to maximum isometric muscle force ($F_{max}$), optimal fibre length ($L_m^0$), maximum muscle contraction velocity ($v_{max}$), and tendon slack length ($L_{ts}$).

The shape of the force-length relationship is based on the linearly scaled model used by Zajac [146], however, we have included an increase in optimal fibre length with a decrease in activation [64], as follows:

$$L_m^0(t) = L_m^0(\gamma(1 - a(t)) + 1)$$

where $\gamma$ is the percentage change in optimal fibre length, $a(t)$ is activation at time $t$, $L_m^0$ is the optimal fibre length at maximum activation, and $L_m^0(t)$ is the optimal fibre length at time $t$.

Passive elastic muscle force in the contractile element is obtained from an exponential relationship, which allows for passive forces to be obtained regardless of fibre length, thus accounting for non-zero passive forces [76]. A tendon force-strain curve scaled by Fmax and Lts is used to interpolate muscle tendon force [146]. Muscle fibre lengths are calculated by forward integration of the fibre velocities obtained from the force-velocity and force-length relationships using a Runge–Kutta–Fehlberg algorithm. The initial muscle fibre lengths and velocities are calculated by apportioning the total muscle tendon velocity to the muscle fibre and tendon based on their relative stiffness. Although numerical integration of ordinary differential equations is reasonable in terms of efficiency, it still represents a bottleneck in the total computation time. Our long-term vision is to use these models in a clinical setting and perform real-time computation of muscle forces. To achieve this, we can assume an infinitely stiff tendon, thus negating the need for numerical integration, increasing computation speed by 250x with no loss in accuracy compared to an elastic tendon model [108]. The rapid uptake of inexpensive wearable sensors linked to smart phones promises to revolutionise clinical motion analysis, bringing musculoskeletal models much closer to clinic use and provide measurements outside of the laboratory.

## 5.6   Calibration

The ability of a model to predict clinical outcome measures is dependent on calibrating a model to match subject-specific geometry, loads and boundary conditions. Calibration of the EMG-informed model involves adjusting physiological model parameters to fit experimental data. During this process we try to match the joint moments from multiple degrees of freedom produced by the EMG-informed model with those estimated from inverse dynamics, which for simplicity we just call the experimental joint moments. The selection of model parameters and their physiological range is important, as we want to avoid a numerical curve fitting exercise. A non-linear optimisation is used to find parameters that best-match inverse dynamics joint moments across a wide range of tasks (n = 4 or 5) and parameters are kept within tight limits. A key point to make here is that following calibration, the parameters in the model are no longer adjusted, and the model is able to predict new trials that were not part of the calibration set [76]. More recent model incarnations ensure the predictions match the experimental joint moments at multiple joints (e.g. hip, knee, and ankle) and multiple degrees of freedom [108].

The models are most sensitive to the muscle-tendon units parameters of moment arms, tendon slack lengths, and to a lesser extent, the optimal fibre lengths [49]. Moment arms have a direct influence on the moment produced by each muscle, so accurate estimates of the muscles origin, insertion, and wrapping is critical, but often neglected due to the difficulty in scaling muscle-tendon geometry to experimental

data. We are developing tools within the Musculoskeletal Atlas Project to address some of these challenges and make it easy to generate accurate models of muscle moment arms (see Sect. 3).

Tendon slack lengths and optimal fibre lengths are difficult to measure experimentally. Therefore, we use a two step numerical method to adjust these parameters for each muscle to ensure that the muscle fibre is acting on the ascending limb of the force-length curve [139]. First, we adjust the tendon slack and optimal fibre lengths for the persons anthropometry using the scaled OpenSim anatomical model [139], and second we further calibrate these parameters to best-fit the experimental joint moments. This muscle-parameter scaling and calibration is often overlooked by the modelling community, but has a profound influence on the force estimates of a simulation.

Pennation angles have less of an effect on the predicted forces and moments, but have the potential to be estimated from ultrasound imaging. Maximum isometric muscle force can also be scaled to fit physiological cross sectional areas of muscles from an accurate geometric model (as in Sect. 2) or measurements from medical imaging data.

Activation parameters can also be adjusted in this calibration and we include the non-linear EMG-to-force shape factor, A, as well as the parameters $C_1$ and $C_2$ that alter the recursive muscle excitation filter coefficients. These activation parameters might be expected to change due to different EMG electrode placement and are thus subject to day-to-day variation. Muscle parameters are not expected to change from day-to-day, so further calibrations performed on an individual across a time period of weeks should only adjust muscle activation parameters. Indeed, we have shown model predictions of equal performance when testing subjects across multiple weeks using the same parameters from the initial calibration (knee joint moment prediction: $R^2 = 0.91$ [76].

At this point the calibrated EMG-informed model is ready to run in open-loop to predict muscle forces, joint moments, joint contact forces etc., driven purely by experimental joint angles and EMG-derived excitations. To date this has been the principle way we have employed the EMG-informed models [15, 41, 76, 108, 140, 141]. However, recent developments can account for problems associated with measuring EMGs.

## 5.7   Accounting for Missing EMGs and Errors in EMGs

EMG signals are affected by cross talk and variations in the EMG electrode placements, and there is loss of neural signal content via EMG signal processing. In addition, it is not possible to record EMGs from all muscles. So our recent efforts have been directed to accommodating missing EMGs and EMG measurement errors [109, 110, 137]. This is achieved by closing the loop on the calibrated EMG-informed model running in open-loop to estimate the excitations of missing EMGs and adjusts the EMG-derived excitations to obtain the best-fit to the experimental data; that is

minimising the least squares errors in predicting both the experimental joint moments and the EMG linear envelopes. Since these methods can select any set of excitation patterns we also minimize total excitations squared, but other criteria could be used, e.g. minimize energy expenditure or joint contact forces. We have begun to call these approaches Hybrid EMG-informed models [109, 110, 137].

Estimating the missing and adjusting the EMG-derived excitations is performed by either static optimisation or synergy based methods. Static optimisation is used to estimate all excitations on a time-point-by-time-point basis, while best-fitting both the experimental joint moments and EMG linear envelopes [110]. Even though this methods excitations very well track the measured EMGs, the same cannot be assumed for the excitations patterns of muscles without EMGs, which are unknown. A method is required to further constrain the excitations solution to follow the underlying neural patterns that people use to move.

Synergy based methods aim to derive the simple underlying synergistic primitives that people use to construct all their muscles activation patterns for movement. In these approaches non-negative matrix factorization is employed to extract a small set of excitation primitives (typically 5 to 6 primitives) and muscle weightings from the recorded EMG linear envelopes. The selected excitation primitives and muscle weightings account for over 90% of variance in EMG data [2, 88, 109, 137]. Muscle excitations to drive the EMG-informed model are then reconstructed by the matrix product of the muscle weightings with the excitation primitives. Optimisation adjusts the muscle weightings to ensure the EMG-informed model well predicts the experimental joint moments and EMG linear envelopes on a trial-by-trial basis [137].

## 5.8 Validation

As with any computational model, it is imperative to validate a model against experimental data. Because it is not feasible to measure muscle forces in vivo, we have relied on indirect validation by comparing model predictions of joint moments with those estimated from inverse dynamics. However, because joint contact forces are dominated by muscle forces, in vivo contact force measurements from patients with an instrumented knee prosthesis provide another valuable source of experimental data for validation [41, 140] (see Grand Knee Challenge - https://simtk.org/home/kneeloads [37]) (Fig. 21). We have used this method to validate the open-loop [41, 140] and synergy based [137] EMG-informed models.

## 5.9 Application

Muscle activation patterns change in response to injury or neurological disorders, so EMG-informed models are well suited to understand muscle function in these cases. As stated previously, muscle forces are the primary determinant of joint contact
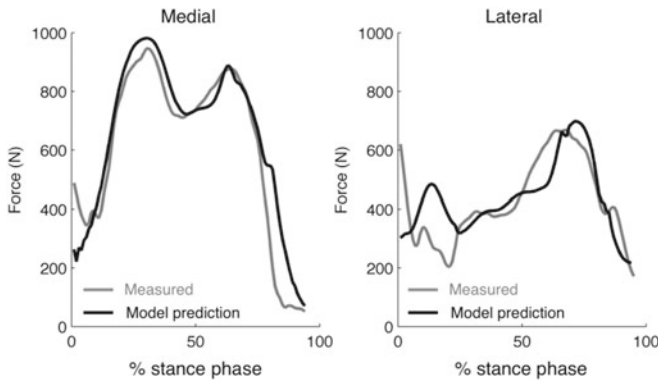
**Fig. 21** Medial and lateral tibiofemoral joint contact force predictions using an EMG-informed model running in open-loop compared to measured contact forces from an instrumented knee implant [41, 140]

force; so accounting for individual muscle activation patterns provides insight to joint loading and stress distribution in the articular cartilage. This has important implications for understanding the onset and development of osteoarthritis, which is believed to have a mechanical pathway. People suffering from knee osteoarthritis have altered muscle activation patterns that include high levels of co-contraction of the hamstrings, quadriceps and gastrocnemii and higher levels activation of lateral versus medial knee muscles [46, 58, 61, 62]. We have also observed high levels of co-contraction in patients who have undergone arthroscopic partial meniscectomy [125]. Using an EMG-informed model of the knee, we have shown how co-contraction increases knee joint contact loads, particularly in the lateral compartment of the tibiofemoral joint, when other models have predicted condylar lift off [140, 141] (Fig. 21). These findings have implications for understanding the load exposure of articular cartilage and how mechanics influence cartilage homeostasis.

Muscle forces obtained from an EMG-informed model can also provide input for finite element models to calculate stress distributions in musculoskeletal tissues. We are using this approach to investigate hip joint bone density distributions [34] and knee joint biomechanics in larger population-based studies to understand hip and knee osteoarthritis and patellofemoral pain [5], the latter being a common knee disorder. Mechanical stress in the patellofemoral joint is hypothesised to be a cause of dull, achy retro-patellar pain [94]. However, testing this hypothesis is difficult as many factors influence patellofemoral joint cartilage stress, including; the geometry of the articulating surfaces, the kinematics of the joint, and the distribution of quadriceps muscle forces. We have estimated muscle forces during walking and running in a large cohort of patellofemoral pain subjects and pain-free controls [6] and shown that patients with pain have higher normalised muscle forces compared to pain-free controls. These are hypothesised to increase cartilage stresses and might also be causing pain.

## *5.10 PET-CT Imaging*

Our long-term goal is to use computational models to predict clinical outcomes from interventions and correlate tissue-level stresses with pain and function. Estimating tissue function is difficult, however, some medical imaging modalities provide a snapshot of tissue function with regard to metabolism. In mineralised bone, areas with high metabolic activity receive the richest sensory and sympathetic innervation, and therefore play an important role in the generation of skeletal pain [79, 115]. Quantifying metabolic activity with functional imaging techniques might offer us a biological metric of bone-related pain that we can use to compare with mechanical stresses. Positron Emission Tomography (PET) is a functional imaging modality that can high-light areas of increased bone metabolic activity and remodelling, in response to local mechanical stresses or injury. Traditionally, $^{18}$F-NaF PET has been used in the field of oncology; however, recent studies have suggested that $^{18}$F-NaF PET is promising for the evaluation of orthopaedic conditions, such as in the assessment of bone fracture healing [60] and the identification of sources of back pain [74]. These relationships exist as the $^{18}$F-NaF tracer localises in areas of bone mineralisation or newly exposed mineralised surface, indicating regions of both osteoblast and osteoclast activity [127]. We acquired MR and $^{18}$F-NaF PET-CT images of 22 patients with chronic patellofemoral pain (>1 year) to assess the regions of bone metabolic activity and determine whether changes in MR signal intensity correlated to $^{18}$F uptake [32]. Taking CT scans at the same time as the PET scans enables accurate co-location of skeletal structures, hence the term PET-CT. Of the 22 patients, 14 exhibited at least one region of increased tracer uptake on PET that did not correspond to bone marrow edema or cartilage damage on MRI. We also found a correlation between increasing tracer uptake and increasing pain intensity ($r^2 = 0.55$) [32] (Fig. 22).
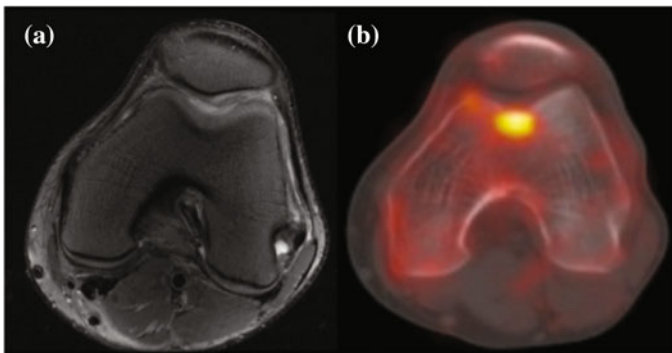


**Fig. 22** Axial MRI of patellofemoral pain patient **a**, showing no abnormalities within bone or cartilage of the patellofemoral joint. Corresponding PET-CT image of the same subject **b** illustrating a hotspot of high metabolic activity in the trochlear groove of the femur

The most common location of increased metabolic activity was the subchondral region on the lateral facet of the patella. In general, abnormalities in the bone and cartilage detected by MRI (e.g. subchondral cysts, bone marrow edema, cartilage damage) correlated with increased tracer uptake in the $^{18}$F-NaF PET-CT images [32]. However, there were a number of regions of increased tracer uptake, indicating increased bone metabolic activity that did not have any structural damage detected by MRI. These findings suggest that $^{18}$F-NaF PET-CT and MRI provide different information about the joint and perhaps $^{18}$F-NaF PET-CT can be used to detect early changes in metabolic activity prior to the development of structural damage in the bones and cartilage. We hypothesise that regions of increased metabolic activity in the bone of PF pain patients correlate to regions of increased mechanical stresses in the tissue [32], which are also related to the development of pain. To test this hypothesis, we will use muscle forces from our EMG-informed model as input to a finite element model of the joint to estimate mechanical stresses throughout the bone and cartilage of the PF joint.

## 5.11 Conclusions

In summary, EMG-informed musculoskeletal modelling provides a robust methods to estimate muscle and joint forces, taking into account individual muscle activation patterns that might be important for understanding musculoskeletal injury and disease. When coupled with finite element models and imaging modalities to non-invasively estimate tissue stress and tissue function, these methods provide us with tools to understand the mechanical aetiology of musculoskeletal injury and disease. These advancements have created avenues for biomedical researchers and those interested in mechanobiology to gain valuable insight and knowledge regarding the form and function of the musculoskeletal system.

# References

1. M.J. Ackerman, The visible human project. Proc. IEEE **86**(3), 504–511 (1998)
2. J.L. Allen, R.R. Neptune, Three-dimensional modular control of human walking. J. Biomech. **45**(12), 2157–63 (2012)
3. D.C. Barratt, C.S. Chan, P.J. Edwards, G.P. Penney, M. Slomczykowski, T.J. Carter, D.J. Hawkes, Instantiation and registration of statistical shape models of the femur and pelvis using 3d ultrasound imaging. Med. Image Anal. **12**, 358–374 (2008)
4. F.T. Bergmann, H.M. Sauro, SBW - a modular framework for systems biology, in *WSC '06, Winter Simulation Conference*, Monterey, California (2009)
5. T.F. Besier, G.E. Gold, G.S. Beaupre, S.L. Delp, A modeling framework to estimate patellofemoral joint cartilage stress in-vivo. Med. Sci. Sports Exerc. **37**(11), 1924–1930 (2005)
6. T.F. Besier, M. Fredericson, G.E. Gold, G.S. Beaupre, S.L. Delp, Knee muscle forces during walking and running in patellofemoral pain patients and pain-free controls. J. Biomech. **42**(7), 898–905 (2009)
7. B.J. Bornstein, S.M. Keating, A. Jouraku, M. Hucka, LibSBML: an API Library for SBML. Bioinformatics **24**(6), 880–881 (2008)
8. C.P. Bradley, A.J. Pullan, P.J. Hunter, Geometric modeling of the human torso using cubic hermite elements. Ann. Biomed. Eng. **25**(1), 96–111 (1997)
9. W.A.M. Brekelmans, H.W. Poort, T.J.J.H. Slooff, A new method to analyse the mechanical behaviour of skeletal parts. Acta Orthop. Scand. **43**(5), 301–317 (1972)
10. D.J. Brooks, *BioSignalML: an abstract model for physiological time-series data*. Thesis, ResearchSpace@Auckland (2013)
11. D.J. Brooks, P.J. Hunter, B.H. Smaill, M.R. Titchener, BioSignalML x2014; a meta-model for biosignals, in *2011 Annual International Conference of the IEEE Engineering in Medicine and Biology Society,EMBC*, pp. 5670–5673 (2011)
12. R. Bryan, P.B. Nair, M. Taylor, Use of a statistical model of the whole femur in a large scale, multi-model study of femoral neck fracture risk. J. Biomech. **42**(13), 2171–2176 (2009)
13. R. Bryan, P.S. Mohan, A. Hopkins, F. Galloway, M. Taylor, P.B. Nair, Statistical modelling of the whole human femur incorporating geometric and material properties. Med. Eng. Phys. **32**(1), 57–65 (2010)
14. T.S. Buchanan, D.G. Lloyd, Muscle activity is different for humans performing static tasks which require force control and position control. Neurosci. Lett. **194**(1–2), 61–64 (1995)
15. T.S. Buchanan, D.G. Lloyd, K. Manal, T.F. Besier, Neuromusculoskeletal modeling: estimation of muscle forces and joint moments and movements from measurements of neural command. J. Appl. Biomech. **20**(4), 367–395 (2004)
16. T.S. Buchanan, D.G. Lloyd, K. Manal, T.F. Besier, Estimation of muscle forces and joint moments using a forward-inverse dynamics model. Med. Sci. Sports Exerc. **37**(11), 1911–1916 (2005)
17. D.R. Carter, G.S. Beaupre, *Skeletal Function and Form. Mechanobiology of Skeletal Development, Aging and Regeneration* (Cambridge University Press, Cambridge, 2001)
18. D.R. Carter, M.C. Van Der Meulen, G.S. Beaupre, Mechanical factors in bone growth and development. Bone **18**(1 Suppl), 5S–10S (1996)
19. D.R. Carter, G.S. Beaupre, M. Wong, R.L. Smith, T.P. Andriacchi, D.J. Schurman, R.L. Smith, The mechanobiology of articular cartilage development and degeneration. Clin. Orthop. **1**(427 Suppl), S69–S77 (2004)

20. G.R. Christie, P.M.F. Nielsen, S.A. Blackett, C.P. Bradley, P.J. Hunter, FieldML: concepts and implementation. Philos. Trans. Ser. A Math. Phys. Eng. Sci. **367**(1895), 1869–1884 (2009)

21. D.D. Cody, G.J. Gross, F.J. Hou, H.J. Spencer, S.A. Goldstein, D.P. Fyhrie, Femoral strength is better predicted by finite element models than QCT and DXA. J. Biomech. **32**(10), 1013–1020 (1999)

22. M.T. Cooling, V. Rouilly, G. Misirli, J. Lawson, T. Yu, J. Hallinan, A. Wipat, Standard virtual biological parts: a repository of modular modeling components for synthetic biology. Bioinformatics **26**(7), 925–931 (2010)

23. T.F. Cootes, C.J. Taylor, D.H. Cooper, J. Graham et al., Active shape models-their training and application. Comput. Vis. Image Underst. **61**, 38–59 (1995)

24. D.M. Corcos, G.L. Gottlieb, M.L. Latash, G.L. Almeida, G.C. Agarwal, Electromechanical delay: an experimental artifact. J. Electromyogr. Kinesiol. **2**(2), 59–68 (1992)

25. M. Courtot, N. Juty, C. Knpfer, D. Waltemath, A. Zhukova, A. Drger, M. Dumontier, A. Finney, M. Golebiewski, J. Hastings, S. Hoops, S. Keating, D.B. Kell, S. Kerrien, J. Lawson, A. Lister, J. Lu, R. Machne, P. Mendes, M. Pocock, N. Rodriguez, A. Villeger, D.J. Wilkinson, S. Wimalaratne, C. Laibe, M. Hucka, N.L. Novre, Controlled vocabularies and semantics in systems biology. Mol. Syst. Biol. **7**(543), 1–12 (2011)

26. A.A. Cuellar, C.M. Lloyd, P.F. Nielsen, D.P. Bullivant, D.P. Nickerson, P.J. Hunter, An overview of cellML 1.1, a biological model description language. Simulation **79**(12), 740–747 (2003)

27. S. Dambreville, Y. Rathi, A. Tannenbaum, A framework for image segmentation using shape models and kernel space shape priors. IEEE Trans. Pattern Anal. Mach. Intell. **30**(8), 1385–1399 (2008)

28. S.J. De Serres, T.E. Milner, Wrist muscle activation patterns and stiffness associated with stable and unstable mechanical loads. Exp. Brain Res. **86**(2), 451–458 (1991)

29. S.L. Delp, F.C. Anderson, A.S. Arnold, P. Loan, A. Habib, C.T. John, E. Guendelman, D.G. Thelen, OpenSim: open-source software to create and analyze dynamic simulations of movement. IEEE Trans. Biomed. Eng. **54**(11), 1940–1950 (2007)

30. C.J. Donnelly, D.G. Lloyd, B.C. Elliott, J.A. Reinbolt, Optimizing whole body kinematics to minimize valgus knee loading during sidestepping: implications for ACL injury risk. J. Biomech. **45**(8), 1491–1497 (2012)

31. R.L. Drake (ed.), *Terminologia Anatomica: International Anatomical Terminology*, 2nd edn. (Thieme, Stuttgart, 2011)

32. C.E. Draper, A. Quon, M. Fredericson, T.F. Besier, S.L. Delp, G.S. Beaupre, G.E. Gold, Comparison of MRI and (18) F-NaF PET/CT in patients with patellofemoral pain. J. Magn. Reson. Imaging **36**(4), 928–932 (2012)

33. I.L. Dryden, K.V. Mardia, *Statistical Shape Analysis*, 1st edn. (Wiley, Oxford, 2001)

34. J. Fernandez, M. Sartori, D. Lloyd, J. Munro, V. Shim, Bone remodelling in the natural acetabulum is influenced by muscle force-induced bone stress. Int. J. Numer. Method Biomed. Eng. **30**(1), 28–41 (2014)

35. J.W. Fernandez, P. Mithraratne, S.F. Thrupp, M.H. Tawhai, P.J. Hunter, Anatomically based geometric modelling of the musculo-skeletal system and other organs. Biomech. Model. Mechanobiol. **2**(3), 139–155 (2004)

36. J.W. Fernandez, A. Ho, S. Walt, I.A. Anderson, P.J. Hunter, A cerebral palsy assessment tool using anatomically based geometries and free-form deformation. Biomech. Model. Mechanobiol. **4**(1), 39–56 (2005)

37. B.J. Fregly, T.F. Besier, D.G. Lloyd, S.L. Delp, S.A. Banks, M.G. Pandy, D.D. D'Lima, Grand challenge competition to predict in vivo knee loads. J. Orthop. Res. **30**(4), 503–513 (2012)

38. J. Fripp, S. Crozier, S.K. Warfield, S. Ourselin, Automatic segmentation of the bone and extraction of the bone-cartilage interface from magnetic resonance images of the knee. Phys. Med. Biol. **52**(6), 1617–1631 (2007)

39. B.A. Garner, M.G. Pandy, The obstacle-set method for representing muscle paths in musculoskeletal models. Comput. Methods Biomech. Biomed. Eng. **3**(1), 1–30 (2000)

40. A. Garny, D.P. Nickerson, J. Cooper, R. Weber dos Santos, A.K. Miller, S. McKeever, P.M.F. Nielsen, P.J. Hunter, CellML and associated tools and techniques. Philos. Trans. Ser. A Math. Phys. Eng. Sci. **366**(1878), 3017–3043 (2008)

41. P. Gerus, M. Sartori, T.F. Besier, B.J. Fregly, S.L. Delp, S.A. Banks, M.G. Pandy, D.D. D'Lima, D.G. Lloyd, Subject-specific knee joint geometry improves predictions of medial tibiofemoral contact forces. J. Biomech. **46**(16), 2778–2786 (2013)

42. H. Gray, *Gray's Anatomy: The Anatomical Basis of Clinical Practice*, 40th edn. (Churchill-Livingstone, Elsevier, 2008)

43. J. Gregory, R.M. Aspden, Femoral geometry as a risk factor for osteoporotic hip fracture in men and women. Med. Eng. Phys. **30**(10), 1275–1286 (2008)

44. A.C. Guimaraes, W. Herzog, M. Hulliger, Y.T. Zhang, S. Day, Effects of muscle length on the EMG-force relationship of the cat soleus muscle studied using non-periodic stimulation of ventral root filaments. J. Exp. Biol. **193**, 49–64 (1994)

45. H. Hatze, Estimation of myodynamic parameter values from observations on isometrically contracting muscle groups. Eur. J. Appl. Physiol. Occup. Physiol. **46**(4), 325–338 (1981)

46. T.L. Heiden, D.G. Lloyd, T.R. Ackland, Knee joint kinematics, kinetics and muscle co-contraction in knee osteoarthritis patient gait. Clin. Biomech. (Bristol) **24**(10), 833–841 (2009)

47. T. Heidlauf, O. Rohrle, Modeling the chemoelectromechanical behavior of skeletal muscle using the parallel open-source software library OpenCMISS. Comput. Math. Methods Med. **2013**, 1–14 (2013)

48. T. Heimann, H.-P. Meinzer, Statistical shape models for 3D medical image segmentation: a review. Med. Image Anal. **13**(4), 543–563 (2009)

49. R. Heine, K. Manal, T.S. Buchanan, Using Hill-type muscle models and EMG data in a forward dynamic analysis of joint moment: evaluation of critical parameters. J. Mech. Med. Biol. **3**(2), 169–186 (2003)

50. R. Henkel, L. Endler, A. Peters, N.L. Novre, D. Waltemath, Ranked retrieval of computational biology models. BMC Bioinform. **11**(1), 1–12 (2010)

51. W. Herzog, J. Sokolosky, Y.T. Zhang, A.C. Guimaraes, Emg-force relation in dynamically contracting cat plantaris muscle. J. Electromyogr. Kinesiol. **8**(3), 147–155 (1998)

52. W. Herzog, D. Longino, A. Clark, The role of muscles in joint adaptation and degeneration. Langenbecks Arch. Surg. **388**(5), 305–315 (2003)

53. A.V. Hill, The heat of shortening and the dynamic constants of muscle. Proc. R. Soc. Lond. B **126**(843), 136–195 (1938)

54. A.L. Hof, J. Van den Berg, EMG to force processing I: an electrical analogue of the Hill muscle model. J. Biomech. **14**(11), 747–758 (1981)

55. N. Hogan, Adaptive control of mechanical impedance by coactivation of antagonist muscle. IEEE Trans. Autom. Control **29**(8), 681–690 (1984)

56. G. Holzer, G. Von Skrbensky, L.A. Holzer, W. Pichl, Hip fractures and the contribution of cortical versus trabecular bone to femoral neck strength. J. Bone Miner. Res. **24**, 468–474 (2009)

57. S. Hoops, S. Sahle, R. Gauges, C. Lee, J. Pahle, N. Simus, M. Singhal, L. Xu, P. Mendes, U. Kummer, COPASIa COmplex PAthway SImulator. Bioinformatics **22**(24), 3067–3074 (2006)

58. T. Hortobagyi, L. Westerkamp, S. Beam, J. Moody, J. Garry, D. Holbert, P. DeVita, Altered hamstring-quadriceps muscle balance in patients with knee osteoarthritis. Clin. Biomech. (Bristol) **20**(1), 97–104 (2005)

59. D.W. Howie, S.D. Neale, R. Stamenkov, M.A. McGee, D.J. Taylor, D.M. Findlay, Progression of acetabular periprosthetic osteolytic lesions measured with computed tomography. J. Bone Joint Surg. Am. **89**(8), 1818–1825 (2007)

60. W.K. Hsu, B.T. Feeley, L. Krenek, D.B. Stout, A.F. Chatziioannou, J.R. Lieberman, The use of 18F-fluoride and 18F-FDG PET scans to assess fracture healing in a rat femur model. Eur. J. Nucl. Med. Mol. Imaging **34**(8), 1291–1301 (2007)

61. C. Hubley-Kozey, K. Deluzio, M. Dunbar, Muscle co-activation patterns during walking in those with severe knee osteoarthritis. Clin. Biomech. (Bristol) **23**(1), 71–80 (2008)

62. C.L. Hubley-Kozey, K.J. Deluzio, S.C. Landry, J.S. McNutt, W.D. Stanish, Neuromuscular alterations during walking in persons with moderate knee osteoarthritis. J. Electromyogr. Kinesiol. **16**(4), 365–378 (2006)

63. M. Hucka, A. Finney, H.M. Sauro, H. Bolouri, J.C. Doyle, H. Kitano, A.P. Arkin, B.J. Bornstein, D. Bray, A. Cornish-Bowden, A.A. Cuellar, S. Dronov, E.D. Gilles, M. Ginkel, V. Gor, I.I. Goryanin, W.J. Hedley, T.C. Hodgman, J.H. Hofmeyr, P.J. Hunter, N.S. Juty, J.L. Kasberger, A. Kremling, U. Kummer, N. Le Novre, L.M. Loew, D. Lucio, P. Mendes, E. Minch, E.D. Mjolsness, Y. Nakayama, M.R. Nelson, P.F. Nielsen, T. Sakurada, J.C. Schaff, B.E. Shapiro, T.S. Shimizu, H.D. Spence, J. Stelling, K. Takahashi, M. Tomita, J. Wagner, J. Wang, The systems biology markup language (SBML): a medium for representation and exchange of biochemical network models. Bioinformatics **19**(4), 524–531 (2003)

64. P.A. Huijing, Important experimental factors for skeletal muscle modelling: non-linear changes of muscle length force characteristics as a function of degree of activity. Eur. J. Morphol. **34**(1), 47–54 (1996)

65. R. Huiskes, E.Y.S. Chao, A survey of finite element analysis in orthopedic biomechanics − the first decade. J. Biomech. **16**(6), 385–409 (1983)

66. R. Huiskes, S.J. Hollister, From structure to process, from organ to cell: recent developments of FE-analysis in orthopaedic biomechanics. J. Biomech. Eng. **115**(4B), 520–527 (1993)

67. P.J. Hunter, The IUPS Physiome Project: a framework for computational physiology. Prog. Biophys. Mol. Biol. **85**(2–3), 551–569 (2004)

68. J.J. Jacobs, K.A. Roebuck, M. Archibeck, N.J. Hallab, T.T. Glant, Osteolysis: basic science. Clin. Orthop. Relat. Res. **1**(393), 71–77 (2001)

69. I. Jolliffe, Principal component analysis, in *Encyclopedia of Statistics in Behavioral Science*, vol. 3, 1st edn., ed. by B.S. Everitt, D.C. Howell (Wiley, 2005), pp. 1580–1584

70. D. Kainmueller, H. Lamecker, S. Zachow, H.-C. Hege, An articulated statistical shape model for accurate hip joint segmentation. EMBC 2009. Annu. Int. Conf. IEEE **2009**, 6345–6351 (2009)

71. J.H. Keyak, J.M. Meagher, H.B. Skinner Jr., C.D. Mote, Automated three-dimensional finite element modelling of bone: a new method. J. Biomed. Eng. **12**(5), 389–397 (1990)

72. J.H. Keyak, S.A. Rossi, K.A. Jones, H.B. Skinner, Prediction of femoral fracture load using automated finite element modeling. J. Biomech. **31**(2), 125–133 (1998)

73. J.H. Keyak, S.A. Rossi, K.A. Jones, C.M. Les, H.B. Skinner, Prediction of fracture location in the proximal femur using finite element models. Med. Eng. Phys. **23**(9), 657–664 (2001)

74. R. Lim, F.H. Fahey, L.A. Drubach, L.P. Connolly, S.T. Treves, Early experience with fluorine-18 sodium fluoride bone PET in young patients with back pain. J. Pediatr. Orthop. **27**(3), 277–282 (2007)

75. C.M. Lloyd, J.R. Lawson, P.J. Hunter, P.F. Nielsen, The CellML Model Repository. Bioinformatics **24**(18), 2122–2123 (2008)

76. D.G. Lloyd, T.F. Besier, An EMG-driven musculoskeletal model to estimate muscle forces and knee joint moments in vivo. J. Biomech. **36**(6), 765–776 (2003)

77. D.G. Lloyd, T.S. Buchanan, Strategies of muscular support of varus and valgus isometric loads at the human knee. J. Biomech. **34**(10), 1257–1267 (2001)

78. A.C. Looker, T.J. Beck, E.S. Orwoll, Does body size account for gender differences in femur bone density and geometry? J. Bone Miner. Res. **16**, 1291–1299 (2001)

79. D.B. Mach, S.D. Rogers, M.C. Sabino, N.M. Luger, M.J. Schwei, J.D. Pomonis, C.P. Keyser, D.R. Clohisy, D.J. Adams, P. O'Leary, P.W. Mantyh, Origins of skeletal pain: sensory and sympathetic innervation of the mouse femur. Neuroscience **113**(1), 155–166 (2002)

80. K. Manal, T.S. Buchanan, A one-parameter neural activation to muscle activation model: estimating isometric joint moments from electromyograms. J. Biomech. **36**(8), 1197–1202 (2003)

81. P.M. Mayhew, C.D.L. Thomas, J.G. Clement, N. Loveridge, T.J. Beck, W. Bonfield, C.J. Burgoyne, J. Reeve, Relation between age, femoral neck cortical stability, and hip fracture risk. The Lancet **366**, 129–135 (2005)

82. A.K. Miller, J. Marsh, A. Reeve, A. Garny, R. Britten, M. Halstead, J. Cooper, D.P. Nickerson, P.F. Nielsen, An overview of the CellML API and its implementation. BMC Bioinform. **11**(178), 1–12 (2010)

83. H.S. Milner-Brown, R.B. Stein, R. Yemm, Changes in firing rate of human motor units during linearly changing voluntary contractions. J. Physiol. **230**(2), 371–390 (1973)

84. T. Miyazaki, M. Wada, H. Kawahara, M. Sato, H. Baba, S. Shimada, Dynamic load at baseline can predict radiographic disease progression in medial compartment knee osteoarthritis. Ann. Rheum. Dis. **61**(7), 617–622 (2002)

85. J.T. Munro, I.A. Anderson, C.G. Walker, V.B. Shim, Finite element analysis of retroacetabular osteolytic defects following total hip replacement. J. Biomech. **46**(14), 2529–2533 (2013)

86. T. Nakamura, C.H. Turner, T. Yoshikawa, C.W. Slemenda, M. Peacock, D.B. Burr, Y. Mizuno, H. Orimo, Y. Ouchi, C.C. Johnston Jr., Do variations in hip geometry explain differences in hip fracture risk between Japanese and white Americans? J. Bone Miner. Res. **9**, 1071–1076 (1994)

87. M.L. Neal, M.T. Cooling, L.P. Smith, C.T. Thompson, H.M. Sauro, B.E. Carlson, D.L. Cook, J.H. Gennari, A reappraisal of how to build modular, reusable models of biological systems. PLoS Comput. Biol. **10**(10), 1–7 (2014)

88. R.R. Neptune, D.J. Clark, S.A. Kautz, Modular control of human walking: a simulation study. J. Biomech. **42**(9), 1282–1287 (2009)

89. D. Nickerson, M. Nash, P. Nielsen, N. Smith, P. Hunter, Computational multiscale modeling in the iups physiome project: modeling cardiac electromechanics. IBM J. Res. Dev. **50**(6), 617–630 (2006)

90. D.P. Nickerson, J.R. Terkildsen, K.L. Hamilton, P.J. Hunter, A tool for multi-scale modelling of the renal nephron. Interface Focus **1**(3), 417–425 (2011)

91. N.L. Novre, A. Finney, M. Hucka, U.S. Bhalla, F. Campagne, J. Collado-Vides, E.J. Crampin, M. Halstead, E. Klipp, P. Mendes, P. Nielsen, H. Sauro, B. Shapiro, J.L. Snoep, H.D. Spence, B.L. Wanner, Minimum information requested in the annotation of biochemical models (MIRIAM). Nat. Biotechnol. **23**(12), 1509–1515 (2005)

92. N.L. Novre, B. Bornstein, A. Broicher, M. Courtot, M. Donizelli, H. Dharuri, L. Li, H. Sauro, M. Schilstra, B. Shapiro, J.L. Snoep, M. Hucka, Biomodels database: a free, centralized database of curated, published, quantitative kinetic models of biochemical and cellular systems. Nucleic Acids Res. **34**(suppl 1), D689–D691 (2006)

93. K. Oberhofer, K. Mithraratne, N.S. Stott et al., Anatomically-based musculoskeletal modeling: prediction and validation of muscle deformation during walking. Vis. Comput. **25**, 843 (2009). doi:10.1007/s00371-009-0314-8

94. R.E. Outerbridge, The etiology of chondromalacia patellae. J. Bone Joint. Surg. Br. **43–B**, 752–757 (1961)

95. J. Partanen, T. Jms, P. Jalovaara, Influence of the upper femur and pelvic geometry on the risk and type of hip fractures. J. Bone Miner. Res. **16**, 1540–1546 (2001)

96. M. Peacock, K.A. Buckwalter, S. Persohn, T.N. Hangartner, M.J. Econs, S. Hui, Race and sex differences in bone mineral density and geometry at the femur. Bone **45**, 218–225 (2009)

97. D.R. Pedersen, R.A. Brand, C. Cheng, J.S. Arora, Direct comparison of muscle force predictions using linear and nonlinear programming. J. Biomech. Eng. **109**(3), 192–199 (1987)

98. D.A. Pierce, D.L. Preston, Radiation-related cancer risks at low doses among atomic bomb survivors. Radiat. Res. **154**, 178–186 (2000)

99. R.P. Pitto, A. Hayward, C. Walker, V.B. Shim, Femoral bone density changes after total hip arthroplasty with uncemented taper-design stem: a five year follow-up study. Int. Orthop. **34**(6), 783–787 (2010)

100. J.R. Potvin, R.W. Norman, S.M. McGill, Mechanically corrected emg for the continuous estimation of erector spinae muscle loading during repetitive lifting. Eur. J. Appl. Physiol. Occup. Physiol. **74**(1–2), 119–132 (1996)

101. P.E. Purdue, P. Koulouvaris, H.G. Potter, B.J. Nestor, T.P. Sculco, The cellular and molecular biology of periprosthetic osteolysis. Clin. Orthop. Relat. Res. **454**, 251–61 (2007)

102. T.A. Quinn, S. Granite, M.A. Allessie, C. Antzelevitch, C. Bollensdorff, G. Bub, R.A.B. Burton, E. Cerbai, P.S. Chen, M. Delmar, D. DiFrancesco, Y.E. Earm et al., Minimum information about a cardiac electrophysiology experiment (MICEE): Standardised reporting for model reproducibility, interoperability, and data sharing. Prog. Biophys. Mol. Biol. **107**(1), 4–10 (2011)
103. K.T. Rajamani, M.A. Styner, H. Talib, G. Zheng, L.P. Nolte, M.A. Gonzalez Ballester, Statistical deformable bone models for robust 3D surface extrapolation from sparse data. Med. Image Anal. **11**, 99–109 (2007)
104. A.J. Ramme, A.J. Criswell, B.R. Wolf, V.A. Magnotta, N.M. Grosland, EM segmentation of the distal femur and proximal tibia: a high-throughput approach to anatomic surface generation. Ann. Biomed. Eng. **39**, 1555–1562 (2011)
105. M.M. Rehani, G. Bongartz, W. Kalender, Managing X-ray dose in computed tomography. ICRP special task force report. Ann. ICRP **30**, 7–45 (2000)
106. N. Rodriguez, M. Donizelli, N.L. Novre, SBMLeditor: effective creation of models in the Systems Biology Markup Language (SBML). BMC Bioinform. **8**(79), 1–8 (2007)
107. D. Rueckert, A.F. Frangi, J.A. Schnabel, Automatic construction of 3D statistical deformation models of the brain using nonrigid registration. IEEE Trans. Med. Imaging **22**(8), 1014–1025 (2003)
108. M. Sartori, M. Reggiani, D. Farina, D.G. Lloyd, Emg-driven forward-dynamic estimation of muscle force and joint moment about multiple degrees of freedom in the human lower extremity. PLoS ONE **7**(12), 1–11 (2012)
109. M. Sartori, L. Gizzia, D.G. Lloyd, D. Farina, A musculoskeletal model of human locomotion driven by a low dimensional set of impulsive excitation primitives. Front. Comput. Neurosci. **7**(79), 1–22 (2013)
110. M. Sartori, D. Farina, D.G. Lloyd, Hybrid neuromusculoskeletal modeling to best track joint moments using a balance between muscle excitations derived from electromyograms and optimization. J. Biomech. **47**(15), 3613–3621 (2014)
111. O.D. Schipplein, T.P. Andriacchi, Interaction between active and passive knee stabilizers during level walking. J. Orthop. Res. **9**(1), 113–119 (1991)
112. R. Schmidt, L. Muller, A. Kress, H. Hirschfelder, A. Aplas, R.P. Pitto, A computed tomography assessment of femoral and acetabular bone changes after total hip arthroplasty. Int. Orthop. (SICOT) **26**(5), 299–302 (2002)
113. H. Seim, D. Kainmueller, M. Heller, H. Lamecker, S. Zachow, H.C. Hege, Automatic segmentation of the pelvic bones from ct data based on a statistical shape model, in *EG VCBM'08 Proceedings of the First Eurographics conference on Visual Computing for Biomedicine* (2008)
114. A. Seireg, R.J. Arvikar, A mathematical model for evaluation of forces in lower extremeties of the musculo-skeletal system. J. Biomech. **6**(3), 313–326 (1973)
115. M.A. Sevcik, N.M. Luger, D.B. Mach, M.A. Sabino, C.M. Peters, J.R. Ghilardi, M.J. Schwei, H. Rohrich, C. De Felipe, M.A. Kuskowski, P.W. Mantyh, Bone cancer pain: the effects of the bisphosphonate alendronate on pain, skeletal remodeling, tumor growth and tumor necrosis. Pain **111**(1–2), 169–180 (2004)
116. M.A. Sherman, A. Seth, S.L. Delp, Simbody: multibody dynamics for biomedical research. Iutam Symp. Hum. Body Dyn. **2**, 241–261 (2011)
117. V.B. Shim, R.P. Pitto, R.M. Streicher, P.J. Hunter, I.A. Anderson, The use of sparse CT datasets for auto-generating accurate FE models of the femur and pelvis. J. Biomech. **40**(1), 26–35 (2007)
118. V.B. Shim, R.P. Pitto, R.M. Streicher, P.J. Hunter, I.A. Anderson, Development and validation of patient-specific finite element models of the hemipelvis generated from a sparse CT data set. J. Biomech. Eng. **130**(5), 1–11 (2008)
119. V.B. Shim, M. Battley, I.A. Anderson, J.T. Munro, Validation of an efficient method of assigning material properties in finite element analysis of pelvic bone. Comput. Methods Biomech. Biomed. Eng. **18**(14), 1495–1499 (2015)
120. P. Shull, A. Silder, R. Shultz, T. Besier, S. Delp, M. Cutkosky, Six-week gait retraining program for knee osteoarthritis patients: Learning retention and symptom changes, in *American Society of Biomechanics* (2012)

121. N.P. Smith, D.P. Nickerson, E.J. Crampin, P.J. Hunter, Multiscale computational modelling of the heart. Acta Numer. **13**, 371–431 (2004)
122. V.M. Spitzer, D. Whitlock, A.L. Scherzinger, M.J. Ackerman, The visible-human (male and female). Radiology **197**, 533–533 (1995)
123. R. Stamenkov, D. Howie, J. Taylor, D. Findlay, M. McGee, G. Kourlis, A. Carbone, M. Burwell, Measurement of bone defects adjacent to acetabular components of hip replacement. Clin. Orthop. Relat. Res. **7**(412), 117–124 (2003)
124. E. Stindel, J.L. Briard, P. Merloz, S. Plaweski, F. Dubrana, C. Lefevre, J. Troccaz, Bone morphing: 3D morphological data for total knee arthroplasty. Comput. Aided Surg. **7**, 156–168 (2002)
125. D.L. Sturnieks, T.F. Besier, D.G. Lloyd, Muscle activations to stabilize the knee following arthroscopic partial meniscectomy. Clin. Biomech. (Bristol) **26**(3), 292–297 (2011)
126. A. Suinesiaputra, A.F. Frangi, T.A. Kaandorp, H.J. Lamb, J.J. Bax, J.H. Reiber, B.P. Lelieveldt, Automated detection of regional wall motion abnormalities based on a statistical model applied to multislice short-axis cardiac MR images. IEEE Trans. Med. Imaging **28**, 595–607 (2009)
127. J.E. Taunton, M.B. Ryan, D.B. Clement, D.C. McKenzie, D.R. Lloyd-Smith, B.D. Zumbo, A retrospective case-control analysis of 2002 running injuries. Br. J. Sports Med. **36**(2), 95–101 (2002)
128. A.A. Tax, J.J. Denier van der Gon, C.C. Gielen, C.M. van den Tempel, Differences in the activation of m. biceps brachii in the control of slow isotonic movements and isometric contractions. Exp. Brain Res. **76**(1), 55–63 (1989)
129. A.A. Tax, J.J. Denier van der Gon, C.J. Erkelens, Differences in coordination of elbow flexor muscles in force tasks and in movement tasks. Exp. Brain Res. **81**(3), 567–572 (1990)
130. A.A. Tax, J.J. Denier van der Gon, C.C. Gielen, M. Kleyne, Differences in central control of m. biceps brachii in movement tasks and force tasks. Exp. Brain Res. **79**(1), 138–142 (1990)
131. M. Theeuwen, C.C. Gielen, L.E. Miller, The relative activation of muscles during isometric contractions and low-velocity movements against a load. Exp. Brain Res. **101**(3), 493–505 (1994)
132. G.M. Treece, A.H. Gee, P.M. Mayhew, K.E.S. Poole, High resolution cortical bone thickness measurement from clinical CT data. Med. Image Anal. **14**(3), 276–290 (2010)
133. M. Viceconti, C. Zannoni, D. Testi, A. Cappello, A new method for the automatic mesh generation of bone segments from ct data. J. Med. Eng. Technol. **23**(2), 77–81 (1999)
134. M. Viceconti, M. Davinelli, F. Taddei, A. Cappello, Automatic generation of accurate subject-specific bone finite element models to be used in clinical studies. J. Biomech. **37**(10), 1597–1605 (2004)
135. J.H. Waarsing, R.M. Rozendaal, J.N. Verhaar, S.M.A. Bierma-Zeinstra, H. Weinans, A statistical model of shape and density of the proximal femur in relation to radiological and clinical OA of the hip. Osteoarthr. Cartil. **18**(6), 787–794 (2010)
136. D. Waltemath, R. Adams, D.A. Beard, F.T. Bergmann, U.S. Bhalla, R. Britten, V. Chelliah, M.T. Cooling, J. Cooper, E.J. Crampin, A. Garny et al., Minimum information about a simulation experiment (MIASE). PLoS Comput. Biol. **7**(4), 1–4 (2011)
137. J.P. Walter, A.L. Kinney, S.A. Banks, D.D. DLima, T.F. Besier, D.G. Lloyd, B.J. Fregly, Muscle synergies improve optimization prediction of knee contact forces during walking. J. Biomech. Eng. **136**(2), 1–9 (2014)
138. T.D. White, P.A. Folkens (eds.), *The Human Bone Manual*, 1st edn. (Elsevier, Amsterdam, 2005)
139. C.R. Winby, D.G. Lloyd, T.B. Kirk, Evaluation of different analytical methods for subject-specific scaling of musculotendon parameters. J. Biomech. **41**(8), 1682–1688 (2008)
140. C.R. Winby, D.G. Lloyd, T.F. Besier, T.B. Kirk, Muscle and external load contribution to knee joint contact loads during normal gait. J. Biomech. **42**(14), 2294–2300 (2009)
141. C.R. Winby, P. Gerus, T.B. Kirk, D.G. Lloyd, Correlation between emg-based co-activation measures and medial and lateral compartment loads of the knee during gait. Clin. Biomech. (Bristol) **28**(9–10), 1014–1019 (2013)

142. J.J. Woods, B. Bigland-Ritchie, Linear and non-linear surface emg/force relationships in human muscles. An anatomical/functional argument for the existence of both. Am. J. Phys. Med. **62**(6), 287–299 (1983)
143. T.A. Wren, D.P. Lindsey, G.S. Beaupre, D.R. Carter, Effects of creep and cyclic loading on the mechanical properties and failure of human achilles tendons. Ann. Biomed. Eng. **31**(6), 710–717 (2003)
144. P. Wriggers, L. Krstulovic-Opara, J. Korelc, Smooth C-1-interpolations for two-dimensional frictional contact problems. Int. J. Num. Methods Eng. **51**(12), 1469–1495 (2001)
145. T. Yu, C.M. Lloyd, D.P. Nickerson, M.T. Cooling, A.K. Miller, A. Garny, J.R. Terkildsen, J. Lawson, R.D. Britten, P.J. Hunter, P.M.F. Nielsen, The physiome model repository 2. Bioinformatics **27**(5), 743–744 (2011)
146. F.E. Zajac, Muscle and tendon: properties, models, scaling, and application to biomechanics and motor control. Crit. Rev. Biomed. Eng. **17**(4), 359–411 (1989)
147. R. Zdero, H. Bougherara, A. Dubov, S. Shah, P. Zalzal, A. Mahfud, E.H. Schemitsch, The effect of cortex thickness on intact femur biomechanics: a comparison of finite element analysis with synthetic femurs. Proc. Inst. Mech. Eng. [H] **224**, 831–840 (2010)
148. J. Zhang, D. Malcolm, J. Hislop-Jambrich, C.D.L. Thomas, P. Nielsen, Automatic meshing of femur cortical surfaces from clinical CT images. Mesh Process. Med. Image Anal. **2012**, 40–48 (2012)
149. J. Zhang, D. Malcolm, J. Hislop-Jambrich, C.D.L. Thomas, P.M.F. Nielsen, An anatomical region-based statistical shape model of the human femur. Comput. Methods Biomech. Biomed. Eng. Imaging Vis. **2**, 176–185 (2014)

# Review of "Universal" Rules Governing Bone Composition, Organization, and Elasticity Across Organizational Hierarchies

**Viktoria Vass, Claire Morin, Stefan Scheiner and Christian Hellmich**

**Abstract** "Universal" organizational patterns in bone are reviewed and presented, in terms of mathematically expressed rules concerning the composition and elasticity of a large variety of tissues. Firstly, experimental data sets gained from dehydration-demineralization tests, dehydration-deorganification tests, and dehydration-ashing tests are thoroughly analyzed. On this basis, bilinear relations can be identified, between the mass density of the extracellular bone matrix on the one hand, and the apparent mass densities of its basic constituents (water, hydroxyapatite, and organic matter), on the other hand. Secondly, the question as to how hydroxyapatite is distributed in bone tissue is addressed. To that end, mass and volume measurements gained from wet, dehydrated, and demineralized tissue samples, as well as optical densities provided by transmission electron microscopy, are studied, confirming a rule on how the mineral is partitioned between fibrillar and extrafibrillar spaces in the ultrastructure of bone. Thirdly, a swelling rule for hydrating collagen is validated through processing of experimental data from X-ray diffraction, vacuum drying, and mass measurements, quantifying the change of the bone tissue composition upon hydration. And fourthly, application of the mass conservation law to extracellular bone matrix considered as closed thermodynamic system, allows for studying the change of bone tissue composition during mineralization. Finally, these compositional rules, which are shown to be "universally" valid throughout the vertebrate kingdom, enter a micromechanical homogenization scheme for upscaling the experimentally accessible elastic properties of the elementary mechanical building blocks

V. Vass · S. Scheiner · C. Hellmich (✉)
Institute for Mechanics of Materials and Structures,
TU Wien – Vienna University of Technology, Vienna, Austria
e-mail: christian.hellmich@tuwien.ac.at

C. Morin
Ecole Nationale Supérieure des Mines de Saint Etienne,
CIS-EMSE-INSERM U1059, SAINBIOSE, F-42023 Saint-Etienne, France
e-mail: claire.morin@emse.fr

of bone (hydroxyapatite minerals, type I collagen, and water with non-collageneous organics) to the macroscopic scale of cortical and trabecular bone.

**Keywords** Bone mechanics · Elasticity · Strength · Micromechanics · Multiscale modeling

**Nomenclature**

| | |
|---|---|
| $\mathbb{A}$ | fourth-order strain concentration tensor |
| $\mathbb{c}, \mathbb{C}$ | fourth-order elasticity tensor at the "microscopic" and "macroscopic" scale, respectively |
| $d$ | lateral/equatorial diffraction spacing |
| $\mathscr{D}$ | characteristic length of the heterogeneities inside the RVE |
| div | divergence (mathematical operator) |
| $\mathbb{D}$ | fourth-order compliance tensor |
| $D_{ijkl}$ | component $ijkl$ of tensor $\mathbb{D}$ |
| $D$ | axial diffraction spacing / axial macroperiod |
| $d\mathbf{x}_i$ | line element along the principal direction $i$ |
| $E$ | Young's modulus |
| $\mathbf{E}$ | macroscopic strain tensor |
| $f$ | volume fraction |
| $g$ | gravitational acceleration |
| GRAD | gradient operator at the structure scale |
| $\mathbb{I}$ | fourth-order identity tensor |
| $J$ | Jacobian, quantifying volume change during hydration process |
| $k$ | elastic bulk modulus |
| $\ell$ | characteristic length of the RVE |
| $\mathscr{L}$ | characteristic length of the structure built up by RVEs, or of its loading |
| $M$ | mass concerning a millimeter-sized bone sample |
| min | minimum value (mathematical operator) |
| $N_r$ | number of phases |
| $\mathbf{n}$ | outwardly pointing vector normal to a surface element of an RVE |
| $\mathbb{P}_r^s$ | fourth-order Hill tensor of inclusion with shape $r$ (or phase $r$) embedded in matrix with stiffness $\mathbb{C}$ (or $\mathbb{C}^0$ if $s = 0$), or with symmetry property $s$ otherwise |
| $\mathscr{R}$ | water-to-organic mass ratio |
| $RVE$ | Representative Volume Element |
| $\mathbf{T}$ | traction vector |
| $v$ | velocity |
| $V$ | volume quantity concerning a millimeter-sized bone sample |
| $W$ | weight quantity concerning a millimeter-sized bone sample |
| $\mathscr{W}$ | work |
| $WF$ | weight fraction |
| $\mathbf{x}$ | location vector |
| $\beta$ | proportionality constant between extrafibrillar space and fibrillar space increase during hydration |

| | |
|---|---|
| $\partial V$ | boundary of volume $V$ |
| $\boldsymbol{\varepsilon}$ | microscopic strain field |
| $\boldsymbol{\varepsilon}_r$ | average (micro-)strain in phase $r$ |
| $\lambda_i$ | principal stretch in direction $i$ |
| $\mu$ | elastic shear modulus |
| $\phi$ | relative mineral portion in extrafibrillar space |
| $\rho$ | mass density |
| $\boldsymbol{\sigma}$ | microscopic stress field |
| $\boldsymbol{\sigma}_r$ | average (micro-)stress in phase $r$ |
| $\boldsymbol{\Sigma}$ | macroscopic stress tensor |
| $\boldsymbol{\xi}$ | displacement field |

*Operators*

| | |
|---|---|
| $\langle(.)\rangle$ | average of quantity (.) over the volume of the RVE |
| : | double contraction |
| . | simple contraction (dot product) |

*Subscripts*

| | |
|---|---|
| air | measured in air |
| ash | ...of ash |
| ax | ...in axial direction |
| can | ...of canalicular porosity |
| col | ...of collagen |
| dev | deviatoric part |
| dry | in dry state |
| excol | ...of extracollageneous space |
| exfib | ...of extrafibrillar space |
| fib | ...of fibril |
| fl | ...of ionic fluid |
| HA | ...of hydroxyapatite |
| $H_2O$ | ...of water |
| $i$ | ...of constituent $i$ |
| lac | ...of lacunar porosity |
| liquid | ...of liquid used for the Archimedes' tests |
| $m$ | ...of the matrix phase |
| max | maximum value (typically related to full saturation) |
| org | ...of organic matter |
| $r$ | ...of phase $r$ |
| $RVE$ | ...of the Representative Volume Element |
| sub | measured when submerged in water |
| tr | ...in transverse direction |
| vas | ...of vascular porosity |
| vol | volumetric part |
| $w$ | ...in wet (hydrated) state |
| wetcol | ...of wet collagen |

| 0 | at the time of osteoid deposition |
| 1, 2 | ...in transverse direction |
| 3 | ...in axial direction |
| $\infty$ | ...in fully mineralized state |
| $\mu$por | ...of microporosity |

*Superscripts*

| col | ...per volume of molecular collagen |
| cort | ...per volume of cortical space |
| dry | ...per volume of dry bone tissue |
| dh | ...of partially dehydrated tissue |
| excel | ...per volume of extracellular space |
| excol | ...per volume of extracollageneous space |
| exfib | ...per volume of extrafibrillar space |
| exp | experimental value |
| ext | ...of external forces acting on the RVE |
| exvas | ...per volume of extravascular space |
| fib | ...per volume of fibrillar space |
| fibsat | at fibrillar saturation limit |
| hom | homogenized |
| int | ...of internal forces acting within the RVE |
| imsat | at intermolecular pore saturation limit |
| pred | model-predicted value |
| $\mu$ | ...of a millimeter-sized bone sample |
| 0 | related to the matrix phase in the auxiliary Eshelby problem |

# 1  Introduction

Many tasks in the diverse field of biomedical engineering involve ensuring the mechanical integrity of structures made up by biological tissues. The mechanical integrity of structures depends on the mechanical loading to which they are subjected, on the specific shapes of the structures (i.e. of the organs), and last, but not least on the mechanical properties of the materials (i.e. of the biological tissues) making up the structures. The aforementioned tissue properties, changing in time and space across the organs, depend on tissue composition and on the micro- and nanostructures within a piece of tissue. The present contribution reviews rigorously derived mathematical relations describing corresponding structure-property relations.

This topic is closely linked to the question on whether there are any non-changing, "universally" valid rules governing the composition and microstructure of biological tissues. Inspired by Rupert Riedl (1925–2005), the eminent Austro-American zoologist of the second half of the twentieth century, who stressed that *"the living world happens to be crowded by universal patterns of organizations, which, most obviously, find no direct explanation through environmental conditions or adaptive radiation"*

[127], we here report on the successful finding of mathematical rules reflecting the aforementioned patterns. Therefore, we apply an engineering science approach to the structural biology of bone tissue, also assessing how such rules or patterns affect the mechanical properties of bone tissue. For this purpose, we take into account the well-known fact that bone tissue features a distinctive hierarchical organization [46, 78, 150], as seen in Fig. 1 and described in greater detail in Sect. 2. The involved organizational patterns (specific arrangements of water, hydroxyapatite-type mineral, and organic matter) can be found throughout different anatomical locations, different organs, and different species. However, the *dosages* of distinctive features within a specific material microstructure may well differ. These dosages follow the aforementioned "universal" composition rules, which arise from a vast amount of experimental data available in literature.

In particular, dehydration-demineralization tests, dehydration-deorganification tests, and dehydration-ashing tests were analyzed in order to quantify the relations between the mass density of extracellular bone matrix and the apparent mass densities of water, hydroxyapatite, and organic matter, see Sect. 3. Furthermore, mass and volume measurements on wet, dehydrated, and demineralized bone tissue samples, as well as optical densities obtained from transmission electron microscopy (TEM) of similar tissues were employed for assessing the distribution of hydroxyapatite within extracellular bone matrix, see Sect. 4. Thereafter, a swelling rule for hydrating collageneous tissues derived from processing and comparing data collected from X-ray diffraction, vacuum drying, and mass measurements, is presented in Sect. 5. Based on a mass conversation law formulated for closed systems representing both the bone ultrastructure, as well as the fibrillar and extrafibrillar spaces, the bone tissue evolution during mineralization can be predicted, see Sect. 6. Finally, we present how the hierarchical organization of bone tissue can be "translated" into a corresponding multiscale homogenization scheme, which allows for prediction of the macroscopic tissue stiffness. The corresponding microelastic model also incorporates the aforementioned four composition rules, so that they eventually govern "universal" structure-property relations in bone, as described in Sect. 7.

## 2 Morphological Patterns of Bone

Bone materials are characterized by an astonishing variability and diversity. Still, the fundamental hierarchical organization, or "once-chosen" basic "construction plans" of bone materials have remained largely unchanged during biological evolution; this has been coined, by Gould and Lewontin [52], as an "architecturally constrained" situation. The aforementioned construction plans are reflected by typical morphological features (or patterns) which can be discerned across most bone organs and tissues occurring in the vertebrate kingdom. The corresponding hierarchical organization of bone can be described by means of the following five levels [78]:
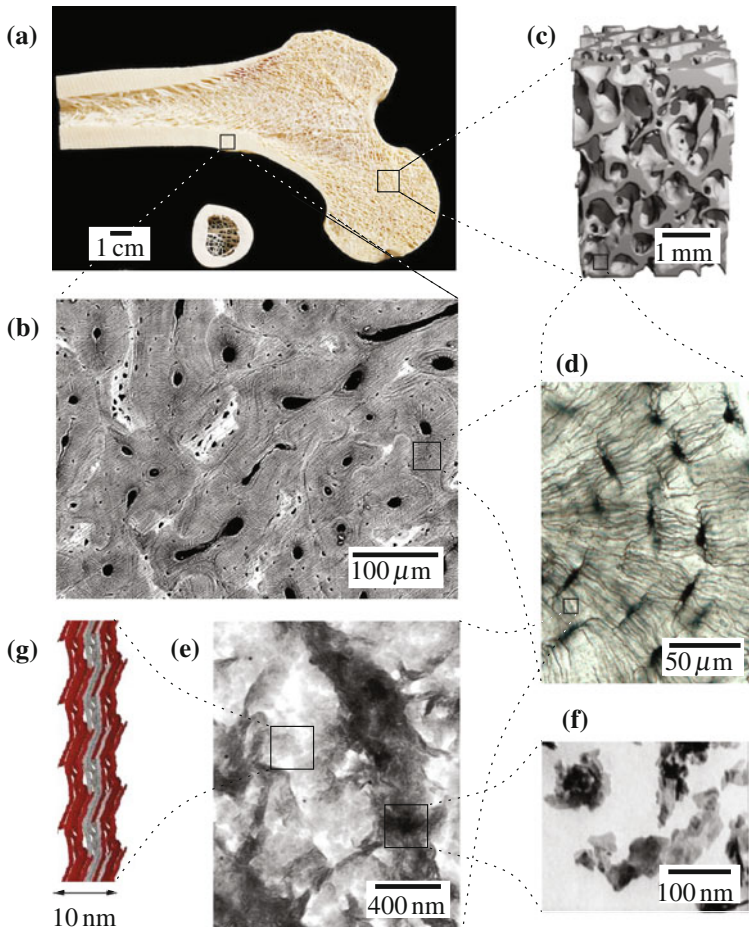
**Fig. 1** Hierarchical organization of bone: **a** photograph of a cross-section through and across a whole long bone (copyright Ralph Hutchings/Visuals Unlimited, Inc.), showing the macrostructure; microstructure featuring either **b** osteonal cortical bone, acquired by SEM [58], or **c** trabecular struts making up trabecular bone, visualized based on micro-computed tomography data [103]; **d** osteocytic lacunae (brightfield light microscopy image taken by Tim Arnett); **e** ultrastructure, [122]; **f** hydroxyapatite crystals, obtained by means of SEM [150]; **g** wet collagen, electron density map of [112] (permission for reproduction requested from publisher: **b** The Royal Society; **c** ASME; **d** Annual Reviews; **e** Springer; **g** PNAS)

- The macrostructure, with a characteristic length of several millimeters to centimeters, features cortical (or compact) bone and trabecular (or spongy) bone, see Fig. 1a.
- Zooming out pieces of cortical bone, see Fig. 1b, or trabecular bone, see Fig. 1c, reveals that actually both materials are porous in nature: The corresponding vascular porosity hosts various biological cells as well as blood vessels; in cortical bone this porosity is organized in a tree-type branching structure of canals (called Haversian canals if parallel to the main bone axis, and Volkmann canals at the branching junctions [24, 29]); and in trabecular bone, these canals are penetrating each other, yielding eventually a microstructure made up by single plates or struts [54]. The vascular pore channels are connected, via much smaller channels called canaliculi, to cave-like single pores called lacunae [138], populated by individual osteocytes, and seen as small black dots in Fig. 1d.
- The entire domain outside the vascular, lacunar, and canalicular porosities is called extracellular space or matrix. It appears as a nanocomposite with a characteristic size of several micrometers, see Fig. 1e. Within this extracellular space, collagen-rich domains, see the light areas in Fig. 1e, and collagen-free domains, see the dark areas in Fig. 1e, can be distinguished, the characteristic length of both of which is several hundred nanometers. Commonly, these domains are referred to as fibrils and extrafibrillar space [122].
- Finally, the so-called elementary components of mineralized tissues can be distinguished, with a characteristic lengths in the range of nanometers:

– plate-shaped mineral crystals consisting of impure hydroxyapatite (HA, $Ca_{10}[PO_4]_6[OH]_2$) with typical 1–5 nm thickness, and 25–50 nm length [150], see Fig. 1f;
– slender, helically round collagen molecules with a diameter of about 1.2 nm and a length of about 300 nm [21, 112, 120], which are self-assembled in staggered organizational schemes (fibrils) with characteristic diameters of 50–500 nm [35, 95, 105, 122, 125, 142, 150, 151], see Fig. 1g – several covalently bonded fibrils are sometimes referred to as fibers;
– different non-collagenous organic molecules, predominantly lipids, proteglycans, and proteins [73, 146]; and
– water.

Both the amount of these components, as well as their distribtution across the hierarchical levels described above, are the focus of the subsequent sections.

## 3   Mineral and Collagen Dosages in Extracellular Bone Matrix

Data from bone drying, demineralization, and deorganification tests, collected over a time span of more than 80 years [13, 25, 51, 57, 87, 90–92, 96], evidence a myriad of different chemical compositions of different bone materials. However, careful

analysis of the data, as to extract the chemical concentrations of hydroxyapatite, water, and organic matter[1] (see Table 1) in the extracellular bone matrix, reveals an astonishing fact [147]: it appears that there exists a unique bilinear relationship between organic concentration and mineral concentration, across different species, different organs, and different age groups, from early childhood to old age.

Corresponding experimental endeavors typically started with the determination of the *"macroscopic"* mass density, i.e. that associated to millimeter-sized bone samples, by means of Archimedes' principle. Therefore, the mass of the (wet) bone sample is first measured in air, delivering the quantity $M_{air}^{\mu}$. Thereafter, the weight of the bone sample when submerged in a liquid, is quantified as $W_{sub}^{\mu}$. Both quantities then give access to the volume of the millimeter-sized sample, through

$$V^{\mu} = \frac{1}{\rho_{liquid}} \left( M_{air}^{\mu} - \frac{W_{sub}^{\mu}}{g} \right) , \tag{1}$$

with $\rho_{liquid}$ as the mass density of the employed liquid, and $g$ as the gravitational acceleration, $g = 9.81 \, \text{m/s}^2$. Finally, the macroscopic mass density of the investigated samples follows from

$$\rho^{\mu} = \frac{M_{air}^{\mu}}{V^{\mu}} . \tag{2}$$

After having determined the samples' mass density, the experimenters typically turned towards determination of the samples' chemical composition; by one of three different experimental modalities, as described next.

***Dehydration-Demineralization Tests***

In a series of seminal experimental campaigns [87, 90, 91, 96], see Tables 1, 2 and 3, numerous millimeter-sized bone samples were first dried in a vacuum desiccator at room temperature, until a constant mass was observed, namely the mass of the dehydrated bone sample, $M_{dry}^{\mu}$. The difference between the mass of wet sample in air and the mass of dehydrated sample obviously equals the mass of water which was originally contained in the sample, $M_{H_2O}^{\mu} = M_{air}^{\mu} - M_{dry}^{\mu}$. This water had filled all the bone pore spaces, from the vascular pore space seen in Fig. 1b, c, via the lacunar and canalicular pore spaces seen in Fig. 1d, down to the inter-crystalline and intermolecular pore spaces, as seen in Fig. 1e, f, g. Next, the samples were rehydrated and then demineralized in a 0.5 mol/L ethylenediaminetetraacetic acid (EDTA) solution at $p$H 7.5, until no calcium was detected anymore by an atomic absorption spectrometer. After drying such a demineralized sample in vacuum, one is left with the organic mass which had been contained in the originally mineralized and wet bone sample, $M_{org}^{\mu}$. Finally, knowledge of the masses of organic matter and water gives access to the hydroxyapatite mass, $M_{HA}^{\mu} = M_{air}^{\mu} - M_{org}^{\mu} - M_{H_2O}^{\mu}$. Thereafter, the constituent masses can be readily converted into weight fractions, through

---

[1]90% of which is collagen [146].

**Table 1** Bone composition from dehydration-demineralization experiments of Lees et al. [91][a] and Lees et al. [96][b]

| Tissue | $\rho^{\mu}$ (g/cm$^3$) | $WF_{HA}^{\mu}$ (-) | $WF_{org}^{\mu}$ (-) | $WF_{H_2O}^{\mu}$ (-) |
|---|---|---|---|---|
| Bovine tibia[a] | 2.06 | 0.658 | 0.219 | 0.123 |
| Bovine tibia[a] | 2.05 | 0.656 | 0.219 | 0.126 |
| Bovine tibia[a] | 2.02 | 0.621 | 0.239 | 0.140 |
| Bovine tibia[a] | 2.02 | 0.627 | 0.232 | 0.140 |
| Bovine tibia[a] | 2.00 | 0.643 | 0.227 | 0.129 |
| Bovine tibia[a] | 2.05 | 0.643 | 0.230 | 0.127 |
| Bovine tibia[a] | 2.10 | 0.671 | 0.211 | 0.118 |
| Bovine tibia[a] | 2.08 | 0.664 | 0.216 | 0.120 |
| Bovine tibia[a] | 2.12 | 0.661 | 0.215 | 0.123 |
| Bovine tibia[a] | 2.08 | 0.663 | 0.221 | 0.116 |
| Bovine tibia[a] | 2.10 | 0.647 | 0.224 | 0.129 |
| Bovine tibia[a] | 1.98 | 0.654 | 0.217 | 0.128 |
| Bovine tibia[a] | 2.05 | 0.644 | 0.227 | 0.129 |
| Bovine tibia[a] | 2.11 | 0.649 | 0.229 | 0.122 |
| Bovine tibia[a] | 2.03 | 0.638 | 0.213 | 0.123 |
| Bovine tibia[a] | 2.06 | 0.699 | 0.184 | 0.117 |
| Bovine tibia[a] | 2.02 | 0.658 | 0.219 | 0.123 |
| Bovine tibia[a] | 1.99 | 0.656 | 0.219 | 0.126 |
| Bovine tibia[a] | 1.95 | 0.640 | 0.228 | 0.131 |
| Bovine tibia[a] | 2.01 | 0.659 | 0.218 | 0.123 |
| Bovine tibia[a] | 2.04 | 0.638 | 0.242 | 0.121 |
| Bovine tibia[a] | 2.05 | 0.674 | 0.210 | 0.116 |
| Whale malleus[b] | 2.49 | 0.860 | 0.100 | 0.040 |
| Whale malleus[b] | 2.45 | 0.800 | 0.130 | 0.070 |
| Whale incus[b] | 2.50 | 0.860 | 0.090 | 0.050 |
| Whale stapes[b] | 2.42 | 0.810 | 0.130 | 0.060 |
| Whale stapes[b] | 2.36 | 0.800 | 0.140 | 0.060 |
| Whale periotic[b] | 2.40 | 0.810 | 0.130 | 0.070 |
| Whale periotic[b] | 2.48 | 0.830 | 0.110 | 0.060 |
| Whale periotic[b] | 2.52 | 0.850 | 0.100 | 0.050 |
| Whale periotic[b] | 2.52 | 0.850 | 0.100 | 0.050 |
| Whale periotic[b] | 2.58 | 0.870 | 0.090 | 0.040 |
| Whale t. bulla[b] | 2.48 | 0.850 | 0.100 | 0.050 |

**Table 2** Mineralized tendon composition from dehydration-demineralization experiments of Lees and Page [90]

| Tissue | $\rho^{\mu}$ (g/cm$^3$) | $\mathrm{WF}_{\mathrm{HA}}^{\mu}$ (-) | $\mathrm{WF}_{\mathrm{org}}^{\mu}$ (-) | $\mathrm{WF}_{\mathrm{H_2O}}^{\mu}$ (-) |
|---|---|---|---|---|
| Mineralized turkey leg tendon | 1.33 | 0.286 | 0.250 | 0.465 |
| Mineralized turkey leg tendon | 1.50 | 0.445 | 0.239 | 0.316 |
| Mineralized turkey leg tendon | 1.50 | 0.410 | 0.217 | 0.374 |
| Mineralized turkey leg tendon | 1.51 | 0.437 | 0.217 | 0.346 |
| Mineralized turkey leg tendon | 1.52 | 0.454 | 0.239 | 0.308 |
| Mineralized turkey leg tendon | 1.52 | 0.437 | 0.219 | 0.343 |
| Mineralized turkey leg tendon | 1.52 | 0.396 | 0.244 | 0.360 |
| Mineralized turkey leg tendon | 1.53 | 0.443 | 0.222 | 0.335 |
| Mineralized turkey leg tendon | 1.54 | 0.459 | 0.244 | 0.297 |
| Mineralized turkey leg tendon | 1.58 | 0.473 | 0.228 | 0.299 |
| Mineralized turkey leg tendon | 1.58 | 0.462 | 0.217 | 0.321 |
| Mineralized turkey leg tendon | 1.59 | 0.476 | 0.228 | 0.297 |
| Mineralized turkey leg tendon | 1.60 | 0.487 | 0.230 | 0.283 |
| Mineralized turkey leg tendon | 1.61 | 0.459 | 0.230 | 0.310 |
| Mineralized turkey leg tendon | 1.61 | 0.495 | 0.244 | 0.261 |
| Mineralized turkey leg tendon | 1.62 | 0.500 | 0.228 | 0.272 |
| Mineralized turkey leg tendon | 1.64 | 0.506 | 0.228 | 0.266 |

$$\mathrm{WF}_i^{\mu} = \frac{M_i^{\mu}}{M_{\mathrm{air}}^{\mu}}, \qquad i = \mathrm{org}, \mathrm{HA}, \mathrm{H_2O}, \tag{3}$$

see Tables 1, 2 and 3. The weight fractions obviously fulfill

$$\mathrm{WF}_{\mathrm{H_2O}}^{\mu} + \mathrm{WF}_{\mathrm{HA}}^{\mu} + \mathrm{WF}_{\mathrm{org}}^{\mu} = 1 . \tag{4}$$

**Table 3** Bone composition from dehydration-demineralization experiments of Lees [87]

| Tissue | $WF_{HA}^{\mu}$ (-) | $WF_{org}^{\mu}$ (-) | $WF_{H_2O}^{\mu}$ (-) | $\rho^{\mu}$ (g/cm$^3$) |
|---|---|---|---|---|
| Horse metacarpal | 0.55 | 0.25 | 0.2 | 1.79 |
| Horse metacarpal | 0.57 | 0.26 | 0.17 | 1.84 |
| Horse metacarpal | 0.55 | 0.26 | 0.19 | 1.80 |
| Horse metacarpal | 0.54 | 0.28 | 0.18 | 1.79 |
| Horse metacarpal | 0.62 | 0.26 | 0.12 | 1.96 |
| Horse metacarpal | 0.62 | 0.27 | 0.11 | 1.97 |
| Horse metacarpal | 0.62 | 0.26 | 0.12 | 1.96 |
| Horse metacarpal | 0.61 | 0.26 | 0.13 | 1.94 |
| Horse metacarpal | 0.62 | 0.25 | 0.13 | 1.95 |
| Horse metacarpal | 0.54 | 0.23 | 0.23 | 1.75 |
| Horse metacarpal | 0.53 | 0.24 | 0.23 | 1.74 |
| Horse metacarpal | 0.54 | 0.27 | 0.19 | 1.79 |
| Horse metacarpal | 0.63 | 0.22 | 0.15 | 1.94 |
| Horse metacarpal | 0.62 | 0.25 | 0.13 | 1.95 |
| Horse metacarpal | 0.62 | 0.26 | 0.12 | 1.96 |
| Horse metacarpal | 0.64 | 0.23 | 0.13 | 1.98 |
| Horse metacarpal | 0.62 | 0.26 | 0.12 | 1.96 |
| Horse metacarpal | 0.66 | 0.23 | 0.12 | 1.99 |
| Horse metacarpal | 0.63 | 0.24 | 0.13 | 1.96 |

### Dehydration-Deorganification Tests

Gong et al. [51] weighed several (macroscopic) bone samples in the wet state, as well as after drying at 80°C for 72 h - thereby getting access to their wet and dry masses, $M_{air}^{\mu}$ and $M_{dry}^{\mu}$. As before, their difference is equal to the mass of water in the investigated bone sample, $M_{H_2O}^{\mu} = M_{air}^{\mu} - M_{dry}^{\mu}$. Next, the samples were freed from fat and other organic material, using, in a soxhlet apparatus, a mixture of 80% ethyl ether and 20% ethanol, as well as an 80% aqueous solution of ethylene diamine. After drying such a deorganified sample at 80°C (until constant weight is attained), one is left with the hydroxyapatite mass contained in the investigated bone sample, $M_{HA}^{\mu}$. Finally, when knowing the mass of hydroxyapatite and water contained in the originally wet bone sample, as well as its original mass, the mass of the organic matter can be readily determined through $M_{org}^{\mu} = M_{air}^{\mu} - M_{HA}^{\mu} - M_{H_2O}^{\mu}$, together with the corresponding weight fractions according to Eq. (3), see Table 4.

### Dehydration-Ashing Tests

In an interesting experimental campaign of Biltz and Pellegrino [13], cortical bone samples were dried until a constant mass, i.e. the dry bone mass, $M_{dry}^{\mu}$, was attained, which, together with the original mass of the sample in air, $M_{air}^{\mu}$, gives access to the mass of water in the investigated bone sample, $M_{H_2O}^{\mu}$. Next, the dried bones

**Table 4** Bone composition from dehydration-deorganification experiments of Gong et al. [51]

| Tissue | $\rho^\mu$ (g/cm$^3$) | $\mathrm{WF}_{\mathrm{HA}}^\mu$ (-) | $\mathrm{WF}_{\mathrm{org}}^\mu$ (-) | $\mathrm{WF}_{\mathrm{H_2O}}^\mu$ (-) |
|---|---|---|---|---|
| Steer tibial shaft | 2.00 | 0.630 | 0.244 | 0.126 |
| Dog femoral shaft | 2.00 | 0.630 | 0.259 | 0.111 |
| Humar femur and tibia | 1.99 | 0.642 | 0.239 | 0.119 |
| Monkey femur | 2.04 | 0.643 | 0.239 | 0.117 |
| Steer atlas bone | 1.93 | 0.588 | 0.266 | 0.146 |
| Dog lumbar vertebrae | 1.91 | 0.582 | 0.265 | 0.153 |
| Human thoracic and lumbar vertebrae | 1.92 | 0.601 | 0.258 | 0.140 |
| Monkey lumbar vertebrae | 1.88 | 0.582 | 0.274 | 0.144 |

were gently incinerated until all organic matter was burned off. Subsequent weighing evidenced the ash mass, $M_{\mathrm{ash}}^\mu$. As also some inorganic matter, namely 6.6% of the ash mass, is burned at an ashing temperature of 600°C [51], the ash mass provides access to the mineral mass, according to $M_{\mathrm{HA}}^\mu = 1.066 \times M_{\mathrm{ash}}^\mu$. The mass of organic matter follows from $M_{\mathrm{org}}^\mu = M_{\mathrm{air}}^\mu - M_{\mathrm{HA}}^\mu - M_{\mathrm{H_2O}}^\mu$. The corresponding weight fractions can be determined through Eqs. (3) and (4), which, in turn, provide access to $\rho^\mu$, through

$$\rho^\mu = \left( \frac{\mathrm{WF}_{\mathrm{org}}^\mu}{\rho_{\mathrm{org}}} + \frac{\mathrm{WF}_{\mathrm{HA}}^\mu}{\rho_{\mathrm{HA}}} + \frac{\mathrm{WF}_{\mathrm{H_2O}}^\mu}{\rho_{\mathrm{H_2O}}} \right)^{-1}, \qquad (5)$$

where $\rho_{\mathrm{org}} = 1.42 \, \mathrm{g/cm^3}$, $\rho_{\mathrm{HA}} = 3 \, \mathrm{g/cm^3}$, and $\rho_{\mathrm{H_2O}} = 1 \, \mathrm{g/cm^3}$ are the constituents' *real* mass densities [51, 60, 86]. For a compilation of data derived from [13], see Table 5. For the sake of completeness, it should be noted that [13] actually reported the volume fraction of water

$$f_{\mathrm{H_2O}}^\mu = \frac{M_{\mathrm{air}}^\mu - M_{\mathrm{dry}}^\mu}{V^\mu}, \qquad (6)$$

and the weight fraction of ash per mass of dried bone

$$\mathrm{WF}_{\mathrm{ash}}^{\mathrm{dry}} = \frac{M_{\mathrm{ash}}^\mu}{M_{\mathrm{air}}^\mu - M_{\mathrm{H_2O}}^\mu}. \qquad (7)$$

Similar test campaigns were performed by Burns and Hammet [25, 57], see Table 6 for a compilation of test results.

**Table 5** Bone composition from dehydration-ashing experiments of Biltz and Pellegrino [13]

| Femoral and tibial samples of | $\rho^{\mu}$ (g/cm$^3$) | $WF_{HA}^{\mu}$ (-) | $WF_{org}^{\mu}$ (-) | $WF_{H_2O}^{\mu}$ (-) |
|---|---|---|---|---|
| Fish | 1.80 | 0.507 | 0.273 | 0.220 |
| Turtle | 1.81 | 0.529 | 0.266 | 0.204 |
| Frog | 1.93 | 0.572 | 0.246 | 0.182 |
| Polar bear | 1.92 | 0.583 | 0.245 | 0.172 |
| Man | 1.94 | 0.657 | 0.263 | 0.080 |
| Elephant | 2.00 | 0.658 | 0.242 | 0.100 |
| Monkey | 2.09 | 0.653 | 0.237 | 0.110 |
| Cat | 2.05 | 0.652 | 0.233 | 0.115 |
| Horse | 2.02 | 0.648 | 0.228 | 0.124 |
| Chicken | 2.04 | 0.653 | 0.227 | 0.120 |
| Dog | 1.94 | 0.637 | 0.219 | 0.144 |
| Goose | 2.04 | 0.669 | 0.218 | 0.113 |
| Cow | 2.05 | 0.660 | 0.212 | 0.128 |
| Guinea Pig | 2.10 | 0.669 | 0.212 | 0.119 |
| Rabbit | 2.12 | 0.685 | 0.199 | 0.116 |
| Rat | 2.24 | 0.713 | 0.197 | 0.090 |

### Determination of Tissue-Specific Volume Fractions

Determination of the extracellular volume fractions of mineral and collagen, $f_{HA}^{excel}$ and $f_{col}^{excel}$, rests on the aforementioned volume and weighing measurements on wet, dehydrated, and demineralized bone specimens, and on techniques revealing the bone microstructure, such as light microscopy, confocal microscopy, or micro-computed tomography. These imaging techniques give access to the so-called microporosity $f_{\mu por}$, the sum of the vascular, lacunar, and canalicular porosities,

$$f_{\mu por} = f_{vas} + f_{lac} + f_{can}. \tag{8}$$

Vascular porosity in cortical bone, also called Haversian porosity in that context, ranges from 2% to typically 8% [19, 20, 30, 36, 140]. Under severe conditions such as bone disease like osteoporosis, overtraining, or drug treatment, it may increase up to 20% [140]. In trabecular bone, the vascular porosity ranges from 30 to 90% [27]. On the other hand, the much smaller lacunar and canalicular porosities lie within a much narrower range of values; in recent years, they were quantified by micro-computed tomography. In this context, Schneider et al. [137, 138] reported 1.3 and 0.7% lacunar and canalicular porosity values, respectively. These values are close to those reported by Palacio-Mancheno [113], Tommasini et al. [144], and Hesse et al. [70]. Considering 3% vascular porosity as relevant for mammalian bone of medium-to-large-sized animals (see e.g. evaluation of microscopic images of Lees et al. [91]

**Table 6** Bone composition from dehydration-ashing experiments of Burns [25][a] and Hammett [57][b]

| Tissue | $WF_{HA}^{\mu}$ (-) | $WF_{org}^{\mu}$ (-) | $WF_{H_2O}^{\mu}$ (-) | $\rho^{\mu}$ (g/cm$^3$) |
|---|---|---|---|---|
| Rabbit limb bones[a] | 0.267 | 0.202 | 0.392 | 1.38 |
| Rabbit limb bones[a] | 0.210 | 0.194 | 0.581 | 1.25 |
| Rat leg bones[a] | 0.389 | 0.231 | 0.313 | 1.54 |
| Rat leg bones[a] | 0.345 | 0.224 | 0.375 | 1.46 |
| Rat leg bones[a] | 0.398 | 0.232 | 0.318 | 1.54 |
| Rat leg bones[a] | 0.378 | 0.218 | 0.334 | 1.52 |
| Rat leg bones[a] | 0.376 | 0.230 | 0.344 | 1.51 |
| Humerus of rat[b] | 0.171 | 0.180 | 0.650 | 1.20 |
| Humerus of rat[b] | 0.176 | 0.191 | 0.633 | 1.21 |
| Humerus of rat[b] | 0.235 | 0.199 | 0.567 | 1.27 |
| Humerus of rat[b] | 0.315 | 0.210 | 0.475 | 1.37 |
| Humerus of rat[b] | 0.337 | 0.208 | 0.456 | 1.40 |
| Humerus of rat[b] | 0.378 | 0.215 | 0.407 | 1.46 |
| Humerus of rat[b] | 0.434 | 0.222 | 0.344 | 1.55 |
| Humerus of rat[b] | 0.175 | 0.194 | 0.631 | 1.21 |
| Humerus of rat[b] | 0.180 | 0.193 | 0.627 | 1.21 |
| Humerus of rat[b] | 0.264 | 0.205 | 0.532 | 1.31 |
| Humerus of rat[b] | 0.315 | 0.209 | 0.476 | 1.37 |
| Humerus of rat[b] | 0.362 | 0.209 | 0.429 | 1.44 |
| Humerus of rat[b] | 0.420 | 0.219 | 0.361 | 1.53 |
| Humerus of rat[b] | 0.451 | 0.229 | 0.320 | 1.58 |
| Femur of rat[b] | 0.133 | 0.182 | 0.685 | 1.17 |
| Femur of rat[b] | 0.144 | 0.191 | 0.665 | 1.18 |
| Femur of rat[b] | 0.201 | 0.204 | 0.595 | 1.24 |
| Femur of rat[b] | 0.283 | 0.217 | 0.500 | 1.34 |
| Femur of rat[b] | 0.315 | 0.210 | 0.475 | 1.37 |
| Femur of rat[b] | 0.356 | 0.217 | 0.427 | 1.43 |
| Femur of rat[b] | 0.413 | 0.230 | 0.357 | 1.52 |
| Femur of rat[b] | 0.143 | 0.197 | 0.660 | 1.18 |
| Femur of rat[b] | 0.150 | 0.195 | 0.655 | 1.19 |
| Femur of rat[b] | 0.235 | 0.208 | 0.557 | 1.28 |
| Femur of rat[b] | 0.288 | 0.213 | 0.499 | 1.34 |
| Femur of rat[b] | 0.338 | 0.214 | 0.448 | 1.41 |
| Femur of rat[b] | 0.401 | 0.222 | 0.377 | 1.50 |
| Femur of rat[b] | 0.430 | 0.235 | 0.336 | 1.55 |

as reported in Fritsch and Hellmich [46]), we account for 5% microporosity $f_{\mu\text{por}}$ when assessing the extracellular (ultrastructural) characteristics of the bones tested by Biltz and Pellegrino [13], Burns [25], Gong et al. [51], Hammet [57], Lees [87], Lees et al. [91]. Accordingly, the extracellular mass density reads as

$$\rho^{\text{excel}} = \frac{\rho^\mu - \rho_{\text{H}_2\text{O}} \times f_{\mu\text{por}}}{1 - f_{\mu\text{por}}}, \tag{9}$$

and the weight fraction of water-filled micropores (i.e. vascular, lacunar, and canalicular pores) in (wet) bone specimens reads as

$$\text{WF}^\mu_{\mu\text{por}} = \frac{\rho_{\text{H}_2\text{O}} \times f_{\mu\text{por}}}{\rho^\mu}. \tag{10}$$

$\text{WF}^\mu_{\mu\text{por}}$ allows for scale transition from the macroscopic (microstructural) to the extracellular (ultrastructural) scale,

$$\text{WF}^{\text{excel}}_{\text{HA}} = \frac{\text{WF}^\mu_{\text{HA}}}{1 - \text{WF}^\mu_{\mu\text{por}}}, \tag{11}$$

$$\text{WF}^{\text{excel}}_{\text{org}} = \frac{\text{WF}^\mu_{\text{org}}}{1 - \text{WF}^\mu_{\mu\text{por}}}, \tag{12}$$

$$\text{WF}^{\text{excel}}_{\text{H}_2\text{O}} = 1 - \text{WF}^{\text{excel}}_{\text{HA}} - \text{WF}^{\text{excel}}_{\text{org}}. \tag{13}$$

From Eqs. (5), (11)–(13), one can determine the apparent mass densities of organics, water, and hydroxyapatite through

$$\rho_i^{\text{excel}} = \text{WF}_i^{\text{excel}} \rho^{\text{excel}}, \qquad i = \text{org, HA, H}_2\text{O}. \tag{14}$$

The microporosity is negligible in size as regards the mineralized turkey leg tendon [34] and otic bones [159]. Thus, weight fractions and mass densities are not to be differentiated between the microstructural and the ultrastructural scale, as concerns the tissue samples of Lees and Page [90] and Lees et al. [96].

### *"Universal" Rules in Bone Fibrillogenesis and Mineralization*

Applying the presented evaluation procedures to the collected experimental data, see Tables 1, 2, 3, 4, 5 and 6, results in a remarkable finding concerning the apparent mass densities of hydroxyapatite mineral, organic, and water; i.e. the masses of these constituents found in a millimeter-sized sample divided by the volume of the extracellular portion within this millimeter-sized sample; across a great variety of species, organs, and ages. The aforementioned apparent mass densities (or concentrations) strongly correlate with each other, see Fig. 2, as well as with the bone tissue mass density, see Fig. 3. Interestingly, all these correlations can be represented by bilinear functions, whereby the increasing branch depicted in Fig. 2a relates to tissues taken

from growing organisms (being in the states of childhood and adolescence), while the descending branch relates to tissues taken from adult organisms. The apparent mass densities can be translated into volume fractions through

$$f_i^{\text{excel}} = \frac{\rho_i^{\text{excel}}}{\rho_i}, \qquad i = \text{org, HA, H}_2\text{O} \,. \tag{15}$$

so that the constituents' volume fractions can be expressed by the following regression functions depending on the extracellular mass density,

$$\text{if} \quad \rho^{\text{excel}} \leq 1.978 \, \text{g/cm}^3 \quad \begin{cases} f_{\text{HA}}^{\text{excel}} = \frac{1}{\rho_{\text{HA}}} \left( 1.3275 \rho^{\text{excel}} - 1.3938 \right), \\ f_{\text{org}}^{\text{excel}} = \frac{1}{\rho_{\text{org}}} \left( 0.3888 \rho^{\text{excel}} - 0.2393 \right), \\ f_{\text{H}_2\text{O}}^{\text{excel}} = 1 - f_{\text{HA}}^{\text{excel}} - f_{\text{org}}^{\text{excel}}, \end{cases} \tag{16}$$

relating to growing organisms, and

$$\text{if} \quad \rho^{\text{excel}} \geq 1.978 \, \text{g/cm}^3 \quad \begin{cases} f_{\text{HA}}^{\text{excel}} = \frac{1}{\rho_{\text{HA}}} \left( 1.7298 \rho^{\text{excel}} - 2.1895 \right), \\ f_{\text{org}}^{\text{excel}} = \frac{1}{\rho_{\text{org}}} \left( -0.5180 \rho^{\text{excel}} + 1.5541 \right), \\ f_{\text{H}_2\text{O}}^{\text{excel}} = 1 - f_{\text{HA}}^{\text{excel}} - f_{\text{org}}^{\text{excel}}, \end{cases} \tag{17}$$

relating to aging organisms. As 90% of the organic matter in bone is collagen [146], the extracellular volume fraction of collagen follows as

$$f_{\text{col}}^{\text{excel}} = 0.9 \times f_{\text{org}}^{\text{excel}}. \tag{18}$$

### *Cell Biology Aspects*

It is interesting to discuss the mineral-versus-organics concentration relation of Fig. 2a from the viewpoint of cell biology: during growth, the mineral-to-organic mass apposition ratio in extracellular bone tissue is a constant, $d\rho_{\text{HA}}^{\text{excel}}/d\rho_{\text{org}}^{\text{excel}} = 3.4$, universally valid throughout different tissues of different growing species at different ages. This constant reflects the working mode of osteoblasts (cuboidal or polygonal bone cells with several tens of micrometers characteristic length [1, 17, 74, 111, 115, 129, 158]. Pre-osteoblasts [41, 97, 115] deposit new osteoid, in the form of seams of some 8 to 10 µm thickness, made of proteoglycan gel reinforced by fairly randomly oriented collagen fibrils [26, 41, 155], see Fig. 4a. Thereafter, osteoblasts order the collagen fibrils through stretching [41], and mediate, through budding of matrix vesicles from cell processes [3], the precipitation of hydroxyapatite, see Fig. 4b. This results in the so-called primary mineralization [115], with a characteristic time of hours to days [152]. From a chemical viewpoint, specially synthesized matrix molecules, such as bone sialoprotein, osteopontin, or osteocalcin [153], induce mineral formation, and such non-collagenous organic molecules typically make up 10% of the overall organic volume fraction [24, 86, 146], regardless of the magnitude of the latter. Accordingly, one would expect the more mineral precipitation, the more
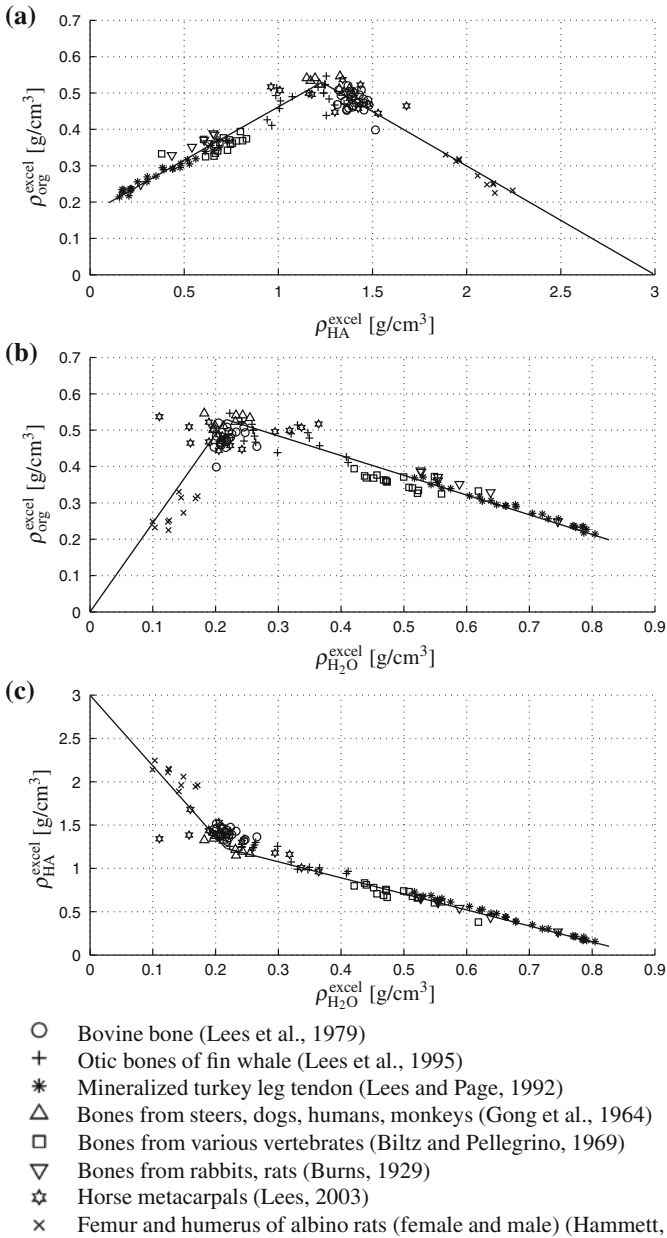
**Fig. 2** Relations between apparent mass densities in extracellular bone matrix in the line of Vuong and Hellmich [147]: **a** hydroxyapatite versus organic matter, **b** water versus organic matter, and **c** water versus hydroxyapatite; across different species, organs, and ages
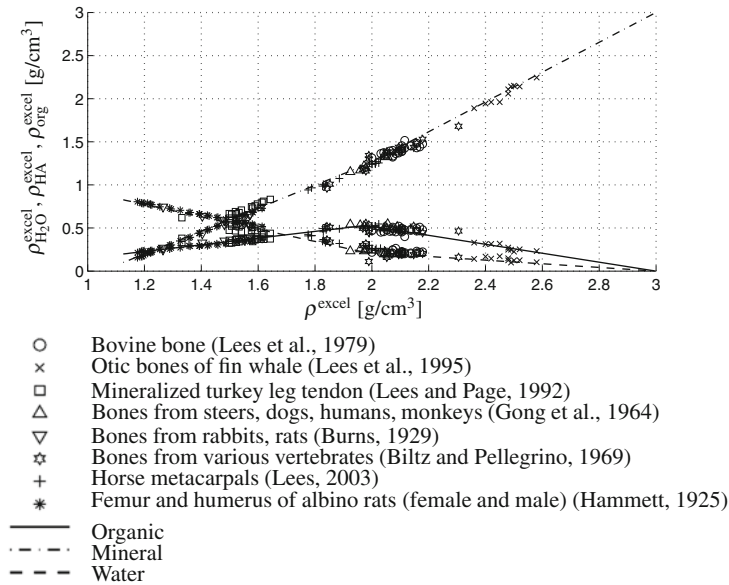
**Fig. 3** Apparent mass densities of water, hydroxyapatite, and organic matter, versus overall mass density of extracellular bone matrix, $\rho^{excel}$, across different species, organs, and ages

non-collagenous organics to be present, the amount of the latter being proportional to that of the overall organic matter. This is perfectly consistent with the aforementioned tissue- and species-independent, "universal" mineral-per-organics apposition ratio of 3.4, suggesting primary mineralization as the dominant mineralization mechanism in growing organisms.

In such organisms, the mineral is hindered from further precipitation in the highly ionic fluids, through the action of the most abundant biological bone cells, namely the osteocytes [1, 10, 11, 18, 111, 115, 143], residing in the lacunar porosity of extravascular bone matrix. Originating from osteoblasts which were buried in the course of ongoing osteoid formation and mineralization, osteocytes maintain a widely spread network, through channels called canaliculi, among themselves and with the osteoblasts located at the bone tissue surface. This network is thought to effectively transfer mechanical stimuli related to tissue deformation, to the osteoblasts [17, 32], so as to trigger their bone formation activity, as described before. In addition to mechanosensing, osteocytes may inhibit mineralization around their lacunae [18], and therefore set an upper limit to the asymptotic mineral concentration which may be attained during the process called secondary mineralization. This process exhibits a characteristic time of weeks to months [9], see Fig. 4c, and before reaching its asymptote, secondary mineralization is not controlled by the local biological cells, but by the diffusion and composition properties of the fluids saturating the extracellular bone tissue [115]. However, at higher ages, the aforementioned inhibitive activity of osteocytes steadily decreases, so that, in the end, even the lacunae themselves
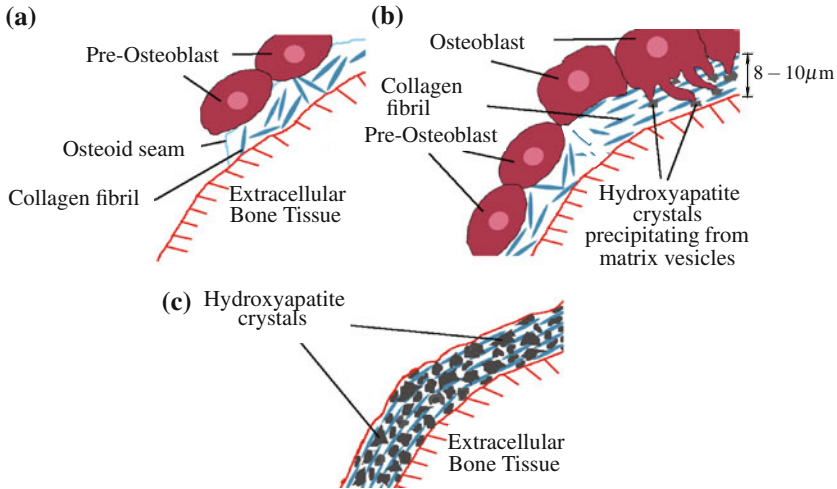
**Fig. 4** Working mode of pre-osteoblasts and osteoblasts: primary and secondary mineralization of an unmineralized osteoid; **a** pre-osteoblasts lay down an osteoid seam, reinforced by randomly oriented collagen fibrils; **b** primary mineralization: osteoblasts order the collagen fibrils through cell-driven stretch, and mediate, through budding of matrix vesicles from cell processes, the precipitation of hydroxyapatite; **c** secondary mineralization: crystals grow without control of local biological cells

may be filled with mineral, as evidenced in [11, 49, 75]. As a consequence, the organic-to-mineral concentration ratio decreases and the mineral-to-organic mass apposition ratio is not equal to 3.4 anymore. At the same time, osteoblastic activity also decreases at more advanced ages [1], leading to a reduction of the (absolute) organic concentration in extracellular bone matrix. This combined effect of both osteoblastic and osteocytic activity reduction is expressed by a (negative) mineral-growth-to-organic-removal ratio, see Fig. 2a, which reveals secondary mineralization as the dominant mineralization mechanism in adult, aging organisms.

We also remark that the results presented here refer to physiologically normal conditions, while drug treatments may lead to considerable deviations from these rules for fibrillogenesis and mineralization, see [147] for further details.

## 4 Mineral Distribution in Extracellular Bone Matrix

At the ultrastructural observation scale (1–10 μm) of fully mineralized tissues, transmission electron micrographs (TEM) reveal that hydroxyapatite is situated both within and outside of the collagen fibrils, and that the majority of hydroxyapatite lies outside the fibrils [2, 101, 121, 122, 139, 159]. The question arises whether the distribution of mineral between the fibrillar and extrafibrillar spaces follows a general rule. And indeed, Hellmich and Ulm [63] found out that the average mineral concentration
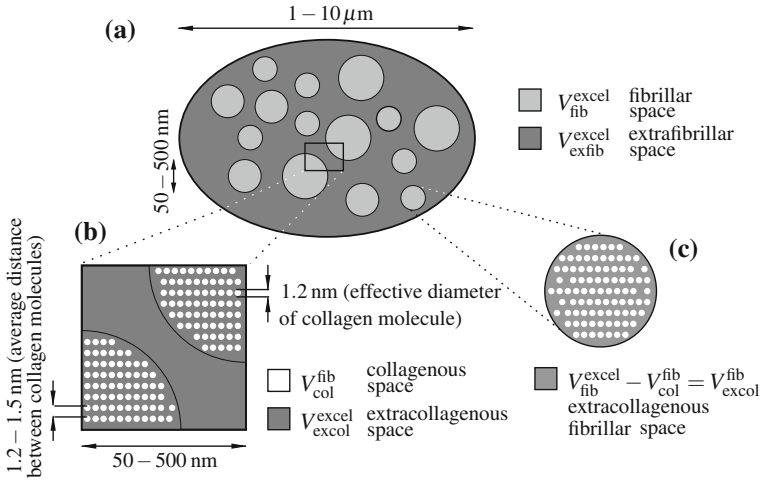
**Fig. 5** Schematical sketch of spaces in the extracellular bone matrix or ultrastructure, **a** section through the ultrastructural representative volume element perpendicular to the direction of the fibrils, **b** and **c** close-ups

in the extrafibrillar space equals that in the extracollageneous space. The underlined arguments are as follows: The ultrastructural volume element with a characteristic size of some micrometers, consists of fibrillar and extrafibrillar space; see Fig. 5a, with corresponding volumes $V_{fib}^{excel}$ and $V_{exfib}^{excel}$. The fibrils are made up by collagen molecules exhibiting a triple helix structure arranged more or less cylindrically, with diameters ranging from 50 to 500 nm [35, 95, 105, 122, 125, 142, 150, 151]. The fibrillar volume $V_{fib}^{excel}$ comprises all fibrils within the ultrastructural (or extracellular) volume $V^{excel}$. $V_{col}^{fib}$, the volume of collagen within the fibrils, is a subspace of $V_{fib}^{excel}$, as is $(V_{fib}^{excel} - V_{col}^{fib})$, see Fig. 5c. The latter is the volume within the fibrils which is not occupied by collagen molecules, subsequently referred to as extracollageneous fibrillar volume, $V_{excol}^{fib}$. The space within the ultrastructure (or extracellular bone matrix) that is not occupied by fibrils is called extrafibrillar space, $V_{exfib}^{excel} = V^{excel} - V_{fib}^{excel}$. The union of the spaces $V_{exfib}^{excel}$ and $V_{excol}^{fib}$, $V_{exfib}^{excel} + V_{excol}^{fib} = V^{excel} - V_{col}^{excel} = V_{excol}^{excel}$, is the total extracollageneous space within the extracellular bone, see Fig. 5b.

Based on these notions, the aforementioned rule would imply that the ratio of the mass of the extrafibrillarly located mineral $\left(M_{HA}^{exfib}\right)$, over the volume of the extrafibrillar space needs to be equal to the ratio of the entire mineral mass $(M_{HA})$, over the extracollageneous volume

$$\rho_{HA}^{exfib} = \frac{M_{HA}^{exfib}}{V_{exfib}^{excel}} \equiv \frac{M_{HA}}{V_{excol}^{excel}} = \rho_{HA}^{excol}, \qquad (19)$$

with $\rho_{HA}^{exfib}$ and $\rho_{HA}^{excol}$ being the apparent mineral densities relating to the extrafibrillar and the extracollageneous volumes, respectively. Equation (19) can be rearranged as follows

$$\phi_{HA}^{exfib} = \frac{M_{HA}^{exfib}}{M_{HA}} \equiv \frac{V_{exfib}^{excel}}{V_{excol}^{excel}} = \frac{f_{exfib}^{excel}}{1 - f_{col}^{excel}} , \qquad (20)$$

where $f_{exfib}^{excel} = V_{exfib}^{excel} / V^{excel}$ is the extrafibrillar volume fraction, $f_{col}^{excel} = V_{col}^{excel} / V^{excel}$ is the collagen volume fraction, both quantified within the volume of extracellular bone, and $\phi_{HA}^{exfib}$ is the relative amount of extrafibrillar mineral.

Two independent sets of experimental observations covering a large range of tissue mass densities were considered for checking the relevance of Eq. (20), as discussed next.

### Experimental Set I: Mass and Volume Measurements

First, $f_{exfib}^{excel} / (1 - f_{col}^{excel})$ is determined from weighing experiments and diffraction spacing measurements. In order to determine the apparent mass density of collagen, we adopt a value of $\rho_{org} = 1.42 \, g/cm^3$ [76, 86], and consider the fact that collagen constitutes approximately 90% by weight of the organic matter in mineralized tissues [13, 86, 146, 150]. The mass of organic matter can be determined from weighing experiments on demineralized and dehydrated specimens [13, 86, 90, 91], harvested from different anatomical locations of different vertebrates at different ages, see Sect. 2, in particular Tables 1, 2, 3 and 5. On the other hand, the determination of the extrafibrillar volume fraction $f_{exfib}^{excel} = 1 - f_{fib}^{excel}$ requires quantification of the fibrillar space within the mineralized tissue. This can be achieved by application of a model for the organization of collagen: we use Lees' generalized packing model [16, 86], as the simplest model to quantify the average crosslink length between collagen molecules, see also [63].

### Experimental Set II: Transmission Electron Microscopy

As a second, independent set of observations, we consider optical density measurements from TEMs, in order to determine $\phi_{HA}^{exfib}$. Figure 6 displays three TEMs of cross sections of mineralized tissues, covering a wide range of extracellular mass densities; from $\rho^{excel} = 1.5 \, g/cm^3$ for mineralized turkey leg tendon, see Fig. 6a, to $\rho^{excel} = 2.6 \, g/cm^3$ for the rostrum of whale, see Fig. 6c. These micrographs reflect the electron density of material phases. The higher the electron density, the darker the respective area of the TEM images. Since hydroxyapatite exhibits by far the largest electron density of all elementary components, the TEM images displayed in Fig. 6 highlight that hydroxyapatite is mainly located outside the fibrils. First, the relative optical density is determined using the protocol of Lees et al. [95]: the TEM images are scanned and then captured by a frame grabber [22]. The optical density is considered linearly proportional to the number of electrons transmitted through the particular area [95], the number of electrons linearly proportional to the local hydroxyapatite mass density in the fibrillar or extrafibrillar space. The average densities are then related to the apparent mineral densities, allowing for the determination of the extrafibrillar volume fraction of tissues, $f_{exfib}^{excel}$, shown in TEM images. $f_{exfib}^{excel}$ turns out to be 60% for the mineralized turkey leg tendon micrograph of Fig. 6a ($\rho^{excel} = 1.5 \, g/cm^3$), 53% for the human tibia ($\rho^{excel} = 2.0 \, g/cm^3$), see Fig. 6b, and 85% for the whale rostrum ($\rho^{excel} = 2.6 \, g/cm^3$), see Fig. 6c.
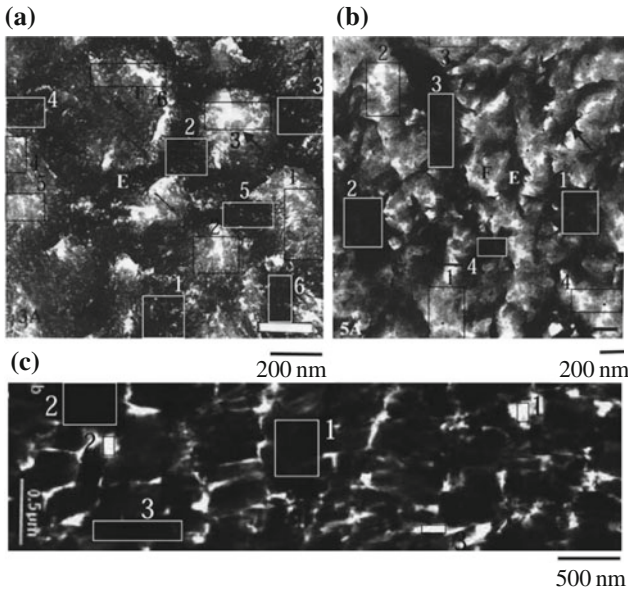
**Fig. 6** Transmission electron micrographs of cross sections through: **a** mineralized turkey leg tendon [122]; **b** human tibia [122] and **c** whale rostrum [159]

### Comparison of Independently Derived Values of the Relative Amount of Extrafibrillar Mineral

Next, the sample-specific relative amount of extrafibrillar mineral, $\phi_{HA}^{exfib}$, of very different bone tissues, derived from the independent methods related to the experiment sets I and II, respectively, are compared, as shown in Fig. 7. It can be seen that the values derived from both experimental data sets are in perfect agreement when comparing similar tissues. This surprisingly good agreement of values obtained from two independent assessment methods provides the sought after evidence that the average mineral concentration in the extrafibrillar and the extracollageneous spaces are indeed equal; see Hellmich and Ulm [63] for further details.

## 5 Hydration-Dependent Evolution of Unmineralized Collagenous Tissues

Hydration of collagenous tissues, consisting of fibrillar and extrafibrillar constituents, causes swelling, as well as mechanical softening (i.e. reduction of stiffness). The underlying mechanism can be quantified in terms of the following mathematical rule [109]: After drying the tissue in air, water remains only in the gap zones between the triple-helical collagen molecules making up 12% of the total volume [88]. Upon
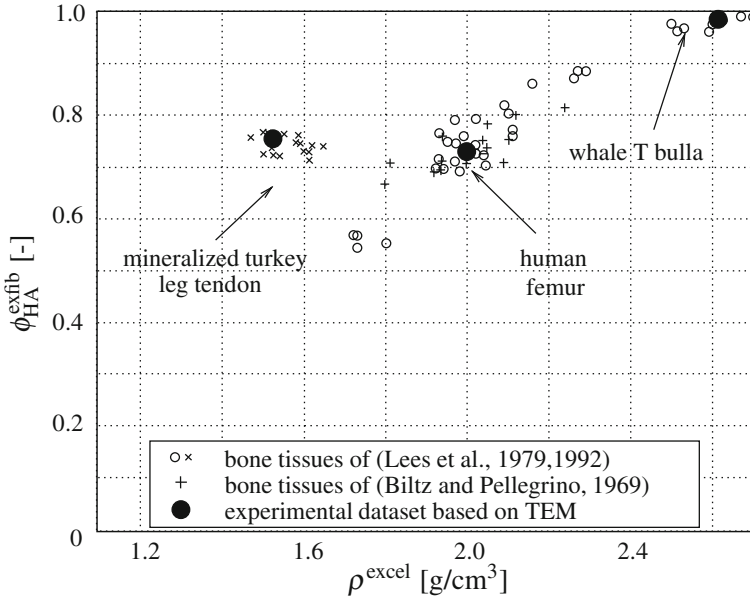
**Fig. 7** Relative amount of extrafibrillar mineral, $\phi_{HA}^{exfib}$, as a function of extracellular mass density $\rho^{excel}$, according to Hellmich and Ulm [63]
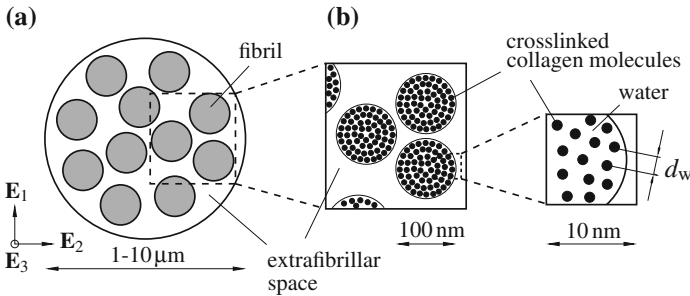


**Fig. 8** Scheme concerning hierarchical structure of collagen: **a** collagenous tissue, **b** wet collagen

rehydration, the extrafibrillar space is established at volumes directly proportional to the hydration-induced swelling of the (micro) fibrils, until the maximum equatorial distance between the long collagen molecules is reached. Thereafter, the volume of the fibrils stays constant, and only the extrafibrillar volume continues to grow. Mathematically, the proportionality between the extrafibrillar space growth and the swelling of fibrils (in case the fibrils still swell, which occurs if they are not fully hydrated) can be expressed as follows

$$V_{exfib}^{excel} = \beta(V_{fib}^{excel} - V_{dry}^{col}), \quad V_{dry}^{col} \leq V_{fib}^{excel} \leq V_{fib,max}^{excel}, \tag{21}$$

with $\beta$ as proportionality constant, with $V_{\text{exfib}}^{\text{excel}}$ as the volume of extrafibrillar space within the collageneous tissue, $V_{\text{fib}}^{\text{excel}}$ as fibrillar volume within the collageneous tissue, which is smaller than or equal to the maximum attainable value $V_{\text{fib,max}}^{\text{excel}}$, and larger than a minimum value $V_{\text{dry}}^{\text{col}}$ corresponding to the dry volume of the collageneous tissue, $V^{\text{excel}}$. The fibrillar and extrafibrillar volumes, $V_{\text{fib}}^{\text{excel}}$ and $V_{\text{exfib}}^{\text{excel}}$, fill the entire tissue volume $V^{\text{excel}}$, $V_{\text{fib}}^{\text{excel}} + V_{\text{exfib}}^{\text{excel}} = V^{\text{excel}}$, yielding, together with (21), a tissue swelling rule in the following form

$$\frac{V^{\text{excel}}}{V_{\text{dry}}^{\text{col}}} = \beta \left( \frac{V_{\text{fib}}^{\text{excel}}}{V_{\text{dry}}^{\text{col}}} - 1 \right) + \frac{V_{\text{fib}}^{\text{excel}}}{V_{\text{dry}}^{\text{col}}}, \quad V_{\text{dry}}^{\text{col}} \leq V_{\text{fib}}^{\text{excel}} \leq V_{\text{fib,max}}^{\text{excel}}. \tag{22}$$

We regard the fibrils as continua with one to several hundreds of nanometers characteristic size, these continua being built up by representative volume elements of several to several tens of nanometers characteristic size, see Fig. 8. Microscopic images [28] show that hydration affects volume changes in a fibril in a homogeneous fashion. Therefore, following the deformation laws of continuum mechanics [131], the current fibrillar volume $V_{\text{fib}}^{\text{excel}}$ is related to the initial volume $V_{\text{dry}}^{\text{col}}$ by the Jacobian $J$, which is standardly expressed by the product of the principal stretches $\lambda_1$, $\lambda_2$, and $\lambda_3$ of the volume elements, thus

$$\frac{V_{\text{fib}}^{\text{excel}}}{V_{\text{dry}}^{\text{col}}} = J = \lambda_1 \times \lambda_2 \times \lambda_3. \tag{23}$$

The principal stretches are defined as the ratio of the current length to the initial length of the line elements $d\mathbf{x}_1$, $d\mathbf{x}_2$, and $d\mathbf{x}_3$ attached to the fibrils and oriented in the principle deformation directions $e_1$, $e_2$, and $e_3$ (see Fig. 8). These principle stretches are related to the ratios of diffraction spacings in the current and initial elementary volumes, in the line of standard stretch measurements in lattice-like microstructures [148, 149]. As regards $\lambda_1$ and $\lambda_2$, the aforementioned diffraction spacings are related to the (on-average) lateral (transversal, equatorial) distances between collagen molecules,

$$\lambda_1 = \lambda_2 = \lambda_{\text{tr}} = \frac{d_{\text{w}}}{d_{\text{dry}}}, \tag{24}$$

with $d_{\text{w}}$ as the lateral diffraction spacing related to some more or less hydrated state of the fibril, and $d_{\text{dry}} = 1.09$ nm as the lateral diffraction spacing in dry tissues [93]. As regards $\lambda_3$, diffraction peaks relate to the axial macroperiod $D_{\text{w}}$ of collagen, comprising repeating units of one gap zone and one overlap zone each, as discovered by Hodge and Petruska [72]; this axial macroperiod increases, albeit only slightly, upon hydration (up to a value of 67 nm). Since this increase is clearly less than 5% when compared to the axial macroperiod measured by dry tissues, $D_{\text{dry}} = 64$ nm, measured in dry tissues, we consider $D_{\text{w}}$ as a constant, and hence

$$\lambda_3 = \lambda_{ax} = \frac{D_w}{D_{dry}} = 1. \tag{25}$$

Finally, the variation of the current fibrillar volume with respect to the initial one reads as

$$\frac{V_{fib}^{excel}}{V_{dry}^{col}} = \lambda_1 \cdot \lambda_2 \cdot \lambda_3 = \left(\frac{d_w}{d_{dry}}\right)^2. \tag{26}$$

However, the diffraction spacings are limited, and cannot exceed a maximum value of 1.38 nm in the equatorial direction [102]. Therefore, the amount of water which can be accommodated in the fibrils is also limited. Upon further hydration, namely beyond the so-called fibrillar saturation limit, only the extrafibrillar volume continues to grow. The mathematically expressed swelling rule (21), together with volume relations (22) to (26), was experimentally validated by means of the measurement results of Meek et al. [102], Robinson [128], Rougvie and Bear [130]. Therefore, the water-to-organic ratios $\mathscr{R}$ given in these papers, were converted into volumes according to

$$\frac{V^{excel}}{V_{dry}^{col}} = 0.88 \frac{\mathscr{R}\rho_{col} + \rho_{H_2O}}{\rho_{H_2O}}, \tag{27}$$

where $\rho_{col} = 1.42\,\text{g/cm}^3$ [88] and $\rho_{H_2O} = 1\,\text{g/cm}^3$ are the mass densities of molecular collagen and water, respectively; obviously, this equation accounts for the existence of 12% gap zones in the collagenous dry matrix [72, 88], relating to an intermolecular pore saturation limit amounting to $\mathscr{R}^{imsat} = 0.096$. Based on relations (22) and (27), combined with the observations of Meek et al. [102], that the fibrillar swelling stops at a water-to-organic mass ratio of $\mathscr{R}^{fibsat} = 0.82$, one can translate the swelling rule (22) into a mathematical relation between water-to-organic mass ratios and corresponding diffraction spacings,

$$\mathscr{R}^{pred} = \frac{1}{\rho_{col}} \left( \frac{\rho_{H_2O}}{0.88} \left[ (\beta + 1) \left(\frac{d_w}{d_{dry}}\right)^2 - \beta \right] - \rho_{H_2O} \right). \tag{28}$$

It is directly tested against respective experimental values provided by Katz and Li [76], Meek et al. [102], Rougvie and Bear [130], see Fig. 9, with a relative error as low as 0.98±12.56 % (mean value plus standard deviation), see [109] for further details. Given the excellent confirmation of the swelling rule, it allows for quantifying the evolution of subvolumes and volume fractions in hydrating tissues: during hydration, the fibrillar volume fraction decreases by more than 50%, see Fig. 10b. At the same time, the tissue is swelling to its triple size, as seen in Fig. 10a. Also during hydration, the volume fraction of molecular collagen within a fibril decreases from 88 to 54.7%, while that of water increases from 0 to 45.3%, see Fig. 11b. At the same time, the fibrils grow by about 60% in volume, see Fig. 11a.
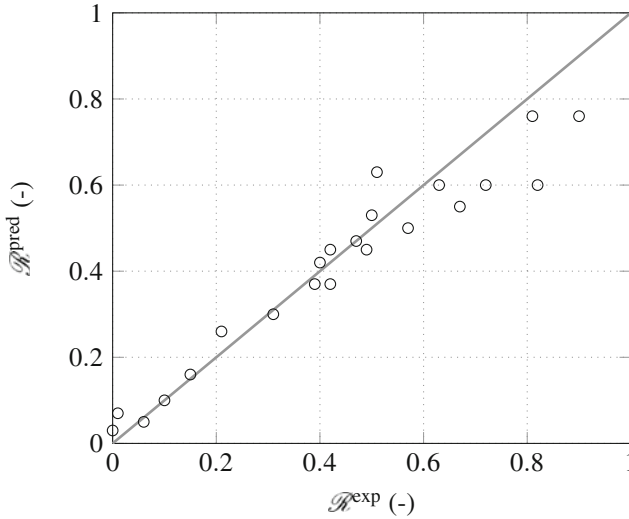
**Fig. 9** Water-to-organic mass ratio: diffraction- and swelling rule-based predictions $\mathscr{R}^{\mathrm{pred}}$ versus direct experiments $\mathscr{R}^{\mathrm{exp}}$
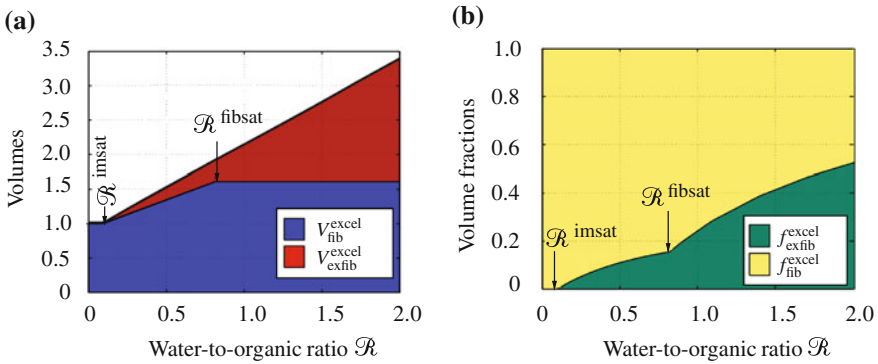


**Fig. 10** Tissue swelling (**a**) and evolution of tissue composition (**b**) during hydration: **a** water-to-organic mass ratio $\mathscr{R}$ over the fibrillar and extrafibrillar volumes making up the tissue; **b** water-to-organic mass ratio $\mathscr{R}$ over the fibrillar and extrafibrillar volume fractions at the tissue scale

## 6 Bone Tissue Evolution During Mineralization

Inspired by an interesting idea of Lees [87], Morin and Hellmich [107] showed that the volume and structure changes in mineralizing bone tissues can be mathematically predicted when considering the extracellular bone tissue and its subvolumes (both the fibrils and the extrafibrillar space) as closed thermodynamic systems: i.e. if no fluid mass leaves or enters these volumes during the mineralization process, then the precipitation of hydroxyapatite crystals entails that the mass of lost ionic fluid

**(a)**

**(b)**
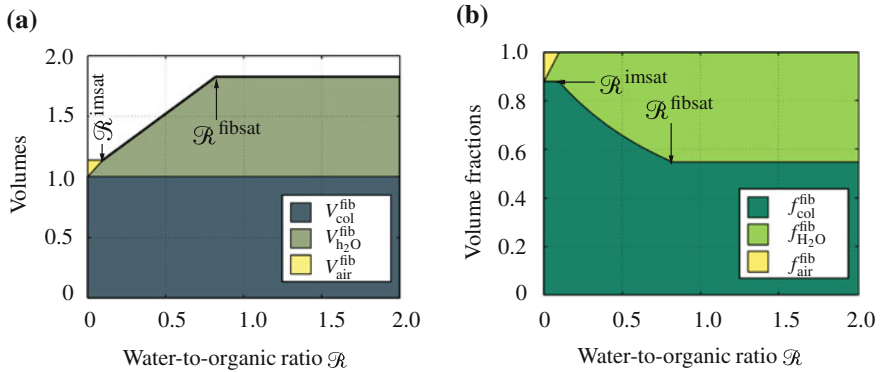


**Fig. 11** Fibrillar swelling (**a**) and evolution of fibrillar composition (**b**) during hydration: **a** water-to-organic mass ratio $\mathscr{R}$ over the volumes of molecular collagen, water, and air making up the fibrils; **b** water-to-organic mass ratio $\mathscr{R}$ over the volume fractions of collagen, water, and air at the tissue scale

equals the mass of formed solid hydroxyapatite crystal in the fibrillar and extrafibrillar subvolumes, as well as in the entire tissue volume, while the collagen mass remains unaltered. The precipitation of dissolved ions into solid mineral crystals is accompanied by an increase in mass density, which, upon overall conservation under closed conditions, leads to a volume decrease (or shrinkage) of the tissues during the biomineralization process. This shrinkage affects both the fibrillar and the extrafibrillar tissue compartments. Thereby, the fibrillar shrinkage can be experimentally accessed through equatorial neutron diffraction spacings $d_{w,\infty}$, measured on fully mineralized tissues [104, 109]

$$\left(\frac{d_{w,\infty}}{d_{w,0}}\right)^2 = \frac{V_{fib,\infty}^{excel}}{V_{fib,0}^{excel}}, \tag{29}$$

with $d_{w,0}$ as the neutron diffraction spacing at the time of osteoid deposition (i.e. the beginning of the mineralization process), and $V_{fib,0}^{excel}$ and $V_{fib,\infty}^{excel}$ as the fibrillar volume in unmineralized and fully mineralized tissues, respectively.

The mass density-diffraction relation ($\rho_\infty^{excel}$-$d_{w,\infty}$-relation) is derived in three consecutive steps: First, the mineralization-induced tissue shrinkage is evaluated at the tissue level, based on the "universal" composition rules described in Sect. 3, yielding [107]

$$\frac{V_\infty^{excel}}{V_0^{excel}} = \frac{1}{1 + (\rho_{HA}/\rho_{fl} - 1) \times f_{HA,\infty}^{excel}(\rho_\infty^{excel})}, \tag{30}$$

with $V_0^{excel}$ and $V_\infty^{excel}$ as the extracellular tissue volumes at the beginning and the end of the mineralization process, $\rho_{HA}$ and $\rho_{fl}$ as the mass densities of hydroxyapatite

and ionic fluid, $f_{\text{HA},\infty}^{\text{excel}}$ as the mineral volume fraction in the fully mineralized tissue, which depends on the tissue mass density, $\rho_\infty^{\text{excel}}$.

Secondly, this relation is downscaled to the extrafibrillar space, by considering the equality of mineral concentrations in the extracollagenous and the extrafibrillar spaces [63], see Sect. 4, and the hydration swelling rule for unmineralized tissues [109], as described in Sect. 5. The corresponding volume change reads as [107]

$$\frac{V_{\text{exfib},\infty}^{\text{excel}}}{V_{\text{exfib},0}^{\text{excel}}} = 1 + \frac{(1 - \rho_{\text{HA}}/\rho_{\text{fl}})}{1 - f_{\text{col},0}^{\text{excel}}} \frac{V_\infty^{\text{excel}}}{V_0^{\text{excel}}} \times f_{\text{HA},\infty}^{\text{excel}}(\rho_\infty^{\text{excel}}), \tag{31}$$

where $V_\infty^{\text{excel}}/V_0^{\text{excel}}$ obeys Eq. (30), $f_{\text{HA},\infty}^{\text{excel}}(\rho_\infty^{\text{excel}})$ follows from the universal composition rules (see Sect. 3), and $f_{\text{col},0}^{\text{excel}}$ is the collagen volume fraction in unmineralized tissue, which can be quantified from the hydration-dependent swelling rules described in Sect. 5, see [109] for details.

Thirdly, the fibrillar shrinkage is analogously derived,

$$\frac{V_{\text{fib},\infty}^{\text{excel}}}{V_{\text{fib},0}^{\text{excel}}} = \frac{f_{\text{fib},\infty}^{\text{excel}}}{f_{\text{fib},0}^{\text{excel}}} \frac{V_\infty^{\text{excel}}}{V_0^{\text{excel}}}, \tag{32}$$

and this ratio is related to the change in diffraction spacing, as given in Eq. (29), with $d_{\text{w},0} = d_{\text{max}} = 1.52$ nm as the diffraction spacing of fully saturated unmineralized collageneous tissues [23, 39, 76, 93]. Finally, these relations are translated into the sought mass density-diffraction spacing relations, according to continuum geometry and considering negligible length changes in the meridional direction of the tissue [109]. In case of fully-hydrated tissues, this relation reads as

$$d_{\text{w},\infty} = d_{\text{max}} \sqrt{\frac{1 - f_{\text{exfib},0}^{\text{excel}} \times \left[1 - (\rho_{\text{HA}}/\rho_{\text{fl}} - 1) \times f_{\text{HA},\infty}^{\text{excel}} \times \frac{f_{\text{col},\infty}^{\text{excel}}}{\rho_{\text{HA}} f_{\text{HA},\infty}^{\text{excel}}/\rho_{\text{fl}} + f_{\text{fl},\infty}^{\text{excel}}}\right]}{(1 - f_{\text{exfib},0}^{\text{excel}}) \times \left[1 + (\rho_{\text{HA}}/\rho_{\text{fl}} - 1) \times f_{\text{HA},\infty}^{\text{excel}}\right]}}, \tag{33}$$

with

$$f_{\text{exfib},0}^{\text{excel}} = 1 - \frac{1}{0.88} \left(\frac{d_{\text{max}}}{d_{\text{dry}}}\right)^2 \frac{f_{\text{col},\infty}^{\text{excel}}}{\rho_{\text{HA}} f_{\text{HA},\infty}^{\text{excel}}/\rho_{\text{fl}} + f_{\text{fl},\infty}^{\text{excel}} + f_{\text{col},\infty}^{\text{excel}}}, \tag{34}$$

where $d_{\text{max}} = 1.52$ nm and $d_{\text{dry}} = 1.09$ nm, and with dependencies $f_{\text{HA},\infty}^{\text{excel}}$, $f_{\text{col},\infty}^{\text{excel}}$, and $f_{\text{fl},\infty}^{\text{excel}}$ on tissue mass density as given in Sect. 3 (see Eqs. (16) and (17)).

In case of partially dehydrated tissues, some fluid mass (and corresponding volume) will be lost during dehydration,

$$\Delta f_{\text{fl},\infty}^{\mu,\text{dh}} = f_{\text{fl},\infty}^\mu - f_{\text{fl},\infty}^{\mu,\text{dh}} = f_{\text{fl},\infty}^\mu - \mathscr{R}^{\infty,dh} f_{\text{col},\infty}^\mu \rho_{\text{col}}/\rho_{\text{fl}}, \tag{35}$$

with $\mathscr{R}^{\infty,dh}$ as the experimentally measured water-to-organic mass ratio of partially dehydrated tissues at the macroscopic scale, as e.g. given by Lees and Mook [89].

The volume fraction of the remaining fluid after dehydration per extracellular bone matrix reads as

$$f_{fl,\infty}^{excel,dh} = \frac{f_{fl,\infty}^{\mu} - \min(\Delta f_{fl,\infty}^{\mu,dh}, f_{\mu por})}{1 - f_{\mu por}} .$$ (36)

The lost fluid volume fraction in the extracellular scale amounts to

$$\Delta f_{fl,\infty}^{excel,dh} = f_{fl,\infty}^{excel} - f_{fl,\infty}^{excel,dh} .$$ (37)

The mass density-diffraction spacing relation for partially dehydrated tissues reads as

$$d_{w,\infty}^{dh} = d_{w,\infty} \sqrt{1 - \frac{\Delta f_{fl,\infty}^{excel,dh} - f_{exfib,0}^{excel} \Delta f_{fl,\infty}^{excel,dh}/(1 - f_{col,0}^{excel})}{f_{fib,\infty}^{excel}}} ,$$ (38)

with

$$f_{fib,\infty}^{excel} = 1 - \left\{ \frac{f_{exfib,0}^{excel}}{\frac{1}{1+(\rho_{HA}/\rho_{fl}-1)\times f_{HA,\infty}^{excel}}} + \frac{f_{exfib,0}^{excel}}{1 - f_{col,0}^{excel}} \times (1 - \rho_{HA}/\rho_{fl}) \times f_{HA,\infty}^{excel} \right\} ,$$ (39)

and

$$f_{col,0}^{excel} = \frac{f_{col,\infty}^{excel}}{\rho_{HA} f_{HA,\infty}^{excel}/\rho_{fl} + f_{fl,\infty}^{excel} + f_{col,\infty}^{excel}} .$$ (40)

Identification of $\Delta f_{fl,\infty}^{excel,dh} = f_{fl,\infty}^{excel}$ delivers model predictions for the diffraction spacings in fully dried tissues. These mass density-diffraction spacing relations are fed with experimental data for tissue mass density and the corresponding predictions for diffraction spacing are validated through comparison with experimental results [87, 89, 93]. Very low prediction errors of $1.8 \pm 3.1\%$ underline the relevance of the model-predicted evolutions of the tissue compartment volumes, and of the model-predicted volume fractions during the mineralization process in different bone tissues (see Fig. 12); and hence, the idea of hydroxyapatite precipitating under closed thermodynamic conditions from an ionic solution in the fibrillar and extrafibrillar spaces of bone tissue. Accordingly, the structural (volumetric) evolution of mineralizing bone tissue can be quantified as follows: during mineralization, the volume of the overall collagenous tissue is shrinking because the mass density of hydroxyapatite is around three times larger than that of liquid ionic solution. In general, the more mineral is present in the tissue, the higher the shrinkage of the volumes of the different compartments (see Fig. 13). More specifically, this volume loss is minimal for low-mineralized tissues at the beginning of the mineralization process (see the left lower corner of Fig. 13), whereas highly mineralized bone tissue has lost up to 60% of its initial (osteoid) volume (see the right upper corner of Fig. 13).

The compositional evolution can be also quantified in terms of volume fractions: the mineralization process leads to a slight increase of the fibrillar volume frac-
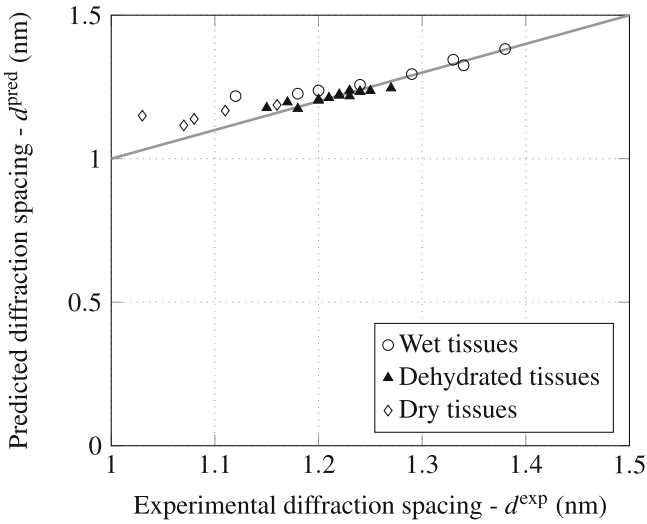
**Fig. 12** Predicted versus experimental diffraction spacing for wet, dry, and partially dehydrated, mineralized tissues
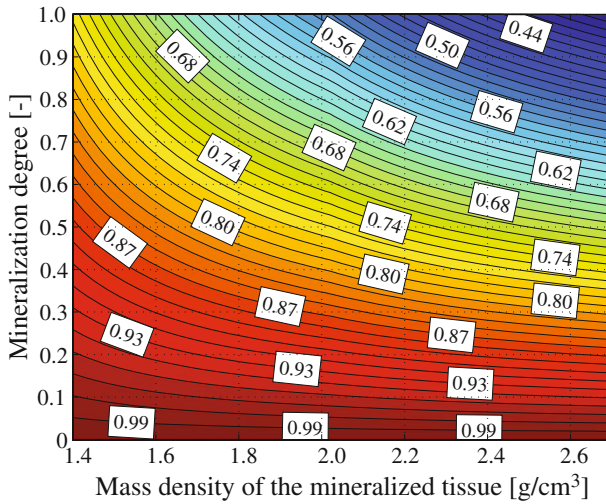


**Fig. 13** Normalized tissue volume as function of the mineralization degree for different final tissue mass densities
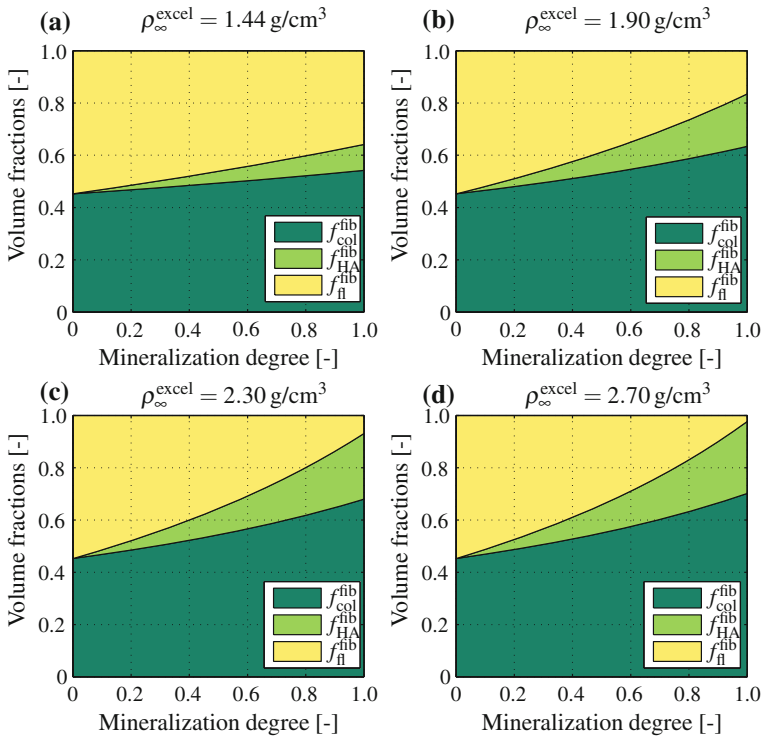
**Fig. 14** Normalized tissue volume as function of the mineralization degree, for different final tissue mass densities

tions, since the fibrils, thanks to the presence of chemically inert collagen, are less affected by the fluid-to-crystal transformation-induced volume loss, as compared to the extrafibrillar space. Within the fibrils, the fluid volume fraction, starting from around 50% in the unmineralized osteoid, is reduced by one third in the case of low-mineralized tissues (see Fig. 14a), while it is almost completely consumed in the case of very highly mineralized tissues (see Fig. 14d). Thereby, lost fluid volume fractions are replaced by collagen and mineral volume fractions, at about the same shares (see Fig. 14a–d). In the extrafibrillar space, mineral volume fractions increase overlinearly with the mineralization degree, the more so the more highly the tissue is mineralized.

# 7 Nano- and Microstructural Patterns Governing Anisotropic Tissue Elasticity

Throughout the last two decades, hierarchical material models for bone [4, 33, 53, 55, 56, 60, 61, 64–66, 98, 108, 110, 116, 118, 119, 124, 132, 154], developed within the frameworks of homogenization theory and continuum micromechanics [7, 37, 157] and validated through a multitude of biochemical, biophysical, and biomechanical experiments [13, 16, 25, 51, 57, 79, 86, 87, 90–92, 94, 96, 100, 126, 145], have opened the way to translate the chemical composition of extracellular bone material (i.e. the volume fractions of organics, water, and hydroxyapatite) into the tissue's anisotropic elasticity. This section is devoted to briefly introducing the fundamentals of continuum micromechanics, and to presenting how this theoretical framework has elucidated the "construction plans" providing the most fascinating mechanical properties of bone.

### *Micromechanical Representation of Bone Tissue by Means of Representative Volume Elements (RVEs)*

In continuum micromechanics [37, 71, 156, 157], a material is understood as a macro-homogeneous, but micro-heterogeneous body filling a representative volume element (RVE) with characteristic length $\ell$, which must be both considerably larger than the dimensions of heterogeneities within the RVE, $\mathscr{D}$, and significantly smaller than the characteristic lengths of geometry or loading of a structure built up by the material defined on the RVE, $\mathscr{L}$. The characteristic length of structural loading typically coincides with wave lengths of signals traveling through the structure, or relates to macroscopic stress gradients according to $\mathscr{L} \approx ||\boldsymbol{\Sigma}||/||\text{GRAD}\boldsymbol{\Sigma}||$ [7], with the "macroscopic" stress tensor $\boldsymbol{\Sigma}$. In mathematical terms, the aforementioned separation of scales requirement reads as

$$\mathscr{D} \ll \ell \ll \mathscr{L}. \tag{41}$$

Hereby, the first inequality sign typically relates to a factor of 2 to 3 [38]; while the second one typically relates to a factor of 5 to 50 [81].

In general, the microstructure within one RVE is so complex that it cannot be described in complete detail. Therefore, quasi-homogeneous subdomains, called material phases, with known physical quantities are reasonably chosen. Quantitative phase properties are volume fractions $f_r$ of phases $r = 1, \ldots, N_r$, (average) elastic properties, as well as the morphological description, as, e.g. the isotropy or the symmetries of anisotropy of the spatial distribution of the phases, the existence of one connected "matrix phase" in which one or several "inclusion phases" with different shapes are embedded (as in reinforced composite material), or the disordered arrangement of all phases (as in a polycrystal).

The central goal of continuum micromechanics is to estimate the mechanical properties (such as elasticity or strength) of the material defined on the RVE from the aforementioned phase properties. This procedure is referred to as homogenization

or one homogenization step. If a single phase exhibits a heterogeneous microstructure itself, its mechanical behavior can be estimated by introduction of an RVE within this phase [46], with dimensions $\ell_2 \leq \mathscr{D}$, comprising again smaller phases with characteristic length $\mathscr{D}_2 \ll \ell_2$, and so on, leading to a multistep homogenization scheme, as in case of bone (see Fig. 15). In this context, the following "universal" microstructural patterns are considered across the hierarchical organization of bone materials:

- an RVE of wet collagen, with a characteristic length of several nanometers (see Fig. 15a), represents the staggered organization of cylindrical collagen molecules (see Fig. 1h), which are attached to each other by ∼1.5 nm long crosslinks [8, 93, 112]. These crosslinks imply the existence of a contiguous matrix built up by molecular collagen, hosting fluid-filled intermolecular spaces, which are represented by cylindrical inclusions;
- an RVE of extrafibrillar space (hydroxyapatite foam), with a characteristic length of several hundred nanometers (see Fig. 15c), hosts crystal needles (represented through infinitely many uniformly oriented cylindrical hydroxyapatite inclusions) oriented in all space directions; in mutual interaction with spherical, water-filled pores in-between;
- an RVE of extracellular bone matrix or ultrastructure, with a characteristic length of several micrometers (see Fig. 15d), hosts cylindrical, mineralized fibrils being embedded into a contiguous matrix built up by hydroxyapatite foam material;
- an RVE of extravascular bone material, with a characteristic length of several hundred micrometers (see Fig. 15e), hosts spherical, osteocyte-filled cavities called lacunae being embedded into a contiguous matrix built up by the extracellular bone material; and
- an RVE of cortical bone material, with a characteristic length of several millimeters (see Fig. 15f), hosts cylindrical vascular pores being embedded into a matrix of extravascular bone material.

### *Elasticity Homogenization*

As concerns the homogenization (or upscaling) of the elastic properties of bone, starting from the level of its basic building blocks, up to the level of the bone microstructure, see Fig. 15, we start with focusing on a single RVE built up by phases enumerated by $r$. The second-order strain tensor, $\boldsymbol{\varepsilon}_r$, is related to the (average "microscopic") second-order stress tensor in phase $r$, $\boldsymbol{\sigma}_r$, by the phase elasticity tensor $\mathbb{c}_r$

$$\boldsymbol{\sigma}_r = \mathbb{c}_r : \boldsymbol{\varepsilon}_r \,. \tag{42}$$

The RVE is subjected to homogeneous (macroscopic) strains $\mathbf{E}$ at its boundary [59], prescribed in terms of displacements

$$\forall \mathbf{x} \in \partial V_{RVE}: \qquad \boldsymbol{\xi}(\mathbf{x}) = \mathbf{E} \cdot \mathbf{x} \,, \tag{43}$$

whereby $\mathbf{x}$ is the position vector for locations within or at the boundary of the RVE. As a consequence, the resulting kinematically compatible microstrains $\boldsymbol{\varepsilon}(\mathbf{x})$ throughout

intermolecular space

$\ell_{\text{wetcol}} \approx 10$ nm

$x_3$

$x_1, x_2$

matrix: molecular collagen

(a) wet collagen

"self-consistent" matrix: with no volume fraction and the elastic properties of the RVE itself

hydroxyapatite (HA)

hydroxyapatite (HA)

$\ell_{\text{fib}} \approx 100 - 500$ nm

$x_3$

$x_1, x_2$

wet collagen

$\ell_{\text{exfib}} \approx 100 - 500$ nm

intercrystalline space

(b) collagen - hydroxyapatite network (fibril)

(c) hydroxyapatite foam (extrafibrillar space)

mineralized collagen fibril

$\ell_{\text{excel}} \approx 5 - 10$ μm

$x_3$

$x_1, x_2$

extrafibrillar space (hydroxyapatite foam)

(d) extracellular bone matrix or ultrastructure

$\ell_{\text{exvas}} \approx 100$ μm

$x_3$

$x_1, x_2$

lacunae     extracellular bone matrix (ultrastructure)

(e) extravascular bone material

$\ell_{\text{cort}} \approx 1$ mm

$x_3$

$x_1, x_2$

Haversian canals     extravascular bone material
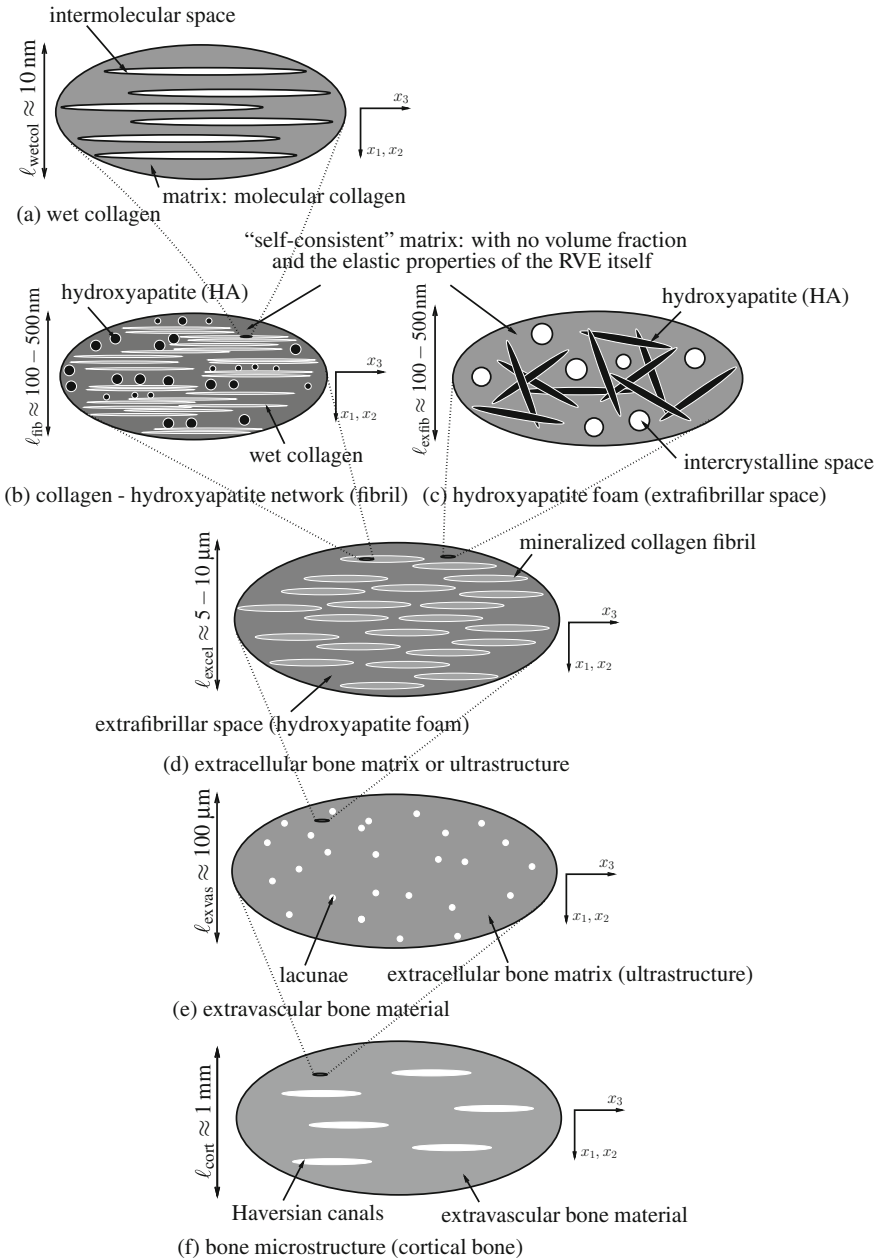
(f) bone microstructure (cortical bone)

**Fig. 15** Micromechanical representation of bone material by means of a six-step homogenization scheme, according to Fritsch et al. [48]

the RVE fulfill the average condition,

$$\mathbf{E} = \frac{1}{V_{RVE}} \int_{V_{RVE}} \boldsymbol{\varepsilon} \, dV = \langle \boldsymbol{\varepsilon} \rangle = \sum_r f_r \boldsymbol{\varepsilon}_r \,, \tag{44}$$

providing a link between the (average) microscopic and macroscopic strains. Furthermore, the aforementioned deformations provoke traction forces $\mathbf{T}(\mathbf{x})$ on the boundary of the RVE, and microstresses $\boldsymbol{\sigma}(\mathbf{x})$ throughout the RVE, fulfilling the equilibrium conditions

$$\begin{aligned}
\forall \mathbf{x} \in V_{RVE} & \quad \text{div}\boldsymbol{\sigma}(\mathbf{x}) = 0 \,, \\
\forall \mathbf{x} \in \partial V_{RVE} & \quad \mathbf{T}(\mathbf{x}) = \boldsymbol{\sigma}(\mathbf{x}) \cdot \mathbf{n}(\mathbf{x}) \,,
\end{aligned} \tag{45}$$

with $\mathbf{n}(\mathbf{x})$ as the normal to the boundary at position $\mathbf{x}$. The external work done by these traction forces reads as

$$\begin{aligned}
\mathscr{W}^{ext} &= \int_{\partial V_{RVE}} \mathbf{T}(\mathbf{x}) \cdot \boldsymbol{\xi}(\mathbf{x}) \, dS = \int_{\partial V_{RVE}} (\mathbf{E} \cdot \mathbf{x}) \cdot [\boldsymbol{\sigma}(\mathbf{x}) \cdot \mathbf{n}(\mathbf{x})] \, dS \\
&= \mathbf{E} : \int_{V_{RVE}} \boldsymbol{\sigma}(\mathbf{x}) \, dV \,,
\end{aligned} \tag{46}$$

whereby we made use of boundary condition (43) and of the divergence theorem. Hence, the force quantity doing work on the macroscopic strains $\mathbf{E}$ is the volume integral over the microscopic stress, which is independent of microscopic position and of dimension "stress times volume". This induces the existence of the macroscopic stress $\boldsymbol{\Sigma}$ in the form

$$\boldsymbol{\Sigma} V_{RVE} = \int_{V_{RVE}} \boldsymbol{\sigma}(\mathbf{x}) \, dV \quad \Leftrightarrow \quad \boldsymbol{\Sigma} = \frac{1}{V_{RVE}} \int_{V_{RVE}} \boldsymbol{\sigma}(\mathbf{x}) \, dV = \langle \boldsymbol{\sigma} \rangle = \sum_r f_r \boldsymbol{\sigma}_r, \tag{47}$$

i.e. the well-known stress average rule. Insertion of (47) into the principle of virtual power [50, 99, 131], which in the case of linearized strains, can be expressed in terms of an expression with the dimension "work",

$$\mathscr{W}^{ext} = -\mathscr{W}^{int} = \int_{V_{RVE}} \boldsymbol{\sigma}(\mathbf{x}) : \boldsymbol{\varepsilon}(\mathbf{x}) \, dV \,, \tag{48}$$

yields the so-called Hill's lemma

$$\boldsymbol{\Sigma} : \mathbf{E} = \frac{1}{V_{RVE}} \int_{V_{RVE}} \boldsymbol{\sigma}(\mathbf{x}) : \boldsymbol{\varepsilon}(\mathbf{x}) \, dV = \langle \boldsymbol{\sigma} : \boldsymbol{\varepsilon} \rangle \,. \tag{49}$$

Linearity of elastic law (42) and of partial differential equation (45)$_1$ imply a multilinear relation between the homogenized (macroscopic) strain $\mathbf{E}$ and the average (microscopic) strain $\boldsymbol{\varepsilon}_r$, expressed by the fourth-order concentration tensors $\mathbb{A}_r$ of each of the phases $r$,

$$\boldsymbol{\varepsilon}_r = \mathbb{A}_r : \mathbf{E}. \tag{50}$$

Insertion of Eq. (50) into (42) and averaging over all phases according to Eq. (47) lead to

$$\boldsymbol{\Sigma} = \sum_r f_r \mathbb{c}_r : \mathbb{A}_r : \mathbf{E}. \tag{51}$$

Equation (51) implies the existence of a macroscopic "homogenized" stiffness tensor linking macroscopic stresses to macroscopic strains in the format

$$\boldsymbol{\Sigma} = \mathbb{C}^{\text{hom}} : \mathbf{E}, \tag{52}$$

yielding $\mathbb{C}^{\text{hom}}$ as

$$\mathbb{C}^{\text{hom}} = \sum_r f_r \mathbb{c}_r : \mathbb{A}_r. \tag{53}$$

The concentration tensors $\mathbb{A}_r$ are estimated from matrix-inclusion problems, pioneered by Eshelby [43]. On a mathematical level, this is achieved by setting the phase strains equal to those in ellipsoidal inclusions in infinitely extending matrices of stiffness $\mathbb{C}^0$ subjected to remote strains, and by combining respective semi-analytical relationships [43, 84] with stress and strain average rules [59, 157], yielding

$$\mathbb{A}_r = \left[ \mathbb{I} + \mathbb{P}_r^0 : \left( \mathbb{c}_r - \mathbb{C}^0 \right) \right]^{-1} : \left\{ \sum_s f_s \left[ \mathbb{I} + \mathbb{P}_s^0 : \left( \mathbb{c}_s - \mathbb{C}^0 \right) \right]^{-1} \right\}^{-1}. \tag{54}$$

Insertion of Eq. (54) into (51) yields an expression for the macroscopic homogenized stiffness tensor as function of their volume fractions, shapes and interactions

$$\mathbb{C}^{\text{hom}} = \sum_r f_r \mathbb{c}_r : \left[ \mathbb{I} + \mathbb{P}_r^0 : \left( \mathbb{c}_r - \mathbb{C}^0 \right) \right]^{-1} : \left\{ \sum_s f_s \left[ \mathbb{I} + \mathbb{P}_s^0 : \left( \mathbb{c}_s - \mathbb{C}^0 \right) \right]^{-1} \right\}^{-1}, \tag{55}$$

where $f_r$ and $\mathbb{c}_r$ are the volume fraction and the elastic stiffness of phase $r$, $\mathbb{I}$ is the fourth-order unity tensor, $\mathbb{P}_r^0$ the fourth-order Hill tensor accounting for the characteristic shape of phase $r$, which, in case of ellipsoidal inclusions in anisotropic media [84, 85], reads as

$$P_{r,ijkl}^0 = \frac{1}{16\pi\alpha^{1/2}} \int_\Omega \frac{1}{t^3} \left\{ \hat{g}_{il} w_j w_k + \hat{g}_{ik} w_j w_l + \hat{g}_{jl} w_i w_k + \hat{g}_{jk} w_i w_l \right\} dS(\boldsymbol{w}). \tag{56}$$

In Eq. (56), the shape of the ellipsoid is considered by $\alpha = \det \alpha_{ij}$, being related to the equation of the ellipsoid, $\alpha_{ij} x_i x_j = 1$, $dS(\boldsymbol{w})$ is a surface element of the unit sphere (with surface $\Omega$); $w_1$, $w_2$ and $w_3$ are the components of the unit length vector $\boldsymbol{w}$ pointing from the origin of the sphere to the surface element $dS(\boldsymbol{w})$, and

$t^2 = \alpha_{ij}^{-1} w_i w_j$. Finally, $\hat{g}_{ik}$ are the components of the inverse of the second-order tensor $C_{ijkl}^0 w_j w_l$, with $C_{ijkl}^0$ denoting the stiffness of anisotropic matrix.

As regards the matrix stiffness, $\mathbb{C}^0$, its choice governs the interactions between the phases inside the RVE: $\mathbb{C}^0 = \mathbb{C}^{\mathrm{hom}}$ relates to a dispersed arrangement of phases where all phases "feel" the overall homogenized material, and the corresponding homogenization scheme is standardly called self-consistent [69, 83], well-suited for polycrystalline materials (applied for RVEs depicted in Fig. 15b, c). On the other hand, the matrix may be identified as a phase $m$ itself, $\mathbb{C}^0 = \mathbb{c}_m$, which relates to matrix-inclusion-type composite, and the corresponding homogenization scheme is standardly referred to as Mori–Tanaka scheme [12, 106] (applied for RVEs depicted in Fig. 15a, d, e, f).

Strictly speaking, the RVE of extrafibrillar space (see Fig. 15c) requires a slight (but important) modification of the aforementioned developments: it consists of one pore space and infinitely many cylindrical solid phases which are oriented in all space directions. This requires modification of Eqs. (44), (47), (53), and (55) in terms of integrals over the unit sphere [47]. Accordingly, the homogenized stiffness of the extrafibrillar RVE of Fig. 15c reads as

$$
\begin{aligned}
\mathbb{C}_{\mathrm{exfib}}^{\mathrm{hom}} &= \left\{ f_{\mathrm{HA}}^{\mathrm{exfib}} \mathbb{c}_{\mathrm{HA}} : \int_{\varphi=0}^{2\pi} \int_{\theta=0}^{\pi} \left[ \mathbb{I} + \mathbb{P}_{\mathrm{cyl}}^{\mathrm{exfib}}(\theta, \varphi) : (\mathbb{c}_{\mathrm{HA}} - \mathbb{C}_{\mathrm{exfib}}^{\mathrm{hom}}) \right]^{-1} \frac{\sin\theta \, d\theta \, d\varphi}{4\pi} + \right. \\
&\quad \left. \left( 1 - f_{\mathrm{HA}}^{\mathrm{exfib}} \right) \mathbb{c}_{\mathrm{H_2O}} : \left[ \mathbb{I} + \mathbb{P}_{\mathrm{sph}}^{\mathrm{exfib}} : (\mathbb{c}_{\mathrm{H_2O}} - \mathbb{C}_{\mathrm{exfib}}^{\mathrm{hom}}) \right]^{-1} \right\} : \\
&\quad \left\{ f_{\mathrm{HA}}^{\mathrm{exfib}} \int_{\varphi=0}^{2\pi} \int_{\theta=0}^{\pi} \left[ \mathbb{I} + \mathbb{P}_{\mathrm{cyl}}^{\mathrm{exfib}}(\theta, \varphi) : (\mathbb{c}_{\mathrm{HA}} - \mathbb{C}_{\mathrm{exfib}}^{\mathrm{hom}}) \right]^{-1} \frac{\sin\theta \, d\theta \, d\varphi}{4\pi} + \right. \\
&\quad \left. \left( 1 - f_{\mathrm{HA}}^{\mathrm{exfib}} \right) \left[ \mathbb{I} + \mathbb{P}_{\mathrm{sph}}^{\mathrm{exfib}} : (\mathbb{c}_{\mathrm{H_2O}} - \mathbb{C}_{\mathrm{exfib}}^{\mathrm{hom}}) \right]^{-1} \right\}^{-1},
\end{aligned}
$$
(57)

with $\mathbb{P}_{\mathrm{cyl}}^{\mathrm{exfib}}$ and $\mathbb{P}_{\mathrm{sph}}^{\mathrm{exfib}}$ standing for the Hill tensor of a cylindrical or a spherical inclusion embedded in a matrix with a stiffness of $\mathbb{C}_{\mathrm{exfib}}^{\mathrm{hom}}$, respectively.

### Elasticity of Elementary Components

The micromechanical representation of Fig. 15 is validated at different observation scales, namely at the extracellular, the extravascular, and the cortical/trabecular scales. All corresponding computations are based on the *same* elasticity properties assigned to bone's elementary constituents: hydroxyapatite, (molecular) collagen, and water (with some non-collagenous organics). The elastic properties of hydroxyapatite are obtained from tests with an ultrasonic interferometer coupled with a solid media pressure apparatus [77], which reveal the isotropic elastic properties of hydroxyapatite powder,

$$
\mathbb{c}_{\mathrm{HA}} = 3k_{\mathrm{HA}} \mathbb{I}_{\mathrm{vol}} + 2\mu_{\mathrm{HA}} \mathbb{I}_{\mathrm{dev}},
$$
(58)

with $\mathbb{I}_{vol}$ and $\mathbb{I}_{dev}$ as the volumetric and deviatoric part of the fourth-order identity tensor $\mathbb{I}$, and with $k_{HA} = 82.6$ GPa and $\mu_{HA} = 44.9$ GPa, as the bulk and shear moduli of hydroxyapatite. In view of the largely disordered arrangement of poorly crystalline minerals [42, 45, 62, 63, 65, 95, 117], this isotropic characterization is sufficient for successful bone elasticity upscaling [33, 47, 61, 66, 154], as is also confirmed by the validation diagrams of Figs. 16, 17, 18, 19, 20 and 21. Sasaki and Odajima [133] determined the Young's modulus of molecular collagen by a hybrid mechanical–X-ray technique, considering Lees' 1987 packing model [86] for the cross-sectional arrangement of collagen molecules. This resulted in an elastic Young's modulus of 2.9 GPa. As they did not account for the additional 12% microporosity which is still present in "fully dehydrated" collagen [88], the aforementioned values relate to the RVE of Fig. 15a with 12% intermolecular space. Adopting a Poisson's ratio of 0.34 for such an RVE [35], the corresponding homogenization relation allows for back-analysis of an isotropic estimate of the stiffness tensor of molecular collagen, which reads in Kelvin–Mandel notation (see e.g. Eq. (44) of [68] or Eq. (2a) of [31]) as

$$\mathbb{C}_{col} = \begin{Bmatrix} 4.86 & 2.39 & 2.39 & 0 & 0 & 0 \\ 2.39 & 4.86 & 2.39 & 0 & 0 & 0 \\ 2.39 & 2.39 & 4.86 & 0 & 0 & 0 \\ 0 & 0 & 0 & 1.23 & 0 & 0 \\ 0 & 0 & 0 & 0 & 1.23 & 0 \\ 0 & 0 & 0 & 0 & 0 & 1.23 \end{Bmatrix} \quad \text{GPa} , \tag{59}$$

with a Young's modulus of 3.28 GPa and a Poisson's ratio of 0.33. We assign the standard bulk modulus of water, $k_{H_2O} = 2.3$ GPa, to phases comprising water with mechanically insignificant amounts of non-collagenous organic matter.

### Model Validation at the Extracellular Scale

At the extracellular level, we compare the micromechanical elasticity predictions to ultrasonic tests with 10 MHz frequency, performed on cortical bone samples of bovine, human, elephant, deer, cod, and dugong tissues [91, 92]. Given the measured wave velocities ranging from 2.38 to 4.18 km/s, the wave exhibited wave lengths between 238 and 418 $\mu$m, being by a factor of 23.8 to 41.8 larger than the RVE of Fig. 15d, hence they characterize the latter according to Eq. (41). As tissue-specific input values for the micromechanical model, the volume fractions entering the RVE descriptions of wet collagen (Fig. 15a), of the fibrillar and extrafibrillar spaces (Fig. 15b, c), and of the extracellular matrix (Fig. 15d) are needed.

As regards the cortical bone samples from bovine tibia [91], the macroscopic mass densities and weight fractions are given, see Table 1. Based on a typical microporosity of $f_{\mu por} = 5\%$, see our discussion around Eq. (9), the aforementioned quantities are transformed into ultrastructural (extracellular) weight fractions and apparent mass densities according to Eqs. (10)–(13), and into extracellular (ultrastructural) volume fractions according to Eqs. (16) and (17). Then, the mineral distribution rules of Sect. 4, and the swelling and shrinkage rules of Sect. 5 and 6 allow for quantification of the extrafibrillar and fibrillar volume fractions per volume of extracellular matrix as

**Table 7** Experimental characterization of various cortical bone samples by Less et al. [91][a], Less et al. [92][b], and Less et al. [96][c]; Macroscopic and extracellular bone mass densities, $\rho^\mu$ and $\rho^{\text{excel}}$, longitudinal ultrasonic velocities in radial material directions, $v_1$, experimental and model-predicted normal stiffness values in radial direction, $C_{1111}^{\text{exp}}$ and $C_{1111}^{\text{pred}}$, respectively

| Tissue | $\rho^\mu$ (g/cm³) | $\rho^{\text{excel}}$ (g/cm³) | $v_1$ (km/s) | $C_{1111}^{\text{exp}}$ (GPa) | $C_{1111}^{\text{pred}}$ (GPa) |
|---|---|---|---|---|---|
| Bovine tibia[a] | 2.02 | 2.07 | 3.18 | 21.0 | 24.1 |
| Bovine tibia[a] | 1.99 | 2.04 | 3.18 | 20.7 | 22.1 |
| Bovine tibia[a] | 1.95 | 2.00 | 3.18 | 20.2 | 19.7 |
| Bovine tibia[a] | 2.01 | 2.06 | 3.16 | 20.6 | 22.3 |
| Bovine tibia[a] | 2.04 | 2.09 | 3.27 | 22.4 | 21.7 |
| Bovine tibia[a] | 2.05 | 2.11 | 3.26 | 22.4 | 24.4 |
| Bovine tibia[b] | 2.07 | 2.13 | 3.32 | 23.4 | 25.7 |
| Dugong rib[b] | 2.02 | 2.07 | 3.00 | 18.7 | 22.5 |
| Elephant radius[b] | 1.94 | 1.99 | 3.05 | 18.5 | 18.1 |
| Human femur[b] | 1.93 | 1.98 | 3.13 | 19.4 | 17.6 |
| Deer antler[b] | 1.78 | 1.82 | 2.38 | 10.3 | 12.5 |
| Deer antler[b] | 1.74 | 1.78 | 2.40 | 10.2 | 11.5 |
| Whale malleus[c] | 2.49 | 2.49 | 4.85 | 58.6 | 57.2 |
| Whale malleus[c] | 2.53 | 2.53 | 4.89 | 60.5 | 61.8 |
| Whale malleus[c] | 2.51 | 2.51 | 4.55 | 52.0 | 59.4 |
| Whale malleus[c] | 2.45 | 2.45 | 4.61 | 52.1 | 52.8 |
| Whale incus[c] | 2.50 | 2.50 | 4.79 | 57.4 | 58.3 |
| Whale incus[c] | 2.46 | 2.46 | 4.70 | 54.3 | 53.9 |
| Whale periotic[c] | 2.40 | 2.40 | 4.15 | 41.3 | 47.7 |
| Whale periotic[c] | 2.48 | 2.48 | 4.60 | 52.5 | 56.0 |
| Whale periotic[c] | 2.50 | 2.50 | 4.53 | 51.3 | 58.3 |
| Whale periotic[c] | 2.52 | 2.52 | 4.65 | 54.5 | 60.6 |
| Whale periotic[c] | 2.58 | 2.58 | 4.84 | 60.4 | 67.9 |
| Whale typamic bulla[c] | 2.54 | 2.54 | 4.60 | 53.7 | 63.0 |
| Whale typamic bulla[c] | 2.50 | 2.50 | 4.53 | 51.3 | 58.3 |
| Whale typamic bulla[c] | 2.53 | 2.53 | 4.53 | 51.9 | 61.8 |
| Whale typamic bulla[c] | 2.54 | 2.54 | 4.54 | 52.4 | 63.0 |
| Whale typamic bulla[c] | 2.49 | 2.49 | 4.48 | 50.0 | 57.2 |

$$f_{\text{exfib}}^{\text{excel}} = \frac{f_{\text{exfib},0}^{\text{excel}}}{\frac{1}{1+(\rho_{\text{HA}}/\rho_{\text{fl}}-1)\times f_{\text{HA}}^{\text{excel}}}} + \frac{f_{\text{exfib},0}^{\text{excel}}}{1 - f_{\text{col},0}^{\text{excel}}} \times (1 - \rho_{\text{HA}}/\rho_{\text{fl}}) \times f_{\text{HA}}^{\text{excel}} ,$$

$$f_{\text{fib}}^{\text{excel}} = 1 - f_{\text{exfib}}^{\text{excel}} , \tag{60}$$

whereby $f_{\text{exfib},0}^{\text{excel}}$ and $f_{\text{col},0}^{\text{excel}}$ are determined from Eqs. (34) and (40), with $f_{\text{col},\infty}^{\text{excel}} = f_{\text{col}}^{\text{excel}}$ according to Eq. (18), with $f_{\text{HA},\infty}^{\text{excel}} = f_{\text{HA}}^{\text{excel}}$ according to Eqs. (16)$_2$ and (17)$_2$. They are the basis for the determination of the phase volume fractions within the lower scale RVEs: In this context, the fact that the average hydroxyapatite concentration in the extracollagenous space is the same inside and outside the fibrils [63], see also Sect. 4, allows for quantification of the mineral and collagen volume fractions within the fibrillar and extrafibrillar compartments. Accordingly, in the extrafibrillar space, the volume fractions of mineral, $f_{\text{HA}}^{\text{exfib}}$, and of the intercrystalline fluid, $f_{\text{ic}}^{\text{exfib}}$, read as [108]

$$f_{\text{HA}}^{\text{exfib}} = \frac{f_{\text{HA}}^{\text{excel}} \phi_{\text{HA}}^{\text{exfib}}}{f_{\text{exfib}}^{\text{excel}}} \qquad \text{with} \qquad \phi_{\text{HA}}^{\text{exfib}} = \frac{1 - f_{\text{fib}}^{\text{excel}}}{1 - f_{\text{col}}^{\text{excel}}} ,$$

$$f_{\text{ic}}^{\text{exfib}} = 1 - f_{\text{HA}}^{\text{exfib}} . \tag{61}$$

Within the fibrillar space, the volume fractions of mineral, $f_{\text{HA}}^{\text{fib}}$, and of wet collagen, $f_{\text{wetcol}}^{\text{fib}}$ read as [108]

$$f_{\text{HA}}^{\text{fib}} = \frac{f_{\text{HA}}^{\text{excel}} \left(1 - \phi_{\text{HA}}^{\text{exfib}}\right)}{f_{\text{fib}}^{\text{excel}}} ,$$

$$f_{\text{wetcol}}^{\text{fib}} = 1 - f_{\text{HA}}^{\text{fib}} . \tag{62}$$

Finally, the volume fractions of molecular collagen and the intermolecular space at the wet collagen level, $f_{\text{col}}^{\text{wetcol}}$ and $f_{\text{im}}^{\text{wetcol}}$, can be calculated from the extracellular volume fractions of collagen as [108]

$$f_{\text{col}}^{\text{wetcol}} = \frac{f_{\text{col}}^{\text{excel}}}{f_{\text{fib}}^{\text{excel}} f_{\text{wetcol}}^{\text{fib}}} ,$$

$$f_{\text{im}}^{\text{wetcol}} = 1 - f_{\text{col}}^{\text{wetcol}} . \tag{63}$$

The corresponding micromechanical elasticity predictions of the bovine tibial bone samples of Lees et al. [91] agree well with the actual experimental data. This is underlined by relative errors of $5.47 \pm 7.01\%$ for the radial normal stiffness, and of $-2.84 \pm 6.70\%$ for the axial normal stiffness components, see also Figs. 16 and 17.

As regards the wet cortical bone samples from deer antler, human femur, elephant radius, and dugong rib of Lees et al. [92], and the various whale bones of Lees et al. [96], the macroscopic mass densities are given, see Table 7. Based on a typical microstructural porosity of $f_{\mu\text{por}} = 5\%$, these macroscopic mass densities are transformed into ultrastructural (extracellular) mass densities, by means of Eq. (9). The

**Table 8** Experimental characterization of various cortical bone samples by Less et al. [91][a] and Less et al. [92][b]; Macroscopic and extracellular bone mass densities, $\rho^\mu$ and $\rho^{excel}$, longitudinal ultrasonic velocities in axial material directions, $v_3$, experimental and model-predicted normal stiffness values in axial direction, $C_{3333}^{exp}$ and $C_{3333}^{pred}$, respectively

| Tissue | $\rho^\mu$ (g/cm³) | $\rho^{excel}$ (g/cm³) | $v_3$ (km/s) | $C_{3333}^{exp}$ (GPa) | $C_{3333}^{pred}$ (GPa) |
|---|---|---|---|---|---|
| Bovine tibia[a] | 2.06 | 2.12 | 3.92 | 32.5 | 32.3 |
| Bovine tibia[a] | 2.05 | 2.11 | 3.92 | 32.4 | 31.6 |
| Bovine tibia[a] | 2.02 | 2.07 | 3.81 | 30.1 | 27.3 |
| Bovine tibia[a] | 2.02 | 2.07 | 3.86 | 30.9 | 27.6 |
| Bovine tibia[a] | 2.00 | 2.05 | 3.90 | 31.2 | 28.3 |
| Bovine tibia[a] | 2.05 | 2.11 | 3.88 | 31.7 | 30.7 |
| Bovine tibia[a] | 2.10 | 2.16 | 3.88 | 32.5 | 35.4 |
| Bovine tibia[a] | 2.08 | 2.14 | 3.92 | 32.8 | 33.8 |
| Bovine tibia[b] | 2.06 | 2.12 | 4.18 | 37.0 | 34.3 |
| Elephant radius[b] | 1.93 | 1.98 | 3.89 | 29.9 | 23.5 |
| Human femur[b] | 1.96 | 2.01 | 3.76 | 28.4 | 25.8 |
| Deer antler[b] | 1.74 | 1.78 | 3.08 | 16.9 | 13.1 |
| Deer antler[b] | 1.73 | 1.77 | 3.15 | 17.5 | 12.8 |



**Fig. 16** Comparison between model predictions and experiments of radial normal stiffness values at the extracellular scale (10 MHz experiments: Lees et al. [91, 92, 96], see also Table 7)
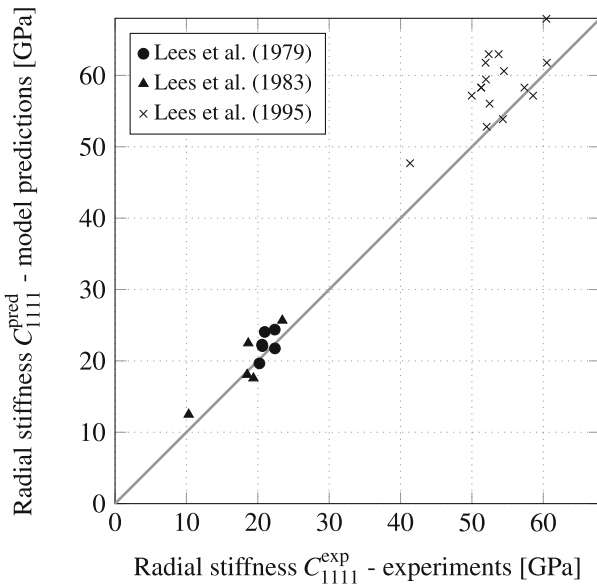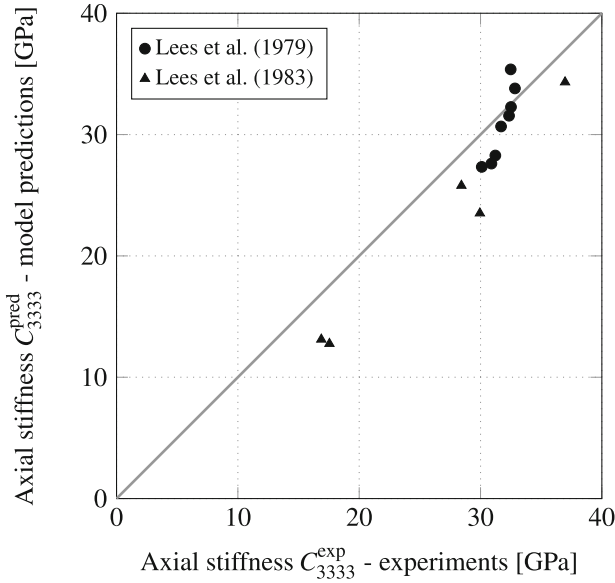
**Fig. 17** Comparison between model predictions and experiments of axial normal stiffness values at the extracellular scale (10 MHz experiments: Lees et al. [91, 92], see also Table 8)

latter mass densities then enter the bilinear relation of Fig. 2a, so as to deliver the extracellular volume fractions of mineral, organic and water according to Eqs. (16) and (17). These volume fractions are then used to quantify the composition of the lower scale RVEs of Fig. 1d, e. The corresponding micromechanical elasticity predictions of the bone samples of Lees et al. [92] and of Lees et al. [96] agree well with the actual experimental data. This is underlined by relative errors of $7.18 \pm 12.13\%$ for the radial normal stiffness, and of $-15.61 \pm 6.17\%$ for the axial normal stiffness components for the different bone tissues reported by Lees et al. [92], and by a relative error of $9.71 \pm 7.21\%$ for the radial normal stiffness of whale bones reported by Lees et al. [96], see Figs. 16 and 17.

### Model Validation at the Extravascular Scale

At the extravascular level, we compare the micromechanical elasticity predictions to ultrasonic tests carried out by McCarthy et al. [100] on equine bones; at a frequency of 2.25 MHz. The measured velocities range from 3.13 to 4.4 km/s, resulting in a wave length ranging from 1.4 to 2.0 mm. The characteristic length of experimentally characterized RVE of Fig. 15e is by a factor of 14 to 20 smaller, hence they characterize the latter according to Eq. (41). As tissue-specific input values for the micromechanical model, the volume fractions entering the RVE descriptions of wet collagen (Fig. 15a), of the fibrillar and extrafibrillar spaces (Fig. 15b, c), of the extracellular matrix (Fig. 15d), and of the extravascular matrix (Fig. 15e) are needed.

**Table 9** Experimental characterization of equine cortical bone samples by McCarthy et al. [100]; Macroscopic and extravascular bone mass densities, $\rho^\mu$ and $\rho^{\text{exvas}}$, longitudinal ultrasonic velocities in radial and axial material directions, $v_1$ and $v_3$, experimental and model-predicted normal stiffness values in radial and axial direction, $C_{1111}^{\text{exp}}$, $C_{3333}^{\text{exp}}$, $C_{1111}^{\text{pred}}$, $C_{3333}^{\text{pred}}$, respectively

| $\rho^\mu$ (g/cm$^3$) | $\rho^{\text{exvas}}$ (g/cm$^3$) | $v_1$ (km/s) | $v_3$ (km/s) | $C_{1111}^{\text{exp}}$ (GPa) | $C_{3333}^{\text{exp}}$ (GPa) | $C_{1111}^{\text{pred}}$ (GPa) | $C_{3333}^{\text{pred}}$ (GPa) |
|---|---|---|---|---|---|---|---|
| 2.03 | 2.14 | 3.60 | 4.30 | 27.8 | 39.7 | 27.4 | 37.5 |
| 2.02 | 2.11 | 3.55 | 4.20 | 26.6 | 37.2 | 25.1 | 34.3 |
| 2.01 | 2.13 | 3.45 | 4.10 | 25.4 | 35.9 | 26.8 | 36.6 |
| 2.01 | 2.09 | 3.65 | 4.40 | 27.8 | 40.4 | 23.7 | 32.4 |
| 2.00 | 2.10 | 3.55 | 4.20 | 26.5 | 37.0 | 24.5 | 33.5 |
| 2.00 | 2.08 | 3.40 | 4.20 | 24.0 | 36.6 | 23.1 | 31.5 |
| 2.00 | 2.06 | 3.58 | 4.30 | 26.5 | 38.2 | 22.4 | 30.5 |
| 1.98 | 2.11 | 3.42 | 4.10 | 24.7 | 35.5 | 25.4 | 34.8 |
| 1.98 | 2.11 | 3.35 | 4.15 | 23.7 | 36.4 | 25.4 | 34.8 |
| 1.98 | 2.09 | 3.50 | 4.15 | 25.6 | 36.0 | 23.9 | 32.6 |
| 1.98 | 2.09 | 3.60 | 4.30 | 27.1 | 38.6 | 23.9 | 32.6 |
| 1.97 | 2.08 | 3.50 | 4.03 | 25.5 | 33.7 | 23.2 | 31.7 |
| 1.97 | 2.10 | 3.35 | 4.20 | 23.6 | 37.1 | 24.7 | 33.8 |
| 1.96 | 2.08 | 3.50 | 4.03 | 25.5 | 33.8 | 23.3 | 31.8 |
| 1.96 | 2.07 | 3.60 | 4.20 | 26.8 | 36.5 | 22.6 | 30.8 |
| 1.95 | 2.10 | 3.52 | 3.95 | 26.1 | 32.8 | 24.9 | 34.0 |
| 1.95 | 2.04 | 3.40 | 4.03 | 23.6 | 33.2 | 21.3 | 28.9 |
| 1.95 | 2.08 | 3.35 | 4.10 | 23.3 | 35.0 | 23.3 | 31.8 |
| 1.95 | 2.16 | 3.42 | 4.10 | 25.2 | 36.3 | 28.4 | 38.8 |
| 1.95 | 2.07 | 3.45 | 4.15 | 24.6 | 35.6 | 22.6 | 30.8 |
| 1.95 | 2.10 | 3.55 | 4.15 | 26.5 | 36.2 | 24.9 | 34.0 |
| 1.93 | 2.06 | 3.35 | 4.03 | 23.1 | 33.4 | 22.0 | 30.0 |
| 1.93 | 2.02 | 3.30 | 4.10 | 22.0 | 34.0 | 20.1 | 27.2 |
| 1.93 | 2.07 | 3.48 | 4.25 | 25.1 | 37.4 | 22.7 | 31.0 |
| 1.92 | 2.05 | 3.35 | 4.00 | 23.0 | 32.7 | 21.4 | 29.1 |
| 1.92 | 2.02 | 3.40 | 4.03 | 23.4 | 32.8 | 20.1 | 27.2 |
| 1.92 | 2.05 | 3.35 | 4.20 | 23.0 | 36.1 | 21.4 | 29.1 |
| 1.92 | 2.03 | 3.40 | 4.20 | 23.5 | 35.9 | 20.7 | 28.1 |
| 1.91 | 2.03 | 3.35 | 4.13 | 22.8 | 34.7 | 20.7 | 28.2 |
| 1.91 | 2.17 | 3.48 | 4.17 | 26.2 | 37.7 | 29.0 | 39.5 |
| 1.91 | 2.11 | 3.45 | 4.35 | 25.1 | 39.9 | 25.2 | 34.4 |
| 1.90 | 2.20 | 3.13 | 3.95 | 21.6 | 34.3 | 31.3 | 42.7 |
| 1.90 | 2.02 | 3.40 | 4.00 | 23.4 | 32.4 | 20.1 | 27.3 |
| 1.82 | 1.90 | 3.30 | 4.00 | 20.7 | 30.4 | 14.9 | 18.9 |
| 1.76 | 2.09 | 3.20 | 3.85 | 21.4 | 30.9 | 23.7 | 32.4 |

McCarthy et al. [100] reported the macroscopic mass densities, $\rho^{\mu}$, and the vascular porosities $f_{\text{vas}}$, which give access, based on the typical lacunar and canalicular porosities of 1.3% and 0.7%, respectively, to the extravascular and extracellular mass densities, $\rho^{\text{exvas}}$ and $\rho^{\text{excel}}$. The latter enters the bilinear relations given by Eqs. (16) and (17), delivering the extracellular volume fractions of hydroxyapatite, collagen and water. The volume fractions of the lower scale RVEs of Fig. 15 follow from Eqs. (60)–(63). The corresponding micromechanical elasticity prediction of the equine metacarpal bone samples of McCarthy et al. [100] agree well with the actual experimental data. This is underlined by relative errors of $-4.23 \pm 11.33\%$ for the radial normal stiffness, and of $-9.78 \pm 10.52\%$ for the axial normal stiffness components, see Fig. 18.

In order to check the predictive capabilities of the micromechanical model concerning the off-diagonal and shear stiffness components of the elasticity tensor, we consider the stiffness tensor given by Ashman et al. [6] on the basis of 2.25 MHz ultrasonic tests on human femoral samples, reading in Kelvin–Mandel notation (see e.g. Eq. (44) of Helnwein [68] or Eq. (20) of Cowin [31]) as

$$
\mathbb{C}^{\text{exp}} = \begin{Bmatrix} 18.0 & 9.98 & 10.1 & 0 & 0 & 0 \\ 9.98 & 20.2 & 10.7 & 0 & 0 & 0 \\ 10.1 & 10.7 & 27.6 & 0 & 0 & 0 \\ 0 & 0 & 0 & 12.46 & 0 & 0 \\ 0 & 0 & 0 & 0 & 11.22 & 0 \\ 0 & 0 & 0 & 0 & 0 & 9.04 \end{Bmatrix} \quad \text{GPa.} \tag{64}
$$

It should be noted that Ashman et al. [6] use macroscopic mass density values for the evaluation of the ultrasonic velocity measurements, while 2.25 MHz, as stated previously, actually refer to the extravascular RVE of Fig. 1d. Accordingly, the values given in (64) need to be corrected by a factor of

$$
\frac{\rho^{\text{exvas}}}{\rho^{\mu}} = \frac{\rho^{\mu} - \rho_{\text{H}_2\text{O}} f_{\text{vas}}}{(1 - f_{\text{vas}}) \rho^{\mu}} = 1.04 \tag{65}
$$

taking $\rho^{\mu} = 1.90 \, \text{g/cm}^3$ from the tests of Ashman et al. [6]. Considering a typical vascular porosity of 8% in human femoral bone [19, 20, 30, 36, 140], yields

$$
\mathbb{C}^{\text{exp}}_{\text{exvas}} = \begin{Bmatrix} 18.74 & 10.39 & 10.52 & 0 & 0 & 0 \\ 10.39 & 21.03 & 11.14 & 0 & 0 & 0 \\ 10.52 & 11.14 & 28.74 & 0 & 0 & 0 \\ 0 & 0 & 0 & 12.97 & 0 & 0 \\ 0 & 0 & 0 & 0 & 11.68 & 0 \\ 0 & 0 & 0 & 0 & 0 & 9.41 \end{Bmatrix} \quad \text{GPa.} \tag{66}
$$

Applying the mass-density based volume fraction evaluation procedure to the same human femur sample provided by Ashman et al. [6] delivers the volume fractions entering the RVEs at all scales of Fig. 15. Based on a microporosity of $f_{\mu\text{por}} =$
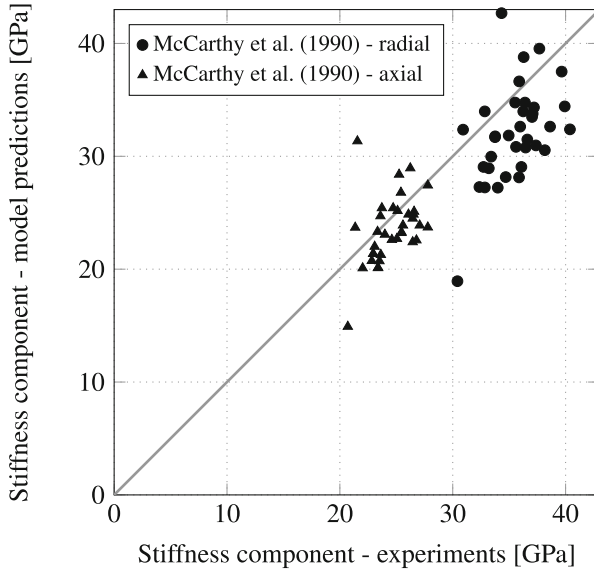
**Fig. 18** Comparison between model predictions and experiments of radial and axial normal stiffness values at the extravascular scale (2.25 MHz experiments: McCarthy et al. [100], see also Table 9)

10% in consistency with the vascular porosity value given further above and the lacunar and canalicular porosities given below Eq. (8), the macroscopic mass density $\rho^\mu = 1.90 \, \text{g/cm}^3$ is translated into an extracellular mass density entering Eq. (16). The volume fractions of the lower scale RVEs then follow from Eqs. (61)–(63). The corresponding micromechanical model prediction reads as

$$
\mathbb{C}^{\text{pred}}_{\text{exvas}} = 
\begin{Bmatrix}
17.71 & 6.88 & 6.76 & 0 & 0 & 0 \\
6.88 & 17.71 & 6.76 & 0 & 0 & 0 \\
6.76 & 6.76 & 23.92 & 0 & 0 & 0 \\
0 & 0 & 0 & 11.09 & 0 & 0 \\
0 & 0 & 0 & 0 & 11.09 & 0 \\
0 & 0 & 0 & 0 & 0 & 9.68
\end{Bmatrix}
\quad \text{GPa.} \tag{67}
$$

The satisfactory agreement between model prediction and experimental data is underlined by an absolute error of $-9.13 \pm 7.8\%$ for the diagonal stiffness components. The off-diagonal stiffness components are less well predicted; however, these components are particularly prone to experimental errors, see e.g. [44, 80, 82, 114].

### Model Validation at the Macroscopic Scale

At the trabecular level, we compare the micromechanical elasticity predictions to ultrasonic tests [126, 145] on bovine femoral and human tibial tissues; at a frequency of 50 kHz, as well as to mechanical tests of Keaveny et al. [79] on bovine tibial tissue samples. Given a typical wave propagation velocity of 3 km/s in the tested bone
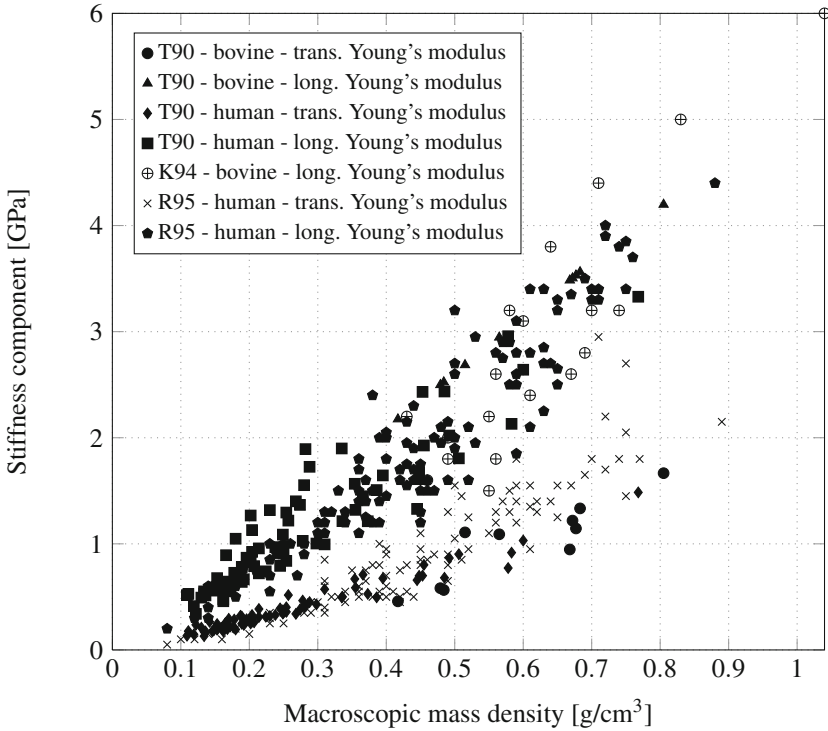
**Fig. 19** Experimental data used for model validation: Macroscopic elastic stiffness constants of trabecular bone as a function of macroscopic mass density $\rho^\mu$; T90...[145], K94... [79], R95... [126]

specimens, the characteristic wave length was of the order of 6 cm, being by a factor of 60 larger than the RVE of Fig. 15f, hence they characterize the latter according to Eq. (41). As tissue-specific input values for the micromechanical model, the volume fractions entering the RVE descriptions of wet collagen (Fig. 15a), of the fibrillar and extrafibrillar spaces (Fig. 15b, c), of the extracellular matrix (Fig. 15d), of the extravascular matrix (Fig. 15e), and of the bone microstructure (Fig. 15f) are needed.

For marrow-cleared trabecular bone, as tested by Keaveny et al. [79], Rho et al. [126], Turner et al. [145], the corresponding volume fractions can be derived from the measured macroscopic mass density, $\rho^\mu$, see Fig. 19. For the extravascular mass density of bone, we take $\rho^{exvas} = 1.74$ g/cm$^3$ for bovine, and $\rho^{exvas} = 1.76$ g/cm$^3$ for human bone specimens [5]. Assuming that the lacunar-canalicular volume fraction per extravascular bone, $f_{lac+can}^{exvas} = 0.021$, is the same in cortical and trabecular bone, the extracellular mass density follows from

$$\rho^{excel} = \frac{\rho^{exvas} - \rho_{H_2O} \times f_{lac+can}^{exvas}}{1 - f_{lac+can}^{exvas}}. \tag{68}$$
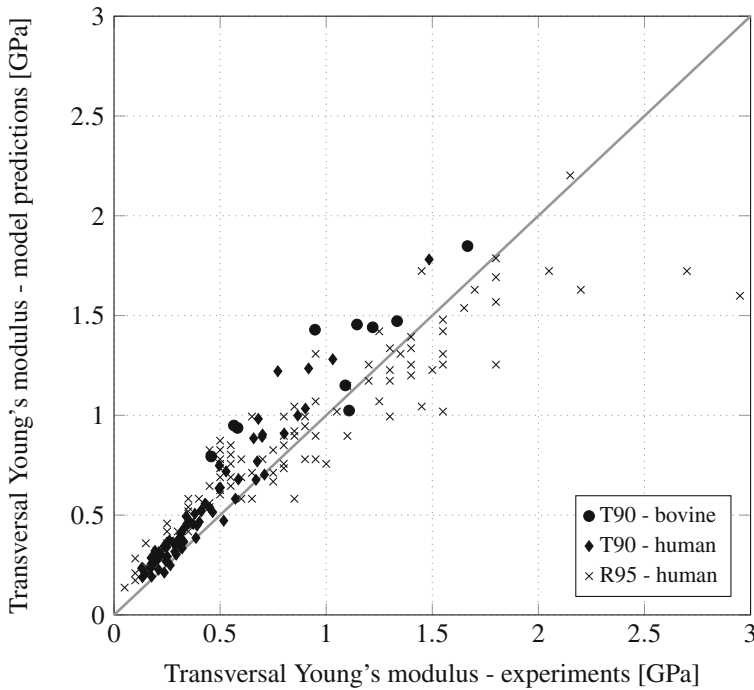
**Fig. 20** Comparison between model predicted and experimental macroscopic elastic stiffness constants of trabecular bone in transversal direction (50 kHz ultrasonic and mechanical experiments); T90...[145], K94... [79], R95... [126]

The sought volume fractions can be computed from Eqs. (16), (17) and (60)–(63). The relative errors of the corresponding micromechanical elasticity predictions amount to $23.62 \pm 16.75\%$ in radial, and $23.39 \pm 30.83\%$ in axial direction for the bovine samples of Turner et al. [145]; $24.67 \pm 20.72\%$ in radial, and $31.45 \pm 25.45\%$ in axial direction for the human samples of Turner et al. [145]; $12.72 \pm 21.40\%$ in radial direction for the bovine samples of Keaveny et al. [79]; and $0.09 \pm 28.44\%$ in radial, and $28.26 \pm 17.03\%$ in axial direction for the human samples of Rho et al. [126], see Figs. 20 and 21.

# 8   Concluding Remarks

Multiscale homogenization schemes similar to the one of Fig. 15 can also be employed for successful upscaling of mechanical properties of bone beyond the realm of elasticity. This was reported for poroelasticity [60, 64, 67, 108], for strength [48], and for viscoelasticity [40]. While we refer to the aforementioned references concerning experimental data bases used for micromechanics model validation, we note
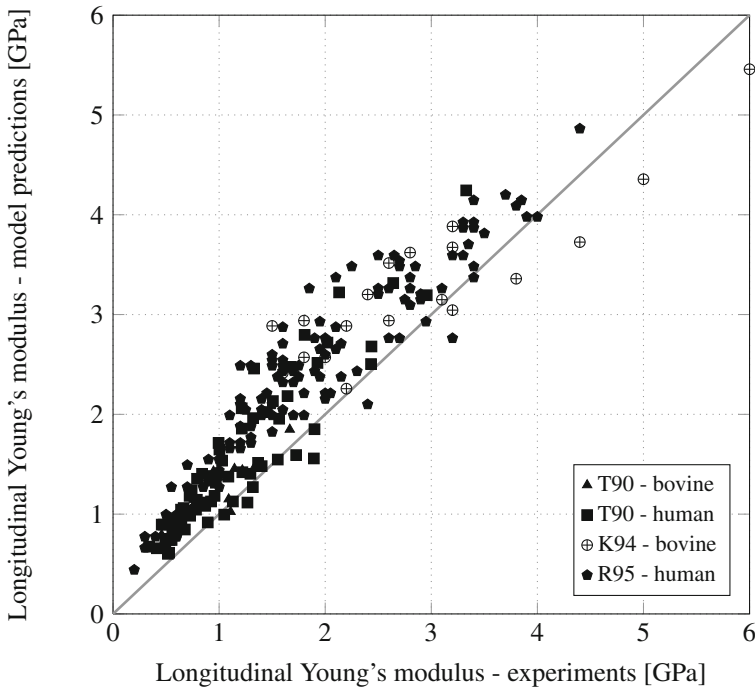
**Fig. 21** Comparison between model predicted and experimental macroscopic elastic stiffness constants of trabecular bone in longitudinal direction (50 kHz ultrasonic and mechanical experiments); T90...[145], K94... [79], R95... [126]

in passing that a satisfactory performance of the strength and viscoelastic upscaling schemes stems from the consideration of sliding processes between the nanoscaled mineral crystals. This is in line with ongoing discussions in the bone materials science at large, be it in the context of Mohr-Coulomb-type, nano-granular behavior elucidated by nanoindentation and atomic force microscopy [141]; or in the context of interface nanomechanics cast in the framework of molecular dynamics simulations [123]. The aforementioned poromechanics approaches are particularly valuable for quantifying the mechanical state in the vascular and lacunar pore spaces when the biological cells reside, i.e. the oscillating hydrostatic pressure to which they respond in a chemical fashion, see [136] and references therein. They also provide a natural link between micromechanics on the one hand, and system biology and cell population models on the other hand [134, 135]. This results in a rather "rigorously" derived "mechano-biology of bone". Finally, multiscale micromechanics models can be readily combined with physics results, then allowing for the in-depth use and evaluation of clinical X-ray data from Computed Tomography yielding micromechanics-based Finite Element models at the organ scale. The latter elucidates the fascinating load carrying behavior of these organs, and also pave the way to patient-specific bone fracture risk assessment [14, 15].

# References

1. J. Aaron, Histology and micro-anatomy of bone, in *Calcium, Phosphate and Magnesium Metabolism: Clinical Physiology and Diagnostic Procedures*, ed. by B.E.C. Nordin (Churchill Livingstone, New York, 1971), pp. 298–356

2. B. Alexander, T.L. Daulton, G.M. Genin, J. Lipner, J.D. Pasteris, B. Wopenka, S. Thomopoulos, The nanometre-scale physiology of bone: steric modelling and scanning transmission electron microscopy of collagen-mineral structure. J. R. Soc. Interface **9**, 1774–1786 (2012)

3. H.C. Anderson, The role of matrix vesicles in growth plate development and biomineralization. Front. Biosci. **10**, 822–837 (2005)

4. B. Aoubiza, J.M. Crolet, A. Meunier, On the mechanical characterization of compact bone structure using the homogenization theory. J. Biomech. **29**(12), 1539–1547 (1996)

5. R.B. Ashman, J. Rho, Elastic modulus of trabecular bone material. J. Biomech. **21**(3), 177181 (1988)

6. R.B. Ashman, S.C. Cowin, W.C. van Buskirk, J.C. Rice, A continuous wave technique for the measurement of the elastic properties of cortical bone. J. Biomech. **17**(5), 349361 (1984)

7. J.-L. Auriault, C. Boutin, C. Geindreau, *Homogenization of Coupled Phenomena in Heterogenous Media* (Wiley, New York, 2009)

8. A.J. Bailey, R.G. Paul, L. Knott, Mechanisms of maturation and ageing of collagen. Mech. Ageing Dev. **106**(1–2), 1–56 (1998)

9. Y. Bala, D. Farlay, P. Delmas, P. Meunier, G. Boivin, Time sequence of secondary mineralization and microhardness in cortical and cancellous bone from ewes. Bone **46**, 1204–1212 (2010)

10. D. Baylink, J. Wergedal, Bone formation and resorption by osteocytes, (1971), pp. 257–289

11. L.S. Bell, M. Kayser, C. Jones, The mineralized osteocyte: a living fossil. Am. J. Phys. Anthropol. **137**, 449–456 (2008)

12. Y. Benveniste, A new approach to the application of Mori–Tanaka's theory in composite materials. Mech. Mater. **6**(2), 147–157 (1987)

13. R. Biltz, E. Pellegrino, The chemical anatomy of bone. J. Bone Joint Surg. **51–A**(3), 456–466 (1969)

14. R. Blanchard, A. Dejaco, E. Bongaers, C. Hellmich, Intravoxel bone micromechanics for microCT-based finite element simulations. J. Biomech. **46**, 2710–2721 (2013)

15. R. Blanchard, C. Morin, A. Malandrino, A. Vella, S. Zdenka, C. Hellmich, Patient-specific fracture risk assessment of vertebrae: a multiscale approach coupling X-ray physics and continuum micromechanics. Numer. Methods Biomed. Eng. **32**(9), e02760 (2016)

16. L.C. Bonar, S. Lees, H.A. Mook, Neutron diffraction studies of collagen in fully mineralized bone. J. Mol. Biol. **181**(2), 265–270 (1985)

17. L. Bonewald, M. Johnson, Osteocytes, mechanosensing and Wnt signaling. Bone **42**(4), 606–615 (2008)

18. E. Bonucci, The osteocyte: the underestimated conductor of the bone orchestra. Rend. Lincei Sci. Fis. e Nat. **20**, 237–254 (2009)

19. V. Bousson, C. Bergot, A. Meunier, F. Barbot, C. Parlier-Cuau, A.-M. Laval-Jeantet, J.-D. Laredo, CT of the middiaphyseal femur: cortical bone mineral density and relation to porosity. Radiology **217**(1), 179–187 (2000)

20. V. Bousson, A. Meunier, C. Bergot, É. Vicaut, M.A. Rocha, M.H. Morais, A.-M. Laval-Jeantet, J.-D. Laredo, Distribution of intracortical porosity in human midfemoral cortex by age and gender. J. Bone Miner. Res. **16**(7), 1308–1317 (2001)

21. L. Bozec, M. Horton, Topography and mechanical properties of single molecules of type I collagen using atomic force microscopy. Biophys. J. **88**(6), 4223–4231 (2005)

22. J. Bradley, Interactive image display for the x window system. version 3.10a, 2nd edn. (1994), http://www.trilon.com/xv/manual/xv-3.10a

23. B. Brodsky, E.F. Eikenberry, K.C. Belbruno, K. Sterling, Variations in collagen fibril structure in tendons. Biopolymers **21**(5), 935–951 (1982)

24. J.A. Buckwalter, M.J. Glimcher, R.R. Cooper, R. Recker, Bone biology, part I: structure, blood supply, cells, matrix, and mineralization. J. Bone Joint Surg. **77–A**(8), 1256–1275 (1995)

25. C.M. Burns, The effect of the continued ingestion of mineral acid on growth of body and bone and on the composition of bone and of the soft tissues. Biochem. J. **23**(5), 860–867 (1929)

26. A. Buxboim, I. Ivanovska, D. Discher, Matrix elasticity, cytoskeletal forces and physics of the nucleus: how deeply do cells feel outside and in? J. Cell Sci. **123**(3), 297–308 (2010)

27. D.R. Carter, W.C. Hayes, The compressive behavior of bone as a two-phase porous structure. J. Bone Joint Surg. **59**(7), 954–962 (1977)

28. K.-H. Chung, K. Bhadriraju, T.A. Spurlin, R.F. Cook, A.L. Plant, Nanomechanical properties of thin films of type I collagen fibrils. Langmuir **26**(5), 3629–3636 (2010)

29. D.M.L. Cooper, A.L. Turinsky, C.W. Sensen, Hallgrímsson, Quantitative 3D analysis of the canal network in cortical bone by micro-computed tomography. Anat. Rec. **4274B**(1), 169–179 (2003)

30. D.M.L. Cooper, C.D.L. Thomas, J.G. Clement, A.L. Turinsky, C.W. Sensen, B. Hallgrímsson, Age-dependent change in the 3D structure of cortical porosity at the human femoral midshaft. Bone **40**, 957–965 (2014)

31. S. Cowin, A recasting of anisotropic poroelasticity in matrices of tensor components. Transp. Porous Media **50**, 35–56 (2003)

32. S. Cowin, The significance of bone microstructure in mechanotransduction. J. Biomech. **40** (2007)

33. J.M. Crolet, B. Aoubiza, A. Meunier, Compact bone: numerical simulation of mechanical characteristics. J. Biomech. **26**(6), 677–687 (1993)

34. J.D. Currey, The effect of porosity and mineral content on the Young's modulus of elasticity of compact bone. J. Biomech. **21**(2), 131–139 (1988)

35. S. Cusack, A. Miller, Determination of the elastic constants of collagen by Brillouin light scattering. J. Mol. Biol. **135**(1), 39–51 (1979)

36. P. Dong, S. Haupert, B. Hesse, M. Langer, P.-J. Gouttenoire, V. Bousson, F. Peyrin, 3D osteocyte lacunar morphometric properties and distributions in human femoral cortical bone using synchrotron radiation micro-CT images. Bone **60**, 172–185 (2014)

37. L. Dormieux, D. Kondo, F.-J. Ulm, Microporomechanics **66**(6), 1036–1059 (2006)

38. W.J. Drugan, J.R. Willis, A micromechanics-based nonlocal constitutive equation and estimates of representative volume element size for elastic composites. J. Mech. Phys. Solids **44**(4), 497–524 (1996)

39. E. Eanes, D. Lundy, G. Marti, X-ray diffraction study of the mineralization of turkey leg tendon. Calcif. Tissue Int. **6**, 239–248 (1970)

40. L. Eberhardsteiner, C. Hellmich, Layered water in crystal interfaces as source for bone viscoelasticity: arguments from a multiscale approach. Comput. Methods Biomech. Biomed. Eng. **17**(1), 48–63 (2014)

41. A. Engler, S. Sen, H. Sweeney, D. Discher, Matrix elasticity directs stem cell lineage specification. Cell **126**(4), 677–689 (2006)

42. M. Epple, Solid-state chemical methods to investigate the nature of calcified deposits. Zeitschrift für Kardiologie **390**(3) (2001)

43. J.D. Eshelby, The determination of the elastic field of an ellipsoidal inclusion, and related problems. Proc. R. Soc. Lond. Ser. A Math. Phys. Sci. **241**(1226), 376–396 (1957)

44. A. Every, W. Sachse, Sensitivity of inversion algorithms for recovering elastic constants of anisotropic solids from longitudinal wavespeed data. Ultrasonics **30**, 43–48 (1992)

45. P. Fratzl, S. Schreiber, K. Klaushofer, Bone mineralization as studied by small-angle x-ray scattering. Connect. Tissue Res. **34**(4) (1996)

46. A. Fritsch, C. Hellmich, Universal microstructural patterns in cortical and trabecular, extracellular and extravascular bone materials: micromechanics-based prediction of anisotropic elasticity. J. Theor. Biol. **244**(4), 597–620 (2007)

47. A. Fritsch, L. Dormieux, C. Hellmich, Porous polycrystals built up by uniformly and axisymmetrically oriented needles: homogenization of elastic properties. Comptes Rendus Mécanique **334**(3), 151–157 (2006)

48. A. Fritsch, C. Hellmich, L. Dormieux, Ductile sliding between mineral crystals followed by rupture of collagen crosslinks: experimentally supported micromechanical explanation of bone strength. J. Theor. Biol. **260**(2), 230–252 (2009)
49. H.M. Frost, Micropetrosis. J. Bone Joint Surg. **42**, 144–150 (1960)
50. P. Germain, The method of virtual power in continuum mechanics. part 2: microstructure. SIAM J. Appl. Math. **25**(3), 556–575 (1973)
51. J. Gong, J. Arnold, S.H. Cohn, Composition of trabecular and cortical bone. The Anat. Rec. **149**, 325–332 (1964)
52. S.J. Gould, R.C. Lewontin, The spandrels of San Marco and the Panglossian paradigm: a critique of the adaptationist programme. Proc. R. Soc. Lond. Ser. B Biol. Sci. **205**, 581–598 (1979)
53. Q. Grimal, G. Rus, W.J. Parnell, P. Laugier, A two-parameter model of the effective elastic tensor for cortical bone. J. Biomech. **44**(8), 1621–1625 (2011)
54. M. Hahn, M. Vogel, M. Pompesious-Kempa, G. Delling, Trabecular bone pattern factora new parameter for simple quantification of bone microarchitecture. Bone **13**(4), 327–330 (1992)
55. E. Hamed, Y. Lee, I. Jasiuk, Multiscale modeling of elastic properties of cortical bone. Acta Mech. **213**(1), 131–154 (2010)
56. E. Hamed, E. Novitskaya, J. Li, I. Jasiuk, J. McKittrick, Experimentally-based multiscale model of the elastic moduli of bovine trabecular bone and its constituents. Mater. Sci. Eng. C **54**, 207–216 (2015)
57. F.S. Hammet, A biochemical study of bone growth. I Changes in the ash, organics matter and water during growth (mus norvegicus albinus). J. Biol. Chem. **64**, 409–428 (1925)
58. F. Hang, A.H. Barber, Nano-mechanical properties of individual mineralized collagen fibrils from bone tissue. J. R. Soc. Interface (2010)
59. Z. Hashin, Analysis of composite materials a survey. J. Appl. Mech. **50**(3), 481 (1983)
60. C. Hellmich, Microelasticity of Bone, in *Applied Micromechanics of Porous Materials - CISM Courses and Lectures*, vol. 480, ed. by L. Dormieux, F.-J. Ulm (2005)
61. C. Hellmich, F.-J. Ulm, Micromechanical model for ultrastructural stiffness of mineralized tissues. J. Eng. Mech. **128**(8), 898–908 (2002)
62. C. Hellmich, F.-J. Ulm, Are mineralized tissues open crystal foams reinforced by crosslinked collagen? – some energy arguments. J. Biomech. **535**(9), 1199–1212 (2002)
63. C. Hellmich, F.-J. Ulm, Average hydroxyapatite concentration is uniform in the extracollagenous ultrastructure of mineralized tissues: evidence at the 1–10-microm scale. Biomech. Model. Mechanobiol. **2**(1), 21–36 (2003)
64. C. Hellmich, F.-J. Ulm, Drained and undrained poroelastic properties of healthy and pathological bone: a poro-micromechanical investigation. Transp. Porous Media **58**(3), 243–268 (2005)
65. C. Hellmich, J.-F. Barthélémy, L. Dormieux, Mineralcollagen interactions in elasticity of bone ultrastructure a continuum micromechanics approach. Eur. J. Mech. A/Solids **23**(5), 783–810 (2004)
66. C. Hellmich, F.-J. Ulm, L. Dormieux, Can the diverse elastic properties of trabecular and cortical bone be attributed to only a few tissue-independent phase properties and their interactions? Biomech. Model. Mechanobiol. **2**(4), 219–238 (2004)
67. C. Hellmich, D. Celundova, F.-J. Ulm, Multiporoelasticity of hierarchically structured materials: micromechanical foundations and application to bone. J. Eng. Mech. **135**(5), 382–394 (2009)
68. P. Helnwein, Some remarks on the compressed matrix representation of symmetric second-order and fourth-order tensors. Comput. Methods Appl. Mech. Eng. **190**(2223), 2753–2770 (2001)
69. A.V. Hershey, The elasticity of an isotropic aggregate of anisotropic cubic crystals. J. Appl. Mech. Trans. ASME **21**(3), 236–240 (1954)
70. B. Hesse, P. Varga, M. Langer, A. Pacureanu, S. Schrof, N. Männicke, H. Suhonen, P. Maurer, P. Cloetens, F. Peyrin, K. Raum, Canalicular network morphology is the major determinant of the spatial distribution of mass density in human bone tissue: evidence by means of synchrotron radiation phase-contrast nano-CT. J. Bone Miner. Res. **30**(2), 346–356 (2015)

71. R. Hill, Elastic properties of reinforced solids: some theoretical principles. J. Mech. Phys. Solids **11**(5), 357–372 (1963)

72. A.J. Hodge, J.A. Petruska, Recent studies with the electron microscope on ordered aggregates of the tropocollagen molecule, in *Aspects of Protein Structure - Proceedings of a Symposium held in Madras 14–18 January 1963 and organized by the University of Madras, India*, ed. by G.N. Ramachandran (Academic Press, New York, 1963), pp. 289–300

73. G.K. Hunter, P.V. Hauschka, R.A. Poole, L.C. Rosenberg, H.A. Goldberg, Nucleation and inhibition of hydroxyapatite formation by mineralized tissue proteins. Biochem. J. **317**(1), 59–64 (1996)

74. R. Jilka, R. Weinstein, T. Bellido, A. Parfitt, S. Manolagas, Osteoblast programmed cell death (apoptosis): modulation by growth factors and cytokines. J. Bone Miner. Res. **13**(5), 793–802 (1998)

75. J. Jowsey, Age changes in human bone. Clin. Orthop. **17**, 210–218 (1960)

76. E.P. Katz, S.T. Li, Structure and function of bone collagen fibrils. J. Mol. Biol. **80**(1), 1–15 (1973)

77. J.L. Katz, K. Ukraincik, On the anisotropic elastic properties of hydroxyapatite. J. Biomech. **4**(3), 221–227 (1971)

78. J.L. Katz, H.S. Yoon, S. Lipson, R. Maharidge, A. Meunier, P. Christel, The effects of remodeling on the elastic properties of bone. Calcif. Tissue Int. **36**(1), 31–36 (1984)

79. T.M. Keaveny, E.F. Wachtel, C.M. Ford, W.C. Hayes, Differences between the tensile and compressive strengths of bovine tibial trabecular bone depend on modulus. J. Biomech. **27**(9), 1137–1146 (1994)

80. C. Kohlhauser, C. Hellmich, Determination of Poissons ratios in isotropic, transversely isotropic, and orthotropic materials by means of combined ultrasonic-mechanical testing of normal stiffnesses: application to metals and wood. Eur. J. Mech. A/Solids **33**, 82–98 (2012)

81. C. Kohlhauser, C. Hellmich, Ultrasonic contact pulse transmission for elastic wave velocity and stiffness determination: influence of specimen geometry and porosity. Eng. Struct. **47**, 115–133 (2013)

82. R. Kriz, W. Stinchcomb, Elastic moduli of transversely isotropic graphite fibers and their composites. Exp. Mech. **19**(2), 41–49 (1979)

83. E. Kröner, Berechnung der elastischen Konstanten des Vielkristalls aus den Konstanten des Einkristalls. Zeitschrift für Physik **151**(4), 504–518 (1958)

84. N. Laws, The determination of stress and strain concentrations at an ellipsoidal inclusion in an anisotropic material. J. Elast. **7**(1), 91–97 (1977)

85. N. Laws, A note on penny-shaped cracks in transversely isotropic materials. Mech. Mater. **4**(2), 209–212 (1985)

86. S. Lees, Considerations regarding the structure of the mammalian mineralized osteoid from viewpoint of the generalized packing model. Connect. Tissue Res. **16**, 281–303 (1987)

87. S. Lees, Mineralization of type I collagen. Biophys. J. **85**, 204–207 (2003)

88. S. Lees, J. Heeley, Density of a sample bovine cortical bone matrix and its solid constituent in various media. Calcif. Tissue Int. **33**, 499–504 (1981)

89. S. Lees, H.A. Mook, Equatorial diffraction spacing as a function of water content in fully mineralized cow bone determined by neutron diffraction. Connect. Tissue Res. **39**, 291–292 (1986)

90. S. Lees, E.A. Page, A study of some properties of mineralized turkey leg tendon. Connect. Tissue Res. **28**(4), 263–287 (1992)

91. S. Lees, P.F. Cleary, J.D. Heeley, E.L. Gariepy, Distribution of sonic plesio-velocity in a compact bone sample. J. Acoust. Soc. Am. **66**(3), 641–646 (1979)

92. S. Lees, J.M. Ahern, M. Leonard, Parameters influencing the sonic velocity in compact calcified tissues of various species. J. Acoust. Soc. Am. **74**(1), 28–33 (1983)

93. S. Lees, L.C. Bonar, H.A. Mook, A study of dense mineralized tissue by neutron diffraction. Int. J. Biol. Macromol. **6**(6), 321–326 (1984)

94. S. Lees, D. Hanson, E.A. Page, H. Mook, Comparison of dosage-dependent effects of beta-aminopropionitrile, sodium fluoride, and hydrocortisone on selected physical properties of cortical bone. J. Bone Miner. Res. **9**(9), 1377–1389 (1994)

95. S. Lees, K.S. Prostak, V.K. Ingle, K. Kjoller, The loci of mineral in turkey leg tendon as seen by atomic force microscope and electron microscopy. Calcif. Tissue Int. **55**, 180–189 (1994)

96. S. Lees, D. Hanson, E.A. Page, Some acoustical properties of the otic bones of a fin whale. J. Acoust. Soc. Am. **99**(4), 2421–2427 (1995)

97. V. Lemaire, F.L. Tobin, L.D. Greller, C.R. Cho, L.J. Suva, Modeling the interactions between osteoblast and osteoclast activities in bone remodeling. J. Theor. Biol. **229**, 293–309 (2004)

98. J. Martínez-Reina, J. Domínguez, J.M. García-Aznar, Effect of porosity and mineral content on the elastic constants of cortical bone: a multiscale approach. Biomech. Model. Mechanobiol. **210**(3), 309–322 (2011)

99. G.A. Maugin, The principle of virtual power: from eliminating metaphysical forces to providing an efficient modelling tool. Contin. Mech. Thermodyn. **5**(2), 127–146 (2013)

100. R.N. McCarthy, L.B. Jeffcott, R.N. McCartney, Ultrasound speed in equine cortical bone: effects of orientation, density, porosity and temperature. J. Biomech. **23**(11), 1139–1143 (1990)

101. E.A. McNally, H.P. Schwarcz, A model for the ultrastructure of bone based on electron microscopy of ion-milled sections. PLOS one **7**(1), e29258 (2012)

102. K.M. Meek, N.J. Fullwood, P.H. Cooke, G.F. Elliott, D.M. Maurice, A.J. Quantock, R.S. Wall, C.R. Worthington, Synchrotron X-ray diffraction studies of the cornea, with implications for stromal hydration. Biophys. J. **60**(2), 467–474 (1991)

103. T.A. Metzger, T.C. Kriepke, T.J. Vaughan, L.M. McNamara, G.L. Niebur, The in situ mechanics of trabecular bone marrow: the potential for mechanobiological response. J. Biomech. Eng. **137**(1), 011006 (2015)

104. C. Miles, M. Ghelashvili, Polymer-in-a-box mechanism for the thermal stabilization of collagen molecules in fibers. Biophys. J. **76**(6), 3243–3252 (1999)

105. A. Miller, S.B. Parker, The organic matrix of bone. Phil. Trans. R. Soc. B **304**, 455–477 (1984)

106. T. Mori, K. Tanaka, Average stress in matrix and average elastic energy of materials with misfitting inclusions. Acta Metall. **21**(5), 571–574 (1973)

107. C. Morin, C. Hellmich, Mineralization-driven bone tissue evolution follows from fluid-to-solid phase transformations in closed thermodynamic systems. J. Theor. Biol. **335**, 185–197 (2013)

108. C. Morin, C. Hellmich, A multiscale poromicromechanical approach to wave propagation and attenuation in bone. Ultrasonics **54**(5), 1251–1269 (2014)

109. C. Morin, C. Hellmich, P. Henits, Fibrillar structure and elasticity of hydrating collagen: a quantitative multiscale approach. J. Theor. Biol. **317**, 384–393 (2013)

110. S. Nikolov, D. Raabe, Hierarchical modeling of the elastic properties of bone at submicron scales: the role of extrafibrillar mineralization. Biophys. J. **94**(11), 4220–4232 (2008)

111. B.S. Noble, The osteocyte lineage. Arch. Biochem. Biophys. **473**, 106–111 (2008)

112. J.P.R.O. Orgel, T.C. Irving, A. Miller, T.J. Wess, Microfibrillar structure of type i collagen in situ. Proc. Nat. Acad. Sci. U. S. A. **103**(24), 9001–9005 (2006)

113. P.E. Palacio-Mancheno, A.I. Larriera, S.B. Doty, L. Cardoso, S. Fritton, 3D assessment of cortical bone porosity and tissue mineral density using high resolution $\mu$CT: effects of resolution and threshold method. J. Bone Miner. Res. **29**(1), 142–150 (2012)

114. E. Papadakis, T. Patton, Y. Tsai, D. Thompson, R. Thompson, The elastic moduli of a thick composite as measured by ultrasonic bulk wave pulse velocity. J. Acoust. Soc. Am. **89**(6), 2753–2757 (1991)

115. A.M. Parfitt, The physiologic and clinical significance of bone histomorphometric data, in *Histomorphometry*, Techniques and Interpretation, ed. by R.R. Recker (CRC Press Inc, Boca Raton, 1983), pp. 143–223

116. W.J. Parnell, Q. Grimal, The influence of mesoscale porosity on cortical bone anisotropy. Investigations via asymptotic homogenization. J. R. Soc. Interface **6**, 97–109 (2009)

117. F. Peters, K. Schwarz, M. Epple, The structure of bone studied with synchrotron X-ray diffraction, X-ray absorption spectroscopy and thermal analysis. Thermochim. Acta **361**(1–2) (2000)

118. R.M.V. Pidaparti, D.B. Burr, Collagen fiber orientation and geometry effects on the mechanical properties of secondary osteons. J. Biomech. **25**(8) (1992)
119. R.M.V. Pidaparti, A. Chandran, Y. Takano, C.H. Turner, Bone mineral lies mainly outside collagen fibrils: predictions of a composite model for osternal bone. J. Biomech. **29**(7) (1996)
120. S. Pradhan, D. Katti, K. Katti, Steered molecular dynamics study of mechanical response of full length and short collagen molecules. J. Micromech. Microeng. **1**(3), 104110 (2011)
121. K. Prostak, S. Lees, The locus of mineral crystallites in bone. Connect. Tissue Res. **18**(1), 41–54 (1988)
122. K.S. Prostak, S. Lees, Visualization of crystal-matrix structure. In situ demineralization of mineralized turkey leg tendon and bone. Calcif. Tissue Int. **59**(6), 474–479 (1996)
123. T. Qu, D. Verma, M. Shahidi, B. Pichler, Mechanics of organic-inorganic biointerfacesImplications for strength and creep properties. MRS Bull. **40**(4), 349–358 (2015)
124. A.G. Reisinger, D.H. Pahr, P.K. Zysset, Sensitivity analysis and parametric study of elastic properties of an unidirectional mineralized bone fibril-array using mean field methods. Biomech. Model. Mechanobiol. **9**(5) (2010)
125. J.-Y. Rho, M.E. Roy, T.Y. Tsui, G.M. Pharr, Elastic properties of microstructural components of human bone tissue as measured by nanoindentation. J. Biomed. Mater. Res. **45**(1), 48–54 (1998)
126. J.Y. Rho, M.C. Hobatho, R.B. Ashman, Relations of mechanical properties to density and CT numbers in human bone. Med. Eng. Phys. **17**(5), 347–355 (1995)
127. R. Riedl, A systems-analytical approach to macro-evolutionary phenomena. Q. Rev. Biol. **52**(4), 351–370 (1977)
128. R.A. Robinson, Chemical analysis and electron microscopy of bone, in *Bone as Tissue*, ed. by K. Rodahl, J.T. Nicholson, E.M. Brown Jr. (McGraw-Hill, New-York, 1960), pp. 186–250
129. P.J.M. Roholl, E. Blauw, C. Zurcher, J.A.M.A. Dormans, H.M. Theuns, Evidence for a diminished maturation of preosteoblasts into osteoblasts during aging in rats: an ultrastructural analysis. J. Bone Miner. Res. **9**(3), 355–366 (1994)
130. M.A. Rougvie, R.S. Bear, An X-Ray diffraction investigation of swelling by collagen. J. Am. Leather Chem. Assoc. **48**(12), 735–751 (1953)
131. J. Salençon, *Handbook of Continuum Mechanics* (Springer, Berlin, 2001)
132. V. Sansalone, S. Naili, V. Bousson, C. Bergot, F. Peyrin, J. Zarka, J.D. Laredo, G. Haiat, Determination of the heterogeneous anisotropic elastic properties of human femoral bone: from nanoscopic to organ scale. J. Biomech. **43**(10) (2010)
133. N. Sasaki, S. Odajima, Stress-strain curve and Young's modulus of a collagen molecule as determined by the X-ray diffraction technique. J. Biomech. **29**(5), 655–658 (1996)
134. S. Scheiner, P. Pivonka, C. Hellmich, Coupling systems biology with multiscale mechanics, for computer simulations of bone remodeling. Comput. Methods Appl. Mech. Eng. **254**, 181–196 (2013)
135. S. Scheiner, P. Pivonka, C. Hellmich, Mathematical modeling of postmenopausal osteoporosis and its treatment by the anti-catabolic drug denosumab. Numer. Methods Biomed. Eng. **30**, 127 (2014)
136. S. Scheiner, P. Pivonka, C. Hellmich, Poromicromechanics reveals that physiological bone strains induce osteocyte-stimulating lacunar pressure. Biomech. Model. Mechanobiol. **15**(1), 928 (2016)
137. P. Schneider, M. Stauber, R. Voide, M. Stampanoni, L.R. Donahue, R. Müller, Ultrastructural properties in cortical bone vary greatly in two inbred strains of mice as assessed by synchrotron light based micro- and nano-CT. J. Bone Miner. Res. **22**(10), 1557–1570 (2007)
138. P. Schneider, M. Meier, R. Wepf, R. Müller, Serial FIB/SEM imaging for quantitative 3D assessment of the osteocyte lacuno-canalicular network. Bone **49**(2), 304–311 (2011)
139. H.P. Schwarcz, E.A. McNally, G.A. Botton, Dark-field transmission electron microscopy of cortical bone reveals details of extrafibrillar crystals. J. Struct. Biol. **188**(3), 240–248 (2014)
140. W.K. Sietsema, Animal models of cortical porosity. Bone **17**(4), 297–305 (1995)
141. K.T. Tai, F.-J. Ulm, C. Ortiz, Nanogranular origins of the strength of bone. Nanoletters **6**(11), 2520–2525 (2006)

142. N.-J. Tao, S.M. Lindsay, S. Lees, Studies of compact hard tissues and collagen by means of brillouin light scattering. Connect. Tissue Res. **24**(3–4), 187–205 (1990)
143. S. Teitelbaum, Bone resorption by osteoclasts. Science **289**, 1504–1508 (2000)
144. S.M. Tommasini, A. Trinward, A.S. Acerbo, F. De Carlo, L.M. Miller, S. Judex, Changes in intracortical microporosities induced by pharmaceutical treatment of osteoporosis as detected by high resolution micro-CT. Bone **50**, 596–604 (2012)
145. C.H. Turner, S.C. Cowin, J.Y. Rho, R.B. Ashman, J.C. Rice, The fabric dependence of the orthotropic elastic constants of cancellous bone. J. Biomech. **23**(6), 549–561 (1990)
146. M.R. Urist, R.J. DeLange, G.A. Finerman. Bone cell differentiation and growth factors. Science (1983)
147. J. Vuong, C. Hellmich, Bone fibrillogenesis and mineralization: quantitative analysis and implications for tissue elasticity. J. Theor. Biol. **287**, 115–130 (2011)
148. B.E. Warren, X-ray diffraction methods. J. Appl. Phys. **12**(5), 375–384 (1941)
149. B.E. Warren, B.L. Averbach, The effect of cold-work distortion on X-ray patterns. J. Appl. Phys. **21**(6), 595–599 (1950)
150. S. Weiner, H.D. Wagner, The material bone: structure-mechanical function relations. Annu. Rev. Mater. Sci. **28**, 271–298 (1998)
151. S. Weiner, T. Arad, I. Sabanay, W. Traub, Rotated plywood structure of primary lamellar bone in the rat: orientations of the collagen fibril arrays. Bone **20**, 509–514 (1997)
152. J. Wergedal, Baylink, Electron microprobe measurements of bone mineralization rate in vivo. Am. J. Physiol. **226**(2), 345–352 (1974)
153. H.P. Wiesmann, U. Meyer, U. Plate, H.J. Hhling, Aspects of collagen mineralization in hard tissue formation. Int. Rev. Cytol. **242**, 121–156 (2005)
154. Y.J. Yoon, S.C. Cowin, The estimated elastic constants for a single bone osteonal lamella. Biomech. Model. Mechanobiol. **7**(1) (2008)
155. A. Zajac, D. Discher, Cell differentiation through tissue elasticity-coupled, myosin-driven remodeling. Curr. Opin. Cell Biol. **20**(6), 609–615 (2008)
156. A. Zaoui, Structural morphology and constitutive behavior of microheterogeneous materials, *Continuum Micromechanics* (Springer, Berlin, 1997), pp. 291–347
157. A. Zaoui, Continuum micromechanics: survey. J. Eng. Mech. **128**(8), 808–816 (2002)
158. J.-X. Zhu, Y. Sasano, I. Takahashi, I. Mizogushi, M. Kagayama, Temporal and spatial gene expression of major bone extracellular matrix molecules during embryonic mandibular osteogenesis in rats. Histochem. J. **33**, 25–35 (2001)
159. L. Zylberberg, W. Traub, V. de Buffrenil, F. Allizard, T. Arad, S. Weiner, Rostrum of a toothed whale: ultrastructural study of a very dense bone. Bone **23**, 241–247 (1998)

# Computational Biomechanics of Bone Adaptation by Remodeling

**Taiji Adachi and Yoshitaka Kameo**

**Abstract**  In bone remodeling, a variety of mechanical and biochemical signaling occurs among osteoclasts and osteoblasts, which are responsible for bone resorption and formation, and osteocytes, which are believed to have a mechanosensing function. Biomechanics research incorporating mathematical modeling and computer simulations is being conducted in order to understand the functional adaptation of bone structure by remodeling that can be observed at a macroscopic level resulted from the complex interaction among these signals at molecular and cellular levels.

**Keywords**  Bone remodeling · Bone adaptation · Osteocytes · Mechanosensing · Micro finite element analysis · Computer simulations

## 1 Introduction

The details of intracellular signaling mechanisms and cell-cell interactions involved in the control of bone metabolism are gradually being clarified [1–4]. Moreover, a further development in biomechanics research [5–7] in order to understand the mechanical adaptation phenomenon, known as Wolff's Law, is anticipated with advances in bone cell mechanobiology researches [8, 9]. However, while our understanding of the detailed mechanism at cellular and molecular levels increases, difficulties are still being faced in understanding the control dynamics of the bone remodeling system that occurs at the macroscopic level and emerges over the hierarchy of interaction between these elements due to the complexity involved.

Mathematical modeling and computational simulation research have recently garnered attention as means of comprehensively understanding the dynamics of complex

T. Adachi (✉) · Y. Kameo
Department of Biosystems Science, Institute for Frontier Life and Medical Sciences,
Kyoto University, Kyoto, Japan
e-mail: adachi@infront.kyoto-u.ac.jp

Y. Kameo
e-mail: kameo@infront.kyoto-u.ac.jp

systems [6, 10, 11]. The phenomenon by which the remodeling activity of osteo-clasts and osteoblasts is regulated via the process of mechanical and biochemical signaling is not only temporally regulated but also spatially regulated, depending on the distance between and the location of cells. Moreover, in order to understand the functional adaptation phenomenon of bone as a result of remodeling, it is necessary to first understand the correlation between mechanical function and changes in bone morphology that arise from both the forces acting on bone and the deformation of the bone matrix. In other words, it is important to not only track the evolution of complex signaling but also to understand the relationship between bone structure and function and the deeply involved dynamic field.

## 2 From the Macroscopic Structure to the Microscopic Cellular Responses of Bone

### 2.1 Hierarchical Structure of Bone

Adaptive bone remodeling can be understood in terms of the relationship between forces and bone structure on a macroscopic level. However, remodeling occurs as a result of the coupling activity of osteoclasts and osteoblasts on a microscopic level. The relationship with osteocyte mechanosensing on a molecular level is also impor-tant. As shown in Fig. 1, cancellous bone is composed of a cancellous, trabecular network structure. A trabecular cross-section of this bone reveals a newly-formed lamellar bone matrix on the trabecular surface as a result of bone resorption and formation activity by osteoclasts and osteoblasts. Furthermore, osteocytes discretely present within the trabecular matrix form a dense network that extends to numerous cell processes.

### 2.2 Bone Remodeling Regulation by Mechanical Stimuli

Bone remodeling is thought to be regulated by the accumulation of microscopic dam-age, localized stress and strain, and mechanical stimuli such as the interstitial fluid flow within bone canaliculi into which cell processes extend [12, 13]. Furthermore, an experiment in which isolated osteocytes were loaded with localized mechanical stimuli demonstrated that the cell processes are particularly sensitive to mechanical stimuli [14]. The magnitude of macroscopic elastic strain that occurs in bone is usu-ally no more than 0.1–0.2%, and even if such small deformation is directly applied to osteocytes and osteoblasts, cellular responses such as an influx of calcium ions or nitric oxide production are not observed. This suggests the presence of an amplifica-tion mechanism for mechanical stimuli on a microscopic cellular and/or molecular level.
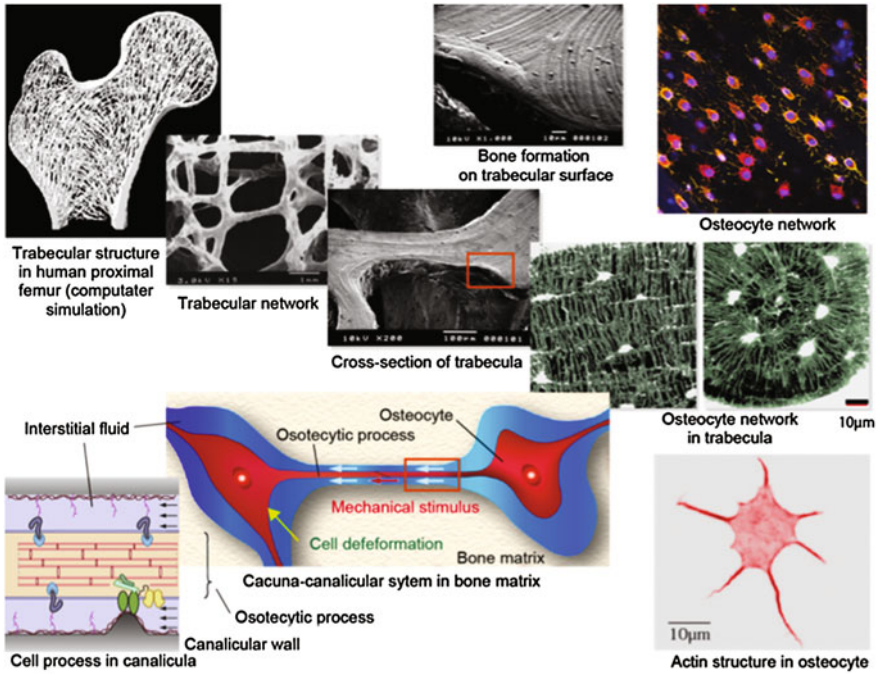
**Fig. 1** Hierarchical structure of bone from the trabecular structure of cancellous bone, the osteocyte networks within bone matrix, to the osteocyte processes within the canaliculi (This figure was partially adapted from Ref. [26] with permission from Elsevier.)

## 2.3 The Mechanobiology of Osteocytes

The processes of osteocytes [9, 15, 16] that have garnered attention as mechanosensor cells of bone contain many actin filament bundles, the morphological characteristics of which are very interesting. It is conceivable that some kind of mechanosensing function exists on the scale of these cell processes. For example, the interstitial fluid flow within bone canaliculi places shear stress on the cell processes, while local linked structures between the walls of the bone canaliculi and the surface of the cell processes may act as a mechanism for transmitting mechanical signals (forces) by amplifying small deformation or stress of the membranes and internal cytoskeletal structure of cell processes [17]. Furthermore, responses to fluid shear stress by micro-patterned osteocyte networks have been observed [18], and models depicting the role of the primary cilia in the mechanosensing mechanism of osteocytes have been proposed [19, 20]. Thus, future detailed clarification of the mechanosensing mechanism of osteocytes is strongly required.

# 3 The Mathematical Modeling and Computational Biomechanics Approach

As shown in Fig. 1, it is not easy to explain the pattern formation of the trabecular structure in cancellous bone on the most macroscopic level based on the detailed mechanisms at a microscopic level. This is due to the size of the gap between the temporal and spatial hierarchy from molecular and cellular level to the tissue and organ level, even when the mechanosensing mechanism at the osteocyte level is elucidated in detail at the molecular level. Mathematical modeling with computational biomechanics is therefore a promising approach.

## 3.1 Classic Mathematical Models of Mechanical Adaptation by Bone Remodeling

Many phenomenological mathematical models of bone remodeling representing bone resorption and formation have been proposed to date, in which bone remodeling occurs by referring to the macroscopic mechanical state of bone, as typified by the mechanostat theory [21–24]. In contrast, we proposed a mathematical model in which local mechanical nonuniformity at the cell level appears to drive trabecular remodeling [25, 26]. The top left image in Fig. 1 shows the cancellous bone structure of the human proximal femur predicted by a large-scale computer simulation using this model [26]. It shows that the three-dimensional trabecular structure, which appears very similar to the actual structural pattern, can be predicted with an extremely simple local rule.

## 3.2 Mechanosensing and Communication of Osteocytes

The bottom-up approach, in which knowledge obtained at the cellular and molecular levels is pieced together, is an important approach in regard to the above-mentioned phenomenological approach. The authors proposed a mathematical model of bone remodeling (Fig. 2a) in which the cell processes of osteocytes and the bone canalicular network are assumed to play an important role in mechanosensing and communication (Adachi et al. 2010; Kameo et al. 2011a). The trabeculae were first modeled as poroelastic media containing a bone lacuno-canalicular network, after which a mathematical model of bone remodeling was constructed from mechanosensing of fluid shear stress by osteocytes up to bone resorption and formation by osteoclasts and osteoblasts. As a result, shear stress placed on the surface of the cell processes due to the interstitial fluid flow associated with the dynamic deformation of the bone matrix was regarded as mechanical stimuli applied to osteocytes. We were thus able to demonstrate that trabecular morphology functionally adapts and changes to make

the stress distribution on the trabecular surface uniform, i.e. to align the trabeculae in the direction of loading.

## 3.3  Flow Analysis Within Bone Canaliculi Using an Image-Based Model

Kamioka et al. visualized a detailed three-dimensional image (Fig. 2c) of the canaliculi and cell processes within the bone matrix using an ultra-high voltage electron microscope and electron tomography (Fig. 2b) [27]. They also analyzed the microscopic flow in the gaps surrounding the cell processes using the obtained digital image model (Fig. 2d). They found that interstitial fluid within the gaps exhibited a complex flow that depended greatly on location as a result of the irregular surfaces of the canalicular walls. This suggested that local force and deformation affect the cell processes. Furthermore, if it is revealed that the microscopic morphology and environment of the bone lacunae and canaliculi change as a result of various factors [28], this could lead to an understanding of changes in the microscopic mechanical environment surrounding osteocytes and changes in mechanosensing characteristics.

## 4  Modeling Mechanosensing Osteocytes in Bone Adaptation

We previously proposed a mathematical model to represent bone cellular activities in response to mechanical loading based on the assumption that osteoclastic bone resorption and osteoblastic bone formation are regulated by mechanosensing osteocytes [5, 6, 29]. In this model, the process of trabecular bone remodeling consists of three parts: (i) cellular mechanosensing, (ii) intercellular signal transmission, and (iii) trabecular surface movement owing to remodeling, as shown in Fig. 3. A summary of each process is explained below by introducing some physiologically rational assumptions.[1]

## 4.1  Cellular Mechanosensing

In the cellular mechanosensing process, osteocytes were assumed to be sensitive to fluid-induced shear stress acting on their cellular processes. For evaluating the shear stress, we adopted the microstructure model of Weinbaum et al. [12], which accounts for the interstitial fluid flow through a fiber matrix in an annular canaliculus. Using the fluid pressure gradient at the trabecular level, $\nabla p$, the fluid-induced shear stress, $\tau_p$, acting on the osteocyte processes aligned in direction $\boldsymbol{n}$ is given as:

---

[1]Sections 4 and 5 in this chapter were modified from Ref. [29] with permission from Springer.
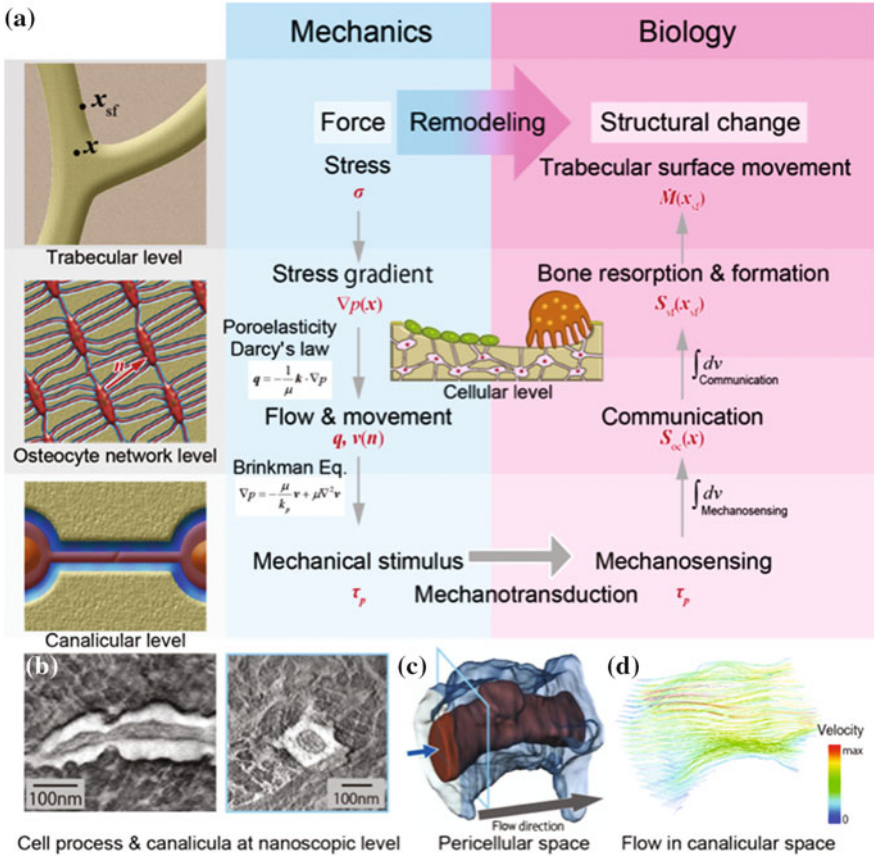
**Fig. 2** Mathematical model of trabecular remodeling considering osteocyte mechanosensing and communication. **a** Force applied to bone causes bone matrix deformation. This results in a pressure gradient in the interstitial fluid within the bone canaliculi network, causing interstitial fluid flow. As a result of this flow, shear stress (force) acts on the surfaces of osteocyte processes, which are sensitive to mechanical stimuli. When osteocytes sense this shear force, signals are transmitted to the trabecular surfaces via intercellular communication, which regulates trabecular remodeling activity by osteoclasts and osteoblasts and results in changes in the trabecular structure of cancellous bone. **b** Using ultra-high voltage electron microscopy computed tomography scans, **c** we created an image-based model of the cell processes and canalicular walls, and **d** analyzed the microscopic flow of interstitial fluid. (b–d were adapted from the Ref. [27] with permission from The Royal Society of Chemistry.)

$$\tau_p\left(\boldsymbol{x},\boldsymbol{n}\right)=\frac{q\tau_p}{\gamma}\left(A_1 I_1(\frac{\gamma}{q})-B_1 K_1(\frac{\gamma}{q})\right)\nabla p(\boldsymbol{x})\cdot\boldsymbol{n} \tag{1}$$

where $q$ is the ratio of the radius of the canaliculus $r_c$ to that of the process $r_p$, i.e., $q=r_c/r_p$, $I_1$ and $K_1$ are the modified Bessel functions of the first order, and the other constants are defined in Weinbaum et al. [12].
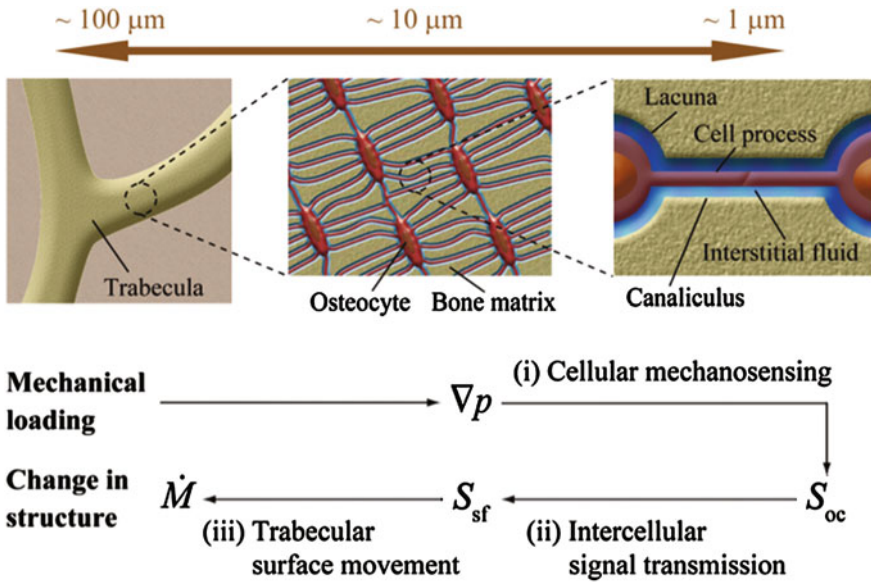
**Fig. 3** Theoretical framework for trabecular bone remodeling considering the mechanical hierarchy from the microscopic level ($\sim$1 µm) to the mesoscopic level ($\sim$100 µm). The remodeling process consists of the following three parts: (i) cellular mechanosensing, (ii) intercellular signal transmission, and (iii) trabecular surface movement. The change in trabecular structure is caused by osteoclastic bone resorption and osteoblastic bone formation. Their remodeling activities are regulated by osteocytes in response to the interstitial fluid flow in canaliculi. (This figure was reproduced from Ref. [29] with permission of Springer.)

Assuming the biochemical signal that osteocytes produce in response to the fluid-induced shear stress $\tau_p$ is proportional to the shear force on their processes, the signal $S_{OC}(x)$ produced by the osteocytes per unit bone volume can be defined, using the volume fraction of the canaliculi oriented in direction $n$, $\rho_c(n)$, introduced in Kameo et al. [30], as follows:

$$S_{OC}(x) = \int_0^{2\pi} d\varphi \int_0^{\pi/2} \alpha \frac{2\tau_p}{r_c^2} \rho_c(n) |\overline{\tau_p(x, n)}| sin\theta d\theta \qquad (2)$$

where $\theta$ is the angle between the vector $n$ and the $x_3-$axis in the arbitrary Cartesian coordinate system, $\varphi$ is the angle between the $x_1-$axis and the projection of $n$ onto the $x_1x_2-$plane measured counterclockwise, $\alpha$ is the mechanosensitivity of the osteocytes, and $|\overline{\tau_p(x, n)}|$ is the time-averaged shear stress over the course of one day. For simplicity, we set $\alpha = 1$ for all of the osteocytes and assumed the isotropy of canalicular orientation, i.e., $\rho_c(n) = \phi/2\pi$, where $\phi$ is the porosity of the trabeculae.

## *4.2  Intercellular Signal Transmission*

The signals produced are modeled to be transmitted to the effector cells on the trabecular surface, such as osteoclasts and osteoblasts, through the intercellular network system of bone cells. With the use of a weight function $w(l)$ that represents the decay in the signal intensity relative to the distance $l$, the total stimulus $S_{sf}$ on the trabecular surface position $\boldsymbol{x}_{sf}$ is obtained in the following integral form:

$$S_{sf}(\boldsymbol{x}_{sf}) = \int_{\Omega} w(l)S_{OC}(\boldsymbol{x})d\Omega, \quad w(l) = 1 - l/l_L \quad (l \le l_L) \tag{3}$$

where $l = |\boldsymbol{x}_{sf} - \boldsymbol{x}|$, and distance $l_L$ denotes the maximum distance for intercellular communication and determines the communication area $\Omega$. The total stimulus $S_{sf}$ is a positive scalar function and is regarded as the driving force of trabecular bone remodeling.

## *4.3  Trabecular Surface Movement*

In order to express the trabecular surface movement owing to remodeling, we introduced a piecewise sinusoidal function that describes the relationship between the rate of trabecular surface remodeling $\dot{M}$ and the total stimulus on the trabecular surface $S_{sf}$, as shown in Fig. 4. This empirical function indicates that bone resorption is initiated by stimuli below the remodeling equilibrium and that bone formation is initiated by stimuli exceeding the equilibrium. In this function, $S_{sf}^U$ is the upper
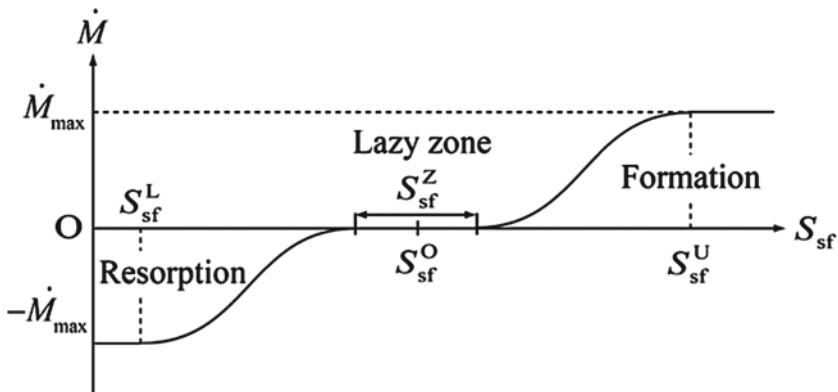


**Fig. 4** Relationship between the rate of trabecular surface remodeling $\dot{M}$ and the total stimulus $S_{sf}$ that the trabecular surface cell receives from the neighboring osteocytes. This relationship is assumed to be represented by a piecewise sinusoidal function. (This figure was reproduced from Ref. [29] with permission of Springer.)

threshold for bone formation, $S_{sf}^L$ is the lower threshold for bone resorption, $S_{sf}^O$ is a stimulus at the remodeling equilibrium, and $S_{sf}^Z$ is the width of the lazy zone. The maximum rates of resorption and formation are assumed to have the same absolute value $\dot{M}_{max}$ in order to simplify the numerical algorithm, whereas, in reality, the formation rate of osteoblasts is much smaller than the resorption rate of osteoclasts. The level set method [31], which is a numerical technique for tracking the interfaces and shapes of materials, was employed to express trabecular surface movement in this simulation.

# 5 Adaptation of a Single Trabecula to a Bending Load

The individual trabecula has a characteristic morphology that is strut-like or plate-like in form depending on its position within cancellous bone. While it is certain that the morphology is associated with the mechanical environment, the determinant remains unclear. Therefore, we hypothesized that the trabecular morphology is influenced by a type of load such as a uniaxial or bending load, and demonstrated the reorientation of the strut-like trabecula under cyclic uniaxial loading [5, 6]. In the present study, we investigated the effects of a bending load on the changes in trabecular morphology [29]. By applying our mathematical model of bone remodeling to the three-dimensional voxel finite element model of a trabecula, we performed a bone remodeling simulation for a single trabecula subjected to a cyclic bending load.

## 5.1 Voxel Finite Element Model of a Single Trabecula

A three-dimensional computational model of a single trabecula for simulating the morphological changes via bone remodeling was constructed as shown in Fig. 5. The region for analysis was $a_1 \times a_2 \times a_3 = 0.8\,\mathrm{mm} \times 1.6\,\mathrm{mm} \times 1.2\,\mathrm{mm}$, which was divided into $20 \times 40 \times 30$ cubic voxel finite elements. A strut-like trabecula having a diameter of $240\,\mu\mathrm{m}$ was placed at the center of the region along the direction of the $x_3$-axis. The trabecula was modeled as a poroelastic material with homogeneous and isotropic material properties (Table 1) [33, 34]. In order to impose external loadings, two parallel plates, each having a thickness of $40\,\mu\mathrm{m}$, were added to the upper and lower surfaces of the region for analysis. The shape of the plates did not change throughout the remodeling process, and the plates were assigned the same material properties as the trabeculae. As mechanical boundary conditions, a shear-free boundary condition was applied to the lower plate, and free leakage of interstitial fluid on the trabecular surfaces was assumed. A cyclic bending load, which was linearly distributed along the $x_2$ direction $\sigma = (2\sigma_3 x_2/a_2)sin(2\pi f t)$ ($f = 1$ Hz), was imposed on the upper plate in the $x_3$ direction for 1.0 s per day. In order to investigate the effects of the magnitude of the applied bending load on the trabecular morphology, the value of $\sigma_3$ was determined as $\sigma_3 = -0.10$ and $-0.15\,\mathrm{MPa}$ based on a previous remodeling simulation of cancellous bone [35]. The physiological parameters
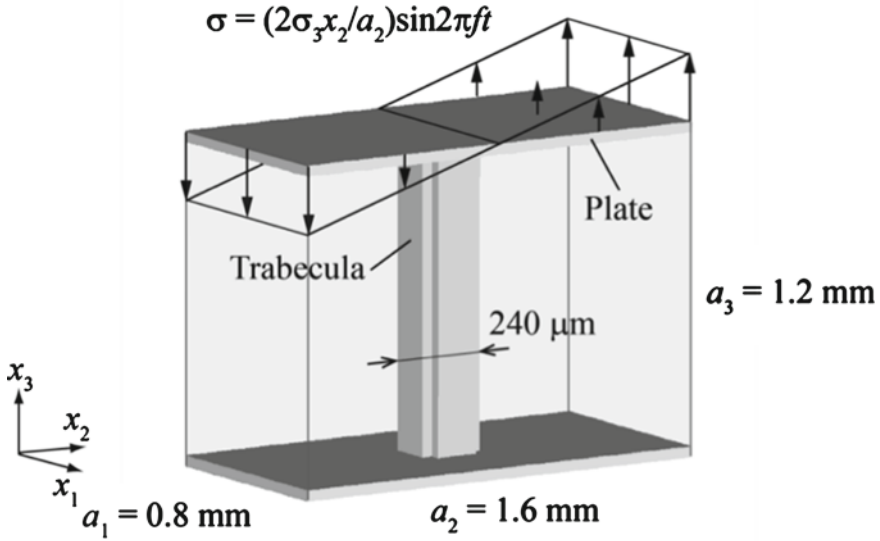
**Fig. 5** Voxel finite element model of a single trabecula having a diameter of 240 m. A cyclic bending load, which was linearly distributed along the $x_2$ direction, was applied to the upper plane along the $x_3$ direction for 1.0 s per day. (This figure was reproduced from Ref. [29] with permission of Springer.)

**Table 1** Material properties of the trabecula as a poroelastic material. Permeability was estimated by the method described in Beno et al. [33], and other constants were taken from the Smit et al. [34]

| Symbol (unit) | Description | Value |
|---|---|---|
| $k$ (m$^2$) | Intrinsic permeability | $1.1 \times 10^{-21}$ |
| $\mu$ (Pa·s) | Fluid viscosity | $1.0 \times 10^{-3}$ |
| $G$ (GPa) | Shear modulus | 5.94 |
| $\nu$ | Drained Poisson's ratio | 0.325 |
| $K_s$ (GPa) | Solid bulk modulus | 17.66 |
| $K_f$ (GPa) | Fluid bulk modulus | 2.3 |
| $\phi$ | Porosity | 0.05 |

introduced in the remodeling model are as listed in Table 2 [8, 36–38]. With the exception of the parameters associated with the mechanical stimulus, i.e., $S_{sf}^U$, $S_{sf}^L$, $S_{sf}^O$, and $S_{sf}^Z$, which were determined arbitrarily, all of the parameter settings were based on experimental findings. Among the above four parameters, $S_{sf}^Z$ representing a remodeling rate sensitivity to the stimulus near the remodeling equilibrium had a greater influence on the changes in bone volume [6]. Therefore, we performed trabecular remodeling simulations under two different settings of parameter $S_{sf}^Z$, as listed in Table 2.

**Table 2** Parameter settings for the trabecular remodeling simulation [8, 36, 37]. ⋆$a$: [36], ⋆$b$: [38], ⋆$c$: [8], ⋆$d$: [37]

| Symbol (unit) | Description | Value |
|---|---|---|
| $r_p$ (nm) | Radius of osteocyte process | $52^a$ |
| $r_c$ (nm) | Radius of canaliculus | $129.5^a$ |
| $l_L$ (μm) | Maximum distance for intercellular communication | $200^{b,c}$ |
| $\dot{M}_{max}$ (μm/day) | Maximum remodeling rate | $40^d$ |
| $S_{sf}^U$ (μN) | Upper threshold for bone formation | 1.5 |
| $S_{sf}^L$ (μN) | Lower threshold for bone resorption | 0.5 |
| $S_{sf}^O$ (μN) | Stimulus at remodeling equilibrium | 1.0 |
| $S_{sf}^Z$ (μN) | Width of lazy zone | 0.6 or 0.4 |
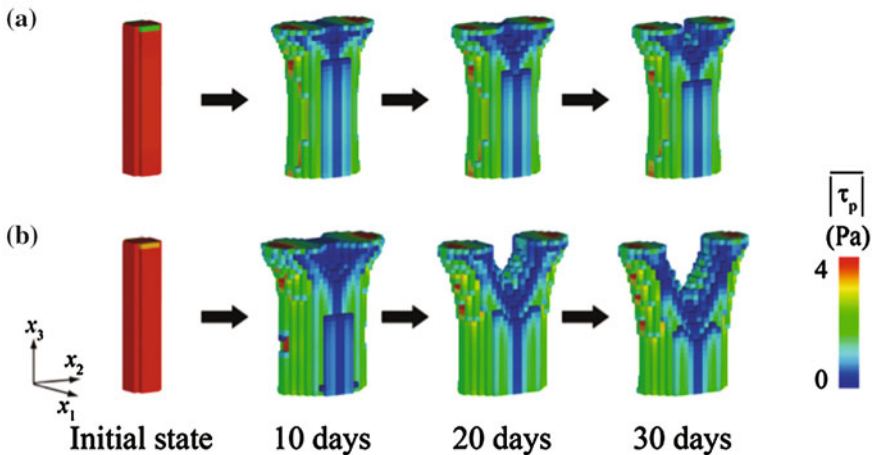


**Fig. 6** Changes in the trabecular morphology and average fluid-induced shear stresses in one day $|\overline{\tau_p}|$ under a cyclic bending load when the width of the lazy zone $S_{sf}^Z$ is 0.6 μN. **a** $\sigma_3 = -0.10$ MPa and **b** $\sigma_3 = -0.15$ MPa. (This figure was reproduced from Ref. [29] with permission of Springer.)

## 5.2 Results: Changes in Single Trabecular Morphology

Applying the proposed mathematical model of bone remodeling to the voxel finite element model of the trabecula, we investigated the morphological changes in a single trabecula subjected to an external cyclic bending load through remodeling simulations. Figures 6 and 7 show the distribution of the one-day average of the fluid-induced shear stress acting on the osteocyte processes $|\overline{\tau_p}|$ at different stages of remodeling when the width of the lazy zone $S_{sf}^Z$ is equal to 0.6 and 0.4 μN, respectively. In both figures, part (a) corresponds to the results for the magnitude
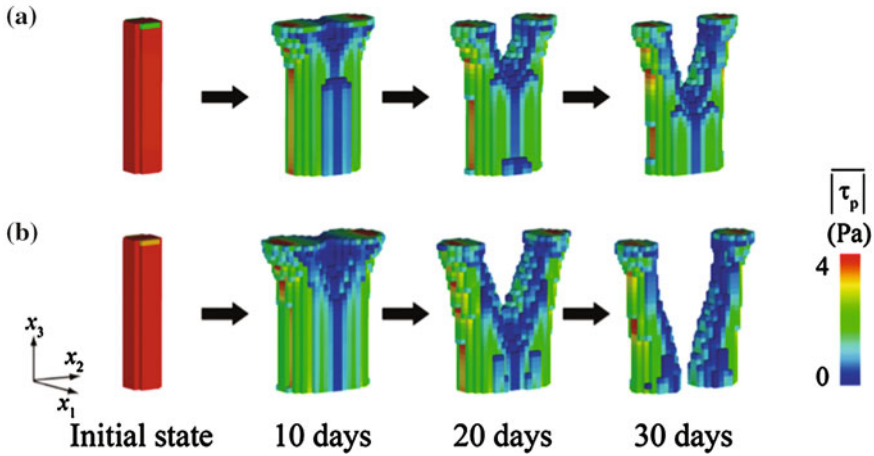
**Fig. 7** Changes in the trabecular morphology and average fluid-induced shear stresses in one day $|\overline{\tau_p}|$ under a cyclic bending load when the width of the lazy zone $S_{sf}^Z$ is $0.4\,\mu$N. **a** $\sigma_3 = -0.10\,$MPa and **b** $\sigma_3 = -0.15\,$MPa. (This figure was reproduced from Ref. [29] with permission of Springer.)

of bending load $\sigma_3 = -0.10\,$MPa, and part (b) corresponds to the results for $\sigma_3 = -0.15\,$MPa.

Under the loading condition of $\sigma_3 = 0.10\,$MPa, as shown in Fig. 6a, bone formation was promoted on all trabecular surfaces in the initial state owing to high fluid-induced shear stress. The bone formation along the $x_2$ direction was dominant because the applied bending load was linearly distributed along the $x_2$ direction. As a result, a plate-like trabecula, the dimension along the $x_2$ direction of which is larger than that along the $x_1$ direction, was formed after 10 days. Afterward, the morphology of the trabecula was almost unchanged, while a small cavity was formed close to the upper end.

The fluid-induced shear stress on the trabecular surfaces increases with the increase in magnitude of the applied bending load. When $\sigma_3 = -0.15\,$MPa, the remarkable bone formation for 10 days produced a plate-like trabecula with a larger width and thickness, as shown in Fig. 6b. After 20 days, unlike the case of $\sigma_3 = -0.10\,$MPa, when $\sigma_3 = -0.15\,$MPa significant bone resorption occurred around the central region of the trabecula near the neutral axis of bending because the fluid-induced shear stress decreased owing to the rapid bone formation along the $x_2$ direction. As a result of subsequent bone resorption in the region, a branching structure was formed at the upper end of the plate-like trabecula.

Comparison of the changes in the trabecular morphology between the two different parameter settings of $S_{sf}^Z$, as shown in Figs. 6 and 7, reveals that both remodeling processes are quite similar for the first 10 days. However, in the case of $S_{sf}^Z = 0.4\,\mu$N, a comparatively large bone volume was lost owing to bone resorption around the central region of the plate-like trabecula. As shown in Fig. 7b, the plate-like trabecula split into two strut-like trabeculae under a large bending load.

## 5.3 Discussion

We demonstrated the morphological changes in a single trabecula under a cyclic bending load based on the remodeling model that incorporates cellular mechanosensing and intercellular signal transmission. As a result of remodeling simulations, a plate-like trabecula was formed after 10 days and the width and thickness increased with the increase in the magnitude of the bending load. The subsequent bone resorption around the central region of the trabecula contributed to the formation of a branching structure or split one plate-like trabecula into two strut-like trabeculae.

The trabeculae of cancellous bone in vivo are generally subjected to cyclic loading due to locomotion and maintenance of posture [12], which results in complex states of stress. The loading condition can be expressed as a superposition of multiple axial and bending loads in the simulation. Since the magnitude and the ratio of each load component are largely position-dependent in cancellous bone, we investigated the effects of uniaxial and bending loads separately in order to understand the basic and primary characteristics of trabecular bone remodeling. In a previous simulation study, we identified the formation of a strut-like trabecula aligned along the loading direction under pure uniaxial loading [5, 6]. In contrast, the results obtained in the present remodeling simulation reveal that the application of the bending loads influences not only the formation of the plate-like trabecula but also the change in trabecular topology. These results suggest the possibility that the characteristic trabecular morphology, such as a strut-like or plate-like form, is determined based on the local mechanical environment.

Whether the plate-like form is maintained for long periods depends on the magnitude of the bending load and the cellular activities at the trabecular surface. Comparing Fig. 6a, b reveals that a large bending load causes remarkable bone loss in the neighborhood of the neutral axis of bending owing to insufficient mechanical stimuli to osteocytes. This structural change appears in a trabecular remodeling simulation based on the phenomenological rule that remodeling progresses toward a locally uniform state of equivalent stress [35]. On the other hand, the decrease in the width of the remodeling lazy zone $S_{sf}^Z$ accelerated the expansion of the resorption cavity around the central region of the trabecula, as shown in Fig. 7a, b. The lazy zone is also introduced in the mechanostat model by Frost [21, 24] as the 'adaptive window' and represents the ability of the surface cells to detect changes in local stimuli. This means that reducing the span of $S_{sf}^Z$ increases the cellular sensitivity to the mechanical stimuli. Considering the biological characteristics of the lazy zone, the simulation results can be interpreted as indicating that a plate-like trabecula is likely to be formed when the cellular response is comparatively stable with respect to the change in local mechanical stimuli.

The proposed remodeling model contains 11 parameters to describe the three processes of trabecular bone remodeling without considering the material properties of the trabecula listed in Table 2: five parameters for (i) cellular mechanosensing ($r_p$, $r_c$, $A_1$, $B_1$, and $\gamma$), one parameter for (ii) intercellular signal transmission ($l_L$), and five parameters for (iii) trabecular surface movement owing to remodeling

($\dot{M}_{max}$, $S_{sf}^U$, $S_{sf}^L$, $S_{sf}^O$, and $S_{sf}^Z$). Among these parameters, the five parameters for cellular mechanosensing do not essentially influence the trabecular bone architecture because we assumed that they are constant by ignoring the position dependence of the geometry and dimensions of canaliculi. In the modeling of intercellular signal transmission, as the maximum distance for intercellular communication $l_L$ increases, the mechanical state of trabeculae within a more global area is reflected in the total stimulus on the trabecular surface $S_{sf}$ and the bone volume fraction will increase due to the enlarged total stimulus. The maximum remodeling rate $\dot{M}_{max}$ is the parameter governing only the rate of bone resorption and formation and has little influence on the trabecular bone architecture in the state of remodeling equilibrium. The roles of the remaining four parameters associated with the mechanical stimulus, $S_{sf}^U$, $S_{sf}^L$, $S_{sf}^O$, and $S_{sf}^Z$, has been discussed in Kameo et al. [6], which reported that the morphological changes in the trabeculae are more sensitive to the parameter set of $S_{sf}^O$, and $S_{sf}^Z$ than to that of $S_{sf}^U$ and $S_{sf}^L$.

In order to validate our results quantitatively, it is crucial to appropriately set the physiological parameters based on a comparison with experimental findings. Unfortunately, such a comparison has not yet been successfully performed because of the difficulty in observing a single trabecula in vivo under a controlled mechanical condition. However, if we can reconstruct the three-dimensional trabecular bone architecture at the entire bone scale in silico with the aid of high-resolution scanners [39, 40], the image-based finite element analysis would help us to investigate the state of stress in the region of interest and to clarify the relationship between the trabecular microstructure and the local mechanical environment. Although it cannot be quantitatively validated, our mathematical model of trabecular bone remodeling has potential for investigating how the well-organized three-dimensional architecture of cancellous bone is produced by complex metabolic activities of numerous bone cells. By incorporating the biochemical features of bone cells, such as the signaling cascade, in our remodeling model, the refined model will contribute not only to the elucidation of the mechanism of bone remodeling but also to future clinical applications.

## 6 Adaptation of Cancellous Bone Tissue

Cancellous bone is porous bone that is composed of strut-like or plate-like trabeculae forming a well-organized three-dimensional architecture.[2] The remodeling simulation proposed in Sect. 5 can represent the functional adaptation of a single trabecula under physiological cyclic loading. In this section, we focus on structural changes in cancellous bone comprising multiple trabeculae in order to validate our model in silico at a more macroscopic level. We combined our remodeling model with the voxel finite element method in order to demonstrate the changes in cancellous bone morphology in response to uniaxial or bending loads and compared the results

---

[2]Section 6 was modified from Ref. [32] with permission of Springer.

with experimental findings and the results of the previous simulation based on the phenomenological law of bone transformation.

## 6.1 Voxel Finite Element Model of Cancellous Bone

For simulating the morphological changes in bone tissue caused by local bone remodeling at the trabecular level, a three-dimensional computational model of cancellous bone was constructed as shown in Fig. 8. The region for analysis was $a_1 \times a_2 \times a_3 = 3.2\,\text{mm} \times 3.2\,\text{mm} \times 3.2\,\text{mm}$ and was divided into $80 \times 80 \times 80$ cubic voxel finite elements having an edge size of $40\,\mu\text{m}$. This sample size was determined based on previous remodeling simulations of cancellous bone [41, 42]. In order to create an isotropic and uniform porous structure as the starting point for the model of cancellous bone, several pieces of torus-like trabeculae having an outer diameter of $360\,\mu\text{m}$ and an inner diameter of $280\,\mu\text{m}$ were placed randomly throughout the entire region in order to yield a bone volume fraction BV/TV of 0.4, which is within the physiological range. The effectiveness of this method was proven through two-dimensional [43, 44] and three-dimensional remodeling simulations [26]. The trabecula was modeled as a poroelastic material [45–47] with homogeneous and isotropic material properties, as listed in Table 2 [33, 34]. Two $200\,\mu\text{m}$-thick plates by which to apply external loads were added to the upper and lower surfaces of the analyzed region. These plates were assigned the same material properties as the trabeculae, and their shapes were not changed by remodeling. A shear-free boundary condition was applied to the lower plane, and free leakage of interstitial fluid over all trabecular surfaces was assumed. In order to investigate the effects of different
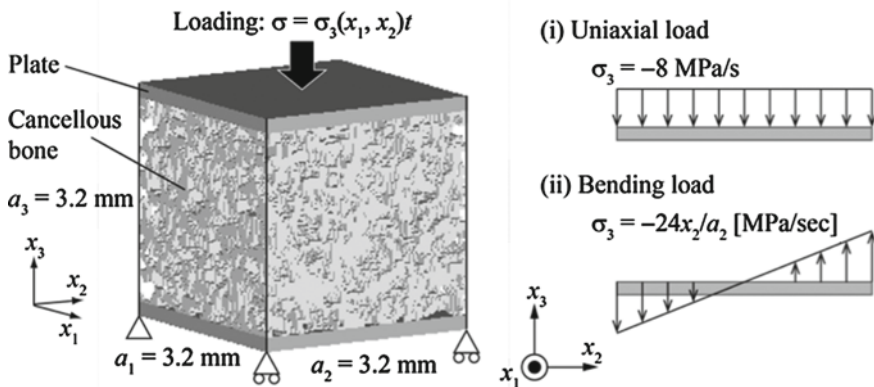


**Fig. 8** Three-dimensional model of cancellous bone for simulation of trabecular remodeling. In the initial configuration, all of the trabeculae are randomly oriented. This model was subjected to two types of monotonically increasing loading through the upper plate: *i* uniaxial loading and *ii* bending loading (This figure was reproduced from Ref. [32] with permission of Springer.)

**Table 3** Parameter settings for the trabecular remodeling simulation [8, 36–38]. ⋆a: [36], ⋆b: [38], ⋆c: [8], ⋆d: [37]

| Symbol (unit) | Description | Value |
|---|---|---|
| $r_p$ (nm) | Radius of osteocyte process | $52^a$ |
| $r_c$ (nm) | Radius of canaliculus | $129.5^a$ |
| $l_L$ (μm) | Maximum distance for intercellular communication | $200^{b,c}$ |
| $\dot{M}_{max}$ (μm/day) | Maximum remodeling rate | $40^d$ |
| $S_{sf}^U$ (μN) | Upper threshold for bone formation | 13 |
| $S_{sf}^L$ (μN) | Lower threshold for bone resorption | 1.0 |
| $S_{sf}^O$ (μN) | Stimulus at remodeling equilibrium | 7.0 |
| $S_{sf}^Z$ (μN) | Width of lazy zone | 10 |

loading patterns on trabecular adaptation, two types of monotonically increasing loads $\sigma = \sigma_3(x_1, x_2)t$ were imposed on the upper plane in the $x_3$ direction for 0.25 s per day, as shown in Fig. 8. One was (i) a uniaxial load $\sigma_3 = -8$ MPa/s and the other was (ii) a bending load that was linearly distributed along the $x_2$ direction from $-12$ to 12 MPa/s, i.e., $\sigma_3 = -24x_2/a_2$ [MPa/s]. The settings of the physiological parameters used in the remodeling model presented in Sect. 4 are summarized in Table 3 [8, 36–38]. With the exception of our parameters associated with mechanical stimulus, $S_{sf}^U$, $S_{sf}^L$, $S_{sf}^O$, and $S_{sf}^Z$, which were determined arbitrarily, all of the parameter settings were based on experimental findings.

## *6.2 Results: Changes in Cancellous Bone Morphology*

We used the mathematical model of trabecular bone remodeling to simulate the remodeling of a cube of cancellous bone over a 30-day period in order to investigate the mechanical adaptation to uniaxial or bending loads. Figure 9 shows the morphological changes in cancellous bone. Figure 9a presents the results for uniaxial loading, and Fig. 9b presents the results for bending loading. In both figures, the color indicates the one-day average of the fluid-induced shear stress acting on the osteocyte processes, which is a driving force of bone remodeling. Independent of the type of external loading, the morphology of the cancellous bone gradually changed over time and the remodeled trabeculae had approximately circular cross-sections, as shown in Fig. 9a, b.

The application of a uniaxial load (Fig. 9a) resulted in bone resorption on all cancellous bone surfaces for the first three days due to the low fluid-induced shear stress, leading to a decrease in the bone volume fraction. After this stage, bone formation
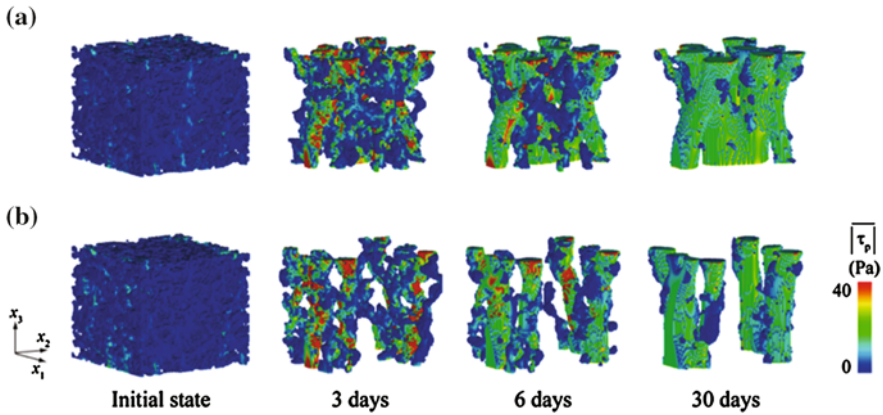
**Fig. 9** Changes of the cancellous bone morphology and average fluid-induced shear stresses in one day $|\overline{\tau_p}|$ **a** under uniaxial loading and **b** under bending loading (This figure was reproduced from Ref. [32] with permission of Springer.)

began on the vertically oriented trabeculae exposed to greater fluid-induced shear stress, despite the preferential loss of the horizontal trabeculae. Successive remodeling gradually decreased the degree of trabecular connectivity, and the trabeculae in the cancellous bone reoriented parallel to the direction of loading by the end of the 30-day simulation.

The application of a bending load to cancellous bone produced significant bone erosion around the central region for analysis, which was close to the neutral axis of bending, during the first three days, as shown in Fig. 9b. During the period from three days to six days, large numbers of trabeculae were lost from this region due to insufficient mechanical stimuli to osteocytes, while bone deposition occurred in the sides of the cancellous bone cube. After 30 days, the cancellous bone architecture reached a state of remodeling equilibrium in which the trabeculae around the central region were essentially absorbed and the remaining trabeculae aligned parallel to the direction of loading. This sequence of bone remodeling resulted in a locally inhomogeneous trabecular pattern within the cancellous bone cube.

## 6.3 Results: Distributions of Equivalent Stress

The spatial distributions of the mechanical quantities of the trabeculae are important determinants of the cancellous bone morphology in the state of remodeling equilibrium. The previously proposed mathematical model for bone remodeling assumed several mechanical quantities to be mechanical stimuli regulating the remodeling process [48]. In order to investigate the relationship between the cancellous bone architecture and the mechanical environment at the trabecular level, we focused on
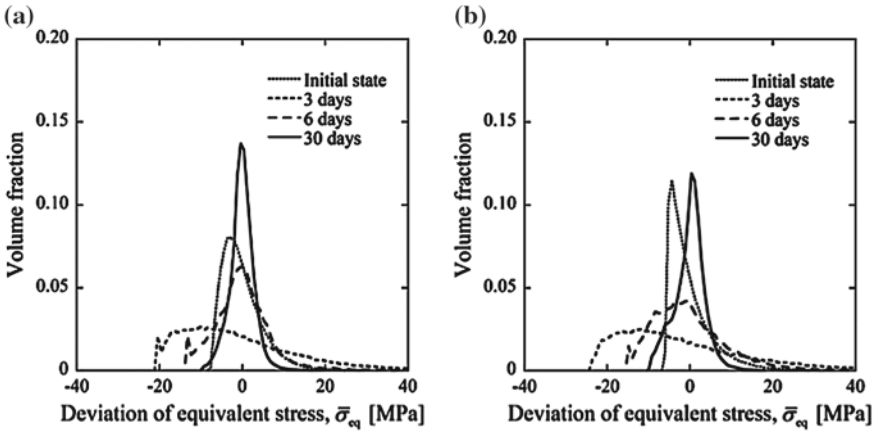
**Fig. 10** Distributions of the volume fraction corresponding to the deviation of equivalent stress $\overline{\sigma_{eq}}$ **a** under uniaxial loading and **b** under bending loading (This figure was reproduced from Ref. [32] with permission of Springer.)

the distribution of von Mises equivalent stress $\sigma_{eq}$ under the maximum load in one day as a typical mechanical quantity. We introduced the deviation of equivalent stress defined as

$$\overline{\sigma_{eq}} = \sigma_{eq} - \text{Mean}(\sigma_{eq}), \tag{4}$$

where $\text{Mean}(\sigma_{eq})$ denotes the mean value of $\sigma_{eq}$ in the cancellous bone included in the region for analysis.

The distributions of the volume fractions corresponding to the deviation of equivalent stress $\overline{\sigma_{eq}}$ are shown in Fig. 10. Figure 10a shows the distributions under uniaxial loading, and Fig. 10b shows the distribution under bending loading. The mean value and the standard deviation (s.d.) of the equivalent stress at different stages of remodeling are listed in Table 4. The initial distributions were asymmetric with respect to the mean value under both types of loading, although there was a slight difference in their kurtosis values. Their distributions shifted to nearly symmetrical bell-shaped curves as bone remodeling progressed. As shown in Table 4, the standard deviation of the equivalent stress decreased by 32% during the 30-day simulation regardless of the type of loading, whereas the mean value increased in both cases.

## 6.4 Discussion

The process by which the cancellous bone architecture adapts to the mechanical environment has a hierarchy from the microscopic cellular level to the macroscopic tissue level. The apparent changes in the density and orientation of cancellous bone result from bone remodeling on the surfaces of the individual trabeculae, and the changes in trabecular morphology are caused by the metabolic activities of numerous bone cells.

**Table 4** Mean value and standard deviation (s.d.) of von Mises equivalent stress during remodeling. (mean $\pm$ s.d.)  (Copyright Kameo and Adachi [32])

|  | von Mises equivalent stress $\sigma_{eq}$ [MPa] | |
|  | Uniaxial load | Bending load |
| --- | --- | --- |
| Initial state | $7.24 \pm 4.93$ | $5.89 \pm 5.46$ |
| 3 days | $20.4 \pm 16.9$ | $24.0 \pm 20.7$ |
| 6 days | $13.1 \pm 7.15$ | $14.5 \pm 9.62$ |
| 30 days | $9.80 \pm 3.36$ | $9.94 \pm 3.72$ |

In the present study, we represented this hierarchical regulatory process in a mathematical model and demonstrated the structural changes in cancellous bone during uniaxial or bending loading in silico. Previous simulation models of the adaptation of the trabecular microstructure have assumed that remodeling is driven by mechanical stimuli, such as stress and strain, at the trabecular level (e.g., [23]). In contrast to these models, the proposed model considers the interstitial fluid flow, which acts directly on the osteocyte processes within the bone matrix, to be the most important stimulus. This simulation method should enable elucidation of the processes by which normal or pathological trabecular architecture develops in response to mechanical conditions at the cellular level.

The simulation results obtained herein indicated that subjecting cancellous bone with randomly arranged trabeculae to external loading resulted in alignment of the trabeculae parallel to the direction of loading and a well-organized architecture specific to the type of external loading, as shown in Fig. 9. Such reorientation of the trabeculae is a reasonable phenomenon from the viewpoint of functional adaptation and agrees qualitatively with in-vivo experimental observations of cancellous bone architecture under controlled mechanical conditions [49–51]. Comparing the cancellous bone morphology in the remodeling equilibrium state between the two loading conditions, as shown in Fig. 9a, b, shows that the trabecular pattern is more inhomogeneous under bending loading due to loss of bone around the central region for analysis, which corresponds to the neutral axis of bending. Although in-vivo experimental studies have not yet succeeded in confirming this phenomenon, a trabecular remodeling simulation based on the phenomenological rule that remodeling progresses toward a locally uniform state of equivalent stress suggested a similar pattern [35]. Under all types of loading, the trabeculae in the remodeling equilibrium state had approximately circular cross-sections because cylindrical trabecular morphology uniformizes the interstitial fluid velocity. The characteristic cross-sectional shape agrees with the anatomical observations of cancellous bone and was first represented by our original remodeling model. These results indicate that our mathematical model for trabecular bone remodeling can successfully predict the macroscopic changes in cancellous bone architecture based on the microscopic cellular activities.

The distributions of the mechanical quantities at the trabecular level are generally non-uniform due to the complexity of cancellous bone architecture. However,

as shown in Table 4, the standard deviation of the equivalent stress decreased during the 30-day simulation under both uniaxial and bending loadings. This suggests that our remodeling model with osteocytes as the mechanosensors can represent the phenomenological law of bone transformation toward a locally uniform state of stress or strain at the trabecular level. The physical meaning of our mathematical model is that bone remodeling is driven by the gradient of interstitial fluid pressure (see Eqs. (1) and (2)) rather than by the hydrostatic pressure itself. This means that the balance of bone resorption and formation is assumed to be regulated by local differences in the mechanical conditions experienced by the trabeculae. In this sense, our model differs distinctly from the previous models in which remodeling was designed to obtain the global reference value of a particular mechanical quantity [23, 52] but is analogous to the model for remodeling caused by the local nonuniformity of equivalent stress [25]. Since the latter model, despite its basis on the phenomenological rule, can successfully describe a three-dimensional trabecular pattern similar to that in the actual human proximal femur [26], it seems reasonable to suppose that bone remodeling is influenced by the local distribution of certain mechanical quantities in the trabeculae rather than by the magnitude of stress or strain.

In our mathematical model, complex three-dimensional architectures of the lacuno-lanalicular porosity and the osteocyte network are ignored for simplicity even though they have a strong anisotropy. The effects of the microstructure on the osteocytic mechanotransduction via interstitial fluid flow can be represented in our simulation by using an anisotropic permeability tensor in the poroelastic analysis and considering the orientation dependence of the volume fraction of the canaliculi $\rho_c(\boldsymbol{n})$ [30]. In addition, our mathematical model is limited by the assumption of an empirical relationship between the rate of trabecular surface remodeling $\dot{M}$ and the total stimulus on the trabecular surface $S_{sf}$, which can be regarded as an index of local fluid pressure gradient. Despite these limitations, our mathematical model has the advantage of being able to investigate the effects of cellular mechanosensing and intercellular communication on the structural changes in cancellous bone. This trabecular remodeling simulation will definitely contribute to elucidating the mechanism of bone functional adaptation as a result of cellular activities. Future incorporation of the signaling cascade of bone cells into the mathematical model will make our simulation model a powerful tool for such clinical applications as the prediction of the effects of drugs targeting specific bone cells and the expected course of bone disease.

# 7 Mathematical Modeling of Spatiotemporal Dynamics at Microscopic Level

After mechanosensing by osteocytes, the remodeling activity of osteoclasts and osteoblasts is regulated by interactions between mechanical signals and intercellular biochemical signaling. These phenomena are not only regulated temporally
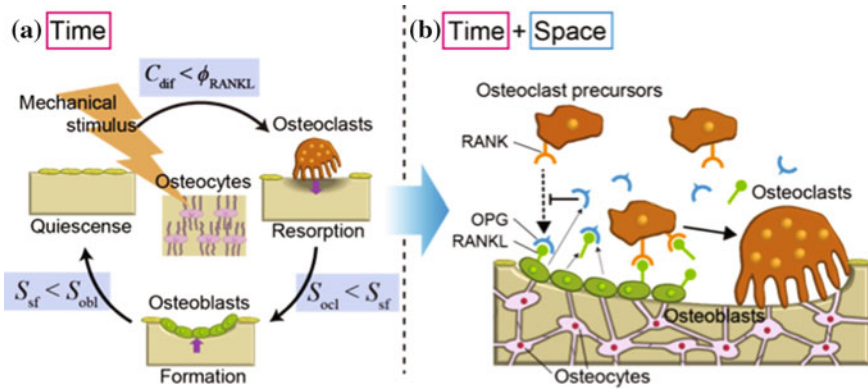
**Fig. 11** Modeling and simulation of the temporal and spatial development of bone remodeling. Bone remodeling is understood as a **a** temporal evolution as a result of osteoclast and osteoblast coupling. **b** However, it is important to understand bone remodeling in terms of the system dynamics, which include spatiotemporal development, such as intercellular interactions via signaling and the diffusion of signaling molecules

(Fig. 11a) but may also be regulated spatially (Fig. 11b), for example through intercellular communication that depends on the distance between and location of cells and the diffusion of signaling molecules. Thus, simultaneously considering the spatiotemporal evolution of mechanical and physical fields, such as the deformation of bone matrix, the fluid flow within bone canaliculi, and the diffusion of signaling molecules, while incorporating morphological changes by bone remodeling, in addition to the conventional systems-biology approach that primarily describes their time evolution, is important.

## 7.1 Remodeling of Trabeculae and Osteons

The trabeculae in cancellous bone and osteons in cortical bone are recognized as bone remodeling units [53]. Here, we propose a model to directly describe the activity of cell groups referred to as remodeling packets at the microscopic structural level. The resorption pit on the trabecular surface in cancellous bone and the cutting cone of the Haversian canals present in the osteons in cortical bone are considered as individual units. The coupling of osteoclasts and osteoblasts in these remodeling units was mathematically modeled, and their activities were merged into a mathematical model for bone remodeling by taking into account both signaling mechanisms and mechanosensing mechanisms.

## 7.2   An Example of Osteoclast Differentiation Signals

Here, we develop a mathematical model of signals related to bone resorption with
the receptor activator of nuclear factor $\kappa$B ligand (RANKL) as an example. As
shown in Fig. 11a, b, RANKL expressed by osteoblasts and osteocytes is a ligand
of RANK, which is expressed on the cell surface of osteoclast progenitors, and
promotes differentiation into osteoclasts. Meanwhile, osteoprotegerin (OPG), which
is secreted by osteoblasts and osteocytes, suppresses differentiation into osteoclasts
by forming an OPG-RANKL complex. An example of this system is that dependent
on spatial distance and time, such as the display of RANKL on the cell surface and/or
its diffusion into the surroundings. Furthermore, by including the diffusion of OPG
with its inhibitory function, the system dynamics are likely to be more complex.

## 7.3   Mathematical Modeling of Signaling Molecules in Bone Remodeling

We develop a model for bone remodeling in which mechanical stimuli to osteo-
cytes activate cellular remodeling activities. First, assuming that osteocytes within
the bone matrix can sense mechanical stimuli, the amount of mechanical stimuli
$S_{ocy}(\boldsymbol{x})$ sensed by osteocytes is estimated based on the stress $\sigma_{eq}(\boldsymbol{x})$ within the bone
matrix at location $\boldsymbol{x}$ (Adachi et al. 2009b, 2010). Next, we consider that the stimuli
$S_{ocy}(\boldsymbol{x})$ sensed by osteocytes is transmitted to the trabecular and Haversian canal
surfaces while decaying depending on the distance, then mechanical stimuli on their
surfaces are evaluated as surface stimuli $S_{sf}(\boldsymbol{x}, t)$. Assuming that the expression of
OPG and RANKL, signal molecules associated with differentiation into osteoclasts,
$\phi_{OPG}(\boldsymbol{x}, t)$ and $\phi_{RANKL}(\boldsymbol{x}, t)$, depends on $S_{sf}(\boldsymbol{x})$, we evaluate the concentrations
of OPG and RANKL using an evolution equation:

$$\dot{\phi}_i(\boldsymbol{x}, t) = \frac{\beta_i S_{sf}(\boldsymbol{x}, t)^{n_i}}{K_i^{n_i} + S_{sf}(\boldsymbol{x}, t)^{n_i}} - k_{on}\phi_i(\boldsymbol{x}, t)\phi_j(\boldsymbol{x}, t) - k_{deg}\phi_i(\boldsymbol{x}, t) + D_i\nabla^2\phi_i(\boldsymbol{x}, t),$$

$$(5)$$

in which the subscripts $(i, j) = $ (RANKL, OPG) or (OPG, RANKL). The first term on
the right hand side of Eq. (5) represents the production of each signal molecule, and
the amount of production is described by a function of the surface stimuli $S_{sf}(\boldsymbol{x})$.
Here, the constant $K_i$ represents the activation coefficient, whereas $\beta$ represents
the maximum level of expression. The second term represents the decrease due to
inactivation by the binding of RANKL and OPG (with a constant $k_{on}$), whereas the
third term represents the decrease due to the degradation of each molecule (with a
constant $k_{deg}$). The fourth term represents the diffusion of each molecule within the
bone marrow with a diffusion coefficient $D_i$.

When the concentration of RANKL, $\phi_{RANKL}$, becomes higher than the threshold
$C_{dif}$ shown in Fig. 11a, we consider this to indicate that new bone resorption will start

on the trabecular surface and Haversian canal surface. Moreover, bone resorption and formation are considered to be controlled by the mechanical stimulation thresholds, $S_{ocl}$ and $S_{obl}$, shown in Fig. 11a. Based on this assumption, we determine the rate (speed) of remodeling on the trabecular surface and Haversian canal surface, and express the morphological changes in bone by bone resorption and formation.

# 8 Computer Simulations of Trabecular and Osteonal Remodeling

## 8.1 Trabecular Remodeling Simulation

We construct a model of an initial single trabecula (Fig. 12a) with a simple shape. The entire volume region for analysis is a $400\,\mu\text{m} \times 1{,}000\,\mu\text{m} \times 1{,}000\,\mu\text{m}$ rectangular solid, which is discretized using $10\,\mu\text{m}$-voxel finite elements. The cylindrical trabecula with a radius of $80\,\mu\text{m}$ is tilted $30°$ on the $z$-axis and is positioned in the center. A rigid plate is then positioned on the upper and lower surfaces and a uniform compression stress of $\sigma_0 = -0.2\,\text{MPa}$ is applied in the direction of the $z$-axis to the surface of the upper rigid plate as a boundary condition. Displacement perpendicular to the lower rigid plate was constrained.

Figure 12b, c show the changes in trabecular morphology and the amount of surface stimuli $S_{sf}$ by remodeling. In their initial state, osteoclasts are randomly located on the trabecular surface. The results of the remodeling simulation confirmed that the morphology of the obliquely oriented trabecula changes to the direction along the compressive loading direction. This is because bone formation and resorption occur repeatedly in regions in which the surface stimulation $S_{sf}$ are large (red) and small (blue), respectively, as shown in Fig. 12b, c.

## 8.2 Osteonal Remodeling Simulation

Figure 12c shows a model of the cutting cone in the Haversian canal of an osteon. The entire volume of analysis is a rectangular solid ($600\,\mu\text{m} \times 600\,\mu\text{m} \times 2{,}000\,\mu\text{m}$) that is regularly discretized using $10\,\mu\text{m}$-voxel finite elements. A cylindrical Haversian canal having a radius of $80\,\mu\text{m}$ and a length of $300\,\mu\text{m}$ was positioned parallel to the $z$-axis under the top surface, and a hemispherical cutting cone was positioned. The displacement in the $z$-direction at the bottom surface was constrained, whereas the lateral surfaces were not. A uniform compression stress, $\sigma_0 = -0.2\,\text{MPa}$, was then applied to the top surface.

Figure 12d shows the changes in morphology of the Haversian canal within the osteon by remodeling. As the initial surface cells, osteoclasts were originally located on the cutting cone, whereas lining cells were located elsewhere. As shown in
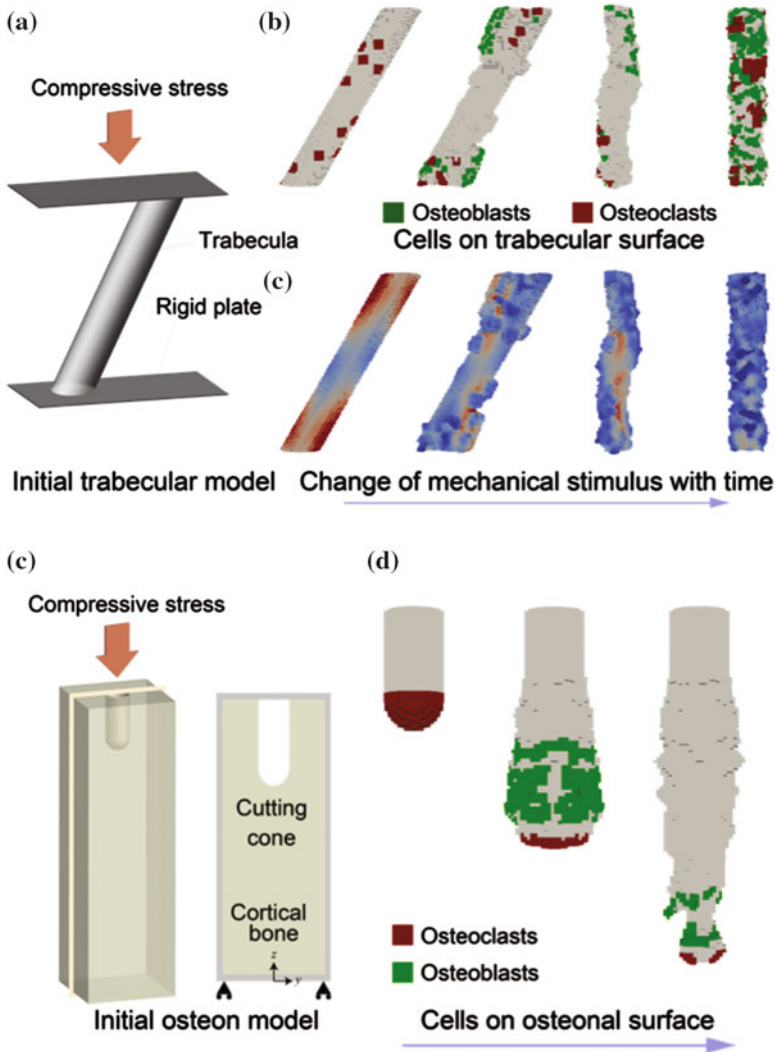
**Fig. 12** Morphological changes by remodeling of a single trabecula and a single osteon under uni-axial compressive loading. **a** Initial trabecular morphology and boundary conditions. **b** Distribution of surface cells associated with changes in trabecular morphology and **c** temporal changes in the surface mechanical stimuli. **d** Initial morphology of an osteon and a Haversian canal. **e** Extension of the Haversian canal and changes in surface cell distribution as a result of osteonal remodeling

Fig. 12d, bone was resorbed by osteoclasts at the tip of the cutting cone, after which osteoblasts formed bone. The osteon was observed to extend in the direction of principal stress.

# 9 Conclusion

In silico experiments of bone remodeling have made it possible to observe morphological changes in bone microstructure as a result of remodeling as well as the spatiotemporal dynamics of osteoclasts and osteoblasts, which were difficult to experimentally observe in vivo. We expect that mathematical modeling and computer simulations of bone remodeling will function as a framework for allowing the discovery of numerous new findings in bone metabolism. Moreover, mathematical modeling and computer simulations of bone remodeling will play an important role in clarifying the behavior of this complex system. We also anticipate that these approaches will be used to elucidate the mechanisms of bone diseases, in which bone morphology and mechanics are closely related, and to predict changes in bone morphology associated with bone metabolic changes caused by therapeutic agents.

# References

1. L.F. Bonewald, M.L. Johnson, Osteocytes, mechanosensing and wnt signaling. Bone **42**(4), 606–615 (2008)
2. T. Nakashima, M. Hayashi, T. Fukunaga, K. Kurata, M. Oh-Hora, J.Q. Feng, L.F. Bonewald, T. Kodama, A. Wutz, E.F. Wagner, J.M. Penninger, H. Takayanagi, Evidence for osteocyte regulation of bone homeostasis through rankl expression. Nat. Med. **17**(10), 1231–1234 (2011)
3. A. Mochizuki, M. Takami, Y. Miyamoto, T. Nakamaki, S. Tomoyasu, Y. Kadono, S. Tanaka, T. Inoue, R. Kamijo, Cell adhesion signaling regulates rank expression in osteoclast precursors. PLoS ONE **7**(11), e48795 (2012)
4. C.A. O'Brien, T. Nakashima, H. Takayanagi, Osteocyte control of osteoclastogenesis. Bone **54**(2), 258–263 (2012)
5. T. Adachi, Y. Kameo, M. Hojo, Trabecular bone remodelling simulation considering osteocytic response to fluid-induced shear stress. Philos. Trans. Royal Soc. a-Math. Phys. Eng. Sci. **368**(1920), 2669–2682 (2010)
6. Y. Kameo, T. Adachi, M. Hojo, Effects of loading frequency on the functional adaptation of trabeculae predicted by bone remodeling simulation. J. Mech. Behav. Biomed. Mater. **4**(6), 900–908 (2011)
7. F.A. Schulte, A. Zwahlen, F.M. Lambers, G. Kuhn, D. Ruffoni, D. Betts, D.J. Webster, R. Muller, Strain-adaptive in silico modeling of bone adaptation a computer simulation validated by in vivo micro-computed tomography data. Bone **52**(1), 485–492 (2013)
8. T. Adachi, Y. Aonuma, K. Taira, M. Hojo, H. Kamioka, Asymmetric intercellular communication between bone cells: propagation of the calcium signaling. Biochem. Biophys. Res. Commun. **389**(3), 495–500 (2009)
9. L.F. Bonewald, The amazing osteocyte. J. Bone Miner. Res. **26**(2), 229–238 (2011)
10. P. Pivonka, J. Zimak, D.W. Smith, B.S. Gardiner, C.R. Dunstan, N.A. Sims, T.J. Martin, G.R. Mundy, Model structure and control of bone remodeling: a theoretical study. Bone **43**(2), 249–263 (2008)
11. P. Pivonka, J. Zimak, D.W. Smith, B.S. Gardiner, C.R. Dunstan, N.A. Sims, T.J. Martin, G.R. Mundy, Theoretical investigation of the role of the rank-rankl-opg system in bone remodeling. J. Theor. Biol. **262**(2), 306–316 (2010)
12. S. Weinbaum, S.C. Cowin, Y. Zeng, A model for the excitation of osteocytes by mechanical loading-induced bone fluid shear stresses. J. Biomech. **27**(3), 339–360 (1994)

13. J. KleinNulend, C.M. Semeins, N.E. Ajubi, P.J. Nijweide, E.H. Burger, Pulsating fluid flow increases nitric oxide (no) synthesis by osteocytes but not periosteal fibroblasts - correlation with prostaglandin upregulation. Biochem. Biophys. Res. Commun. **217**(2), 640–648 (1995)

14. T. Adachi, Y. Aonuma, M. Tanaka, M. Hojo, T. Takano-Yamamoto, H. Kamioka, Calcium response in single osteocytes to locally applied mechanical stimulus: differences in cell process and cell body. J. Biomech. **42**(12), 1989–1995 (2009)

15. R.Y. Kwon, D.R. Meays, A.S. Meilan, J. Jones, R. Miramontes, N. Kardos, J.C. Yeh, J.A. Frangos, Skeletal adaptation to intramedullary pressure-induced interstitial fluid flow is enhanced in mice subjected to targeted osteocyte ablation. Plos One **7**(3) (2012)

16. J. Klein-Nulend, A.D. Bakker, R.G. Bacabac, A. Vatsa, S. Weinbaum, Mechanosensation and transduction in osteocytes. Bone **54**(2), 182–90 (2013)

17. Y.F. Han, S.C. Cowin, M.B. Schaffler, S. Weinbaum, Mechanotransduction and strain amplification in osteocyte cell processes. Proc. Natl. Acad. Sci. U.S.A. **101**(47), 16689–16694 (2004)

18. X.L. Lu, B. Huo, M. Park, X.E. Guo, Calcium response in osteocytic networks under steady and oscillatory fluid flow. Bone **51**(3), 466–473 (2012)

19. R.Y. Kwon, S. Temiyasathit, P. Tummala, C.C. Quah, C.R. Jacobs, Primary cilium-dependent mechanosensing is mediated by adenylyl cyclase 6 and cyclic amp in bone cells. FASEB J. **24**(8), 2859–2868 (2010)

20. S. Temiyasathit, W.J. Tang, P. Leucht, C.T. Anderson, S.D. Monica, A.B. Castillo, J.A. Helms, T. Stearns, C.R. Jacobs, Mechanosensing by the primary cilium: deletion of kif3a reduces bone formation due to loading. Plos One **7**(3), e33368 (2012)

21. H.M. Frost, Bone mass and the mechanostat - a proposal. Anat. Rec. **219**(1), 1–9 (1987)

22. H.M. Frost, Defining osteopenias and osteoporoses: Another view (with insights from a new paradigm). Bone **20**(5), 385–391 (1997)

23. R. Huiskes, R. Ruimerman, G.H. van Lenthe, J.D. Janssen, Effects of mechanical forces on maintenance and adaptation of form in trabecular bone. Nature **405**(6787), 704–706 (2000)

24. H.M. Frost, Bone's mechanostat: a 2003 update. Anat. Rec. Part A **275A**(2), 1081–1101 (2003)

25. T. Adachi, Y. Tomita, H. Sakaue, M. Tanaka, Simulation of trabecular surface remodeling based on local stress nonuniformity. Jsme Int. J. Ser. C-Mech. Syst. Mach. Elem. Manuf. **40**(4), 782–792 (1997)

26. K. Tsubota, Y. Suzuki, T. Yamada, M. Hojo, A. Makinouchi, T. Adachi, Computer simulation of trablecular remodeling in human proximal femur using large-scale voxel fe models: Approach to understanding wolff's law. J. Biomech. **42**(8), 1088–1094 (2009)

27. H. Kamioka, Y. Kameo, Y. Imai, A.D. Bakker, R.G. Bacabac, N. Yamada, A. Takaoka, T. Yamashiro, T. Adachi, J. Klein-Nulend, Microscale fluid flow analysis in a human osteocyte canaliculus using a realistic high-resolution image-based three-dimensional model. Integr. Biol. **4**(10), 1198–1206 (2012)

28. D. Sharma, C. Ciani, P.A.R. Marin, J.D. Levy, S.B. Doty, S.P. Fritton, Alterations in the osteocyte lacunar-canalicular microenvironment due to estrogen deficiency. Bone **51**(3), 488–497 (2012)

29. Y. Kameo, T. Adachi, Modeling trabecular bone adaptation to local bending load regulated by mechanosensing osteocytes. Acta Mech. **225**(10), 2833–2840 (2014)

30. Y. Kameo, T. Adachi, N. Sato, M. Hojo, Estimation of bone permeability considering the morphology of lacuno-canalicular porosity. J. Mech. Behav. Biomed. Mater. **3**(3), 240–248 (2010)

31. S. Osher, J.A. Sethian, Fronts propagating with curvature-dependent speed - algorithms based on hamilton-jacobi formulations. J. Comput. Phys. **79**(1), 12–49 (1988)

32. Y. Kameo, T. Adachi, Interstitial fluid flow in canaliculi as a mechanical stimulus for cancellous bone remodeling: in silico validation. Biomech. Model. Mechanobiol. **13**(4), 851–860 (2014)

33. T. Beno, Y.J. Yoon, S.C. Cowin, S.P. Fritton, Estimation of bone permeability using accurate microstructural measurements. J. Biomech. **39**(13), 2378–2387 (2006)

34. T.H. Smit, J.M. Huyghe, S.C. Cowin, Estimation of the poroelastic parameters of cortical bone. J. Biomech. **35**(6), 829–835 (2002)

35. K. Tsubota, T. Adachi, Spatial and temporal regulation of cancellous bone structure: characterization of a rate equation of trabecular surface remodeling. Med. Eng. Phys. **27**(4), 305–311 (2005)
36. L.D. You, S. Weinbaum, S.C. Cowin, M.B. Schaffler, Ultrastructure of the osteocyte process and its pericellular matrix. Anat. Rec. Part a-Discov. Mol. Cell. Evol. Biol. **278A**(2), 505–513 (2004)
37. Z.F. Jaworski, E. Lok, Rate of osteoclastic bone erosion in haversian remodeling sites of adult dogs rib. Calcif. Tissue Res. **10**(2), 103–112 (1972)
38. B. Huo, X.L. Lu, C.T. Hung, K.D. Costa, Q.B. Xu, G.M. Whitesides, X.E. Guo, Fluid flow induced calcium response in bone cell network. Cell. Mol. Bioeng. **1**(1), 58–66 (2008)
39. S. Majumdar, M. Kothari, P. Augat, D.C. Newitt, T.M. Link, J.C. Lin, T. Lang, Y. Lu, H.K. Genant, High-resolution magnetic resonance imaging: Three-dimensional trabecular bone architecture and biomechanical properties. Bone **22**(5), 445–454 (1998)
40. R. Muller, T. Hildebrand, P. Ruegsegger, Noninvasive bone-biopsy - a new method to analyze and display the 3-dimensional structure of trabecular bone. Phys. Med. Biol. **39**(1), 145–164 (1994)
41. T. Adachi, K. Tsubota, Y. Tomita, S.J. Hollister, Trabecular surface remodeling simulation for cancellous bone using microstructural voxel finite element models. J. Biomech. Eng.-Trans. ASME **123**(5), 403–409 (2001)
42. R. Ruimerman, P. Hilbers, B. van Rietbergen, R. Huiskes, A theoretical framework for strain-related trabecular bone maintenance and adaptation. J. Biomech. **38**(4), 931–941 (2005)
43. K. Tsubota, T. Adachi, Y. Tomita, Functional adaptation of cancellous bone in human proximal femur predicted by trabecular surface remodeling simulation toward uniform stress state. J. Biomech. **35**(12), 1541–1551 (2002)
44. I.G. Jang, I.Y. Kim, Computational study of wolff's law with trabecular architecture in the human proximal femur using topology optimization. J. Biomech. **41**(11), 2353–2361 (2008)
45. S.C. Cowin, Bone poroelasticity. J. Biomech. **32**(3), 217–238 (1999)
46. Y. Kameo, T. Adachi, M. Hojo, Transient response of fluid pressure in a poroelastic material under uniaxial cyclic loading. J. Mech. Phys. Solids **56**(5), 1794–1805 (2008)
47. Y. Kameo, T. Adachi, M. Hojo, Fluid pressure response in poroelastic materials subjected to cyclic loading. J. Mech. Phys. Solids **57**(11), 1815–1827 (2009)
48. F.A. Gerhard, D.J. Webster, G.H. van Lenthe, R. Muller, In silico biology of bone modelling and remodelling: adaptation. Philos. Trans. R. Soc. a-Math. Phys. Eng. Sci. **367**(1895), 2011–2030 (2009)
49. S.A. Goldstein, L.S. Matthews, J.L. Kuhn, S.J. Hollister, Trabecular bone remodeling - an experimental-model. J. Biomech. **24**, 135–150 (1991)
50. R.E. Guldberg, N.J. Caldwell, X.E. Guo, R.W. Goulet, S.J. Hollister, S.A. Goldstein, Mechanical stimulation of tissue repair in the hydraulic bone chamber. J. Bone Miner. Res. **12**(8), 1295–1302 (1997)
51. R.E. Guldberg, M. Richards, N.J. Caldwell, C.L. Kuelske, S.A. Goldstein, Trabecular bone adaptation to variations in porous-coated implant topology. J. Biomech. **30**(2), 147–153 (1997)
52. L.M. McNamara, P.J. Prendergast, Bone remodelling algorithms incorporating both strain and microdamage stimuli. J. Biomech. **40**(6), 1381–1391 (2007)
53. A.M. Parfitt, Osteonal and hemi-osteonal remodeling - the spatial and temporal framework for signal traffic in adult human bone. J. Cell. Biochem. **55**(3), 273–286 (1994)

# Biology of Bone and the Interaction of Bone with Other Organ Systems

**David M. Findlay**

**Abstract** Bone has essential functions to support and protect the soft tissues of the body and to enable locomotion. The formation and maintenance of bone is orchestrated by the three major cell types resident within it- osteoblasts, osteocytes and osteoclasts. These cells confer on bone its ability to respond to increased or decreased biomechanical requirements, bone matrix repair and to regulate a variety of extraskeletal functions. For locomotion, bone is dependent on the actions of muscles, and bone also depends on the strains produced by muscles for its proper functioning. Unloading of bone results in rapid loss of bone mass, as seen in space flight or bed rest. Recent findings suggest that, in addition to biomechanical interaction, bone and muscle may also communicate biochemically. Bone also interacts closely with the vasculature and the nervous system, and is highly perfused and innervated. The latter suggests roles for the central nervous system in bone function, and this has increasingly been found to be the case. Vascular pathology also has implications for bone health, which is demonstrated in avascular bone necrosis and fracture non-union. Articulating joints in the skeleton depend on cartilage providing a frictionless surface and spreading load across the underlying bone. Thus osteoarthritis is a disease of the whole joint, with important effects in both bone and cartilage tissue compartments. This chapter will introduce the biology of bone tissue and discuss its interaction with muscle, cartilage, the nervous system and the vasculature, since all of these organ systems underpin an understanding of the biomechanics of bone.

**Keywords** Biology of bone · Interaction of bone with muscle · Vasculature · Cartilage and the central nervous system

D.M. Findlay (✉)
Discipline of Orthopaedics and Trauma, University of Adelaide,
Adelaide, SA 5000, Australia
e-mail: david.findlay@adelaide.edu.au

# 1   Introduction

Bone is a fascinating organ system, with amazing capacity to bear weight, support locomotion, adapt to increased strength demands, and self-repair. Recently, bone has also been shown to both communicate with other organs and to participate in the control of diverse functions such as energy metabolism and haematopoiesis. An understanding of the biomechanics of bone requires at least a basic appreciation of the biology of bone- its composition, the cells that build and maintain the bone matrix, the factors that regulate those cells- as well as the ways that bone interacts with other organ systems. The final decision making in bone is a synthesis of biomechanical signals, interacting with biochemical and neural signals, in order to maintain bone mass and bone matrix quality sufficient to tolerate the loads imposed on it.

# 2   Biology of Bone

## 2.1   Bone Tissue

Bone comprises mineralised matrix and cells, with extensive blood vessels and accompanying nerves (see Fig. 1). Bone exists in two morphologies, compact or cortical bone, which is the dense bone typically found in the midshaft of long bones or forming a shell on the external surface of bones, and cancellous or trabecular or spongy bone, which consists of interconnecting rods and plates. Cancellous bone provides strength with reduced weight penalty and, because it has greater capacity to flex under load than cortical bone, is found at the ends of long bones.



**Fig. 1** Cartoon of bone taken from http://www.alearned.com/weight/ Figure shows cortical bone, organised into osteons around blood vessels and accompanying nerves
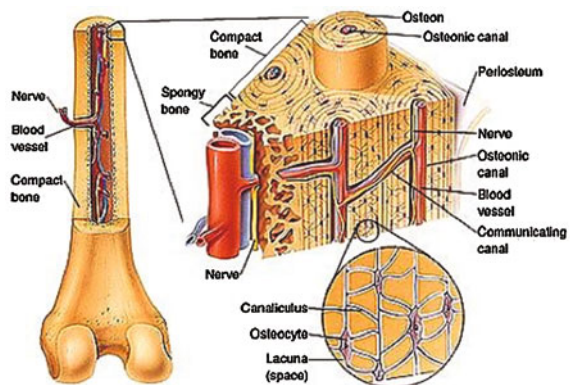
## *2.2 Bone Matrix*

Bone matrix consists of mineral, calcium phosphate in the form of hydroxyapatite $[Ca_5(PO_4)_3(OH)]$, which is laid down on an organic scaffold that is approximately 85% type I collagen. Typically, bone is 75% mineral, 22% organic material and the reminder water, although bone can be mineralised to different extents, with newly formed bones less mineralised than older bone. A number of non-collagenous proteins also have important roles in bone [15, 103], such as regulating mineralisation, in the case of bone sialoprotein (BSP).

## *2.3 Bone Cells*

Bone is built and shaped and remodelled by the cells that reside within it. Rather than being quiescent blocks of mineral, bone is dynamic and responsive to a wide range of stimuli, these responses all being mediated by cells of the osteoblast lineage [8, 96], including osteocytes [7, 13] and lining cells, and osteoclasts [118]. Each of these cell types is described in some detail below and in the cited references.

**Osteoclasts**: Osteoclasts are large multinucleated cells, derived from the monocyte/macrophage cell lineage [118] and are specially adapted to remove both the mineral and organic phases of bone. They do so in response to a number of stimuli, but primarily to shape the bone during growth, to repair bone that is either non-vital or has sustained matrix damage, and to release calcium from the bone store to meet systemic demands and to enable blood calcium to remain within tight healthy limits. Osteoclast formation requires the proliferation, differentiation and fusion of precursor mononuclear cells. An important cytokine molecule that regulates both the formation of osteoclasts from precursor cells and the resorptive activity of mature osteoclasts is Receptor Activator of $NF_\kappa B$ Ligand (RANKL), a member of the TNF family of molecules [83]. RANKL is produced by a number of cells types but in bone primarily by cells of the osteoblast lineage in response to resorptive stimuli, such as bone matrix damage or parathyroid hormone (PTH), or cytokines such as interleukin 11 (IL-11). RANKL binds to its receptor on osteoclast precursors and collaborates with macrophage colony-stimulating factor (M-CSF), causing these cells to differentiate into functional osteoclasts. This process can be inhibited by osteoprotegerin (OPG) [117], a soluble RANKL-binding member of the TNF receptor family, which competes for RANKL binding. RANKL signalling is therefore a function of the relative local concentrations of RANKL and OPG, which are therefore key determinants of whether bone resorption takes place at a given site in the skeleton. Expression of these molecules is in turn controlled by anabolic or catabolic factors, to inhibit or promote resorption, respectively [118]. The relative excess of RANKL has been shown to be a factor in both systemic and focal bone loss pathologies [51].

Osteoclasts degrade the bone matrix by secreting protons, which dissolve the hydroxyapatite crystal mineral, and enzymes that act at low pH to cleave the proteins

that comprise the organic matrix of bone. Resorption is controlled physiologically by the hormone calcitonin [35] and OPG, which inhibit osteoclast resorption by different mechanisms. In trabecular bone, osteoclasts resorb the surface (endosteum) of bone. In cortical bone, they tunnel through the bone, in intimate association with a blood vessel, creating a cutting cone. In both cases, resorption of bone is followed by infilling of the resorbed space with new bone by osteoblasts. This coupled process works less well in older individuals, giving rise to a net loss of bone (osteoporosis) because of incomplete infill of resorption spaces. The most common treatments for osteoporosis are agents that inhibit resorption, so they only prevent further loss of bone. These agents include bisphosphonates [36], which prevent osteoclast action, and anti-RANKL therapy, which prevents osteoclast formation [88].

**Osteoblasts**: Osteoblasts are the cells responsible for bone formation in development, as well as in bone remodelling and repair. They arise from the differentiation of primitive stem cells to multipotential progenitor cells that, under particular environmental conditions, can develop into chondrocytes, adipocytes, muscle cells or osteoblasts [96]. Osteoblasts produce the collagen-rich matrix called osteoid, which mineralises to form bone. These differentiation and functional processes are regulated by a large number of factors, many of which have been identified, and include members of the Wnt family of proteins [11], TGF$\beta$ and members of the bone morphogenetic proteins (BMPs) [121], and PTH. BMPs were identified due to the ability of bone extracts to produce ectopic bone in muscle [126] and were subsequently shown to be useful as promoters of fracture repair [21]. A genetic mutation that gives rise to constitutively activated BMP receptors was shown to the underlying cause of Fibrodysplasia Ossificans Progressiva (FOP), a heritable disorder of severe heterotopic ossification [29]. This discovery may lead to small molecule inhibitor therapeutic approaches to this life-threatening condition [129]. After their bone forming activity, osteoblasts may apoptose (die by programmed cell death), become bone lining cells, or differentiate into osteocytes.

**Osteocytes**: Osteocytes reside within the bone matrix, since they derive from bone-forming osteoblasts. Osteocytes are responsible for laying down mineral within newly formed osteoid, to make bone. Osteocytes are the most abundant cell type in mammalian bones, making up 95% of all bone cells and human cortical bone contains >20,000 osteocytes/mm$^3$. Osteocytes have a unique morphology, with a small cell body linked to surrounding osteocytes, and osteoblasts on the bone surface, by numerous cell processes (40–60/cell) extending through microscopic tunnels, canaliculi, in the bone matrix. Osteocytes are long lived cells, with an average life span estimated at 25 years. Once thought to be quiescent and functionally unimportant, osteocytes appear to have many roles, both within bone and systemically [13].

Firstly, osteocytes are well placed to sense bone strains, and play a key role in mechanosensing and the response of bone to loading. There are various theories as to the exact mechanism, by which osteocytes transduce loads applied to bone to chemical signals [14], and there is a large literature on the mediators that enable an anabolic response to repeated loading of bone [14]. An important such mediator is the molecule sclerostin, whose expression by osteocytes decreases as a function of applied strain in bone [104]. Sclerostin is an inhibitor of the Wnt pathway [11] and

appears to provide tonic suppression of bone formation, such that genetic loss [60] or neutralisation of sclerostin results in an impressive increase in bone formation. Anti-sclerostin antibody administration to animals and humans has been shown to increase bone formation and decrease bone resorption, and such an approach is in advanced trials as an anabolic treatment in osteoporosis [85]. Secondly, osteocytes detect and respond to microscopic damage within the bone matrix, caused by repeated flexing of the relatively inflexible bone material. This damage, and other causes of osteocyte cell death, induces the release of signals from dying cells to stimulate nearby viable osteocytes to increase their expression of RANKL and other molecules to recruit osteoclasts to the site of damaged bone [61]. Agents that prevent osteocyte cell death under these circumstances can prevent osteoclast resorption in response to matrix damage and other toxic stimuli [62]. Upon resorption of the damaged bone, new bone is formed to maintain the integrity of the bone tissue. In addition, it appears that osteocytes constantly renew the mineral surrounding them, in order to keep the bone matrix healthy. Inhibition of this process by knocking out one of the molecules important in this process, matrix metalloproteinase-13 (MMP-13), leads to brittle and fragile bone in mice [3]. A recent publication shows evidence that osteocytes can directly repair diffuse damage in cortical bone, without osteocyte death or the activation of remodelling [113]. Although the mechanisms for this have not been elucidated, it is possible that these relate to this ability of osteocytes to renew the bone matrix.

Thirdly, osteocyte ability to remove adjacent mineral seems to be important in maintaining calcium homeostasis in some circumstances, such as the high calcium demand of lactation [100]. The process, known as osteocytic osteolysis, is dependent on functional osteocyte PTH receptors, at least in lactation. Fourthly, osteocytes appear to participate in phosphate homeostasis by producing FGF23, which acts on the kidney to prevent phosphate reabsorption and also to inhibit the production of 1,25vitaminD, which in turn reduces uptake of calcium and phosphate from the intestine. Thus, excess FGF23 results in phosphate wasting and too little FGF23 can lead to high phosphate levels and inappropriate mineral formation in soft tissues [42]. There is evidence that osteocytes may have additional roles, such as influencing haematopoiesis and may act in distant organs to regulate fat storage and energy usage. These latter actions remain to be confirmed.

## 3 Interaction of Bone with Muscle

### 3.1 Integration of Muscle and Bone

Muscles and bones are functionally linked to enable movement of the skeleton and locomotion. Muscle contraction exerts force on bone via tendon attachments at the insertion sites on bone (entheses). Ligaments constrain the movement of bones relative to each other, for example at the wrist and knee. Because of the functional

interdependence of muscle and bone, it is perhaps not surprising that there are strong relationships between muscle size and strength and bone size and strength. Lebrasseur et al. related measures of muscle mass to trabecular and cortical bone architecture, at various skeletal sites and in men and women of a wide age range [72]. In women, associations were found between muscle mass and cortical thickness (CtTh) at the femoral neck, lumbar spine, radius, and tibia as well as with trabecular volumetric bone mineral density (vBMD) at the femoral neck and spine. In men, muscle mass was associated with CtTh at all skeletal sites and with trabecular architecture at the femoral neck and the radius. The authors concluded that 'These data add to the growing body of evidence supporting the highly-integrated nature of skeletal muscle and bone'.

Mutant mouse strains with reduced muscle or lacking muscle altogether have been examined to determine the effect of muscle on the development of the skeleton [91]. While it is clear from these experiments that muscle plays an important role in skeletal size and shape, considerable variability was seen between effects on different bones. Thus, it appears that in embryonic formation of the skeleton, complex interactions exist between muscle-generated biomechanical forces, and perhaps biochemical signals from muscles (see below). Muscles also seem to drive bone development in postnatal development. Thus, in both boys and girls, the peak in muscle mass, or lean body mass (LBM) accrual preceded the peak in bone mineral content (BMC, i.e., a measure of bone mass) accretion [101]. It is also possible that muscle and bone respond to the same genetic cues. There are a number of clinical implications of a role for muscle in bone development and function, including the effects on the skeleton of muscular dystrophies, and possible links between sarcopenia and osteoporosis.

## 3.2   Muscle Imparts Strain in Bone

As will be covered in more detail by other authors, muscle contraction produces strains in bone. This was demonstrated in rather heroic experiments, in which strain gauges were attached to the human tibial shaft so that bone deformation could be recorded during activities such as walking [70]. Peak strains of 300–500 microstrains were recorded, depending on walking speed and added weight. More recently, Martelli et al. [81, 82] have calculated strains experienced in different regions of the femur during a range of physical activities. They showed, for example, that bone regions subjected to tensile strains are associated with atypical femoral fractures, and that walking is the daily activity that induces the highest tensile strain in the lateral femoral shaft, and they used their data to describe exercises predicted to specifically strengthen the femoral neck, a frequent site of osteoporotic fractures.

Strain gauges attached to a sheep tibia, while the animal was standing, showed, over a 12 h period, tens of thousands of small strain events (<10 microstrain), several hundred strains in the order of 200 microstrain and very few large strain events (>2000 microstrain). When the strains of various magnitude were plotted against the number of occurrences, remarkably similar strain recordings were observed from

the tibia of a diverse range of animals over a 12-h period [93]. These data raised the question of whether bone could detect and respond to these strains, provoking a large number of experiments to test this hypothesis. Rubin et al. [107] found that both the quantity and quality of trabecular bone in sheep femurs were enhanced by mechanical stimulation delivered by an underfoot vibrating platform. This group went on to show concurrent increases in muscle and bone mass when women stood for a period each day on a vibrating platform [58]. However, whether muscle-induced strain is the mechanism underlying these changes is not clear, since these authors also describe altered blood perfusion induced by vibration.

Other authors have shown long lasting changes in circulating muscle metabolic products after a short bout of high force eccentric exercise [122]. Interestingly, circulating levels of anabolic hormones and bone turnover markers were also increased by these exercises. Taken together, these experiments suggested multiple possible drivers of bone changes in response to muscle activity, including applied bone strain, secreted muscle products and elevated anabolic hormones.

### 3.3 Bone Loading and Bone Homeostasis

A large number of experiments have supported the concept that bone not only responds to loading but that the integrity of bone is dependent on loading of the appropriate magnitude and frequency. Using the turkey ulna model to examine the relationship between strain magnitude and the frequency of strain application, Ozcivici et al. [93] proposed that bone mass can be maintained by a small number of large applied strains (for example, 2000 microstrain) or by more frequent application of, for example 1000 microstrain, or hundreds of thousands of cycles of strains of the order of 10 microstrain. These and other data indicate that falling below this total strain delivery stimulates bone loss, while exceeding this interrelationship is anabolic and can stimulate bone gain [93]. These findings are consistent with the paradigm proposed by [38], his so-called 'mechanostat' theory [39], in which the skeleton adapts to changes in physical activity and that these adaptations are due to loading forces produced by skeletal muscles. In this paradigm, regular loading of the skeleton producing no net gains or losses in strain delivery, maintains bone mass. Net unloading of the skeleton, produced for example by disuse, leads to remodelling, with a net loss of bone mass and strength to the new requirements of the system. In contrast, mild overloading of the bone and increased total strain delivery is anabolic and produces increased bone mass and strength. Overload of the skeleton produces first microdamage in the bone matrix, and then fracture of the bone at strains of around 25000 microstrain in young adult bone.

Unloading of the skeleton in space flight has proven to rapidly reduce bone mass and predicted strength. Quantitative CT (QCT) measurement of proximal femur of astronauts after space flight missions lasting 46 months showed total femoral bone loss of around 10%, made up of cortical bone losses of around 8% and trabecular bone losses exceeding 16% [69]. Conversion of similar QCT data into bone strength,

using finite element analysis, predicted significant reduction in proximal femoral strength due to long-duration spaceflight [63]. In fact, some astronauts had predicted bone strength down into the range of elderly osteoporotic fracture patients. In these human subjects, it is difficult to ascertain the contributing factors to this bone loss, since these could include absence of muscle forces to overcome gravity, fluid redistribution in the body, lack of heel strike, reduced intake of protein and other nutrients and difficulty performing aerobic exercises. However, in the hindlimb suspension model of unloading in mice, electrically simulated resistance training in the unloaded limbs was sufficient to both maintain muscle strength and abolish the bone loss that characterise this model [120]. Simulated resistance training in the unloaded limbs also maintained bone formation at the tibia diaphysis [77]. The mouse data therefore suggest that loading of bone by muscle contraction is important in maintaining bone mass, as predicted by the mechanostat theory. In humans, spasticity of muscles results in low bone mass, and bone is rapidly and profoundly lost in the lower limbs after spinal cord injury. Similar to the mouse experiments, electrically stimulated contraction of the upper leg muscles, in this case to enable cycling, could partially reverse femoral bone loss in people with chronic spinal cord injury [40]. Interestingly, there was no change in the tibial bones, suggesting that in the absence of contraction of the lower limb muscles, simple axial loading of these bones was insufficient to achieve an anabolic stimulus.

### 3.4 Mechanotransduction in Bone

There has been great interest in determining how bone loading is transduced into signals that maintain or build bone mass. A theory advanced by Cowin and coworkers is that applied bone strains cause flexion of the bone matrix, which in turn induces fluid flow in the porosity of bone (the osteocyte canaliculi) and that this fluid flow amplifies the loading signal at the bone cellular level [23]. The theory further proposes that fluid transiting the canaliculi deforms the osteocyte cell walls because of molecular tethers between the osteocyte cell extensions and the canalicular walls [128], as well as other pericellular molecules such as perlican [125] forming a semi-permeable barrier within the extracellular space.

A number of cell signalling molecules are induced by bone loading or by cell models of osteocyte loading, including Wnt family members [66]. As mentioned above, one molecule that has risen to prominence in this context is the Wnt antagonist, sclerostin, whose expression in bone is reduced as a function of bone strain [104]. Conversely, unloading of bone increases sclerostin expression [74]. In the hindlimb suspension experiments mentioned above, sclerostin expression increased in the tibial cortical bone of the unloaded limbs, and this effect was prevented by simulated resistance training [77]. Sclerostin acts to suppress bone formation in response to anabolic stimuli, such as loading, by antagonising the canonical Wnt signalling pathway [11]. Wnts signal by binding to their cognate frizzled receptors and co-receptors LRP5 and LRP6, and sclerostin blocks Wnt binding to LRPs (see Fig. 2).
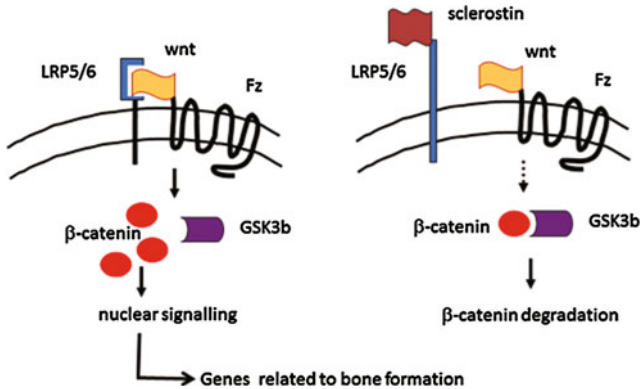
**Fig. 2** Schematic of canonical Wnt signalling. *Left panel* Wnt engages with Frizzled receptor (Fz) and LRP coreceptor to release catenin for transport to the nucleus and activation of transcription of genes related to bone formation. *Right panel* Wnt binding to LRP coreceptor is blocked by sclerostin, preventing Wnt signalling, so that catenin is targeted for degradation

Thus, LRP5 is essential to mechanotransduction in bone and deletion of the Lrp5 gene in osteocytes dramatically reduces the anabolic response of bone to mechanical loading [133]. Wnt signalling releases intracellular catenin to translocate to the nucleus, where it acts as a transcription factor in bone formation. Deletion of a single catenin allele specifically in osteocytes abolishes the bone anabolic response to loading [56]. Thus, disruption of the Wnt signalling pathway at several levels consistently interferes with mechanotransduction in bone. Many other molecules are also important in this process, including estrogen. Estrogen deficiency has been reported to increase canalicular volume, which has been suggested to alter solute transport and interstitial fluid velocities around osteocytes during mechanical loading. This in turn may impair the osteocyte perception of mechanical stimuli [114]. Consistent with these findings, deficiency of the estrogen receptor abolished the load-induced anabolic response of bone [109].

### 3.5 Myokines and Bone

As reviewed by Hamrick, muscle secretes a variety of cytokines and growth factors [48], collectively referred to as myokines, with potential roles in health and disease. Myokines include Myostatin, IGF1, FGF2, and IL5, 6 and 15. Myokine secretion by muscle is stimulated by muscle contraction and these factors may influence multiple organ systems, including bone. Thus, in addition to biomechanical influences of muscle on bone, muscle may act as an endocrine organ for bone anabolism [17]. This concept is supported by experiments such as those showing that muscle cell (myoblast and myotube) secreted factors can prevent glucocorticoid-induced

osteocyte apoptosis in vitro [55]. Conversely, it has also been shown that bone cells may secrete factors that affect muscle; MLO-Y4 osteocyte-like cell conditioned medium significantly enhanced myogenic differentiation of C2C12 myoblasts in vitro [89]. It has been proposed that, in addition to loss of muscle contraction causing bone loss due to loss of biomechanical stimulation of bone, there may also be a biochemical component. Myostatin is a member of the TGF family and a negative regulator of skeletal muscle growth. Interestingly, and as reviewed by [48], myostatin deficiency increases bone density, the osteogenic differentiation of bone-marrow derived stem cells, and bone repair. The intimate physical association of muscle and bone, together with a shared vasculature in many cases [89], further lends credence to the possibility of functionally important biochemical crosstalk between muscle and bone.

### 3.6　Muscle and Fracture Repair

There is an extensive literature on the role for muscle in fracture repair [45, 75, 123]. It is well known in clinical orthopaedics that bone with little muscle coverage, in particular the tibia, has less good outcomes for fracture than bone with good muscle coverage. Muscles appear to have intrinsic capacity to promote bone repair. Experiments in mouse models comparing the healing of open tibial fractures covered with either muscle or fasciocutaneous tissue, have shown superior healing and biomechanical characteristics obtained with good muscle coverage [49]. In elegant experiments using cell lineage labelling, Liu et al. showed that myogenic progenitors can contribute to open, but not closed, fracture repair [75].

## 4　Interaction of Bone with the Vasculature

Bone is a highly vascular structure (see Fig. 3) and the vascular supply of bone has been well reviewed by Rhinelander [102] and more recently by Brandi and Collin-Osdoby [16]. The vasculature is intimately and pivotally involved in the growth, maintenance and repair of bone. Bones have multiple arterial inlets and venous outlets, comprising, in the case of long bones, four arterial inputs, the nutrient artery, periosteal arteries, metaphyseal arteries and epiphyseal arteries. Nutrient, metaphyseal, and epiphyseal vessels enter bone through foramina in the cortex and then ramify and anastomose to supply marrow, cancellous bone and cortex in a centrifugal direction. On the outside surface of bone, the vasculature of the periosteum consists of relatively small arterioles that pierce the cortex from outside, supplying blood to the bone in a centripetal direction. The periosteal arteries probably play only a minor role in the nutrition of the healthy mature cortex, and then, primarily, the outer cortex and in regions where there are strong fascial attachments. The blood supply to bones serves both the marrow and the calcified bone tissue and, as

**Fig. 3** Blood vessels of the proximal humerus, showing feeding vessel branching to fine vessels ascending to the epiphysis and subchondral bone and descending to the metaphysis



reviewed by Compston [20], these two tissue types are functionally interdependent with respect to blood supply, haematopoiesis, bone modelling and bone remodelling.

## 4.1 Bone Tissue Vasculature

Bone tissue is highly vascularised, with arterial and venous vessels at the centre of each osteon in compact bone. In cancellous bone, scanning electron microscopy reveals numerous vessels lying on and penetrating through trabeculae [90]. It has been estimated that for cell survival, osteocytes must be within 200 $\mu$m of a blood vessel. Therefore, as elegantly shown by Schneider et al. [110], blood capillaries penetrate compact bone at high density. Blood vessels appear to be in functional continuity with osteocyte canaliculi [19], at least for small molecules, because dye injected into the circulation rapidly appears in the osteocyte porosity [37]. Transport of nutrients into the osteocyte porosity clearly depends on more than pulsatile blood flow, however, since it was shown in a turkey model that disuse increased osteocyte hypoxia, which was overcome by a brief loading regimen.

## 4.2 Relationship Between Blood Vessels and Bone Remodelling

Bone remodelling is dependent on blood vessels, which bring osteoclast precursors to begin resorption, as well as osteoblast precursors, energy and waste disposal (Fig. 4).
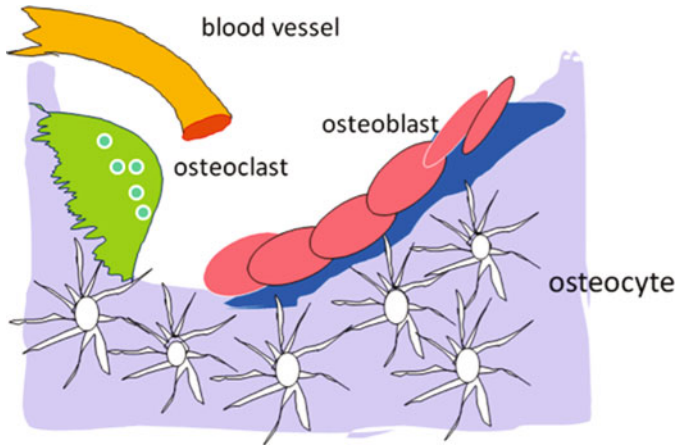
**Fig. 4** Blood vessels are intimately related to bone remodelling, bringing firstly osteoclast precursors from the circulation to remodelling sites and then osteoblast precursors, which are closely allied to the vessel wall

In trabecular bone, resorption begins on the bone surface, and there is evidence that this remodelling occurs within a 'Bone Remodelling Compartment (BRC)', with a canopy of bone-lining cells and an associated capillary [64]. There is evidence that these small vessels are dynamic, as demonstrated by experiments investigating the anabolic action of PTH [98]. PTH is anabolic when delivered intermittently, where it increases both bone resorption and formation, with a net gain of bone. Such treatment concomitantly increases local concentrations of vascular endothelial growth factor (VEGF) and its receptor, neurophilin-1. When VEGF was blocked by neutralising antibodies, PTH lost its osteoanabolic action [98]. Intriguingly, the action of intermittent PTH seemed to relocate small bone marrow blood vessels closer to bone forming sites on the endosteal surface, suggesting that these vessels could be removed and replaced by the action of PTH. In addition, intermittent PTH was shown to increase blood perfusion in bone [106].

Recently, a new capillary subtype was described in the mouse skeletal system, characterised by Type H endothelial cells, which couples angiogenesis and osteogenesis [68]. These vessels have distinct morphological, molecular and functional properties and are found in specific locations, where they mediate growth of the bone vasculature, generate distinct metabolic and molecular microenvironments, maintain perivascular osteoprogenitors and, as stated, couple angiogenesis to osteogenesis. The abundance of these vessels was strongly reduced in bone from aged animals, and pharmacological reversal of this decline allowed the restoration of bone mass in older animals.

The remodelling unit of cortical bone is referred to as the Basic Remodeling Unit (RBU). The RBU comprises a blood vessel that serves as the conduit, through which osteoclast precursors are delivered to the remodelling site. The front edge of the

BMU forms a cutting cone, which tunnels through the bone matrix. Moller et al. published high resolution scanning electron micrographs of a vascular loop from a cutting cone in cortical bone [90].

### 4.3  Bone Vasculature in Fracture and Bone Regeneration

Fracture of bone results in disruption of blood vessels and bone healing is critically dependent upon an adequate vascular supply. Although the cartilaginous callus is avascular, replacement of callus with new bone requires angiogenesis, and inhibition of this process prevents fracture healing (reviewed by Bahney et al. [9]). Ingrowth of new vessels into the fracture callus was elegantly described by Mark et al. [80]. Rhinelander showed the dramatic effects on the vasculature following long bone fracture in dogs [102]. Initially, the somewhat sluggish blood flow in the (undamaged) marrow vessels was greatly enhanced after fracture, after which there was vigorous sprouting of new vessels during the healing phase of the fracture. Some of these events are replicated during bone regeneration. In experiments also performed by Rhinelander, microangiographs of dog tibia one week after insertion of autologous bone graft into a bone defect showed vigorous penetration of the graft by blood vessels [102]. Likewise, in impaction grafting experiments in the sheep proximal femur, the replacement of graft bone by host bone was preceded by vascular invasion into the graft. This vascularisation was greatly enhanced, and occurred earlier, when BMP-7 was added to the engrafted bone [87], consistent with the known action of BMPs to stimulate angiogenesis through a VEGF-mediated mechanism [24].

### 4.4  Bone Vasculature and Surgical Intervention

Because of the importance of bone vasculature and perfusion, the vasculature clearly needs to be respected during surgery involving the skeleton, either to bone per se or to vessels flowing to the bone. Examples of unavoidable damage to the bone and its vasculature are sawing and cutting of bone, drilling and placing pins and screws into bone, reaming of the marrow space and placing nails or prostheses where the marrow vessels normally reside, and placing of hot bone cement onto bone to bone joint prostheses. In these cases, attempts need to be made to contain the damage in order to minimise bone trauma and maximise healing [31]. In order to spare vessels adjacent to, and perfusing, the bone, Solomon and co-workers devised novel surgery for tibial plateau fractures [116]. Critically, with the approach used in these novel surgeries, the proximal tibial soft tissue envelope and its blood supply were preserved. The authors described an outcome, in which all the fractures healed uneventfully and without infection, compared with the high rates of infection and poor rates of healing described in the literature for tibial plateau fractures.

## *4.5 Bone Vasculature and Osteoporosis*

While a clear link between vascular pathology and osteoporosis has not been established, there is good evidence that both the number and quality of nutrient vessels in the bone marrow decreases with age. London and colleagues showed the dramatic reduction in patent vessels in the human femoral diaphysis with age [76], and this is consistent with MRI data showing that osteoporosis and osteopenia are associated with reduced perfusion of the proximal femur compared with subjects with normal BMD [46]. Further, these authors found that as bone perfusion decreased there was a corresponding increase in marrow fat. They went on to show reduced bone perfusion in osteoporosis in the ovariectomy rat model [47]. Another group have shown in one mouse strain that the loss of bone volume with age associates with reduced blood vessel density in the marrow, increased blood pressure and bone vascular resistance, decreased perfusion and increased adipocyte density [105]. Suggesting a causal link between perfusion and bone mass, these associations were not observed in another mouse strain that lost much less bone during aging.

The risk of osteoporotic fracture has been shown to increase with cardio-vascular disease- heart failure, stroke and peripheral atherosclerosis [112]. Yearly percentage gains in aortic calcification associate with yearly decrements in bone mineral density and increase the risk of hip and vertebral fracture [111]. Recently, Prisby made the remarkable discovery of severe calcification of the bone vascular network in older rats and humans [99], whereby the bone marrow blood vessels actually turn into bone. Vessel ossification was associated with increased marrow adipocyte number. The author postulated that ossified vessels in patients would result in diminished bone blood flow, bone marrow ischemia, diminished interstitial pressure and fluid flow, and that these changes may create hypoxic and acidic conditions in the bone and alter osteoblast and osteoclast activity, culminating in reduced bone mass.

A large amount of research has been focussed on understanding the mechanisms leading to vascular calcification (reviewed by Johnson and collagues [57]. For example, it has been shown that isoprostanes, derivatives of oxidised fatty acids, have opposite effects on vascular smooth muscle cells and osteoblasts, increasing mineralisation by vascular smooth muscle cells and decreasing mineralisation by MC3T3-E1 osteoblast-like cells [95]. These data show how increased circulating oxidisation products and inflammatory mediators, as seen in aging and diabetes, could potentially lead to the changes described above. Vascular calcification is a hallmark of chronic kidney disease, the incidence of which is steadily rising, with likely important implications for bone health.

## *4.6 Bone Vasculature and Osteoarthritis*

This aspect is dealt with in more detail below. However, suffice to say that reduced perfusion and elevated intraosseous blood pressure have been consistently observed

in both animal models of osteoarthritis [1, 73], and in patients [65]. It is not clear whether these changes are the cause or effect of this condition.

## 5   Interaction of Bone with Cartilage

This section deals with the interaction of bone with articular cartilage, since this osteo-chondral structure is essential for ambulation. Cartilage acts as a bearing surface and its unique lubrication gives joints an extremely low coefficient of friction of around $10^{-3}$ [86]. Since cartilage degradation is the characteristic feature of osteoarthritis (OA), much of the research to understand OA has been focussed on the cartilage. However, it is now recognised that the whole joint is involved in the progression of OA and that the interaction between cartilage and subchondral bone is central to this process.

### 5.1   Cartilage: Bone Interface

The interface between articular cartilage and bone of articulating long bones is a unique zone that has received attention due to its particular relevance to the initiation and progression of OA (reviewed by Findlay [33, 34]. The zone comprises articular cartilage, below which is calcified cartilage sitting on and intercalated into the sub-chondral bone plate. Below the subchondral plate is the trabecular bone at the end of the respective long bones. In OA, there are well described progressive destruc-tive changes in the articular cartilage [54], which parallel characteristic changes in the underlying bone. These include sclerosis and increased volume of subchondral bone, cyst formation, osteophyte formation at the joint margins, and reduced bone mineralisation.

### 5.2   Subchondral Bone Vasculature

The subchondral bone is richly vascularised by fine vessels originating in the epiph-ysis and this vasculature is important for both the bone and the overlying cartilage. It has been estimated that perfusion from the subchondral bone accounts for at least 50% of glucose, oxygen and water requirements of cartilage [53], the remainder coming from the synovial fluid via the synovial circulation. Elegant work by Pan and co-workers [94], showed, at least in the mouse and for small molecules, biochemical continuity between articular cartilage and subchondral bone. These and other authors [44] further showed that diffusion of small and macromolecules through cartilage was significantly enhanced by physiological loading of the cartilage.

In OA, there are multiple perturbations of the subchondral vasculature and per-fusion. There is vascular invasion into the calcified cartilage and not infrequently the cartilage itself [79]. Increased vascularization was noted in the monosodium

iodoacetate (MIA)-induced rat model of early OA [127]. Using dynamic-enhanced MRI, decreased subchondral bone perfusion was seen in the Duncan Hartley guinea pig model of OA, which temporally preceded and spatially localized (medial compartment) at the same sites as the eventual bone and cartilage lesions. The data suggested that this impaired venous blood flow had outflow obstruction as an underlying mechanism [73]. Earlier studies in patients with hip pain of short duration (<1 year) but who did not yet show severe degenerative changes, intraosseous pressure was raised, while PO$_2$ was reduced [65]. Finally, in the area defined by MRI as a bone marrow lesion (BML), perfusion was found to be reduced compared to normal subchondral bone [1]. This is consistent with the earlier proposal by Arnoldi that decreased bone blood perfusion, and the consequent decreased interstitial fluid flow in the subchondral bone [5], lead to ischaemia and bone death. BMLs are reported to represent areas of bone necrosis, above which the cartilage is more likely to be degraded [32, 33]. Thus, a potential outcome of venous stasis in subchondral bone is that poor perfusion may also result in a decrease in nourishment to the overlying cartilage.

## 5.3 Chondrocyte-Osteoblast Interaction

Given the possibility of bidirectional molecular transfer between the cartilage and bone, biochemical crosstalk between bone cells and chondrocytes in the cartilage may also occur. In ex vivo experiments using bovine osteochondral tissue, chondrocyte survival in the articular cartilage was favored by the co-presence in culture of healthy subchondral bone, either contiguous with, or separated but co-incubated with, the cartilage, compared with cartilage cultures alone (Fig. 5) [4]. These experiments suggested the secretion of chondrocyte survival factors by the bone cells.



**Fig. 5** Amin and colleagues showed that incubation of bovine articular cartilage with subchondral bone, either contiguous or co-incubated, protected chondrocytes from apoptosis, compared with cartilage incubated alone [4]

On the other hand, osteoblasts from sclerotic OA subchondral bone were found to upregulate catabolic metalloproteinase expression by chondrocytes, an effect mimicked by known cartilage catabolic factors, IL-1, IL-6 and oncostatin M [108]. This was associated with decreased expression of the cartilage structural protein, aggrecan. It has also been shown that conditioned medium collected from compressed osteoblasts in culture upregulates catabolic enzyme production in mouse articular chondrocytes [97], with the active agent identified as 14-3-3$\varepsilon$. The authors demonstrated that conditioned medium from OA subchondral bone contains elevated levels of 14-3-3$\varepsilon$. Conversely, increased production of IL-1$\beta$ and TNF$\alpha$ by chondrocytes from OA patients, which decrease collagen matrix production and increase production of degradative enzymes, may also affect the metabolism of the underlying bone.

## 5.4  Bone Remodelling in OA

As reviewed by Burr and Gallant, OA is associated with major changes in remodelling of the subchondral bone [18]. These authors argue that, at least in animal models of OA, remodelling is spatially related and also changes as a function of disease progression. Thus, animal models typically show increased remodelling early in OA, during which there is loss of subchondral bone and this is followed by bone sclerosis as the disease progresses [50]. Gene microarray analysis of subchondral bone in the rat meniscectomy model of OA showed increased expression of many catabolic factors early in the disease [131]. It has been shown that antiresorptive agents, which reduce bone remodelling, have good efficacy to reduce cartilage degradation in a number of animal models. It is thought that inhibiting resorption and metabolism in subchondral bone indirectly affects chondrocytes because in most cases these agents are not known to have direct effects on cartilage. Altered expression of genes associated with bone remodelling has been found in bone relatively distant from the joint. For example, the relationship between RANKL and OPG was different in cancellous bone from the intertrochanteric region in human OA, compared with bone from unaffected controls [28] and there was differential gene expression of osteocalcin in OA and control bone from the same site [67]. These results suggest that there may be skeleton-wide differences in bone turnover in OA, perhaps predisposing to the disease or as a result of the disease.

## 5.5  The Potential Role of TGF$\beta$ in OA

A potential role for TGF$\beta$ in OA has been identified. There were early reports of an increased level of the growth factors IGF-I, IGF-II and TGF$\beta$ in OA subchondral bone [25]. Later, increased production of TGF$\beta$ was seen in isolated human subchondral osteoblasts from OA patients [84]. Subsequent observations of reduced mineralisation in primary cultures of human osteoblasts derived from OA bone and

an increased ratio of $\alpha_1 : \alpha_2$ chains of type I collagen in OA bone, are potentially explained by increased TGF$\beta$ expression. Experimentally, silencing of the TGF$\beta$ gene in osteoblasts from OA subchondral bone reduced $\alpha_1 : \alpha_2$ ratio and normalised mineralisation by these cells [22]. A recent publication by Zhen and co-workers shows that changes in bone and cartilage in the mouse ACTL model of OA are accompanied by increased TGF$\beta$ signaling in the subchondral bone [134]. When TGF$\beta$ signalling was over-activated specifically in osteoblasts, the mice spontaneously developed OA. Conversely, deletion of TGF$\beta$ signalling specifically in pre-osteoblasts reduced OA in the mouse ACLT model [134]. These data highlight an important role for TGF$\beta$ in OA, although what is responsible for the increased TGF$\beta$ in the subchondral bone remains to be determined.

## 5.6  The Significance of Bone Marrow Lesions

Bone marrow lesions (BML) in OA are regions in the subchondral bone that can be imaged using MRI. Depending on the MRI sequence used, they may be brighter than the surrounding bone. BML are frequently seen in painful knees and from early to late OA but are rarely seen in normal joints. BML are of interest because they seem to offer diagnostic and predictive value: longitudinal studies have shown that BML are a potent risk factor for structural detrioration in knee OA [26, 30]. BML underly regions of cartilage degradation and loss and enlargement of BML has been strongly associated with increased cartilage loss [78]. Conversely, a reduction in the extent of bone marrow abnormalities on MRI is associated with a decrease in cartilage degradation [52]. Mechanical loading is considered a likely causal factor for BMLs [12], although metabolic and vascular factors may also contribute [32]. Histologically, BML contain sclerotic bone, which may be necrotic and/or fibrotic [130]. Since BML are associated with pain and cartilage degradation, they may provide sensitive biomarkers for disease modification in OA. Laslett and co-workers found in a preliminary study, treating subjects with moderate OA (significant knee pain on most days) [71], that the antiresorptive agent zoledronic acid decreased the size of BMLs and also pain over 12 months.

## 6  Interaction of Bone with the Central Nervous System

## 6.1  Nerves in Bone

There is extensive innervation of bone, with nerves accompanying blood vessels throughout the bone matrix (Fig. 1) and the periosteum richly innervated. However, the role of nerves and the interactions between the central nervous system (CNS) and bone has not been well understood and is only relatively recently begun to be elucidated. Clearly, disruption of nerves in bone, as in fracture, results in significant pain.
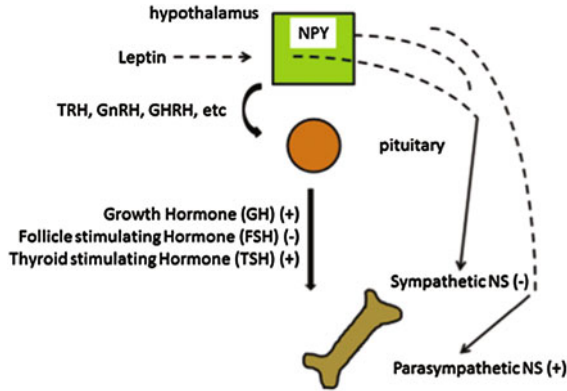
**Fig. 6** Summary of Central Nervous System-bone interactions. Shown are Leptin and NPY, which act via the hypothalamic-Sympathetic Nervous System (SNS) axis to reduce bone accrual. The parasympathetic NS appears to favour bone accrual. A number of pituitary hormones, thought to act secondarily on bone, may in fact have direct positive or negative effects on bone mass

Indeed bone pain, seen in numerous conditions, such as arthritis, bone cancer, bone surgery, fracture, Pagets Disease of Bone, Osteogenesis Imperfecta, osteonecrosis and osteomyelitis, is the most obvious manifestation of the interaction of the CNS with bone, although its causes are usually not well understood. The CNS appears to have roles both in the development of the skeleton and it exerts important control over remodelling in the mature skeleton. The essential requirement of intact links between CNS and bone is apparent in the massive rapid loss of cortical and trabecular bone after spinal cord injury [27]. The CNS communicates with bone through nerve endings terminating in bone and by the release of hormonal factors, primarily from the pituitary gland. The latter are the result of sophisticated feedback loops that affect the hypothalamic-pituitary axis.

## 6.2 Hypothalamic Control of Bone

In response to a range of environmental, hormonal, nutritional and other cues, the hypothalamus selectively directs the release into the circulation of at least nine hormones from the pituitary gland (Fig. 6). These factors, such as thyroid stimulating hormone (TSH), growth hormone (GH), follicle-stimulating hormone (FSH) and luteinising hormone (LH) are thought of as acting on particular organs and tissues, as their name suggests, but in fact act widely throughout the body, including the musculoskeletal system. Several examples of the actions of pituitary hormones are given here. Growth hormone release is stimulated by Growth Hormone Releasing Hormone from the hypothalamus, which in turn is regulated by complex nutritional and other cues. GH is a stimulator of bone and muscle growth, so that GH deficiency leads to dwarfism and GH excess leads to gigantism. GH acts directly on the skeleton,

as well as via the Insulin Like Growth Factors I and II (IGFI and II), whose production GH stimulates in the liver, and in the end organs themselves. Thus, GH directly and through IGF-I stimulates osteoblast proliferation and activity, promoting bone formation. It also stimulates osteoclast differentiation and activity, promoting bone resorption. The result is an increase in the overall rate of bone remodeling, with a net effect of bone accumulation. The actions of GH have been reviewed by Olney [92].

Follicle stimulating Hormone (FSH) stimulates secondary sexual characteristics in both males and females but has been found to be a negative regulator of bone. In mice, FSH receptor deficiency leads to hypogandism but the mice do not lose bone, whereas ovariectomised controls lost substantial bone and had higher serum bone resorption markers [119]. Serum bone turnover markers were raised in the ovariectomised controls but not in the FSH Receptor knockout animals. Consistent with this, the FSH Receptor null mice produced fewer osteoclasts in vitro, which resorbed less bone. In mice in which one allele of the FSH$\beta$ gene was deleted, these animals had reduced serum FSH$\beta$ but were eugonadal: they nevertheless had increased bone mass [119]. Thus, as with FSHR deletion, FSH$\beta$ elimination prevented bone loss and even increased bone mass, despite the severe hypogonadism. These findings suggested a direct effect of FSH on bone to down regulate bone mass. The in vitro correlate of the in vivo results was that FSH was shown to increase both osteoclast formation and bone resorption [119]. Evidence for a role for FSH in humans is that women in the 4th quartile of serum FSH levels had statistically higher circulating resorption markers than women in the 1st quartile [43].

The pituitary secretes thyroid stimulating hormone (TSH), which stimulates the thyroid gland to secrete thyroid hormones T3 and T4, which have an essential role in body metabolism. TSH has been shown to have independent positive effects on bone. Thyroid hormones are required for skeletal development and establishment of peak bone mass. Hypothyroidism in children results in growth retardation with delayed skeletal development, whereas thyrotoxicosis accelerates bone maturation. In adults, T3 regulates bone turnover and bone mineral density, and normal euthyroid status is essential to maintain optimal bone strength. Population studies indicate that hypothyroidism and hyperthyroidism are both associated with an increased risk of fracture.

In seeking evidence for a direct action of TSH on bone, Abe et al. investigated the effects on the skeleton of deletion of the TSH receptor (TSHR) [2]. They found that reduction or deletion of the TSHR produced profound osteoporosis. Probing the mechanisms for this, the authors showed that deletion of the TSHR increased osteoclast and osteoblast formation. On the other hand, recombinant TSH, added to cells in culture, inhibited osteoclast formation and survival by attenuating RANKL signalling. TSH also inhibited osteoblast differentiation. These studies suggest that TSH maintains bone mass and strength by controlling the balance between osteoclast formation and resorption and osteoblast differentiation and bone formation. However, the above in vivo studies are complicated by the effects of reduced TSH on thyroid hormone levels. In more recent studies, the TSHR gene deficient mice were again studied, but this time with T4 normalisation [132]. These studies supported those

cited above, in that TSHR gene deletion resulted in reduced bone mass, and reduced bone biomechanical properties, despite adequate serum T4 levels.

## *6.3  Functions of Nerves in Bone*

There is evidence that bone function is controlled by both the sympathetic and parasympathetic nervous systems. Several examples of the complex biology involved in this control will be given, although there is a growing literature, to which the reader is referred. No further mention will be made here of the fat-derived molecule, leptin, but there is good genetic evidence indicating central action of leptin to inhibit the accrual of bone mass (reviewed by Karsenty and Ferron [59]). Likewise, members of the neuropeptide Y family have been shown to have potent centrally-mediated and local effects on bone formation, and the reader is referred to an excellent recent review on this topic [115].

As summarised by Vignaux et al., the skeleton is richly innervated by sympathetic neurons [124], which are found in close vicinity to osteoblasts, and stimulation of the sympathetic nervous system postnatally causes bone loss, due to reduced bone formation and increased bone resorption. On the other hand, inhibition of the sympathetic nervous system leads to a high bone mass phenotype caused by an increase in bone formation and a decrease in bone resorption. Recent evidence shows that the sympathetic nervous system is also involved in bone development [41]. Mice globally lacking the semaphorin 3 A gene (Sema3a/mice) have low bone mass, apparently due to reduced bone formation. Semaphorin 3A (Sema3A) is a diffusable axon-guidance molecule that is abundantly expressed in bone and can affect osteoblast differentiation. Mice lacking Sema3A expression specifically in osteoblasts showed no effect on bone mass, whereas mice in which the gene was specifically knocked out in neurons showed reduced bone mass. Further investigation revealed that neuron-derived Sema3A is indispensable for sensory nerve innervation into bone, and that this innervation is in some way important for bone development.

A second example of interaction between the sympathetic nervous system and bone relates to G-CSF-mediated mobilisation of bone marrow stem cells. This process has marked effects on osteocytes [6], suggesting a potential role for this cell type in mobilisation. Moreover, ablation of osteocytes greatly reduced stem cell mobilisation. Evidence that the sympathetic nervous system was also involved was that nerves could be identified histologically adjacent to osteocytes, that osteocytes were found to express the $\beta2$-adrenergic receptor (a sympathetic neurotransmitter), and that surgical denervation of the bone prevents mobilisation [6]. Thus, G-CSF leads to activation of the sympathetic nervous system, which suppresses osteocytes via the $\beta2$-adrenergic system. It is proposed that this secondarily suppresses the osteoblastic stem cell niche, releasing stem cells into the circulation [6].

Roles for the parasympathetic nervous system in bone metabolism are less well explored but recent research suggests that the parasympathetic-bone axis favours bone mass accrual. Bajayo et al. found parasympathetic innervation in bone [10],

together with receptors for acetylcholine (parasympathetic neurotransmitter) on osteoblasts and osteoclasts. They then showed that mice deficient in functional nicotinic acetylcholine receptors (those found on bone cells) have increased bone resorption and low bone mass, together with a large increase in osteoclast number and bone resorption. The authors previously reported that central IL-1 signaling, as opposed to peripheral IL-1 signalling, increases bone mass by suppressing bone resorption. Bajayo and co-wokers showed that silencing of IL-1 receptor signalling in the central nervous system by brain-specific over-expression of the human IL-1 receptor antagonist led to very low skeletal ACh levels [10]. These mice also exhibit increased bone resorption and low bone mass. These findings describe a novel central IL-1-parasympathetic-bone axis that favours bone mass accrual.

**Summary**: The biology of bone is clearly complex and interdependent on the biology of many other organ systems. This review gives a glimpse of that complexity. In many cases, consideration of the biomechanical aspects of bone will not require a detailed understanding of the bone biology. However, awareness that bone is a vital and biologically responsive organ system, whose behaviour is linked to the adjacent structures of muscle and cartilage, and that it integrates signals arriving from the circulation, the nervous system and from skeletal loading, is essential to the informed interpretation of findings from biomechanical experiments.

# References

1. R.K. Aaron, J.P. Dyke, D.M. Ciombor, D. Ballon, J. Lee, E. Jung, G.A. Tung, Perfusion abnormalities in subchondral bone associated with marrow edema. Ann. N. Y. Acad. Sci. **1117**, 124–137 (2007)
2. E. Abe, R.C. Marians, W. Yu, X.B. Wu, T. Ando, Y. Li, J. Iqbal, L. Eldeiry, G. Rajendren, H.C. Blair, T.F. Davies, M. Zaidi, TSH is a negative regulator of skeletal remodeling. Cell **115**(2), 151–162 (2003)
3. T. Alliston, Biological regulation of bone quality. Curr. Osteoporos. Rep. **12**(3), 366–375 (2014)
4. A.K. Amin, J.S. Huntley, A.H. Simpson, A.C. Hall, Chondrocyte survival in articular cartilage: the influence of subchondral bone in a bovine model. J. Bone Joint Surg. Br. **91**(5), 691–699 (2009)
5. C.C. Arnoldi, Vascular aspects of degenerative joint disorders: a synthesis. Acta Orthop. Scand. **65**(Sup 261), 1–82 (1994)
6. N. Asada, Y. Katayama, M. Sato, K. Minagawa, K. Wakahashi, H. Kawano, Y. Kawano, A. Sada, K. Ikeda, T. Matsui, M. Tanimoto, Matrix-embedded osteocytes regulate mobilization of hematopoietic stem/progenitor cells. Cell Stem Cell **12**(6), 737–747 (2013)
7. G.J. Atkins, D.M. Findlay, Osteocyte regulation of bone mineral: a little give and take. Osteoporos. Int. **23**(8), 2067–2079 (2012)
8. J.E. Aubin, Advances in the osteoblast lineage. Biochem. Cell Biol. **76**(6), 899–910 (1998)
9. C.S. Bahney, D.P. Hu, T. Miclau, R.S. Marcucio, The multifaceted role of the vasculature in endochondral fracture repair. Front. Endocrinol. **6**(4), 1–10 (2014)

10. A. Bajayo, A. Bar, A. Denes, M. Bachar, V. Kram, M. Attar-Namdar, A. Zallone, K.J. Kovács, R. Yirmiya, I. Bab, Skeletal parasympathetic innervation communicates central IL-1 signals regulating bone mass accrual. Proc. Natl. Acad. Sci. USA **109**(38), 15455–15460 (2012)

11. R. Baron, M. Kneissel, WNT signaling in bone homeostasis and disease: from human mutations to treatments. Nat. Med. **19**(2), 179–192 (2013)

12. K.L. Bennell, M.W. Creaby, T.V. Wrigley, K.A. Bowles, R.S. Hinman, F. Cicuttini, D.J. Hunter, Bone marrow lesions are related to dynamic knee loading in medial knee osteoarthritis. Ann. Rheum. Dis. **69**(6), 1151–1154 (2010)

13. L.F. Bonewald, The amazing osteocyte. J. Bone Miner. Res. **26**(2), 229–238 (2011)

14. L.F. Bonewald, Osteocyte biology, in *Osteoporosis*, ed. by R. Marcus, D. Feldman, D.W. Dempster, M. Luckey, J.A. Cauley (Academic Press, New York, 2013), pp. 209–234. (Chapter 10)

15. A.L. Boskey, Biomineralization: conflicts, challenges, and opportunities. J. Cell. Biochem. **72**(S30), 83–91 (1998). doi:10.1002/(SICI)1097-4644(1998)72:30/31+<83::AID-JCB12>3.0.CO;2-F. ISSN 1097-4644

16. M.L. Brandi, P. Collin-Osdoby, Vascular biology and the skeleton. J. Bone Miner. Res. **21**(2), 183–192 (2006)

17. M. Brotto, M.L. Johnson, Endocrine crosstalk between muscle and bone. Exerc. Sport Sci. Rev. **12**(2), 135–141 (2014)

18. D.B. Burr, M.A. Gallant, Bone remodelling in osteoarthritis. Nat. Rev. Rheumatol. **8**(11), 665–673 (2012)

19. C. Ciani, S.B. Doty, S.P. Fritton, An effective histological staining process to visualize bone interstitial fluid space using confocal microscopy. Bone **44**(5), 1015–1017 (2009)

20. J.E. Compston, Bone marrow and bone: a functional unit. J. Endocrinol. **173**(3), 387–394 (2002)

21. S.D. Cook, D.C. Rueger, Osteogenic protein-1: biology and applications. Clin. Orthop. Relat. Res. **324**, 29–38 (1996)

22. D. Couchourel, I. Aubry, A. Delalandre, M. Lavigne, J. Martel-Pelletier, J.P. Pelletier, D. Lajeunesse, Altered mineralization of human osteoarthritic osteoblasts is attributable to abnormal type I collagen production. Arthritis Rheum. **60**(5), 1438–1450 (2009)

23. S.C. Cowin, The significance of bone microstructure in mechanotransduction. J. Biomech. **40**(Suppl 1), S105–S109 (2007)

24. M.M. Deckers, R.L. van Bezooijen, G. van der Horst, J. Hoogendam, C. van Der Bent, S.E. Papapoulos, C.W. Löwik, Bone morphogenetic proteins stimulate angiogenesis through osteoblast-derived vascular endothelial growth factor A. Endocrinology **143**(4), 1545–1553 (2002)

25. J. Dequeker, S. Mohan, R.D. Finkelman, J. Aerssens, D.J. Baylink, Generalized osteoarthritis associated with increased insulin-like growth factor types i and ii and transforming growth factor beta in cortical bone from the iliac crest. possible mechanism of increased bone density and protection against osteoporosis. Arthritis Rheum. **36**(12), 1702–1708 (1993)

26. D. Dore, S. Quinn, C. Ding, T. Winzenberg, G. Zhai, F. Cicuttini, G. Jones, Natural history and clinical significance of MRI-detected bone marrow lesions at the knee: a prospective study in community dwelling older adults. Arthritis Res. Ther. **12**(6), R223 (2010)

27. S. Dudley-Javoroski, R.K. Shields, Regional cortical and trabecular bone loss after spinal cord injury. J. Rehabil. Res. Dev. **49**(9), 1365–1376 (2012)

28. N.L. Fazzalari, J.S. Kuliwaba, G.J. Atkins, M.R. Forwood, D.M. Findlay, The ratio of messenger RNA levels of receptor activator of nuclear factor kappaB ligand to osteoprotegerin correlates with bone remodeling indices in normal human cancellous bone but not in osteoarthritis. J. Bone Miner. Res. **16**(6), 1015–1027 (2001)

29. G. Feldman, M. Li, S. Martin, M. Urbanek, J.A. Urtizberea, M. Fardeau, M. LeMerrer, J.M. Connor, J. Triffitt, R. Smith, M. Muenke, F.S. Kaplan, E.M. Shore, Fibrodysplasia ossificans progressiva, a heritable disorder of severe heterotopic ossification, maps to human chromosome 4q27-31. Am. J. Hum. Genet. **66**(1), 128–135 (2000)

30. D.T. Felson, S. McLaughlin, J. Goggins, M.P. LaValley, M.E. Gale, S. Totterman, W. Li, C. Hill, D. Gale, Bone marrow edema and its relation to progression of knee osteoarthritis. Ann. Intern. Med. **139**(5 Pt 1), 330–336 (2003)

31. J.R. Field, G. Sumner-Smith, Bone blood flow response to surgical trauma. Injury **33**(5), 447–451 (2002)

32. D.M. Findlay, Vascular pathology and osteoarthritis. Rheumatology (Oxford) **46**(12), 1763–1768 (2007)

33. D.M. Findlay, Subchondral bone in osteoarthritis, in *Principles of Osteoarthritis*, ed. by B.M. Rothschild (InTech, Croatia, 2012), pp. 139–154

34. D.M. Findlay, Long overlooked: the role of subchondral bone in osteoarthritis pathophysiology and pain. Medicographia **35**(2), 221–227 (2013)

35. D.M. Findlay, P.M. Sexton, Calcitonin. Growth Factors **22**(4), 217–224 (2004)

36. H. Fleisch, Bisphosphonates in osteoporosis. Eur. Spine J. **12**(Suppl 2), S142–S146 (2003)

37. S.P. Fritton, S. Weinbaum, Fluid and solute transport in bone: flow-induced mechanotransduction. Annu. Rev. Fluid Mech. **41**, 347–374 (2009)

38. H. M Frost, Bone "mass" and the "mechanostat": a proposal. Anat. Rec. **219**(1), 1–9 (1987)

39. H.M. Frost, The Utah paradigm of skeletal physiology: an overview of its insights for bone, cartilage and collagenous tissue organs. J. Bone Miner. Metab. **18**(6), 305–316 (2000)

40. A. Frotzler, S. Coupaud, C. Perret, T.H. Kakebeeke, K.J. Hunt, N. Donaldson Nde, P. Eser, High-volume FES-cycling partially reverses bone loss in people with chronic spinal cord injury. J. Appl. Physiol. **43**(1), 169–176 (2008)

41. T. Fukuda, S. Takeda, R. Xu, H. Ochi, S. Sunamura, T. Sato, S. Shibata, Y. Yoshida, Z. Gu, A. Kimura, C. Ma, C. Xu, W. Bando, K. Fujita, K. Shinomiya, T. Hirai, Y. Asou, M. Enomoto, H. Okano, A. Okawa, H. Itoh, Inner ear vestibular signals regulate bone remodeling via the sympathetic nervous system. Nature **497**(7450), 490–493 (2013)

42. S. Fukumoto, T.J. Martin, Bone as an endocrine organ. Trends Endocrinol. Metab. **20**(5), 230–236 (2009)

43. A. García-Martín, R. Reyes-García, J.M. García-Castro, P. Rozas-Moreno, F. Escobar-Jiménez, M. Muñoz-Torres, Role of serum FSH measurement on bone resorption in postmenopausal women. Endocrine **41**(2), 302–308 (2012)

44. B.S. Gardiner, D.W. Smith, P. Pivonka, A. Grodzinsky, E. Frank, L. Zhang, Solute transport in cartilage undergoing cyclic deformation. Comput. Methods Biomech. Biomed. Eng. **10**(4), 265–278 (2007)

45. S. Gopal, S. Majumder, A.G. Batchelor, S.L. Knight, P. De Boer, R.M. Smith, Fix and flap: the radical orthopaedic and plastic treatment of severe open fractures of the tibia. J. Bone Joint Surg. Br. **82**(7), 959–966 (2000)

46. J.F. Griffith, D.K. Yeung, P.H. Tsang, K.C. Choi, T.C. Kwok, A.T. Ahuja, K.S. Leung, P.C. Leung, Compromised bone marrow perfusion in osteoporosis. J. Bone Miner. Res. **23**(7), 1068–1075 (2008)

47. J.F. Griffith, Y.X. Wang, H. Zhou, W.H. Kwong, W.T. Wong, Y.L. Sun, Y. Huang, D.K. Yeung, L. Qin, A.T. Ahuja, Reduced bone perfusion in osteoporosis: likely causes in an ovariectomy rat model. Radiology **254**(3), 739–746 (2010)

48. M.W. Hamrick, Role for myokines in muscle-bone interactions. Exerc. Sport Sci. Rev. **39**(1), 43–47 (2011)

49. L.E. Harry, A. Sandison, E.M. Paleolog, U. Hansen, M.F. Pearse, J. Nanchahal, Comparison of the healing of open tibial fractures covered with either muscle or fasciocutaneous tissue in a murine model. J. Orthop. Res. **26**(9), 1238–1244 (2008)

50. T. Hayami, M. Pickarski, Y. Zhuo, G.A. Wesolowski, G.A. Rodan, L.T. Duong, Characterization of articular cartilage and subchondral bone changes in the rat anterior cruciate ligament transection and meniscectomized models of osteoarthritis. Bone **38**(2), 234–243 (2006)

51. D.R. Haynes, T.N. Crotti, A.E. Potter, M. Loric, G.J. Atkins, D.W. Howie, D.M. Findlay, The osteoclastogenic molecules RANKL and RANK are associated with periprosthetic osteolysis. J. Bone Joint Surg. Br. **83**(6), 902–911 (2001)

52. D.J. Hunter, Y. Zhang, J. Niu, J. Goggins, S. Amin, M.P. LaValley, A. Guermazi, H. Genant, D. Gale, D.T. Felson, Increase in bone marrow lesions associated with cartilage loss: a longitudinal magnetic resonance imaging study of knee osteoarthritis. Arthritis Rheum. **54**(5), 1529–1535 (2006)

53. H. Imhof, I. Sulzbacher, S. Grampp, C. Czerny, S. Youssefzadeh, F. Kainberger, Subchondral bone and cartilage disease: a rediscovered functional unit. Invest. Radiol. **35**(10), 581–588 (2000)

54. H. Imhof, I.M. Nöbauer-Huhmann, C. Krestan, A. Gahleitner, I. Sulzbacher, S. Marlovits, S. Trattnig, MRI of the cartilage. Eur. Radiol. **12**(11), 2781–2793 (2002)

55. K. Jähn, N. Lara-Castillo, L. Brotto, C.L. Mo, M.L. Johnson, M. Brotto, L.F. Bonewald, Skeletal muscle secreted factors prevent glucocorticoid-induced osteocyte apoptosis through activation of catenin. Eur. Cell Mater. **24**, 197–209 (2012)

56. B. Javaheri, A.R. Stern, N. Lara, M. Dallas, H. Zhao, Y. Liu, L.F. Bonewald, M.L. Johnson, Deletion of a single catenin allele in osteocytes abolishes the bone anabolic response to loading. J. Bone Miner. Res. **29**(3), 705–715 (2014)

57. R.C. Johnson, J.A. Leopold, J. Loscalzo, Vascular calcification: pathobiological mechanisms and clinical implications. Circ. Res. **99**(10), 1044–1059 (2006)

58. S. Judex, C.T. Rubin, Is bone formation induced by high-frequency mechanical signals modulated by muscle activity? J. Musculoskelet. Neuronal Interact. **10**(1), 3–11 (2010)

59. G. Karsenty, M. Ferron, The contribution of bone to whole-organism physiology. Nature **481**(7381), 314–320 (2012)

60. H.Z. Ke, W.G. Richards, X. Li, M.S. Ominsky, Sclerostin and Dickkopf-1 as therapeutic targets in bone diseases. Endocr. Rev. **33**(5), 374–378 (2012)

61. O.D. Kennedy, B.C. Herman, D.M. Laudier, R.J. Majeska, H.B. Sun, M.B. Schaffler, Activation of resorption in fatigue-loaded bone involves both apoptosis and active pro-osteoclastogenic signaling by distinct osteocyte populations. Bone **50**(5), 1115–1122 (2012)

62. O.D. Kennedy, D.M. Laudier, R.J. Majeska, H.B. Sun, M.B. Schaffler, Osteocyte apoptosis is required for production of osteoclastogenic signals following bone fatigue in vivo. Bone **64**, 132–137 (2014)

63. J.H. Keyak, A.K. Koyama, A. LeBlanc, Y. Lu, T.F. Lang, Reduction in proximal femoral strength due to long-duration spaceflight. Bone **44**(3), 449–453 (2009)

64. S. Khosla, J.J. Westendorf, M.J. Oursler, Building bone to reverse osteoporosis and repair fractures. J. Clin. Invest. **118**(2), 421–428 (2008)

65. T. Kiaer, N.W. Pedersen, K.D. Kristensen, H. Starklint, Intra-osseous pressure and oxygen tension in avascular necrosis and osteoarthritis of the hip. J. Bone Joint Surg. Br. **72**(6), 1023–1030 (1990)

66. J. Klein-Nulend, A.D. Bakker, R.G. Bacabac, A. Vatsa, S. Weinbaum, Mechanosensation and transduction in osteocytes. J. Bone Miner. Res. **54**(2), 182–190 (2013)

67. J.S. Kuliwaba, D.M. Findlay, G.J. Atkins, M.R. Forwood, N.L. Fazzalari, Enhanced expression of osteocalcin mrna in human osteoarthritic trabecular bone of the proximal femur is associated with decreased expression of interleukin-6 and interleukin-11 mRNA. J. Bone Miner. Res. **15**(2), 332–341 (2000)

68. A.P. Kusumbe, S.K. Ramasamy, R.H. Adams, Coupling of angiogenesis and osteogenesis by a specific vessel subtype in bone. J. Bone Miner. Res. **507**(7492), 323–328 (2014)

69. T.F. Lang, A.D. Leblanc, H.J. Evans, Y. Lu, Adaptation of the proximal femur to skeletal reloading after long-duration spaceflight. J. Bone Miner. Res. **21**(8), 1224–1230 (2006)

70. L.E. Lanyon, W.G. Hampson, A.E. Goodship, J.S. Shah, Bone deformation recorded in vivo from strain gauges attached to the human tibial shaft. Acta Orthop. Scand. **46**(2), 256–268 (1975)

71. L.L. Laslett, D.A. Doré, S.J. Quinn, P. Boon, E. Ryan, T.M. Winzenberg, G. Jones, Bone marrow edema pattern in osteoarthritic knees: correlation between MR imaging and histologic findings. Radiology **71**(8), 1322–1328 (2012)

72. N.K. Lebrasseur, S.J. Achenbach, L.J. Melton 3rd, S. Amin, S. Khosla, Skeletal muscle mass is associated with bone geometry and microstructure and serum insulin-like growth factor

binding protein-2 levels in adult women and men. J. Bone Miner. Res. **27**(10), 2159–2169 (2012)

73. J.H. Lee, J.P. Dyke, D. Ballon, D.M. Ciombor, M.P. Rosenwasser, R.K. Aaron, Subchondral fluid dynamics in a model of osteoarthritis: use of dynamic contrast-enhanced magnetic resonance imaging. Osteoarthr. Cartil. **17**(10), 1350–1355 (2009)

74. C. Lin, X. Jiang, Z. Dai, X. Guo, T. Weng, J. Wang, Y. Li, G. Feng, X. Gao, L. He, Sclerostin mediates bone response to mechanical unloading through antagonizing Wnt/beta-catenin signaling. J. Bone Miner. Res. **24**(10), 1651–1661 (2009)

75. R. Liu, O. Birke, A. Morse, L. Peacock, K. Mikulec, D.G. Little, A. Schindeler, Myogenic progenitors contribute to open but not closed fracture repair. BMC Musculoskelet. Disord. **12**(1), 288–297 (2011)

76. G.M. London, Soft bone - hard arteries: a link? Kidney Blood Press. Res. **34**(4), 203–208 (2011)

77. B.R. Macias, J.M. Swift, M.I. Nilsson, H.A. Hogan, S.D. Bouse, S.A. Bloomfield, Simulated resistance training, but not alendronate, increases cortical bone formation and suppresses sclerostin during disuse. J. Appl. Physiol. **112**(5), 918–925 (2012)

78. V. Mandalia, A.J. Fogg, R. Chari, J. Murray, A. Beale, J.H. Henson, Bone bruising of the knee. Clin. Radiol. **60**(6), 627–636 (2005)

79. P.I. Mapp, D.A. Walsh, Mechanisms and targets of angiogenesis and nerve growth in osteoarthritis. Nat. Rev. Rheumatol. **8**(7), 390–398 (2012)

80. H. Mark, A. Penington, U. Nannmark, W. Morrison, A. Messina, Microvascular invasion during endochondral ossification in experimental fractures in rats. Bone **35**(2), 535–542 (2004)

81. S. Martelli, M.E. Kersh, A.G. Schache, M.G. Pandy, Strain energy in the femoral neck during exercise. J. Biomech. **47**(8), 1784–1791 (2014a)

82. S. Martelli, P. Pivonka, P.R. Ebeling, Femoral shaft strains during daily activities: implications for atypical femoral fractures. Clin. Biomech. (Bristol, Avon) **29**(8), 869–876 (2014)

83. T.J. Martin, Historically significant events in the discovery of RANK/RANKL/OPG. World J. Orthop. **4**(4), 186–197 (2013)

84. F. Massicotte, D. Lajeunesse, M. Benderdour, J.P. Pelletier, G. Hilal, N. Duval, J. Martel-Pelletier, Can altered production of interleukin-1beta, interleukin-6, transforming growth factor-beta and prostaglandin E(2) by isolated human subchondral osteoblasts identify two subgroups of osteoarthritic patients. Osteoarthr. Cartil. **10**(6), 491–500 (2002)

85. M.R. McClung, A. Grauer, S. Boonen, M.A. Bolognese, J.P. Brown, A. Diez-Perez, B.L. Langdahl, J.Y. Reginster, J.R. Zanchetta, S.M. Wasserman, L. Katz, J. Maddox, Y.C. Yang, C. Libanati, H.G. Bone, Romosozumab in postmenopausal women with low bone mineral density. N. Engl. J. Med. **370**(5), 412–420 (2014)

86. C.W. McCutchen, The frictional properties of animal joints. Wear **5**(1), 1–17 (1962)

87. M.A. McGee, D.M. Findlay, D.W. Howie, A. Carbone, P. Ward, R. Stamenkov, T.T. Page, W.J. Bruce, C.I. Wildenauer, C. Toth, The use of op-1 in femoral impaction grafting in a sheep model. J. Orthop. Res. **22**(5), 1008–1015 (2004)

88. T. Miyazaki, F. Tokimura, S. Tanaka, A review of denosumab for the treatment of osteoporosis. Patient Prefer. Adher. **8**, 463–471 (2014)

89. Ch. Mo, S. Romero-Suarez, L.F. Bonewald, M.L. Johnson, M. Brotto, Prostaglandin E2: from clinical applications to its potential role in bone-muscle crosstalk and myogenic differentiation. Recent Pat. Biotechnol. **6**(3), 223–229 (2012)

90. J.F. Moller, K. Robertsen, C. Bunger, E.S. Hansen, Improved method for examination of microvascular structures in bone tissue. Clin. Orthop. **334**, 15–23 (1997)

91. N.C. Nowlan, C. Bourdon, G. Dumas, S. Tajbakhsh, P.J. Prendergast, P. Murphy, Developing bones are differentially affected by compromised skeletal muscle formation. Bone **46**(5), 1275–1285 (2010)

92. R.C. Olney, Regulation of bone mass by growth hormone. Med. Pediatr. Oncol. **41**(3), 228–234 (2003)

93. E. Ozcivici, Y.K. Luu, B. Adler, Y.X. Qin, J. Rubin, S. Judex, C.T. Rubin, Mechanical signals as anabolic agents in bone. Nat. Rev. Rheumatol. **6**(1), 50–59 (2010)

94. J. Pan, X. Zhou, W. Li, J.E. Novotny, S.B. Doty, L. Wang, In situ measurement of transport between subchondral bone and articular cartilage. J. Orthop. Res. **27**(10), 1347–1352 (2009)

95. F. Parhami, A.D. Morrow, J. Balucan, N. Leitinger, A.D. Watson, Y. Tintut, J.A. Berliner, L.L. Demer, Vascular calcification: pathobiological mechanisms and clinical implications. Arterioscler. Thromb. Vasc. Biol. **17**(4), 680–687 (1997)

96. M.F. Pittenger, A.M. Mackay, S.C. Beck, R.K. Jaiswal, R. Douglas, J.D. Mosca, M.A. Moorman, D.W. Simonetti, S. Craig, D.R. Marshak, Multilineage potential of adult human mesenchymal stem cells. Science **284**(5411), 143–147 (1999)

97. S. Priam, C. Bougault, X. Houard, M. Gosset, C. Salvat, F. Berenbaum, C. Jacques, Identification of soluble 14-3-3ε as a novel subchondral bone mediator involved in cartilage degradation in osteoarthritis. Arthritis Rheum. **65**(7), 1831–1842 (2013)

98. R. Prisby, A. Guignandon, A. Vanden-Bossche, F. Mac-Way, M.T. Linossier, M. Thomas, N. Laroche, L. Malaval, M. Langer, Z.A. Peter, F. Peyrin, L. Vico, M.H. Lafage-Proust, Intermittent pth(1–84) is osteoanabolic but not osteo-angiogenic and relocates bone marrow blood vessels closer to bone-forming sites. J. Bone Miner. Res. **26**(11), 2583–2596 (2011)

99. R.D. Prisby, Bone marrow blood vessel ossification and 'microvascular dead space' in rat and human long bone. Bone **64**, 195–203 (2014)

100. H. Qing, L. Ardeshirpour, P.D. Pajevic, V. Dusevich, K. Jhn, S. Kato, J. Wysolmerski, L.F. Bonewald, Demonstration of osteocytic perilacunar-canalicular remodeling in mice during lactation. J. Bone Miner. Res. **27**(5), 1018–1029 (2012)

101. F. Rauch, D.A. Bailey, A. Baxter-Jones, R. Mirwald, R. Faulkner, The muscle-bone unit during the pubertal growth spurt. Bone **34**(5), 771–775 (2004)

102. F.W. Rhinelander, Circulation in bone, in *The Biochemistry and Physiology of Bone*, vol. II, ed. by G.H. Bourne (Academic Press, New York, 1972), pp. 2–78. (Chapter 1)

103. P.G. Robey, A.L. Boskey, The biochemistry of bone, in *Osteoporosis*, ed. by R. Marcus, D. Feldman, J. Kelsey (Academic Press, New York, 1996), pp. 95–156. (Chapter 4)

104. A.G. Robling, P.J. Niziolek, L.A. Baldridge, K.W. Condon, M.R. Allen, I. Alam, S.M. Mantila, J. Gluhak-Heinrich, T.M. Bellido, S.E. Harris, C.H. Turner, Mechanical stimulation of bone in vivo reduces osteocyte expression of sost/sclerostin. J. Biol. Chem. **283**(9), 5866–5875 (2008)

105. B. Roche, A. Vanden-Bossche, M. Normand, L. Malaval, L. Vico, M.H. Lafage-Proust, Validated laser doppler protocol for measurement of mouse bone blood perfusion - response to age or ovariectomy differs with genetic background. Bone **55**(2), 418–426 (2013)

106. B. Roche, A. Vanden-Bossche, L. Malaval, M. Normand, M. Jannot, R. Chaux, L. Vico, M.H. Lafage-Proust, Parathyroid hormone 1–84 targets bone vascular structure and perfusion in mice: impacts of its administration regimen and of ovariectomy. J. Bone Miner. Res. **29**(7), 1608–1618 (2014)

107. C.T. Rubin, A.S. Turner, R. Mller, E. Mittra, K. McLeod, W. Lin, Y.X. Qin, Quantity and quality of trabecular bone in the femur are enhanced by a strongly anabolic, noninvasive mechanical intervention. J. Bone Miner. Res. **17**(2), 349–357 (2002)

108. C. Sanchez, M.A. Deberg, N. Piccardi, P. Msika, J.Y. Reginster, Y.E. Henrotin, Osteoblasts from the sclerotic subchondral bone downregulate aggrecan but upregulate metalloproteinases expression by chondrocytes. this effect is mimicked by interleukin-6, -1β and oncostatin m pretreated non-sclerotic osteoblasts. Osteoarthr. Cartil. **13**(11), 979–987 (2005)

109. L.K. Saxon, C.H. Turner, Estrogen receptor beta: the antimechanostat? Bone **36**(2), 185–192 (2005)

110. P. Schneider, M. Stauber, R. Voide, M. Stampanoni, L.R. Donahue, R. Müller, Ultrastructural properties in cortical bone vary greatly in two inbred strains of mice as assessed by synchrotron light based micro- and nano-CT. J. Bone Miner. Res. **22**(10), 1557–1570 (1997)

111. E. Schulz, K. Arfai, X. Liu, J. Sayre, V. Gilsanz, Aortic calcification and the risk of osteoporosis and fractures. J. Clin. Endocrinol. Metab. **89**(9), 4246–4253 (2004)

112. U. Sennerby, H. Melhus, R. Gedeborg, L. Byberg, H. Garmo, A. Ahlbom, N.L. Pedersen, K. Michaëlsson, Cardiovascular diseases and risk of hip fracture. JAMA **302**(15), 1666–1673 (2009)

113. Z. Seref-Ferlengez, J. Basta-Pljakic, O.D. Kennedy, C.J. Philemon, M.B. Schaffler, Structural and mechanical repair of diffuse damage in cortical bone in vivo. J. Bone Miner. Res. **29**(2), 2537–2544 (2014)

114. D. Sharma, C. Ciani, P.A. Marin, J.D. Levy, S.B. Doty, S.P. Fritton, Alterations in the osteocyte lacunar-canalicular microenvironment due to estrogen deficiency. Bone **51**(3), 488–497 (2012)

115. Y.C. Shi, P.A. Baldock, Central and peripheral mechanisms of the NPY system in the regulation of bone and adipose tissue. Bone **50**(2), 430–436 (2012)

116. L.B. Solomon, P.R. Boopalan, A. Chakrabarty, S.A. Callary, Can tibial plateau fractures be reduced and stabilised through an angiosome-sparing antero-lateral approach? Injury **45**(4), 766–774 (2014)

117. W.S. Simonet, D.L. Lacey, C.R. Dunstan, M. Kelley, M.-S. Chang, R. Luthy et al., Osteoprotegerin: a novel secreted protein involved in the regulation of bone density. Cell **89**(2), 309–319 (1997)

118. N.S. Soysa, N. Alles, K. Aoki, K. Ohya, Osteoclast formation and differentiation: an overview. J. Med. Dent. Sci. **59**(3), 65–74 (2012)

119. L. Sun, T.F. Davies, H.C. Blair, M. Abe, M. Zaidi, TSH and bone loss. Ann. N. Y. Acad. Sci. **309–318**, 2006 (1068)

120. J.M. Swift, M.I. Nilsson, H.A. Hogan, L.R. Sumner, S.A. Bloomfield, Simulated resistance training during hindlimb unloading abolishes disuse bone loss and maintains muscle strength. J. Bone Miner. Res. **25**(3), 564–574 (2010)

121. S.Y. Tang, T. Alliston, Regulation of postnatal bone homeostasis by TGF. Bonekey Rep. **2**, 255 (2013)

122. Y. Tsuchiya, K. Sakuraba, E. Ochi, High force eccentric exercise enhances serum tartrate-resistant acid phosphatase-5b and osteocalcin. J. Musculoskelet. Neuronal Interact. **14**(1), 50–57 (2014)

123. S.E. Utvag, K.B. Iversen, O. Grundnes, O. Reikeras, Poor muscle coverage delays fracture healing in rats. Acta Orthop. Scand. **73**(4), 471–474 (2002)

124. G. Vignaux, J. Ndong, D. Perrien, F. Elefteriou, Inner ear vestibular signals regulate bone remodeling via the sympathetic nervous system. J. Bone Miner. Res. **30**(6), 1103–1111 (2015)

125. B. Wang, X. Lai, C. Price, W.R. Thompson, W. Li, T.R. Quabili, W.J. Tseng, X.S. Liu, H. Zhang, J. Pan, C.B. Kirn-Safran, M.C. Farach-Carson, L. Wang, Perlecan-containing pericellular matrix regulates solute transport and mechano-sensing within the osteocytelacunar-canalicular system. J. Bone Miner. Res. **29**(4), 878–891 (2014)

126. J.M. Wozney, V. Rosen, A.J. Celeste, L.M. Mitsock, M.J. Whitters, R.W. Kriz, R.M. Hewick, E.A. Wang, Novel regulators of bone formation: molecular clones and activities. Science **242**(4885), 1528–1534 (1988)

127. L. Xie, A.S.P. Lin, K. Kundu, M.E. Levenston, N. Murthy, R.E. Guldberg, Quantitative imaging of cartilage and bone morphology, reactive oxygen species, and vascularization in a rodent model of osteoarthritis. Arthritis Rheum. **64**(6), 1899–1908 (2012)

128. L.D. You, S. Weinbaum, S.C. Cowin, M.B. Schaffler, Ultrastructure of the osteocyte process and its pericellular matrix. Anat. Rec. A Discov. Mol. Cell Evol. Biol. **278**(2), 505–513 (2004)

129. P.B. Yu, D.Y. Deng, C.S. Lai, C.C. Hong, G.D. Cuny, M.L. Bouxsein, D.W. Hong, P.M. McManus, T. Katagiri, C. Sachidanandan, N. Kamiya, T. Fukuda, Y. Mishina, R.T. Peterson, K.D. Bloch, BMP type I receptor inhibition reduces heterotopic ossification. Nat. Med. **14**(12), 1363–1369 (2008)

130. M. Zanetti, E. Bruder, J. Romero, J. Hodler, Bone marrow edema pattern in osteoarthritic knees: correlation between mr imaging and histologic findings. Radiology **215**(3), 835–840 (2000)

131. R. Zhang, H. Fang, Y. Chen, J. Shen, H. Lu, C. Zeng, J. Ren, H. Zeng, Z. Li, S. Chen, D. Cai, Q. Zhao, Gene expression analyses of subchondral bone in early experimental osteoarthritis by microarray. PLoS One **7**(2), e32356 (2012)

132. W. Zhang, Y. Zhang, Y. Liu, J. Wang, L. Gao, C. Yu, H. Yan, J. Zhao, J. Xu, Thyroid-stimulating hormone maintains bone mass and strength by suppressing osteoclast differentiation. J. Biomech. **47**(6), 1307–1314 (2014)

133. L. Zhao, J.W. Shim, T.R. Dodge, A.G. Robling, H. Yokota, Inactivation of Lrp5 in osteocytes reduces young's modulus and responsiveness to the mechanical loading. Bone **54**(1), 35–43 (2013)

134. G. Zhen, C. Wen, X. Jia, Y. Li, J.L. Crane, S.C. Mears, F.B. Askin, F.J. Frassica, W. Chang, J. Yao, J.A. Carrino, A. Cosgarea, D. Artemov, Q. Chen, Z. Zhao, X. Zhou, L. Riley, P. Sponseller, M. Wan, W.W. Lu, X. Cao, Inhibition of tgf-$\beta$ signaling in mesenchymal stem cells of subchondral bone attenuates osteoarthritis. Nat. Med. **19**(6), 704–712 (2013)